FIRE & GLOBAL CHANGE DURING KEY INTERVALS OF THE LATE TRIASSIC & EARLY JURASSIC WITH A FOCUS ON THE CENTRAL POLISH BASIN

Submitted by Robyn Pointer to the University of Exeter as a thesis for the degree of Doctor of Philosophy in Geology, in November 2018.

I certify that all material in this thesis which is not my own work has been identified and that no material has been previously submitted and approved for the award of a degree by this or any other University.

Signature……………………………………………

ABSTRACT

Core from modern-day Poland recovering fluvial and paralic strata provides an excellent record of climatic and environmental changes in the Central Polish Basin during two key intervals of the Early Jurassic. Thick successions of Rhaetian-Hettangian and Pliensbachian-Toarcian age are examined using a number of techniques in order to understand the wildfire activity history, carbon-cycle interactions, and organic matter composition of sediments at two sites in the Central Polish Basin. Physical and geochemical proxies for wildfire activity show evidence of increased wildfire activity both prior to and after the Toarcian Oceanic Anoxic Event (OAE) at the Kazewy-1 site, with suppression of wildfire activity during the negative carbon-isotope excursion of the OAE. Correlation with published wildfire activity proxy records from additional sites in the Tethyan realm shows that this pattern was not limited to the Central Polish Basin, but is part of a wider, regional change. Additionally, new wildfire activity proxy records show increased wildfire activity across the Triassic-Jurassic Boundary at the Kaszewy-1 and Niekłań PIG-1 sites in the Central Polish Basin, correlating with other contemporaneous proxy records from Denmark and Greenland. New carbon-isotope records generated from terrestrial organic matter from the Niekłań PIG-1 core show trends towards heavier $\delta^{13}C$ values immediately after the Triassic-Jurassic Boundary, providing evidence of a perturbation to the carbon-cycle at this time. Exploratory investigation of sediments from the Kaszewy-1 core provides a new record of BIT indices of Early Jurassic sediments, surpassing the oldest-known use of this terrestrial organic matter input proxy. Additionally, a newly-developed technique is used to investigate carbon-isotope variability in fossil terrestrial organic matter across the Toarcian Oceanic Anoxic Event carbon-isotope excursions. A new record of individual phytoclast $\delta^{13}C$ values demonstrates that, despite $\delta^{13}C$ variability between phytoclasts from a single horizon, larger overall trends in $\delta^{13}C$ values can be identified from single phytoclast $\delta^{13}C$ measurements.

ACKNOWLEDGEMENTS

CONTENTS

LIST OF FIGURES & TABLES IN THIS THESIS

Table 7.2 R^2 values calculated from cross-plots of coarse and fine fossil charcoal, and fine fossil non-charcoal abundances against various lithological properties for the Niekłan PIG-1 samples. R^2 values range between 0 and 1, with lower values indicating a weaker relationship between the two variables (Taylor, 1990). Samples were assigned numerical values based on their lithological characteristics which were then used to calculate R2 values. Maximum and median grain sizes were assigned a number between 1 and 5, corresponding to mud, silt, fine sand, medium sand, and coarse sand. Depositional setting was assigned a number between 1 and 9, based on the inferred marine influence; the value 1 was assigned to samples thought to be deposited in fully terrestrial

ABBREVIATIONS USED IN THIS THESIS

[cren] concentration of crenarchaeol

[sum brGDGT] concentration of the sum of all branched GDGTs

^{12}C Carbon-12; the lighter of the two stable isotopes of carbon

^{13}C Carbon-13; the heavier of the two stable isotopes of carbon

δ^{13}C Carbon-isotope signature (ratio of ^{13}C to ^{12}C)

δ^{13}C$_{carb}$ Carbon-isotope signature of bulk carbonate material

δ^{13}C$_{org}$ Carbon-isotope signature of bulk organic matter material

δ^{13}C$_{phytoclast}$ Carbon-isotope signature of individual phytoclasts

δ^{13}C$_{plant}$ Carbon-isotope signature of macrofossil plant material

δ^{13}C$_{wp}$ Carbon-isotope signature of bulk woody phytoclasts

BIT index branched and isoprenoid tetraether index

CBT index cyclisation index of branched tetraethers

CIE carbon-isotope excursion

GDGT glycerol dialykyl glycerol tetraether

MAAT mean annual air temperature

MBT index methylation index of branched tetraethers (as defined by Weijers *et al.* (2007))

MBT' index methylation index of branched tetraethers (as revised by Peterse *et al.* (2012))

OAE oceanic anoxic event

OM organic matter

PAH(s) polycyclic aromatic hydrocarbon(s)

Pl-To Pliensbachian-Toarcian

T-J Triassic-Jurassic

CHAPTER 1 INTRODUCTION

The Early Jurassic (201.3 ± 0.2 – 174.1 ± 1.0; Cohen et al., 2013) was a time in Earth's history that is thought to have experienced extreme climatic conditions, including major perturbations to the global carbon cycle. Two key intervals, the Triassic-Jurassic Boundary, and the Toarcian, are particularly focused on due to major climatic changes that are thought to have occurred during these times. In particular, the role of wildfire within the Earth System at these times is explored, investigating its links with atmospheric composition, global temperatures, soil erosion, and primary productivity.

Wildfire activity is linked to a number of other components of the Earth System and has the potential to make a significant contribution to major environmental changes. Increased wildfire activity has been linked to both increasing atmospheric oxygen levels and decreasing atmospheric carbon dioxide levels on long-term scales (e.g. Berner et al., 2003). Wildfire activity can also affect global temperatures via the release of aerosols into the atmosphere, causing short-term warming, and by increasing the Earth's albedo, leading to long-term cooling (e.g. Bowman et al., 2009). The removal of biomass from the Earth's surface can also contribute to increased soil erosion and weathering (e.g. Berner et al., 2003) A positive feedback link between wildfire activity and transport of phosphorous to the oceans has also been identified. With phosphorous playing an important role in marine primary productivity, wildfire activity has the ability to influence primary production and the potential to contribute to marine anoxic events (Belcher et al., 2010). The role of wildfire within the Earth System is a complex one, and there is still much to be gained from studying wildfire activity proxies.

The Triassic-Jurassic Boundary (201.3 ± 0.2 Ma; Hillebrandt et al., 2013) followed the end-Triassic mass extinction and emplacement of the Central Atlantic Magmatic Province. Evidence of a major carbon-cycle perturbation across the boundary is observed in both marine and terrestrial, organic and inorganic, carbon-isotope records; characteristic large negative carbon-isotope excursions point to a massive input of light carbon into the ocean-atmosphere system at the time of the Triassic-Jurassic Boundary (e.g. Hesselbo et al., 2002). Rising temperatures and increasing levels of atmospheric carbon dioxide across the

boundary are also inferred from palaeobotanical, computer modelling, and stable-isotope studies (e.g. McElwain et al., 1999; Beerling and Berner, 2002; Korte et al., 2009). Evidence of increased wildfire activity across the Triassic-Jurassic Boundary is also observed at sites in Europe, suggesting perhaps a regional change to the fire regime (e.g. Belcher et al., 2010). The majority of palaeoenvironmental and climatic studies of Triassic-Jurassic Boundary successions focus on marine sediments, with there being a relatively small number of studies examining terrestrial deposits. While there is a relatively large body of work examining the effects of climatic changes in the marine realm at this time, current knowledge of climatic changes in the terrestrial realm is somewhat limited.

The Toarcian (182.7 ± 0.7 Ma – 174.1 ± 1.0 Ma; Cresta et al., 2001; Rocha et al., 2016) was another interval during the Early Jurassic thought to have experienced a global increase in temperatures, resulting in possibly the warmest period of the Early Jurassic (e.g. Korte et al., 2015). The Toarcian world was also likely wetter than before, with isotope records indicating increased continental weathering (e.g. osmium; Cohen et al., 2004). The main climatic event of the Toarcian, however, was the Toarcian Oceanic Anoxic Event, characterised by the widespread deposition of organic-rich shales in marine environments, and accompanied by a major extinction of marine organisms (e.g. Jenkyns, 1988; Caruthers et al., 2014). The oceanic anoxic event is also characterised by a large negative carbon-isotope excursion, preceded and followed by smaller magnitude positive excursions (e.g. Hesselbo et al., 2007). It is thought that the negative carbon-isotope excursion reflects the input of a large amount of isotopically-light carbon into the atmosphere during the oceanic anoxic event (e.g. Hesselbo et al., 2000, 2007). Wildfire activity proxy records from sites in Europe indicate a regional suppression of wildfire activity coinciding with the negative carbon-isotope excursion of the oceanic anoxic event, and increasing activity towards the end of the oceanic anoxic event (e.g. Baker et al., 2017). Similar to palaeoenvironmental studies of the Triassic-Jurassic Boundary, studies of the Toarcian focus on marine sediments, due to the scarcity of available terrestrial sequences, leaving a gap in our knowledge of environmental and climatic changes affecting the terrestrial realm during this time.

The carbon-isotope record of the Toarcian Oceanic Anoxic Event is well-studied and well-constrained: a large negative carbon-isotope excursion is separated by two smaller positive CIEs at the beginning and end of the OAE. These characteristic CIEs have been observed in numerous Toarcian-aged sequences from a wide range of sites across the globe. A high-resolution carbon-isotope record generated from bulk organic matter samples from a sedimentary core recovered from Llanbedr, Wales, UK, shows these characteristic CIEs associated with the Toarcian OAE (Xu et al., 2018). A newly-developed technique combining laser ablation and nano-combustion isotope-ratio mass spectrometry allows for the investigation of carbon-isotope variations both within and between individual phytoclasts from this same site. This experimental work included in this thesis attempts to quantify the variation in carbon-isotope values of individual terrestrial fossil organic matter particles (phytoclasts), which is currently unknown (**Chapter 5**). The newly-generated data are also compared to the characteristic positive and negative CIEs of the Toarcian OAE.

The Polish Basin is a large, now tectonically inverted, epeiric basin covering most of modern-day Poland (Dadlez, 2003). During the Early Jurassic thick sequences of sediments were deposited in the Basin, with the thickest sediments deposited in the Mid-Polish Trough, which defines an axis northwest-southeast through central Poland (Pieńkowski, 2004). Lower Jurassic sediments reach a maximum thickness of ~1400 metres in the Mid-Polish Trough. Previous studies of Polish Basin sediments have been limited in scope, and there is still much to gain from palaeoenvironmental studies of the Lower Jurassic Polish Basin sediments.

A series of sedimentary cores recovered in recent years from across the Polish Basin has provided an increasing number of opportunities to study the sedimentary and palaeoenvironmental history of the Polish Basin throughout the Mesozoic. Two particular cores recovered from the Kaszewy-1 and Niekłań PIG-1 boreholes, both located in the Mid-Polish Trough, provide thick sequences of Rhaetian-Hettangian and Pliensbachian-Toarcian sediments ideal for palaeoenvironmental studies. Both cores provide the opportunity to investigate the wildfire activity history of the Central Polish Basin across the Triassic-Jurassic Boundary through palaeobotanical and geochemical analyses (**Chapter 7**); the Kaszewy-1 core also provides the opportunity to investigate variations in wildfire

activity across the Toarcian Oceanic Anoxic Event (**Chapter 6**). Comparison with contemporaneous wildfire activity proxy records from other sites in Europe allows for a regional reconstruction of wildfire activity during these key time intervals of the Early Jurassic. Carbon-isotope analysis of terrestrial organic matter from the Niekłań PIG-1 core allows for the investigation of the terrestrial component of the carbon cycle across the Triassic-Jurassic Boundary, supplementing the current, relatively-limited, knowledge of this topic. The sediments of the Kaszewy-1 core represent deposition in a range of terrestrial and shallow-marine environments, and are relatively thermally immature. A exploratory investigation of samples from the T-J Boundary and Pliensbachian-Toarcian sections of the Kazewy-1 core attempts to apply the BIT index and MBT'-CBT proxies to Early Jurassic-aged sediments, producing possibly the oldest-known records of organic matter input reconstructions as well as palaeotemperature and soil pH estimates using these proxies (**Chapter 8**).

CHAPTER 2 THESIS AIMS

The overall aim of this thesis is to produce new records of palaeoenvironmental changes within the Polish Basin during the Early Jurassic: across the Triassic-Jurassic Boundary, and during the Toarcian Oceanic Anoxic Event. Investigation of wildfire activity proxies, carbon-isotope compositions of organic matter, and palaeoenvironmental organic geochemistry proxies provide an insight into climatic conditions in terrestrial environments. These investigations aim to identify the significance of wildfire in past major environmental change events, ascertaining the impact of wildfire on atmospheric oxygen levels, global temperatures, and weathering during the Early Jurassic. Additionally, investigation of carbon-isotope compositions of individual terrestrial phytoclasts provide an insight into terrestrial organic matter carbon-isotope variations on a smaller-scale than has typically been investigated before.

The core aims of this thesis are to address the following questions:

- How does the carbon-isotope composition vary both within and between individual terrestrial phytoclasts, and how does this compare to larger organic matter samples?

- Is there evidence of wildfire activity in the Polish Basin across two key intervals during the Early Jurassic, and how does it compare to wildfire activity records from other sites at these times?

- Is there evidence of the characteristic Triassic-Jurassic Boundary negative carbon-isotope excursions in fossil terrestrial organic matter from the Polish Basin?

- Can the BIT index and MBT'-CBT proxies be successfully used on Lower Jurassic sediment samples, pushing their oldest-known use further back in the Mesozoic?

- What implications do the new datasets have for our understanding of environmental conditions in the Central Polish Basin, and a wider context, during the Early Jurassic?

CHAPTER 3 INDICATORS OF GLOBAL CHANGE AND VARIATIONS IN WILDFIRE ACTIVITY

3.1. Global Changes Across the Triassic-Jurassic Boundary

The Triassic-Jurassic Boundary (T-J Boundary; 201.3 ± 0.2 Ma; Hillebrandt et al., 2013) was a time of known global environmental and climatic changes and has been the subject of extensive study by many (see **Figure 3.1** for a map of key T-J Boundary study sites). The T-J Boundary followed the end-Triassic mass extinction, one of the largest extinction events of the Phanerozoic (541.0 ± 0.1 Ma – present day), and experienced extreme changes in environmental and climatic conditions, including a major perturbation to the global carbon-cycle (e.g. McElwain et al., 1999; Hesselbo et al., 2002; Guex et al., 2004; Korte et al., 2009). Studies carried out thus far show that these environmental and climatic events are intricately linked, though there are still many disagreements about the nature of the relationships. Correlating the T-J Boundary between different study sites, and particularly between marine and terrestrial deposits, has also proved difficult, adding to the debate about the exact nature of climatic changes across the world at this time (e.g. Pálfy and Kocsis, 2014). This section outlines key research that has been carried out thus far and identifies where there is still great potential for further studies to be carried out.

3.1.1. Defining the Triassic-Jurassic Boundary & Correlation Issues

The base of the Jurassic System (i.e. the T-J Boundary) is currently defined by the Global Stratotype Section and Point (GSSP) located at Kuhjoch, Austria, and correlates with the first appearance of the ammonite *Psiloceras spelae tirolicum* (Hillebrandt et al., 2013). The base of the Jurassic is dated at 201.3 ± 0.2 Ma (Hillebrandt et al., 2013).

Difficulties have arisen with identifying the T-J Boundary in sedimentary successions, as the indicator species of ammonite occurs very rarely, and due to conflicting palynological, magnetostratigraphy, and carbon-isotope stratigraphy records. The ammonite *P. spelae* has been identified at sites in North America, South America and Europe (Hillebrandt and Krystyn, 2009), making correlation
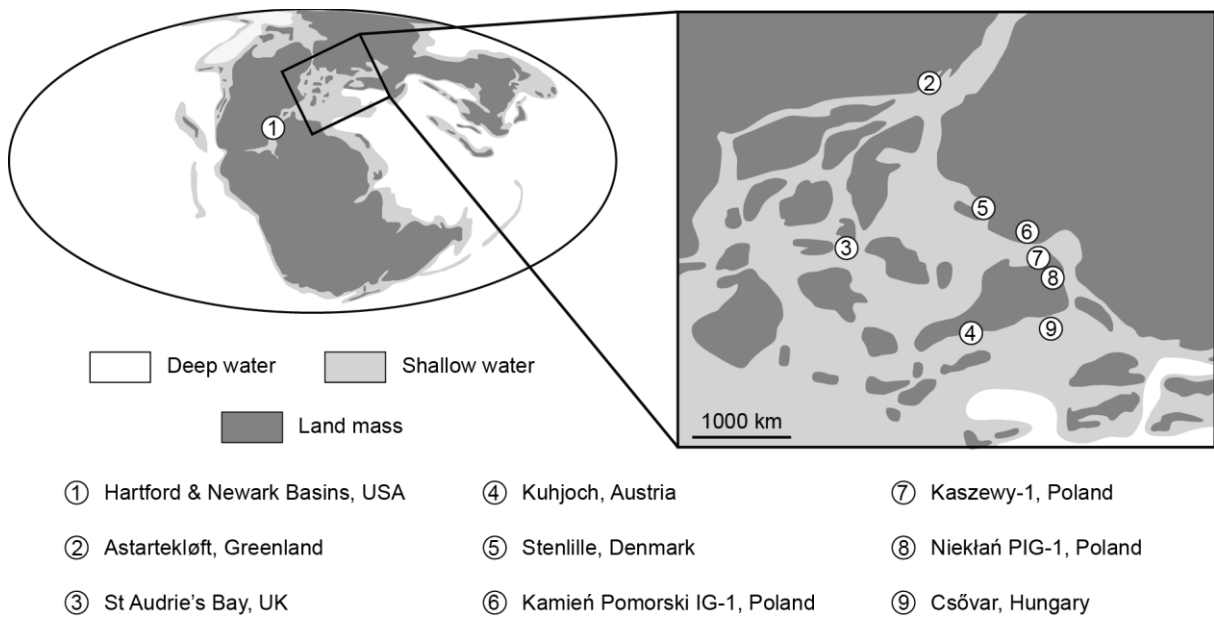
Figure 3.1 Global palaeogeographic map of the Triassic-Jurassic Boundary (~200 Ma) and, inset, palaeogeographic map of northwest Europe with key T-J Boundary study sections labelled. Base maps redrawn from Blakey (2018a, 2018b).

between these sites relatively simple, but it is missing at many key Lower Jurassic sites, such as those in the southwest United Kingdom. In terrestrial sedimentary sequences, ammonites are, obviously, not present, and other methods have to be used to identify the T-J Boundary, and correlate between sites.

Palynological assemblages have also been used to place the T-J Boundary. Late Triassic assemblages include the marine and terrestrial palynomorphs such as *Granuloperculatipollis rudis, Limbosporites lundbladiae, Lunatisporites rhaeticus, Ovalipollis ovalis, Polypodiisporites polymicroforatus, Rhaetipollis germanicus, Rhaetogonyaulax rhaetica, Ricciisporites tuberculatus,* and *Semiretisporis gothae* (e.g. Bonis et al., 2009; van de Schootbrugge et al., 2009; Lindström et al., 2016). The last occurrences of these palynomorphs have been used to identify the end of the Triassic, along with the first occurrence of the Jurassic pollen *Cerebropollenites thiergartii* (*C. thiergartii*) (e.g. Bonis et al., 2009; van de Schootbrugge et al., 2009; Hillebrandt et al., 2013). Hillebrandt et al. (2013) suggest that although the basal Jurassic marker *C. thiergartii* is found below the ammonite *P. spelae*, *C. thiergartii* can be used for correlations between terrestrial and marine sites since it is the closest first occurrence of a terrestrial palynomorph to that of *P. spelae*.

Attempts to define the Triassic-Jurassic boundary using magnetostratigraphy have proven difficult, with little consensus, and relatively little sample material. Though it is generally agreed that the Earth's magnetic field had a normal polarity across the Triassic-Jurassic boundary (e.g. Pálfy et al., 2007), a short-lived reversal across the boundary has been discovered in the SW United Kingdom (e.g. Hounslow et al., 2004) and in the NE USA (e.g. Whiteside et al., 2007; Kent et al., 2017). Identifying and correlating the T-J Boundary using magnetostratigraphy still remains difficult and a contentious issue.

Negative carbon-isotope excursions (CIEs) across the T-J Boundary have been identified at multiple sites around the world, and have been used to correlate, and identify the T-J Boundary. Negative CIEs have been identified in a wide range of materials from different depositional settings (e.g. Hesselbo et al., 2002; Guex et al., 2004; Whiteside et al., 2010; Ruhl and Kürschner, 2011). However, there are still ongoing discussions about the precise nature of these negative CIEs, which can cause issues with identifying the T-J Boundary. Carbon-isotope stratigraphy of the T-J Boundary is discussed in more detail in **Section 3.1.3.** (p. 41).

3.1.2. Environmental Conditions Across the T-J Boundary & Their Effects

The Late Triassic-Early Jurassic was a time of severe environmental change: it is inferred that atmospheric carbon dioxide concentrations increased, global temperatures rose, fire activity increased, and sea level varied. However, there is widespread disagreement about the magnitude and timing of these changes and their subsequent effects. Volcanic activity at the Central Atlantic Magmatic Province is also thought to have occurred during the end of the Triassic (e.g. Guex et al., 2004), along with a widespread sea level fall (e.g. Hallam and Wignall, 1999). The Late Triassic-Early Jurassic also coincided with the break-up of Pangaea (e.g. Ciarapica, 2007; Golonka, 2007).

A rise in atmospheric carbon dioxide (CO_2) levels across the T-J Boundary has been inferred by several authors, with a peak of 600 ppm estimated by authors McElwain et al. (1999) based on stomatal density. Other estimates of peak atmospheric CO_2, based on stomatal studies and computer modelling, include 1500 ppm (Royer, 2001; Beerling and Berner, 2002). A rise of ~2000 ppm across the T-J Boundary has been inferred from soil carbonate $\delta^{13}C$ values (Schaller et al., 2011). The consensus is that there were increases in atmospheric carbon

dioxide levels at the T-J Boundary, and that this likely contributed to temperature rises.

Increased atmospheric carbon dioxide levels likely caused a temperature rise of ~3-4°C at the T-J Boundary (e.g. McElwain et al., 1999; Belcher et al., 2010; Pienkowski et al., 2012), based on changes in leaf stomatal densities and changes in spore/pollen ratios. Estimated rises of ~6°C have been suggested by Beerling and Berner (2002) and Huynh and Poulsen (2005) based on computer modelling experiments. Oxygen-isotope data suggest that temperatures could have increased by as much as 10°C during this time (Pálfy et al., 2007; Korte et al., 2009). Despite differences in magnitude, most authors agree that evidence points towards increasing temperatures across the T-J Boundary. However, a recent study suggests that sea-surface temperatures declined during the Rhaetian (Knobbe and Schaller, 2018).

Storm activity would likely have also increased with elevated atmospheric temperatures, potentially resulting in increased wildfire activity (e.g. Reeve and Toumi, 1999). Despite there being a generally poor record of wildfire during the Late Triassic and Early Jurassic (Scott, 2000), evidence of increased wildfire activity at the T-J Boundary has been documented by a number of authors. Increases in fossil charcoal abundance have been documented in both Europe and the USA, indicating increased wildfire activity across the T-J Boundary (e.g. Jones et al., 2002; Belcher et al., 2010; Uhl and Montenari, 2011; Marynowski and Simoneit, 2009). Elevated concentrations of pyrolytic polycyclic aromatic hydrocarbons in T-J Boundary sediments have also been noted by Marynowski and Simoneit (2009) and Petersen and Lindström (2012). Wildfire activity across the T-J Boundary is discussed in greater depth in **Section 3.5.4.1.** (p. 84).

3.1.2.1. The End-Triassic Mass Extinction & Possible Causes

The end-Triassic Extinction (ETE) affected both the flora and fauna of the marine and terrestrial realms: up to 80% of all living species became extinct during this time (e.g. Bond and Grasby, 2016, and references therein). Though it is accepted that this extinction is one of the 'big five' mass extinctions of the Phanerozoic, there is little consensus on the exact magnitude; some authors claim it to be the third largest extinction (e.g. McElwain *et al.* 1999) while others claim it to be the

second (e.g. Cirilli *et al.* 2009). There is also significant debate about the cause(s) of the end-Triassic extinction.

Marine organisms were strongly affected in this mass extinction. Reef ecosystems suffered high extinction rates with several authors claiming total collapse of these ecosystems (e.g. Hallam and Goodfellow, 1990; Pálfy et al., 2001; Hautmann, 2004). The ETE was one of the most severe for both ammonites and radiolarians (e.g. Bown and Lord, 1990; Guex et al., 2004). Other marine organisms that decreased in number during the ETE include bivalves, brachiopods, cephalopods, coccolithophorids, conodonts, dinoflagellates, foraminifers, gastropods and ostracods (e.g. Bown and Lord, 1990; Hallam and Wignall, 1999).

Terrestrial fauna were also affected by the ETE. Tetrapods were particularly affected, with an estimated ~50% of tetrapod species going extinct in this time (Benton, 1995). However, other studies suggest that terrestrial vertebrates were relatively unaffected during the end-Triassic extinction, with only minor changes in species diversity (e.g. Benton, 1991; Weems, 1992; Lucas, 1994).

Losses have been identified in terrestrial plants at both the macro- and micro-scales. Evidence from plant macrofossils from Greenland suggests that there was a >95% species turnover at the T-J boundary (McElwain et al., 1999). However, further studies of the Greenland macrofloral fossils suggest that terrestrial plants did not experience a mass extinction but instead saw a gradual decline in species biodiversity throughout the Late Triassic and across the boundary with the Jurassic (e.g. McElwain et al., 2007, 2009)

A palynofloral turnover has been reported across the Triassic-Jurassic boundary by several authors. An abrupt change in flora has been reported from North America from palynomorph records (e.g. Embry and Suneby, 1994; Cirilli et al., 2009). However, reports from Europe indicate that there was either a gradual change in palynology (Pienkowski et al., 2012) or a minor extinction (Cirilli et al., 2009). Sporomorph records from East Greenland also show little evidence of a mass extinction (Mander et al., 2010). Little palynofloral change has been identified in Australia (Helby, 1987). It has been suggested that a palynofloral extinction may not be represented in European sections due to reworking of sporomorphs or, possibly, that certain plant groups are underrepresented in the

palynological record (Mander et al., 2010). The general consensus is that there was a global disturbance of terrestrial flora across the Triassic-Jurassic boundary (Bond and Grasby, 2016).

Although there is general agreement that the Late Triassic mass extinction was caused by an environmental crisis, several different mechanisms have been proposed, including: volcanism associated with the Central Atlantic Magmatic Province (e.g. Deenen et al., 2010; Ruhl, Deenen, et al., 2010); increased atmospheric carbon dioxide (e.g. McElwain et al., 1999; Guex et al., 2004; Marzoli et al., 2004; Galli et al., 2005; Bacon et al., 2011; Pienkowski et al., 2012), increased atmospheric sulphur dioxide (e.g. Guex et al., 2004), methane release from seafloor gas hydrates (e.g. Galli et al., 2005; Pálfy et al., 2007; Williford et al., 2007; Pienkowski et al., 2014), primary productivity declines (e.g. Beerling and Royer, 2002; Schoene et al., 2010), ocean acidification (e.g. Hautmann et al., 2008; Greene et al., 2012), rapid sea level changes (e.g. Hallam, 1990b; Hallam and Wignall, 1999; Tanner et al., 2001) and bolide impact (e.g. Bice et al., 1992; Olsen et al., 2002). It is likely that no mechanism was solely responsible for instigating the end-Triassic mass extinction, and that it was the result of a number of these mechanisms interacting with each other, e.g. the release of greenhouse gases from CAMP volcanism leading to destabilisation of seafloor gas hydrates due to increasing global temperatures. Ocean acidification and primary productivity collapse can potentially also be linked to increasing atmospheric carbon dioxide levels.

3.1.3. Carbon-isotope Stratigraphy

Carbon-isotope signatures in organic matter from across the Triassic-Jurassic Boundary have been well-studied. Characteristic negative $\delta^{13}C_{org}$ excursions have been identified in both terrestrial and marine materials from a wide range of locations around the world (e.g. Hesselbo et al., 2002; Guex et al., 2004; Deenen et al., 2010; Kuroda et al., 2010; Whiteside et al., 2010; Ruhl and Kürschner, 2011), suggesting a global perturbation to the carbon-cycle across the T-J Boundary.

3.1.3.1. The Marine $\delta^{13}C_{org}$ & $\delta^{13}C_{carb}$ Records

Marine bulk organic matter $\delta^{13}C_{org}$ comprises the majority of published Triassic-Jurassic Boundary carbon-isotope records. The majority of these marine $\delta^{13}C_{org}$
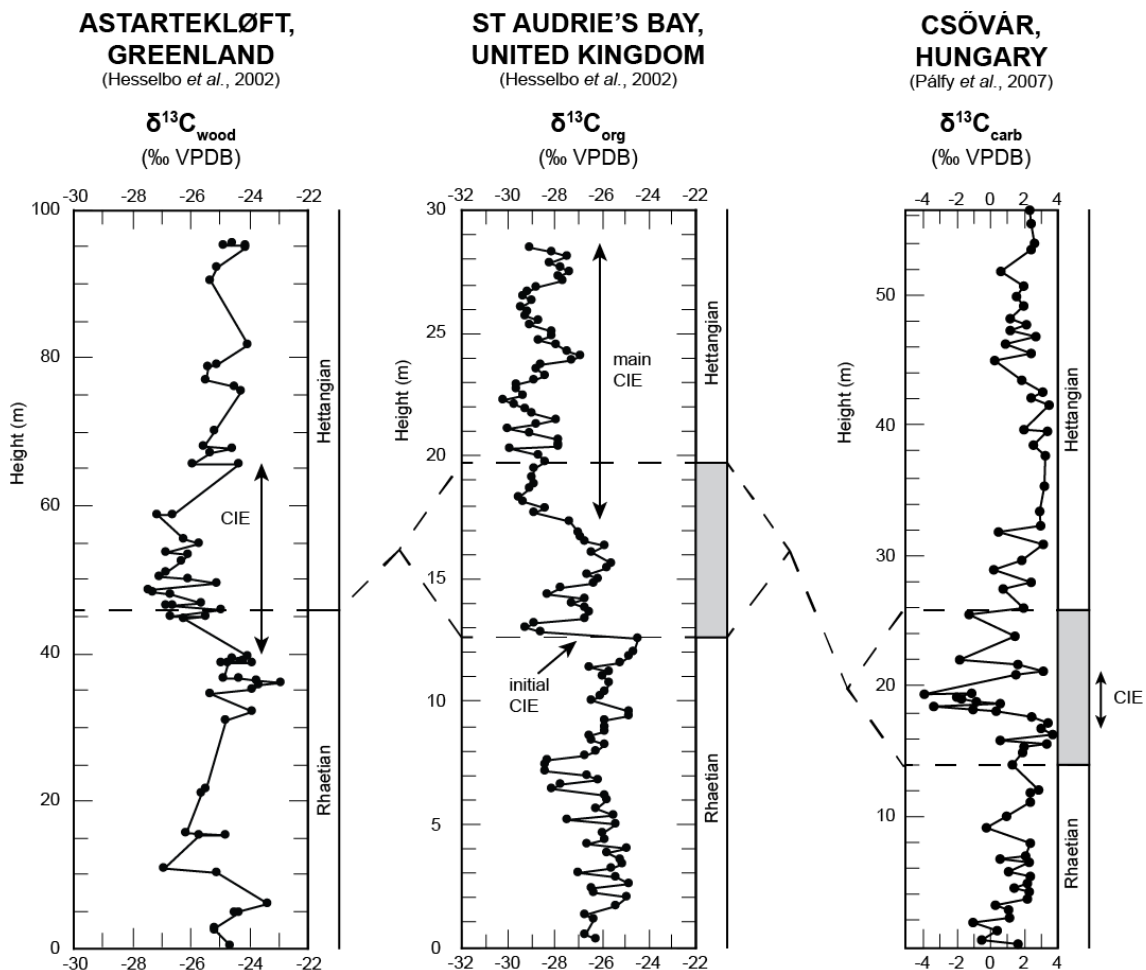
Figure 3.2 Carbon-isotope records showing examples of negative CIEs recorded at the T-J Boundary at: Astartekløft, East Greenland (terrestrial fossil wood record; Hesselbo et al., 2002); St Audrie's Bay, Southwest UK (marine bulk organic matter record; Hesselbo et al., 2002); and Csővár, Hungary (marine bulk carbonate record; Pálfy et al., 2007). Dashed lines represent correlation between the T-J Boundary at the three sites.

records show at least one negative carbon-isotope excursion (CIE), and there is a general consensus that the T-J Boundary is marked by negative CIEs at sites in Europe, North America and from around the Pacific Ocean (**Figure 3.2**; e.g. Ward et al. (2001), Ruhl et al. (2009), Akikuni et al. (2010), Bartolini et al. (2012), Lindström et al. (2012)). However, there are some records from Austria and Canada which show negative CIEs occurring prior to the T-J Boundary (Hillebrandt et al., 2013; Percival et al., 2017); geochemical evidence (mercury concentrations and mercury/TOC ratios) suggests that these pre-T-J Boundary CIEs coincided with increased volcanic activity (Percival et al., 2017). A number of marine bulk carbonate (i.e. inorganic carbon) records also show negative CIEs

at the T-J Boundary (**Figure 3.2**; e.g. Galli et al. (2007), Pálfy et al. (2007), Felber et al. (2015)).

Some of the earliest marine $\delta^{13}C_{org}$ records include carbon-isotope curves published from sites in Denmark and Austria (Morante and Hallam, 1996; Nielsen and Japsen, 1991). A negative CIE of ~2‰ was identified in bulk organic matter samples of Hettangian age by Nielsen and Japsen (1991), possibly the earliest-published record of a negative carbon-isotope excursion in organic matter at the Triassic-Jurassic Boundary. In contrast, the bulk organic matter carbon-isotope record from Austria shows a positive CIE of ~2‰ at the Triassic-Jurassic Boundary, though the authors attribute this signal as the result of diagenesis and not an indicator of changing environmental conditions (Morante and Hallam, 1996). An increasing number of bulk organic matter carbon-isotope records began being published at the start of the 21st century, with authors such as Pálfy et al. (2001) and Ward et al. (2001) identifying single negative carbon-isotope excursions of ~2‰ at the Triassic-Jurassic Boundary at sites in Hungary and Western Canada, respectively.

The first record of multiple negative carbon-isotope excursions across the Triassic-Jurassic Boundary was published by Hesselbo et al. (2002) from St Audrie's Bay in the southwest United Kingdom. The authors identified one relatively short-lived negative C-isotope excursion of ~4‰ followed by a brief return to more positive values before a more prolonged negative carbon-isotope excursion of ~4.5‰, which the authors estimated to have lasted >300 kyr, based on obliquity cycles. Hesselbo et al. (2002) termed the first and shorter of these excursions the 'initial' negative carbon-isotope excursion, and the second and longer excursion the 'main' negative carbon-isotope excursion, nomenclature that has subsequently been adopted by other authors and which will be used in the discussion chapters of this thesis.

Negative carbon-isotope excursions correlating to the initial excursion seen at St Audrie's Bay have been identified by a number of authors at many sites in Europe, the Pacific, and the United States of America (e.g. Guex et al., 2004; Kürschner et al., 2007; van de Schootbrugge et al., 2008; Ruhl et al., 2009; Kuroda et al., 2010). The magnitude of the initial negative CIEs seen at these sites ranges from ~2‰ to ~8‰, with the majority of records showing an excursion

of ~4 – 5‰. The initial negative CIE is often recorded in materials of Rhaetian age, though some records show the initial excursion occurring across the Rhaetian-Hettangian Boundary (Hesselbo et al., 2002; Kürschner et al., 2007; Lindström et al., 2012), however it is important to note that the same method has not been used to define the stratigraphic framework at each site (e.g. marine biostratigraphy at St Audrie's Bay (Hesselbo et al., 2002); sequence stratigraphy and palynology at Kamień Pomorski, Poland (Pienkowski et al., 2012)). The duration of the initial negative carbon-isotope excursion is debated, though there is consensus that the initial excursion is shorter and more abrupt than the second main negative excursion (Pálfy and Kocsis, 2014).

The main negative carbon-isotope excursion has also been identified by several authors at a number of sites in Europe and the United States of America (e.g. Gómez et al., 2007; Bonis et al., 2009; Clémence et al., 2010; Ruhl and Kürschner, 2011; Lindström et al., 2012). In contrast to the initial negative carbon-isotope excursion, the main negative CIE often has a smaller magnitude, ranging from ~2‰ to ~4‰, with most of the identified main CIEs showing a magnitude of ~4‰. The main negative carbon-isotope excursion is often recorded in samples of Rhaetian-Hettangian boundary age, with few records confining the main excursion in entirety to the Hettangian stage. Similar to the initial excursion, the duration of the main negative CIE is debated, though the duration appears to be greater than that of the initial negative CIE at sites where both negative carbon-isotope excursions have been identified (Hesselbo et al., 2002; Ruhl et al., 2009; Lindström et al., 2012).

An additional negative carbon-isotope excursion has been identified at sites in Austria and Denmark which occurs before the initial negative excursion (Ruhl and Kürschner, 2011; Lindström et al., 2012; Hillebrandt et al., 2013). Both studies termed this additional negative excursion the 'precursor' excursion, and at both sites it occurs in Rhaetian-aged material. The magnitude of the pre-cursor negative CIE in both records is relatively small; the Austrian negative CIE has a magnitude of ~3‰ and the Danish negative CIE has a magnitude of ~2‰. Both the initial and main negative carbon-isotope excursions are also identified at these two sites.

Further negative carbon-isotope excursions have been identified at sites in Europe and North America which have not been correlated to the either the initial or main negative excursions of Hesselbo et al. (2002). These negative CIEs occur in both the Rhaetian and the Hettangian, and range in magnitude from ~1‰ to ~6‰ (e.g. Gómez et al., 2007; Ward et al., 2007; Williford et al., 2007; Haas et al., 2010; Van de Schootbrugge et al., 2013; Lindström et al., 2016). It is likely that these unnamed negative carbon-isotope excursions represent both the initial and main negative CIEs.

Marine carbonate $\delta^{13}C_{carb}$ records show evidence of negative CIEs across the T-J Boundary similar to the $\delta^{13}C_{org}$ record (**Figure 3.2**). Early records show negative CIEs of ~-8‰ and ~-10‰ at sites in Hungary and Western Canada during the Rhaetian–Hettangian transition and Rhaetian, respectively (Pálfy et al., 2001; Ward et al., 2004). Records from a number of sites in Northern Italy show a short, sharp negative CIE of ~2‰ magnitude immediately above the T-J Boundary followed by a return to more positive $\delta^{13}C_{carb}$ values (Galli et al., 2007); a second negative CIE of smaller magnitude is also observed in most sections. Additional records from other sites in Europe show negative CIEs across the T-J Boundary, ranging from ~1‰ to ~8‰ in magnitude (e.g. Pálfy et al., 2007; Haas et al., 2010; Črne et al., 2011; Felber et al., 2015). Negative CIEs of ~2–3‰, which correlate with the initial negative CIE, are also recorded from sites in New Zealand and the United Arab Emirates in Rhaetian and Rhaetian – Hettangian successions (Akikuni et al., 2010; Hönig et al., 2016).

3.1.3.2. The Terrestrial $\delta^{13}C_{org}$ Record

Organic matter carbon-isotope records from terrestrial sites are fewer in number compared to those from marine sites, though a small number of $\delta^{13}C_{org}$ records do exist from Africa, Europe and North America. The lack of terrestrial $\delta^{13}C_{org}$ records stems from a lack of precisely identified continuous successions from across the Triassic-Jurassic Boundary. The few published terrestrial carbon-isotope curves all identify at least one negative CIE at the Triassic-Jurassic Boundary, most of which are correlated to the initial negative excursion first identified at St Audrie's Bay, United Kingdom (**Figure 3.2**).

Hesselbo et al. (2002) published the first detailed T-J Boundary terrestrial $\delta^{13}C_{org}$ record, from macrofossil wood samples from Astartekløft, East Greenland. The

authors discovered a negative CIE of ~3.5‰ across T-J Boundary. Bacon et al. (2011) have also identified a negative CIE of ~4‰, recorded in taxonomically-identified plant cuticle samples from the same location across the T-J Boundary. An additional macrofossil wood $\delta^{13}C$ record from Whiteside et al. (2010) also shows a negative carbon-isotope excursion of similar magnitude (~4‰) in Rhaetian-aged material from the northeastern USA, which the authors correlate with the initial negative carbon-isotope excursion of Hesselbo et al. (2002). It is important to note though, that this negative CIE is based on a single-data point.

A small number of terrestrial bulk organic matter carbon-isotope records from Rhaetian-aged sediments have been published thus far. Terrestrial bulk OM $\delta^{13}C_{org}$ records from Morocco, northeastern USA, and the Polish Basin all show negative CIEs, ranging in magnitude from ~3‰ to ~5‰ (Deenen et al., 2010; Whiteside et al., 2010; Pienkowski et al., 2012). The authors of these records correlate their negative carbon-isotope excursions with the initial negative CIE of Hesselbo et al. (2002). Whiteside et al. (2010) estimate that the negative CIE in the northeastern USA records had a duration of 20–40 kyr based on cyclostratigraphy.

Carbon-isotope records from plant wax lipids also show negative CIEs at the T-J Boundary. A study by Whiteside et al. (2010) identified a negative carbon-isotope excursion of ~4‰ in Rhaetian-aged plant wax lipids from the northeastern USA. The authors correlate this excursion with the initial negative CIE. Ruhl et al. (2011) also discovered a negative CIE in plant wax lipids from Rhaetian-aged material from Austria, though the magnitude of the excursion was much greater: ~8‰. Another plant wax lipid $\delta^{13}C$ record from Astartekløft, East Greenland, shows a negative CIE of relatively small magnitude, ~2‰, in Rhaetian-Hettangian-aged samples (Williford et al., 2014).

3.1.3.3. Possible Causes of the T-J Boundary Negative $\delta^{13}C$ Excursions

It is evident from the marine and terrestrial $\delta^{13}C_{org}$ records that there was a major perturbation to the global carbon-cycle during the latest Triassic-earliest Jurassic, with several different causes proposed (see **Table 3.1** for a summary). There is a general consensus that a massive release of isotopically-light carbon (^{12}C) into the atmosphere-ocean system was responsible for producing the negative CIEs. Alternative hypotheses include: primary productivity collapse, variations in bulk

Hypothesis	Supporting studies	Opposing studies
Unspecified perturbation to the carbon cycle	Ruhl et al., 2009; Akikuni et al., 2010; Haas et al., 2010; Pienkowski et al., 2012; Williford et al., 2014	-
Seafloor methane hydrate release	Pálfy et al., 2001; Hesselbo et al., 2002; Gómez et al., 2007; Kürschner et al., 2007; Whiteside et al., 2010; Ruhl et al., 2011	Guex et al., 2004; Clémence et al., 2010
Greenhouse gas release from CAMP volcanic activity	Hesselbo et al., 2002; Gómez et al., 2007; Lucas and Tanner, 2007; Clémence et al., 2010; Deenen et al., 2010; Kuroda et al., 2010; Whiteside et al., 2010; Bacon et al., 2011; Ruhl and Kürschner, 2011; Lindström et al., 2012	Tanner et al., 2001; Beerling and Berner, 2002
Thermal metamorphism of organic-rich sediments	Korte et al. (2009); cf. Svensen et al. (2009); van de Schootbrugge et al. (2009); Whiteside et al. (2010); Ruhl et al. (2011)	-
Primary productivity collapse	McRoberts et al., 1997; Pálfy et al., 2001; Ward et al., 2001; Beerling and Royer, 2002; Guex et al., 2004; Williford et al., 2007; Kuroda et al., 2010; Ruhl et al., 2010	-
Changes in bulk OM composition	van de Schootbrugge et al., 2008; Bonis et al., 2009; Ruhl et al., 2011; Van de Schootbrugge et al., 2013	Whiteside et al., 2010; Bacon et al., 2011
Recycling of isotopically-light bottom waters	Ward et al., 2001	-

Table 3.1 Summary of suggested possible causes of TJB C-isotope excursions with supporting and opposing studies.

OM composition, and recycling of isotopically-light bottom waters (**Table 3.1**). Of course, it is entirely possible, and likely, that no one factor was solely responsible and that it was, in fact, a combination of different factors that caused a major perturbation to the carbon-cycle across the T-J Boundary.

The release of massive amounts of ^{12}C into the atmosphere has been suggested by numerous authors as the cause of the T-J Boundary negative carbon-isotope excursions (e.g. Ruhl et al., 2009; Haas et al., 2010; Pienkowski et al., 2012; Williford et al., 2014). A relatively sudden input of large amounts of ^{12}C into the atmosphere could cause negative shifts in both terrestrial and marine organic matter via isotopic exchange at the atmosphere-ocean interface. This hypothesis is favoured by many authors since it accounts for the changes seen in organic matter from both the terrestrial and marine realms. However, there is still an

ongoing debate regarding the source of massive amounts of isotopically-light carbon at the T-J Boundary.

Three different sources are considered for the ^{12}C which may have caused the negative CIEs: methane released from seafloor gas hydrates; greenhouse gases released during CAMP volcanic activity; and thermal metamorphism of organic-rich sediments. Whilst most authors consider one of the aforementioned to be the main source of isotopically-light carbon, some have suggested that both all three sources likely made a significant contribution of ^{12}C into the atmosphere (e.g. Hesselbo et al., 2002; Gómez et al., 2007; Whiteside et al., 2010).

The release of isotopically-light methane from seafloor gas hydrates is considered by a number of authors to be the main cause of the negative carbon-isotope shifts seen in organic matter at the T-J Boundary (e.g. Pálfy et al., 2001; Kürschner et al., 2007; Whiteside et al., 2010; Ruhl et al., 2011). It is thought that the melting of seafloor gas hydrates as global temperatures increased would have released large amounts of ^{12}C into the ocean and subsequently, the atmosphere; methane in gas hydrates has a very light carbon-isotope signature, reaching values of ~-70‰ (Kvenvolden, 1995). The negative carbon-isotope shifts seen at the T-J Boundary would have resulted from this massive release of isotopically-light methane into the ocean-atmosphere system.

Although this hypothesis is favoured by several authors, there are some that dismiss the release of methane from gas hydrates as the cause of the T-J Boundary negative carbon-isotope shifts. Guex et al. (2004) argue that the duration of the negative excursions is not abrupt enough to have been caused by a sudden massive input of isotopically-light carbon into the atmosphere from methane hydrates. Clémence et al. (2010) also reject the release of methane from gas hydrates as the cause of the negative carbon-isotope shifts. The authors claim that both the organic and inorganic carbon-isotope records would register a negative shift if methane were the ^{12}C-source but, at some sites (e.g. UK, Clémence et al., 2010; Italy, Bachan et al., 2012), the inorganic carbon-isotope records show a positive shift at the T-J Boundary.

Carbon dioxide and methane released during CAMP magmatism, including thermogenic methane, is favoured by some authors as the source of the ^{12}C which caused T-J Boundary negative carbon-isotope shifts (e.g. Hesselbo et al.,

2002; Lucas and Tanner, 2007; Clémence et al., 2010; Deenen et al., 2010; Kuroda et al., 2010; Ruhl et al., 2010; Bacon et al., 2011; Lindström et al., 2012). The release of isotopically-light carbon dioxide and methane (e.g. Javoy et al., 1986; Chiodini et al., 2011; Rizzo et al., 2015) during CAMP magmatism would have released large amounts of ^{12}C into the atmosphere. The direct input of carbon dioxide and methane into the atmosphere from the CAMP eruptions would have likely been accompanied by thermal metamorphism of organic-rich sediments during sill emplacement, which would have also contributed to the input of ^{12}C into the atmosphere.

Numerical modelling by Beerling and Berner (2002) indicates that the amount of carbon dioxide released during CAMP volcanism alone would not have been sufficient to produce the negative carbon-isotope shifts seen at the T-J Boundary. However, the modelling does not take into account the release of thermogenic CO_2. Timing of CAMP volcanism is still debated, casting doubt on its role in causing the T-J Boundary negative carbon-isotope shifts.

The intrusion of sills into organic-rich sediments has also been proposed by some authors as an alternative or additional cause of the T-J Boundary negative CIEs. As magma is intruded into organic-rich sediments, the heat from the magma can cause the sediments to undergo thermal metamorphism; ^{12}C-rich carbon, in the form of carbon dioxide and methane, is released from the organic matter in the sediments, increasing the proportion of ^{12}C relative to ^{13}C in the atmospheric carbon reservoir. The intrusion of CAMP volcanics into organic-rich sediments could have induced a release of carbon dioxide and methane into the atmosphere sufficient to produce the lighter $\delta^{13}C_{org}$ values seen at the T-J Boundary (e.g. Korte et al., 2009; van de Schootbrugge et al., 2009; Ruhl et al., 2011).

It was initially suggested by McRoberts et al. (1997) and then later by Pálfy et al. (2001) and Ward et al. (2001), that primary productivity collapse may be responsible for the negative carbon-isotope excursions seen at the Triassic-Jurassic Boundary. A reduction or collapse of primary productivity can result in higher atmospheric CO_2 levels as less carbon dioxide is drawn down for photosynthesis. Consequently, remaining primary producers and dissolved inorganic carbon will be relatively enriched in ^{12}C instead of ^{13}C (due to its increased abundance in the atmosphere-ocean system) during photosynthesis

which will lead to lighter $\delta^{13}C_{org}$ values (Sarmiento and Toggweiler, 1984). The primary productivity collapse hypothesis gained some support from other authors such as Beerling and Royer (2002), Guex et al. (2004), Williford et al. (2007), and Kuroda et al. (2010); however, it remains one of the lesser-supported hypotheses amongst T-J Boundary carbon-isotope stratigraphers.

Primary productivity collapse at the T-J Boundary is sometimes discussed as a consequence of rising atmospheric CO_2 levels as primary producers struggle to cope with higher global temperatures brought about by the higher levels of carbon dioxide in the atmosphere (Ruhl, Veld, et al., 2010; Guex et al., 2004). It is possible that the input of large amounts of carbon dioxide (and other greenhouse gases) from CAMP volcanism and/or methane from seafloor gas hydrates into the atmosphere could have caused large amounts of primary producers to die off, resulting in a positive feedback loop where atmospheric carbon dioxide levels were pushed even higher (Guex et al., 2004, and references therein). This scenario would also produce negative shifts in $\delta^{13}C_{org}$ values, such as those seen at the Triassic-Jurassic Boundary.

The carbon-isotopic composition of organic matter can vary greatly dependent on its source (a more detailed discussion is provided in **Section 3.4.**; p. 61). Modern terrestrial organic matter at the present day tends to have more negative $\delta^{13}C_{org}$ values than marine organic matter (e.g. Lamb et al., 2006; and references therein). However, prior to the mid-Miocene, terrestrial OM may have more positive $\delta^{13}C$ values than marine OM (Tyson, 1995). It has been suggested by some authors that atmospheric isotopic-compositions changes may only be identified using biomarker $\delta^{13}C$ analyses (Kürschner et al., 2007; Ruhl et al., 2009; Ruhl et al., 2010). Both van de Schootbrugge et al. (2008, 2013) and Bonis et al. (2009) have suggested that variations in bulk organic matter samples may have played a role in the negative carbon-isotope shifts seen in samples from Germany and Austria, respectively. However, Bacon et al. (2011) have shown that even after taking into consideration organic matter composition, a negative carbon-isotope excursion is still seen in the $\delta^{13}C_{org}$ record from Greenland. Analyses by Whiteside et al. (2010) of different types of organic matter from the north-eastern USA have also shown that a negative carbon-isotope excursion is present in all types of organic matter studied, regardless of their source. It is also worth noting that negative carbon-isotope excursions are seen in $\delta^{13}C_{org}$ records

from many sites, both terrestrial and marine, which would have varying amounts of terrestrial and marine organic matter in the bulk OM samples. Therefore, it is likely that variation in bulk organic matter composition does not play an overriding role in the variation of $\delta^{13}C_{org}$ values, and that the trends seen across the Triassic-Jurassic Boundary are representative of a wider, global perturbation to the carbon cycle.

3.2. Global Changes During the Toarcian

3.2.1. Environmental Conditions During the Toarcian

The Toarcian stage (182.7 ± 0.7 Ma – 174.1 ± 1.0 Ma; Cresta et al., 2001; Bordalo Da Rocha et al., 2016) is thought to have been the warmest period of the Early Jurassic, and experienced severe environmental and climatic conditions. Oxygen-isotope and Mg/Ca ratio data indicates a rise in seawater temperature during the Toarcian (Saelen et al., 1996; McArthur et al., 2000; Bailey et al., 2003; Jenkyns, 2003; Rosales et al., 2004; Suan et al., 2010). A rise in seawater temperature of ~7-10°C has been estimated from $\delta^{18}O$ measurements of various fossil invertebrate hard parts (McElwain et al., 2005; Gómez et al., 2008; Dera et al., 2011; Gómez and Goy, 2011; Korte et al., 2015). As well as a rise in seawater temperature, evidence points to multiple periods of sea-level rise throughout the Toarcian (e.g. Haq et al., 1987; Hallam, 1997; Hallam, 2001; Gómez and Goy, 2005). Evidence from calcium, strontium and osmium isotopes indicate periods of extreme continental weathering throughout the Toarcian stage (Cohen et al., 2004; Xu et al., 2018). There is also limited evidence of increased levels of wildfire activity preceding and following the Toarcian Oceanic Anoxic Event (OAE; Baker et al., 2017).

The Toarcian oceanic anoxic event was recognised originally on the basis of widespread deposition of organic-rich shales in marine settings (Jenkyns, 1988; Hesselbo et al., 2007). The OAE is also marked by a characteristic negative carbon-isotope excursion, between two positive CIEs (discussed in further detail in the following section). A major extinction of marine organisms is also associated with the Toarcian OAE (e.g. Little and Benton, 1995; Aberhan and Fürsich, 1996; Harries and Little, 1999; Gröcke et al., 2011; Sandoval et al., 2012; Caruthers et al., 2014; Danise et al., 2015).

3.2.2. Organic and Inorganic Carbon-isotope Stratigraphy

Evidence from multiple studies indicates a global perturbation to the carbon cycle during the Toarcian; records from various sites show a large negative carbon-isotope excursion separating two positive CIEs, corresponding to the Toarcian OAE (**Figure 3.3**). These carbon-isotope excursions have been identified in both terrestrial and marine organic matter.

A large negative carbon-isotope excursion has been identified in marine bulk organic matter records from Europe (Küspert, 1982; Jimenez et al., 1996; Jenkyns and Clayton, 1997; Duarte, 1998; Hesselbo et al., 2000; Jenkyns et al., 2002; Kemp et al., 2005; Hesselbo et al., 2007; Hesselbo and Pienkowski, 2011; Xu et al., 2018), North America (Caruthers et al., 2011; Them et al., 2017), South America (Al-Suwaidi et al., 2010; Fantasia et al., 2018) and Asia (Caruthers et al., 2011; Suan et al., 2011; Kemp and Izumi, 2014; Xu et al., 2017; Izumi et al., 2018). The magnitude of the negative CIE varies between localities, ranging from 2‰ (Duarte, 1998) to 8‰ (Jenkyns and Clayton, 1997). This negative CIE has also been identified in a fossil wood $\delta^{13}C$ record from Argentina, of similar magnitude (~6‰) to the marine bulk organic matter record from the same site (Al-Suwaidi et al., 2010). Negative CIEs are also recorded in fossil wood material from Denmark and Yorkshire (-7‰ and -6‰, respectively; Hesselbo et al. (2000)), and Portugal (-8‰; Hesselbo et al., 2007). At some sites, the negative carbon-isotope excursion occurs in several steps (Jenkyns et al., 2002; Kemp et al., 2005; Hesselbo and Pienkowski, 2011). Records from various sites in Europe record a negative carbon-isotope excursion, ~3-6‰ in magnitude, in marine bulk carbonate material (Jenkyns and Clayton, 1997; Hesselbo, Jenkyns, et al., 2007; Hermoso et al., 2009) and, more subtly in brachiopod and belemnite macrofossil calcite (Suan, Pittet, et al., 2008; Ullmann et al., 2014; Rosales et al., 2018).

Positive carbon-isotope excursions, ranging in magnitude from 2‰ to 4‰, in marine bulk organic matter have been identified in records from multiple sites in Europe (Jenkyns and Clayton, 1986; Jimenez et al., 1996; Jenkyns and Clayton, 1997; Duarte, 1998). Positive CIEs have also been identified at multiple sites in Europe, with a magnitude of 4‰ (Jenkyns and Clayton, 1997).
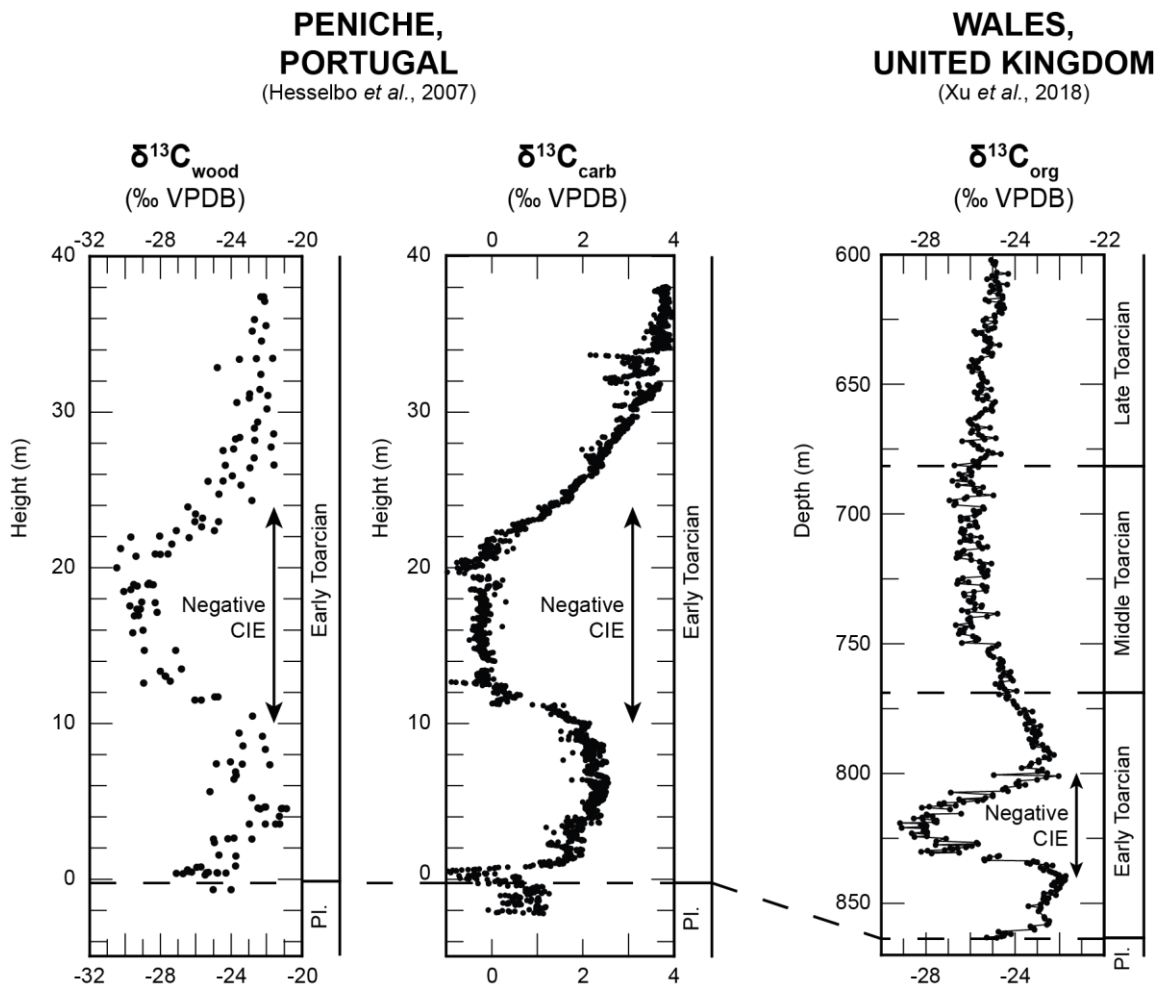
Figure 3.3 Carbon-isotope records showing examples of the negative CIE recorded during the Toarcian at: Peniche, Portugal (terrestrial fossil wood and bulk carbonate records; Hesselbo et al., 2007); and Wales, UK (bulk OM record; Xu et al., 2018). Pl. = Pliensbachian.

3.2.2.1. Causes of the Toarcian OAE Negative CIEs

It is thought that the large negative CIE was caused by a rapid input of a large amount of isotopically-light carbon into the ocean-atmosphere system (e.g. Al-Suwaidi et al., 2010; Caruthers et al., 2011; Xu et al., 2017). This influx of ^{12}C is thought to have originated from methane from seafloor hydrates, and/or from the thermal metamorphism of organic-rich sediments, likely related to emplacement of the Karoo-Ferrar large igneous province (LIP). The release of large amounts of ^{12}C-rich gases during Karoo-Ferrar volcanism is thought to have contributed to the negative CIE (Suan et al., 2008a; Gröcke et al., 2011; Suan et al., 2011; Them et al., 2017). U-Pb dating of zircon crystals from Karoo-Ferrar LIP deposits, mercury concentration records and spectral analysis studies support a link to the Karoo-Ferrar LIP emplacement (Suan et al., 2008b; Sell et al., 2014; Burgess et

al., 2015; Percival et al., 2015). The thermal metamorphism of organic rich sediments as a result of LIP emplacement has also been suggested as an alternative or additional mechanism (McElwain et al., 2005; Them et al., 2017), however evidence from geochemical studies by Gröcke et al. (2009) argue against this. The release of large amounts of methane from seafloor gas hydrates is more widely-supported, and could have resulted from rising ocean temperatures caused by Karoo-Ferrar volcanism (Hesselbo, Meister, et al., 2000; Jenkyns, 2003; Kemp et al., 2005; Hesselbo, Jenkyns, et al., 2007; Svensen et al., 2007; Gröcke et al., 2011; Hesselbo and Pienkowski, 2011; Izumi et al., 2018). The positive CIEs are thought to reflect increased burial of carbon in the form of marine black shales (e.g. Jenkyns, 1985, 1988; Jenkyns and Clayton, 1997).

3.3. The Polish Basin: Early Jurassic Records

The Polish Basin is a large (~700 x ~100 km) inverted epeiric sedimentary basin covering most of modern-day Poland (**Figure 3.4**). Formation of the basin began in the late Permian and was likely caused by a combination of cooling of the crust and trans-tensional tectonic stresses (Dadlez, 2003; Pieńkowski, 2004). Both terrestrial and marine/marginal-marine sediments were deposited in the basin during the Mesozoic, with sediments being delivered predominantly from the northeast (Baltic Syneclise), southeast (Fore-Carpathian Land) and southwest (Sudety Land; Pieńkowski, 2004; Pieńkowski et al., 2008). Throughout the Early Jurassic, changes in sediment delivery were greatly influenced by sea level change; as sea level fell within the basin, sediments were typically delivered from a smaller catchment area (Pieńkowski, 2004). Further study is needed to improve our understanding of sediment routing in the Polish basin during the Early Jurassic. Mesozoic sediments reach a maximum thickness of ~1400 m in the Mid-Polish Trough which runs approximately northwest- southeast along the axis of the basin (Pieńkowski, 2004). Lower Jurassic sediments of the Polish Basin comprise the Kamienna Group and dominant lithofacies are sandstones, heteroliths and mudstones (Pieńkowski, 2004; see also **Section 3.3.1.**; p.52). The basin was inverted during the Late Cretaceous-Early Cenozoic, likely due to crustal compression (Dadlez, 2003) associated with the Alpine orogeny (Krzywiec, 2002).
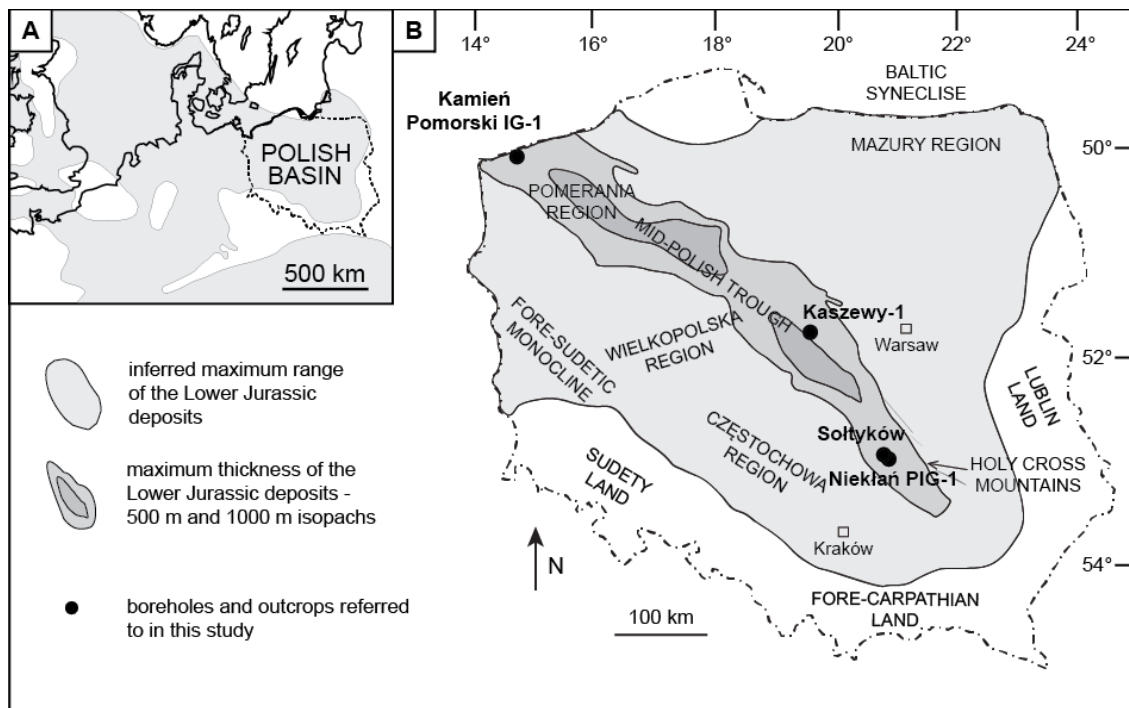
Figure 3.4 A) Map of Lower Jurassic deposits in northwest Europe. B) Map of Lower Jurassic Polish Basin deposits within modern-day Poland, along with key regions, boreholes, and outcrops referred to in this thesis labelled. Longitude and latitude also shown. Both modified from Pieńkowski (2004).

3.3.1. Lower Jurassic Stratigraphy of the Polish Basin

The Lower Jurassic of the Polish Basin is well documented in a monograph by Pieńkowski (2004). Prior to this work lithostratigraphic studies focussed on specific areas within the Polish Basin, rather than the basin as a whole, and there were over 60 informal stratigraphic units in use (e.g. Znosko, 1959; Marcinkiewicz, 1960; Unrug and Calikowski, 1960; Mossoczy, 1961; Dadlez, 1962; Karaszewski, 1962; Wyrwicki, 1996; Jurkiewiczowa, 1967; Kozydra, 1968; Dadlez and Kopik, 1972; Cieśla, 1979; Deczkowski, 1997). Deczkowski (1997) provided an outline for Early Jurassic sedimentation within the Polish Basin, which forms the basis of the work by Pieńkowski (2004). A summary of the Lower Jurassic of Pieńkowski (2004) is given here; ages of the Polish Basin sediments are constrained using sequence stratigraphy. Since the publication of this monograph, sediment age constraints are constantly being re-evaluated as new records (e.g. palynology, carbon-isotope stratigraphy) are published, providing a more accurate chronostratigraphic classification of the Lower Jurassic Polish Basin sediments. The occurrence of limited marine sediments in the Basin

hinders the use of ammonite biostratigraphy which is commonly utilised for dating other Lower Jurassic deposits. There is little information regarding palaeogeography and drainage patterns within the basin.

During the Early Jurassic sediments were deposited across the Polish Basin, and are divided into twelve formations, forming the Kamienna group (**Figure 3.5**). The Kamienna Group consists of siliciclastic sediments deposited in terrestrial, marginal-marine, and marine environments. Key formations included in this thesis include the following: Zagaje, Skłoby, Drzewica, Ciechocinek, and Borucice Formations (**Table 3.2**).

The Zagaje Formation consists mainly of cross-bedded sandstones, with mudstones in the lower part, and conglomerates in the upper part. Plant remains and coals are common in the mudstones. The sediments of this formation were thought to have been deposited in alluvial and lacustrine environments during the Rhaetian (Triassic), Hettangian and Sinemurian, and reach a maximum thickness of ~157 m. The coal- and plant-bearing mudstones of the Zagaje Formation are dominant in the upper part of the formation in the Holy Cross Mountains region and central Poland, and are distinguished as the Huta Mudstone Member within the Zagaje Formation.

Well-sorted sandstones and heteroliths up to 160 m thick form the Skłoby Formation, which can be found in the Mid-Polish Trough and Fore-Sudetic Monocline (**Figure 3.4**). This formation is absent in other parts of the Polish Basin and is sometimes replaced by the Zagaje Formation. The Skłoby Formation represents sediment deposited during the Middle-Late Hettangian in a nearshore depositional environment. Towards the margins of the basin, these sediments were deposited in deltaic and lagoonal settings.

The Drzewica Formation is found in central Poland and the Holy Cross Mountains and reaches a maximum thickness of 100 m. The formation consists of sandstones which were deposited in nearshore, deltaic, and barrier-lagoonal environments. Deposition of these sediments occurred from the Early to the Late Pliensbachian. The Drzewica Formation is equivalent to the Komorowo Formation (Pomerania region) and the upper part of the Blanowice Formation (Częstochowa region).

Formation	Age	Maximum thickness (m)	Geographic extent	Dominant lithofacies	Depositional environment	Notes
Borucice	Late Toarcian	120	All parts of the Polish Basin	Coarse-grained sandstones dominant, with lesser amounts of fine-grained sandstones and mudstones	Alluvial	
Ciechocinek	Early Toarcian	140	All parts of the Polish Basin	Heteroliths, mudstones, and fine-grained sandstones	Large, shallow, brackish embayment	
Olsztyn	Pliensbachian	180	Baltic Syneclise	Sandstones	Alluvial	Equivalent to the Gielniow and Drzewica Formations (Holy Cross Mountains and central Poland) and Lobez and Komorowo Formations (Pomerania regions)
Blanowice	Pliensbachian	42	Częstochowa region	Sandstones dominant, with mudstones, heteroliths and coal seams	Deltaic, alluvial, lacustrine	Equivalent to the Gielniow and Drzewica Formations (Holy Cross Mountains and central Poland) and Lobez and Komorowo Formations (Pomerania regions)
Komorowo	Late Pliensbachian	165	Pomerania region, Fore-Sudetic Monocline	Sandstones with heteroliths and mudstones	Alluvial, deltaic	Equivalent to the Drzewica Formation (Holy Cross Mountains and central Poland) and Blanowice Formation (Częstochowa region)
Drzewica	Early-Late Pliensbachian	100	Central Poland, Holy Cross Mountains	Sandstones	Nearshore, deltaic, barrier/lagoonal	Equivalent to the Komorowo Formation (Pomerania region) and Blanowice Formation (Częstochowa region)
Łobez	Early Pliensbachian	160	Pomerania region	Mudstones	Marine	Equivalent to the Gielniow Formation and Blanowice Formation (Częstochowa region)

Table 3.2 Key information about the Lower Jurassic deposits of the Polish Basin. Summarised from Pieńkowski (2004).

Formation	Age	Maximum thickness (m)	Geographic extent	Dominant lithofacies	Depositional environment	Notes
Gielniów	Early Pliensbachian	75	Holy Cross Mountains, Fore-Sudetic Monocline, Wielkopolska region	Heteroliths, mudstones and fine-grained sandstones	Nearshore	Equivalent to the Lobez Formation (Pomerania region) and Blanowice Formation (Częstochowa region)
Ostrowiec	Sinemurian	240	Mid-Polish trough, Fore Sudetic Monocline	Bedded sandstones and heterolith dominant. Three distinct units of alluvial/deltaic sediments	Nearshore, except for the three alluvia/deltaic units	
Przysucha Ore-bearing	Middle-Late Hettangian	80	Holy Cross Mountains	Clay- and mudstones with characteristic siderite bands dominant. Heteroliths and sandstones also common	Nearshore and deltaic/lagoonal	Equivalent to the Skłoby Formation deposits found in the Pomerania region
Skłoby	Middle-Late Hettangian	160	Mid-Polish Trough, Fore-Sudetic Monocline	Well-sorted sandstones and heteroliths	Deltaic and lagoonal	Absent in other parts of the Polish Basin, sometimes replaced by the Zagaje Formation
Zagaje	Rhaetian – Sinemurian	157		Cross-bedded sandstones dominant, with mudstones in the lower part, and conglomerates in the upper part	Alluvial and lacustrine	Contains the Huta Mudstone Member, found in the Holy Cross Mountains and central Poland, and formed of plant-bearing mudstones

Table 3.2 (continued) Key information about the Lower Jurassic deposits of the Polish Basin. Summarised from Pieńkowski (2004).

	Western and central Poland		Holy Cross Mountains region		Częstochowa region	Baltic Syneclise
	NW	SE	NW	SE		
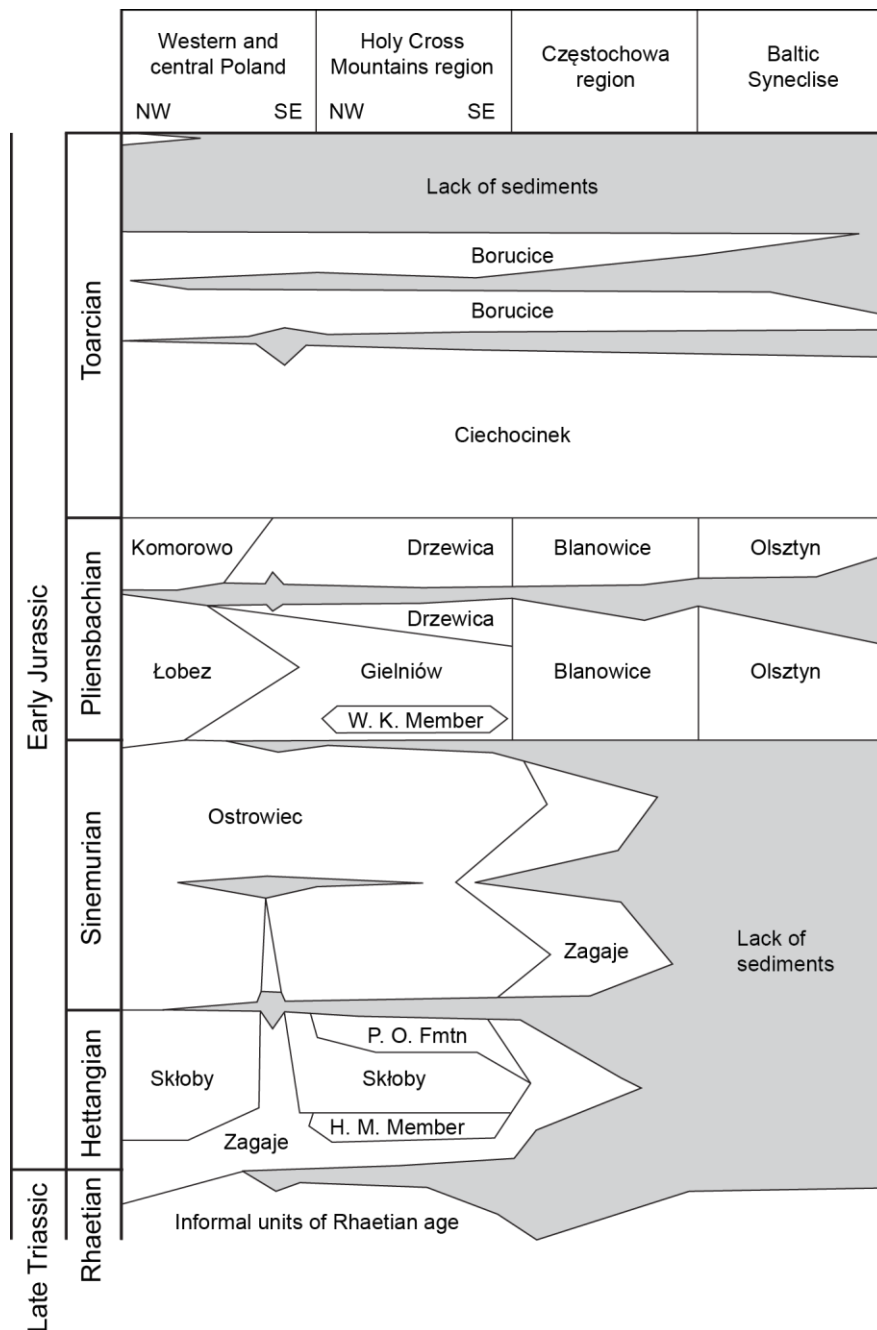
Figure 3.5 Lower Jurassic lithostratigraphy of the Polish Basin. H. M. member = Huta Mudstone Member; P. O. Fmtn = Przysucha Ore-bearing Formation; W. K. Member = Wola Korzeniowa Member. Modified from Pieńkowski (2004).

Heteroliths, mudstones, and fine-grained sandstones comprise the main lithofacies of the Ciechocinek Formation, which can reach up to 140 m in thickness. The sediments of this formation were thought to have been deposited in a large, shallow, brackish embayment during the Early Toarcian. The Ciechocinek Formation can be found in all parts of the Polish Basin.

The Borucice Formation can be found in all parts of the Polish Basin and reaches a maximum thickness of 120 m. The formation is dominated by coarse-grained sandstones which were deposited in alluvial environments; lesser amounts of fine-grained sandstones and mudstones can also be found. The Borucice Formation was deposited during the Late Toarcian and is the youngest of the Lower Jurassic formations within the Polish Basin.

3.3.2. Environmental Conditions in the Polish Basin During the Early Jurassic

3.3.2.1. The Triassic-Jurassic Boundary

Previously published studies provide evidence for a warm and wet climate in the Polish Basin across the Triassic-Jurassic Boundary. An increased marine influence affected the Polish Basin during the middle Hettangian, but decreased during the Late Hettangian (**Figure 3.6**; Pieńkowski, 2004).

During the Late Rhaetian, the climate within the Polish Basin was warm with seasonal rainfall, as indicated by clay mineral assemblages dominated by smectite (Brański, 2014, 2009). Humidity levels in the Polish Basin increased towards the Triassic-Jurassic Boundary, with kaolinite and illite becoming the dominant clay minerals, indicating a shift to year-round rainfall while maintaining warm temperatures (Brański, 2009, 2014; Pienkowski et al., 2014). A number of episodic, abrupt changes kaolinite-illite ratios are evident in Hettangian-age samples, indicating several periods of intense climate change (Brański, 2014).

Fossil insects (mostly beetles) found in the Hettangian-aged Sołtyków deposit (central Poland) are similar to assemblages found in Europe and China and are thought to indicate a warm, subtropical habitat (Wegierek and Zherikhin, 1997), supporting clay mineral evidence. However, *in situ* fossil evidence of the xeromorphic conifer genus *Hirmeriella* has been found at the Sołtyków site, suggesting a dry habitat or season during the Hettangian (Reymanówna, 1991). Other fossil plant remains found at the site include specimens of non-xeromorphic conifers and ferns (Wcislo-Luraniec, 1991).
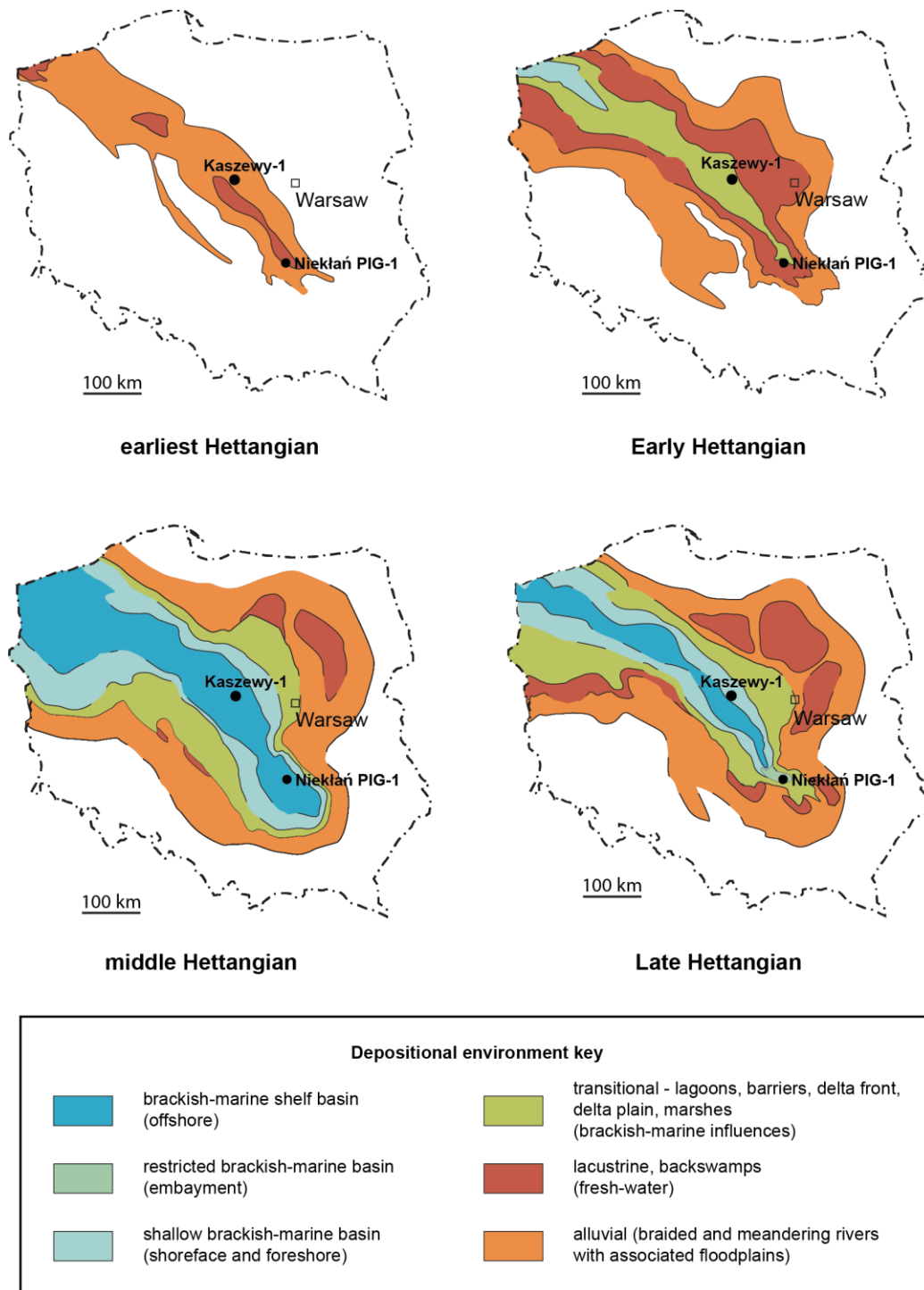
Figure 3.6 Generalised map of depositional environments within the Polish Basin during the Hettangian. The locations of the Kaszewy-1 and Niekłań PIG-1 cores are also shown. Modified from Pieńkowski (2004).

The presence of fossil charcoal and elevated levels of polycyclic aromatic hydrocarbons (PAHs) in the Polish Basin also supports the suggestion of drier periods around the Triassic-Jurassic Boundary (Reymanówna, 1993; Marynowski and Simoneit, 2009; Gierliński et al., 2004).

3.3.2.2. The Toarcian

There are few published studies regarding climatic and environmental conditions in the Polish Basin during the Toarcian period.

During the Early Toarcian there was an extensive rise in sea level which reached marginal parts of the Polish Basin; this was followed by a progressive sea level fall in the Late Toarcian (**Figure 3.7**; Pieńkowski, 2004). Carbon-isotope data from terrestrial organic matter samples from a number of sites within the Polish Basin show a stepped negative carbon-isotope excursion during the Toarcian, coinciding with the global Toarcian OAE (Hesselbo and Pienkowski, 2011). Clay mineralogy from multiple sites around the Polish Basin show a dominant illite-chlorite assemblage in the lower part of the Ciechocinek Formation, likely corresponding to a cooling event with reduced humidity (Brański, 2012). This illite-chlorite assemblage is then replaced by a kaolinite-dominated assemblage in the middle and upper part of the Ciechocinek Formation, which Brański (2012) interprets as a period of extreme continental weathering in a humid sub-tropical environment with increased rainfall.

There is currently a distinct lack of published climatic conditions studies of Toarcian-aged sediments from the Polish Basin, leaving the potential for a wide-range of new studies to be carried out, improving our understanding of climatic conditions in the Polish Basin during the Toarcian.

3.3.3. Previous Studies & Scope for Future Work

Published work focussing on the Polish Basin in the Early Jurassic includes a large body of work investigating dinosaur palaeontology and trace fossils (e.g. Gierliński, 1991; Pieńkowski, 1998; Niedźwiedzki and Pienkowski, 2005; Niedźwiedzki and Pieńkowski, 2016). Non-dinosaur trace fossil studies include work by Leonowicz (2004), Pienkowski and Niedźwiedzki (2010), and Pieńkowski and Uchman (2010). There are significant number of invertebrate palaeontology studies, focussing on ammonites, bivalves and dinoflagellates (e.g. Kopik, 1964; Barski and Leonowicz, 2002; Kozłowska et al., 2016). There are few published studies of the flora of the Polish Basin during the Early Jurassic (e.g. Lund, 1977; Barbacka et al., 2010; Pacyna, 2013, 2014; Barbacka et al., 2016). Published palynology studies are also few in number (Ziaja, 2006; Pienkowski and Waksmundzka, 2009).
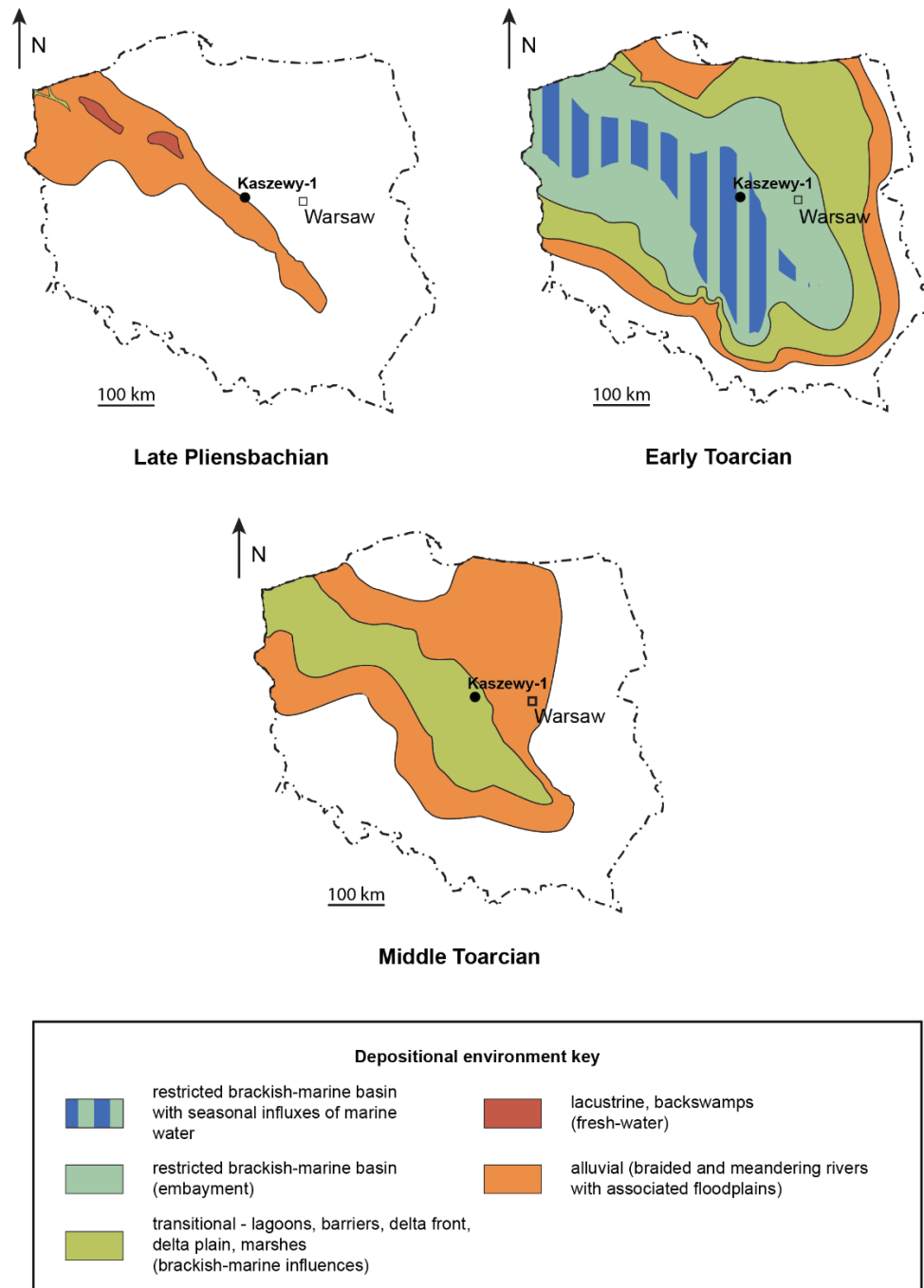
Figure 3.7 Generalised map of depositional environments within the Polish Basin during the Late Pliensbachian – Middle Toarcian. The locations of the Kaszewy-1 borehole is also shown. Modified from Pieńkowski (2004).

Over the last ~20 years, the Polish government has encouraged a number of boreholes, recovering sediment cores, as part of an investigation into carbon capture and storage. The recovered cores, once sampled and analysed as part of this investigation, have since been made available to researchers and new

work is continuing to be published. Two cores in particular are of interest to this thesis: the Kaszewy-1 and Niekłań PIG-1 cores, both located in central Poland. The Kazewy-1 core comprises ~1400 m of Late Triassic and Early Jurassic sediments, allowing for palaeoenvironmental studies of both the Triassic-Jurassic Boundary and Toarcian periods of time (Brański, 2014). The Niekłań PIG-1 core, on the other hand, spans the Norian-Hettangian time periods and provides the possibility of high-resolution palaeoenvironmental studies (Pienkowski et al., 2014).

3.4. Carbon-isotopes in Organic Matter

3.4.1. A Brief Introduction to Stable Carbon-isotopes and $\delta^{13}C$ Values

Isotopes of the same element have the same number of protons but different number of neutrons in the atomic nucleus, and therefore have different atomic weights but the same chemical properties; isotopes which are not radioactive are termed 'stable'.

Carbon has two abundant stable isotopes: carbon-12 (^{12}C) and carbon-13 (^{13}C). Carbon-12 is the more abundant, and lighter (mass: 12.000000), of the two, and accounts for ~99% of all elemental carbon on Earth (Meija et al., 2016a, 2016b). Carbon-13 is heavier (mass: 13.003355) and accounts for ~1% of all elemental carbon on Earth (Meija et al., 2016a, 2016b). The ratio of ^{13}C:^{12}C in an entity is known as delta-13-C, or $\delta^{13}C$, and measured in parts per thousand (per mil, ‰); the following equation (**3.1**) is used to calculate $\delta^{13}C$ (Urey et al., 1951):

$$(3.1) \quad \delta^{13}C = \left(\frac{\frac{^{13}C}{^{12}C} \, sample}{\frac{^{13}C}{^{12}C} \, standard} - 1 \right) \times 1000$$

The original standard reference material for $\delta^{13}C$ measurements was the Pee Dee Belemnite (PDB), a Cretaceous belemnite from the Peedee Formation, South Carolina, USA (Urey et al., 1951; Craig, 1953). The Pee Dee Belemnite had a ^{13}C:^{12}C ratio of 0.01118, however the source material was depleted in the 1970s and was replaced by a new scale: the Vienna PDB (Friedman et al., 1982; Coplen, 1995; Brand et al., 2014). Stable carbon-isotope signatures are often used in palaeoclimate studies to reconstruct past environmental conditions.

3.4.2. Carbon-isotope Variability in Organic Matter

The carbon-isotope signatures and ratio of organic carbon to total nitrogen (C_{org}/N_{total}) of modern organic matter vary greatly, dependent on its origin. Characteristic values of $\delta^{13}C$ and C_{org}/N_{total} ratios can be used to identify the source of unknown organic matter (**Figure 3.8**). A new $\delta^{13}C$ record generated from fossil woody phytoclasts presented in this thesis (**Chapter 5**) aims to help understanding of carbon-isotope variability in fossil organic matter.

Terrestrial plants fall into one of three types, dependent on the photosynthetic pathway that they utilise (see following section for further discussion). These three different types of plants have characteristic $\delta^{13}C$ and C_{org}/N_{total} values. So-called C3 plant $\delta^{13}C$ values range between ~-32‰ and ~-21‰ with C_{org}/N_{total} ratios upwards of 12, whereas C4 plant $\delta^{13}C$ values range between ~-17‰ and ~-9‰ with C_{org}/N_{total} ratios upwards of ~20 (Deines, 1980; Prahl et al., 1980; Meyers, 1994; Tyson, 1995; Lamb et al., 2006). The ratio of organic carbon to total nitrogen can vary greatly between plants, mainly due to large variations in plant nitrogen content (Lamb et al., 2006). Plants utilising the CAM photosynthetic pathway typically show a wide range of $\delta^{13}C$ values, ranging between ~-28‰ and ~-11‰ (Schleser, 1995; Lamb et al., 2006). A study by Meyers (1994) suggests that $\delta^{13}C$ and C_{org}/N_{total} ratios are relatively unaffected by diagenesis.

Modern freshwater and marine algae have low C_{org}/N_{total} ratios between 4 and 10 (Meyers, 1994; Tyson, 1995). Marine algae typically show a wider range in $\delta^{13}C$ values, ranging between ~-24‰ and ~-16‰; freshwater algae $\delta^{13}C$ values typically range between ~-30‰ and ~-26‰ (Haines, 1976; Schidlowski et al., 1983; Meyers, 1994). Modern freshwater and marine particulate organic carbon (i.e. phytoplankton and zooplankton mixed with detrital terrestrial OM; POC) have similar $\delta^{13}C$ values and C_{org}/N_{total} ratios to freshwater and marine algae. Modern freshwater POC has $\delta^{13}C$ values that typically range between ~-25‰ and ~-33‰ and C_{org}/N_{total} ratios between 4 and 10 (Salomons and Mook, 1981; Barth et al., 1998; Lamb et al., 2006). Marine POC typically has $\delta^{13}C$ values between ~-24‰ and ~-18‰ and C_{org}/N_{total} ratios between 4 and 10 (Peters et al., 1978; Middelburg and Nieuwenhuize, 1998; Lamb et al., 2006). Modern marine and freshwater dissolved organic carbon (DOC) typically has a relatively wide range of C_{org}/N_{total} values, between ~7 and ~26, but have different $\delta^{13}C$ signatures (Peterson et al.,
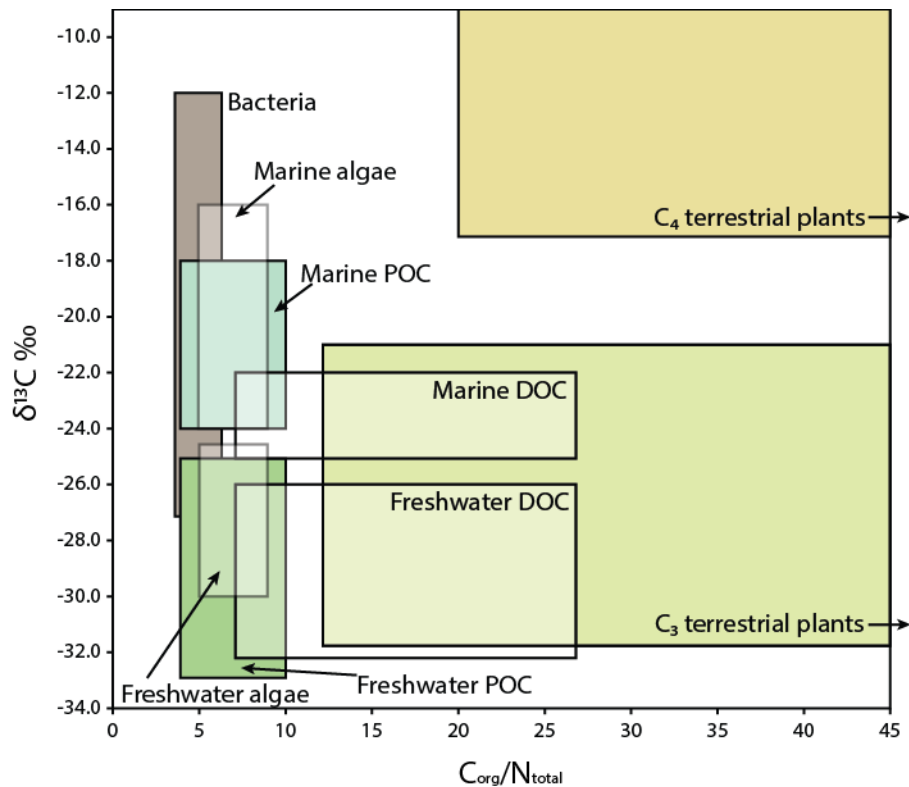
Figure 3.8 Characteristic $\delta^{13}C$ and C_{org}/N_{total} ratios of modern organic matter recorded at coastal sites. Redrawn from Lamb et al. (2006).

1994; Lamb et al., 2006). Marine DOC $\delta^{13}C$ values are more positive, ranging between ~-25‰ and ~-22‰, whereas freshwater DOC $\delta^{13}C$ values are more negative, ranging between ~-32‰ and ~-26‰ (Peterson et al., 1994; Lamb et al., 2006).

3.4.3. Carbon-isotope Signatures of Plants

Studies of modern plants show that their carbon-isotopic composition primarily depends on the rate of photosynthesis and/or stomatal conductance, and the carbon-isotopic composition of the atmosphere, but is also affected by the plant type and tissue, as well as other environmental factors.

3.4.3.1. Intrinsic Factors

A number of intrinsic factors affect the overall carbon-isotope composition of plants. There are variations in $\delta^{13}C$ values between different tissue types within a plant, which are also controlled by the overall plant type, and its photosynthetic pathway (**Table 3.3**).

Factor	Relationship with $\delta^{13}C$	Notes	Reference(s)
Photosynthetic pathway	C3 plants more depleted than C4 plants	$\delta^{13}C$ ~-28‰	O'Leary, 1988; Hobbie and Werner, 2004
	C4 plants more enriched than C3 plants	$\delta^{13}C$ ~-14‰	O'Leary, 1988; Hobbie and Werner, 2004
	CAM plants show signatures intermediate between C3 and C4 plants	$\delta^{13}C$ ~-10‰ – ~-20‰	Hobbie and Werner, 2004
Photosynthetic rate	Increase in photosynthetic rate shifts $\delta^{13}C$ values to more positive		McCarroll et al., 2009
Tissue Type	Whole plant most enriched		Hobbie and Werner, 2004; Lamb et al., 2006
	Cellulose & lignin depleted relative to whole plant	Cellulose enriched relative to lignin. Lignin depleted by 3-4‰ relative to whole plant	Hobbie and Werner, 2004. Lamb et al., 2006
	Lipids depleted relative to cellulose & lignin	Lipids depleted by ~5‰ relative to cellulose	Hobbie and Werner, 2004; Lamb et al., 2006
	Alkanes depleted relative to lipids	Based on $\delta^{13}C$ values of fossil plant material	Whiteside et al., 2010; Ruhl et al., 2011
Plant Type	Evergreen plants tend to have more positive $\delta^{13}C$ values than deciduous ones		Brooks et al., 1997
Plant Height (within canopy)	Increase in plant height shifts $\delta^{13}C$ to more positive values		Vogel, 1978; Medina and Minchin, 1980; Schleser, 1992; Brooks et al., 1997, 1998
Plant Age	No apparent effect on $\delta^{13}C$	Based on conifer tree ring data	Saurer et al., 2004

Table 3.3 Summary of intrinsic factors affecting $\delta^{13}C$ values of modern plants (unless otherwise stated), and supporting studies.

Photosynthesis is the process by which a plant converts carbon dioxide (from the atmosphere) and water into energy (in the form of glucose) and oxygen (Hall and Rao, 1999; Taiz and Zeiger, 2010). During photosynthesis, plants discriminate

against ^{13}C because ^{13}C forms stronger bonds that require more energy to break (O'Leary, 1988); diffusion of the heavier $^{13}CO_2$ is also slower than diffusion of the lighter $^{12}CO_2$. Carbon- isotope discrimination initially occurs during the fixation of CO_2 from the atmosphere and is dependent on the photosynthetic pathway of a plant.

The three different types of photosynthetic pathway (C3, C4, and crassulacean acid metabolism (CAM)) each have their own rates of carbon-isotope discrimination. C3 plants fix carbon dioxide using the enzyme ribulose bisphosphate carboxylase whereas C4 plants fix carbon dioxide through carboxylation of phosphoenolpyruvate (O'Leary, 1988). The C4 photosynthetic pathway is relatively new, thought to have evolved ~20 Ma (Hobbie and Werner, 2004; Sage, 2004). Plants which utilise the CAM pathway (mostly desert plants) absorb carbon dioxide at night to synthesise malic acid which they then decarboxylate the following morning (O'Leary, 1988). Thus plants utilising the C3 pathway tend to be more depleted in ^{13}C than C4 plants, with $\delta^{13}C$ values ~-28‰ and ~-14‰, respectively, whereas plants utilising the CAM pathway tend to have an isotopic signature ranging from ~-10‰ to ~-20‰ (O'Leary, 1988). An increase in the rate of photosynthesis also results in more positive $\delta^{13}C_{plant}$ values (McCarroll et al., 2009).

Carbon-isotope discrimination continues throughout the whole photosynthetic process, and during other process within plants, leading to different tissue types becoming more depleted in ^{12}C than others. In general, whole plant $\delta^{13}C$ values are the most positive and leaf wax-derived alkanes are the most negative (Hobbie and Werner, 2004, and references therein). It would appear that the general order of $\delta^{13}C$ is: whole plant > cellulose > lignin > lipids > alkanes (Collister et al., 1994; Hobbie and Werner, 2004; Lamb et al., 2006).

Other, more minor, factors affecting $\delta^{13}C$ values in plants include the plant type and its height within the canopy. Brooks et al. (1997) found that evergreen plants tend to have more positive $\delta^{13}C$ values than deciduous ones, and also that plants higher up in the canopy tend to have more positive $\delta^{13}C$ values than ones lower. This relationship between plant height and $\delta^{13}C$ value is supported by data from other studies (Vogel, 1978; Medina and Minchin, 1980; Schleser, 1992; Brooks

et al., 1998). Saurer et al. (2004) found that plant age does not appear to affect $\delta^{13}C$ value.

3.4.3.2. External Factors

There are a multitude of environmental factors that affect the carbon-isotope composition of modern plants by influencing the rate of photosynthesis (**Table 3.4**; Hall and Rao, 1999).

The carbon-isotope composition of the atmosphere plays a significant role in determining the $\delta^{13}C$ value of a plant (McCarroll et al., 2009). Carbon is present in the atmosphere as carbon dioxide, so as atmospheric carbon dioxide levels increase, the gradient between external atmospheric pCO_2 and the internal pCO_2 of a plant increases (Taiz and Zeiger, 2010). A larger pressure gradient between external pCO_2 and internal pCO_2 increases the rate of diffusion of CO_2 into the plant, causing greater carbon-isotope discrimination (Taiz and Zeiger, 2010). The effect of air temperature on $\delta^{13}C$ values is less clear; previously published studies show mixed results, with some finding a positive relationship, others finding a negative relationship, and some finding no apparent relationship between air temperature and $\delta^{13}C$ values (Smith et al., 1973, 1976; Troughton et al., 1974; Troughton and Card, 1975; Bender and Berge, 1979; Saurer et al., 2004).

Water availability and salinity also affect $\delta^{13}C$ values; increased water availability appears to increase carbon-isotope discrimination, shifting $\delta^{13}C$ values towards more negative values (Farquhar et al., 1989; Saurer et al., 1995). The effect of salinity on $\delta^{13}C$ values is debatable; conflicting evidence shows that salinity can shift $\delta^{13}C$ values in either direction (Guy et al., 1980; Farquhar et al., 1989). Similarly, the effect of light availability on $\delta^{13}C$ values is also questionable. A study on tomato plants show negligible variations in $\delta^{13}C$ values in response to changing light availability (Park and Epstein, 1960), but a later study by Smith et al. (1976) showed that light availability appears to cause random variations in $\delta^{13}C$ values. Further studies by O'Leary (1981) and (Farquhar et al., 1989) show that increasing light availability causes shifts towards more negative and more positive $\delta^{13}C$ values, respectively. Increasing availability of nutrients appears to shift $\delta^{13}C$ towards more positive values (O'Leary, 1981). Tree ring data shows that material grown in the spring (earlywood) tends to have more negative $\delta^{13}C$

Factor	Relationship with $\delta^{13}C$	Notes	Reference(s)
Atmospheric CO_2 content	Increasing atmospheric CO_2 shifts $\delta^{13}C$ to more negative values		Park and Epstein, 1960; McCarroll et al., 2009
Air temperature	Increase in air temperature shifts $\delta^{13}C$ to more positive values	Based on data from conifer tree rings	Saurer et al., 2004
	Increase in air temperature shifts $\delta^{13}C$ to more negative values		Smith et al., 1973, 1976; Bender and Berge, 1979
	No change in $\delta^{13}C$ with changes in air temperature		Troughton et al., 1974; Troughton and Card, 1975
Water availability	Increase in water availability shifts $\delta^{13}C$ to more negative values		Farquhar et al., 1989; Saurer et al., 1995
Salinity	Increase in water salinity shifts $\delta^{13}C$ to more positive values		Farquhar et al., 1989
	Increase in water salinity shifts $\delta^{13}C$ to more negative values		Guy et al., 1980
Light availability	Increased light availability shifts $\delta^{13}C$ to more negative values	Based on plants using CAM photosynthesis	O'Leary, 1981
	Increased light availability shifts $\delta^{13}C$ to more positive values		Farquhar et al., 1989
	Variation in light availability causes seemingly random variations $\delta^{13}C$ values		Smith et al., 1976
	Negligible variation in $\delta^{13}C$ with changes in light availability	Based on data from tomato plants	Park and Epstein, 1960
Nutrient availability	Increased nutrition shifts $\delta^{13}C$ to more positive values		O'Leary, 1981
Growing season	Earlywood $\delta^{13}C$ values more negative than latewood $\delta^{13}C$ values	Based on tree ring data	(Freyer, 1980; Leavitt and Long, 1991; Brooks et al., 1998
Elevation	No change in $\delta^{13}C$ with elevation variation		Saurer et al., 2004
Latitude	Increase in latitude shifts $\delta^{13}C$ to more negative values		Saurer et al., 2004
Longitude	No change in $\delta^{13}C$ with longitude variation		Saurer et al., 2004

Table 3.4 Summary of external factors affecting $\delta^{13}C$ values of modern plants, and supporting studies.

values than that grown in the summer (latewood; Freyer, 1980; Leavitt and Long, 1991; Brooks et al., 1998).

A study by Saurer et al. (2004) showed that $\delta^{13}C$ values tend to become more negative as latitude increases, but found no relationship between longitude or elevation and $\delta^{13}C$ values.

Although local environmental conditions do influence the carbon-isotopic composition of plants, the consensus is that these become less important when investigating changes in plant carbon-isotope composition over time because the integrated magnitudes are relatively small. On geological timescales, it is thought that stratigraphic excursions in plant $\delta^{13}C$ values generally represent changes in atmospheric carbon-isotope composition, with secondary effects from environmental differences.

3.5. Wildfire Activity in the Fossil Record

3.5.1. Physical Evidence: Fossil Charcoal

3.5.1.1. Fossil Charcoal: Characteristics, Formation & Identification

Charcoal is a black, brittle and lustrous organic material (Scott, 2010) and typically contains a high percentage of carbon (Eckmeier, Rosch, et al., 2007; Eckmeier, Gerlach, et al., 2007). Formation of charcoal occurs in oxygen-depleted environments, where the incomplete combustion of organic matter results in pyrolysis (Goldberg, 1985; Scott and Jones, 1991). Charcoal usually
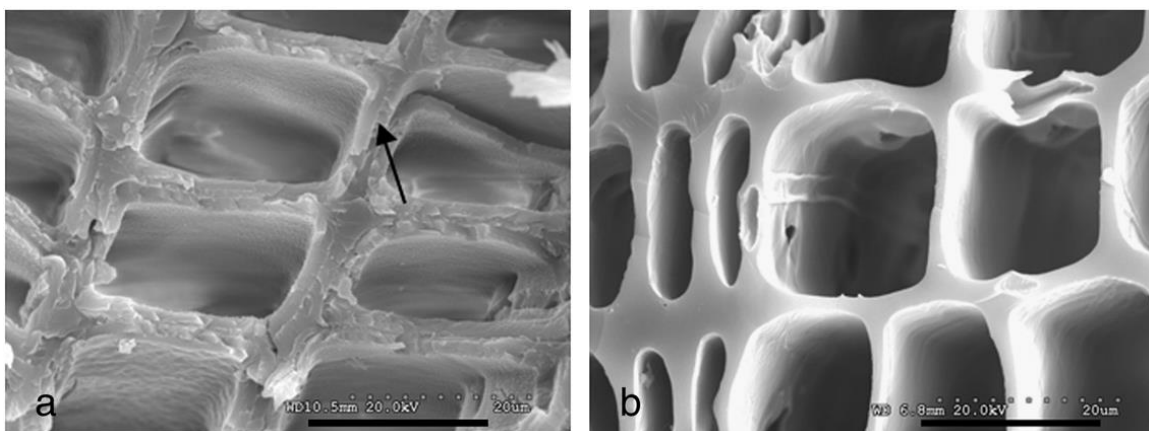
Figure 3.9 From Scott (2010). Scanning electron micrographs of charred Sequoia wood showing a) middle lamella (arrow), and b) lack of middle lamella (cell wall homogenisation).

shows exceptional preservation of the anatomy of the original vegetation (e.g. Bird et al., 2008; Scott, 2009, 2010). Charcoal is a relatively inert material which is easily preserved and, as a result, is common in the fossil record (e.g. Scott and Jones, 1991; Scott, 2000; Scott and Glasspool, 2007).

Charcoal is usually produced by fire activity but can also be produced by volcanic activity, when organic matter is buried in high-temperature ashes or pyroclastic flow deposits and kept at high enough temperatures for pyrolysis of organic matter to occur (Scott and Glasspool, 2006; Scott, 2010; Scott and Damblon, 2010). Volcanogenic charcoal is physically distinct from charcoal produced by wildfire and far less common (e.g. Scott and Glasspool, 2005, 2006). In the geological record, charcoal is usually indicative of past wildfire activity, particularly when there is a lack of preserved volcanic material.

Identification of fossil charcoal can be carried out using optical microscopy; its black appearance, preservation of original plant structures, and highly reflective surfaces distinguishes charcoal from non-charcoalified organic matter (**Figure 3.9**; Scott, 2000). Due to its brittle nature and resistance to degradation, charcoal fragments are often angular, unlike non-charcoal organic matter fragments which are often more rounded due to their low resistance to degradation (Scott, 2000). Wood cell walls have a layered structure, showing primary and secondary walls separated by a middle lamella. During pyrolysis, cell wall homogenisation can occur, resulting in the cell walls losing their distinctive layered structure; this can be identified using scanning electron microscopy (Jones and Chaloner, 1991; Scott, 2000, 2010; Chaloner, 1989). It is thought that the presence of homogenised cell walls is a key feature of charcoal, but recent experiments by Hudspith and Belcher (2017) have shown that cell wall homogenisation only occurs during the early stage of charring, and can be overprinted by subsequent thermal degradation, resulting in the thinning and breakdown of the cell walls. Consequently, evidence of cell wall homogenisation may not be visible in all fossil charcoal samples, and the lack of homogeneity cannot be used to categorically rule out identification of charcoal.

3.5.1.2. Fossil Charcoal as an Indicator of Past Wildfire Activity

Several authors have suggested that that variations in charcoal abundance provide a record of biomass burned in wildfires (e.g. Carcaillet et al., 2002;

Thevenon et al., 2004; Marlon et al., 2006; Higuera et al., 2007; Power et al., 2007). It is thought that the amount of charcoal present in a sediment is linked to wildfire characteristics such as size, severity and proximity (Whitlock et al., 2006). However, fossil charcoal abundance can be affected by several other factors besides wildfire activity, such as vegetation type, transport distance, and depositional environment, and these must be considered carefully when interpreting fossil charcoal abundance data.

Vegetation type can influence the amount of charcoal produced during a wildfire; some plants are more susceptible to burning than others, and hence are more likely to produce larger amounts of charcoal. For example, leaf size and shape, and plant moisture content can affect the flammability of a plant (e.g. Watson, 1978; Whelan, 1995; Bond and van Wilgen, 1996; Cornelissen et al., 2003). The presence of volatile components such as oils and waxes in plant material can also contribute to the flammability of vegetation (Cornelissen et al., 2003). A change in vegetation type from less flammable to more flammable will likely produce more charcoal during wildfire events, and as a result, could bias the wildfire activity record. The effect of vegetation type on wildfire activity levels is discussed in greater detail in **Section 3.5.3.2.** (p. 82).

Due to its robust nature and its ability to float, charcoal is capable of being transported large distances before its final deposition (Scott, 2010). Elliott and Parker (2001) suggest that rainstorms can transport substantial amounts of charcoal for long distances. Charcoal can also be transported long distances by wind, though this applies to smaller fragments of charcoal only (Griffin & Goldberg, 1979; Herring, 1985). Microscopic charcoal is usually transported by wind whereas macroscopic charcoal is usually transported by water (e.g. Scott, 2000; Marynowski and Simoneit, 2009; Scott, 2009). Consequently, the depositional environment of fossil charcoal may not reflect the environment in which the wildfire occurred (Scott 2010). Macroscopic charcoal is thought to be deposited local to the fire that produced it (e.g. Long et al., 1998; Tinner et al., 1998; Carcaillet et al., 2001; Sadori and Giardini, 2007; Whitlock, 2001; Kawano et al., 2012). Microscopic charcoal is usually transported further before deposition due to its small size, and many authors suggest that its presence alone in deposits records the regional fire activity (e.g. Scott 2010). However, experiments have shown that large pieces of charcoal can be transported for long distances

by water before becoming waterlogged and falling out of suspension (Scott, 2010). This observation suggests that the presence of macroscopic charcoal in a deposit is not a definitive marker of local wildfire activity.

Since charcoal is a robust material, it can survive being transported long distances without showing evidence of wear, therefore making it difficult to interpret how far it has travelled prior to deposition. Nichols et al. (2000) suggest that to determine how far charcoal has been transported, it would be more appropriate to examine the sorting of a charcoal assemblage. Charcoal fragments which have been transported long distance would show greater amounts of sorting than those that have only travelled a short distance before being deposited (e.g. Marynowski and Simoneit, 2009; Scott, 2010; Uhl and Montenari, 2011).

It is also important to consider the amount of fossil charcoal present as a proportion of the total phytoclasts in a sample when interpreting fossil charcoal abundance in terms of wildfire activity levels. An increase in the total amount of organic matter deposited at a site, e.g. by increased runoff, could create an artificial increase in fossil charcoal without there being an actual increase in wildfire activity and charcoal production at the time. An increase in fossil charcoal abundance without a corresponding increase in total organic matter is much more likely to reflect an increase in wildfire activity and charcoal production.

Fossil charcoal abundance in a deposit can also be altered by sediment reworking. Evidence of reworking, such as the presence of trace fossils, should be looked for in deposits sampled for fossil charcoal abundance analyses. Sediment reworking should be considered when interpreting fossil charcoal abundance as a wildfire activity proxy, along with the final depositional environment.

The depositional environment plays a role in the amount of charcoal deposited and preserved in sediments. High-energy environments, such as rivers and shallow marine sites, are likely to transport and deposit charcoal away from its production site. Smaller charcoal particles are likely to be transported further away than larger particles. High-energy environments may also increase the chance of charcoal being broken up before deposition. Low-energy environments, such as small lakes and the deep sea, are likely to see higher

amounts of microscopic charcoal deposited. Since smaller charcoal particles can be transported further before deposition, fossil charcoal abundance data from low-energy environments may reflect the wildfire activity of a wider area than high-energy environments. To minimise bias from depositional environments it would preferable to study a section which represents one, or very few, depositional environments (Belcher, Mander, et al., 2010). If this is not possible, then there must be careful consideration of the sedimentology and lithology of the study sites when interpreting fossil charcoal abundance data.

A number of authors suggest that charcoal formation temperatures can be estimated from the light reflected from the surface of a sample of charcoal under oil (reflectance value; e.g. Ascough et al., 2010). Reflectance values show a positive relationship with charcoal formation temperature, and that this holds up for both modern and fossil charcoal (Jones et al., 1991; Scott and Jones, 1991; Scott and Glasspool, 2005, 2007; McParland et al., 2009). This relationship has been used to infer wildfire temperatures from fossil charcoal reflectance values (Jones et al., 1991; Scott and Glasspool, 2005; McParland et al., 2009; Marynowski et al., 2011; Petersen and Lindström, 2012; Hudspith and Belcher, 2017). However, Ascough et al. (2010) have suggested this relationship is less reliable for charcoal formed at temperatures lower than 400°C because such charcoal is prone to degradation. Also, when charring time is unknown, reflectance values will only yield minimum formation temperatures (Ascough et al., 2010).

Recent experimental work has also raised caveats. The use of oven-created charcoals to create reflectance–temperature curves does not fully recreate the conditions experienced in a wildfire (Belcher and Hudspith, 2016). Instead, maximum reflectance values are reached at the transition between pyrolysis and oxidation of the organic matter in wildfires, and this process is not recreated in oven-formed charcoal. Belcher and Hudspith (2016) conclude that the relationship between reflectance values and charring temperatures needs revision, and that wildfire temperatures cannot be inferred from existing calibrations.

3.5.2. Geochemical Evidence: Pyrolytic Polycyclic Aromatic Hydrocarbons

3.5.2.1. Polycyclic Aromatic Hydrocarbons: Formation & Characteristics

Polycyclic aromatic hydrocarbons (PAHs) are organic compounds consisting of carbon and hydrogen atoms arranged in aromatic rings (**Table 3.5**; Jiang et al., 1998; Shen et al., 2011). Polycyclic aromatic hydrocarbons can originate from a variety of sources, though certain PAHs are produced only during the pyrolysis of organic matter; these are known as pyrolytic PAHs (Killops and Massoud, 1992; Jiang et al., 1998; Belcher et al., 2009; Shen et al., 2011). Polycyclic aromatic hydrocarbons can also be derived from petroleum and bituminous sources, without the occurrence of pyrolysis, and produced directly by land plants, such as the PAH retene.

Pyrolysis usually occurs above temperatures of 350°C, and up to temperatures >1200°C (Abdel-Shafy and Mansour, 2016). It has been suggested by Zhou et al. (2015) that higher molecular weight PAHs may be formed from PAH compounds with lower molecular weights. This is a finding supported by computer modelling by Kislov et al. (2013), which shows that pyrolytic PAHs can be formed sequentially, producing new compounds with an increased number of aromatic rings from those that came before. Experiments involving the pyrolysis of tar show that PAHs are produced sequentially in addition steps, producing PAHs with greater numbers of aromatic rings as reaction time increases (Ledesma et al., 2006). An experimental burning study by McGrath et al. (2003) shows that there is a positive correlation between pyrolysis temperature and the number of aromatic rings in the pyrolytic PAH compounds. While there is still debate about the precise chemical pathway that leads to the formation of pyrolytic PAHs, it is generally agreed that pyrolytic PAHs are produced sequentially, with higher molecular weight molecules being produced from those with lower molecular weights (e.g. Frenklach, 2002; Zhou et al., 2015).

As PAHs can also originate from other sources, it is important to distinguish these from pyrolysis-derived PAHs. Alkylated PAHs (with additional alkyl chains stemming from the aromatic hydrocarbon rings) are thought to originate from a petroleum or bituminous source and not from the pyrolysis of organic matter (henceforth termed petrogenic PAHs; **Table 3.5**; Venkatesan and Dahl, 1989; Jiang et al., 1998; Shen et al., 2011).
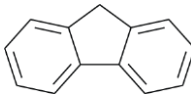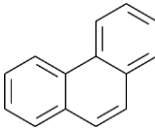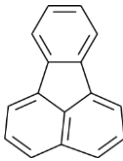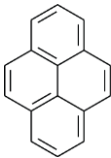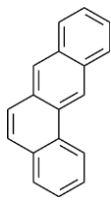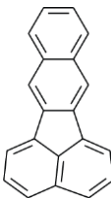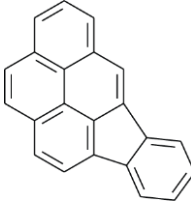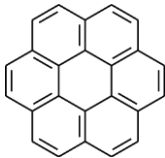
Polycyclic aromatic hydrocarbon	Molecular weight (*m/z*)	Number of aromatic rings	Structure	Source
fluorene	166	3		
phenanthrene	178	3		
fluoranthene	202	4		
pyrene	202	4		Combustion of organic matter (e.g. Jiang et al., 1998; Belcher et al., 2009)
benz-anthracene	228	4		
benzo(k)fluoranthene	252	5		
indeno[1,2,3-cd]pyrene	276	6		
coronene	300	7		Combustion of organic matter AND petroleum/ bitumen (e.g. Jiang et al., 1998; Belcher et al., 2009; Shen et al., 2011)

Table 3.5 Key PAHs discussed in this thesis.
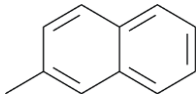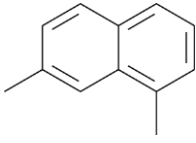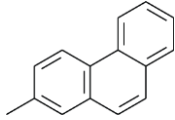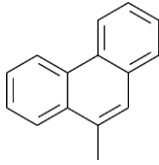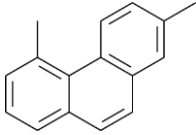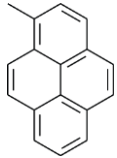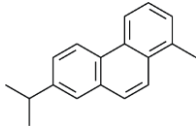
Polycyclic aromatic hydrocarbon	Molecular weight (m/z)	Number of aromatic rings	Structure	Source
2-methylnaphthalene	142	2		
1,7-dimethylnaphthalene	156	2		
2-methylphenanthrene	192	3		Petroleum/ bitumen (e.g. Jiang et al., 1998; Belcher et al., 2009)
9-methylphenanthrene	192	3		
2,5-dimethylphenanthrene	206	3		
1-methylpyrene	216	4		
retene	234	3		Higher-plant biomarker (e.g. Ellis et al., 1995; Jiang et al., 1998; Peters et al., 2007)

Table 3.5 (continued) Key PAHs discussed in this thesis.

Coronene is a PAH which can originate from both petroleum and bituminous sources, as well as from the pyrolysis of organic matter (**Table 3.5**; Oros and Simoneit, 2000; Simoneit, 2002). Belcher et al. (2005) suggest that if coronene is present in significant quantities it is more likely to have originated from a petrogenic source rather than from the combustion of organic matter.

Retene is a PAH which is well-known as a higher land plant biomarker (**Table 3.5**; Jiang et al., 1998; Peters et al., 2007, and references therein). In particular,

retene is thought to be a biomarker originating from conifers (e.g. Ellis et al., 1995; Jiang et al., 1998; Peters et al., 2007; Belcher et al., 2009).

3.5.2.2. Pyrolytic PAHs as Indicators of Past Wildfire Activity

Pyrolytic PAHs can be found preserved in sediments and are thought to indicate periods of past wildfire activity (e.g. Killops and Massoud, 1992; Venkatesan and Dahl, 1989; Jiang et al., 1998). Pyrolytic PAHs can also be formed from organic matter which is in contact with volcanic intrusions and undergoes pyrolysis (George, 1992; Murchison and Raymond, 1989), though this is apparently much rarer. Wildfire activity records based on pyrolytic PAH concentrations have been produced for various Mesozoic-aged sedimentary sequences, including the Cretaceous (e.g. Finkelstein et al., 2005; Belcher et al., 2009), the Jurassic (e.g. Marynowski and Filipiak, 2007) and the Triassic (e.g. Nabbefeld et al., 2010).

Although the presence of pyrolytic PAHs is used as an indicator of past wildfire activity, it has been suggested that they could also be formed during diagenesis or that they may migrate in sediments (Scott 2009). However, Abdel-Shafy and Mansour (2016) suggest that due to their non-polar nature, PAHs are relatively immobile in sediments as they are poorly water-soluble, and that transport of PAHs in the sediment pile is not significant.

Degradation of pyrolytic PAHs over geological timescales does not appear to be widely studied, though it is thought that PAHs are relatively resistant to degradation (e.g. Johnsen et al., 2005) due to the compounds adhering to sediments during burial (Page et al., 1999). Abdel-Shafy and Mansour (2016) suggest that different PAHs degrade at different rates; they suggest that phenanthrene, in particular, degrades at a much slower rate than other pyrolytic PAHs. Studies by Landrum (1989), Brannon et al. (1995) and Hatzinger and Alexander (1995) show that stability of PAHs may actually increase as the contact time with sediment increases.

It is very easy for PAHs to be transported by aerosols before deposition into sediments, and long-distance transport to the site of deposition is possible (e.g. Aceves and Grimalt, 1993; Leister and Baker, 1994; Fernandez et al., 2000; Halsall et al., 2001; Tsapakis et al., 2003; Abdel-Shafy and Mansour, 2016). When interpreting polycyclic PAH concentration records in terms of wildfire

activity it is, therefore, important to consider that they may represent wildfire activity on a more regional scale, rather than local.

It has been suggested by Venkatesan and Dahl (1989) that elevated levels of pyrolytic PAHs are only indicative of wildfire activity when they are much more abundant than petrogenic PAHs, though the authors do not quantify how much more abundant they must be. The authors claim that sediments which contain similar concentrations of both pyrolytic and petrogenic PAHs do not represent periods of increased wildfire activity, though this appears to be a little-researched topic (Page et al., 1999).

Given the uncertainties involved with analysis of pyrolytic PAHs in geological samples, it has been suggested that pyrolytic PAH concentration data be combined with other wildfire activity proxies, such as fossil charcoal abundance, for more reliable interpretations (Finkelstein et al., 2005; Marynowski and Filipiak, 2007; Marynowski and Simoneit, 2009; van de Schootbrugge et al., 2009). Concentrations of retene that also covary with pyrolytic PAH concentrations are thought to be a good indicator of burning biomass (e.g. Belcher et al., 2009). Pyrolytic PAH concentration and fossil charcoal abundance datasets that covary are harder to dispute as reliable indicators of wildfire activity levels than lone pyrolytic PAH concentration records.

3.5.3. Causes of Changes in Wildfire Activity Levels

3.5.3.1. Initiation of Wildfires

A wildfire is a fire that occurs in an area of combustible vegetation and requires fuel (vegetation), heat, oxygen and a source of ignition (Pyne et al., 1996).

Wildfires are usually caused by the ignition of vegetation by lightning strikes during storms (e.g. Komarek, 1967; Cope and Chaloner, 1980; Tinner et al., 1998; Scott, 2000; Jones et al., 2002; Petersen and Lindström, 2012). Wildfires can also be initiated by volcanic activity, sparks from rock falls, extraterrestrial impacts, and spontaneous combustion, though these are much rarer (e.g. Batchelder, 1967; Scott, 1988; Jones and Lim, 2000; Scott, 2000). Ignition requires both increased temperatures and a supply of oxygen which, in turn, help the wildfire to spread, providing there is sufficient fuel available (Scott, 2000).

Lower Oxygen Limit (% of atmosphere)	Reference	Notes
7	Cope and Chaloner (1980)	Based on experimental work involving burning of methane and carbon monoxide in oxygen-containing atmospheres.
12	Wildman Jr et al. (2004)	Based on results of flame-spread experiments.
13	Clark and Russell (1981)	Reply to Cope and Chaloner (1980). Based on experimental burning work by Rasbash and Langford (1968).
13	Cope and Chaloner (1981)	Revision of estimate by Cope and Chaloner (1980) based on experimental burning work by Rasbash and Langford (1968).
13	Scott (2000)	Review paper. Lower oxygen limit based on previously-published work by other authors in this table.
13	Bowman et al. (2009)	Based on modelling work by Berner et al. (2003) and Berner (2006).
15	Watson et al. (1978)	Based on experimental work and derived as a function of both fuel moisture and oxygen level.
15	Belcher and McElwain (2008)	Based on data from experimental burns of modern plant material.
16	Belcher, Yearsley, et al. (2010)	Based on data from experimental burns of modern plant material.

Table 3.6 Lower atmospheric oxygen limit estimates, and supporting studies.

Fire cannot be sustained without free oxygen in the atmosphere (Pyne et al., 1996), though there are upper and lower limits to the amount of oxygen present that will sustain wildfire, also known as the 'fire window'. Jones and Chaloner (1991) suggested that the fire window comprises atmospheres which contain 15-35% oxygen. Various studies have estimated that the lower limit of atmospheric oxygen ranges from 7-16%, though 15% is generally the accepted lower limit (**Table 3.6**; Cope and Chaloner, 1980; Wildman et al., 2004; Bowman et al., 2009; Belcher and McElwain, 2008; Belcher, et al., 2010b). The upper limit of atmospheric oxygen ranges between 25-35%; above this level of atmospheric oxygen, wildfires would rage and prevent the recovery of vegetation (**Table 3.7**; Watson, 1978; Lenton and Watson, 2000). Key burning experiments by Belcher and McElwain (2008) helped to establish the 15% lower limit and computer

Upper Oxygen Limit (% of atmosphere)	Reference	Notes
25	Watson et al. (1978)	Based on experimental work and derived as a function of both fuel moisture and oxygen level.
25-35	Lenton and Watson (2000)	Based on computer modelling experiments.
35	Lenton (2003)	Based on computer modelling experiments and previously-published work by other authors in this table.

Table 3.7 Upper atmospheric oxygen limit estimates, and supporting studies.

modelling by Lenton (2003) helped to establish the 35% upper limit.

Increased temperatures are required during ignition and afterwards to enable the wildfire to spread, along with a sufficient source of fuel (i.e. vegetation). If there is not enough fuel or heat, then the wildfire will either fail to ignite, or will burn out shortly after ignition. Work by Belcher et al. (2005) has shown that while increased temperatures are required for wildfires to catch alight, it is the oxygen content of the atmosphere which is a much more important factor in destruction of vegetation by wildfires. Different types of vegetation have different susceptibilities to ignition, and differ in their ability to spread a wildfire (e.g. Albini, 1976; Uhl and Kauffman, 1990; Bond and van Wilgen, 1996; McElwain et al., 2007; Belcher et al., 2010). The behaviour of different vegetation types as wildfire fuel is discussed in more detail in the following section.

3.5.3.2. Factors Influencing Wildfire Activity Level

The duration, extent, and intensity of a wildfire is affected by multiple factors, often interacting with one another (**Figure 3.10**). A simplified explanation is that as the availability of fuel, oxygen, heat, and ignition sources increases, so does the level of wildfire activity; however, each of these factors are, themselves, influenced by other factors (**Table 3.8**).

Different types of vegetation have different properties, making some types more susceptible to burning during wildfires than others. Increased availability of flammable vegetation is linked to an increased level of wildfire activity (e.g. Batchelder, 1967; Scott, 2000, and references therein; McElwain et al., 2007). High flammability is linked to both plant moisture content and leaf surface area.

As one might expect, the higher the moisture content of a plant, the less likely it is to ignite or sustain a wildfire (e.g. Uhl and Kauffman, 1990; Belcher and McElwain, 2008). Fire calorimetry experiments by Belcher et al. (2010) have shown that as leaf surface area increases, flammability decreases, a finding that is supported by other published studies (e.g. Bond and van Wilgen, 1996; Steinthorsdottir et al., 2011; Petersen and Lindström, 2012). The ideal vegetation for fuelling wildfires comprises plants with low moisture contents and small leaf surface areas. Narrow-leaved plants are often associated with higher atmospheric temperatures, which also contribute to increased levels of wildfire activity.

As outlined in the previous section (**Section 3.5.3.1.**; p. 80), there are upper and lower limits to the volume of atmospheric oxygen required to initiate and sustain wildfire activity. Above the lower limit of 15% oxygen, studies show that as atmospheric oxygen content increases, so does the level of wildfire activity (e.g. Pyne et al., 1996; Lenton and Watson, 2000; Scott, 2010). Models by Belcher et al. (2010) show that below 18.5% atmospheric oxygen, wildfire activity levels would be low, but sharply increase between 19% and 22%. The authors do not place an upper limit on the amount of atmospheric oxygen, but suggest that wildfire activity would still continue above an atmospheric oxygen concentration of 22%, though the level would not increase much. Upon reaching an upper limit of 35% atmospheric oxygen, the level of wildfire activity would likely be so high that it would be incompatible with a sustained flora (e.g. Lenton, 2003).

Concentrations of atmospheric carbon dioxide have a negative relationship with wildfire activity levels: as atmospheric CO_2 goes up, atmospheric O_2 goes down, decreasing the amount of oxygen available for wildfires (e.g. Scott and Glasspool, 2006; Belcher et al., 2010a). However, increased atmospheric carbon dioxide is linked with increased atmospheric temperatures, which is positively linked with wildfire activity.

Air temperature has a positive relationship with wildfire activity levels. Studies show that increased temperatures are often associated with increased storminess (e.g. Reeve and Toumi, 1999; Power et al., 2007) which, in turn, are associated with increased numbers of lightning strikes, increasing the likelihood of ignition (e.g. Belcher, Mander, et al., 2010). A study by Price and Rind (1994)
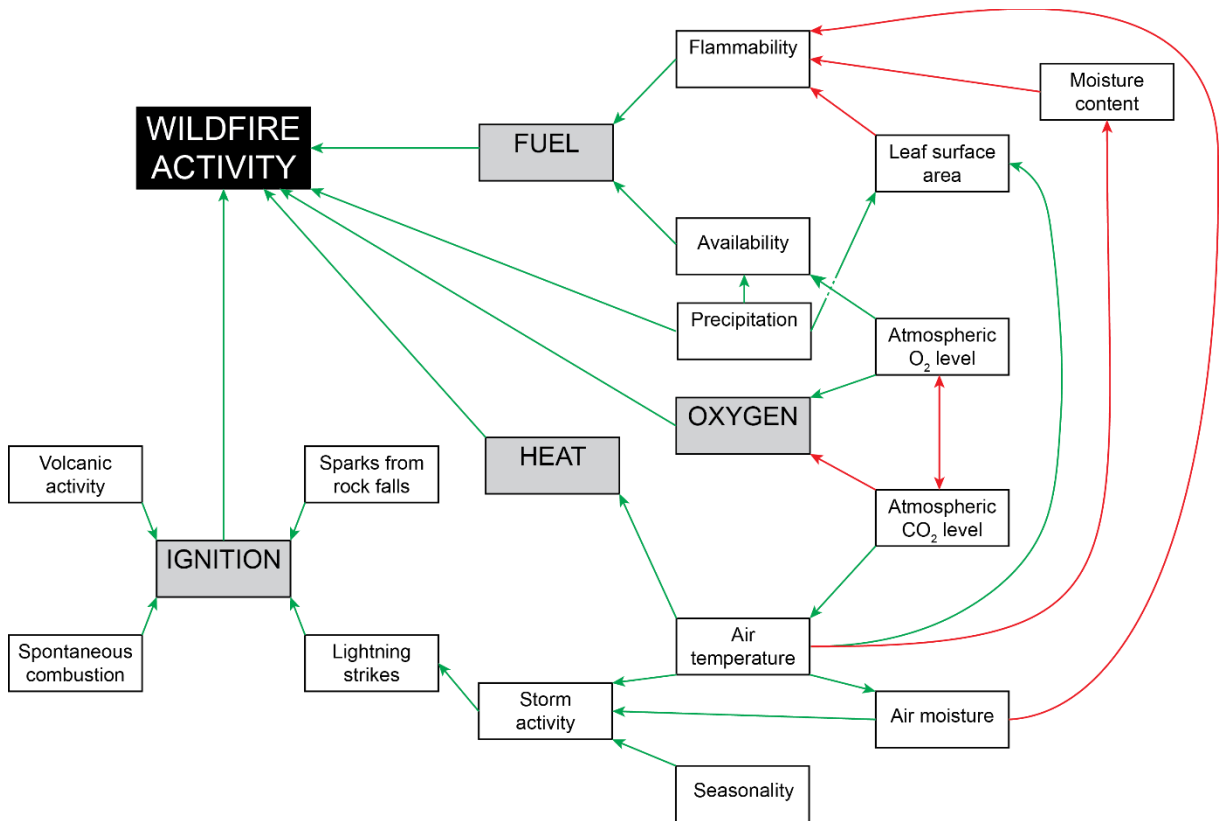
Figure 3.10 Diagram showing how various factors affect wildfire activity levels. Green arrows indicate a positive relationship; red arrows indicate a negative relationship.

has also shown that higher air temperatures are linked to increased drying of vegetation, increasing its flammability.

Increasing the chances for ignition of plant material increases the likelihood of wildfires initiating and sustaining. Wildfires can sometimes be initiated by volcanic activity, rock falls or spontaneous combustion (e.g. Batchelder, 1967; Scott, 2000), but are most commonly initiated by lightning strikes during storms. Increasing storm activity increases the number of lightning strikes that occur, and is affected by air moisture, and seasonality. Increasing air moisture and seasonality are both associated with increased storminess (e.g. Petersen and Lindström, 2012), however, increased storminess can also be linked to increased levels of precipitation which can limit the initiation and extent of wildfires (e.g. Price and Rind, 1994).

	Correlation with wildfire activity		References
FUEL			
Availability	Positive	Increasing amount of vegetation increases the amount of fuel available.	Sanford et al., 1985; Batchelder, 1967; Scott, 2000; Glasspool and Scott, 2010
		Not all vegetation is fuel. Dependent upon environmental conditions, and vegetation type; Narrow leaves associated with higher temperatures	Price, 2000; McElwain et al., 2007; Belcher, Mander, et al., 2010; Steinthorsdottir, Jeram, et al., 2011
Flammability	Positive	Increasing vegetation flammability increases likelihood of initiating and sustaining wildfires	
Moisture content	Negative	Increasing moisture content decreases plant flammability	Albini, 1976; Watson, 1978; Uhl and Kauffman, 1990; Jones and Chaloner, 1991; Whelan, 1995; Scott, 2000; Scott and Glasspool, 2006; Belcher and McElwain, 2008; Glasspool and Scott, 2010
Leaf surface area	Negative	Increasing leaf surface area decreases plant flammability	Bond and van Wilgen, 1996; Price, 2000; Cornelissen et al., 2003; Belcher, Mander, et al., 2010; Steinthorsdottir, Jeram, et al., 2011; Petersen and Lindström, 2012
ATMOSPHERIC COMPOSITION			
Atmospheric O_2 concentration	Positive	Increasing atmospheric O_2 concentrations increases the availability of oxygen required for fire	Watson, 1978; Cope and Chaloner, 1980; Clark and Russell, 1981; Cope and Chaloner, 1981; Berner and Canfield, 1989; Chaloner, 1989; Scott and Jones, 1991; Pyne et al., 1996; Lenton and Watson, 2000; Scott, 2000; Berner et al., 2003; Scott and Glasspool, 2006; Scott, 2010
Atmospheric CO_2 concentration	Negative	Increasing atmospheric CO_2 concentrations decreases the availability of oxygen required for fire, but increasing atmospheric CO_2 concentration can cause air temperatures to rise	Pyne et al., 1996; Scott, 2000; Scott and Glasspool, 2006; Belcher, Mander, et al., 2010
HEAT			
Air temperature	Positive	Increasing air temperature increases storminess	Reeve and Toumi, 1999; Power et al., 2007; Belcher, Mander, et al., 2010; Petersen and Lindström, 2012
		Increasing temperatures increases air moisture	Belcher et al., 2010a
		Increasing air temperature increases drying of vegetation	Price and Rind, 1994

Table 3.8 Summary of factors affecting wildfire activity levels and supporting references.

	Correlation with wildfire activity		References
IGNITION			
Lightning strikes	Positive	Increasing number of lightning strikes increases chance of ignition	Batchelder, 1967; Komarek, 1967; Watson, 1978; Cope and Chaloner, 1980; Pyne et al., 1996; Tinner et al., 1998; Reeve and Toumi, 1999; Scott, 2000; Jones et al., 2002; Scott and Glasspool, 2006; Belcher and McElwain, 2008; Glasspool and Scott, 2010; Petersen and Lindström, 2012
Storm activity	Positive	Increasing storm activity increases number of lightning strikes	Price and Rind, 1994; Belcher, Mander, et al., 2010; Petersen and Lindström, 2012
Volcanic activity	Positive	Increasing volcanic activity increases chance of ignition	Batchelder, 1967; Scott, 1988, 1990, 2000, Scott and Glasspool, 2005, 2006
Rock Falls	Positive	Increasing rock falls increases chance of ignition from sparks	(Batchelder, 1967; Scott, 2000)
Spontaneous combustion	Positive	Increasing spontaneous combustion increases chance of ignition	(Batchelder, 1967; Scott, 2000)
OTHER			
Precipitation levels	Negative	Increasing precipitation decreases number and extent of wildfires	Price and Rind, 1994
Seasonality	Positive	Increases storminess	Petersen and Lindström, 2012
Humidity	Positive; negative	Increasing air moisture increases storminess. Increasing humidity decreases combustibility of vegetation	Power et al., 2007; Petersen and Lindström, 2012 Batchelder, 1967; Scott, 2000

Table 3.8 (continued) Summary of factors affecting wildfire activity levels and supporting references.

It is evident that there is a complex relationship between environmental factors and the level of wildfire activity, all of which must be taken into consideration when interpreting wildfire activity records. However, this relationship can be simplified if wildfire activity levels increase, then there must have been an increase in fuel, oxygen, heat or ignition sources, or any combination of these four factors.

3.5.4. Wildfire Activity During the Early Jurassic

3.5.4.1. The Triassic-Jurassic Boundary

There are a limited number of published fossil charcoal abundance and pyrolytic PAH concentration studies spanning the T-J Boundary. Data from a number of sites in Europe and Greenland show evidence of increased wildfire activity across the T-J Boundary in the form of increased abundances of fossil charcoal and/or increased concentrations of pyrolytic PAHs in sediments.

Fossil charcoal in the Polish Basin has already been the subject of a 2009 study by Marynowski and Simoneit (2009), in combination with pyrolytic PAHs. Total organic content (TOC) and the presence of pyrolytic PAHs in samples from the Sołtyków outcrop were analysed, along with samples from the Upper Gromadzice outcrop (Hettangian) and Kamien Pomorski IG-1 core (Norian-Hettangian). Marynowski and Simoneit (2009) found elevated levels of TOC and pyrolytic PAHs in the lower sections of both the Sołtyków and Upper Gromadzice outcrops. Three different periods of elevated TOC and PAHs were found in the Kamien Pomorski IG-1 core: one in Rhaetian-aged samples, the other two in Hettangian-aged samples. The authors suggest that the elevated levels of TOC and PAHs, along with the presence of macrofossil charcoal, is evidence for periods of elevated wildfire activity in the Polish Basin both before and after the Triassic-Jurassic Boundary, but do not discuss the possible causes of the increased levels of wildfire activity.

Belcher et al. (2010) analysed fossil charcoal abundance across the Triassic-Jurassic transition at Astartekløft, Greenland, as well as vegetation type. The authors found a five-fold increase in fossil charcoal abundance across the T-J Boundary, following a change from less flammable leaf types in the Triassic to more flammable leaf types at the T-J Boundary. The authors sampled beds from the same depositional setting to eliminate the possibility of changes in fossil

charcoal abundance occurring as a result of changing environment. Belcher et al. (2010) attributed the rise in fossil charcoal abundance to an increase in wildfire activity due to a change from less flammable to more flammable vegetation types at Astartekløft. The authors suggest that the change in vegetation type to more flammable leaf morphologies could have been caused by the extinction of less flammable plants due to climate change (global warming and its associated effects) at the T-J Boundary. Global warming at the TJB would have also likely increased the frequency of lightning strikes and ignition of wildfires, according to Belcher et al. (2010). To summarise, the Belcher et al. (2010) study shows an increase in fossil charcoal abundance across the Triassic-Jurassic Boundary which the authors suggest is most likely caused by climate-driven changes in vegetation type leading to an increase in wildfire activity and increase in charcoal production.

A study of fossil charcoal from deposits in the Danish Basin by Petersen and Lindström (2012) found an increase in average inertinite (fossil organic matter particles high in carbon matter showing preserved original structures with high reflectance values, analogous to modern charcoal; ICCP (2001)) content from ~17% to ~75% in sediments spanning the Triassic-Jurassic Boundary, along with the presence of pyrolytic PAHs. Samples were collected from coal and coaly beds interpreted to have been deposited in a mire-type environment. A change from forested mires to fern- and shrub-dominated mires across the Triassic-Jurassic Boundary in the Danish Basin is also documented by the authors. Petersen and Lindström (2012) propose two possible causes for the increase in wildfire activity: CAMP volcanic activity forcing a warmer climate, and the establishment of a seasonal climate and large marine area increasing water vapour and, in turn, increasing storm activity and lightning strikes.

Van de Schootbrugge et al. (2009) performed geochemical analyses of samples from the Mariental core, located in northern Germany, and found increased amounts of PAHs in the Triletes Beds of Triassic-Jurassic Boundary age. However, palynological analyses of the samples did not find coinciding increased amounts of black opaque phytoclasts that could be identified as charcoal. Van de Schootbrugge et al. (2009) analysed the ratios of various PAHs present to determine the origin of the PAHs and concluded that, due to high coronene to benzo(a)pyrene ratios, the PAHs present in the Mariental core samples likely

originated from a source other than wildfires; they also suggest that increased wildfire activity in the Late Rhaetian is unlikely due to humid environmental conditions concluding that the increased level of PAHs present in the Triletes Beds (spanning the T-J Boundary) are likely to have been produced by the intrusion of CAMP basalts into sediments, causing incomplete combustion of buried organic matter, and not by increased wildfire activity.

3.5.4.2. The Toarcian Oceanic Anoxic Event

There are also a limited number of published studies examining wildfire activity during the Toarcian, in particular across the Oceanic Anoxic Event. Fossil charcoal and pyrolytic PAH concentration datasets exist from a small number of sites within modern-day Europe, though the authors of these studies do not necessarily discuss the data in terms of wildfire activity levels. One study that does examine wildfire activity across the Toarcian OAE, in the form of changes in fossil charcoal abundance, is by Baker et al. (2017).

Baker et al. (2017) examined fossil charcoal abundance at sites in Portugal and Wales, UK, and found increased abundances prior to and after the Toarcian OAE, with a generally low abundance of fossil charcoal during the Toarcian OAE. The increased abundances of fossil charcoal coincide with relatively positive $\delta^{13}C_{org}$ values, and the low abundances with extremely negative $\delta^{13}C_{org}$ values which coincide with the OAE. The authors interpret these two records of fossil charcoal abundance as indicating elevated levels of wildfire activity at the beginning of the Toarcian OAE, and afterwards, during the recovery phase. Baker et al. (2017) suggest that wildfire activity, and therefore the production of charcoal, was driven by increasing atmospheric oxygen levels, and formed a positive feedback loop, driving recovery from the Toarcian OAE.

Fossil charcoal has been found in Toarcian-aged sediments from the island of Bornholm, Denmark, by Hesselbo et al. (2000) though the authors make no mention of wildfire in the study. Additional studies of charcoalified and coalified leaf fossils from Bornholm by McElwain et al. (2005) suggest that the fossil charcoal record at this site is incompatible with an elevated level of wildfire activity during the Toarcian due to indicators of wetter climate.

A wide range of polycyclic PAHs have been detected in Early Toarcian-aged sediments from Yorkshire, UK, by French et al. (2014), but there is a lack of fossil charcoal data and the authors make no interpretation of the data in terms of wildfire activity. Elevated concentrations of pyrolytic PAHs correlate with the *tenuicostatum* ammonite biozone. Correlation of the pyrolytic PAH concentration data with $\delta^{13}C_{org}$ data from Hesselbo et al. (2007) suggests that the elevated pyrolytic PAH concentrations occur prior to the Toarcian OAE. A smaller increase of pyrolytic PAH concentrations at the end of the *exeratum* ammonite subzone appears to correlate with the end of the Toarcian OAE, and a return to more positive $\delta^{13}C_{org}$ values.

A record of wildfire activity in the Polish Basin during the late Pliensbachian and earlier Toarcian by Rybicki et al. (2016) shows co-occurrences of inertinite, fossil charcoal, and unsubstantiated PAHs, which the authors suggest are evident of wildfire activity. A lack of stratigraphic information in the study makes it difficult to compare the authors' findings with other wildfire records from the Toarcian.

It is evident that there are a lack of published datasets relating to wildfire activity during the Toarcian and across the Triassic-Jurassic Boundary. There is great scope for additional work to be carried out investigating the wildfire activity records of these time periods.

3.6. The BIT and MBT'-CBT indices

A detailed discussion of the background of the BIT and MBT'-CBT indices is provided in **Chapter 8, Sections 8.3.2. – 8.3.4.**

3.6.1. The BIT Index

The Branched and Isoprenoid Tetraether (BIT) Index is a proxy used for estimating the input of soil organic matter in sediments, developed by Hopmans et al. (2004). Glycerol dialkyl glycerol tetraethers (GDGTs) are a type of lipid thought to be derived from terrestrial soil bacteria (Peterse et al., 2012) and known to be derived from marine planktonic archaea (Hopmans et al., 2004) and can be found in immature sediments. Branched GDGTs are usually produced by terrestrial organisms, though some branched GDGTs can be produced *in situ* in

marine sediments; isoprenoid GDGTs are produced by marine organisms (Peterse et al., 2009). The presence of GDGTs in sediments is detected using high performance liquid chromatography/atmospheric pressure positive ion chemical ionization mass spectrometry (HPLC/APCI-MS). The BIT Index is based on the relative abundance of 3 branched GDGTs in comparison to the isoprenoid GDGT crenarchaeol.

In general, the higher the BIT Index, the greater the input of terrestrial organic matter to the sediments analysed. There are concerns that isoprenoid GDGTs can be produced in terrestrial environments as well as marine, calling into doubt the efficacy of this proxy (Xie et al., 2012; Weijers, Schouten, van den Donker, et al., 2007).

The BIT Index proxy was developed using Recent surface sediment samples and is best used on immature sediments (Hopmans et al., 2004). As a result, it is commonly used on relatively young sediments (e.g. Cenozoic) and is more rarely used on older sediments. However, branched GDGTs and crenarchaeol have both been detected in sediments of Cretaceous age (Kuypers et al., 2001; Hopmans et al., 2004), suggesting that the BIT Index can be used on older (e.g. Mesozoic) immature sediments. Jenkyns et al. (2012) successfully detected branched GDGTs in and calculated BIT indices from Middle Jurassic-Early Cretaceous-age sediments as part of a study reconstructing sea-surface temperatures. Robinson et al. (2017) attempted to analyse BIT Index values of sediments of Sinemurian and Pliensbachian age (~199-183 Ma), though the amount of branched GDGTs in these Early Jurassic sediments was either below the limit of detection or not abundant enough to be quantified.

3.6.2. The MBT'-CBT Index

The MBT'-CBT proxy is a revision by Peterse et al. (2012) of the original MBT-CBT proxy (methylation index and cyclisation ratio of branched tetraethers) by Weijers et al. (2007) and is used for reconstructing palaeotemperature and soil pH. A study by Weijers et al. (2007) showed that the assemblage of branched GDGTs *in situ* is related to mean annual air temperature (MAAT) and soil pH. The authors found that the number of methyl groups in these

compounds is related to MAAT, and that the number of cyclopentane moieties is related to soil pH. Weijers et al. (2007) developed the Methylation index of Branched Tetraethers (MBT) and Cyclisation ratio of Branched Tetraethers (CBT) to quantify the relative amounts of methyl groups and cyclopentane moieties, respectively, in branched GDGTs. Peterse et al. (2012) revised these original indices using additional data from soil studies to produce the updated MBT' and CBT indices.

Peterse et al (2012) also updated the equations used to calculate mean annual air temperature and soil pH using their revised MBT' and CBT indices. The revised equations by Peterse et al. (2012) are now the standard formulae used for reconstructing MAAT and soil pH from branched GDGTs.

CHAPTER 4 LABORATORY METHODS USED IN THIS THESIS

4.1. Single-phytoclast δ¹³C Measurements

4.1.1. St Audrie's Bay, UK, Samples

Organic matter was liberated from the sediments using the acid digestion method used for fossil charcoal abundance quantification studies at the wildFIRE Lab, University of Exeter, by the author and M. Grosvenor; a detailed discussion of this method is provided in **Section 4.2.1.** Bulk rock samples were treated with 37% hydrochloric acid and 40% hydrofluoric acid to remove all carbonate and silicate material, respectively. The samples were then washed until neutral and the remaining organic matter sieved using a 125 μm mesh into a coarse fraction and a fine fraction.

Up to ten phytoclasts from the coarse fraction (>125 μm) of each sample were described, photographed, and picked (**Figure 4.1**). A Wild Heerbrugg binocular stereo microscope with reflected and transmitted light sources, located at Camborne School of Mines, University of Exeter, was used. The picked phytoclasts were assigned a new sample number each and stored separately until analysis.

A newly-developed technique combining laser ablation, nano-combustion gas chromatography and isotope ratio mass spectrometry (LA/nC/GC/IRMS) by van Roij et al., (2017) was used to measure the carbon-isotope ratios of the individual phytoclasts at the Department of Earth Sciences, Utrecht University (**Figure 4.2**). Prior to the actual measurements being made, the phytoclasts were prepared for analysis. Fourteen phytoclasts were placed and then pressed onto a nickel disc using a hydraulic press at a pressure of ~1 bar. The remaining eleven phytoclasts were placed directly onto the nickel disc and were not pressed (**Table 4.1**).

A piece of polyethylene (PE) film standard was then placed next to the phytoclast on the nickel disc. The standard material used for the analyses is the international IAEA-CH-7 polyethylene standard. The PE standard has a certified δ¹³C value of
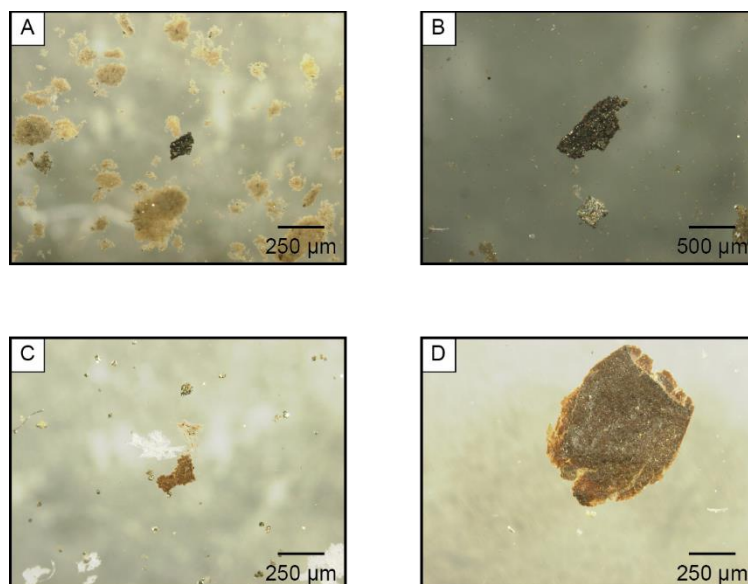
Figure 4.1 Photographs of St Audrie's Bay phytoclasts suspended in water under reflected and transmitted light. A) StAB1, fragment 3, non-structured amorphous phytoclast; B) StAB40, fragment 2, non-structured amorphous phytoclast; C) StAB205, fragment 5, non-structured amorphous phytoclast; StAB206, fragment 6, non-structured amorphous phytoclast. Non-structures amorphous phytoclasts are thought to be derived from woody plant parts.

-32.151 ± 0.050‰ (1σ), relative to the international Vienna Pee Dee Belemnite (VPDB) standard (Coplen et al., 2006).

An individual nickel disc holding both a phytoclast and piece of PE film was placed into the sample chamber and flushed with helium until the background argon and carbon dioxide levels stabilised. Once the background gas levels were stable, the ablation sequence was started. A range of different ablation sequences were used during this pilot study; each involved bookending the sequence with three measurements of reference gases and at least one measurement of the PE standard. Multiple ablations and measurements of both the PE film and phytoclast were made in each ablation sequence.

The laser energy setting was varied between low energy (~25 kV) and high energy (~27 kV) during the pilot study (**Table 4.1**). Phytoclasts were approached from the side with the laser during ablation.

The peak areas measured from the ablation of the reference gases, PE film, and phytoclast sample were converted into $\delta^{13}C_{instrument}$ values. The $\delta^{13}C_{instrument}$
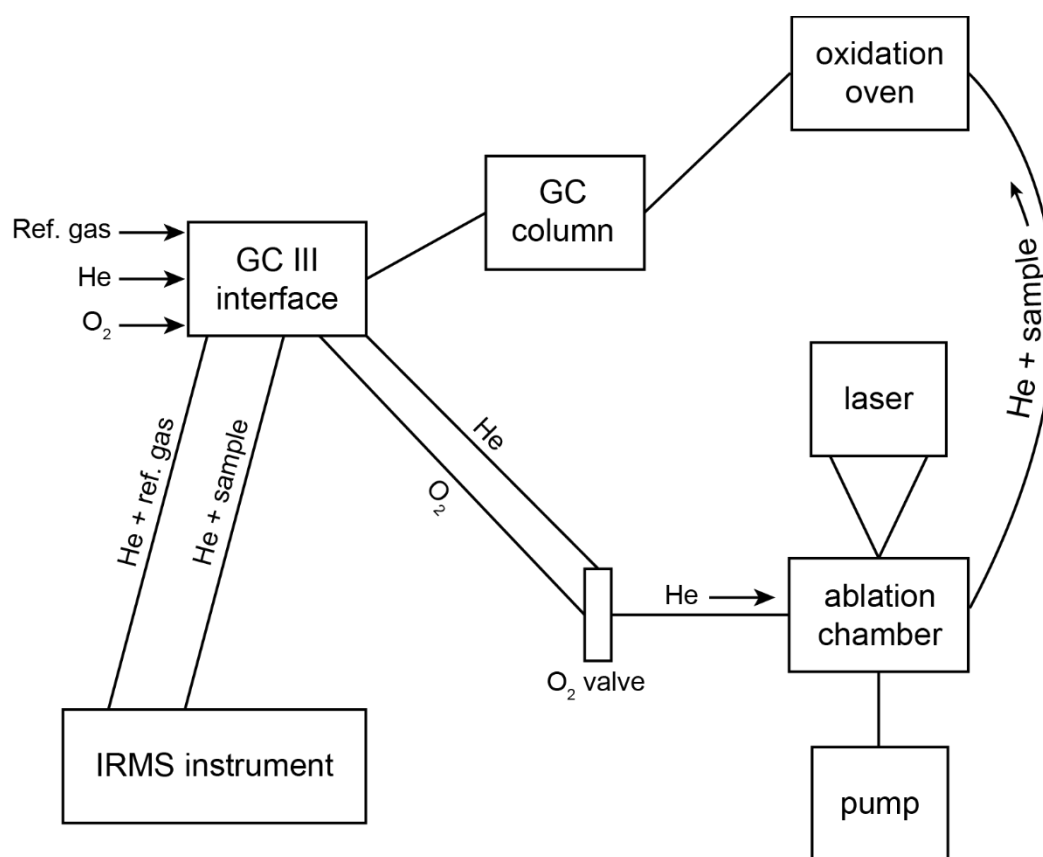
Figure 4.2 A schematic diagram of the LA/nC/GC/IRMS system developed by van Roij et al. (2017). GC = gas chromatography; He = helium; Ref. gas = reference gas. Redrawn from Figure S1 (van Roij et al., 2017).

values calculated by the software were detrended ($\delta^{13}C_{detrend}$) and then corrected for instrument drift ($\delta^{13}C_{corr}$). The final corrected $\delta^{13}C$ values ($\delta^{13}C_{corr}$) are reported and discussed in this thesis.

A total of 155 PE standard measurements were taken during the pilot study and were found to show a nonlinear relationship with peak size. These $\delta^{13}C_{insturment}$ values were detrended relative to peak size to avoid the effect of peak size distorting reported $\delta^{13}C$ values. The PE standard $\delta^{13}C_{insturment}$ values were detrended using the nonlinear least squares fit method (obtained using R software package), resulting in **Equation 4.1**:

(4.1) $\delta^{13}C_{detrend} = \delta^{13}C_{instrument} - \log(\text{peak area, base} = 3.068396)$

Sample	Height	Phytoclast	Phytoclast pressed?	Laser energy
		1A	Yes	Low
		2A	Yes	Low
		3A	Yes	Low
StAB205	12.7	2B	No	Low
		3B	No	Low
		4B	No	Low
		5B	No	Low
		1	No	Low
		2	No	Low
		3	No	Low
		3	No	High
StAB206	13.0	3	No	Low
		1	Yes	Low
		2	Yes	Low
		5	Yes	High
		4	Yes	High
		6	Yes	High
StAB1	16.1	1	No	Low
		3	No	Low
		1	Yes	High
		2	Yes	High
StAB40	24.2	3	Yes	High
		4	Yes	High
		5	Yes	High
		6	Yes	High

Table 4.1 Pressing and laser energy settings used for the St Audrie's Bay phytoclasts analysed in the pilot study.

This detrending calculation (**Equation 4.1**) was then applied to all $\delta^{13}C_{instrument}$ measurements (standards, reference gases, samples) in the pilot study to eliminate the influence of peak area on $\delta^{13}C$ value.

The PE standard has a certified $\delta^{13}C$ value of -32.151‰. Reported PE standard $\delta^{13}C_{detrend}$ values deviated from the certified value as a result of instrument drift. By correcting the PE $\delta^{13}C_{detrend}$ values for instrument drift, it was then possible to

correct the reference gas and sample $\delta^{13}C_{detrend}$ values for instrument drift. All $\delta^{13}C_{detrend}$ values were then corrected for this drift using **Equation 4.2**:

$$(4.2) \quad \delta^{13}C_{corr} = \delta^{13}C_{detrend} - (\delta^{13}C_{PE(av)} + 32.151)$$

The average PE $\delta^{13}C$ value $(\delta^{13}C_{PE(av)})$ of all detrended PE $\delta^{13}C$ measurements in a sample run was calculated to measure the deviation from the certified value. The certified $\delta^{13}C$ absolute value of the PE standard, 32.151, was then added to the average PE $\delta^{13}C_{detrend}$ value. Following this step, **Equation 4.2** could then be used correct all $\delta^{13}C_{detrend}$ values in a run for instrument drift. The value of $\delta^{13}C_{PE(av)}$ + 32.151 was then subtracted from all of the $\delta^{13}C_{detrend}$ values in a run to calculate the corrected $\delta^{13}C$ value $(\delta^{13}C_{corr})$. After drift correction, the average value of the PE $\delta^{13}C_{corr}$ values measured in a run should now be -32.151‰. While detrending the data involved processing all measured PE $\delta^{13}C_{instrument}$ values from every run together, correcting the $\delta^{13}C_{detrend}$ values had to be processed per run as the extent of instrument drift varied between runs.

Following the process of measuring > detrending > correcting, the $\delta^{13}C$ values were then ready for analysis and interpretation. The full results are discussed in **Chapter 5, Section 5.5.1.**

4.1.2. Llanbedr, Wales, UK, Samples

Ten bulk rock sediment samples were processed at the wildFIRE Lab, University of Exeter, by S. Baker and M. Grosvenor, using the method described in **Section 4.2.1.** Standard acid maceration techniques were used to liberate organic matter from sediment samples (Baker et al., 2017). The organic matter particles were sieved using a 125 µm mesh into a coarse fraction and a fine fraction.

Fifteen phytoclasts were described, photographed and picked from the coarse fraction (>125 µm) of each of the 10 samples (**Figure 4.3**). A Wild Heerbrugg binocular stereo microscope with reflected and transmitted light sources, located at Camborne School of Mines, University of Exeter, was used. Each phytoclast was given a new unique sample number and stored individually until analysis.

Phytoclasts were prepared before $\delta^{13}C$ measurement using the LA/nC/GC/IRMS system. An individual phytoclast was placed in the centre of a nickel disc (6 mm diameter) before an additional disc was placed on top of the phytoclast-bearing
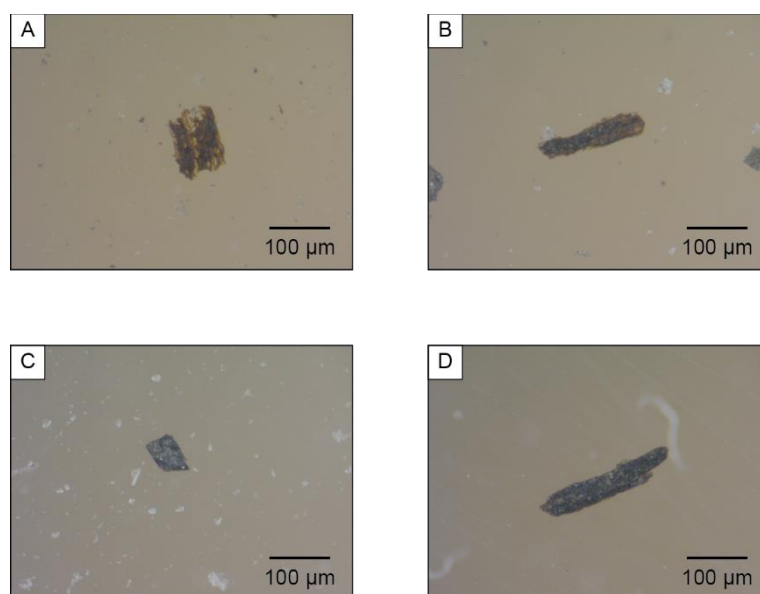
Figure 4.3 Photographs of Llanbedr phytoclasts suspended in water under reflected and transmitted light. A) M2560311; B) M2592714; C) M2729212; D) M276547. Phytoclasts are thought to be derived from woody plant parts.

disc. The two discs were then placed in a hydraulic press and pressed together at a pressure of ~1 bar, to stick the phytoclast to the surface of one of the nickel discs. A piece of polyethylene film standard was then placed onto the nickel disc next to the pressed phytoclast.

A single nickel disc holding both a pressed phytoclast and piece of PE film was placed into the sample chamber, which was then flushed with helium until the background argon and carbon dioxide levels stabilised. Once the background argon and carbon dioxide levels were stable, the ablation sequence was initiated. Three reference gases were run first, followed by one ablation of the PE film, one ablation of the phytoclast sample, a second ablation of the PE film, and the 3 reference gases again.

The peak areas measured during the ablation sequence were then converted to $\delta^{13}C$ values and drift correction calculations performed (**Equation 4.3**).

$$(4.3) \quad \delta^{13}C_{corr} = \delta^{13}C_{instrument} - (\delta^{13}C_{PE(av)} + 32.151)$$

$\delta^{13}C$ measurements of the Mochras PE standards did not show a relationship with peak size and therefore did not require detrending. The reason for this lack of relationship is currently unknown; it may relate to improved ablation quality, or

perhaps the composition of the phytoclasts. The drift-corrected $\delta^{13}C$ values are the values reported for the Llanbedr samples in this thesis, unless stated otherwise.

A random number generator was used to create carbon-isotope curves for the Mochras study section to determine whether the Toarcian OAE negative CIE could be reproduced using one single-phytoclast $\delta^{13}C$ measurement from each sample horizon. Each $\delta^{13}C_{phytoclast}$ measurement within a sample was assigned a number, ordered sequentially starting at 1. Using the =RANDBETWEEN function in Microsoft Excel 2013, a random $\delta^{13}C_{phytoclast}$ measurement was selected from each sample. The randomly-selected $\delta^{13}C_{phytoclast}$ measurements were then plotted against depth. This process was repeated 20 times.

The full results are discussed in **Chapter 5, Section 5.5.2.** (p. 129) The raw data generated is provided in **Appendix A** (p. 308); the full results of the random number generator study is provided in **Appendix B** (p. 356).

4.2. Fossil Charcoal Quantification

4.2.1. Acid Maceration & Sieving

Standard palynological acid maceration techniques were used to extract fossil organic matter from bulk sediment samples (e.g. Belcher et al., 2010; Baker et al., 2017). Hydrochloric (HCl) and hydrofluoric (HF) acids were used to remove carbonate and silicate material, respectively, leaving only fossil organic matter.

Approximately 10 g of bulk sediment sample was placed in a polypropylene sample pot (resistant to HF; 180 ml total volume); samples were kept as whole as possible so as to avoid breaking up organic matter particles into smaller fragments. Samples were initially wetted with ~10 ml of 10% HCl to acidify the samples, before ~50 ml of 37% HCl was added in two stages. The stronger HCl was added in two stages to avoid producing a violent reaction; ethanol was used to slow any reaction that was too violent. The sediment and HCl mixture was then left overnight at room temperature to react, before being topped up with deionised (DI) water and left overnight at room temperature for the particles to settle.

The supernatant liquid was then carefully poured away, leaving only sediment in the sample pot. Approximately 50 ml of 40% HF was then added to the sample in two stages, again, to avoid causing too violent a reaction. Ethanol was used to slow down any reaction that was too violent. The HF and sediment mixture was then agitated for 1 hour at room temperature on a shaker. After this, the samples were left for 72 hours at room temperature to react, before being topped up with DI water and left to settle. The solute would usually settle at the bottom of the sample pot within 1-2 hours, though some samples took up to 24 hours.

The supernatant liquid was then carefully decanted and ~10-20 ml of 37% HCl added to the sample pot to prevent the formation of gels, along with enough deionised water to top up the pot. The samples were then left to settle again (1-24 hours) before the supernatant liquid was decanted and the washing process started. Sample pots were topped up with deionised water and the solute left to settle out of the solution (between 1 and 24 hours) before the supernatant liquid was decanted carefully, avoiding pouring out the particles of organic matter. The washing step was repeated until the solution in each sample pot had reached a neutral pH. Samples were washed between six and fourteen times to become neutral. Neutralised samples were sieved using a 125 μm mesh, collecting both the coarse (>125 μm) and fine fractions (<125 μm) for analysis, with the coarse and fine fractions reflecting local and regional wildfire activity, respectively (e.g. Whitlock, 2001; Sadori and Giardini, 2007; Kawano et al., 2012).

Up to twenty bulk rock samples were processed at a time, with the acid maceration and sieving process taking up to three weeks.

4.2.2. Coarse Fraction Preparation & Particle Quantification

The coarse fraction (>125 μm) of each sample was analysed using a Wild Herring binocular stereo microscope at Camborne School of Mines, University of Exeter, by the author. Under transmitted and reflected light at x50 magnification, the entire sample (organic matter particles suspended in deionised water) was analysed, and the number of charcoal particles in each field of view counted; this process could take up to an hour per sample. Non-charcoal organic matter particles and inorganic matter particles were not counted. The number of charcoal particles per sample was then standardised and expressed as the number of particles per 10 g of bulk rock sediment.

The full results are discussed in **Chapter 6, Section 6.5.1.1.** and **Chapter 7, Section 7.5.1.** The particle counts from all samples is provided in **Appendix C**.

4.2.3. Fine Fraction Preparation & Particle Quantification

The fine fraction (<125 μm) of each sample was used to produce a microscope slide for analysis. The fine fraction was sieved again using a 15 μm mesh to remove the finest material (e.g. clay and pollen) from each sample, allowing for easier analysis of the microscope slides. The organic matter fragments were suspended in a known amount of deionised water and 58 μl of this mixture was dropped onto a glass slide. A cube of glycerine jelly was added to the mixture on the slide before being heated until the glycerine jelly had melted. The melted glycerine jelly and sample were mixed together and heated for a few seconds before a glass cover slip was placed on the sample/jelly mixture, taking care to spread the sample/jelly mixture evenly and to minimise air bubble formation under the cover slip. The whole slide was briefly heated for a third time, and the slide left to set for ~24 hours. The edges of each cover slip were sealed with clear nail varnish.

The fine fraction slides were analysed using a Nikon Polarizing Microscope (model: ECLIPSE E600 POL). Under transmitted light at x20 magnification, ~80-90 fields of view were analysed (~15-46% of total sample area) and the number of both charcoal and non-charcoal organic matter fragments in each field of view were counted; this process took ~1-1.5 hours per slide. Inorganic matter was not counted. After ~50 fields of view, the ratio of charcoal to non-charcoal organic matter fragments stabilised. The total number of charcoal and non-charcoal organic matter fragments counted per slide was then scaled up to express the number of fragments per 10 grams of bulk rock (Belcher et al., 2005). Two individual slides were prepared and analysed for each sample, with the two sets of particle counts being averaged and presented in this thesis.

The full results are discussed in **Chapter 6, Sections 6.5.1.2. – 6.5.1.4.** (p. 154) and **Chapter 7, Section 7.5.1.** (p. 185). The particle counts from all slides is provided in **Appendix C** (p. 360).

4.3. Polycyclic Aromatic Hydrocarbon Quantification

4.3.1. Extraction & Separation of Polycyclic Aromatic Hydrocarbons from Sediments

Samples were prepared at the University of Southampton, Organic Geochemistry and Compound Specific Isotope Ratio Mass Spectrometry Laboratory, under the supervision of J. Whiteside, using a standard extraction technique (e.g. Jiang et al., 1998). Approximately 15 g of bulk rock sample was crushed to a fine, homogeneous powder using an agate pestle and mortar. The total lipid extract (TLE) was taken from the powdered samples using a Dionex ASE 350 Accelerated Solvent Extractor. Approximately 5 g of powdered sample was mixed with clean sand and then placed into an ASE sample chamber. A 1:1 mix of dichloromethane & methanol were then used to obtain the total lipid extract from the samples. The TLE and solvent solution was collected in a large vial (**Figure 4.4**) which was then dried down using a Genevac EZ-2 Centrifugal Evaporator. The dried TLE samples were then transferred to smaller, working vials using ~5 ml of dichloromethane, before being dried down under a constant stream of nitrogen.

The total lipid extract was then separated into three fractions (non-polar, aromatic, and polar molecules) using column separation. The non-polar fraction was separated out first, followed by the aromatic fraction, and then finally the
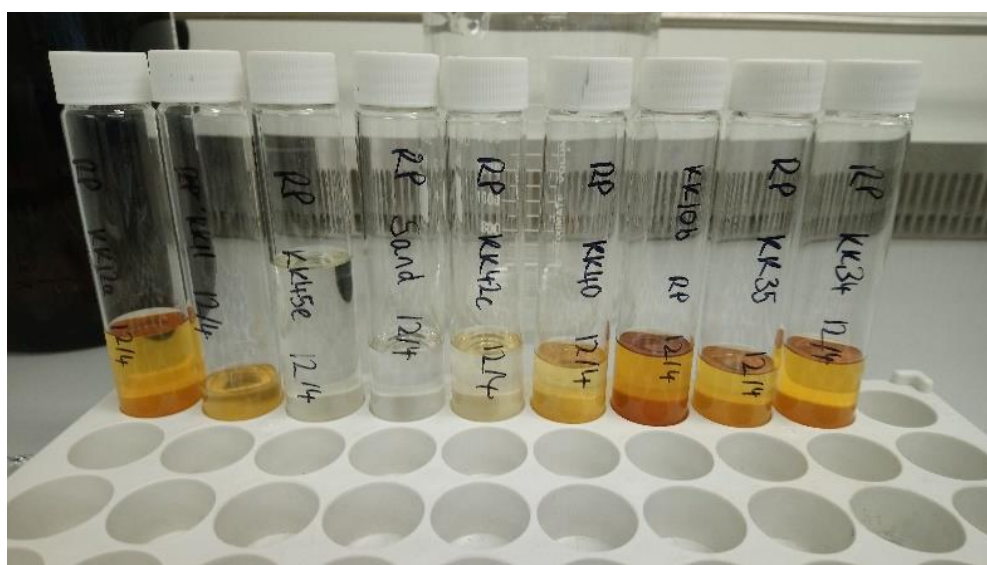
Figure 4.4 TLE after extraction using the Dionex ASE 350 Accelerated Solvent Extractor.
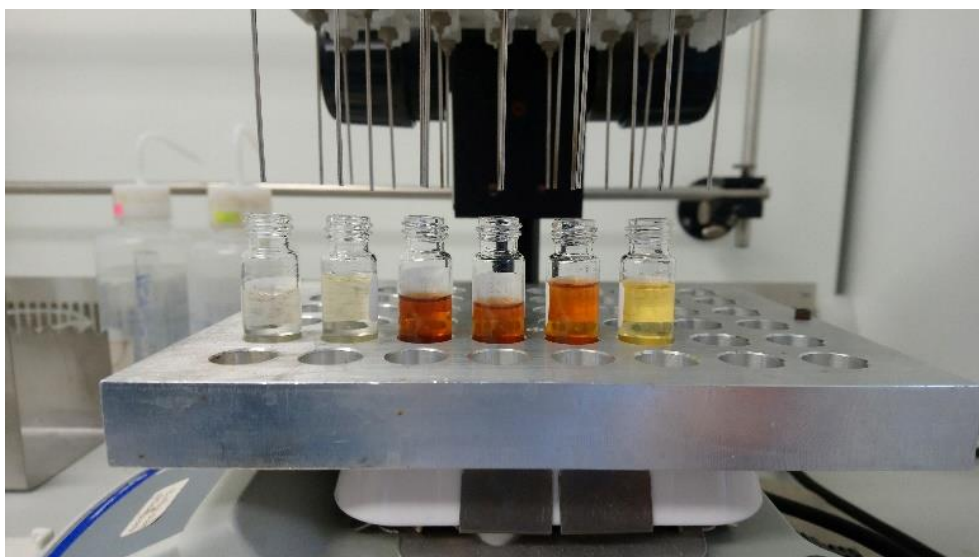
Figure 4.5 Aromatic fractions drying under the nitrogen blow-down system.

polar fraction. The columns used were glass pipettes with a piece of glass cotton at the bottom of the column, and then filled with silica gel. The columns were then saturated with hexane. For each fraction, ~1 ml of solvent was added to the TLE vial, and then slowly dripped through the column using a pipette. An additional ~3 ml of the same solvent was then added to the column, and a constant stream of nitrogen used to push the solvent through the column. The extracted fractions were collected in separate small vials placed underneath the column. A single column was used for the extraction of each fraction from each sample. Pure hexane was used to extract the non-polar fraction from the total lipid extract. A 4:1 mix of hexane and dichloromethane was used to extract the aromatic fraction, and a 1:1 mix of dichloromethane and methanol was used to extract the polar fraction from the TLE.

The separated aromatic fractions (**Figure 4.5**) were dried down until <1 ml of solvent was left in the vials, which was then transferred to a GC-MS vial. The GC-MS vials were then dried down under a constant stream of nitrogen before 200 µl of dichloromethane was added to each GC-MS vial. The GC-MS vials were capped immediately after adding the dichloromethane and stored in a freezer until analysis.

4.3.2. Analysis & Quantification of Extracted Polycyclic Aromatic Hydrocarbons

GC-MS analyses were carried out on a Thermo Scientific TRACE 1310 Gas Chromatograph coupled with a Thermo Scientific TSQ 8000 Triple Quadrupole Mass Spectrometer. A 1 µl sample was injected into the coupled GC-MS system for analysis.

Peak identification of the mass chromatograms was carried out by the comparison of retention times and mass spectra with known standards (**Figures 4.6 – 4.8**).

A total of fifteen different polycyclic aromatic hydrocarbons were identified, including those produced during the pyrolysis of organic matter (8; pyrolytic PAHs), PAHs from a petroleum/bituminous source (6; petrogenic PAHs), and the higher-plant biomarker, retene (see **Table 4.2** for complete list of PAHs identified and quantified).

The abundances of the chosen compounds were calculated by comparison of the peak areas of a known standard (anthracene) with the peak areas of the PAHs from the GC-MS chromatograms (**Equation 4.4**).

The PAH concentration (ng/1 g sediment) was corrected to account for material loss during sample processing. New samples containing only known amounts of anthracene standard were subjected to the same extraction, separation and GC-MS processes as the Polish Basin samples. The abundance of anthracene in these samples was then calculated using the peak areas from the GC-MS chromatograms and **Equation 4.4**.

The concentration of anthracene, as quantified using the GC-MS data, was then compared to the known amounts of anthracene in the starting samples. The loss of anthracene was found to be 20%. The Polish Basin samples were assumed to have lost this proportion of PAHs as well. The PAH concentrations calculated using the peak areas from the GC-MS chromatograms have been corrected for this loss of material (**Equation 4.5**). Any mention of PAH concentration from this point forward refers to the corrected PAH concentrations unless otherwise stated.

Polycyclic aromatic hydrocarbon	Retention time (min)	Molecular weight	Number of aromatic rings	Source
fluorene	18.11	166	3	
phenanthrene	21.65	178	3	
fluoranthene	26.28	202	4	
pyrene	27.01	202	4	Combustion of organic matter
benz-anthracene	31.96	228	4	
benzo(k)fluoranthene	36.64	252	5	
indeno[1,2,3-cd]pyrene	40.90	276	6	
coronene	44.8	300	7	Combustion of organic matter AND petroleum/bitumen
2-methylnaphthalene	12.16	142	2	
1,7-dimethylnaphthalene	14.93	156	2	
2-methylphenanthrene	23.80	192	3	
9-methylphenanthrene	24.10	192	3	Petroleum/bitumen
2,5-dimethylphenanthrene	26.04	206	3	
1-methylpyrene	28.58	216	4	
retene	28.91	234	3	Higher-plant biomarker

Table 4.2 Polycyclic aromatic hydrocarbons identified in this study, including retention time (minutes), molecular weight, number of aromatic rings, and source of the PAHs.

$$(4.4) \quad PAH\ concentration\ (ng\ /1\ g\ sediment) = \frac{\frac{peak\ area + 20000000}{20000000}*200}{grams\ of\ sediment\ processed}$$

$$(4.5) \quad Corrected\ PAH\ concentration\ (ng\ /1\ g\ sediment) = \frac{PAH\ concentation\ (eqtn\ 1)}{0.8}$$

The full results are discussed in **Chapter 6, Section 6.5.2.** (p. 160) and **Chapter 7, Section 7.5.2.** (p. 195). The peak areas, uncorrected PAH concentrations, and corrected PAH concentrations is provided **Appendix D** (p. 365).

1
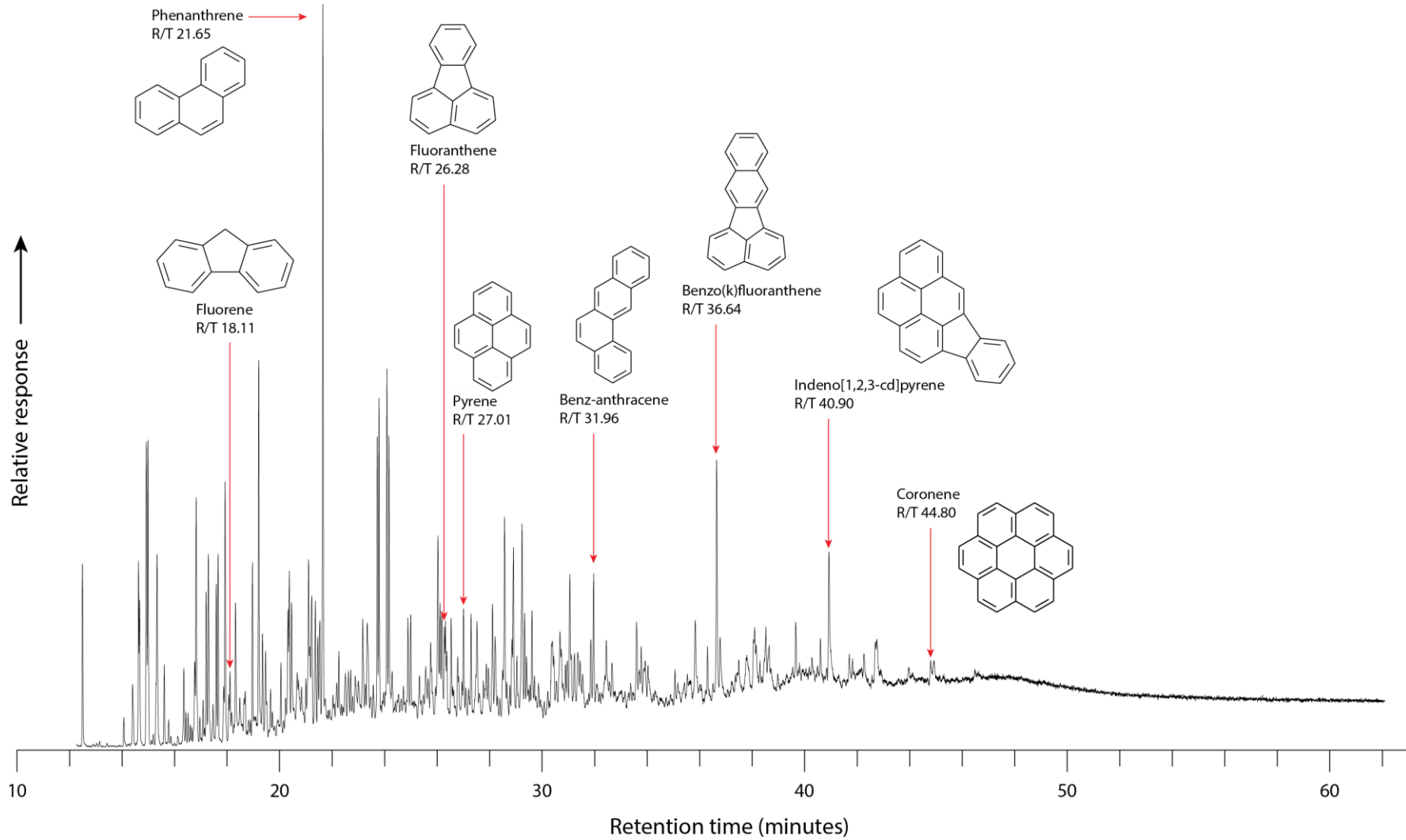
Figure 4.6 Total ion chromatogram (TIC) mass spectra of sample kk_34 showing the peaks associated with the eight pyrolytic PAHs identified, along with their chemical structures and retention times (R/T). N.B. Coronene can also be produced from petroleum and bitumen sources.

1
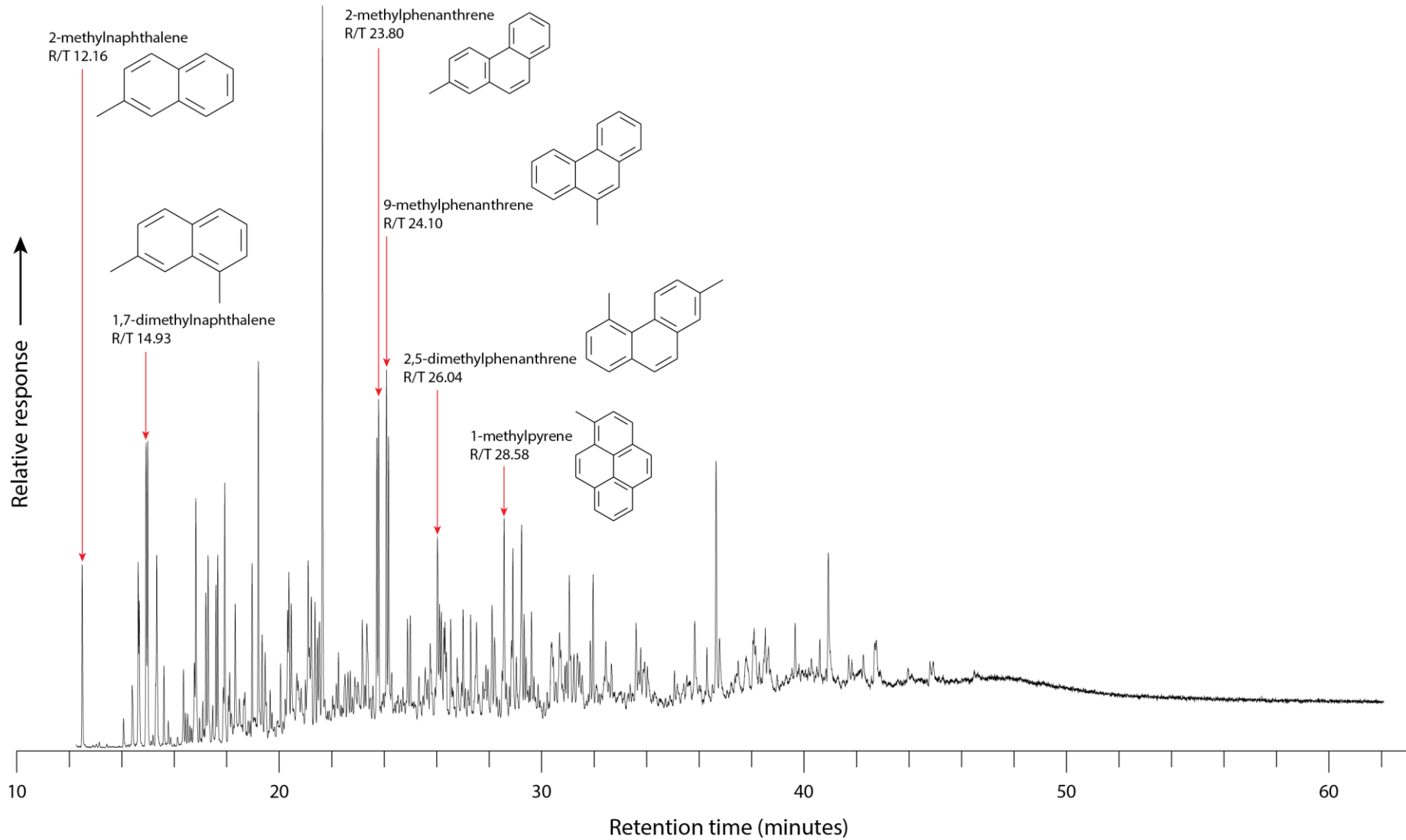
Figure 4.7 TIC mass spectra of sample kk_34 showing the peaks associated with the six petrogenic PAHs identified, along with their chemical structures

and retention times (R/T).

Retene
R/T 28.91

Relative response

Retention time (minutes)

10   20   30   40   50   60

1
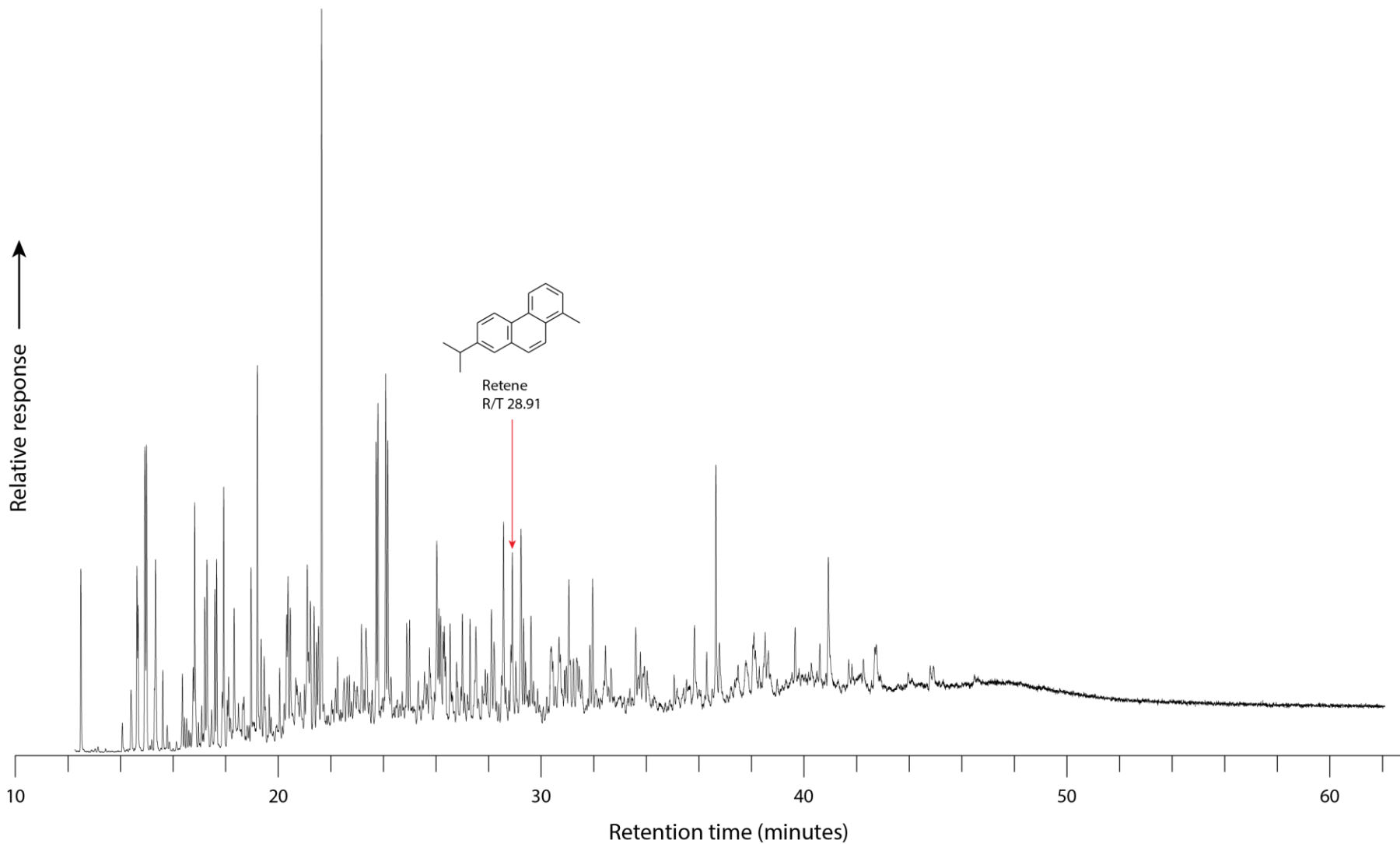
Figure 4.8 TIC mass spectra of sample kk_34 showing the peak associated with the higher-plant biomarker retene, along with its chemical structures and retention time (R/T).

4.4. Carbon-isotope Measurements

4.4.1. Terrestrial Bulk Organic Matter $\delta^{13}C$ Measurements

Bulk rock samples were collected from the Niekłan PIG-1 core for bulk organic matter $\delta^{13}C$ analyses; samples were processed at Camborne School of Mines, University of Exeter. Between 240 and 280 milligrams of each bulk rock sample was crushed to a fine powder using an agate pestle and mortar before decarbonation. Approximately 5 ml of 10% HCl was added to each sample, which was then agitated to ensure thorough mixing of the powder and HCl. Samples were left to react for 24 hours at room temperature before being topped up with deionised water to a total volume of 50 ml. Each sample was centrifuged for 2 minutes at 2500 rpm and then the liquid poured off. The samples were then topped up with deionised water again, and the centrifuge step repeated, bringing the powders to a neutral pH. The neutralised powders were then dried at 40°C for 24 hours to remove all remaining liquid. The dried powders were then reground to a fine homogeneous powder using an agate pestle and mortar for analysis. Carbon- and nitrogen-isotope measurements were carried out at the British Geological Survey Stable Isotope Facility using a Finnigan DELTAplusXP stable-isotope ratio mass spectrometer. Approximately 100 mg of treated powder was measured out into a tin capsule and then analysed using the mass spectrometer. A relatively large quantity of treated powder was analysed due to a lack of carbon-content data; TOC was not determined.

The raw data are provided in **Appendix E** (p. 378).

4.4.2. Macrofossil Plant Material $\delta^{13}C$ Measurements

Macrofossil plant samples were collected from the Niekłań PIG-1 core for carbon-isotope analysis; the samples were processed at Camborne School of Mines, University of Exeter. The macrofossil plant samples are thought to represent vascular plant material from a range of different plant types. The samples were crushed to a fine powder using a porcelain pestle and mortar before being treated for 24 hours at room temperature with ~5 ml of 10% hydrochloric acid to remove any carbonate material present. Samples were then washed several times with deionised water until a neutral pH was reached. The decarbonated and neutralised powders were then dried for 24 hours at 50°C to remove all remaining

liquid. Approximately 1 mg of treated powder was measured out into a tin capsule before placing into an Integra2 combined isotope ratio mass spectrometer and elemental analyser for carbon- and nitrogen-isotope analyses.

4.4.3. Woody Phytoclast δ¹³C Measurements

Bulk rock samples were collected from the Niekłań PIG-1 core for carbon-isotope analysis of picked woody phytoclasts. The samples were prepared by M. Hodbod at the Polish Geological Institute – National Research Institute. Approximately 30-50 mg of bulk rock was crushed and then underwent two rounds of acid digestion, first using cold 30% hydrochloric acid then using 38% hydrofluoric acid. The samples were then washed with a water and hydrogen iodide solution. Cadmium iodide and potassium iodide salt solutions were then used to separate out heavy minerals before the samples were washed with distilled water until neutrality was reached. Woody phytoclast particles were then picked from the remaining organic matter using an optical microscope. The assemblages of picked woody phytoclasts were then analysed at the British Geological Survey Stable Isotope Facility using a Finnigan DELTAplusXP stable-isotope ratio mass spectrometer. All picked woody phytoclasts (<1 mg) from each sample were placed in a tin capsule and then analysed for carbon- and nitrogen-isotope values.

4.5. BIT & MBT'-CBT Indices

4.5.1. Sample Preparation & Analysis

Bulk rock samples were collected from several sites located in the Polish Basin and prepared using a standard extraction method (Lopes dos Santos and Vane, 2016). Samples were cleaned and powdered at Camborne School of Mines, University of Exeter, and the remaining processing and analysis was carried out at Organic Geochemistry Facility at the British Geological Survey.

The surfaces of most bulk rock samples were initially scraped off to reduce the possibility of contamination from modern soil bacteria. The bulk rock samples from the Kozłowice outcrop were highly friable and simply disintegrated when trying to remove the outer surface of the sample. Contamination of the Kozłowice

samples by modern-day soil bacteria is highly likely and have to be taken into consideration when interpreting the results.

Approximately 15 g of bulk rock sample was crushed into a fine homogeneous powder using an agate pestle and mortar prior to extraction using a Dionex 200 automated solvent extractor (ASE). A 9:1 mixture of dichloromethane and methanol was used with the ASE to extract the total lipid extract (TLE) from the powdered samples. The TLE was separated into apolar and polar fractions using column separation. The column separation was carried out using glass pipettes containing aluminium oxide (Al_2O_3). The apolar fraction was extracted using a 9:1 mixture of hexane and dichloromethane, and the polar fraction extracted with a 1:1 mixture of dichloromethane and methanol.

The polar fraction of the TLE was filtered using a polytetrafluoroethylene filter (PTFE, 0.45 µm) prior to analysis using a high-performance liquid chromatography–mass spectrometry (LC–MS) with a Thermo TSQ Quantiva MS instrument coupled to an Ultimate 3000 series HPLC instrument. GDGTs were identified from the chromatograms and converted to concentrations by comparison of the GDGT peak areas with that of an internal standard.

4.5.2. BIT Index Calculations

The Branched and Isoprenoid Tetraether (BIT) Index is a proxy used for estimating the input of terrestrial organic matter in sediments, developed by Hopmans et al. (2004). The BIT Index is based on the relative abundance of 3 branched GDGTs (Ia, IIa, IIIa) in comparison to the isoprenoid GDGT crenarchaeol. The BIT Index is calculated using the following equation (**4.6**):

$$(4.6) \quad BIT = \frac{Ia + IIa + IIIa}{Ia + IIa + IIIa + crenarchaeol}$$

4.5.3. MBT'-CBT Palaeothermometer & Soil pH Reconstructions

The MBT'-CBT proxy is a revision by Peterse et al. (2012) of the original MBT-CBT proxy by Weijers et al. (2007) and is used for reconstructing palaeotemperature and soil pH. Weijers et al. (2007) developed the Methylation index of Branched Tetraethers (MBT) and Cyclisation ratio of Branched Tetraethers (CBT) to quantify the relative amounts of methyl groups and cyclopentane moieties, respectively, in branched GDGTs. Peterse et al. (2012)

revised these original indices using additional data from soil studies to produce the updated MBT' and CBT indices (**Equations 4.7 and 4.8**).

$$(4.7) \quad MBT' = \frac{Ia + Ib + Ic}{Ia + Ib + Ic + IIa + IIb + IIc + IIIa}$$

$$(4.8) \quad CBT = -\log(\frac{Ib + IIb}{Ia + IIa})$$

Peterse et al. (2012) also updated the equations used to calculate mean annual air temperature (**Equation 4.9**) and soil pH (**Equation 4.10**) using their revised MBT' and CBT indices. The revised equations by Peterse et al. (2012) are now the standard formulae used for reconstructing MAAT and soil pH from branched GDGTs.

$$(4.9) \quad MAAT = 0.81 - (5.67 \times CBT) + (31.0 \times MBT')$$

$$(4.10) \quad pH = 7.9 - (1.97 \times CBT)$$

CHAPTER 5 TERRESTRIAL CARBON-ISOTOPE STRATIGRAPHY FOR KEY INTERVALS OF THE EARLY JURASSIC

5.1. Introduction

Carbon-isotope (C-isotope) stratigraphy of the Early Jurassic is a well-studied topic, with much focus on key intervals, such as the Triassic-Jurassic Boundary (201.3 ± 02. Ma; T-J Boundary) and Toarcian Oceanic Anoxic Event (~183 Ma; Toarcian OAE). Notable negative carbon-isotope excursions (CIEs) occur during both of these times, and are recorded in both marine and terrestrial settings from sites across the globe (e.g. Jenkyns, 1988; Hesselbo et al., 2002; Hesselbo, Jenkyns, et al., 2007; Pálfy et al., 2007; Al-Suwaidi et al., 2010; Hesselbo and Pienkowski, 2011).

It is well known that the carbon-isotope composition of plants is influenced by a number of different factors, but most importantly by the carbon-isotope composition of the atmosphere and C-isotope discrimination during photosynthesis (Farquhar et al., 1982, 1989). However, little work has been done to determine how much carbon-isotope values (δ^{13}C) in fossil terrestrial organic matter vary within a sample, and how much this affects the magnitude of carbon-isotope excursions.

A newly-developed technique combining laser ablation, nano-combustion gas chromatography and isotope ratio mass spectrometry (LA/nC/GC/IRMS) (van Roij et al., 2017) provides the opportunity to study δ^{13}C variations of terrestrial organic matter within samples. By using this new method to analyse δ^{13}C values of individual particles of terrestrial organic matter from key Early Jurassic intervals, it will be possible to evaluate the effect of terrestrial plant matter composition on overall bulk organic matter δ^{13}C values.

This newly-developed technique could prove invaluable when investigating the carbon-isotope signatures of organic matter from sediments deposited in environments which experience(d) both marine and terrestrial influences. This new technique could allow for the disentangling of marine and terrestrial organic

matter records. Carbon-isotope analysis of individual organic matter particles could support other methods of organic matter classification and quantification (e.g. hydrogen index), providing a better understanding of organic matter input to marine- and terrestrial-influenced deposition sites. In addition, the coupling of single-phytoclast carbon-isotope data with palynology records could also allow for the generation of carbon-isotope profiles for different types of plants and plant matter. Single-phytoclast carbon-isotope measurements could also prove useful for samples with extremely low organic matter content, where traditional techniques would fail to provide reliable data.

5.2. Aims

This study attempts to capitalise on the use of a recently-developed, novel technique to investigate a number of objectives. With the new data generated using this technique, the following questions are addressed:

- How isotopically-homogeneous are individual phytoclasts?
- How much variation in carbon-isotope values is there between single phytoclasts from the same sediment sample?
- Can single-phytoclast carbon-isotope values be linked to phytoclast appearance?
- How do single-phytoclast carbon-isotope measurements compare against bulk organic matter carbon-isotope measurements from the same sediments?
- How do single-phytoclast carbon-isotope measurements compare against macrofossil wood carbon-isotope measurements from the same time period?
- Is it possible to reproduce the characteristic T-J Boundary negative carbon-isotope excursions and Toarcian Oceanic Anoxic Event negative carbon-isotope excursion with single-phytoclast carbon-isotope measurements?

5.3. Study Sections

5.3.1. Triassic-Jurassic Boundary: St Audrie's Bay, Southwest UK

5.3.1.1. Geological Setting

A mainly marine sedimentary sequence can be found at St Audrie's Bay in the southwest United Kingdom (**Figure 5.1**). The sediments at St Audrie's Bay consist of a thick succession of mudstones and limestones, deposited during the Late Triassic and Early Jurassic. The mudstones and limestones record the upper Rhaetian, entire Hettangian, and lower Sinemurian stages. The Triassic-Jurassic Boundary (201.3 ± 0.2 Ma (Cohen et al., 2013; T-J Boundary) is signified by the first appearance of the Early Jurassic ammonite *Psiloceras spelae* (Hillebrandt and Krystyn, 2009) though it is not present at St Audrie's Bay.

During the Late Triassic-Early Jurassic, the Bristol Channel Basin was located at a mid-palaeolatitude in a shallow sea on the northwest margin of the Tethys Ocean (figure 1; Korte et al., 2015). Sediment deposition occurred in a shallow marine environment (Hesselbo et al., 2004), though the abundance of mudstones suggests that water depth was sufficient enough that the seafloor was below the
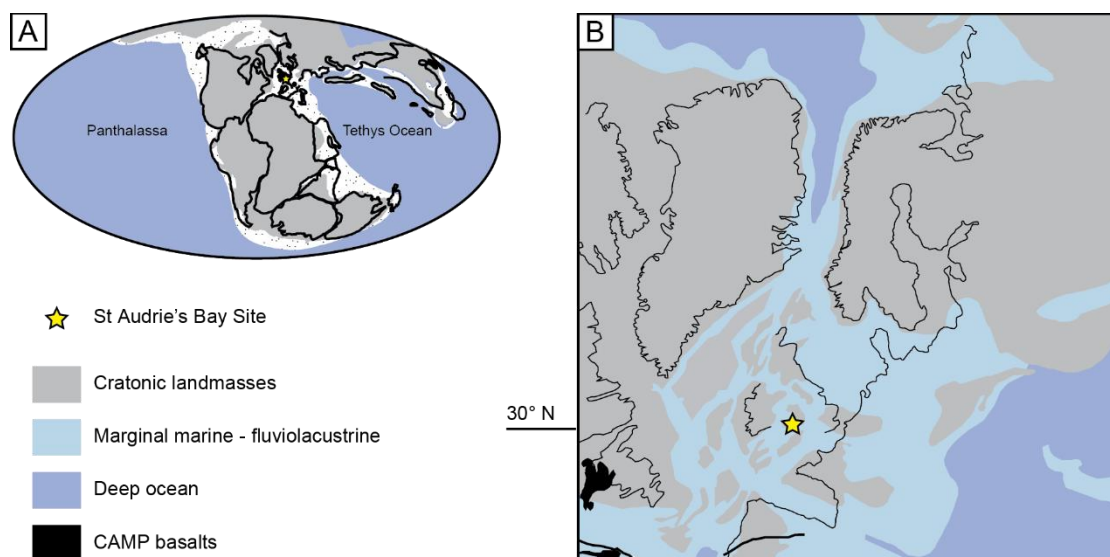
Figure 5.1 Palaeogeography from the Late Triassic. A) Location of St Audrie's Bay on the northwest margin of the Tethys Ocean. B) Detailed palaeogeography of, and depositional settings around, the St Audrie's Bay site within the shallow epicontinental sea on the northwest margin of the Tethys Ocean. Redrawn in part from Quan et al. (2008).

wave base of all but the largest storms. The presence of non-marine palynomorphs in the sediments also suggests that there was not an insignificant terrestrial influence on deposition at the St Audrie's Bay site (Bonis et al., 2010).

Evidence of Milankovitch forcing is seen in both the sedimentology and palynology of St Audrie's Bay. Cyclic changes in palynomorph records show evidence of the ~20-kyr precession cycle (Bonis et al., 2010). Evidence of both ~20-kyr precession and ~100-kyr eccentricity cycles have also been found in sedimentological and geochemical records (Ruhl et al., 2010).

5.3.1.2. Carbon-isotope Stratigraphy

Carbon-isotope stratigraphy across the Triassic-Jurassic Boundary has been extensively studied in the northern hemisphere, particularly in Europe and North America; the southern hemisphere record is poor due to the lack of suitably-aged successions. Negative carbon-isotope excursions, termed 'precursor', 'initial' and 'main', across the T-J Boundary have been reported in organic matter from multiple sites worldwide (Hesselbo et al., 2002; Guex et al., 2004; Ruhl et al., 2009). The carbonate record is less definitive, with both negative and positive CIEs recorded across the T-J Boundary at different sites (Pálfy et al., 2007; Bachan et al., 2012; Al-Suwaidi et al., 2016).

The earliest published marine δ¹³C$_{TOC}$ record from St Audrie's Bay identifies two negative excursions, separated by a short positive excursion (**Figure 5.2**; Hesselbo et al., 2002). The first, 'initial', negative CIE is a stratigraphically confined and presumably short-lived excursion of ~-5‰ and is followed by an apparently short-lived return to positive values. The second, larger negative excursion is termed the 'main' CIE and is characterised by a long-term excursion of ~-4‰. The 'main' CIE is also characterised, at St Audrie's Bay, by smaller scale fluctuations superimposed on the long-term negative trend. The sediments at St Audrie's Bay provide an excellent opportunity to study the δ¹³C values of individual phytoclasts.
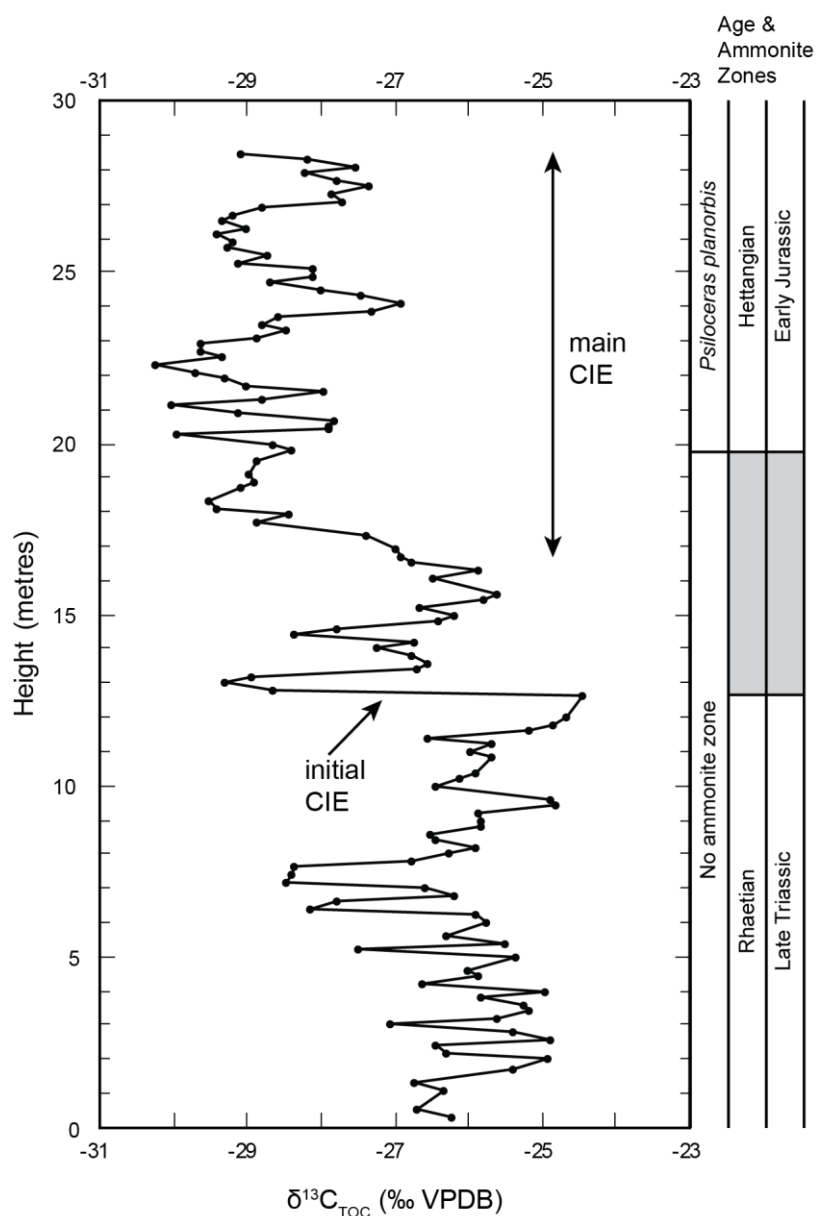
Figure 5.2 Marine bulk organic matter carbon-isotope curve from the Triassic-Jurassic Boundary section of St Audrie's Bay, southwest UK. Redrawn from Hesselbo et al., (2002).

5.3.2. Toarcian Oceanic Anoxic Event: Llanbedr, Wales, UK

5.3.2.1. Geological Setting

The Llanbedr (Mochras farm) borehole (henceforth referred to as Mochras) was drilled onshore in northwest Wales (**Figure 5.3**), between 1967 and 1969 in a joint venture between the British Geological Survey and Aberystwyth University, recovering ~1300 metres of marine sediments of Early Jurassic age (~201 – 174 Ma). This Early Jurassic sequence of sediments is much thicker than many other contemporaneous deposits in Europe, except for the Kaszewy-1 core from the
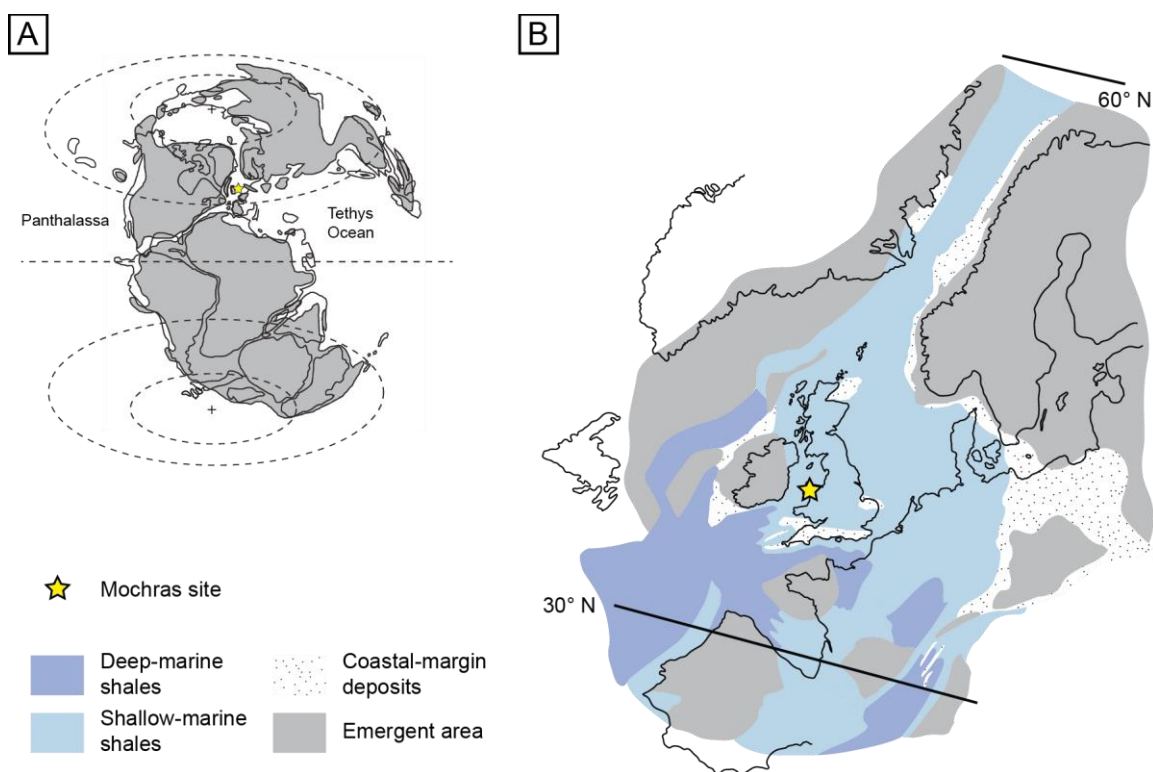
Figure 5.3 Palaeogeography of the Late Early Jurassic. A) Location of Mochras site on the northwest margin of the Tethys Ocean. B) Detailed palaeogeography of, and depositional settings around, the Mochras site within the shallow epicontinental sea on the northwest margin of the Tethys Ocean. Redrawn in part from Korte et al. (2015).

Polish Basin. The Mochras core has a well-constrained biostratigraphy, and has been studied extensively, including its carbon-isotope stratigraphy, making it an excellent candidate for this study.

During the Early Jurassic, the Cardigan Bay Basin was located on the northwest margin of the Tethys Ocean, in a shallow seaway connecting the Tethys Ocean to the Boreal Sea (**Figure 5.3**). Western Europe, including the Mochras site, was located at a mid- palaeolatitude during this time (Sellwood and Jenkyns, 1975). At the Mochras

site, sediments were deposited in a shallow-marine setting and consist mostly of marine mudstones; coarser siliciclastic material can also be found in minor amounts (Hesselbo et al., 2013; Xu et al., 2018). The Toarcian (182.7 – 174.1 Ma) section of the Mochras core consists of ~260 metres of marine mudstones.

5.3.2.2. Carbon-isotope Stratigraphy

Toarcian carbon-isotope stratigraphy has been well studied within Europe. A large negative carbon-isotope excursion, preceded and followed by positive excursions, in the Early Toarcian has long been documented in organic and carbonate matter, from both marine and terrestrial settings (Jenkyns and Clayton, 1986; Jenkyns et al., 2002; Hesselbo et al., 2007; Al-Suwaidi et al., 2010; Kemp and Izumi, 2014; Them et al., 2017). The Early Toarcian negative CIE is thought to be indicative of the Toarcian Oceanic Anoxic Event (OAE), occurring during the *tenuicostatum-serpentinum* ammonite zones.

A recently-published high-resolution bulk organic matter carbon-isotope curve (δ¹³C$_{TOC}$) from the Mochras core shows a large negative excursion of ~-7‰ between depths ~800-840 m, beginning in the *tenuicostatum* ammonite zone, and continuing into the *serpentinum* zone (**Figure 5.4**; Xu et al., 2018). The δ¹³C values drop in a stepwise fashion from pre-excursion values of ~-24‰, before reaching a minimum of ~-31‰ at the beginning of the *serpentinum* ammonite zone. Recovery to post-excursion values of ~-25‰ also occurs in a somewhat stepwise fashion. Small-scale fluctuations in δ¹³C$_{TOC}$ values can be seen super-
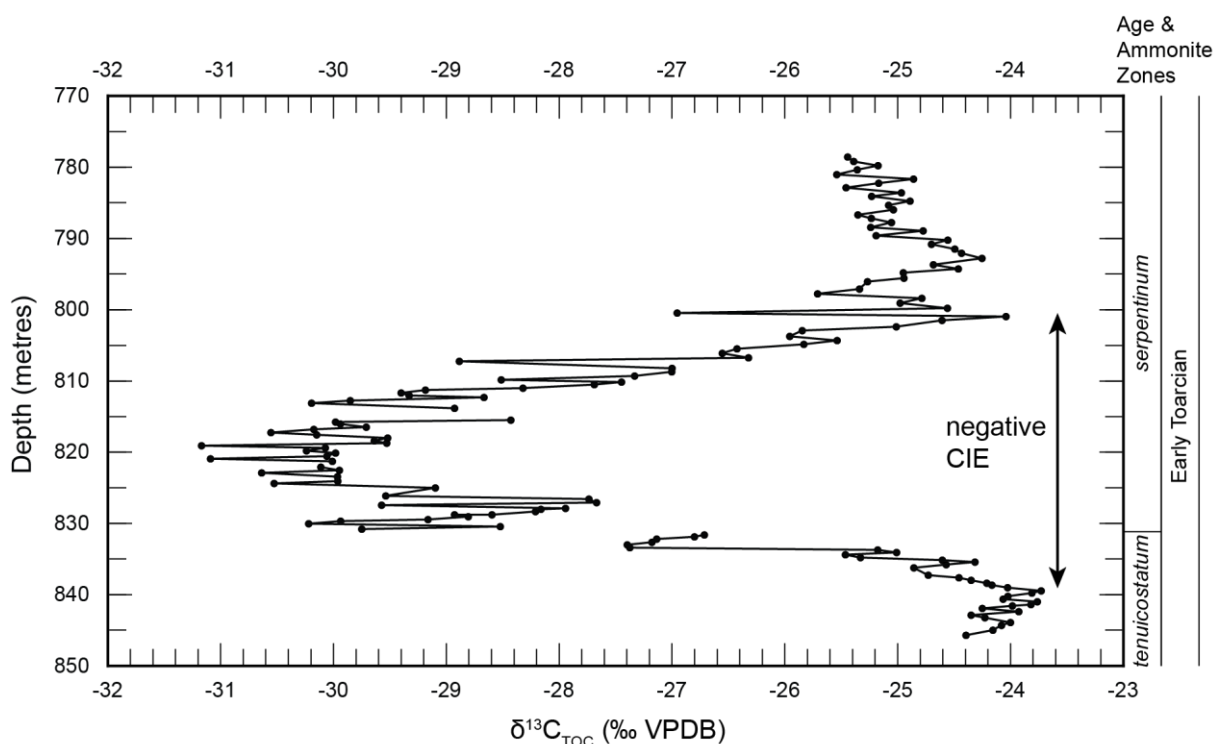
Figure 5.4 Bulk organic matter carbon-isotope curve from the Toarcian Oceanic Anoxic Event section of the Mochras core. Redrawn in part from Xu et al. (2018).

imposed over the long-term trend. This recently-published δ^{13}C$_{TOC}$ curve provides an excellent record to compare the new single-phytoclast carbon-isotope measurements to.

5.4. Materials & Methods

5.4.1. St Audrie's Bay, Southwest UK

5.4.1.1. Materials

Four samples were studied from across the Triassic-Jurassic transition zone, and Hettangian section of the St Audrie's Bay outcrop. The four samples were collected for this study between heights 12.7 m and 24.2 m and were chosen to coincide with high and low points of the Hesselbo et al., (2002) δ^{13}C$_{TOC}$ curve. The samples chosen for this study consist of a mixture of limestones and mudstones that were thought to have been deposited in a marine environment. Phytoclasts were chosen based on their appearance, size and fragility. The largest phytoclasts from each sample, providing they did not disintegrate upon contact with the picking brush. Phytoclasts similar in appearance were chosen to minimise the effect of composition variability amongst the measured carbon-isotope values.

5.4.1.2. Methods

A detailed discussion of the methods used to prepare and analyse the samples is provided in **Section 4.1.** and **Section 4.2.1.**

5.4.2. Mochras, Wales, UK

5.4.2.1. Materials

Ten samples from across the Toarcian Oceanic Anoxic Event, between depths 780.36 – 842.87 m, were originally collected for fossil charcoal abundance studies (Baker et al., 2017). The samples chosen consist of marine mudstones, deposited in a shallow marine environment. The 10 samples were chosen to correspond to key points of the Xu *et al*. (2018) bulk organic matter carbon-isotope curve. Again, phytoclasts were chosen based on their appearance, size and fragility, comparable to the St Audrie's Bay samples.

5.4.2.2. Methods

A detailed discussion of the methods used to prepare and analyse the samples is provided in **Section 4.1.** (p. 93) and **Section 4.2.1.** (p. 99).

5.5. Results & Discussion

5.5.1. Pilot Study: St Audrie's Bay, UK

5.5.1.1. Ideal Preparation & Analysis Settings

Samples which were pressed into the nickel disc were less often moved by the laser during ablation than those that were not pressed. Phytoclasts were also less likely to be blasted away by the laser if they were approached from the side during ablation rather than directly.

The laser energy has to be sufficiently high that the sample and standard material ablates well, but a higher-energy laser also risks moving the sample, or blasting it away. It was found that the phytoclasts ablated with a lower laser energy setting were less likely to move during the ablation, but ablate less material, resulting in an unreliable $\delta^{13}C$ measurement. In contrast, phytoclasts that were ablated at a higher energy setting ablated better, but were more likely to be moved by the laser during the ablation. Too high an energy setting could also result in the ablation of too much material, leading to the peak tails overlapping with the next peak in the mass spectrum, and producing an unreliable $\delta^{13}C$ value.

From the results of the pilot study, pressing the phytoclasts into the nickel disc and using a moderate-high laser energy setting (~25 kV) appears to be the ideal preparation and settings to use for the ablation of phytoclasts. These settings were then used going forward with the larger Mochras study.

5.5.1.2. Size-sample Relationship

During the St Audrie's Bay pilot study, 155 PE standard $\delta^{13}C$ measurements were made. The instrument $\delta^{13}C$ values of the PE standard measurements show a logarithmic relationship with peak area, which corresponds to amount of material ablated (**Figure 5.5**). The R-squared value of this dataset is 0.3512 for the regression line $y = 0.8919\ln(x) - 35.64$. The $\delta^{13}C$ values of all PE standards and
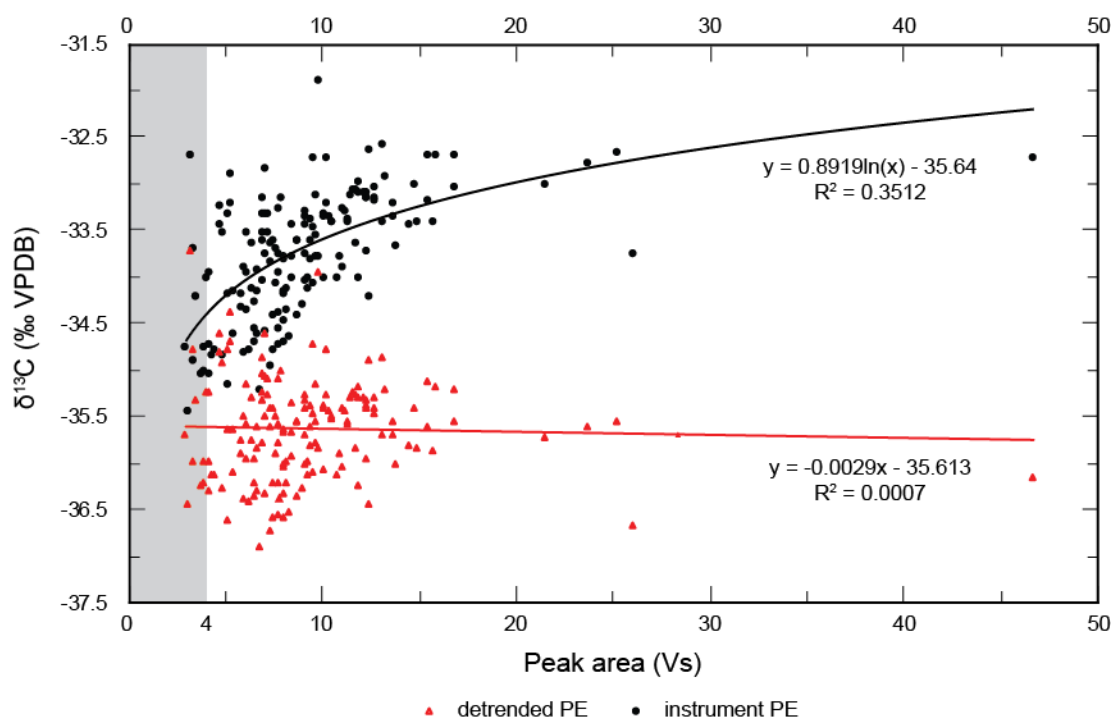
Figure 5.5 Peak area (in the mass spectra) plotted against PE standard δ^{13}C measurements showing the logarithmic relationship between the δ^{13}C values as measured by the instrument and peak area, as well as the relationship with the detrended data. Shaded region highlights samples with peak areas <4 Vs.

samples measured have been corrected for this size-sample relationship and for instrument drift.

5.5.1.3. Reliability of δ^{13}C$_{phytoclast}$ Measurements

A total of 130 individual δ^{13}C$_{phytoclast}$ measurements were made on the St Audrie's Bay phytoclast samples (**Table 5.1**). However, only 64 of these measurements (49%) are reliable; samples which were ablated using a high laser energy setting ablated enough material for a reliable δ^{13}C$_{phytoclast}$ value. Sixty six of the 130 δ^{13}C$_{phytoclast}$ measurements were made using a low laser energy setting, resulting in insufficient material being ablated (as determined by peak sizes (<4 Vs) in the mass spectra), and the measured δ^{13}C$_{phytoclast}$ value being unreliable.

Reliable δ^{13}C$_{phytoclast}$ measurements were made on 10 phytoclasts from samples StAB40 and StAB206, and show a range of values. These reliable δ^{13}C$_{phytoclast}$ measurements are the ones discussed in the rest of this section.

A total of 29 measurements were made across 6 different phytoclasts from sample StAB40, with a minimum average δ^{13}C$_{phytoclast}$ value of -29.64‰ and a

Sample	Height (m)	Pressed?	Laser energy	Phytoclast number	Number of measurements	Instrument measurements		Detrended & drift-corrected values	
						$\delta^{13}C$ (‰)	St. dev. (‰)	$\delta^{13}C$ (‰)	St. dev. (‰)
		N	Low	all	4	-27.42	0.72	-26.09	0.69
StAB1	16.1	N	Low	1	2	-27.95	0.67	-26.28	0.93
		N	Low	3	2	-26.89	0.03	-25.91	0.65
		Y	Low	all	10	-31.64	2.42	-30.15	2.30
StAB205	12.7	Y	Low	1A	2	-28.15	1.51	-27.16	1.22
		Y	Low	2A	3	-33.84	2.00	-32.57	1.85
		Y	Low	3A	5	-31.72	0.95	-29.88	0.94
		N	Low	all	15	-27.21	2.41	-25.76	2.24
		N	Low	2B	3	-29.43	2.22	-27.84	2.10
StAB205	12.7	N	Low	3B	1	-25.12	0.00	-22.19	0.00
		N	Low	4B	5	-28.96	0.92	-27.35	0.70
		N	Low	5B	6	-24.99	0.92	-23.99	0.68
		N	Low	all	63	-27.28	3.16	-26.62	2.42
		N	Low	1	12	-33.08	1.34	-30.83	1.73
StAB206	13.0	N	Low	2	5	-29.56	1.08	-27.95	0.98
		N	Low	3	22	-25.89	0.47	-25.11	0.91
		N	**High**	**3**	**24**	**-25.19**	**0.71**	**-25.61**	**0.76**
		Y	Low	all	9	-27.82	1.43	-25.81	1.49
StAB206	13.0	Y	Low	1	7	-27.96	0.89	-26.02	0.72
		Y	Low	2	2	-27.31	3.33	-25.07	3.65
		Y	**High**	**all**	**11**	**-29.46**	**1.39**	**-28.50**	**1.83**
StAB206	13.0	**Y**	**High**	**5**	**6**	**-28.63**	**1.06**	**-27.10**	**0.86**
		Y	**High**	**4**	**3**	**-29.81**	**0.29**	**-29.56**	**0.06**
		Y	**High**	**6**	**2**	**-31.39**	**1.24**	**-31.08**	**1.16**
		Y	**High**	**all**	**29**	**-28.56**	**2.14**	**-27.64**	**2.06**
		Y	**High**	**1**	**10**	**-30.16**	**0.57**	**-29.64**	**0.33**
		Y	**High**	**2**	**7**	**-29.89**	**1.97**	**-28.34**	**1.56**
StAB40	24.2	**Y**	**High**	**3**	**3**	**-27.12**	**0.81**	**-26.07**	**0.74**
		Y	**High**	**4**	**2**	**-26.51**	**1.87**	**-26.37**	**1.38**
		Y	**High**	**5**	**5**	**-26.34**	**0.66**	**-25.18**	**0.35**
		Y	**High**	**6**	**2**	**-25.62**	**0.42**	**-24.91**	**0.12**

Table 5.1 Results from the St Audrie's Bay pilot study. Rows in bold indicate reliable $\delta^{13}C_{phytoclast}$ measurements.

maximum average $\delta^{13}C_{phytoclast}$ value of -24.91‰. The average $\delta^{13}C_{phytoclast}$ value shows a 4.5‰ range between the individual phytoclasts of sample StAB40. The average $\delta^{13}C_{phytoclast}$ of the 6 $\delta^{13}C_{phytoclast}$ values is -27.64‰, with a 1σ uncertainty of 2.06‰.

Four individual phytoclasts from sample StAB206 ablated sufficient material for reliable $\delta^{13}C_{phytoclast}$ measurements. One of these phytoclasts was not pressed prior to ablation with a high energy laser. Phytoclast number 3 was measured a total of 24 times, resulting in a $\delta^{13}C_{phytoclast}$ value of -25.61‰, with a 1σ uncertainty of 0.76‰. Phytoclasts 4-6 were measured a total of 11 times, with a minimum $\delta^{13}C_{phytoclast}$ value of -31.08‰, and a maximum value of -27.10‰, showing a range of ~4‰. The average $\delta^{13}C_{phytoclast}$ value of phytoclasts 4-6 is -28.50‰, with a 1σ uncertainty of 1.83‰

5.5.1.4. Intra-phytoclast Variability

A total of 29 measurements were made across 6 phytoclasts from sample StAB40, and 35 measurements were made across 4 phytoclasts from sample StAB206 to investigate the homogeneity of carbon-isotopes within individual phytoclasts (**Table 5.2; Figure 5.6**). Phytoclasts were described & characterised

| Sample | Height (m) | Phytoclast number | Number of measurements | $\delta^{13}C_{phytoclast}$ (‰ VPDB) | | | | |
				Average	1σ	Maximum	Minimum	Range
StAB40	24.2	1	10	-29.64	0.33	-29.10	-30.02	1
		2	7	-28.34	1.56	-25.76	-30.71	5
		3	3	-26.07	0.74	-25.63	-26.92	1
		4	2	-26.37	1.38	-25.40	-27.35	2
		5	5	-25.18	0.35	-24.76	-25.62	1
		6	2	-24.91	0.12	-24.83	-24.99	0.1
StAB206	13.0	3	24	-25.61	0.76	-24.31	-27.59	3
		4	3	-29.56	0.06	-29.52	-30.09	0.5
		5	6	-27.10	0.86	-27.52	-30.04	3.5
		6	2	-31.08	1.16	-30.52	-32.27	1.5

Table 5.2 Number of measurements, average, maximum and minimum $\delta^{13}C_{phytoclast}$ values for the St Audrie's Bay samples with reliable $\delta^{13}C_{phytoclast}$ measurement.
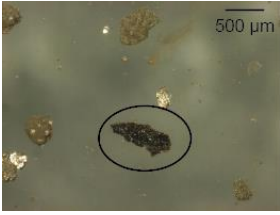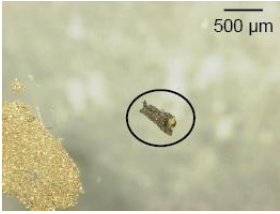
Sample	Phytoclast number	Description	
StAB40	1	Dark grey/black, sub-angular woody phytoclast	
	2	Dark grey/black, sub-angular woody phytoclast	
	3	Dark grey/black, sub-angular, elongate woody phytoclast	
	4	Dark grey/black, elongate tapered woody phytoclast	
	5	Dark grey/black, sub-rounded woody phytoclast	
	6	Dark grey/black, sub-angular woody phytoclast	
StAB206	3	Dark grey/black, sub-angular woody phytoclast	
	4	Dark grey/black, sub-rounded woody phytoclast	

Table 5.3 Phytoclast descriptions and images. Descriptions are based on view under microscope and not on images.
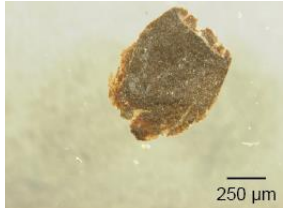
Sample	Phytoclast number	Description	
StAB 206	5	Dark grey/black, sub-angular, elongate woody phytoclast	
	6	Dark grey with brown translucent edges, sub-rounded woody phytoclast	

Table 5.3 (cont.) Phytoclast descriptions and images. Descriptions are based on view under microscope and not on images.

based on their appearance (shape, colour, reflectivity; woody phytoclast, charcoal) and photographed prior to analysis (**Table 5.3**).

The measurements of the individual StAB40 phytoclasts generally show a low range of $\delta^{13}C_{phytoclast}$ values, with a ~0.1-2‰ difference between the minimum and maximum $\delta^{13}C_{phytoclast}$ values. This low range of $\delta^{13}C_{phytoclast}$ values shows that the carbon-isotope signature of an individual phytoclast does not vary by a significant amount in most cases. However, the 7 measurements of phytoclast 2 show a $\delta^{13}C_{phytoclast}$ range of ~5‰, with a minimum and maximum of -30.71‰ and -25.76‰, respectively. There is no obvious apparent reason for this large range of $\delta^{13}C_{phytoclast}$ values compared to the other phytoclasts from sample StAB40; phytoclast 2 has a similar appearance, and therefore likely a similar composition, to the other phytoclasts from sample StAB40.

The measurements of the individual StAB206 phytoclasts show a range of $\delta^{13}C_{phytoclast}$ values, with a ~0.5-3.5‰ difference between the minimum and maximum values. The phytoclasts of sample StABG206 show a greater range of $\delta^{13}C_{phytoclast}$ values than the StAB40 phytoclasts. Again, there is no obvious apparent reason for this: the phytoclasts analysed from sample StAB206 have a very similar visual appearance to each other, and are likely to have a similar composition.
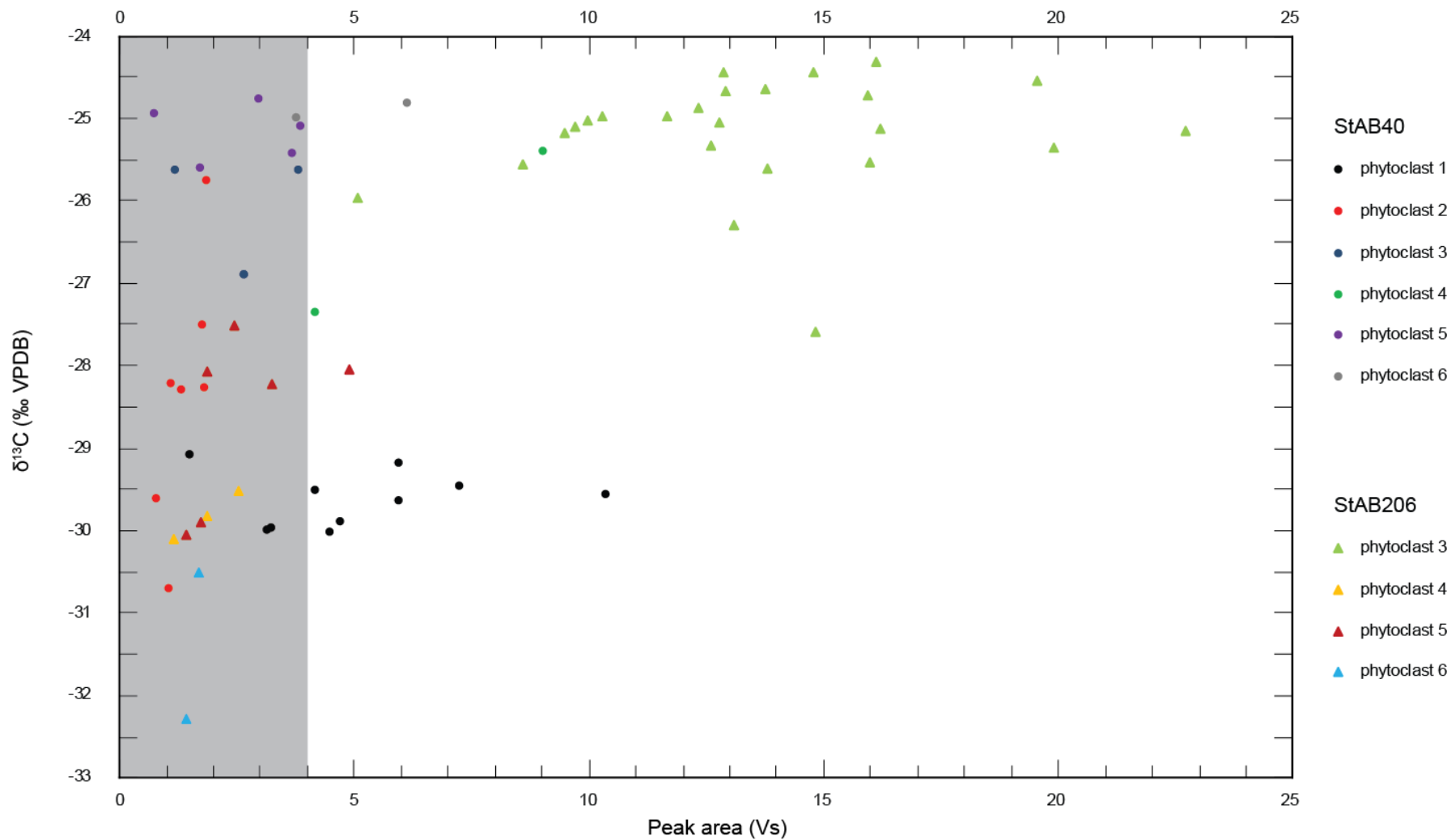
Figure 5.6 δ¹³C$_{phytoclast}$ plotted against peak area (of the measurement in the mass spectra) for each measurement of each phytoclast analysed from samples StAB40 and StAB206. The δ¹³C$_{phytoclast}$ values plotted are the detrended and drift-corrected values. Shaded region highlights samples with peak areas <4 Vs.

The multiple δ^{13}C$_{phytoclast}$ measurements of individual phytoclasts show that, in most cases, a single measurement is sufficient to obtain a reliable δ^{13}C$_{phytoclast}$ value. However, it would be wise to always check intra-phytoclast δ^{13}C variability prior to investigating inter-phytoclast.

5.5.1.5. Comparison with the Bulk Organic Matter δ^{13}C Record

The small number of phytoclasts measured reliably in the St Audrie's Bay pilot study do not show any long-term trends, but can be compared to the bulk organic matter C-isotope curve published by Hesselbo et al. (2002). Comparison with this previously-published record allows us to see how δ^{13}C$_{phytoclast}$ values differ from the carbon-isotope signature of the bulk organic matter at the same, or similar, horizons (**Figure 5.7**).

Sample StAB206 (height: 13.0 m) shows a wide range of δ^{13}C$_{phytoclast}$ values that are both more positive and more negative than the bulk OM curve. At the height of 13.0 m, the δ^{13}C$_{TOC}$ value is -29.30‰, and the average δ^{13}C$_{phytoclast}$ value is -28.34‰, a difference of ~1‰.

Sample StAB40 (height: 24.2 m) also shows a wide range of δ^{13}C$_{phytoclast}$ values that are more positive and more negative than the bulk OM curve. No samples are available for the height of 24.2 m from the bulk OM curve, but there are δ^{13}C$_{TOC}$ measurements from heights 24.1 m and 24.3 m, which are -26.91‰ and -27.46‰, respectively. The average δ^{13}C$_{phytoclast}$ value is -26.75‰, similar to the δ^{13}C$_{TOC}$ values at heights 24.1 m and 24.3 m.

Modern terrestrial C3 plant δ^{13}C values are generally more negative than marine bulk organic matter (Lamb et al., 2006). Mesozoic terrestrial plant δ^{13}C values have been shown to have more positive signals than bulk marine OM (Bocherens et al., 1993; Nordt et al., 2016). There is a wide range of δ^{13}C$_{phytoclast}$ values from both St Audrie's Bay samples, both above and below then δ^{13}C$_{TOC}$ curve; the average δ^{13}C$_{phytoclast}$ values of the St Audrie's Bay samples are more positive than the mixed marine-terrestrial δ^{13}C$_{TOC}$ curve of Hesselbo et al. (2002), as expected.
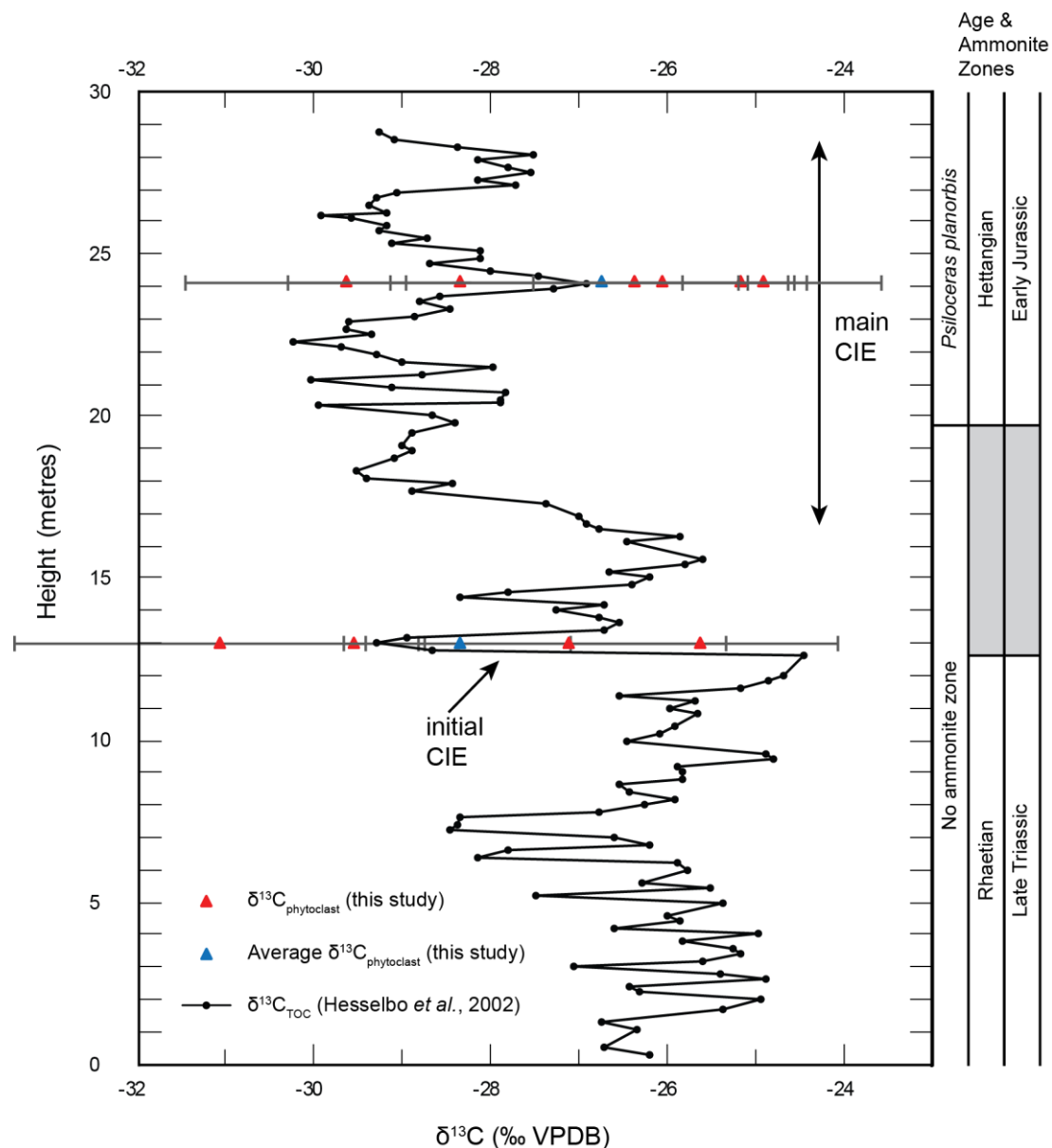
Figure 5.7 Reliable average $\delta^{13}C_{phytoclast}$ measurements from the St Audrie's Bay pilot study plotted against the bulk organic matter carbon-isotope curve ($\delta^{13}C_{TOC}$) of Hesselbo et al., (2002). Grey error bars show 2σ error.

5.5.2. Reproducing the Toarcian Oceanic Anoxic Event Negative Carbon-isotope Excursion Using Single Phytoclast δ¹³C Measurements: Mochras, UK

5.5.2.1. Size-sample Relationship

A total of 137 polyethylene standard $\delta^{13}C_{standard}$ measurements were made across all of the Mochras sample runs. The drift-corrected values of these 137 $\delta^{13}C_{standard}$ measurements show very little correlation with peak area (**Figure 5.8**).
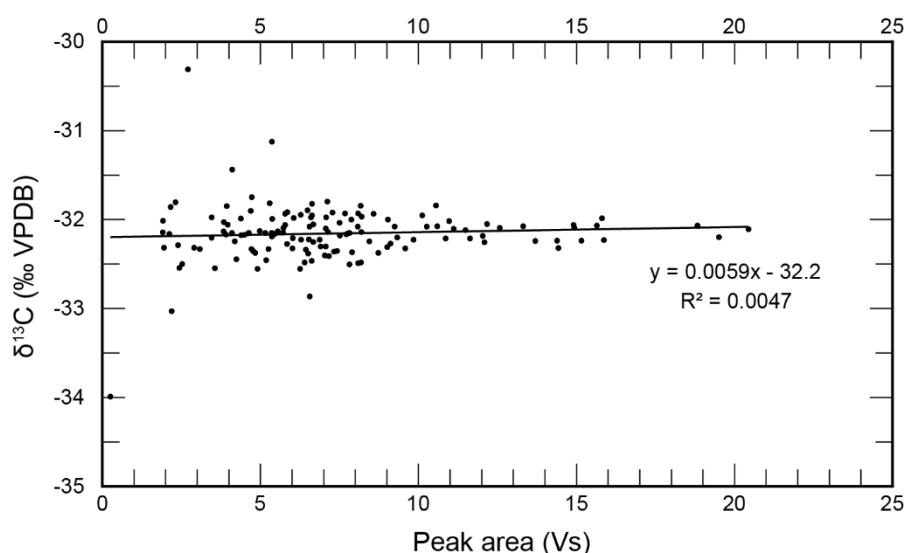
Figure 5.8 Peak area plotted against PE $\delta^{13}C_{standard}$ measurements showing the lack of relationship between the $\delta^{13}C$ values as measured by the instrument and peak area.

The R-squared value of this dataset is 0.0047 for the regression line $y = 0.0059x - 32.2$, where $y = \delta^{13}C$ and $x =$ peak area. The R-squared value is so low that there is effectively no relationship between drift-corrected $\delta^{13}C_{standard}$ values and peak areas. For this reason, all following reported $\delta^{13}C$ values from the Mochras sample set have only been corrected for instrument drift.

5.5.2.2. Intra-phytoclast Variability

Multiple $\delta^{13}C$ measurements of the same phytoclast were performed for the first two Mochras samples analysed to investigate carbon-isotopic homogeneity. Four $\delta^{13}C$ measurements of sample M256037 and six $\delta^{13}C$ measurements of sample M270161 were made. Both sets of measurements show a narrow range in $\delta^{13}C_{phytoclast}$ values, with low 1σ values.

Drift-corrected $\delta^{13}C_{phytoclast}$ measurements of sample M256037 give values of -26.174‰, -26.156‰, -26.252‰, and -26.024‰ (**Figure 5.9**). The average of the four drift-corrected values from sample M256037 is -26.152‰, with a 1σ uncertainty of 0.09. Five measurements of the PE standard were made during the same run, producing a drift-corrected average $\delta^{13}C_{standard}$ value of -32.151, with a 1σ uncertainty of 0.24‰.

Drift-corrected $\delta^{13}C_{phytoclast}$ measurements of sample M270161 give values of -30.546‰, -30.544%, -30.587‰, -30.286‰, -30.150‰, and -30.497‰ (**Figure**
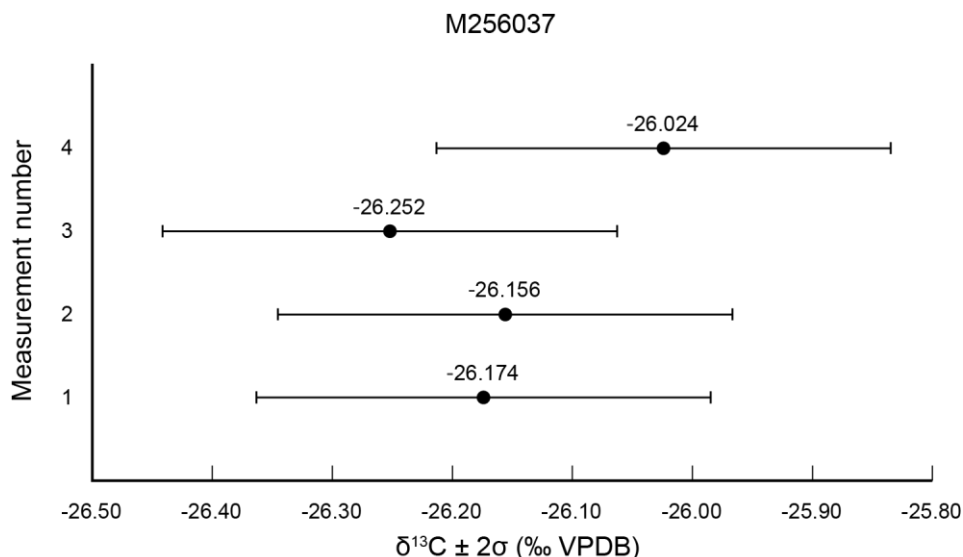
M256037

Figure 5.9 $\delta^{13}C_{phytoclast}$ values as measured multiple times on sample M256037. Standard deviation calculated using the measured $\delta^{13}C_{standard}$ values from this sample run.
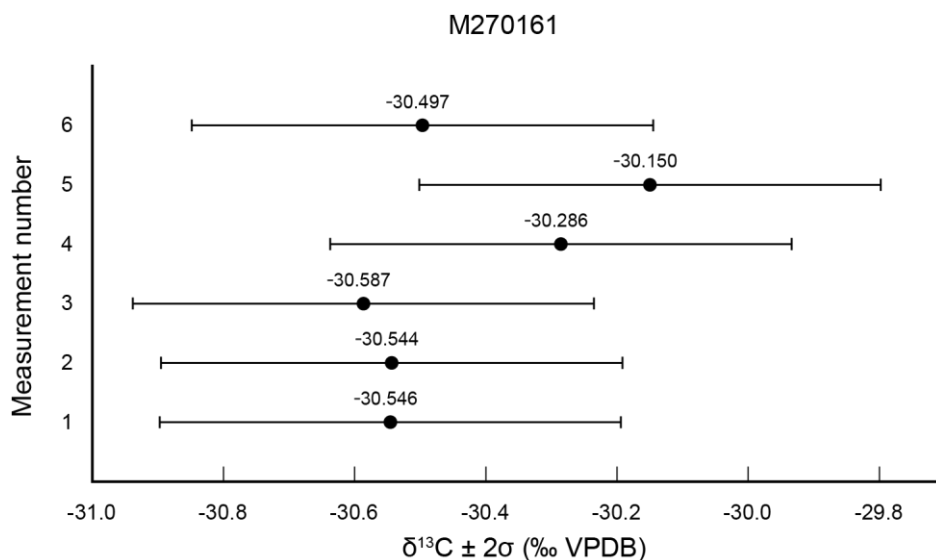
M270161

Figure 5.10 $\delta^{13}C_{phytoclast}$ values as measured multiple times on sample M270161. Standard deviation calculated using the measured $\delta^{13}C_{standard}$ values from this sample run.

5.10). The average of the six drift-corrected $\delta^{13}C_{phytoclast}$ measurements from sample M270161 is -30.435‰, with a 1σ uncertainty of 0.18. Five $\delta^{13}C_{standard}$ measurements of the PE standard were also made during the same run, with a drift-corrected average $\delta^{13}C_{standard}$ value of -32.151‰ and 1σ uncertainty of 0.27‰.

The low 1σ uncertainties of the two sets of drift-corrected $\delta^{13}C_{phytoclast}$ values suggest that both phytoclasts are isotopically-homogeneous. The 1σ uncertainties of the $\delta^{13}C_{phytoclast}$ values are both less than the 1σ uncertainties of

their respective PE standard measurements, suggesting that the phytoclasts are more isotopically-homogenous than the standard used. For these reasons, and coupled with the data from the St Audrie's Bay samples, only one δ^{13}C$_{phytoclast}$ measurement of subsequent Mochras samples was made, bracketed by two δ^{13}C$_{standard}$ measurements of the PE standard.

5.5.2.3. Single-phytoclast Carbon-isotope Curve

The Mochras single-phytoclast δ^{13}C$_{phytoclast}$ dataset shows that δ^{13}C$_{phytoclast}$ can vary greatly within a sediment sample (**Figure 5.11;** see **Appendix A** (p. 308) for phytoclast descriptions and images; raw carbon-isotope data). Variation between single-phytoclast measurements is expected, considering that whole plant δ^{13}C$_{phytoclast}$ values are not homogeneous (e.g. Leavitt and Long, 1991; see **Chapter 3, Section 3.4** (p. 64) for a detailed discussion). The Mochras dataset also shows that the single-phytoclast measurements record a negative carbon-isotope excursion. A small number of δ^{13}C$_{phytoclast}$ measurements fall outside of the normal range of δ^{13}C$_{phytoclast}$, and are not considered in the following discussion, but are included in figures. Here, an outlier is defined as any value falling further than 1.5 x interquartile range from either the first or third quartile (Tukey, 1977).

The negative carbon-isotope excursion recorded by the single-phytoclast data occurs between depths 831.85 m and 805.18 m and had a magnitude of ~-4‰. The average δ^{13}C$_{phytoclast}$ values pre-excursion range between ~-25-26‰, before dropping to excursion values of ~-30‰. Post-excursion, the average δ^{13}C$_{phytoclast}$ values fluctuate between -26‰ and -27‰, and do not recover to as heavy values as prior to the negative excursion. The negative excursion recorded by the single-phytoclast δ^{13}C$_{phytoclast}$ measurements corresponds to the Toarcian Oceanic Anoxic Event. The Toarcian OAE has previously been recorded in terrestrial material from other sites (Hesselbo et al., 2007), so it was expected that the new Mochras single-phytoclast δ^{13}C$_{phytoclast}$ dataset would also show a negative carbon-isotope excursion of some magnitude.

There are only three δ^{13}C$_{phytoclast}$ measurements (and one outlier) for sample M26418, which has an intra-sample δ^{13}C$_{phytoclast}$ range of 0.56‰. Sample M26418 is not considered in this discussion due to the small number of data points; it is likely that the δ^{13}C$_{phytoclast}$ range will increase as more single-phytoclast
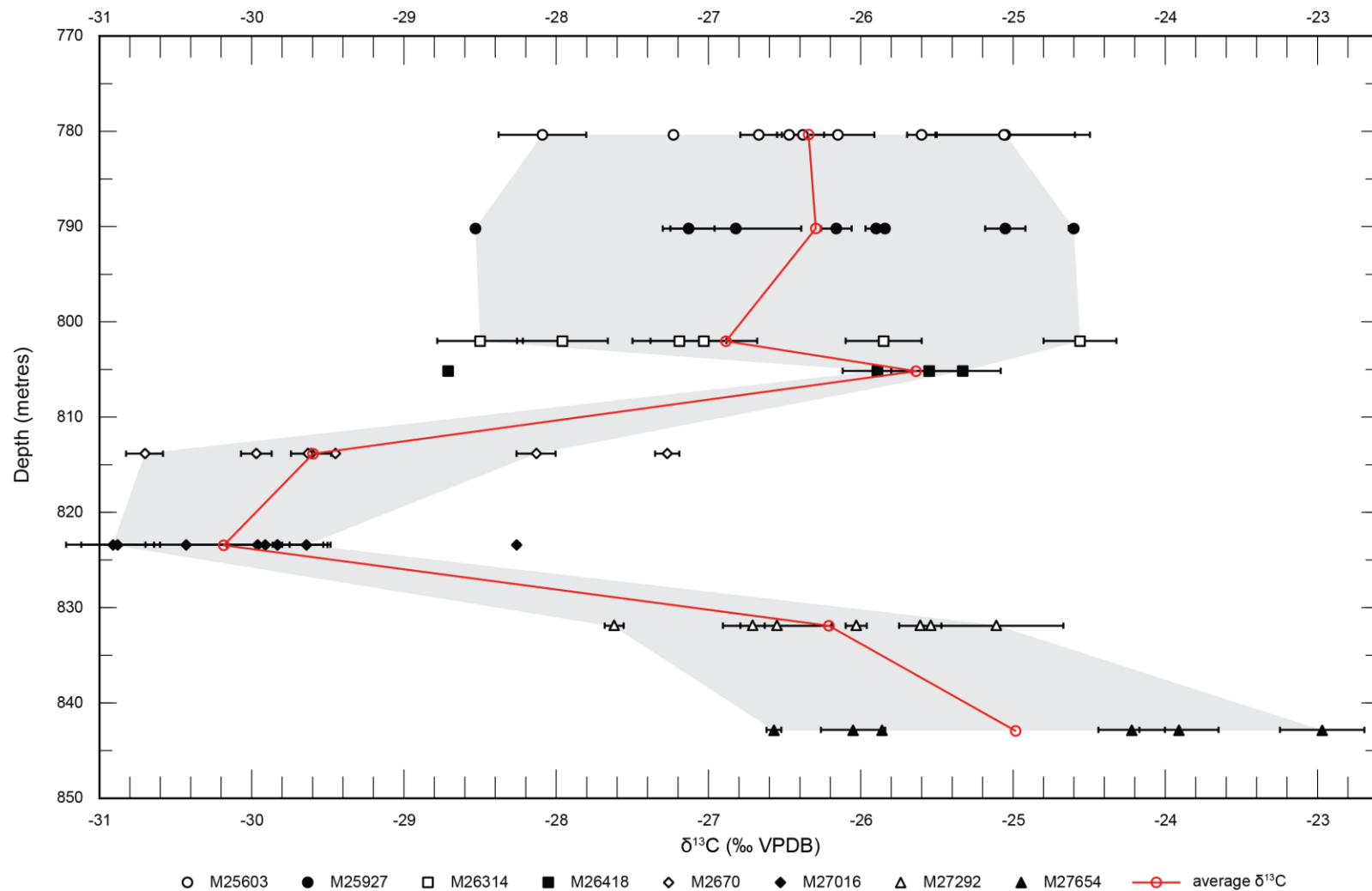
Figure 5.11 Results from the Mochras δ¹³C$_{phytoclast}$ study showing individual δ¹³C$_{phytoclast}$ measurements plotted against depth. The grey band encompasses all values that are not outliers. The average δ¹³C$_{phytoclast}$ value from each horizon is shown plotted in red. Error bars represent 2σ.

Sample	Depth (m)	Number of measurements	δ^{13}C$_{phytoclast}$ (‰ VPDB)			
			Average	Maximum	Minimum	Range
M25603	780.36	9	-26.30	-25.05	-28.09	-3.04
M25927	790.22	8	-26.25	-24.60	-28.53	-3.93
M26314	802.03	6	-26.85	-24.56	-28.50	-3.94
M26418	805.18	3	-25.59	-25.33	-25.89	-0.56
M2670	813.82	6	-29.58	-28.13	-30.70	-2.57
M27016	823.42	8	-30.17	-29.64	-30.91	-1.27
M27292	831.85	7	-26.17	-25.11	-27.62	-2.51
M27654	842.87	6	-24.93	-22.97	-26.57	-3.60

Table 5.4 Average, maximum and minimum δ^{13}C$_{phytoclast}$ values, and δ^{13}C$_{phytoclast}$ intra-sample ranges from the Mochras samples. Outliers are excluded from the calculations in this table.

measurements are made from sample M26418, in line with the other Mochras samples analysed.

Within a sample, the δ^{13}C$_{phytoclast}$ range varies between ~1‰ and ~4‰, excluding outliers (**Table 5.4**). The intra-sample δ^{13}C$_{phytoclast}$ range is greater both before and after the negative carbon-isotope excursion. In the pre-excursion samples M27654 and M27292 (depths 842.87 m and 831.85 m), δ^{13}C$_{phytoclast}$ varies between ~-23‰–26.5‰ and ~-25‰–27.6‰, respectively. The magnitude of variation in samples M27654 and M27292 is ~3.6‰ and ~2.5‰. As δ^{13}C$_{phytoclast}$ values become lighter, the intra-sample δ^{13}C$_{phytoclast}$ range becomes narrower: samples M27016 and M2670 record d13Cphyto values ~-29-31‰ and ~-28-31‰, ranges ~1.3‰ and ~2.6‰ in magnitude, respectively. Post-excursion, intra-samples δ^{13}C$_{phytoclast}$ ranges vary between ~3-4‰ in magnitude, with minimum δ^{13}C$_{phytoclast}$ values of ~-28‰ and maximum δ^{13}C$_{phytoclast}$ values of ~-24‰.

It has been well-established that different types of plant tissue within a plant have different carbon-isotope signatures; whole-plant C-isotope signatures are typically heavier than leaf signatures which, in turn, are heavier than cellulose, lignin, lipids and alkanes (Leavitt and Long, 1991; Hobbie and Werner, 2004). The phytoclasts analysed for as part of this study are mostly woody phytoclasts, with a small number of charcoal phytoclasts, from undetermined plants, and therefore should consist of mostly lignin-derived organic molecules. There appears to be no relationship between the type or appearance of phytoclast and
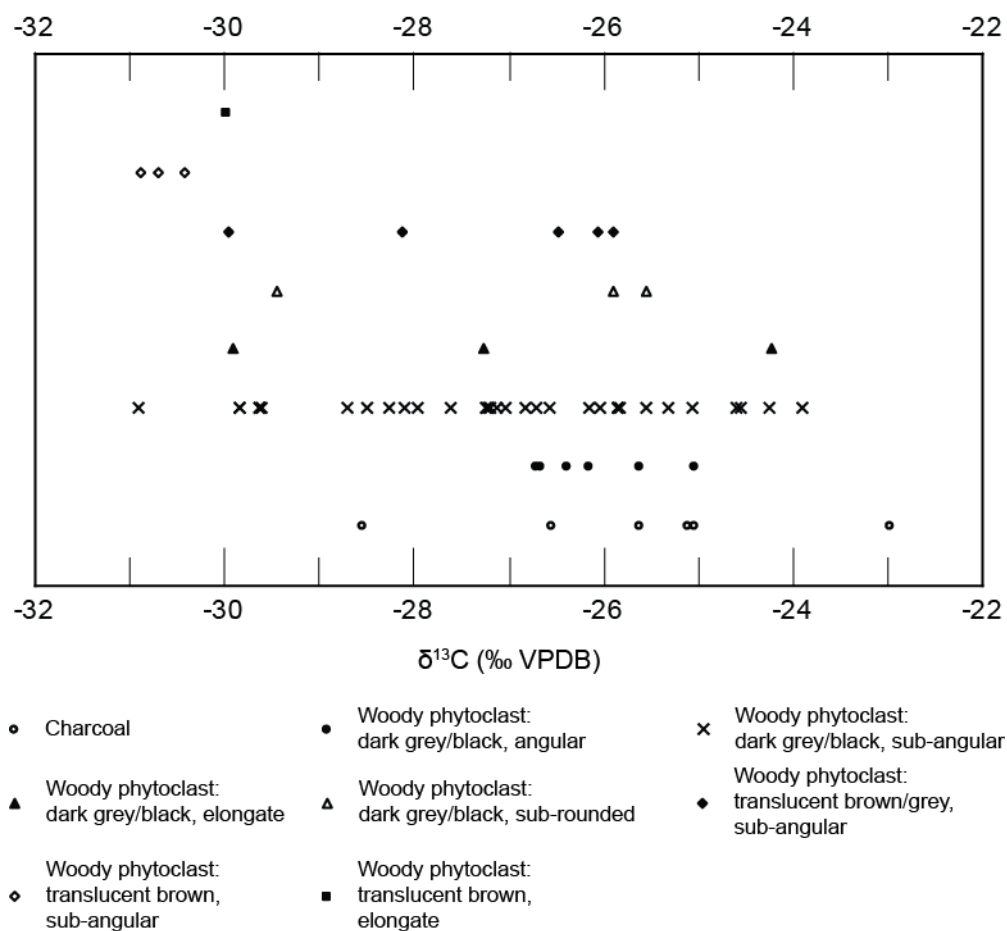
Figure 5.12 Spread of $\delta^{13}C_{phytoclast}$ values, grouped by appearance and classification.

its $\delta^{13}C_{phytoclast}$ value (**Figure 5.12**); the colour, shape or structure of the phytoclasts do not correlate with $\delta^{13}C_{phytoclast}$ values, though it is important to note that some categories of phytoclasts are only represented by a small number of samples. It is unlikely that the range of $\delta^{13}C_{phytoclast}$ values within a sample is due to the presence of different tissue types.

The range of $\delta^{13}C_{phytoclast}$ values seen within a sample are most likely to reflect different sources for the phytoclasts. The same parts of different plants can have different carbon-isotope signatures. It is more probable that the phytoclasts from the Mochras core represent material originating from a variety of sources, producing the range in intra-sample $\delta^{13}C_{phytoclast}$ values reported here.

The carbon-isotope values of plant material are known to vary dependent on the type of plant and the type of plant tissue (Hobbie and Werner, 2004), so it is unsurprising that within each sample, a range of $\delta^{13}C_{phytoclast}$ values are recorded. The recorded values all fall within the range for modern C3 plants (**Figure 3.8**;

Lamb et al., 2006), as expected. Two mechanisms are proposed for the decreased range in $\delta^{13}C_{phytoclast}$ values during the negative CIE: increased carbon-isotope discrimination during photosynthesis, and/or a change in plant assemblage.

Carbon-isotope discrimination during C3 photosynthesis is mostly controlled by the ratio of ambient CO_2 pressure (p_a) to intercellular CO_2 pressure (within the plant; p_i) (Farquhar et al., 1989). However, plants prefer to maintain a constant p_a/p_i ratio, altering factors such as stomatal conductance to achieve this (Ehleringer and Cerling, 1995). A constant p_a/p_i ratio would result in a constant level of C-isotope discrimination, regardless of atmospheric CO_2 levels. It is possible that plants altered their carbon-isotope discrimination during the Toarcian OAE, due to changes in the isotopic composition of carbon in the atmosphere. Without being able to measure the p_a/p_i ratio of Toarcian plants, it is impossible to quantify their rate of carbon-isotope discrimination. Changes in plant discrimination of carbon during photosynthesis cannot be ruled out as contributing towards the CIEs observed across the Toarcian OAE.

A change in plant assemblage during the Toarcian OAE could also explain the narrower range of intra-sample $\delta^{13}C_{phytoclast}$ values seen in samples M27016 and M2670. Rising atmospheric carbon dioxide levels could, indirectly, alter the plant assemblage from which plant material at the Mochras site originated by increasing atmospheric temperatures, leading to a dominance of thermophilic taxa, such as *Classopollis* (Vakhrameev, 1981). It is known that different plants have different carbon-isotope signatures, therefore a change in plant assemblage could lead to a change in carbon-isotope values, and the range between them. It is likely that the decreased range in $\delta^{13}C_{phytoclast}$ values across the most negative part of the CIE are partly a result of a change in plant assemblage. New palynology studies of the Mochras core would allow for this relationship to be investigated.

The C-isotope curve produced from the analysis of single phytoclasts from the Mochras core shows that the C-isotopic signatures of individual components of a bulk terrestrial organic matter sample can vary greatly.

5.5.2.4. Comparison with the Bulk Organic Matter δ¹³C Record

The new Mochras δ¹³C$_{phytoclast}$ data clearly show a negative carbon-isotope excursion during the Early Toarcian which corresponds to the Toarcian Oceanic Anoxic Event. The Toarcian OAE has previously been recorded by a number of geological materials at numerous sites around the world, including at the Mochras site in bulk organic matter. Comparison of the new Mochras δ¹³C$_{phytoclast}$ data with the most recent, and highest resolution, bulk organic matter δ¹³C record (δ¹³C$_{TOC}$; Xu et al., 2018) shows that new δ¹³C$_{phytoclast}$ record correlates well with the bulk OM record, accurately reproducing the Toarcian OAE negative carbon-isotope excursion (**Figure 5.13**).

The δ¹³C$_{TOC}$ curve shows a negative CIE of ~-7‰ beginning at the end of the *tenuicostatum* ammonite zone, and continuing into the *serpentinum* ammonite zone. δ¹³C$_{TOC}$ values fall from ~-24‰ to ~-31‰ in a stepwise fashion before returning to more stable values. Small fluctuations in δ¹³C$_{TOC}$ values can be seen superimposed on the long-term trend. Similarly, the δ¹³C$_{phytoclast}$ curve also shows a negative CIE of ~-5‰, from an average value of ~-25‰ to ~-30‰, which when superimposed over the Xu et al. (2018) data, correlates well.

The most noticeable difference between the new δ¹³C$_{phytoclast}$ dataset and the previously published δ¹³C$_{TOC}$ dataset is the divergence of the two carbon-isotope curves both pre- and post-excursion. The difference between the δ¹³C$_{TOC}$ and average δ¹³C$_{phytoclast}$ values (Δ$_{TOC-phytoclast}$) at a given horizon ranges from ~0-2‰. Δ$_{TOC-phytoclast}$ values are greatest in the recovery phase after the negative CIE, where δ¹³C values return to more positive values. Some disparity between the two C-isotope curves is expected; the δ¹³C$_{TOC}$ measurements reflect the carbon-isotope signatures of all organic matter present in the sample, from both marine and terrestrial sources. Considering that the Toarcian-aged Mochras sediments were deposited in a shallow-marine environment, the bulk OM samples will reflect a mixture of both marine and terrestrial organic matter and it is not surprising that the δ¹³C$_{TOC}$ and δ¹³C$_{phytoclast}$ values differ at a given horizon. It should be noted, however, that while the average δ¹³C$_{phytoclast}$ values deviate from the δ¹³C$_{TOC}$ curve, the individual phytoclast δ¹³C measurements from each sample show a range of values, including those which are much closer to the δ¹³C$_{TOC}$ values at their respective horizons.
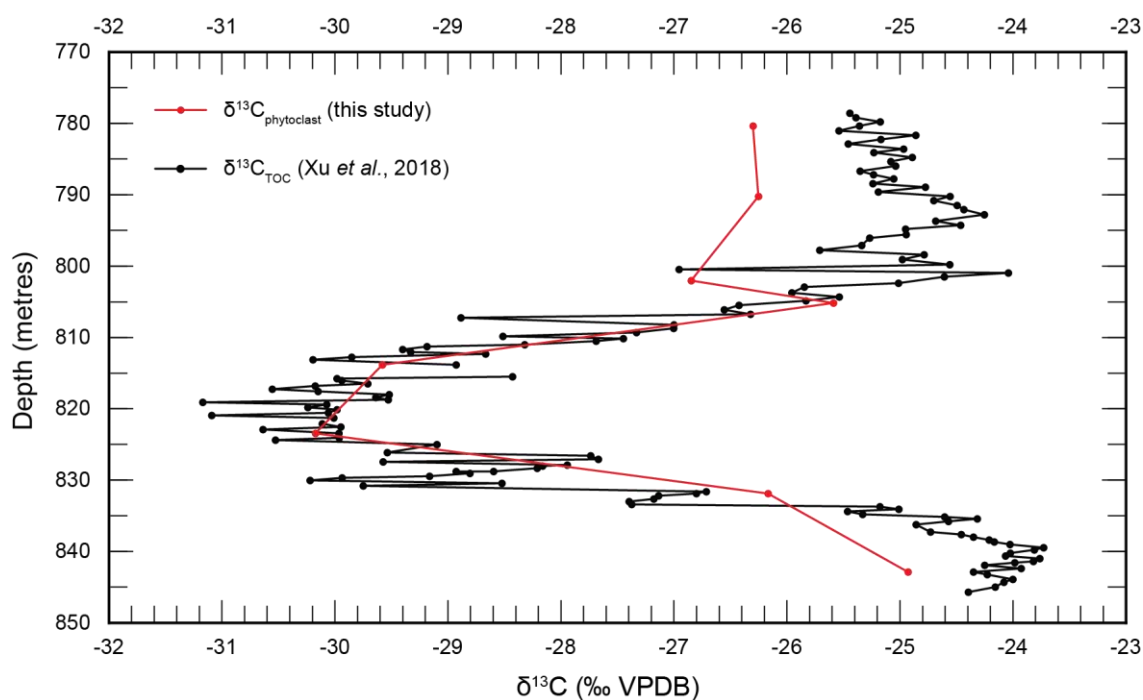
Figure 5.13 Average δ¹³C$_{phytoclast}$ values from this Mochras study plotted against the bulk organic matter carbon-isotope curve of Xu et al. (2018).

Hydrogen Index (HI) data published by (Xu et al., 2018) shows that the HI of the Mochras sediments varies between ~0 and ~350 mg hydrocarbons/g total organic carbon across the Toarcian OAE negative carbon-isotope excursion, indicating a change in organic matter composition and/or preservation throughout the T-OAE Mochras core section (**Figure 5.14**). The authors suggest that the increased HI values are the result of an increase in marine algal primary productivity, and/or an increase in marine organic matter preservation. Comparison of the two carbon-isotope curves with the HI curve shows that there is little correlation between HI and Δ$_{TOC-phytoclast}$. The poor correlation between HI and Δ$_{TOC-phytoclast}$ suggests that the divergence between the phytoclast and TOC C-isotope curves is not caused by a significant change in bulk organic matter composition.

Similar to the wider range of δ¹³C$_{phytoclast}$ values seen within both pre- and post-excursion samples, the greater Δ$_{TOC-phytoclast}$ difference both pre- and post-excursion could be explained by a change in plant assemblage. Different plant assemblages will have different carbon-isotopic signatures, and it is possible that the plant assemblage present during the most negative part of the Toarcian CIE had an overall carbon-isotope signature that was more similar to that of other
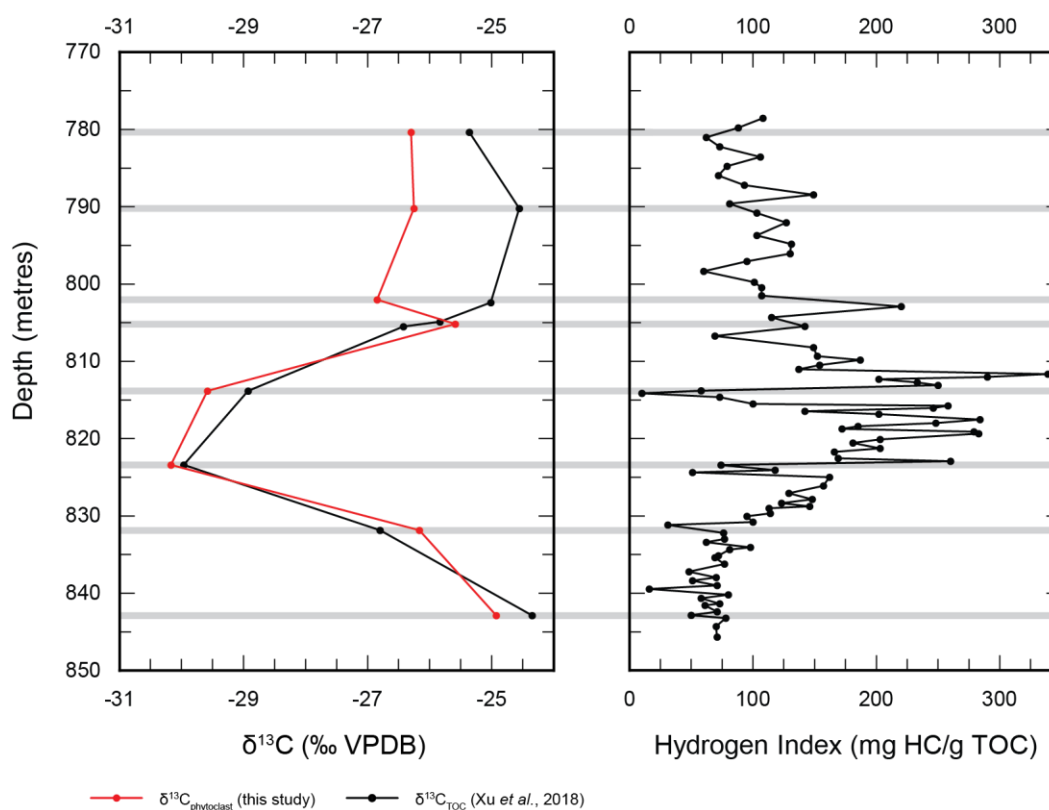
Figure 5.14 Average $\delta^{13}C$phytoclast (this study) and $\delta^{13}C$TOC (Xu et al., 2018) plotted alongside hydrogen index data from Xu et al. (2018).

types of organic matter, compared to the plant assemblages present both pre- and post-CIE.

The new Mochras $\delta^{13}C$phytoclast data correlate well with the $\delta^{13}C$TOC data of Xu et al. (2018), showing that even using a small number of $\delta^{13}C$ measurements on very small terrestrial phytoclast samples, it is possible to identify the Toarcian OAE negative carbon-isotope excursion. The disparity seen between the average $\delta^{13}C$phytoclast and $\delta^{13}C$TOC values could be caused by a number of factors, likely working in combination: changes in C-isotope discrimination by plants during photosynthesis, changes in plant assemblage, changes in composition and/or preservation of TOC.

5.5.2.5. Comparison with a Fossil Wood δ¹³C Record

The Mochras $\delta^{13}C$phytoclast data show a good correlation with the bulk organic matter $\delta^{13}C$ data of Xu et al. (2018), but the bulk OM samples analysed consist of a mixture of both terrestrial and marine matter, as discussed previously. A previously published fossil wood $\delta^{13}C$ record ($\delta^{13}C$wood) from a Toarcian

succession in Peniche, Portugal (Hesselbo, Jenkyns, et al., 2007), allows us to compare the new Mochras δ^{13}C$_{phyto}$ data to a purely terrestrial record.

The Peniche δ^{13}C$_{wood}$ record shows a negative carbon-isotope excursion of ~6‰ in the *levisoni* biozone, during the Early Toarcian, which correlates with the negative CIE of the Mochras δ^{13}C$_{phytoclast}$ record (**Figure 5.15**). The δ^{13}C values between the two sites are consistent, further confirming that the new Mochras δ^{13}C$_{phyto}$ data show a genuine record of the Toarcian OAE. There are some disparities, however, between the two datasets which require further discussion.

The magnitudes of the negative CIE recorded at the sites differs significantly by ~2‰ (~4‰ at Mochras; ~6‰ at Peniche). This could caused by a number of factors such as differences in plant assemblage, differing plant responses to climatic changes in the different locations, and/or differences in type of plant material analysed (e.g. cellulose vs lignin). Without published palynology studies of Mochras, it is not possible to compare plant assemblages at Mochras and Penice. Similarly, without palynology data, it is not possible to investigate how plants near the Mochras site adapted to climatic changes throughout the Toarcian. The Mochras samples consist primarily of lignin whereas the Peniche samples consist of a mixture of plant materials, including cellulose and lignin; this could perhaps partly-account for the difference in CIE magnitude at the two sites.

Both the pre- and post-excursion δ^{13}C values are more negative in the Mochras δ^{13}C$_{phytoclast}$ record than the Peniche δ^{13}C$_{wood}$ record, though the negative CIE δ^{13}C values at both sites are similar, ~-29‰ to ~-31‰.

The more negative pre- and post-excursion Mochras δ^{13}C$_{phytoclast}$ values can be explained by the sample material type. As discussed previously, whole macrofossil wood δ^{13}C values tend to be more positive compared to lignin and cellulose δ^{13}C values, however cellulose decays easily and will likely be absent in the fossil record (Scott, 2000). The Mochras δ^{13}C$_{phytoclast}$ values reflect samples that consist mainly of lignin, whereas the Peniche δ^{13}C$_{wood}$ values reflect samples that consist of several different types of plant tissue, including lignin and cellulose. The Peniche δ^{13}C$_{wood}$ values are the result of an averaging effect of the different tissue types present in the samples, resulting in more positive overall δ^{13}C values. The CIE δ^{13}C values at both sites are similar, most likely the result of increased
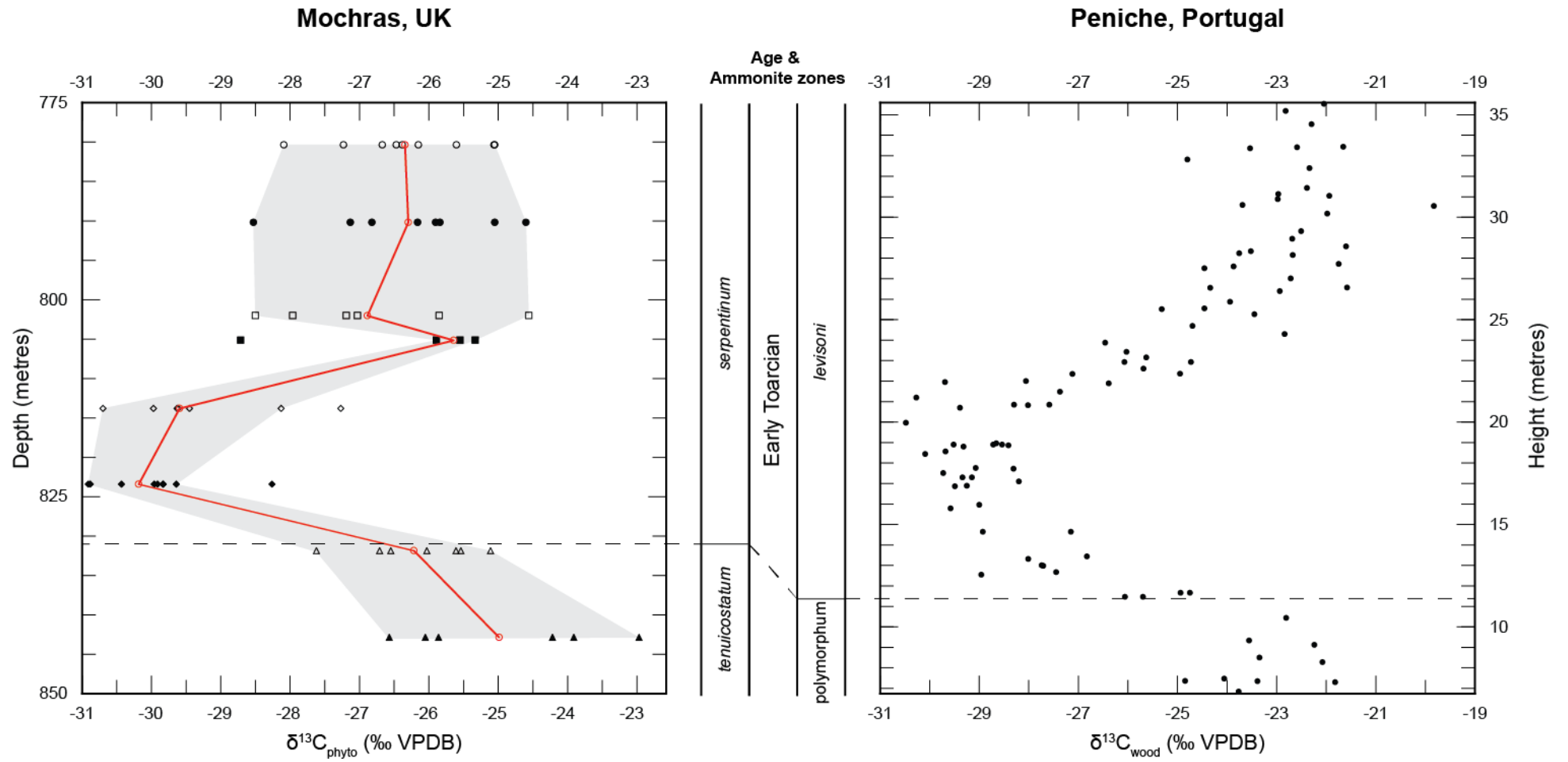
Figure 5.15 δ¹³C$_{phytoclast}$ data from this study plotted alongside δ¹³C$_{wood}$ data from Peniche, Portugal (Hesselbo, Jenkyns, et al., 2007). Correlation is based on Baker et al. (2017) and references therein. Note different horizontal scales.

carbon-isotope discrimination due to the input of massive amounts of ^{12}C into the atmosphere.

The Peniche $\delta^{13}C_{wood}$ curve also shows variation between fossil wood samples from the same sample horizon, similar to the Mochras $\delta^{13}C_{phytoclast}$ data. The Peniche fossil wood samples, however, show a narrower range in $\delta^{13}C$ values, with no greater than a ~2‰ difference between fossil wood samples from the same horizon. In contrast, the Mochras $\delta^{13}C_{phytoclast}$ values vary by up to ~4‰ between samples from the same horizon; this is likely a result of the amount of sample material analysed. Using the LA/nC/GC/IRMS method, several nanograms of carbon from each phytoclast sample were analysed, whereas a greater amount of carbon, on the order of micro- to milligrams, from each Peniche wood sample was analysed. With such small sample sizes, it is far less likely that the Mochras $\delta^{13}C_{phytoclast}$ data represent values that have been averaged by the different types of tissues present, such as in the Peniche wood samples. It is also possible that the two sites, Mochras and Peniche, have different plant assemblages present, which could also lead to the differences in $\delta^{13}C$ variation seen in this study.

Despite their differences, the Mochras $\delta^{13}C_{phytoclast}$ and Peniche $\delta^{13}C_{wood}$ isotope curves show a good correlation. The new Mochras $\delta^{13}C_{phytoclast}$ demonstrates here that even extremely small samples can be used to successfully reconstruct known large-magnitude carbon-isotope events.

5.5.2.6. Reproducing the Toarcian OAE Negative Carbon-isotope Excursion Using Single $\delta^{13}C_{phytoclast}$ Measurements

A random number generator was used to produce single $\delta^{13}C_{phytoclast}$ measurement curves in order to determine how accurately single $\delta^{13}C$ measurements could reproduce the known carbon-isotope pattern across the Toarcian OAE interval. All carbon-isotope curves produced by the random number generator show negative carbon-isotope excursions across the OAE, however, the overall shape of the C-isotope curves vary significantly, along with the magnitude.

The random number generator (RNG) C-isotope curves show negative CIEs between depths 800-830 m (**Figure 5.16**), similar to the negative CIE seen in the whole $\delta^{13}C_{phytoclast}$ dataset (**Figure 5.11**). The magnitude, however, of the RNG
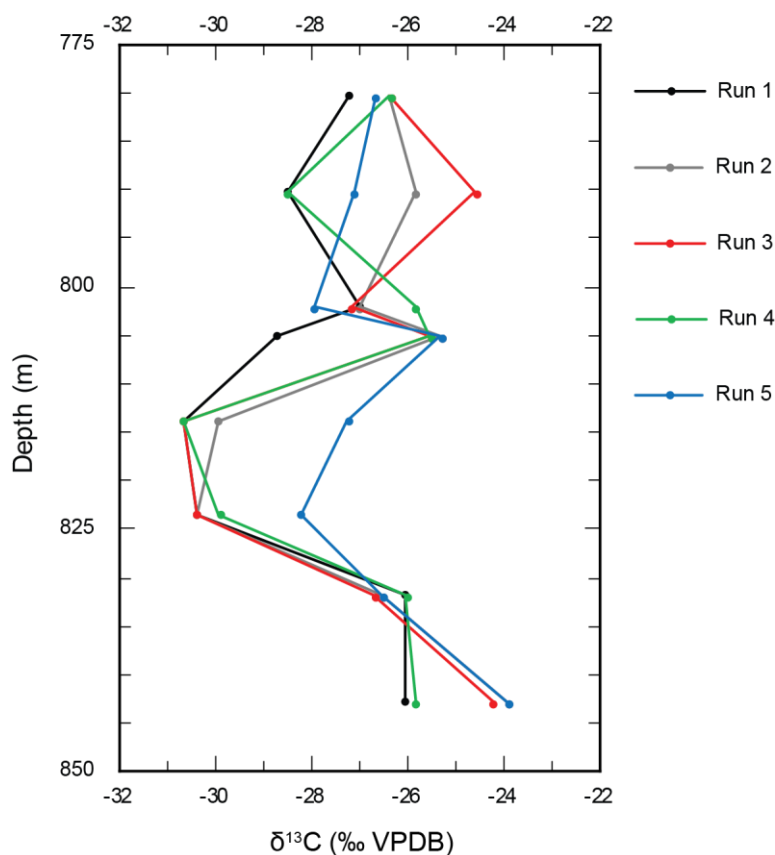
Figure 5.16 Carbon-isotope curves produced using a random number generator to select one δ^{13}C$_{phytoclast}$ measurement from each sample horizon. Outliers were included in the selection. See **Appendix B** for the RNG carbon-isotope curves from runs 6-20.

C-isotope curves varies from ~-2‰ to ~-7‰; the whole δ^{13}C$_{phytoclast}$ dataset shows a negative CIE of ~-7‰. The shape of the RNG C-isotope curves also differ greatly between runs, e.g. run 4 shows a large initial negative CIE followed by a second, smaller negative CIE, but run 3 shows a large negative CIE followed by a small positive CIE, similar to the whole δ^{13}C$_{phytoclast}$ dataset.

The RNG C-isotope curves show that even with one single phytoclast δ^{13}C measurement from multiple horizons, it is possible to identify major, in length and magnitude, carbon isotope excursions. Carbon-isotope curves generated from single phytoclast measurements, however, are less accurate at reproducing smaller fluctuations in δ^{13}C values. When δ^{13}C values return to more stable, normal values, it is much more likely that a single δ^{13}C$_{phytoclast}$ measurement will not accurately represent the average value of multiple single δ^{13}C$_{phytoclast}$ measurements.

5.6. Challenges Using the LA/nC/GC/IRMS Method

Using the LA/nC/GC/IRMS system presented a number of challenges, with only 60 out of a total of 118 samples resulting in a successful $\delta^{13}C$ measurement (~51% success rate). This technique is both time-consuming and sensitive, leading to a total of 58 samples which resulted in either no $\delta^{13}C$ measurement, or an unreliable one (**Table 5.5**). Reasons for the failed 58 measurements are discussed as follows.

One of the main difficulties of this technique is that it is extremely time-consuming, and no part of the process is automatable. Each single phytoclast sample is mounted on its own individual nickel disc, which can only be loaded into the sample chamber one at a time. Each time the sample chamber is opened and closed again, it must be flushed with helium gas until the background argon and carbon dioxide levels stabilise within the acceptable limits. Dependent upon several factors, it can take a minimum of ~30 minutes, and upwards of 2 hours, for the background argon and carbon dioxide levels to stabilise at suitable levels for analysis. The length of time that the sample chamber has been opened prior to flushing, and the quality of the seal between the O-rings and glass both affect how much time it takes for the background argon and carbon dioxide levels to stabilise. Sometimes it is not obviously apparent why the background argon and carbon levels are stabilising slowly, and one must simply wait until they have stabilised before carrying out the ablation and isotope analysis. The sequence used to measure the carbon-isotope values of the PE standard and phytoclast sample is completed in ~20 minutes. Considering the length of time it takes to prepare the phytoclast sample, the flushing of the sample chamber, and the length of the analysis sequence, it can easily take more than 1 hour to measure and analyse 1 single phytoclast.

The phytoclast samples are extremely fragile and it is not uncommon for them to become damaged or lost whilst being transferred from the sample tube to the nickel disc. Some phytoclasts had already broken in their sample tubes during transit. Once the phytoclast has been transferred to the nickel disc, there is a risk of dropping the disc and losing the phytoclast during each following stage of sample preparation.

No. of samples	Reason for failure
13	Phytoclast lost during transfer to sample chamber
8	Poor ablation of PE standard
7	Phytoclast destroyed during picking
7	Phytoclast lost during transfer to disc
6	Phytoclast moved away by laser during ablation
5	PE standard peak areas too small (i.e. not enough material ablated
2	Laser settings not correct
2	No visible phytoclast in sample tube
1	Background Ar and CO_2 levels not stabilising
1	PE standard moved by laser during ablation
1	PE standard took too long to ablate
1	PE standard σ too high
1	Phytoclast too close to edge of nickel disc for ablation
1	Sample chamber not in correct position
1	Stopped to check background Ar and CO2 levels
1	Wrong sequence started
58	**Total**

Table 5.5 Number of failed sample runs, and reasons for failure.

Applying too much pressure with the hydraulic press can also result in damaged phytoclasts, breaking up the samples into a number of smaller fragments, unsuitable for analysis. The pressed nickel discs must be separated carefully after the hydraulic pressing to prevent the phytoclast moving out of its pressing; phytoclasts that have moved out of their pressing are more likely to be blasted away by the laser during ablation. In some cases, phytoclasts could be pressed a second time prior to ablation, but this increases the risk of damaging the phytoclast and fragmenting it into smaller pieces. During pressing, it is possible for the phytoclasts to move from the centre of the nickel disc towards the edge; if the phytoclast (or PE film) is placed too close to the edge of the nickel disc, it will

be harder to focus the laser on the material, and the ablation quality will be poorer, sometimes failing.

Addition of the polyethylene film to the nickel disc with the phytoclast after pressing also carries a risk of knocking the phytoclast out of its pressing if the PE film is placed too close to the phytoclast. The PE film must also be placed onto the nickel disc at flatly as possible to ensure a good ablation. If the surface of the PE film is curved, there is an increased risk of the PE film not ablating properly. Without good ablation of the PE film, it is not possible to correct the δ^{13}C measurements for instrument error.

The nickel disc with the phytoclast sample and PE film must be loaded into the sample chamber from underneath, a procedure that carries an increased risk of dropping the disc. Care must also be taken not to knock the nickel disc on the sides of the sample chamber when securing it in place, to avoid knocking either the phytoclast out of its pressing, or the PE film towards the edge of the disc or on top of the phytoclast. Knocking the nickel disc on the sides of the sample chamber also carries a risk of the vacuum pump sucking up the phytoclast or PE film, losing the sample.

The phytoclasts and PE standard are both sensitive to the laser settings used, which can affect the quality of ablation and therefore, the carbon-isotope measurement made. During ablation, the laser can sometimes move the phytoclast or PE film, causing insufficient ablation; if the laser energy settings are too high, the phytoclast or PE film can be launched away by the laser, and lost, resulting in very little, or no, material ablated. In other cases, the laser can gently move the phytoclast or PE film, resulting in less material being ablated. It is extremely difficult to tell which phytoclasts might move during ablation, meaning that the analysis must be run to determine whether a reliable measurement can be made. Insufficient ablation of the material will result in a low peak area. Peak areas >4 Vs are ideal for carbon-isotope measurements, and required for reliable PE standard δ^{13}C measurements, though sample peak areas 1-4 Vs can be used providing the PE standard ablations produce peak areas >4 Vs. Dirty glass on the sample chamber can also result in low peak areas.

There is a fine balance between the laser energy settings being too high, or too low. Lengthy ablations result in the peak tail overlapping with the following ablation peak; this will result in an unreliable carbon-isotope measurement.

5.7. Conclusions & Future Work

The following conclusions can be drawn from this study:

- The Mochras core samples show no relationship between the mass of macrofossil wood analysed and $\delta^{13}C_{phytoclast}$.
- Variations in intra-sample $\delta^{13}C_{phytoclast}$ values are possibly caused by phytoclasts originating from different types of plants, or phytoclasts derived from different parts of the same plant taxon.
- The range of intra-sample $\delta^{13}C_{phytoclast}$ values is likely narrower during times of high levels of atmospheric carbon dioxide, due to a change in plant assemblage, either one with a dominance of a single taxon, or just fewer taxa in general.
- Single-phytoclast $\delta^{13}C$ measurements can be used to reproduce large excursions in bulk $\delta^{13}C$ values (>4‰) but are unable to accurately reproduce smaller variations (<2‰).
- Single-phytoclast $\delta^{13}C$ measurements can be used to reproduce large excursions as recorded in whole wood samples.

The work presented here in this chapter is only a small glimpse of what is possible using LA/nC/GC/IRMS method recently-developed by van Roij *et al.* (2017). The LA/nC/GC/IRMS method has already proven beneficial in the study of Palaeogene dinoflagellate cysts (Sluijs et al., 2018), and could prove extremely useful in the study of organic matter from other time intervals, particularly for samples with extremely low OM content.

The scope to continue this work further is huge and could include, but would not be limited to: measuring additional phytoclasts from the Mochras samples analysed in this study; measuring amorphous organic matter from the Mochras samples analysed in this study; measuring single phytoclasts from additional Mochras samples across the Toarcian OAE; further palynology studies of the T-OAE section of the Mochras core, to compare with the new data presented here;

measuring single phytoclasts from across other intervals with characteristic carbon-isotope stratigraphy, such as the Triassic-Jurassic Boundary; measuring single phytoclasts from different identified plant types, and tissues.

CHAPTER 6 FIRE AND GLOBAL CHANGE ACROSS THE TOARCIAN OCEANIC ANOXIC EVENT IN THE CENTRAL POLISH BASIN

6.1. Introduction

The Pliensbachian to Toarcian time interval (190.8 ± 1.0 – 174.1 ±1.0 Ma; Meister et al., 2006; Bordalo Da Rocha et al., 2016) was a time thought to have experienced extreme climatic conditions, including the global Toarcian Oceanic Anoxic Event (~183 Ma; Jenkyns, 1988) during which there was widespread deposition of organic-rich shales and a widespread increase in temperatures and rainfall/humidity (e.g. Jenkyns, 1988; Cohen et al., 2004; Korte et al., 2015).

Investigations of palaeoenvironmental conditions during the Pliensbachian and Toarcian often focus on the Pliensbachian-Toarcian Boundary and for the duration of the Toarcian Oceanic Anoxic Event. A significant number of $\delta^{13}C$ records during the Toarcian have been generated from multiple sites around the globe (e.g. Jenkyns et al., 2002; Hesselbo et al., 2007; Xu et al., 2018), as well as other geochemical palaeoenvironmental proxy records (e.g. Cohen et al., 2004; Percival et al., 2016; Xu et al., 2018). A very small number of studies investigating wildfire activity across the Toarcian Oceanic Anoxic event have been published, these suggesting significant changes in wildfire activity levels throughout the Toarcian. The deposition of a thick sequence of sediments in the central Polish Basin during the Early Jurassic (Pieńkowski, 2004) provides an excellent opportunity to not only study wildfire activity in the Polish Basin during the Pliensbachian and Toarcian, but also to examine this new record in a global context, aiding understanding of the climate across the world during this time.

6.2. Aims

This study aims to investigate wildfire activity in the central Polish Basin across the Toarcian Oceanic Anoxic Event, as well as identify geochemical palaeoenvironmental signals. New data from the Polish Basin will complement

published palaeoenvironmental data from other Tethyan realm localities, and will help to ascertain the geographic extent and variability in magnitude of climatic changes during the Toarcian. With the new data collected as part of this study, the following questions are addressed:

- Is there evidence of wildfire activity at the Kaszewy-1 site across the Toarcian Oceanic Anoxic Event?
- How does the wildfire activity history of the Kaszewy-1 site compare to other palaeoenvironmental records from within the Polish Basin?
- How does the wildfire activity history of the Kaszewy-1 site compare to other sites in the Tethyan realm across the Toarcian Oceanic Anoxic Event?

6.3. Background

6.3.1. Study Section: The Kaszewy-1 Core, Poland

The Kaszewy-1 borehole is located in present day central Poland (52°11'59.00"N, 19°29'28.82"E), approximately 100 km west of Warsaw, and was drilled in 2008 as part of an investigation by the Polish government of potential CO_2 sequestration reservoirs (**Figures 3.4 and 3.7**). A ~1500 metre long core of Upper Triassic-Middle Jurassic sediments was recovered. The Pliensbachian section of the Kaszewy-1 core comprises ~220 m of terrestrial and shallow marine siliciclastic sediments, while the Toarcian section is smaller, ~150 m, and also consists of terrestrial and marine siliciclastic sediments.

6.3.2. Wildfire Activity Proxies

6.3.2.1. Fossil Charcoal

A detailed discussion of the use of fossil charcoal abundance as a wildfire proxy is provided in **Section 3.5.1.2.** (p. 72).

Charcoal is formed during the pyrolysis (burning in the absence of oxygen) of organic matter (OM; Scott and Jones, 1991) and is often found in the fossil record due to its robustness (e.g. Scott and Glasspool, 2007). The presence of fossil charcoal in sediments is used as an indicator of past wildfire activity (e.g.

Carcaillet et al., 2002; Power et al., 2007), and it is thought that changes in fossil charcoal abundance reflect changes in wildfire activity (e.g. Whitlock et al., 2006). Generally, an increase in fossil charcoal abundance reflects an increase in wildfire activity level. Different size fractions of fossil charcoal are thought to reflect the wildfire activity signal from different areas; fine fossil charcoal abundance reflects a more regional signal, while coarse fossil charcoal abundance reflects a more local signal (e.g. Kawano et al., 2012). Other factors should also be considered when interpreting fossil charcoal abundance records, such as the lithology and inferred depositional environments of sediment samples analysed (e.g. Belcher et al., 2010). The influence of pre-depositional transport, preservation, reworking, and diagenesis should also be taken into consideration.

6.3.2.2. Pyrolytic Polycyclic Aromatic Hydrocarbons

A detailed discussion of the use of polycyclic aromatic hydrocarbons (PAHs) as a wildfire proxy is provided in **Section 3.5.2.2.** (p. 79).

Polycyclic aromatic hydrocarbons are a group of organic molecules that have ringed structures. Some PAHs are formed during the pyrolysis of organic matter, known as pyrolytic PAHs, and can be used as a proxy for wildfire activity (e.g. Jiang et al., 1998; Belcher et al., 2009). Generally, it is thought that an increase in pyrolytic PAH abundance reflects an increase in wildfire activity, and *vice versa* (e.g. Shen et al., 2011). There is conflicting evidence about the spatial extent of pyrolytic PAH records; some studies suggest they record a local signal, while others suggest pyrolytic PAHs record a regional signal (Scott, 2009; Abdel-Shafy and Mansour, 2016). Pyrolysis is not the only source of PAHs; some PAHs originate from petrogenic sources, though these typically have a different structure to pyrolytic PAHs (e.g. Jiang et al., 1998; Shen et al., 2011). The land plant biomarker retene is also a PAH that is not produced during pyrolysis of organic matter (e.g. Peters et al., 2007). Similar to fossil charcoal as a proxy for wildfire activity, other factors should be considered when interpreting pyrolytic PAH data, such as lithology, depositional environments, and the occurrence, if any, of petrogenic PAHs alongside pyrolytic PAHs (e.g. Venkatesan and Dahl, 1989; Abdel-Shafy and Mansour, 2016).

6.3.3. Previous Work

A detailed discussion of previous studies of Toarcian sediments from the Polish Basin and Toarcian wildfire records in general is provided in **Sections 3.3.2.2.** (p. 52) and **3.5.4.2.** (p. 89).

There are few studies published in the English language regarding the Toarcian of the Polish Basin. The characteristic large negative CIE of the Toarcian OAE, preceded and followed by smaller positive CIEs, is documented at a number of sites in the Polish Basin (Hesselbo and Pienkowski, 2011). Clay mineral analyses of Toarcian-aged sediments from the Polish Basin indicate changes in weathering regime, humidity and temperatures (Brański, 2012).

A small number of published wildfire activity proxy datasets show evidence of increased wildfire activity prior to the Toarcian OAE negative CIE, and during the recovery period. Fossil charcoal abundance records from Portugal and the UK correlate well with each other and carbon-isotope records from the same sites (Baker et al., 2017). Another study of sediments from the UK shows elevated concentrations of PAHs prior to the Toarcian OAE and during the recovery period, also correlating well with carbon-isotope records from the site (French et al., 2014). Despite the lack of wildfire activity proxy records, the abundance and high-resolution of accompanying carbon-isotope records allows for confident correlations between these sites.

6.4. Materials & Methods

6.4.1. Materials

Nine samples from the Pliensbachian and Toarcian sections of the Kaszewy-1 core were collected for fossil charcoal abundance quantification and polycyclic aromatic hydrocarbon analyses. The 9 samples were collected from between depths 1169.10 m and 1297.20 m, at an average resolution of 1 sample per 14.23 m. All 9 samples comprise either mudstones thought to have been deposited in terrestrial or shallow marine environments. Sediments of the same lithology were chosen so as to minimise the bias caused by sedimentology.

6.4.2. Methods

6.4.2.1. Fossil Charcoal Quantification

A detailed discussion of the method used for fossil charcoal quantification is provided in **Section 4.2.** (p. 99). Samples were prepared by the author at the University of Exeter, with the assistance of M. Grosvenor, and analysed by the author.

Standard acid maceration techniques were used to liberate fossil organic matter (OM) from bulk rock samples. Hydrochloric and hydrofluoric acids were used to remove all carbonate and silicate material, respectively. The remaining fossil OM was then sieved at 125 µm into a coarse (>125 µm) fraction and a fine (<125 µm) fraction. Sub-samples of the fine fraction of each sample were used to create microscope slides for fossil charcoal quantification. The number of fossil charcoal particles in both the coarse and fine fractions were counted, along with the number of fossil non-charcoal particles in the fine fraction. Final counts were normalised per 10 grams of sediment.

6.4.2.2. Polycyclic Aromatic Hydrocarbon Quantification

A detailed discussion of the method used for polycyclic aromatic hydrocarbon quantification is provided in **Section 4.3.** (p. 102). Samples were prepared and analysed by the author at the National Oceanography Centre, Southampton.

Standard organic geochemical techniques were used to extract PAHs from sediment samples and quantify them. The total lipid extract (TLE) was taken from sediments using a 1:1 mix of dichloromethane and methanol. The TLE was separated into three fractions (non-polar, aromatic, polar) using column separation and 3 different solvents. The aromatic fraction was analysed using GC-MS; a total of 20 different PAH molecules were identified and quantified using the GC-MS chromatograms and reference material. Final concentrations of PAHs were normalised per gram of sediment.

6.5. Results & Discussion

6.5.1. Fossil Charcoal Abundance

6.5.1.1. Coarse Fossil Charcoal Abundance

The abundance of coarse fossil charcoal particles (>125 μm) in the Pliensbachian and Toarcian sections of the Kaszewy-1 core is very low, ranging from 0 particles/10 g sediment to 15 particles/10 g sediment (**Figure 6.1**). Three samples (kk_42, depth: 1238.07 m; kk_42c, depth: 1215.75 m; kk_47, depth: 1169.10 m) were lacking in coarse fossil charcoal particles. The coarse fossil charcoal abundance of sample kk_35 (depth: 1289.70 m) was not counted due to excess sediment clouding the sample and hindering counting.

Coarse fossil charcoal abundance is very low in the two oldest samples from the Pliensbachian part of the study section: 1 and 0 particles/10 g sediment. The abundance of coarse fossil charcoal particles increases slightly just above the Pliensbachian-Toarcian boundary, to 2 particles/10 g sediment. Coarse fossil charcoal abundance then decreased to 0 particles/10 g sediment in the next two Toarcian samples (kk_42, kk_42c), moving up the core. Peak coarse fossil charcoal abundance is observed in sample kk_45y, with a value of 15 particles/10 g sediment, before abundance drops moving up the core, first to 4 particles/10 g sediment in sample kk_46b and then 0 particles/10 g sediment in sample kk_47.

6.5.1.2. Fine Fossil Charcoal Abundance

Fine fossil charcoal particles (<125 μm) are much more abundant in all of the Pliensbachian and Toarcian samples than coarse fossil charcoal particles (**Figure 6.2**). Fine fossil charcoal abundance ranges from ~12,000 particles/10 g sediment (sample kk_42c; depth: 1215.75 m) to ~256,000 particles/10 g sediment (sample kk_39; depth: 1250.75 m). Fine fossil charcoal abundance is generally low in the Pliensbachian part of the study section, ranging from ~59,800 particles/10 g sediment to ~130,000 particles/10 g sediment. Fine fossil charcoal abundance peaks immediately above the Pliensbachian-Toarcian Boundary, with a value of ~256,000 particles/10 g sediment. Fine fossil charcoal abundance does not peak in the same sample as coarse fossil charcoal abundance. In the following four Toarcian-aged samples, moving up the core, fine fossil charcoal
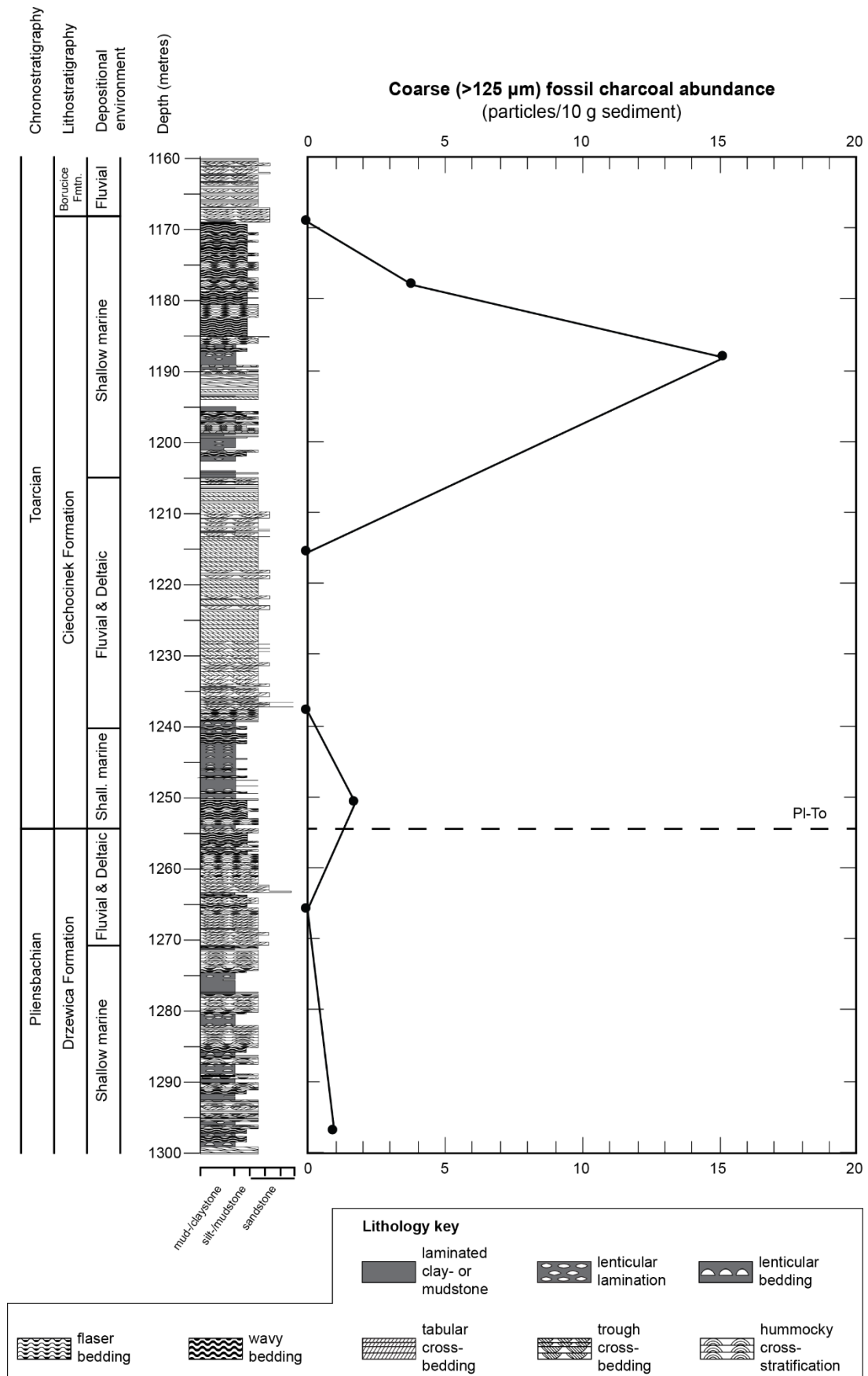
Figure 6.1 Coarse fossil charcoal abundance through the study section of the Kaszewy-1 core. Pl-To = Pliensbachian-Toarcian Boundary. Lithological succession from Pieńkowski (pers. comm.).

abundance drops to low values ranging from ~12,000 particles/10 g sediment to ~26,600 particles/10 g sediment. Fine fossil charcoal abundance increases in the uppermost sample of the study section (Late Toarcian age), with a value of ~175,000 particles/10 g sediment.

6.5.1.3. Fine Fossil Non-charcoal Abundance

Fine fossil non-charcoal particles (i.e. preserved organic matter that has not been charcoalified; <125 µm) are more abundant than, and show a similar abundance pattern to, fine fossil charcoal particles (**Figure 6.2**). The abundance of fine fossil non-charcoal particles is an order or magnitude greater than fine fossil charcoal particle abundance, and ranges from ~132,000 – ~8,160,000 particles/10 g sediment. Fine fossil non-charcoal abundance is generally low in the Pliensbachian part of the study section, ranging from ~154,000 particles/10 g sediment to ~789,000 particles/10 g sediment. The abundance of fine fossil non-charcoal particles peaks immediately above the Pliensbachian-Toarcian Boundary, at a value of ~8,160,000 particles/10 g sediment; this is the same sample in which fine fossil charcoal abundance peaks. Fine fossil non-charcoal abundance then rapidly declines and remains low for the rest of the samples in the Toarcian part of the study section. The abundance of fine fossil non-charcoal particles in this part of the section ranges from ~132,000 particles/10 g sediment to ~1,200,000 particles/10 g sediment.

6.5.1.4. Percentage of Fine Fossil Charcoal

The percentage of fine fossil charcoal particles, in terms of total fine OM particle abundance, varies throughout the Pliensbachian-Toarcian study section from 3.0% to 16.1% and does not show a similar pattern to either coarse or fine fossil charcoal abundance (**Figure 6.2**). The percentage of fine fossil charcoal particles in the fine fraction is relatively high at the bottom of the study section (14.2%) but then declines moving up the core towards the Pliensbachian-Toarcian Boundary. The percentage of fine fossil charcoal particles present reaches a low of 3.0% in sample kk_39 (depth: 1250.75 m), immediately above the Pliensbachian-Toarcian Boundary. The percentage of fine fossil charcoal particles then increases moving up through the Toarcian part of the study section, ranging from 6.1% to 16.1%, with some fluctuations at the top of the study section. The sample containing the highest proportion of fine fossil charcoal particles is sample kk_45y
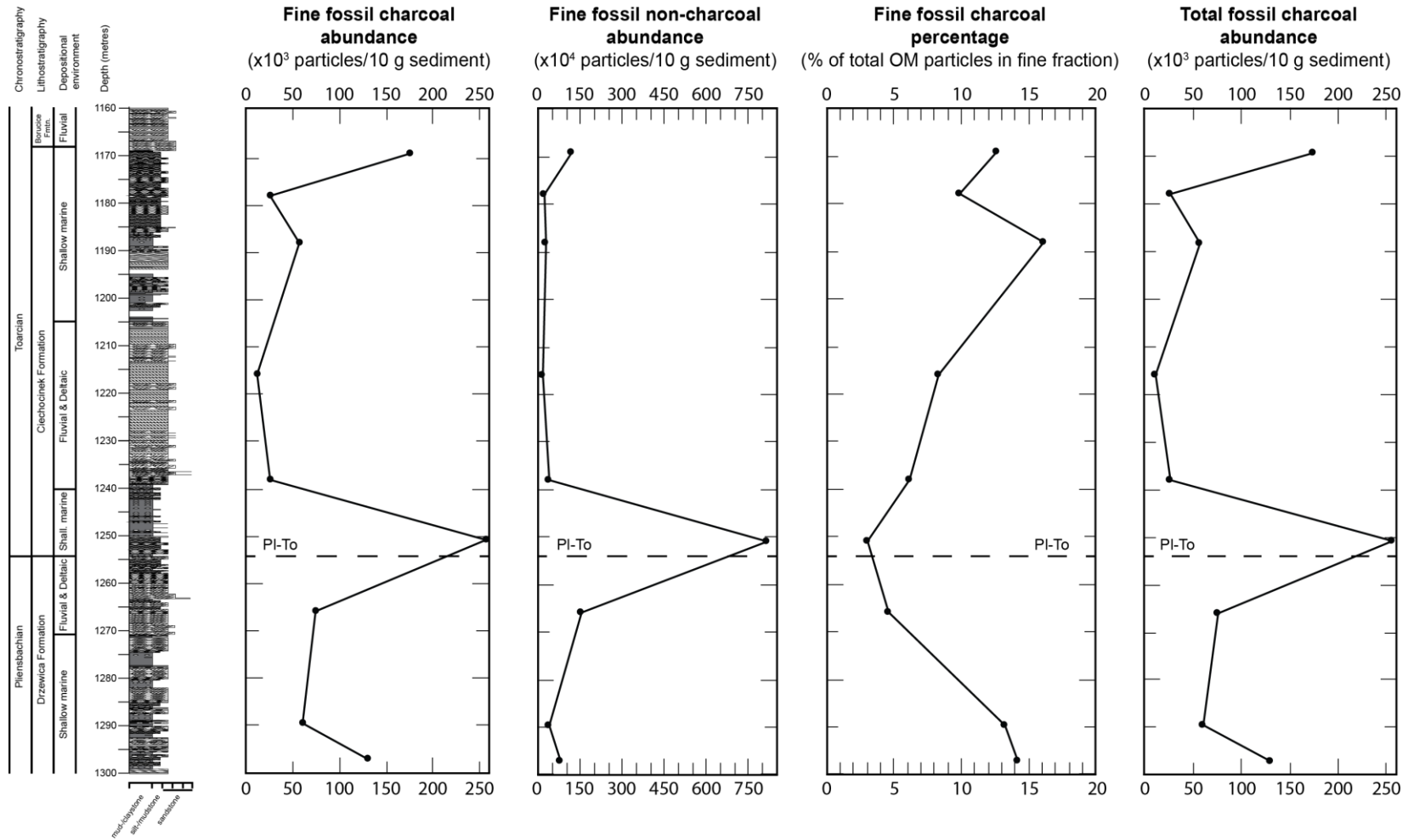
Figure 6.2 Kaszewy-1 core: Abundance of fine fossil charcoal & non-charcoal; percentage of fine fossil charcoal present; total fossil charcoal abundance (i.e. sum of coarse and fine fossil charcoal abundance). See **Figure 6.1** for lithology key. Pl-To = Pliensbachian-Toarcian Boundary; based on sequence stratigraphy. Lithological succession from Pieńkowski (pers. comm.).

(16.1%; depth: 1188.15 m); this is not the sample containing the highest absolute value of fine fossil charcoal particles, though it is the sample containing the highest absolute value of coarse fossil charcoal particles. The varying proportion of fine fossil charcoal particles in the Pliensbachian-Toarcian Kaszewy-1 samples shows that absolute fine fossil charcoal abundance is not controlled by the total number of fine organic matter particles (i.e. fine fossil charcoal + fine fossil non-charcoal), but is being controlled by another factor, such as changes in lithology, depositional environment, or wildfire activity.

The percentage of charcoal in terms of total OM particles is rarely discussed in published studies (see e.g. Baker et al. (2017) as an exception). It is generally accepted that changes in absolute charcoal abundance are sufficient to assess wildfire activity levels qualitatively, once other factors (e.g. lithology, depositional environment) have been taken into consideration. Changes in absolute charcoal abundance are usually interpreted qualitatively, discussing them in terms of increased or decreased wildfire activity, rather than quantitatively. This presents a challenge when comparing the new Polish Basin data to published records, and for this reason, absolute fossil charcoal abundance is discussed when compared to other published charcoal records, and other palaeoenvironmental records. This does limit the interpretation of the data somewhat, and conclusions are made with caveats. Refining the techniques involved with fossil charcoal studies is needed, and as this area of work grows, the interpretation of fossil charcoal records will improve and lead to more robust conclusions.

6.5.1.5. Total Fossil Charcoal Abundance

The total number of fossil charcoal particles (>125 μm and <125 μm) present in each sample is heavily biased by the abundance of fine fossil charcoal particles (**Figure 6.2**). Total fossil charcoal abundance is generally low in the Pliensbachian part of the study section, before peaking immediately above the Pl-To Boundary. The abundance of total fossil charcoal declines moving up through the Toarcian section of the core, before increasing again at the top of study section.

6.5.1.6. Effect of Lithology & Depositional Environment on Fossil Organic Matter Abundance

The depositional environment and lithology of the sediments in which charcoal is eventually deposited in can affect the abundance of preserved charcoal in those sediments (e.g. Scott, 2010). The sedimentology of the Kaszewy-1 core changes frequently, and reflects sediment deposition in a range of terrestrial and shallow-marine environments. Sedimentary facies were assigned based on lithological, sedimentary structural, trace fossil, and body fossil evidence, as well as sequence stratigraphy (Pieńkowski, pers. comm.).

The samples analysed for this study are all mudstones, therefore eliminating the potential for variations in fossil charcoal abundance due to major changes in grain size and lithology. The median and maximum grain size of the horizons sampled show very weak correlations with coarse and fine fossil charcoal abundance, and fine non-fossil charcoal abundance (**Table 6.1**); similarly, the lithofacies shows a very weak correlation with organic matter abundance (**Table 6.1**).

The inferred depositional environments of the sediments sampled vary from fluvial to shallow-marine, with different inferred energies. The abundance of organic matter in the Kaszewy-1 samples does not appear to correlate with either the inferred energy of the depositional environments, or the marine influence of

	Coarse Fossil Charcoal Abundance	**Fine Fossil Charcoal Abundance**	**Fine Fossil Non-Charcoal Abundance**
Maximum grain size	0.112	0.024	0.259
Median grain size	0.181	0.030	0.086
Depositional setting – marine influence	0.224	0.123	0.057

Table 6.1 R^2 (coefficient of determination) values calculated from cross-plots of coarse and fine fossil charcoal, and fine fossil non-charcoal abundances against various lithological properties for the Kaszewy-1 samples. R^2 values range between 0 and 1, with lower values indicating a weaker relationship between the two variables (Taylor, 1990). The lithological properties were assigned a numerical value by the author in order to calculate the degree of correlation between pyrolytic PAH concentration and lithology.

the depositional environment (**Table 6.1**). The lack of strong correlations between various lithological and depositional environment-related parameters and fossil organic matter abundance suggests that another factor is responsible for producing the changes in fossil organic matter abundance throughout the Pliensbachian-Toarcian section of the Kaszewy-1 core. Changes in climatic conditions and wildfire activity could explain the patterns seen here in the Pl-To Kaszewy-1 samples (see **Section 6.5.3.** for further discussion).

6.5.2. Polycyclic Aromatic Hydrocarbon Concentrations

6.5.2.1. Pyrolytic PAH Concentrations

Pyrolytic PAHs were detected in all nine samples in concentrations ranging from 37 ng/g sediment to 985 ng/g sediment (**Figure 6.3**). Benz-anthracene, benzo(k)fluoranthene, fluoranthene, indeno[1,2,3-cd]pyrene, phenanthrene and pyrene were detected in all nine samples. Coronene was detected in quantifiable amounts in seven samples and fluorene was detected in quantifiable amounts in only six samples.

The most abundant pyrolytic PAH in every sample is phenanthrene, with concentrations ranging from 55 ng/g sediment to 986 ng/g sediment. The least abundant pyrolytic PAH in every sample is coronene (37-83 ng/g sediment), closely followed by fluorene (46-147 ng/g sediment). The low concentrations of coronene relative to the other pyrolytic PAHs in the Pliensbachian-Toarcian samples of the Kaszewy-1 core suggest that coronene was produced during the pyrolysis of organic matter, rather than originating from a petrogenic source (cf. Belcher et al., 2005, and references therein).

The general shape of the pyrolytic PAH concentration records shows relatively low concentrations (58-600 ng/g sediment) at the bottom of the study section, in the Pliensbachian part, before a relatively large increase in concentrations (49-985 ng/g sediment) in the last sample before the Pliensbachian-Toarcian Boundary. The concentration of pyrolytic PAHs generally decreases sharply above the Pl-To Boundary to relatively low values (45-172 ng/g sediment). An increase in pyrolytic PAH concentrations (49-430 ng/g sediment) is seen in samples at the top of the study section, in the uppermost Toarcian part.

Figure 6.3 Concentrations of 8 different pyrolytic PAHs throughout the Kaszewy-1 study section. Pl-To = Pliensbachian-Toarcian Boundary.

Pyrolytic PAHs typically form at temperatures above 350°C, and will continue to form at temperatures greater than 1200°C (Abdel-Shafy and Mansour, 2016), with lower molecular weight (*m/z*) molecules forming prior to those with higher *m/z* (Ledesma et al., 2006; Kislov et al., 2013). Fluorene and phenanthrene have the lowest molecular weights (166 and 176, respectively) but differ greatly in concentration throughout the study section; phenanthrene is the most abundant pyrolytic PAH in each sample, whereas fluorene is one of the least abundant, sometimes missing entirely. A number of studies suggest that phenanthrene can also be produced during sediment diagenesis as well as during the pyrolysis of organic matter (e.g. Jiang et al., 1998). Given the large discrepancy in concentrations of phenanthrene and fluorene (both low *m/z* pyrolytic PAHs), it is likely that diagenetic phenanthrene is present in these samples and is masking the pyrolysis-derived phenanthrene signal. For this reason, phenanthrene is no longer included as a pyrolytic PAH in the discussion of the Kaszewy-1 Pliensbachian-Toarcian samples.

	Maximum grain size	Median grain size	Depositional setting – marine influence
Fluorene	0.308	0.051	0.057
Fluoranthene	0.016	0.013	0.050
Pyrene	0.006	0.045	0.096
Benz-anthracene	0.186	0.103	0.053
Benzo(k)fluoranthene	0.100	0.010	0.041
Indeno[1,2,3-cd]pyrene	0.162	0.014	0.028
Coronene	0.208	0.041	0.001

Table 6.2 R^2 (coefficient of determination) values calculated from cross-plots of pyrolytic PAH concentrations against various lithological properties for the Kaszewy-1 samples. R^2 values range between 0 and 1, with lower values indicating a weaker relationship between the two variables (Taylor, 1990). The lithological properties were assigned a numerical value by the author in order to calculate the degree of correlation between pyrolytic PAH concentration and lithology.

The concentrations of each pyrolytic PAH do not appear to correlate with lithological or depositional environment-related parameters, suggesting that another factor, such as wildfire activity controlled the changes in concentrations of the pyrolytic PAHs discussed here (**Table 6.2**).

6.5.2.2. Petrogenic PAH Concentrations

Significant concentrations of petrogenic PAHs were detected in all of the samples from the Pliensbachian-Toarcian study section of the Kaszewy-1 core (**Figure 6.4**). In some samples, petrogenic PAHs are more abundant than pyrolytic PAHs, suggesting that the pyrolytic PAHs may not reflect particularly high levels of wildfire activity (cf. Venkatesan and Dahl, 1989). The high total concentration of PAHs with additional alkyl chains suggests that there is/was a significant source of hydrocarbons proximal to the Kazewy-1 site. Unpublished Rock-Eval data suggest that the sediments between ~1250 m and ~1275 m depth have a good source rock potential, with relatively high TOC values (~3.3% – ~5.8%) and T_{max} values indicating mature organic matter (437-441°C) (Pieńkowski, pers. comm.).
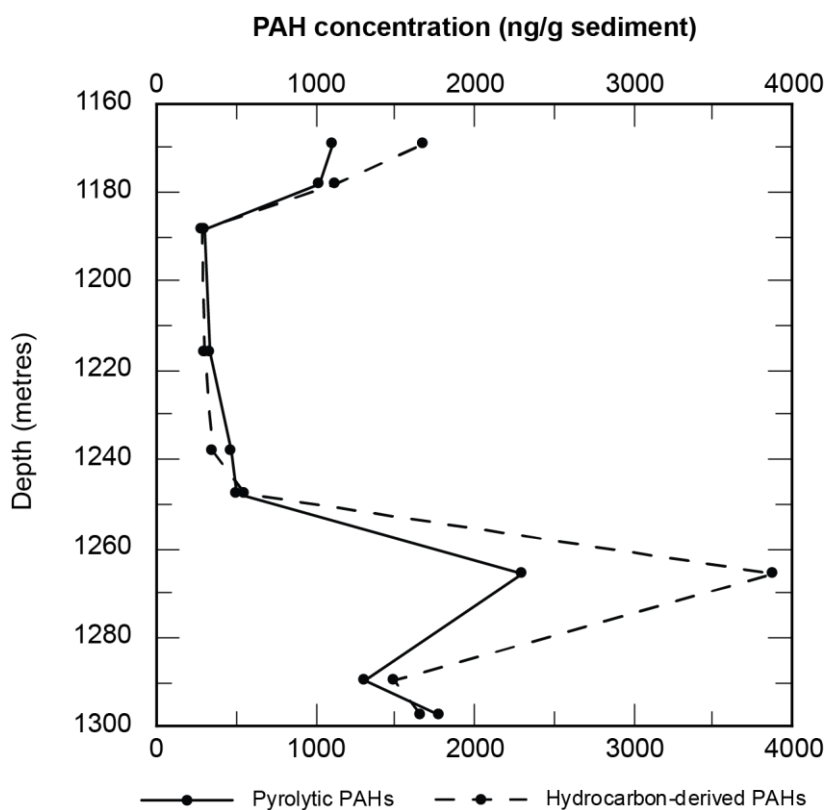
Figure 6.4 Total concentration of petrogenic PAHs plotted alongside total concentration of pyrolytic PAHs for the Kaszewy-1 core Pliensbachian-Toarcian section.

Sample kk_38 (depth: 1265.90 m) has an extremely high total concentration of petrogenic PAHs (~3878 ng/g sediment) which, along with the unpublished Rock-Eval data, suggests that this sample is likely contaminated with PAHs derived from petrogenic sources. Rock-Eval data from the rest of the study section suggests that only sediments between ~1250 – 1275 m depth have a good source rock potential. It is likely that the Pliensbachian-Toarcian PAH sediment samples are contaminated with petrogenic PAHs that possibly formed during burial of sediments containing organic matter. Comparison of the new pyrolytic PAH data with new fossil charcoal abundance data, and with wildfire activity records from other sites should help to clarify the origin and interpretation of the pyrolytic PAHs.

6.5.3. Wildfire Activity History at the Kaszewy-1 Site

Increases in both fossil charcoal abundance and pyrolytic PAH concentration throughout a sedimentary succession are thought to indicate periods of increased wildfire activity (e.g. Jiang et al., 1998; Carcaillet et al., 2002; Belcher et al., 2009; Scott, 2010). Distance from wildfire activity can be indicated by comparing the records of different size fractions of fossil charcoal and geochemical data (e.g. Tinner et al., 1998; Carcaillet et al., 2001; Abdel-Shafy and Mansour, 2016). Fossil charcoal abundance and pyrolytic PAH concentration data indicate up to six potential levels and three overall periods of increased wildfire activity recorded at the Kaszewy-1 site during the Pliensbachian and Toarcian (**Figure 6.5**).

The levels of increased wildfire activity indicated here do not appear to be biased by depositional environment (as discussed in **Section 6.5.1.6.**, p. 159). Samples were sieved at 125 µm, sorting the particles into a coarse fraction, representing material derived from the local area (short transport distance), and a fine fraction, representing material derived from the wider region (larger transport distance). There was not sufficient time to sieve the samples at additional size thresholds; sieving at 125 µm is the accepted standard, though sieving at additional thresholds would provide a more complete picture of size sorting and therefore transport distance. The addition of TOC and microfossil data would also allow for a better understanding of changes in sedimentation rate and reworking, respectively.
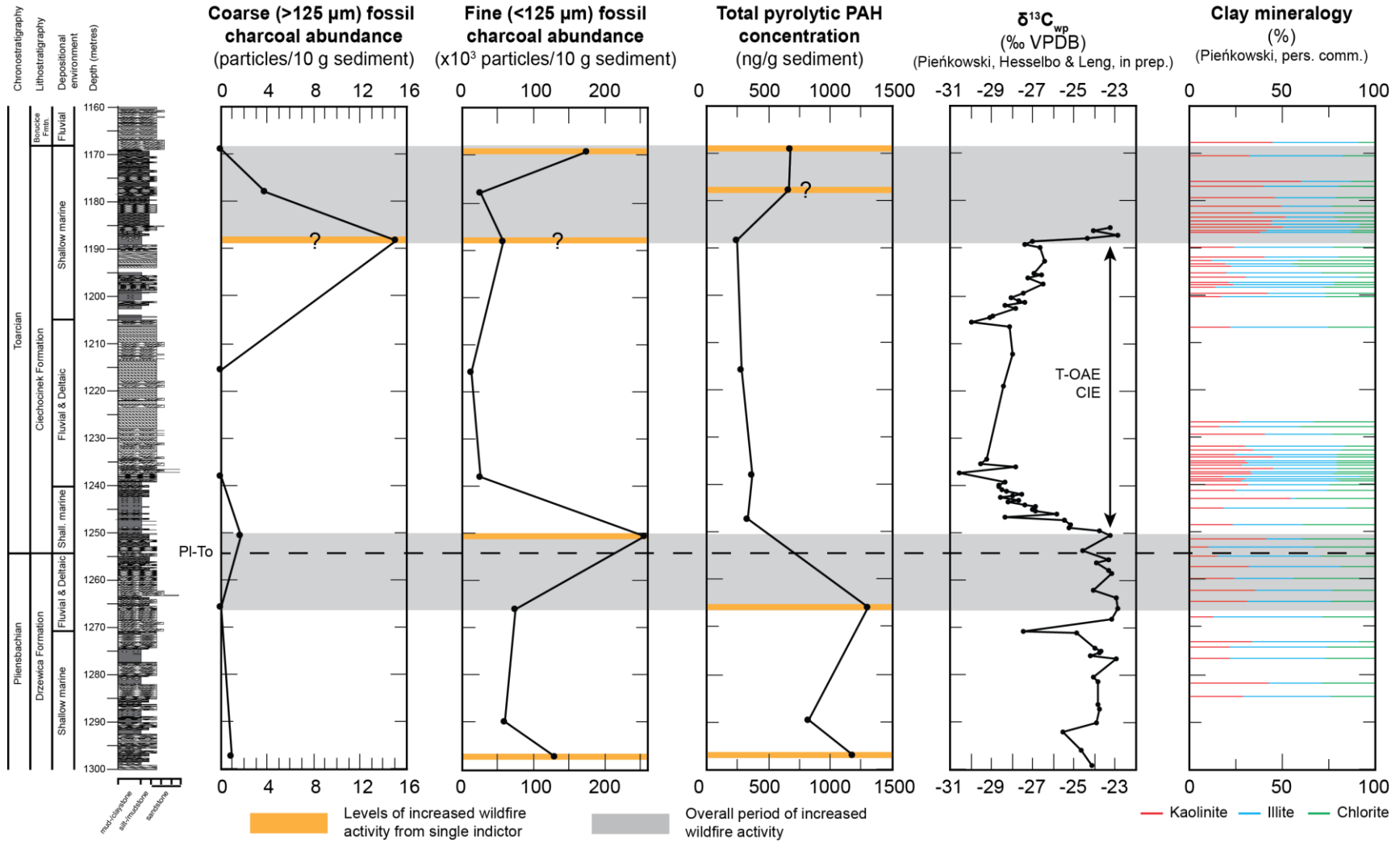
Figure 6.5 New fossil charcoal abundance and pyrolytic PAH concentration records from the Kaszewy-1 core correlated with δ¹³C$_{wp}$ records (Pieńkowski, Hesselbo & Leng, in prep.) and clay mineralogy records (Pieńkowski, pers. comm.). Levels of increased wildfire activity from a single indicator are highlighted in orange; overall periods of increased wildfire activity are highlighted in grey. Pl-To = Pliensbachian-Toarcian Boundary. Lithological succession from Pieńkowski (pers. comm.).

The first level of increased wildfire activity is indicated by increased fine fossil charcoal abundance and total pyrolytic PAH concentration at the bottom of the study section (sample: kk_34; depth: 1297.20 m). A significant lack of coarse fossil charcoal in the same sample suggests that the Kaszewy-1 site itself did not experience increased wildfire activity, but instead that the fine fossil charcoal abundance and pyrolytic PAH concentration records have recorded a more regional wildfire signal (cf. Scott, 2010; Abdel-Shafy and Mansour, 2016).

A second level of increased wildfire activity is indicated by only increased pyrolytic PAH concentrations in sample kk_38 (depth: 1265.90 m) prior to the inferred Pliensbachian-Toarcian boundary. Neither coarse nor fine fossil charcoal abundance is particularly high in this sample, perhaps suggesting that wildfire activity occurred further from the Kaszewy-1 site than during the previous level of increased wildfire activity.

Fine fossil charcoal abundances peaks in sample kk_39 (depth: 1250.75 m), immediately after the inferred Pliensbachian-Toarcian Boundary; there is also a relatively small increase in coarse fossil charcoal abundance. Pyrolytic PAH concentrations for this sample could not be analysed due to insufficient sample material. The increase in fine fossil charcoal abundance and, to a much lesser extent, coarse fossil charcoal abundance suggests a third level of increased wildfire activity, perhaps closer to the Kaszewy-1 site than the two previous levels of increased wildfire activity. This third level of increased wildfire activity coincides with the beginning of the Toarcian OAE negative carbon-isotope excursion, as $\delta^{13}C_{wp}$ values begin to shift towards more negative values from relatively positive ones.

During the negative carbon isotope excursion associated with the Toarcian OAE, there is a significant decline in both coarse and fine fossil charcoal abundance. Similarly, the total concentration of pyrolytic PAHs declines and remains low for the duration of the negative carbon-isotope excursion. A lack of fossil charcoal and low pyrolytic PAH concentration in this section suggests that there was a significant decline in wildfire activity during the Toarcian OAE. Contemporaneous wildfire activity records from other European sites also indicated a period of suppressed wildfire activity associated with the negative CIE of the Toarcian OAE (**Section 6.5.3.2.**).

At the end of the Toarcian OAE negative CIE, during the recovery period as $\delta^{13}C_{org}$ values become more positive, a potential fourth level of increased wildfire activity is indicated by an increase in coarse fossil charcoal abundance (sample: kk_45y; depth 1188.15 m). An increase in fine fossil charcoal abundance is also observed in the same sample, though this is relatively small. The total concentration of pyrolytic PAHs in this sample is also very low. Considering these three separate wildfire activity records together, it is possible that sample kk_45y does not record a fourth level of increased wildfire activity, but is the result of sedimentary bias. Sample kk_45y is a mudstone thought to have been deposited in an offshore environment; it is possible that the charcoal found at this horizon has been transported a large distance by water (charcoal is extremely buoyant) prior to deposition at the Kaszewy-1 site. If, however, the fossil charcoal records are faithfully recording a fourth level of increased wildfire activity, the fire would have been local to the Kaszewy-1 site, likely the closest of all of the six levels of increased wildfire activity recorded by the Kaszewy-1 sediments.

A potential fifth level of increased wildfire activity is indicated by an increase in the total concentration of pyrolytic PAHs in sample kk_46b (depth: 1178.00 m), though both coarse and fine fossil charcoal abundances are low in this sample. The total concentration of pyrolytic PAHs is not the highest concentration observed in the Kaszewy-1 samples which, when also coupled with a relative lack of fossil charcoal particles in the same sample, indicates low confidence in this fifth level of increased wildfire activity.

The final, sixth, level of increased wildfire activity is indicated in the uppermost sample (kk_47) of the study section (depth: 1169.10 m). An increase in both fine fossil charcoal abundance and total pyrolytic PAH concentration, and lack of coarse fossil charcoal particles, suggests a period of increased wildfire activity distal to the Kaszewy-1 site at this time during the Toarcian.

The higher land-plant biomarker retene was detected in all nine of the Kaszewy-1 samples and varies in concentration from 49 ng/g sediment to 471 ng/g sediment (**Figure 6.6**). Retene concentration covaries with total pyrolytic PAH concentration, supporting the suggestion that there were variations in the amount of organic matter burning throughout the Pliensbachian and Toarcian sections of the Kaszewy-1 core (cf. Jiang et al., 1998).

PAH concentration (ng/g sediment)
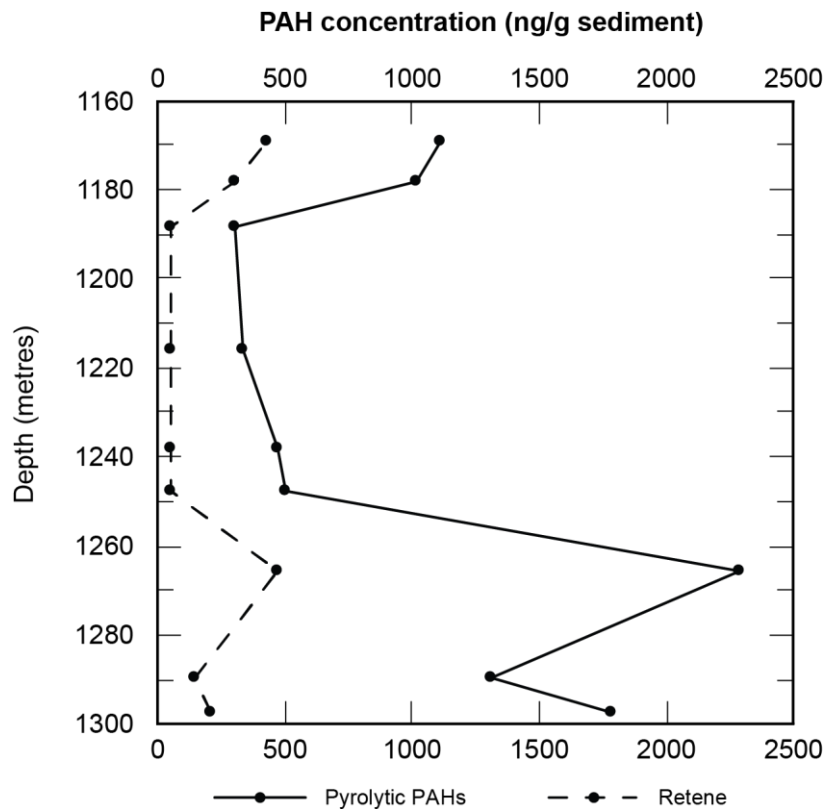
Figure 6.6 Total concentration of pyrolytic PAHs plotted alongside retene concentration for the Kaszewy-1 core Pliensbachian-Toarcian section.

The fossil charcoal abundance and geochemical data from Pliensbachian- and Toarcian-aged samples show evidence of at least four, and possible another two, levels of increased wildfire activity, and that these can be grouped into two larger periods of increased wildfire activity. The datasets presented here also indicate a significant decline in wildfire activity during the negative carbon-isotope excursion of the Toarcian OAE. Variations in the level of wildfire activity level can be caused by a number of different factors, and it is likely that multiple factors contributed to the periods of increased wildfire activity recorded by the Kaszewy-1 samples.

6.5.3.1. Causes of Changes in Wildfire Activity Level

Changes in wildfire activity as recorded in the Kaszewy-1 sediments could be explained by changes in weather patterns, vegetation type and abundance, oxygen availability, or, more realistically, a combination of these factors (**Figure 3.10; Table 3.8**). Unfortunately, a current lack of published palaeoclimatic and palynology studies of the Polish Basin makes identifying the cause(s) of the two

periods of increased wildfire activity difficulty. Unpublished clay mineralogy data suggests that the climate was relatively warm and wet at the Kaszewy-1 site during the Pliensbachian and Toarcian (**Figure 6.5**). Comparison of the new wildfire activity records from the Kaszewy-1 site to published datasets from other contemporaneous sites helps to identify potential causes.

Palaeofloral and palynological data from Bornholm, Denmark, shows a marked increase in thermophilic plant taxa prior to the Toarcian OAE negative carbon-isotope excursion, suggesting higher global temperatures and a decrease in rainfall and humidity prior to the Toarcian OAE (McElwain et al., 2005; Hesselbo and Pienkowski, 2011). Higher temperatures and decreased rainfall and humidity increase the potential for wildfires to ignite and spread (e.g. Power et al., 2007), and could explain the two levels of increased wildfire activity recorded in the Pliensbachian part of the study section. These climatic changes would likely have contributed to the third level of increased wildfire activity, observed after the inferred Pliensbachian-Toarcian Boundary.

The positive carbon-isotope excursion below the Toarcian OAE negative CIE is associated with increased carbon burial, which would likely have increased atmospheric oxygen levels (e.g. Jenkyns and Clayton, 1997). The oldest three levels of increased wildfire activity (in the Pliensbachian section and immediately after the inferred Pliensbachian-Toarcian Boundary) are all associated with relatively positive $\delta^{13}C_{wp}$ values, suggesting that atmospheric oxygen levels were relatively high due to increased carbon burial. A high level of atmospheric oxygen during the Toarcian OAE is also supported by a positive correlation between increased carbon burial and heavier seawater $\delta^{34}S$ values (Jenkyns, 2010). Computer modelling also suggests that anoxia can increase primary production (and therefore oxygen levels within the atmosphere-ocean system) via more efficient recycling of phosphorous from marine sediments (Handoh and Lenton, 2003). Given the relatively long residence time of oxygen in the atmosphere-ocean system (Handoh and Lenton, 2003), it is possible that positive CIE below the Toarcian OAE negative CIE promoted a rise in atmospheric oxygen levels which persisted throughout the Toarcian OAE. Higher atmospheric oxygen levels increase wildfire activity level (e.g. Scott, 2010), and it is possible that relatively high atmospheric oxygen levels contributed to the first extended period of

increased wildfire activity in the Kaszewy-1 Pliensbachian-Toarcian study section.

The Toarcian OAE negative carbon-isotope excursion is associated with a massive input of light carbon into the atmosphere that occurred along with continued high rates of carbon burial (e.g. Hesselbo et al., 2007). Osmium-isotope data from sites in the UK show evidence of increased weathering during the negative CIE associated with the Toarcian OAE (Percival et al., 2016). It is generally agreed that the climate was warmer and wetter during the Toarcian OAE (e.g. Cohen et al., 2004; Korte et al., 2015). Wetter environments can supress wildfire activity, despite the warmer temperatures and higher atmospheric O_2 which encourage wildfire activity (Price and Rind, 1994). Considering that the Toarcian section of the Kaszewy-1 core is dominated by a kaolinite-illite clay mineral assemblage (**Figure 6.5**; Pieńkowski, pers. comm.), it is unlikely that a wetter environment alone was responsible for supressing wildfire activity during the negative CIE; wildfire activity was successfully sustained as recorded at multiple horizons in the Toarcian section of the Kazewy-1 core. Instead, it is possible that wildfire activity was supressed by a lack of suitable fuel during the negative CIE (due to increased wildfire activity occurring below the negative CIE). Throughout the negative CIE, it is possible that the plant assemblages recovered, eventually providing enough fuel for periods of sustained wildfire activity, as seen at the end of the Toarcian OAE, where $\delta^{13}C$ values return to more positive values.

After the negative CIE associated with the Toarcian OAE, $\delta^{13}C_{wp}$ increases to more positive values, and is associated with a continued period of high carbon burial (e.g. Jenkyns and Clayton, 1997), which would have likely maintained the level of atmospheric oxygen. A number of studies provide evidence of cooling and drying at the end of the Toarcian OAE during the recovery phase (Cohen et al., 2004; Dera et al., 2009; Korte et al., 2015). The combination of a relatively high level of atmospheric oxygen and decreasing precipitation and humidity levels at the end of the Toarcian OAE would likely have caused an increase in wildfire activity, despite the cooling of the climate (cf. Price and Rind, 1994; Scott, 2010).

6.5.3.2. Wildfire Activity at the Kaszewy-1 Site in a Global Context

There is a limited collection of published wildfire activity proxy datasets spanning the Toarcian Oceanic Anoxic Event (**Figure 6.7**). A low-resolution study of pyrolytic PAH content of sediment from Yorkshire, UK, shows high pyrolytic PAH content correlating with positive $\delta^{13}C_{org}$ values prior to the negative CIE associated with the Toarcian OAE (French et al., 2014); pyrolytic PAH content generally remains low throughout the negative CIE of the Toarcian OAE, but fluctuates towards the top of the section, correlating with a return to more positive $\delta^{13}C_{org}$ values after the negative CIE. Fossil charcoal abundance studies from sites at Mochras, Wales, UK, and Peniche, Portugal, also show low total fossil charcoal abundances during the negative CIE of the Toarcian OAE, with increases in total fossil charcoal abundance occurring during the recovery period of the OAE, as $\delta^{13}C_{wood}$ values return to more positive values (Baker et al., 2017).

Correlation between these three sites (Yorkshire, Wales, and Peniche) and the Kaszewy-1 site is necessarily imprecise due to differences in sample resolution and sediment thickness. The new Kaszewy-1 wildfire activity proxy data identify up to six potential levels and two extended periods of elevated wildfire activity during the Pliensbachian and Toarcian: both before after the negative CIE of the Toarcian OAE.

Evidence of periods of increased wildfire activity prior to the Toarcian OAE is also seen at both the Yorkshire and Peniche sites (French et al., 2014; Baker et al., 2017). The sedimentary sequences at these two sites are relatively condensed in comparison to that of the Kaszewy-1 site; it is difficult to determine with high confidence if the periods of increased wildfire activity indicated by geochemical and fossil charcoal data at sites in Yorkshire and Peniche correlate with the periods identified in the Kaszewy-1 datasets. Using carbon-isotope data to correlate between sites, it would appear that the period of increased wildfire activity associated with elevated pyrolytic PAH content at the Yorkshire site may correlate to the second level of increased wildfire activity from the Kaszewy-1 core. Again, using carbon-isotope data, it would appear that the elevated total fossil charcoal abundance observed at Peniche (height in section: ~10 m) correlates with the peak in fine fossil charcoal abundance observed in the Kaszewy-1 core; both correlate with relatively positive $\delta^{13}C$ values immediately
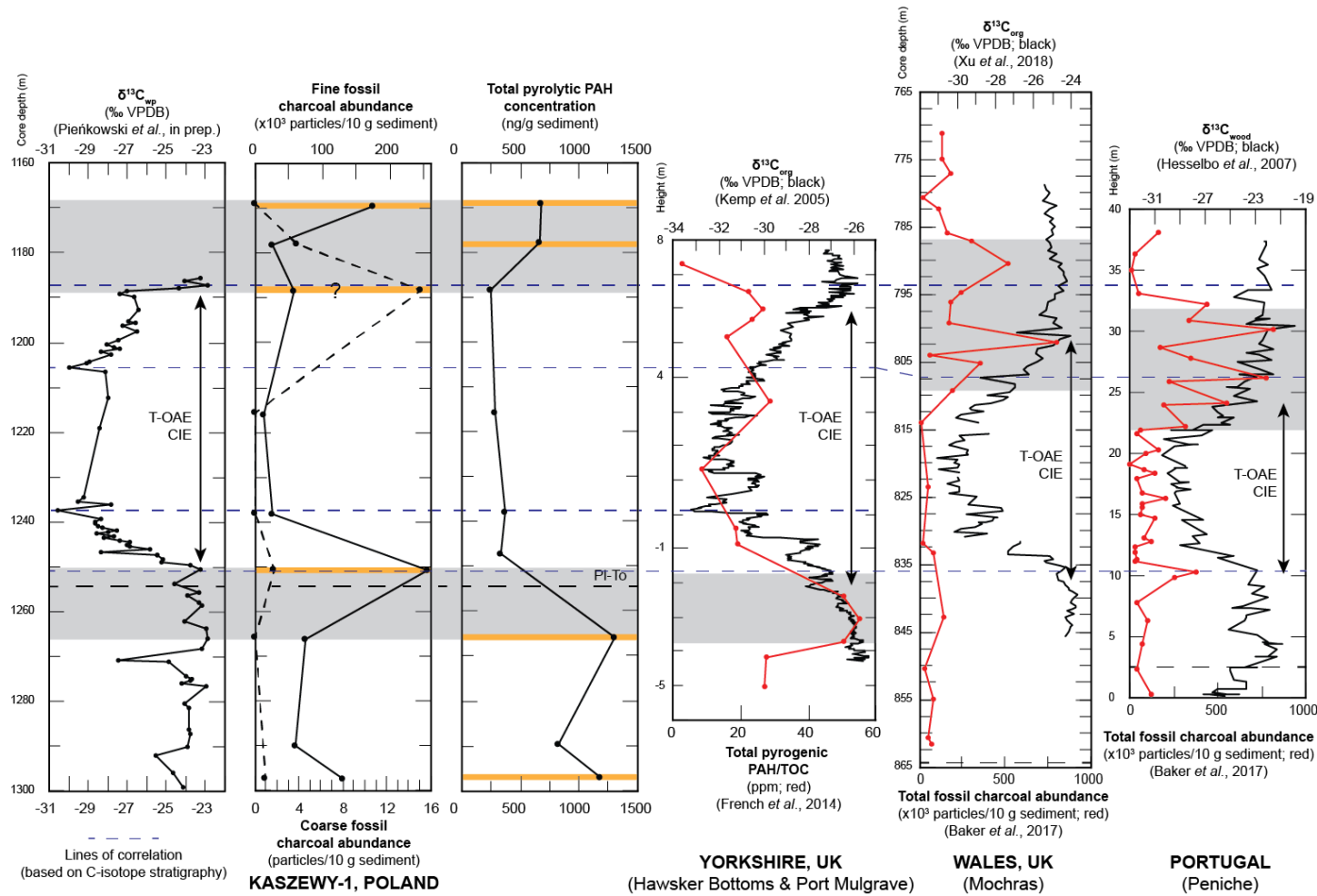
Figure 6.7 New fossil charcoal abundance and pyrolytic PAH concentration records, and a δ¹³C$_{wp}$ record (Pieńkowski, Hesselbo & Leng, in prep.) from the Kaszewy-1 core correlated with δ¹³C and wildfire activity proxy records from two sites in the UK (Yorkshire and Wales; Kemp et al., 2005; French et al., 2014; Baker et al., 2017; Xu et al., 2018) and one site in Portugal (Peniche; Hesselbo et al., 2007; Baker et al., 2017). Levels of increased wildfire activity from a single indicator are highlighted in orange; overall periods of increased wildfire activity are highlighted in grey. Pl-To = Pliensbachian-Toarcian Boundary. Dashed blue lines = correlation lines.

before $\delta^{13}C$ values begin to shift to more negative values during the onset of the Toarcian OAE, and occur after the Pliensbachian-Toarcian Boundary. Latitudinal and environmental differences should also be considered when correlating wildfire activity proxies between sites. For example, the Mochras charcoal record does not show increased charcoal abundance during the first positive CIE of the Toarcian OAE, which could perhaps be explained by differences in depositional setting, or the area's palaeogeography. Further work is needed to understand the impact of latitudinal and palaeogeographical differences on the wildfire activity records discussed here.

Wildfire activity proxy records from all four sites show evidence of low levels of wildfire activity during the negative carbon-isotope excursion of the Toarcian OAE. As discussed previously (**Section 6.5.3.1.**; p. 168), climatic conditions during the Toarcian OAE would likely have hindered the spread of wildfire, and numerous studies show evidence of widespread climatic changes across the globe during the Toarcian OAE. It is likely that the lack of evidence for high levels of wildfire activity during the Toarcian OAE negative CIE at sites in Poland, Portugal and the UK reflect changes in climatic conditions that affected at least the Tethyan realm during this time, and likely extended across the supercontinent at mid-latitudes.

The abundance of fossil charcoal at sites in both Wales and Portugal increases towards the inferred end of the Toarcian OAE, as $\delta^{13}C$ values return to more stable positive values (Baker et al., 2017). A general increase in the pyrolytic PAH content of sediments is also observed in samples from Yorkshire (French et al., 2014), also correlating with a return to more positive $\delta^{13}C_{org}$ values (Kemp et al., 2005). Again, the low resolution of these previously published studies and the new Kaszewy-1 data makes it difficult to determine with confidence precisely how these inferred periods of high wildfire activity correlate. It would appear that these peaks in fossil charcoal abundance at Kaszewy-1, Mochras and Peniche may be a record of the same period of increased wildfire activity, though a more confident correlation could be made with additional data, increasing the resolution of the datasets presented here. The pyrolytic PAH content data from Yorkshire is less clear and does not appear to correlate in particular with any one of the three possible periods of increased wildfire activity recorded by the Kaszewy-1

samples. Additional fossil charcoal data would help to better correlate the Yorkshire geochemical data with the fossil charcoal data from other sites, and understand the pattern of wildfire activity at the Yorkshire site after the Toarcian OAE. Again, differences between the wildfire activity proxy records at these sites could perhaps be explained by latitudinal differences, though further work is needed, particularly, increasing the resolution of the proxy records. Latitudinal differences in rainbelts during the Toarcian could perhaps provide an explanation, though there appear to be no published studies regarding predicted Toarcian rainbelts at the time of writing.

Despite differences in sample resolution and sediment thickness, what is apparent is that there appears to be a significant decline in wildfire activity during the negative CIE of the Toarcian OAE, and periods of elevated wildfire activity both prior to and after this negative CIE. The periods of increased wildfire activity indicated at each site correlate with $\delta^{13}C$ values that are more positive.

6.6. Conclusions & Future Work

The following conclusions can be drawn from this study:

- New fossil charcoal abundance and pyrolytic PAH datasets show evidence of up to six levels of increased wildfire activity recorded at the Kaszewy-1 site during the Pliensbachian and Toarcian, thought to be the first record of wildfire activity in the Polish Basin during this time.
- New fossil charcoal abundance and pyrolytic PAH datasets show evidence of a significant decline in wildfire activity during the Toarcian OAE negative CIE, as defined by $\delta^{13}C_{org}$ data.
- New wildfire activity proxy datasets from the Kaszewy-1 core appear to correlate with wildfire activity proxy datasets from other sites in the Tethyan realm, indicating at least a regional increase in wildfire activity during the onset of and recovery from the Toarcian OAE.

There is the potential for significant further study of Toarcian wildfire activity to be carried out on the basis of the work presented here in this chapter. Increasing the resolution of both fossil charcoal abundance and pyrolytic PAH concentration records from the Kaszewy-1 core, as well as from other sites in the Tethyan

realm, will be key to understanding changes in wildfire activity during the Pliensbachian and Toarcian. The Kaszewy-1 core offers the opportunity to produce a high-resolution record of wildfire activity in the Polish Basin during the Pliensbachian and Toarcian due to how expanded the sedimentary sequence is; this would also allow for the further investigation of wildfire activity across the Tethyan realm during the Toarcian, assessing the regional extent of wildfires at this time. The generation of new records of pyrolytic PAH content from the Mochras and Peniche sites to complement published fossil charcoal data, as well as new fossil charcoal abundance record to complement the geochemical data from Yorkshire, will help to improve correlation between different sites in the Tethyan realm, and help to understand the regional wildfire activity history.

CHAPTER 7 ENVIRONMENTAL CHANGES IN THE CENTRAL POLISH BASIN ACROSS THE TRIASSIC-JURASSIC BOUNDARY

7.1. Introduction

The Triassic-Jurassic Boundary time interval (201.3 ± 0.2 Ma; T-J Boundary; Cohen et al., 2013) was a time thought to have had extreme climatic conditions, including rising atmospheric carbon dioxide levels and increasing temperatures, which may have caused or exacerbated the end Triassic extinction and contributed to a major floral turnover in some regions (e.g. Huynh and Poulsen, 2005; Pálfy et al., 2007; Korte et al., 2009; Pienkowski et al., 2012). Geochemical and palaeobotanical evidence from multiple sites within the Tethyan realm also points to periods of increased wildfire activity across the T-J Boundary (e.g. Marynowski and Simoneit, 2009; Belcher et al., 2010a; Petersen and Lindström, 2012).

Palaeoenvironmental conditions across the T-J Boundary have been well-studied at numerous sites around the globe, but the vast majority of records are from marine deposits (e.g. Pálfy et al., 2001; Hesselbo et al., 2002; Guex et al., 2004; Marzoli et al., 2004; Whiteside et al., 2007; Hautmann et al., 2008; Ruhl et al., 2009; Greene et al., 2012). This bias towards marine palaeoenvironmental records leaves the terrestrial realm relatively under-studied. During the Late Triassic-Early Jurassic, the Polish Basin was dominated by terrestrial depositional environments, resulting in a thick sequence of predominantly terrestrial-derived sediments (e.g. Pieńkowski, 2004).

The Kaszewy-1 and Niekłań PIG-1 sites, both located in the central Polish Basin (Kaszewy-1: 52°11'59.00"N, 19°29'28.82"E; Niekłan PIG-1: 51°09'50.00"N, 20°38'55.00"E), provide an excellent opportunity to investigate wildfire activity and environmental changes in central Europe across the Triassic-Jurassic Boundary, via sedimentary core material. Similar to the Kaszewy-1 borehole (**Chapter 6**), the Niekłan PIG-1 borehole was also drilled in order to characterise

CO_2 sequestration reservoirs. Analysis of the cores facilitates understanding of environmental conditions within the Polish Basin across the T-J Boundary and identification of the extent of increased levels of wildfire activity at this time, as detected at other sites in northwest Europe.

7.2. Aims

This study aims to investigate wildfire activity at a central Polish Basin site across the Triassic-Jurassic Boundary, as well as identify geochemical palaeoenvironmental signals. With the new data collected as part of this study, the following questions are addressed:

- Is there evidence of wildfire activity in the central Polish Basin across the Triassic-Jurassic Boundary?
- How does the wildfire activity history of the central Polish Basin compare to other palaeoenvironmental records?
- How does the wildfire activity history of the central Polish Basin compare to other sites in the NW Tethyan realm across the Triassic-Jurassic Boundary?
- Is there evidence of the characteristic Triassic-Jurassic Boundary negative carbon-isotope excursions in terrestrial organic matter from the Niekłan PIG-1 site?
- What do carbon-isotope records from terrestrial organic matter indicate about the palaeoenvironmental conditions at the Niekłan PIG-1 site across the T-J Boundary?

7.3. Background

7.3.1. Study Sites

Relative sea level change greatly influenced sedimentation within the basin during the Early Jurassic (**Figure 3.6**; Pieńkowski, 2004). During the Hettangian, sea level changed within the Polish Basin, leading to a range of terrestrial and marine depositional environments (Pieńkowski, 2004). The Kaszewy-1 and

Niekłań PIG-1 sites are located in the central Polish Basin, with sedimentary profiles that generally reflect deposition in a terrestrial environment.

In the earliest Hettangian, sediment deposition occurred in fully terrestrial fluvial and lacustrine environments. A marine influence on the basin increased through the Early Hettangian and culminated in the Middle Hettangian, resulting in a brackish-marine environment running NW-SE through the Polish Basin. Marine influence in the basin decreased from the Middle to the latest Hettangian, resulting in a terrestrial-marine transitional environment along the NW-SE axis of the basin, and fluvial depositional environments moving away from this axis towards the edges of the basin.

7.3.1.1. The Kaszewy-1 Core

A ~1500 metre long core of Late Triassic-Middle Jurassic sediments was recovered from the Kazewy-1 borehole (see **Figure 3.4** for location). The upper Rhaetian section of the Kaszewy-1 core comprises ~220 m of terrestrial siliciclastic deposits thought to have been deposited in fluvial and lacustrine settings. The Hettangian section of the core consists of ~100 m of terrestrial and marine siliciclastic deposits, thought to have been laid down in a range of environments, including fluvial, lacustrine and shallow marine.

7.3.1.2. The Niekłań PIG-1 Core

The Niekłan PIG-1 borehole is located in the central Polish Basin (modern-day central Poland; see **Figure 3.4** for location) and was drilled in 2010, recovering a mostly-complete ~200-metre-long core of sedimentary material of Late Triassic and Early Jurassic age (Barbacka et al., 2016). The Late Triassic-aged section of the core comprises ~40 m of fluvial siliciclastic material belonging to the Zbąszynek and Wielichowo Beds (Pienkowski et al., 2014). The Hettangian-aged section of the core comprises ~130 m of fluvial siliciclastic material belonging to the Zagaje Formation, topped with ~30 m of shallow-marine siliciclastic material belonging to the Skłoby Formation (Barbacka et al., 2016). Plant remains are abundant throughout the Niekłan PIG-1 core, with trace evidence of plant roots, and both micro- and macroscopic fossilised plant remains present (Pienkowski et al., 2014; Barbacka et al., 2016).

7.3.2. Carbon-isotopes & C_{org}/N_{total} Ratios of Terrestrial Organic Matter

7.3.2.1. Carbon-isotopes in Terrestrial Organic Matter

A detailed discussion of carbon-isotopes in terrestrial organic matter is provided in **Section 3.4.** (p. 64).

The carbon-isotope signatures of terrestrial organic matter can be used to determine changes in organic matter sources and track palaeoenvironmental changes (e.g. Lamb et al., 2006). In particular, the carbon-isotope signatures of modern plant material can be used to track changes in the carbon-isotope composition of the atmosphere, since plants take in and utilise atmospheric carbon dioxide during photosynthesis (e.g. McCarroll et al., 2009). Modern plants also show changes in carbon-isotope composition in response to variations in other environmental factors, such as light, nutrient, and water availability (e.g. Farquhar et al., 1989; Saurer et al., 2004). On long-term scales, it is thought that changes in plant $\delta^{13}C$ values primarily reflect changes in atmospheric carbon-isotope composition, with other environmental factors making a relatively minor contribution to whole plant $\delta^{13}C$ values. Different tissues within a plant also show variations in $\delta^{13}C$ values, with whole plant $\delta^{13}C$ values generally being the heaviest, and cellulose, lignin, lipids and alkanes being lighter (e.g. Hobbie and Werner, 2004; Lamb et al., 2006); tissue type should be considered when interpreting $\delta^{13}C$ values of fossil plant material. Changes in the carbon-isotope composition of fossil terrestrial organic matter are widely used to reconstruct changes in the carbon cycle in the geological record (e.g. Lamb et al., 2006).

7.3.2.2. C_{org}/N_{total} Ratios As Indicators of Organic Matter Sources

A detailed discussion of C_{org}/N_{total} ratios as an indicator of organic matter source is provided in **Section 3.4.** (p. 64).

Studies of modern organic matter show that the ratio of carbon to nitrogen (C/N) in organic matter can be used to identify its source when combined with $\delta^{13}C$ values (e.g. Lamb et al., 2006, 2007 and references therein). Different types of marine and terrestrial organic matter tend to plot within certain areas of a C_{org}/N_{total} ratio-$\delta^{13}C$ cross-plot (**Figure 3.8**). However, some studies have shown that sediment grain size appears to have some control on the C_{org}/N_{total} ratios of organic matter, with OM from coarser-gained sediments tending to have higher

C_{org}/N_{total} ratios, due increased bacterial decomposition of OM, than OM from finer-grained sediments (Thornton and McManus, 1994). Sediment grain size should therefore be taken into account when interpreting C_{org}/N_{total} ratios of organic matter. Various studies have also shown that C_{org}/N_{total} ratios of organic matter can be altered over time due to degradation and decomposition of the organic matter (e.g. Meyers and Ishiwatari, 1993; Meyers, 1997; Lamb et al., 2006). Considering that most studies of C_{org}/N_{total} ratios of organic matter tend to be on modern samples, it is important to consider the degradation of fossil organic matter both at its time of deposition, and during diagenesis, when interpreting C/N ratios of fossil organic matter.

7.3.3. Wildfire Activity Proxies

7.3.3.1. Fossil Charcoal

A brief discussion of the use of fossil charcoal as a wildfire activity proxy is provided in **Section 6.3.2.1.** (p. 150); a detailed discussion is provided in **Section 3.5.1.2.** (p. 72).

7.3.3.2. Pyrolytic Polycyclic Aromatic Hydrocarbons

A brief discussion of the use of pyrolytic PAHs as a wildfire activity proxy is provided in **Section 6.3.2.2.** (p. 151); a detailed discussion is provided in **Section 3.5.2.2.** (p. 79).

7.3.4. Previous Work

A detailed discussion of previous work pertaining to the topics discussed in the chapter is provided in **Section 3.3.2.1.** (p. 60) and **Section 3.5.4.1.** (p. 87).

The Kaszewy-1 and Niekłan PIG-1 boreholes were originally drilled as part of a government investigation into carbon capture and storage and as such, the core materials have only recently been made available for other studies.

Clay mineralogy and rare earth element studies of the Kaszewy-1 and Niekłan PIG-1 cores, amongst others, provide insight into weathering and palaeoenvironmental conditions in the Polish Basin across the Triassic-Jurassic Boundary (Brański, 2009, 2014; Brański and Mikulski, 2016). A palaeobotanical study of the Niekłan PIG-1 core provides additional evidence of environmental conditions in the central Polish Basin during the Hettangian (Barbacka et al.,

2016). Ammonite palaeontology and carbon capture storage studies of the Kaszewy-1 core have also been published (Pieńkowski, 2014, 2015). A recent high-resolution biostratigraphy and sequence stratigraphy study, including of the Kaszewy-1 core, was published by Barth et al. (2018). There are also unpublished carbon-isotope and Rock-Eval datasets from the Kaszewy-1 core (G. Pieńkowski, pers. comm.). Other studies of relevant Early Jurassic Polish Basin sediments, not including the Kaszewy-1 and Niekłan PIG-1 cores, include dinosaur palaeontology (e.g. Pieńkowski, 1998; Gierliński et al., 2004), sedimentology (Pieńkowski, 2004; Pienkowski et al., 2012) and carbon-isotope stratigraphy (Pienkowski et al., 2012).

There are a limited number of studies published regarding wildfire activity across the Triassic-Jurassic Boundary, with some evidence of increased wildfire activity at sites in Denmark, Germany, Greenland, and Poland. A study of fossil charcoal from deposits in the Danish Basin by Petersen and Lindström (2012) found an increase in average inertinite content from ~17% to ~75% in sediments spanning the Triassic-Jurassic Boundary, along with the presence of pyrolytic PAHs. The authors concluded that the increase in inertinite content and the presence of pyrolytic PAHs resulted from a period of increased wildfire activity across the T-J Boundary, and culminating during the Hettangian. A similar study of core material from Germany by van de Schootbrugge et al. (2009) found increased levels of PAHs in sediments of T-J Boundary-age, but a lack of phytoclasts that could be identified as charcoal; the authors concluded that the PAHs detected in the German core sediments likely originated from a non-wildfire source, and were insufficient evidence for increased wildfire activity at the site. A five-fold increase in fossil charcoal across a T-J Boundary section in Greenland was found by Belcher et al. (2010), with the authors concluding that the increase in fossil charcoal reflected a period of increased wildfire activity. Elevated levels of PAHs have been found in Late Triassic-Early Jurassic sediments at multiple sites in Poland by Marynowski and Simoneit (2009), along with macrofossil charcoal at some of these sites, though the fossil charcoal was not quantified. The authors concluded from their study that the elevated levels of PAHs in multiple horizons at the Polish outcrops reflect periods of increased wildfire activity.

7.4. Materials & Methods

7.4.1. Materials

7.4.1.1. The Kaszewy-1 Core

Eleven samples from the Rhaetian and Hettangian sections of the Kaszewy-1 core were collected for analysis of fossil charcoal abundance and polycyclic aromatic hydrocarbon content. The 11 samples were collected from between depths 1925.56 m and 1803.80 m, at an average resolution of 1 sample per 11.07 m. Nine mudstones and sandstone samples were collected from sediments thought to have been deposited in terrestrial fluvial and lacustrine environments, and two mudstones and sandstone samples were collected from sediments thought to have been deposited in transitional shoreface settings. Samples were collected so as to span the inferred Triassic-Jurassic Boundary and correlate with available $\delta^{13}C_{org}$ data. Due to the frequently changing lithology of the Kaszewy-1 core, and limited sampling time (the core is stored at one of the regional branches of the Polish Geological Institute; access was only provided for a few days whereas the Niekłań PIG-1 core is stored in Warsaw and more easily accessible), it was not possible to identify samples of the same lithology and inferred depositional environment at suitable horizons in the core.

7.4.1.2. The Niekłań PIG-1 Core

Eleven samples in total were collected from the Rhaetian and Hettangian sections of the Niekłan PIG-1 core for fossil charcoal abundance and pyrolytic polycyclic aromatic hydrocarbon studies. Ten samples were originally collected for both analyses, but there was not enough material left to analyse pyrolytic PAH content of sample NC6 after processing for the fossil charcoal abundance study. Sample NC2 was included in the pyrolytic PAH study in place of sample NC6. The eleven samples collected for fossil charcoal abundance counts were collected between depths 165.20 m and 141.10 m. Eleven mudstone and sandstone samples were collected from sediments thought to have been deposited in a mixture of terrestrial fluvial and lacustrine environments. The average resolution of each sample set is 1 sample per 2.41 m. The samples chosen for this analysis were selected in order to minimise lithological and depositional environment bias (cf. Belcher et al., 2010).

A total of 92 bulk sediment samples were collected from the Rhaetian and Hettangian sections of the Niekłan PIG-1 core for bulk organic matter carbon-isotope analyses. The samples were collected from between depths 163.00 m and 15.50 m, at an average resolution of 1 sample per 1.60 m. The sediment samples consist of both mudstone and sandstone thought to have been deposited in both fluvial and lacustrine environments. The bulk sediment samples did not typically contain large pieces of fossil plant material, as these had already been collected prior to bulk sediment sample collection. Samples were taken at regular intervals from the majority of the core, in order to produce a long-term carbon-isotope record of the Niekłan PIG-1 core.

A total of 43 macrofossil plant material samples were collected from the Rhaetian and Hettangian sections of the Niekłan PIG-1 core. The samples were collected between depths 161.70 m and 37.10 m, at an average resolution of 1 sample per 2.90 m. Samples were collected wherever macrofossil plant material was visible on the surfaces of the core. The macrofossil plant material samples range in size from <1 cm to >5 cm long, and represent a range of different plant types. Identification of samples beyond 'vascular plant material' was not possible due to the small sample size and lack of identifying structures or marks. The macrofossil plant samples were collected from both fluvial and lacustrine mudstones and sandstones, from horizons wherever macrofossil plant material was visible on the surface(s) of the core.

Thirty-one bulk sediment samples were collected for bulk carbon-isotope measurements of the woody phytoclast content. The samples were collected from the Rhaetian and Hettangian sections of the core. Twenty-nine of the samples were collected between depths 166.70 m and 144.20 m, at an average resolution of 1 sample per 0.78 m, with an additional two samples collected at depths 105.70 m and 74.60 m. The samples collected consisted of both mudstone and sandstone thought to have been deposited in fluvial and lacustrine environments. Samples were picked by M. Hodbod at the Polish Geological Institute and shared as part of the research in this thesis.

7.4.2. Methods

7.4.2.1. Terrestrial Bulk Organic Matter Carbon-isotopes

A detailed discussion of the method used for carbon-isotope analysis of bulk organic matter is provided in **Section 4.4.1.** (p. 109). Samples were prepared by the author at Camborne School of Mines and analysed at the British Geological Survey by M. Leng.

Standard decarbonation techniques were used to remove all inorganic carbon from bulk rock samples. Hydrochloric acid was added to ~240 – 280 mg of crushed homogenous bulk rock samples, which was then agitated and left to react at room temperature for 24 hours; this was repeated twice. Samples were then washed with deionised water until neutral and then dried. The decarbonated powders were then crushed again to a fine homogeneous powder, prior to carbon- and nitrogen-isotope analysis using a Finnigan DELTAplusXP stable-isotope ratio mass spectrometer.

7.4.2.2. Macrofossil Plant Material Carbon-isotopes

A more detailed discussion of the method used for carbon-isotope analysis of macrofossil plant material is provided in **Section 4.4.2.** (p. 109). Samples were prepared by the author at Camborne School of Mines and analysed at the British Geological Survey by M. Leng.

Standard decarbonation techniques were used to remove all inorganic carbon from macrofossil plant material samples. The samples were crushed to a fine homogeneous powder and then treated with two rounds of hydrochloric acid at room temperature, leaving 24 hours after the addition of hydrochloric acid. Samples were then washed with deionised until neutral and then dried. Samples were then analysed using an Integra2 combined isotope ratio mass spectrometer and elemental analyser for carbon- and nitrogen-isotope analyses

7.4.2.3. Bulk Woody Phytoclast Carbon-isotopes

A more detailed discussion of the method used for carbon-isotope analysis of bulk woody phytoclasts is provided in **Section 4.4.3.** (p. 110). Samples were prepared by M. Hodbod at the Polish Geological Institute and analysed at the British Geological Survey by M. Leng.

Samples were prepared using standard palynological preparation techniques. Bulk rock samples underwent two rounds of acid maceration with cold hydrochloric and hydrofluoric acids, before being washed with a water and hydrogen iodide solution. Heavy minerals were separated out of the samples before the remaining material was washed with distilled water until neutral. Woody phytoclast particles of the same appearance (to minimise $\delta^{13}C$ variability caused by compositional changes) were picked from the palynological residues and analysed using a Finnigan DELTAplusXP stable-isotope ratio mass spectrometer.

7.4.2.4. Fossil Charcoal Quantification

A brief discussion of the methods used for fossil charcoal quantification is provided in **Section 6.4.2.1.** (p. 153); a detailed discussion is provided in **Section 4.2.** (p. 99).

7.4.2.5. Polycyclic Aromatic Hydrocarbon Quantification

A brief discussion of the methods used for PAH quantification is provided in **Section 6.4.2.2.** (p. 153); a detailed discussion is provided in **Section 4.3.** (p. 102).

7.5. Results & Discussion

7.5.1. New Carbon-isotope & C_{org}/N_{total} Ratio Records from the Niekłań PIG-1 Core

7.5.1.1. Bulk Organic Matter Carbon-isotope Stratigraphy

Carbon-isotope analysis of the bulk organic matter samples show a very wide range of $\delta^{13}C_{org}$ values: -6.2‰ – -27.8‰ (**Figure 7.1**).

A number of samples (17) show abnormally heavy $\delta^{13}C_{org}$ values, which is likely due to the remaining presence of inorganic carbonate, such as siderite. During sampling of the Niekłan PIG-1 core several bands of siderite nodules were observed on the surface of the core below ~165m depth. The sediments below this depth are thought to be part of the Huta Mudstone Member which is known
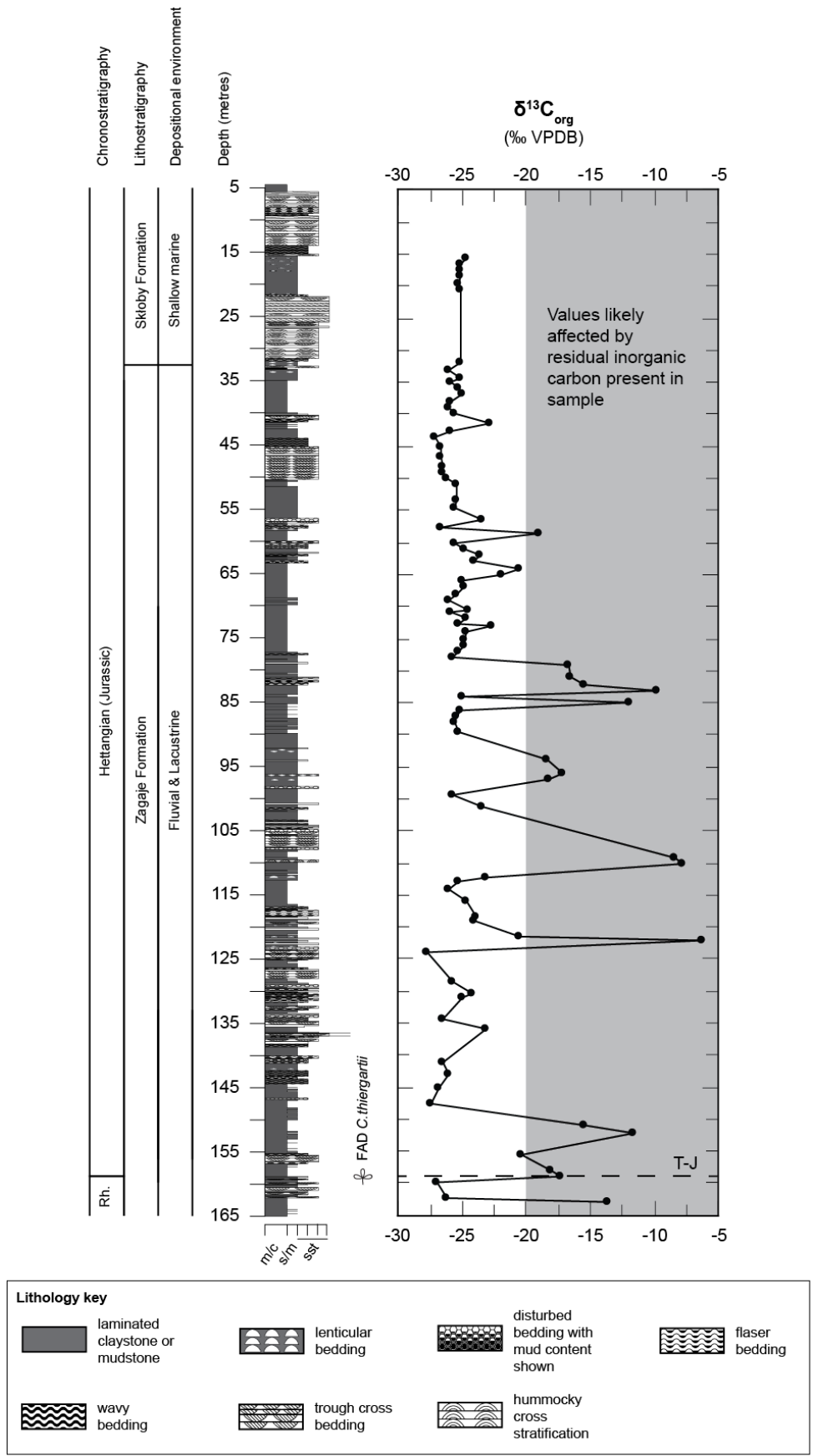
Figure 7.1 New δ¹³Corg record from the Niekłan PIG-1 core. Lithological succession from G. Pieńkowski (pers. comm.). Residual inorganic carbon likely from incomplete removal of calcium carbonate from samples.

for containing siderite nodules (Pieńkowski, 2004). Siderite nodules were not observed on the surface of the core above ~165m depth, therefore decarbonation at higher temperatures and with stronger acids was not carried out on the Niekłan PIG-1 samples analysed as part of this study. Modern C3 plants usually have a $\delta^{13}C$ signature <-20‰ (Lamb et al., 2006), therefore all $\delta^{13}C_{org}$ values <-20‰ have been disregarded as reflecting the true carbon-isotope signature of bulk organic matter. In addition, the new $\delta^{13}C_{org}$ data was also filtered to remove any data points which varied by >2‰ than neighbouring data points. These anomalous values are not included in further discussion of the new Niekłan PIG-1 $\delta^{13}C_{org}$ dataset, unless explicitly stated.

The new $\delta^{13}C_{org}$ record shows a large variation in values, ranging from -20.3‰ – -27.8‰, with an average $\delta^{13}C_{org}$ value of -25.1‰. Samples from the Rhaetian-aged part of the core, just below the inferred T-J Boundary, have relatively light $\delta^{13}C_{org}$ values of ~-29‰. The first sample above the inferred T-J Boundary shows a shift to a more positive $\delta^{13}C_{org}$ value of -20.3‰. Carbon-isotope values then decrease to more negative values between the depths 147.50 m and 123.85 m, fluctuating between -23.2‰ and -27.8‰. Moving up the core, $\delta^{13}C_{org}$ values become slightly heavier, fluctuating between -20.6‰ and -26.1‰ between the depths of 121.40 m and 99.40 m. For the remaining section of the core, between depths 89.60 m and 15.50 m, $\delta^{13}C_{org}$ values are generally heavier, ranging between -20.5‰ and -26.7‰.

The $\delta^{13}C_{org}$ record does not show clear negative carbon-isotope excursions that could be correlated to either the initial or main negative CIE, both characteristic of T-J Boundary carbon-isotope stratigraphy. The fact that some samples from this dataset show very heavy $\delta^{13}C_{org}$ values, likely a result of incomplete decarbonation, also hinders the identification of negative CIEs.

Nitrogen-concentration data are not available to calculate C_{org}/N_{total} ratios for the bulk organic matter samples.

7.5.1.2. Macrofossil Plant Material Carbon-isotope Stratigraphy

Macrofossil plant carbon-isotope values ($\delta^{13}C_{plant}$) vary between -22.1‰ and -29.9‰, with an average value of -27.1‰; C_{org}/N_{total} ratios of the macrofossil plant

samples analysed vary between 2.0 and 123.7, with an average value of 53.7 (**Figure 7.2**).

The new $\delta^{13}C_{plant}$ record shows fluctuating values throughout most of the Hettangian-aged, and part of the Rhaetian-aged, sections of the Niekłan PIG-1 core (between depths 37.10 m and 161.70 m). Plant $\delta^{13}C$ values fluctuate between -27.9‰ and -25.9‰ in the Rhaetian-aged part of the study section, showing a general shift to heavier values towards the inferred T-J Boundary. The $\delta^{13}C_{plant}$ record shows a continued shift towards heavier values immediately above the inferred T-J Boundary, reaching a value of -24.8‰, before a general trend towards lighter values between the depths of 155.30 m and 144.57 m; between these depths, $\delta^{13}C_{plant}$ values fluctuate between -27.1‰ and -29.9‰. From the depth 143.83 m upwards, $\delta^{13}C_{plant}$ values show a general increase towards heavier values, fluctuating between -22.1‰ and -28.7‰. Sample N22 (depth: 130.25 m) has a much heavier $\delta^{13}C_{plant}$ value (-22.1‰) than other samples in this dataset; although it is possible that this sample was not fully decarbonated (siderite may have been present in the sample; the decarbonating process may not have been aggressive enough to remove all inorganic carbon), the $\delta^{13}C_{plant}$ signature does fall within the typical range of $\delta^{13}C$ values for modern terrestrial C3 plants (cf. Lamb et al., 2006).

There appears to be a double-peaked negative excursion of ~5‰ magnitude in this new $\delta^{13}C_{plant}$ record, between the depths 155.30 m and 142.10 m where $\delta^{13}C_{plant}$ values reach lightest values of -29.9‰. The initial negative CIE associated with the T-J Boundary sometimes occurs with a double peak (Pienkowski et al., 2012) and is generally ~4-6‰ in magnitude (e.g. Hesselbo et al., 2002; Kürschner et al., 2007; Ruhl et al., 2009). The double-peaked negative CIE observed in the new Niekłan PIG-1 $\delta^{13}C_{plant}$ record is possibly the same as the initial negative T-J Boundary CIE, as recorded at multiple sites. However, the initial negative CIE recorded in other T-J Boundary-aged successions usually correlates to Rhaetian-aged sediments (e.g. Whiteside et al., 2010; Ruhl and Kürschner, 2011), whereas in the new Niekłan PIG-1 record it correlates with Hettangian-aged sediments, occurring above the inferred T-J Boundary. The T-J Boundary in the Niekłan PIG-1 core is currently defined by the first occurrence of the basal Jurassic palynomorph *C. thiergartii* at ~160 m depth, correlating with
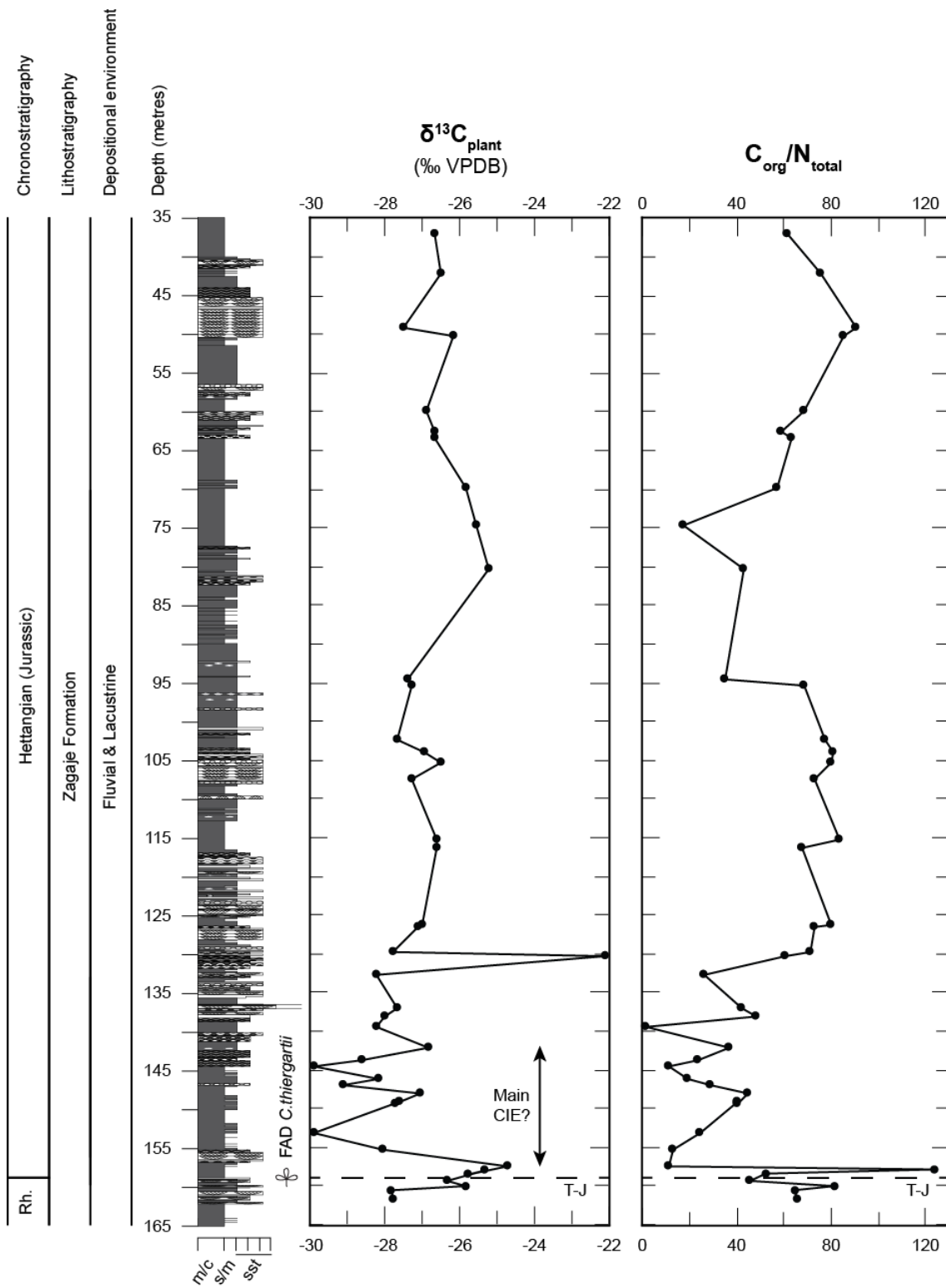
Figure 7.2 New $\delta^{13}C_{plant}$ and C_{org}/N_{total} ratio records from the Niekłan PIG-1 core. See **Figure 7.1** for lithology key. Lithological succession from G. Pieńkowski (pers. comm.). T-J Boundary position is based on the first occurrence of *C. thiergartii*.

the onset of the double-peaked negative CIE. There does not appear to be a clear shift towards lighter $\delta^{13}C_{plant}$ values further up the core. Despite the double-peaked nature of the new $\delta^{13}C_{plant}$ CIE, current evidence suggests that the this negative CIE observed at the bottom of the Hettangian section of the Niekłań PIG-1 core correlates with the 'main' CIE as observed at St Audrie's Bay, and other contemporaneous sites. Increasing the resolution of this new $\delta^{13}C_{plant}$ record would allow for a more confident identification of the negative CIE.

The double-peaked negative excursion observed in the $\delta^{13}C_{plant}$ record is likely caused by a massive input of light carbon (^{12}C) into the atmosphere around the Triassic-Jurassic Boundary. The initial and main negative CIEs associated with the T-J Boundary are thought to be caused by a massive input of ^{12}C into the atmosphere-ocean system, from a combination of volcanogenic gases (carbon dioxide, methane) and methane from the melting of seafloor gas hydrates (e.g. Pálfy et al., 2001; Hesselbo et al., 2002; Kürschner et al., 2007; Whiteside et al., 2010; Lindström et al., 2012).

The C_{org}/N_{total} ratios of the macrofossil plant samples fluctuate frequently between a minimum of 2.0 and a maximum of 123.7, and appear to covary with the $\delta^{13}C_{plant}$ record. The majority of samples have C_{org}/N_{total} values greater than 10, confirming the visual identification of the samples as macrofossil plant material (cf. Meyers, 1994; Lamb et al., 2006). Sample N18 at 155.30 m depth has the lowest C_{org}/N_{total} value of 2.0, but was visually identified as macrofossil plant material; the unusually low C_{org}/N_{total} value remains unexplained, but is possibly related to organic matter degradation (Lamb et al., 2006).

7.5.1.3. Bulk Woody Phytoclast Carbon-isotope Stratigraphy

A newly-generated bulk woody phytoclast $\delta^{13}C$ ($\delta^{13}C_{wp}$) record shows values ranging between -24.8‰ and -28.7‰, with an average value of -26.9‰, in the Niekłan PIG-1 core (**Figure 7.3**). The C_{org}/N_{total} ratios of 30 of the bulk woody phytoclast samples were also calculated and vary between 14.8 and 99.6, with an average C_{org}/N_{total} value of 48.4 (**Figure 7.3**).

The new $\delta^{13}C_{wp}$ record shows values gradually becoming heavier in the Rhaetian-aged part of the study section, ranging from -26.9‰ to -27.6‰, before showing a sharp shift to lighter values (~-26.5‰) immediately above the inferred
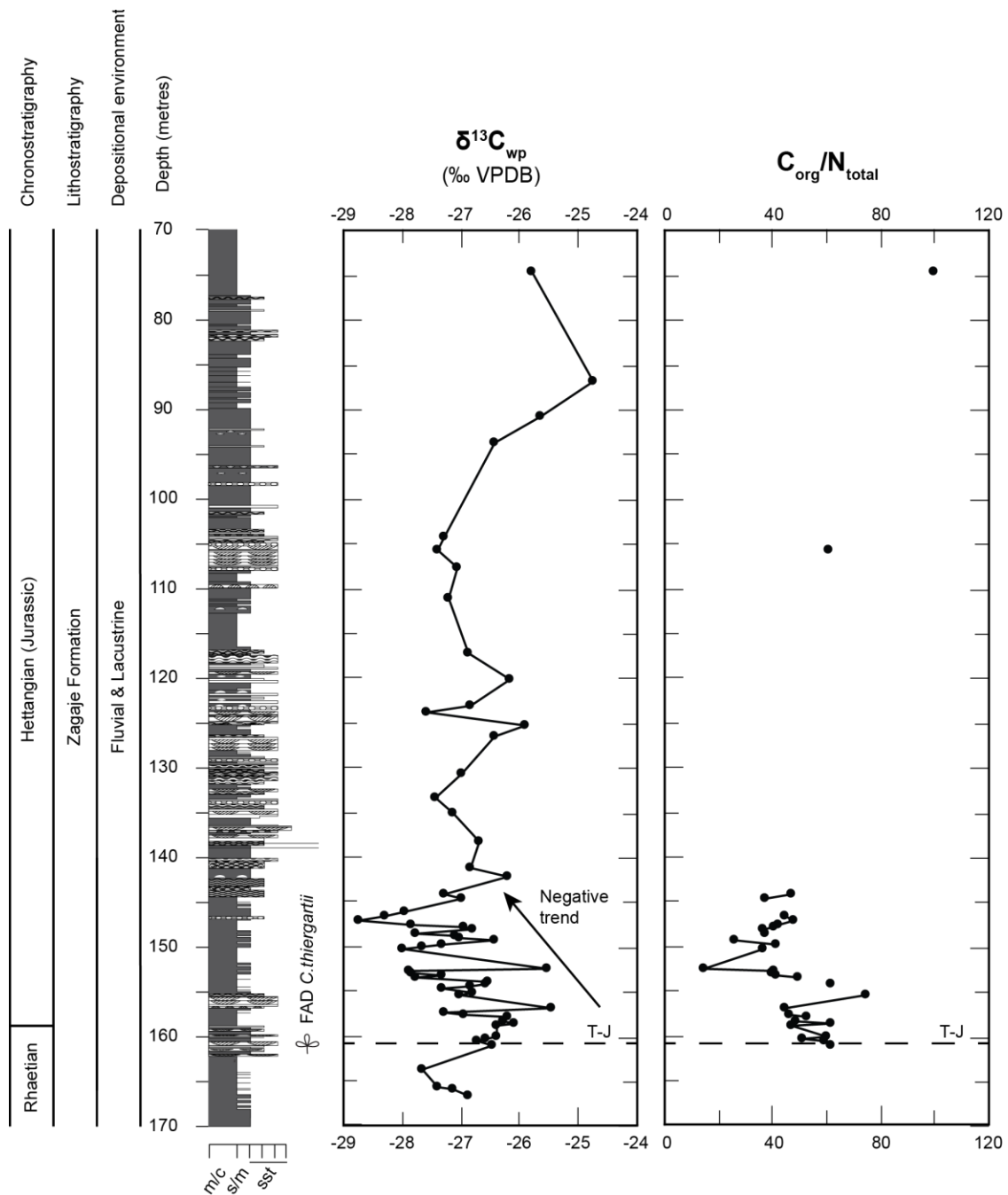
Figure 7.3 New $\delta^{13}C_{wp}$ and C_{org}/N_{total} ratio records from the Niekłan PIG-1 core. See **Figure 7.1** for lithology key. Lithological succession from G. Pieńkowski (pers. comm.). T-J Boundary position is marked by the first occurrence of *C. thiergartii*.

T-J Boundary. Between the depths of 160.70 m and 144.60 m, above the inferred T-J Boundary, $\delta^{13}C_{wp}$ values show a general trend towards more negative values, with multiple fluctuations between -25.5‰ and -28.7‰. From the depth 144.20 m upwards, $\delta^{13}C_{wp}$ appear to recover from this negative trend, with values ranging from -27.6‰ to -24.8‰. The $\delta^{13}C_{wp}$ values are generally lighter than the new

$\delta^{13}C_{org}$ record, as expected, and similar to the new $\delta^{13}C_{plant}$ record, suggesting that the tissue composition of the bulk woody phytoclast samples is similar to that of the macrofossil plant samples. The $\delta^{13}C_{wp}$ values fall within the expected range for modern terrestrial C3 plants (cf. Lamb et al., 2006).

The negative trend in $\delta^{13}C_{wp}$ values observed between depths of 160.70 m and 144.60 m, where $\delta^{13}C_{wp}$ values show an overall shift of ~-4‰, is possibly an expression of the main negative CIE associated with the T-J Boundary. This negative trend correlates with the double-peaked negative CIE observed in the new $\delta^{13}C_{plant}$ record ($\delta^{13}C_{wp}$: 160.70 – 144.60 m; $\delta^{13}C_{plant}$: 155.30 – 142.10 m). The main negative CIE associated with the T-J Boundary is not apparent in the new $\delta^{13}C_{wp}$ record, likely due to a lower resolution of data points in the upper ~70 m of the study section, compared to the lower ~25 m.

The C_{org}/N_{total} ratios of the bulk woody phytoclast samples show a wide variation from 14.8 to 99.6 (**Figure 7.3**), but all fall within the expected range for modern C3 terrestrial plants. The C_{org}/N_{total} ratios appear to show a negative trend in the lower part of the study section, similar to the $\delta^{13}C_{wp}$ record.

7.5.1.4 Niekłan PIG-1 $\delta^{13}C$ Records in a Global Context

The initial negative carbon-isotope excursion associated with the T-J Boundary is recorded at numerous sites worldwide in various geological materials, and varies in magnitude from ~2‰ (Whiteside et al., 2010) to ~8‰ (Ruhl et al., 2011). The majority of records show an initial negative CIE with a magnitude of ~4-5‰ (Pálfy and Kocsis, 2014). The initial negative CIE is now identified in Rhaetian-aged strata as a result of definition of the GSSP in Kuhjoch, Austria, on the first occurrence of the ammonite *Psiloceras tilmani*. Following a brief return to more positive $\delta^{13}C$ values, the majority of carbon-isotope records also show a longer duration second negative CIE (termed the main CIE by Hesselbo et al. (2002)), with a smaller magnitude (Kürschner et al., 2007; van de Schootbrugge et al., 2009). This pattern of a relatively short, sharp negative CIE (the initial CIE) followed by a return to more positive $\delta^{13}C$ values, and then a second, longer negative CIE (the main CIE) of smaller magnitude is characteristic of T-J Boundary carbon-isotope stratigraphy and has been used to correlate between marine and terrestrial sites around the globe.

The double-peaked negative $\delta^{13}C_{plant}$ CIE and negative trend in $\delta^{13}C_{wp}$ values observed immediately above the inferred T-J Boundary in the Niekłan PIG-1 core shows both similarities and differences with other $\delta^{13}C$ records from across the T-J Boundary (**Figure 7.4**). The Niekłan PIG-1 negative $\delta^{13}C_{plant}$ CIE and negative $\delta^{13}C_{wp}$ trend have magnitudes of ~5‰ and ~4‰, respectively, and are thought to correlate with the main negative CIE associated with the T-J Boundary. There are limited published $\delta^{13}C_{wood}$ records from across the T-J Boundary; one such record from Astartekløft, Greenland, shows a negative CIE of similar magnitude, ~3.5‰, occurring across the T-J Boundary (**Figure 7.4**; Hesselbo et al., 2002; Bacon et al., 2011). Another $\delta^{13}C_{wood}$ record from the northeastern USA shows a negative CIE of ~-4‰, occurring immediately after the T-J Boundary (Whiteside et al., 2010).

The negative CIEs identified in the Niekłan PIG-1 $\delta^{13}C_{plant}$ and $\delta^{13}C_{wp}$ records show a double-peaked negative CIE and a general trend towards lighter values, respectively, unlike the abrupt initial CIEs that are identified in most T-J Boundary $\delta^{13}C$ records (e.g. Pálfy and Kocsis, 2014). The extended nature of the Niekłan PIG-1 negative CIEs may result from the seemingly relatively high sediment thickness in comparison to other T-J Boundary sections. However, without a better-defined age model for the Niekłan PIG-1 core, it is difficult to assess quantitatively the sedimentation rate at the Niekłan site across the T-J Boundary relative to other T-J Boundary sites. Increasing the resolution of the Niekłań PIG-1 $\delta^{13}C$ records would improve correlation with other sites as well.

The new Niekłan PIG-1 $\delta^{13}C$ records show evidence of the T-J Boundary main negative CIE (**Figure 7.4**). The $\delta^{13}C_{plant}$ and $\delta^{13}C_{wp}$ records show a shift towards heavier $\delta^{13}C$ values between the depths of ~95 m and ~60 m, perhaps correlating with a return to more positive $\delta^{13}C$ values after the main CIE, as observed from other records. Additional $\delta^{13}C_{plant}$ and $\delta^{13}C_{wp}$ data from the top ~40 m of the Niekłan PIG-1 core would help with interpretation of the carbon-isotope stratigraphy of this core, along with increasing the resolution of the current records.

The timing of the Niekłan PIG-1 negative CIEs is similar to that of the Astartekløft and northeastern USA negative CIEs, but all three apparently occur later than the majority of $\delta^{13}C_{org}$ records, whereas the initial negative CIE occurs in Rhaetian-
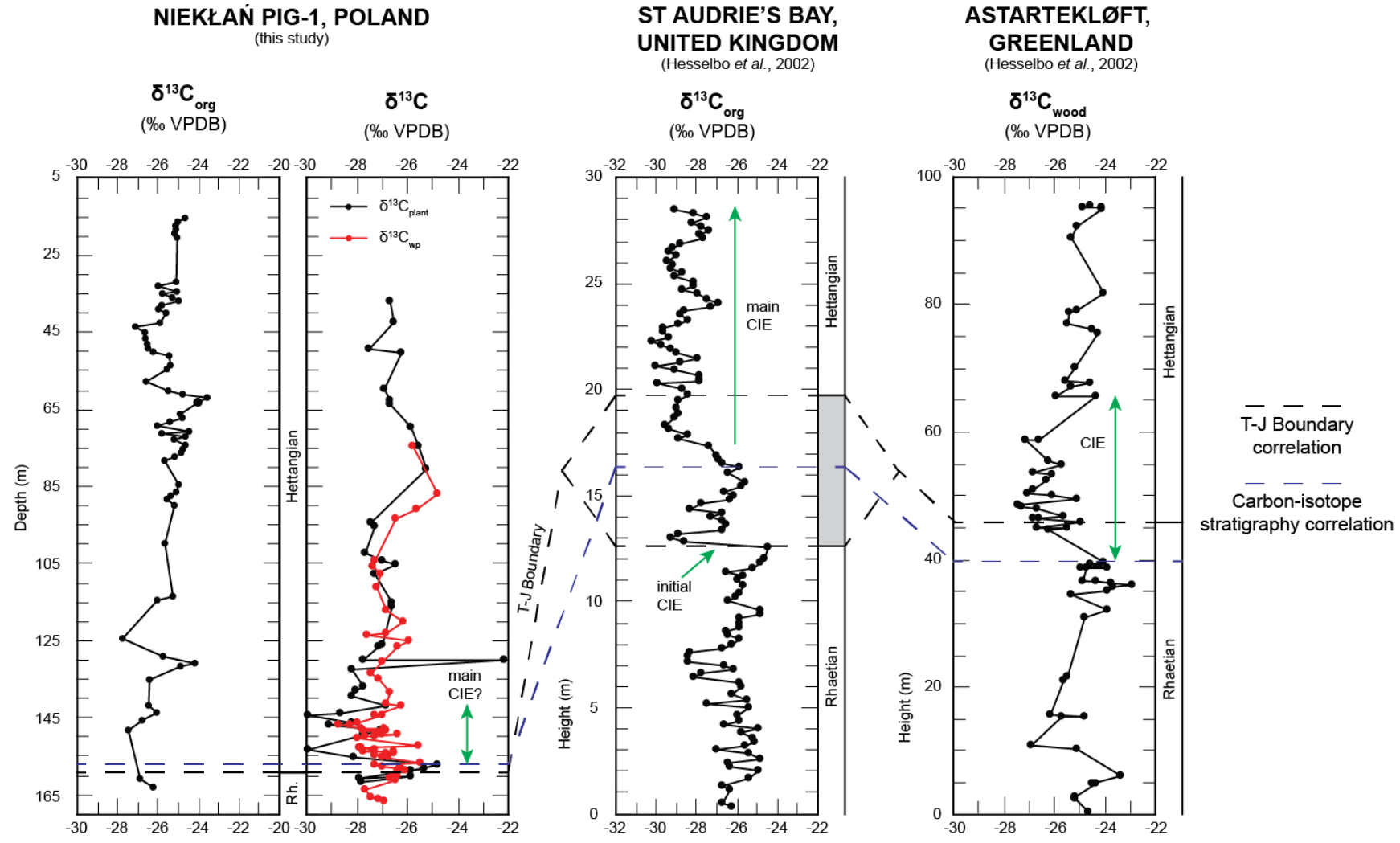
Figure 7.4 New $\delta^{13}C$ records from the Niekłan PIG-1 core correlated with a $\delta^{13}C_{org}$ record from St Audries Bay, UK, and Astartekløft, Greenland (Hesselbo et al., 2002). The T-J Boundary is based on: the first occurrence of *C. thiergartii* in the Niekłań PIG-1 Core; ammonite and non-ammonite biostratigraphy, and palynological changes at St Audrie's Bay; changing floral assemblages at Astartekløft.

aged strata. The majority of $\delta^{13}C_{org}$ records from across the T-J Boundary are from marine successions; one possibility is that there is a lag between the marine and terrestrial realms, though gas exchange between the ocean and atmosphere occurs very rapidly. More likely, this is a dating issue, or other environmental factors are affecting the Niekłań PIG-1 carbon-isotope curves. Extension of the new Niekłan PIG-1 $\delta^{13}C$ records down into the Rhaetian-aged section of the core would help to constrain the nature of the negative CIEs identified in the $\delta^{13}C_{plant}$ and $\delta^{13}C_{wp}$ records.

7.5.2. Fossil Charcoal Abundance

7.5.2.1. The Kaszewy-1 Core

The abundance of coarse fossil charcoal particles (>125 µm) in the Kaszewy-1 core samples is generally low, ranging from 0 particles/10 g sediment to 1256 particles/10 g sediment (**Figure 7.5**). Coarse fossil charcoal abundance is very low at the bottom of the study section with 3 and 0 particles/10 g sediment in the two oldest Rhaetian-aged samples. Coarse fossil charcoal abundance then peaks at a depth of 1896.70 m (sample kk_10) towards the top of the Rhaetian section with a value of 1256 particles/10 g sediment. The following Rhaetian sample at depth 1885.67 m (sample kk_10b) marks a return to low coarse fossil charcoal abundance, with 9 charcoal particles/10 g sediment. Coarse fossil charcoal abundance remains low above the Triassic-Jurassic Boundary, with the remaining Hettangian samples containing 5-24 charcoal particles/10 g sediment. Two samples from the Kaszewy-1 core (kk_8 and kk_10d) were not analysed due to undigested sediment clouding the samples.

Fine fossil charcoal particles (<125 µm) are much more abundant in the Kaszewy-1 sediments than coarse fossil charcoal particles (**Figure 7.6**). Fine fossil charcoal abundance shows a similar pattern to coarse fossil charcoal abundance, and peaks in the same sample as coarse fossil charcoal abundance (sample kk_10). Fine fossil charcoal abundance is generally low in the Upper Rhaetian sediments, ranging from ~24,100 particles/10 g sediment to ~82,500 particles/10g sediment, and increases towards the T-J Boundary. Fine fossil charcoal abundance peaks at a depth of 1896.70 m (sample kk_10), towards the top of the Rhaetian section, with ~385,000 particles/10 g sediment. Fine fossil
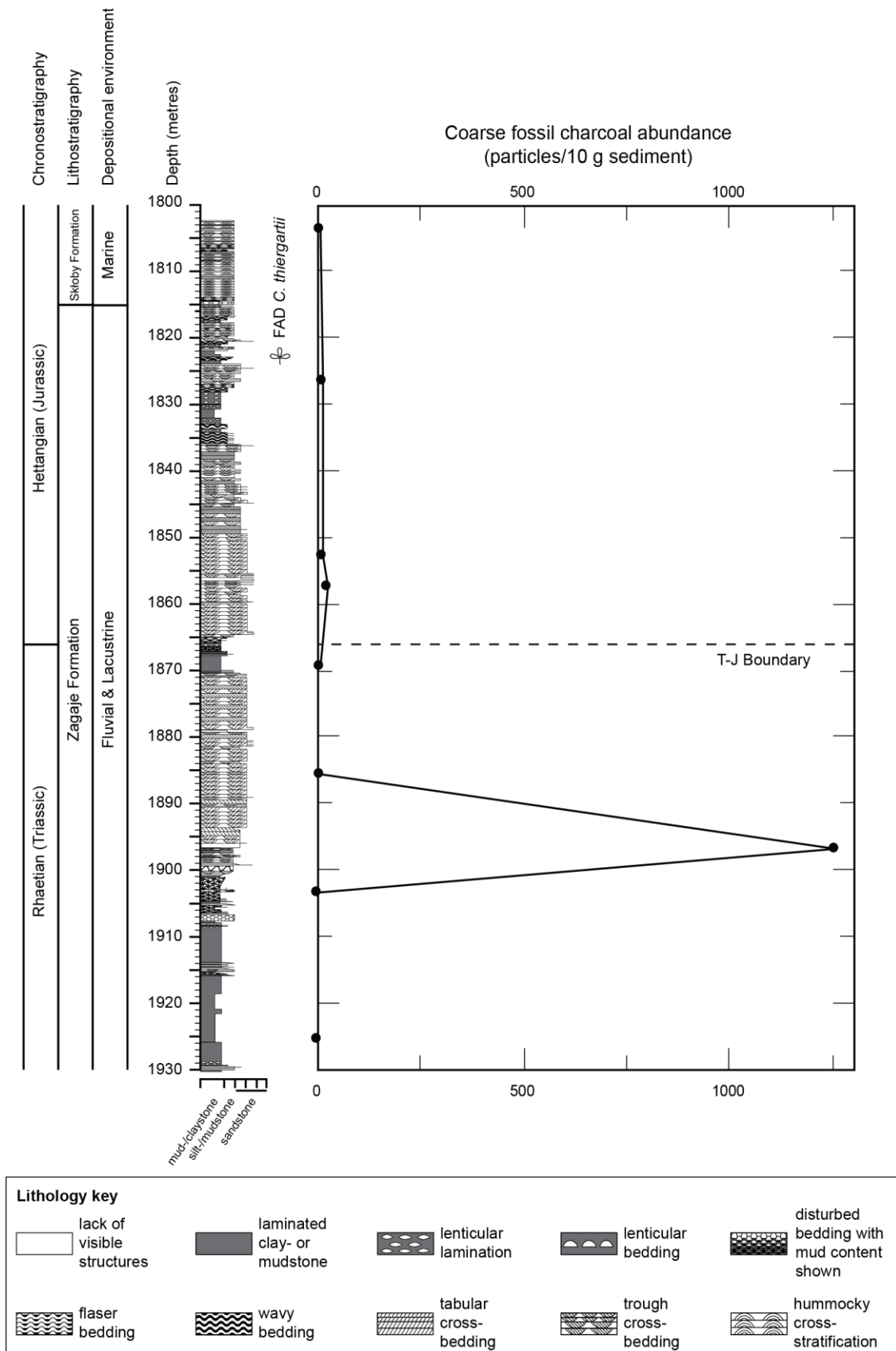
Figure 7.5 Coarse fossil charcoal abundance through the study section of the Kaszewy-1 core. The first occurrence of *Cerebropollenites thiergartii* is commonly used as a basal Jurassic palynomorph marker; the T-J Boundary here is based on sequence stratigraphy. Lithological succession from Grzegorz Pieńkowski (pers. comm.).

charcoal abundance then returns to low values, but still fluctuates, throughout the remaining Rhaetian section, and the Hettangian section above the T-J Boundary. Fine fossil charcoal abundance above the peak in abundance fluctuates between ~15,800 particles/10 g sediment and ~84,900 particles/10 g sediment.

Fine fossil non-charcoal particles (i.e. organic matter that has not been charcoalified; <125 µm) are more abundant than, and show a similar abundance pattern to, fine fossil charcoal particles (**Figure 7.6**). Fine fossil non-charcoal particle abundance is an order or magnitude greater than fine fossil charcoal particle abundance. The abundance of fine fossil non-charcoal particles in the lowest part of the Rhaetian section ranges from ~174,000 particles/10 g sediment to ~275,000 particles/10 g sediment, before reaching a peak abundance of ~2,000,000 particles/10 g sediment at a depth of 1896.70 m (sample kk_10). Fine fossil non-charcoal abundance fluctuates in the remaining Rhaetian and Hettangian section between ~64,800 particles/10 g sediment and ~346,000 particles/10 g sediment.

The percentage of fine fossil charcoal particles in the Kaszewy-1 samples ranges from 12.2% to 37.7%, and does not show a similar pattern to either coarse or fine fossil charcoal abundance (**Figure 7.6**). Fine fossil charcoal percentage fluctuates in the Rhaetian section of the core between 12.2% and 23.1%, reaching a peak of 37.7% in sample kk_10b, the sample above that which shows peak coarse and fine fossil charcoal abundance. Fine fossil charcoal percentage then decreases in the remaining Rhaetian and Hettangian sections further up the core, but still fluctuates between 15.4% and 27.3%. The changing percentage of fine fossil charcoal particles in the Kaszewy-1 samples shows that the fine fossil charcoal abundance is not a function of the total number of organic particles (charcoalified and non-charcoalified) present in a sample, but is being controlled by some other factor, such as changes in wildfire activity. A constant percentage of fine fossil charcoal particles would suggest that increases in absolute abundance are the result of an increased input of total organic matter particles.

The total number of fossil charcoal particles, both greater and less than 125 µm in size, is heavily skewed by the abundance of fine (<125 µm) fossil charcoal particles present in all samples. As a result, the shape of the total charcoal particle abundance curve looks very similar to the shape of the fine charcoal
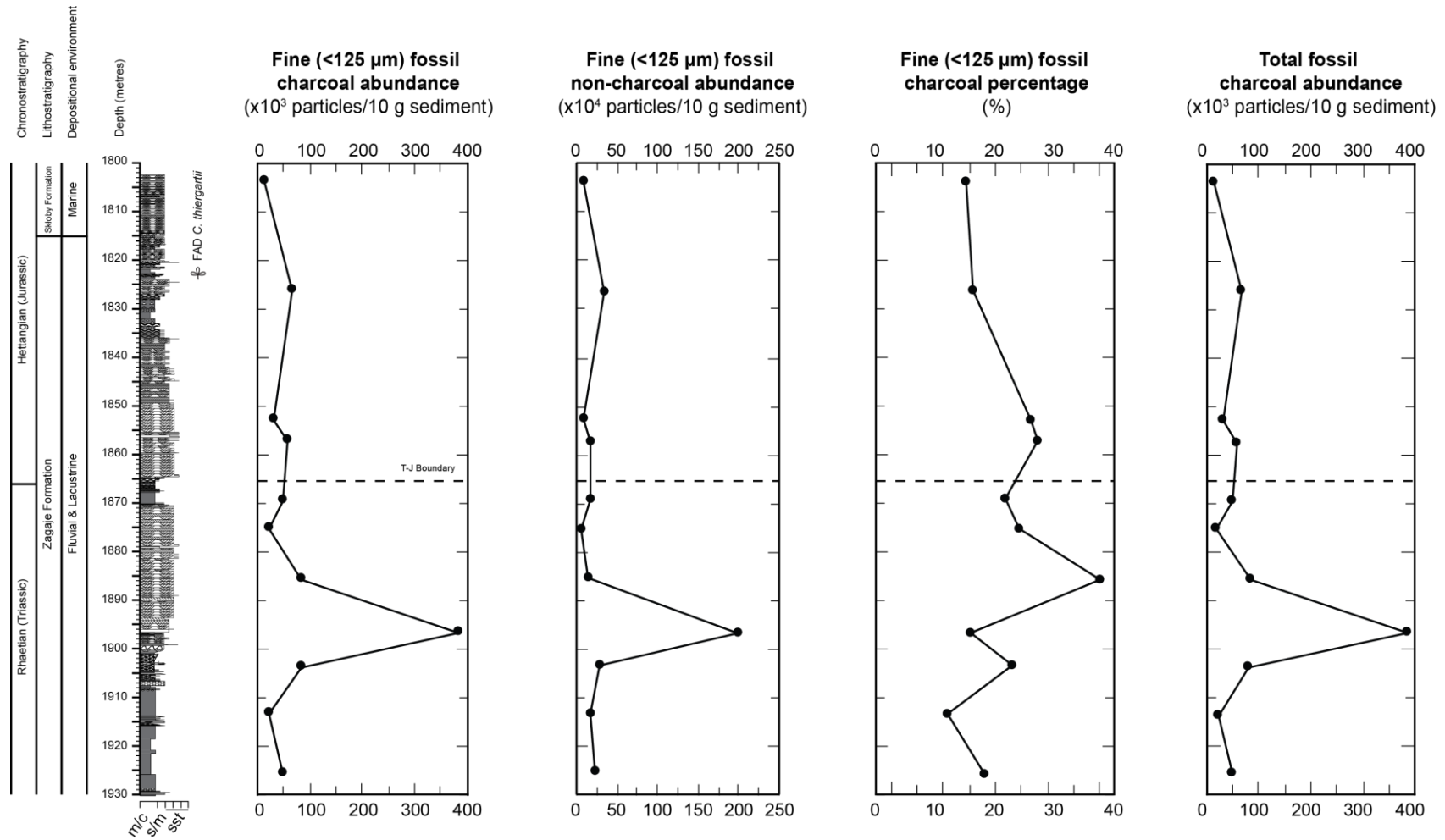
Figure 7.6 Kaszewy-1 core: Abundance of fine fossil charcoal & non-charcoal; percentage of fine fossil charcoal present; total fossil charcoal abundance (i.e. sum of coarse and fine fossil charcoal abundance). See **Figure 7.5** for lithology key. m-c = mudstone/claystone; s-m = siltstone/mudstone; sst = sandstone. Lithological succession from Grzegorz Pieńkowski (pers. comm.). The T-J Boundary here is based on sequence stratigraphy.

	Coarse charcoal abundance	Fine charcoal abundance	Fine non-charcoal abundance
Maximum grain size	0.107	0.030	0.049
Median grain size	0.085	0.017	0.036
Depositional setting – marine influence	0.094	0.059	0.044

Table 7.1 R^2 values calculated from cross-plots of coarse and fine fossil charcoal, and fine fossil non-charcoal abundances against various lithological properties for the Kaszewy-1 samples. R^2 values range between 0 and 1, with lower values indicating a weaker relationship between the two variables (Taylor, 1990). Samples were assigned numerical values based on their lithological characteristics which were then used to calculate R^2 values. Maximum and median grain sizes were assigned a number between 1 and 5, corresponding to mud, silt, fine sand, medium sand, and coarse sand. Depositional setting was assigned a number between 1 and 9, based on the inferred marine influence; the value 1 was assigned to samples thought to be deposited in fully terrestrial environments, with increasing values corresponding to an increasing marine influence.

particle abundance curve (**Figure 7.6**). Total charcoal abundance is relatively low in the bottom of the studied section, and reaches a peak towards the top of the Rhaetian section before it decreases to low levels again in the latest Rhaetian section, across the Triassic-Jurassic Boundary, and throughout the Hettangian part of the studied section.

Lithology and depositional environment can also affect the abundance of charcoal preserved in sediments. The samples collected for this study cover a range of lithologies, thought to have been deposited in a variety of settings. Sedimentary facies were assigned based on lithological, sedimentary structural, trace fossil, and body fossil evidence, as well as sequence stratigraphy (Pieńkowski, pers. comm.). However, as argued below, it would appear that lithology and depositional environment have little control on the fossil charcoal content of the Kaszewy-1 samples (**Table 7.1**). Changes in fossil charcoal content of the Kaszewy-1 samples are more likely the result of changes in wildfire activity across the Triassic-Jurassic Boundary.

A mixture of both mudstone and sandstone beds were collected from the Kaszewy-1 core, due to the frequent changes of lithology in the core. Since sand is deposited in higher energy environments than clays and silts, it would be

expected that a larger number of coarse fossil charcoal particles would be present in sandstone samples than mudstones samples, and fewer fine fossil charcoal particles would be present in sandstone samples than mudstone samples. The fossil charcoal abundance data from the Kasewy-1 core does not show this relationship and there is little correlation between grain size and fossil charcoal abundance (**Table 7.1**). Mudstone samples from the Kaszewy-1 core show a similar range to the sandstone samples in both coarse and fine fossil charcoal abundance. Inferred depositional environment also appears to have little correlation with coarse and fine fossil charcoal abundance (**Table 7.1**); both low and high energy environments show similar abundances of coarse and fine fossil charcoal particles.

7.5.2.2. The Niekłań PIG-1 Core

The abundance of coarse fossil charcoal particles (>125 µm) in the Niekłan PIG-1 core is generally low, ranging from 0 particles/10 g sediment to ~4100 particles/10 g sediment (**Figure 7.7**). The two lowest samples at 165.20 m and 163.00 m (NC1; NC4) in the study section both lack any coarse fossil charcoal particles (0 particles/10 g sediment). A massive increase in coarse fossil charcoal abundance to ~4100 particles/10 g sediment) is then seen in the next sample moving up the core at depth 160.00 m (sample NC6). Sample NC6 is just below the inferred Triassic-Jurassic Boundary and contains the highest abundance of coarse fossil charcoal particles of any of the Niekłan PIG-1 samples. Immediately above the T-J Boundary, coarse fossil charcoal abundance decreases to 126 particles/10 g sediment at depth 158.05 m (sample NC8). An increase in coarse fossil charcoal abundance is observed in the next sample moving up the core at depth 155.50 m (sample NC9), to ~950 particles/10 g sediment. Coarse fossil charcoal abundance then decreases to very low values (0 – 30 particles/10 g sediment) in the remaining samples moving up through the Hettangian section of the core.

Fine (<125 µm) fossil charcoal particles are much more abundant in the Niekłan PIG-1 samples than coarse fossil charcoal particles (**Figure 7.8**). The abundance of fine fossil charcoal particles is generally low in the Rhaetian-aged part of the section, with values of ~2,100 to ~5,200 particles/10 g sediment. Fine fossil charcoal abundance increases slightly to ~69,200 particles/10 g sediment in the
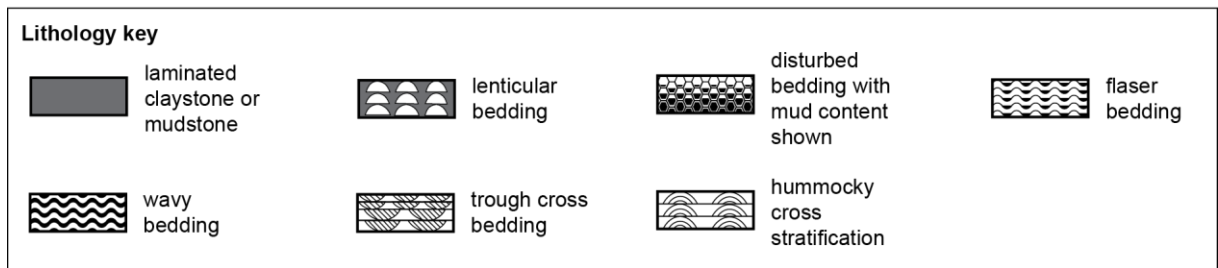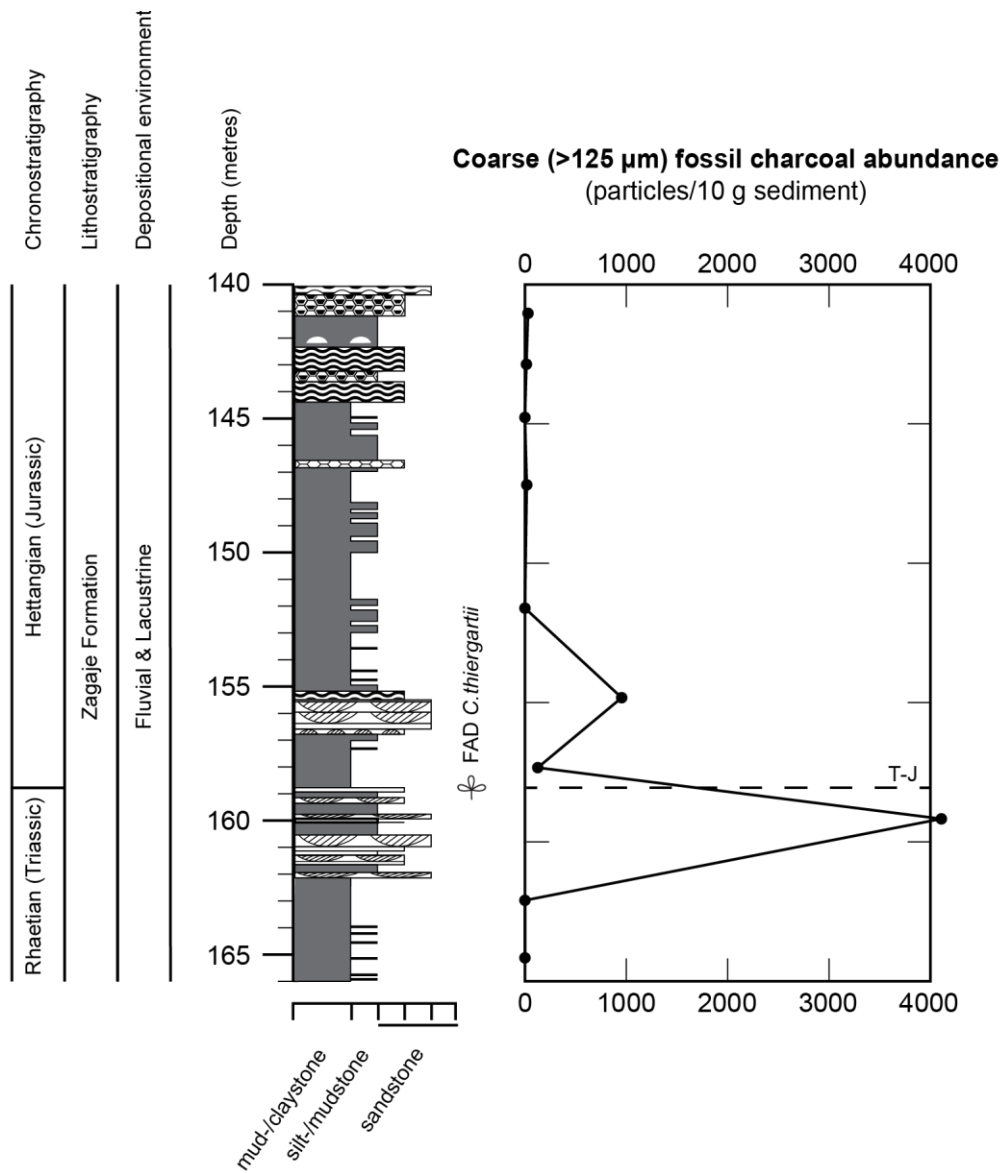
Figure 7.7 Coarse fossil charcoal abundance through the study section of the Niekłan PIG-1 core. *Cerebropollenites thiergartii* is commonly used as a basal Jurassic palynomorph marker and is used here to identify the Triassic-Jurassic Boundary (labelled T-J). Lithological succession from Grzegorz Pieńkowski (pers. comm.).

last sample below the inferred T-J Boundary (160.00 m in depth), before increasing massively to ~314,000 particles/10 g sediment in sample NC8 at

158.05 m in depth, above the inferred T-J Boundary. Fine fossil charcoal abundance then decreases and remains generally low in the remaining part of the Hettangian section, fluctuating between ~28,100 particles/10 g sediment and ~187,000 particles/10 g sediment.

The abundance of fine fossil non-charcoal (i.e. non-charcoalified organic matter) particles shows a similar pattern to that of fine fossil charcoal abundance, but one order of magnitude larger (**Figure 7.8**). Fine fossil non-charcoal abundance is generally low in the lowermost part of the study section (~73,200 – ~77,300 particles/10 g sediment) before increasing in the uppermost sample below the inferred T-J Boundary to ~386,000 particles/10 g sediment. The abundance of fine fossil non-charcoal particles peaks in sample NC8, above the inferred T-J Boundary, at ~1,890,000 particles/10 g sediment; the largest peak in fine fossil charcoal also occurs in this sample. Fine fossil non-charcoal abundance then declines in the remaining samples of the Hettangian section, similar to fine fossil charcoal abundance, fluctuating between ~223,000 particles/10 g sediment and ~824,000 particles/10 g sediment.

The percentage of fine fossil charcoal particles present in the fine fraction of the Niekłan PIG-1 samples ranges between 2.8% and 20.3% (**Figure 7.8**). The proportion of fossil charcoal in the fine fraction of these samples fluctuates throughout the study section, suggesting that fine fossil charcoal abundance is not a function of total organic matter particles present, but that it is controlled by other factors. The percentage of fine fossil charcoal particles present in the lowest samples of the study section is relatively low (2.8% to 6.4%). Fine fossil charcoal percentage then increases to 14.3% – 15.2% in samples both immediately below (160.00 m) and above (158.05 m) the inferred T-J Boundary. The highest percentage of fine fossil charcoal is at depth 155.50 m in sample NC9, with a value of 20.3%. The percentage then decreases to 4.6% in the next sample moving up the core, before increasing first to 12.6% and then again to values between 17.9% and 18.5% in the three uppermost samples of the study section.

Similar to the charcoal abundance data presented in the previous chapter, wildfire activity is discussed in terms of changing absolute charcoal abundance. It is generally accepted that changes in absolute charcoal abundance reflect changes in wildfire activity level (e.g. Scott, 2010). Further work is required to improve our
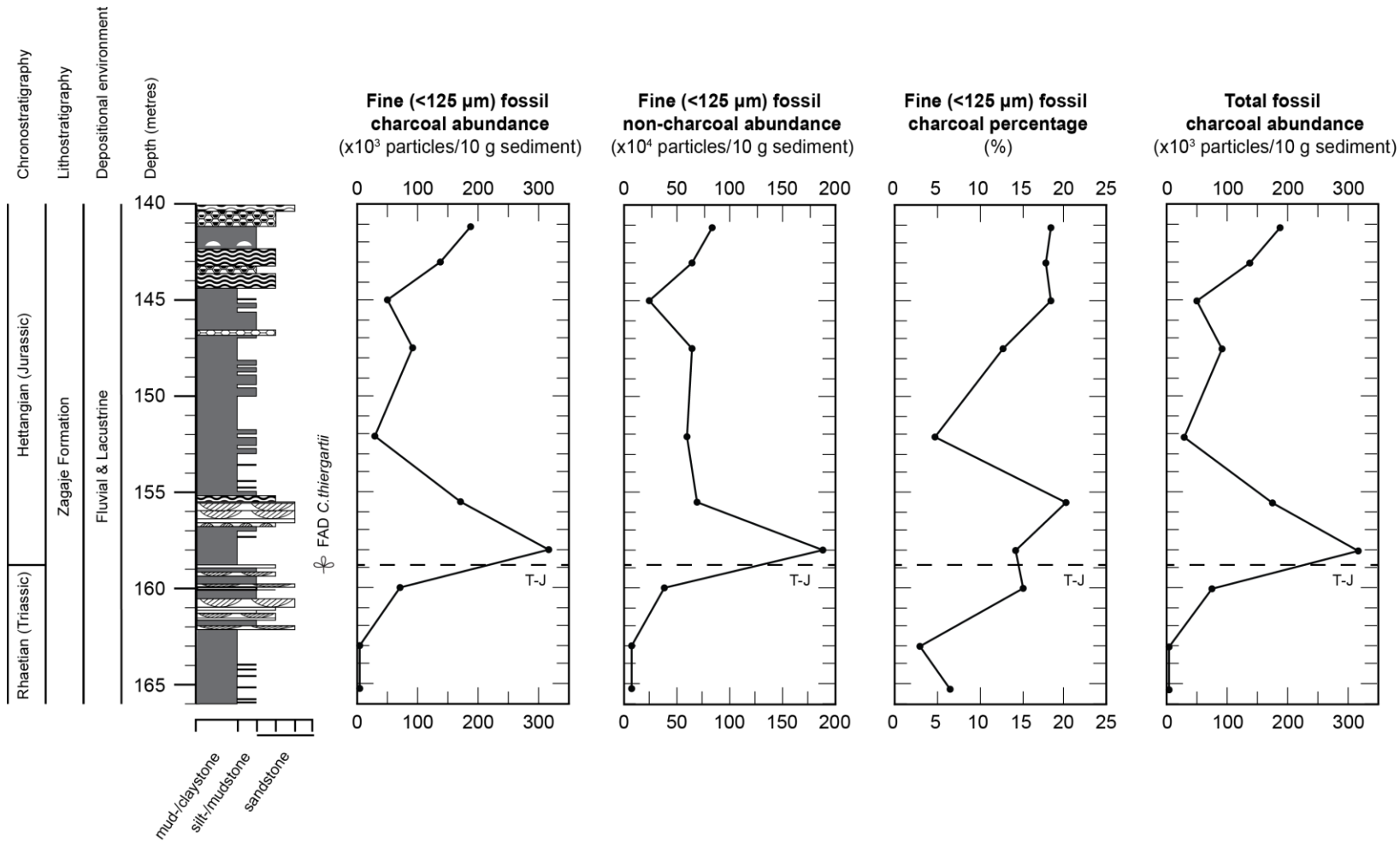
Figure 7.8 Abundance of fine fossil charcoal & non-charcoal; percentage of fine fossil charcoal present; total fossil charcoal abundance (i.e. sum of coarse and fine fossil charcoal abundance). See **Figure 7.7** for lithology key. m-c = mudstone/claystone; s-m = siltstone/mudstone; sst = sandstone. Lithological succession from Grzegorz Pieńkowski (pers. comm.).

	Coarse charcoal abundance	Fine charcoal abundance	Fine non-charcoal abundance
Maximum grain size	0.048	0.062	0.001
Median grain size	0.019	0.051	0.000
Depositional setting – marine influence	0.306	0.000	0.003

Table 7.2 R^2 values calculated from cross-plots of coarse and fine fossil charcoal, and fine fossil non-charcoal abundances against various lithological properties for the Niekłan PIG-1 samples. R^2 values range between 0 and 1, with lower values indicating a weaker relationship between the two variables (Taylor, 1990). Samples were assigned numerical values based on their lithological characteristics which were then used to calculate R^2 values. Maximum and median grain sizes were assigned a number between 1 and 5, corresponding to mud, silt, fine sand, medium sand, and coarse sand. Depositional setting was assigned a number between 1 and 9, based on the inferred marine influence; the value 1 was assigned to samples thought to be deposited in fully terrestrial environments, with increasing values corresponding to an increasing marine influence.

understanding of the relationship between fossil charcoal and past wildfire activity. The total abundance of fossil charcoal particles (both coarse and fine) is heavily controlled by the abundance of fine fossil charcoal particles, and consequently, the total fossil charcoal abundance record shows a very similar pattern to that of the fine fossil charcoal abundance record (**Figure 7.8**). Total fossil charcoal abundance is generally low in the Rhaetian-aged part of the study section, increasing just below the T-J Boundary, and peaking immediately above it. Total fossil charcoal abundance then declines and remains generally low for the remaining part of the Hettangian-aged section of the core, with a relatively small increase towards the top of the study section.

The lithology and inferred depositional environments of the Niekłan PIG-1 samples appear to have little effect on the abundance of fossil organic matter particles (**Table 7.2**), suggesting that the changes in fossil charcoal abundance reflects changes in another factor, likely wildfire activity. Sedimentary facies were assigned using the same criteria as those for the Kaszewy-1 samples (Pieńkowski, pers. comm.). Both mudstones and sandstone bulk rock samples were processed and analysed as part of this study, yet there appears to be no pattern between sedimentology and fossil organic matter abundance; both

mudstones and sandstone samples show a range of fossil organic matter particle counts. The sediments analysed represent sediments which were thought to have been deposited in backswamp, deltaic, fluvial and lacustrine environments. There is little correlation between inferred depositional environment and fossil organic matter abundance.

Samples thought to have been deposited in low-energy lacustrine environments show a wide range of fossil organic matter particle counts. Samples thought to have been deposited in higher energy environments do appear to have generally higher abundances of fossil organic matter, but overall there is insignificant correlation between inferred depositional environment and fossil organic matter abundance.

7.5.3. Polycyclic Aromatic Hydrocarbon Concentrations

7.5.3.1. The Kaszewy-1 Core

Pyrolysis-derived PAHs were detected in all eleven sediment samples in varying concentrations (**Figure 7.9**). Benz-anthracene, benzo(k)fluoranthene, fluoranthene, indeno[1,2,3-cd]pyrene, phenanthrene, and pyrene were detected in all eleven samples, whereas coronene and fluorene were only detected in 9 of 11 samples.

Overall, the most abundant pyrolytic PAH detected was phenanthrene, with concentrations ranging from 60 ng/g sediment to 2078 ng/g sediment. Phenanthrene is the most abundant pyrolytic PAH in 10 of 11 samples; benzo(k)fluoranthene is the most abundant pyrolytic PAH in sample kk_5 at 1925.56 m depth. The least abundant pyrolytic PAH detected was coronene, with concentrations ranging from 43 ng/g sediment to 71 ng/g sediment. Indeno[1,2,3-cd]pyrene and fluorene were also detected in low concentrations, similar to coronene. The low concentrations of coronene relative to the other pyrolytic PAHs detected in the Kaszewy-1 samples suggests that it was produced during the combustion of organic matter (cf. Belcher et al., 2005).

The general shape of the pyrolytic PAH concentration curves show low values at the bottom of the study section followed by two peaks in concentration separated by low values, and then followed by a decrease in pyrolytic PAH concentration
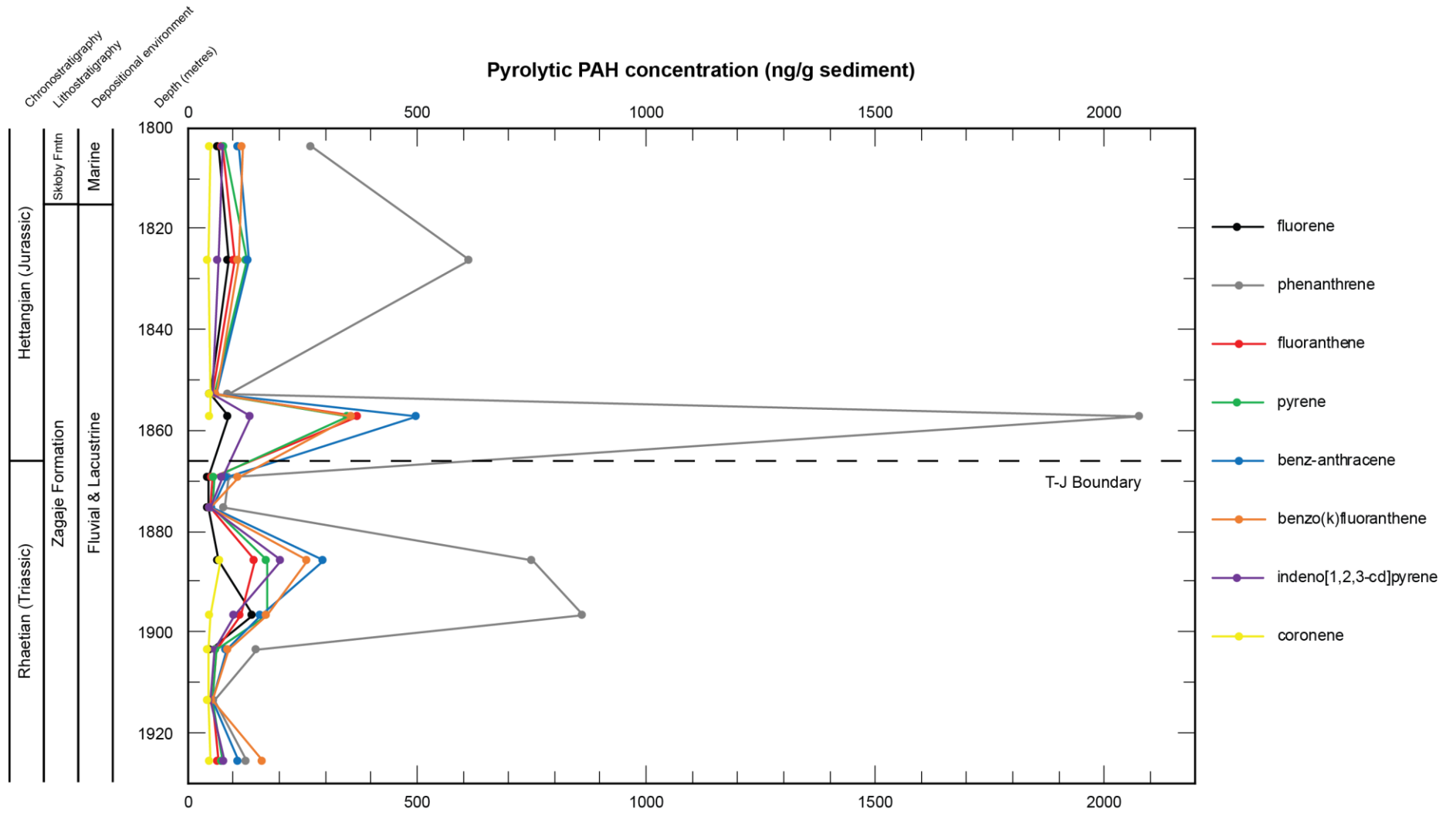
Figure 7.9 Concentrations of 8 different pyrolytic PAHs throughout the Kaszewy-1 study section. T-J Boundary position is based on sequence stratigraphy by G. Pieńkowski.

towards the top of the study section (**Figure 7.9**). At the bottom of the study section, in the lowest Rhaetian-aged sediments, the concentration of each pyrolytic PAH is generally low, ranging from ~50-163 ng/g sediment, though increases between depths 1885.67-1896.70 m to highs of 71-863 ng/g sediment.

Pyrolytic PAH concentrations then decrease to lows of 47-79 ng/g sediment between depths 1869.30-1885.67 m, before increasing and peaking again at depth 1857.30 m, just below the Triassic-Jurassic Boundary. The second peak in pyrolytic PAH concentrations ranges from 88 ng/g sediment to 2078 ng/g sediment. Pyrolytic PAH concentrations then decrease in the remaining Hettangian section of the core. With the exception of phenanthrene, pyrolytic PAH concentrations fall to 47-134 ng/g sediment in the remaining Hettangian section of the core; phenanthrene is more abundant in this section, ranging from 88 ng/g sediment to 616 ng/g sediment.

Pyrolytic PAHs typically form above temperatures of 350°C, and will continue to form at temperatures greater than 1200°C (Abdel-Shafy and Mansour, 2016), with lower molecular weights (*m/z*) forming prior to those with higher molecular weights (Richter and Howard, 2000; Kislov et al., 2013). Pyrolytic PAHs with lower molecular weights form the building blocks of those with higher *m/z* (Richter and Howard, 2000; Kislov et al., 2013). Fluorene and phenanthrene are the pyrolytic PAHs with the lowest molecular weights detected in the Kaszewy-1 samples (166 and 176, respectively). Consequently, it would be expected the concentrations of these two pyrolytic PAHs would be the highest per sample. Phenanthrene is present in far greater concentrations than any other pyrolytic PAHs in the Kaszewy-1 samples (**Figure 7.9**). It has been suggested that phenanthrene can also be produced by diagenetic processes (e.g. Jiang et al., 1998), which most likely explains the discrepancy between the concentrations of fluorene and phenanthrene in the Kaszew-1 T-J Boundary samples, similar to the Kaszewy-1 Toarcian OAE samples discussed in **Chapter 6**. Phenanthrene is not included in the total concentration of pyrolytic PAHs for the Kaszewy-1 T-J Boundary samples due to it likely reflecting a mixture of both pyrolysis- and diagenesis-derived phenanthrene.

Significant concentrations of petrogenic PAHs were detected in all of the Kaszewy-1 samples (**Figure 7.10**). Alkylated (petrogenic) PAHs are usually

PAH concentration (ng/g sediment)
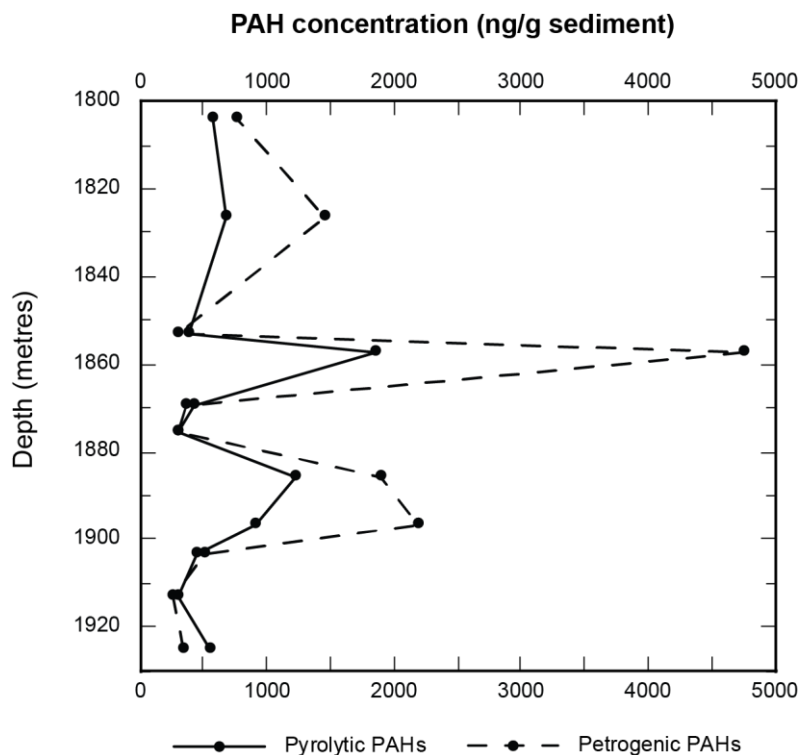
Figure 7.10 Total concentration of petrogenic PAHs plotted alongside total concentration of pyrolytic PAHs for the Kaszewy-1 core Rhaetian-Hettangian section.

derived from hydrocarbon sources, rather than the burning of biomass (Laflamme and Hites, 1978; Lake et al., 1979; Venkatesan and Dahl, 1989), suggesting that there is a hydrocarbon-source in the area surrounding the Kaszewy-1 site. Venkatesan and Dahl (1989) suggest that, within a sample, the concentration ofpyrolytic PAHs should be higher than that of petrogenic PAHs in order to be convincing evidence of wildfire activity. The total concentration of petrogenic PAHs in the Kaszewy-1 samples shows a similar pattern to that of the total concentration of pyrolytic PAHs (**Figure 7.10**). Total petrogenic PAH concentration ranges between 312-4759 ng/g sediment, similar to the total pyrolytic PAH concentration (313-1853 ng/g sediment). Assuming the conclusion of Venkatesan and Dahl (1989) is correct, the pyrolytic PAH data from the Kaszewy-1 samples should not be a convincing argument for fluctuations in wildfire activity at the site across the T-J Boundary. However, the co-occurrence of fossil charcoal with the geochemical evidence, would suggest that wildfire activity did indeed change over time at the Kaszewy-1 site, despite the significant presence of petrogenic PAHs in the same samples.
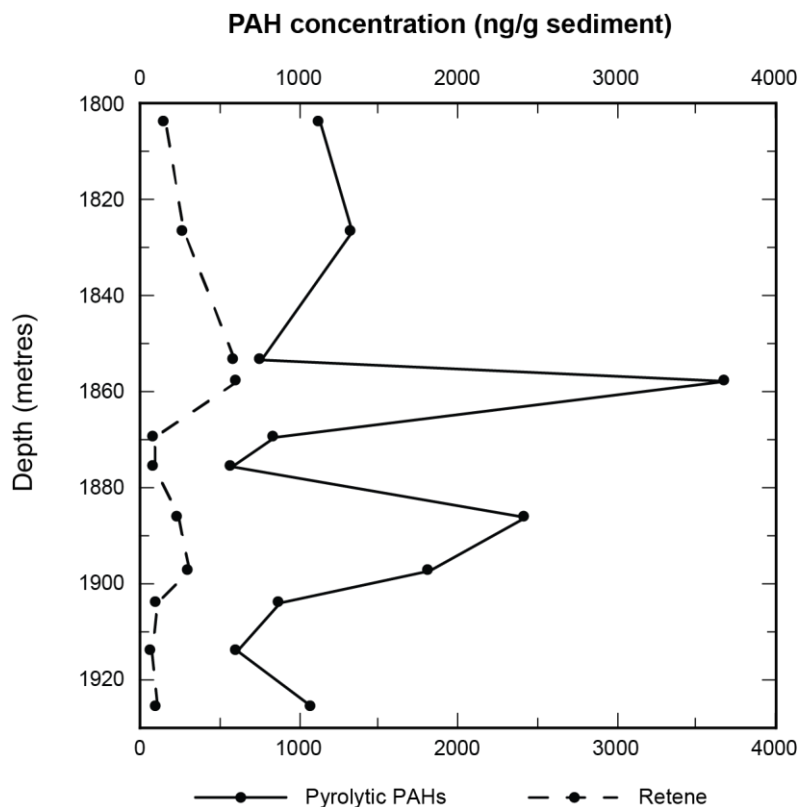
Figure 7.11 Total concentration of pyrolytic PAHs plotted alongside retene concentration for the Kaszewy-1 core Rhaetian-Hettangian section.

The land-plant biomarker retene was detected in all the Kaszewy-1 samples and varies in concentration from 46 ng/g sediment to 307 ng/g sediment (**Figure 7.11**). Retene concentration covaries with total pyrolytic PAH concentration, further confirming that significant amounts of plant material were burning at the Kaszewy-1 site throughout the Late Triassic and Early Jurassic.

7.5.3.2. The Niekłań PIG-1 Core

Pyrolytic PAHs were detected in all ten samples from the Niekłan PIG-1 core in varying concentrations (**Figure 7.12**). Benz-anthracene, benzo(k)fluoranthene, fluoranthene, indeno[1,2,3-cd]pyrene, phenanthrene, and pyrene were detected in all eleven samples, whereas coronene was detected in nine samples, and fluorene detected in only three.

Generally, the most abundant pyrolytic PAH in the Niekłan PIG-1 study section is benzo(k)fluoranthene, with concentrations ranging from 41 ng/g sediment to 836

ng/g sediment, followed by indeno[1,2,3-cd]pyrene (41 – 713 ng/g sediment) and phenanthrene (48 – 495 ng/g sediment). Whilst fluorene was detected in only three samples, it is present in those samples in higher concentrations (53 – 72 ng/g sediment) than coronene is in most of the nine samples that it was detected in (41 – 78 ng/g sediment). It is thought that relatively low concentrations of coronene reflects pyrolysis-derived rather than petrogenic coronene (cf. Belcher et al., 2005).

The general shape of the pyrolytic PAH concentration curves shows two peaks in concentration separated by relatively low values (**Figure 7.12**); these two peaks both occur in the Hettangian-aged part of the study section, above the inferred Triassic-Jurassic Boundary. In the lowest Rhaetian-aged sediments, the concentration of each pyrolytic PAH is relatively low, ranging between 41 ng/g sediment and 64 ng/g sediment. Generally, pyrolytic PAH concentrations remain low in the first sample above the inferred T-J Boundary, except for the PAH phenanthrene, which shows a peak in concentration offset from peaks in concentration of most other pyrolytic PAHs; fluorene and coronene concentrations remain relatively stable throughout the entire study section. The first peak in pyrolytic PAH concentrations is observed in sample NC9 at depth 155.50 m, with values ranging from 50 ng/g sediment to 797 ng/g sediment.

Moving up the core, pyrolytic PAH concentrations decrease dramatically in sample NC10 at depth 152.10 m, ranging between 53 ng/g sediment and 104 ng/g sediment. The second peak in pyrolytic PAH concentrations occurs at depth 147.50 m (sample NC12) and is similar in magnitude to the first peak, ranging from 72 ng/g sediment to 836 ng/g sediment. Moving up the study section, the concentrations of pyrolytic PAHs decline rapidly and remain low for the remaining samples, ranging between 47 ng/g sediment and 215 ng/g sediment.

Unlike the contemporaneous pyrolytic PAH record from the Kaszewy-1 core (**Section 7.5.3.1.**), phenanthrene is not the most abundant PAH in the Niekłan PIG-1 samples, though it is still possible that there is a component of diagenetic phenanthrene in the Niekłan PIG-1 samples. As was the case for the Kaszewy-1
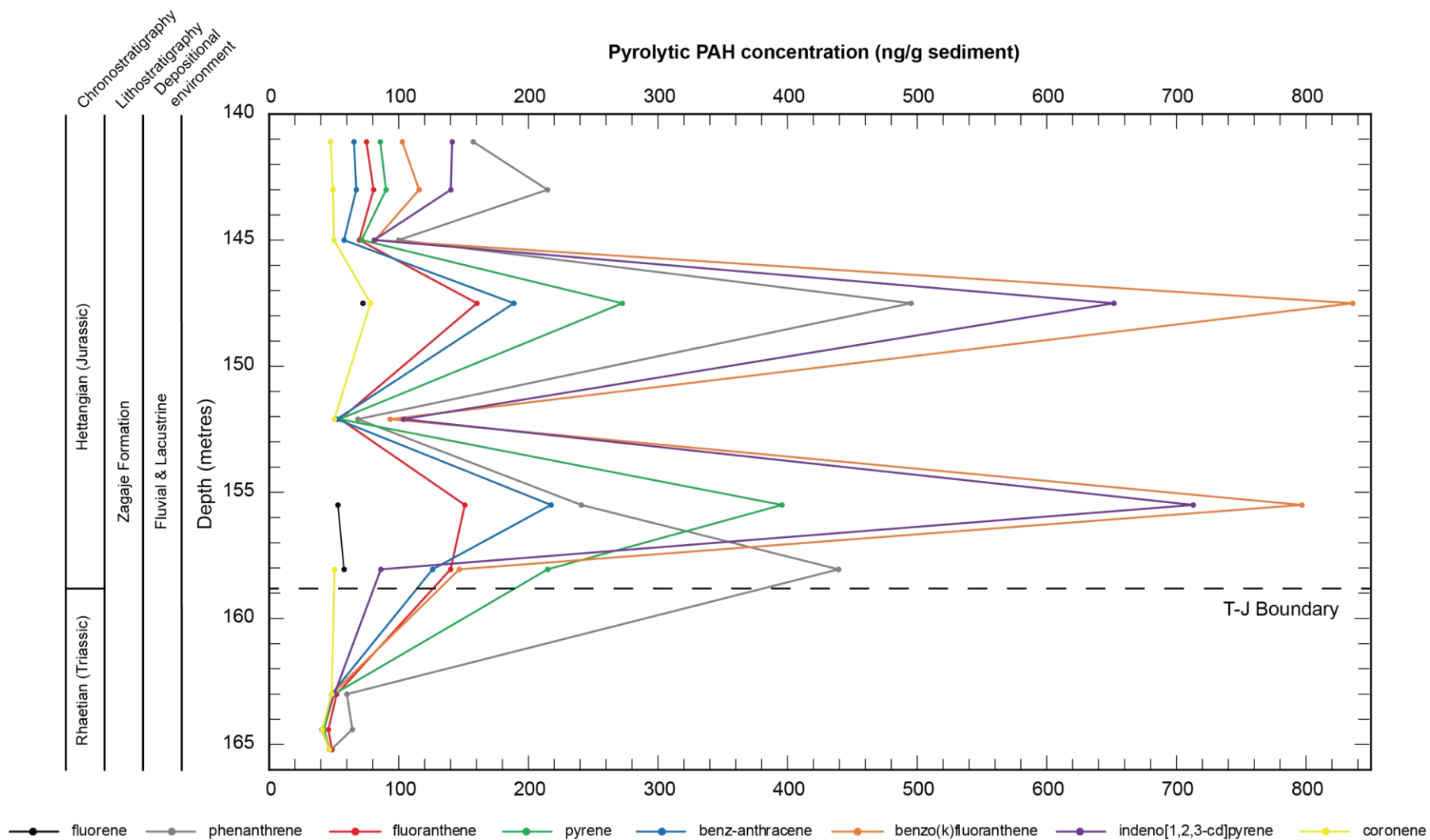
Figure 7.12 Concentrations of 8 different pyrolytic PAHs throughout the Niekłan PIG-1 study section. T-J Boundary position is marked by the first occurrence of *C. thiergartii*.

PAH concentration (ng/g sediment)
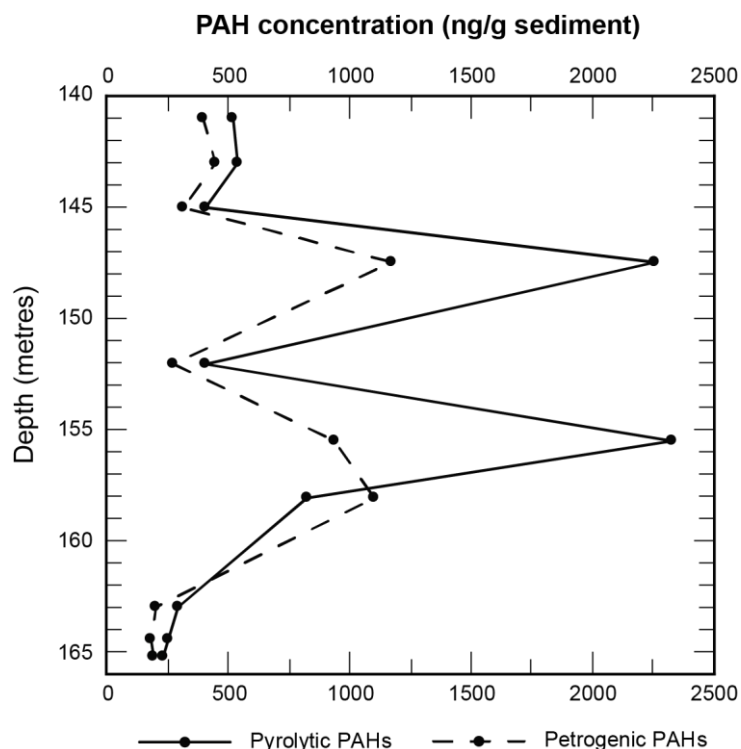
Figure 7.13 Total concentration of petrogenic PAHs plotted alongside total concentration of pyrolytic PAHs for the Niekłan PIG-1 core Rhaetian-Hettangian section.

dataset, phenanthrene is not included in any total concentrations of pyrolytic PAHs of Niekłan PIG-1 samples discussed further in this thesis. Petrogenic PAHs are less abundant in the T-J Boundary Niekłan PIG-1 samples than they are in the T-J Boundary Kaszewy-1 samples; total pyrolytic PAH concentration is generally higher than total petrogenic PAH concentration (**Figure 7.13**). At depths 155.50 m and 147.50 m (samples NC9 and NC12), which both

show peaks in pyrolytic PAH concentrations, the total concentration of pyrolytic PAHs is approximately twice as great as the total concentration of petrogenic PAHs, suggesting that the pyrolytic PAHs detected in the Niekłan PIG-1 samples highly likely originate from burning of organic matter, rather than petrogenic sources (Venkatesan and Dahl, 1989).

The land-plant biomarker retene was also detected in all the Niekłan PIG-1 samples and varies in concentration from 49 ng/g sediment to 253 ng/g sediment (**Figure 7.14**). Similar to the Kaszewy-1 record, retene concentration covaries
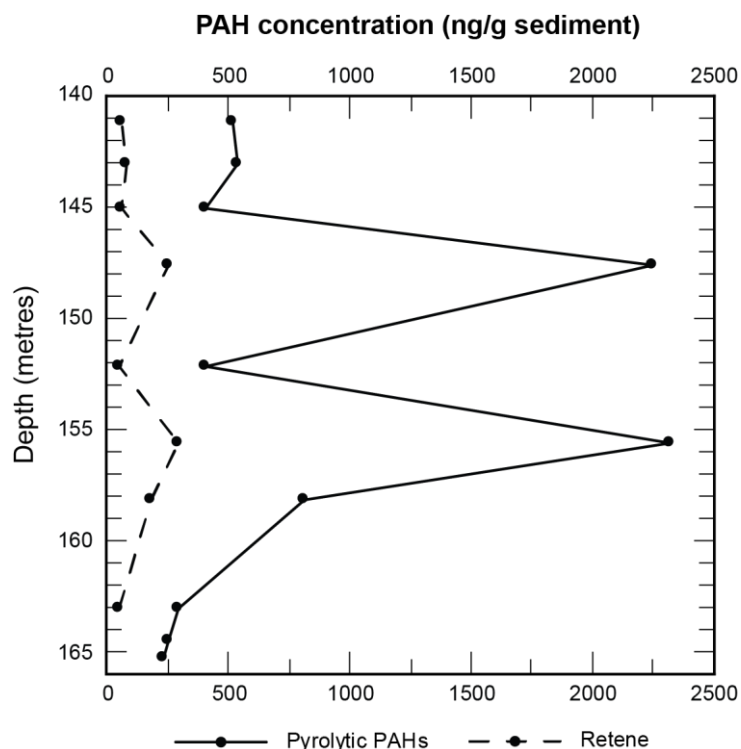
Figure 7.14 Total concentration of pyrolytic PAHs plotted alongside retene concentration for the Niekłan PIG-1 core Rhaetian-Hettangian section.

with total pyrolytic PAH concentration, confirming the burning of biomass at the Niekłan PIG-1 site throughout the Late Triassic and Early Jurassic.

7.5.4. Wildfire Activity History in the Central Polish Basin Across the Triassic-Jurassic Boundary

The co-occurrence of fossil charcoal and geochemical markers of organic matter pyrolysis in the Kaszewy-1 and Niekłan PIG-1 samples provides an insight into the history of wildfire activity in the central Polish Basin across the Triassic-Jurassic Boundary. Changes in both fossil charcoal abundance and pyrolytic PAH concentrations suggest that the Kaszewy-1 site experienced two periods of intense wildfire activity around the T-J Boundary (**Figure 7.15**), whereas at least five periods of intense wildfire activity are indicated by the Niekłan PIG-1 fossil charcoal abundance and pyrolytic PAH concentration records (**Figure 7.16**).

The abundance of fossil charcoal in the sedimentary record is thought to be a reliable indicator of past wildfire activity (e.g. Scott, 2010). An increase in fossil charcoal abundance through a sedimentary sequence is thought to reflect increased rates of charcoal formation caused by increased wildfire activity, and *vice versa* (e.g. Carcaillet et al., 2002; Thevenon et al., 2004; Marlon et al., 2006; Higuera et al., 2007; Power et al., 2007; Scott, 2010). Similarly, an increase in the concentration of pyrolytic PAHs in sediments is also thought to reflect increased rates of incomplete combustion of organic matter (e.g. Jiang et al., 1998; Belcher et al., 2009; Shen et al., 2011). The levels of increased wildfire activitity indicated in these two cores do not appear to be biased by depsitional setting (as discussed in **Sections 7.5.2.**). Analysis of size sorting was not carried out beyond <125 µm and >125 µm due to time constraints. TOC and microfossil data was not available to assess changes in sedimentation rate or extent of reworking. Additional work would include investigating these aspects further.

7.5.4.1. A Period of Increased Wildfire Activity Recorded in the Rhaetian of the Kaszewy-1 Core

The abundance of both coarse and fine fossil charcoal in the Kaszewy-1 core indicate low levels of wildfire activity in the lower Rhaetian section, before increasing and peaking in the mid-Rhaetian section at a depth of 1896.70 m (**Figure 7.15**). The peaks in both coarse and fine fossil charcoal abundance are fairly sharp, suggesting that this first level of increased wildfire activity was relatively short-lived. Both coarse and fine fossil charcoal abundance decrease across the Triassic-Jurassic Boundary and remain relatively low in the rest of the Hettangian section of the core, indicating lower levels of wildfire activity across the T-J Boundary and during the Early Hettangian. The T-J Boundary in the Kaszewy-1 core is based on sequence and carbon-isotope stratigraphy. The FAD of *C. thiergartii* occurs ~40 m above the currently-accepted position of the T-J Boundary; a lack of palynology data from the study section between the FAD of *C. thiergartii* and the T-J Boundary currently prevents the basal Jurassic marker being used to define the boundary.
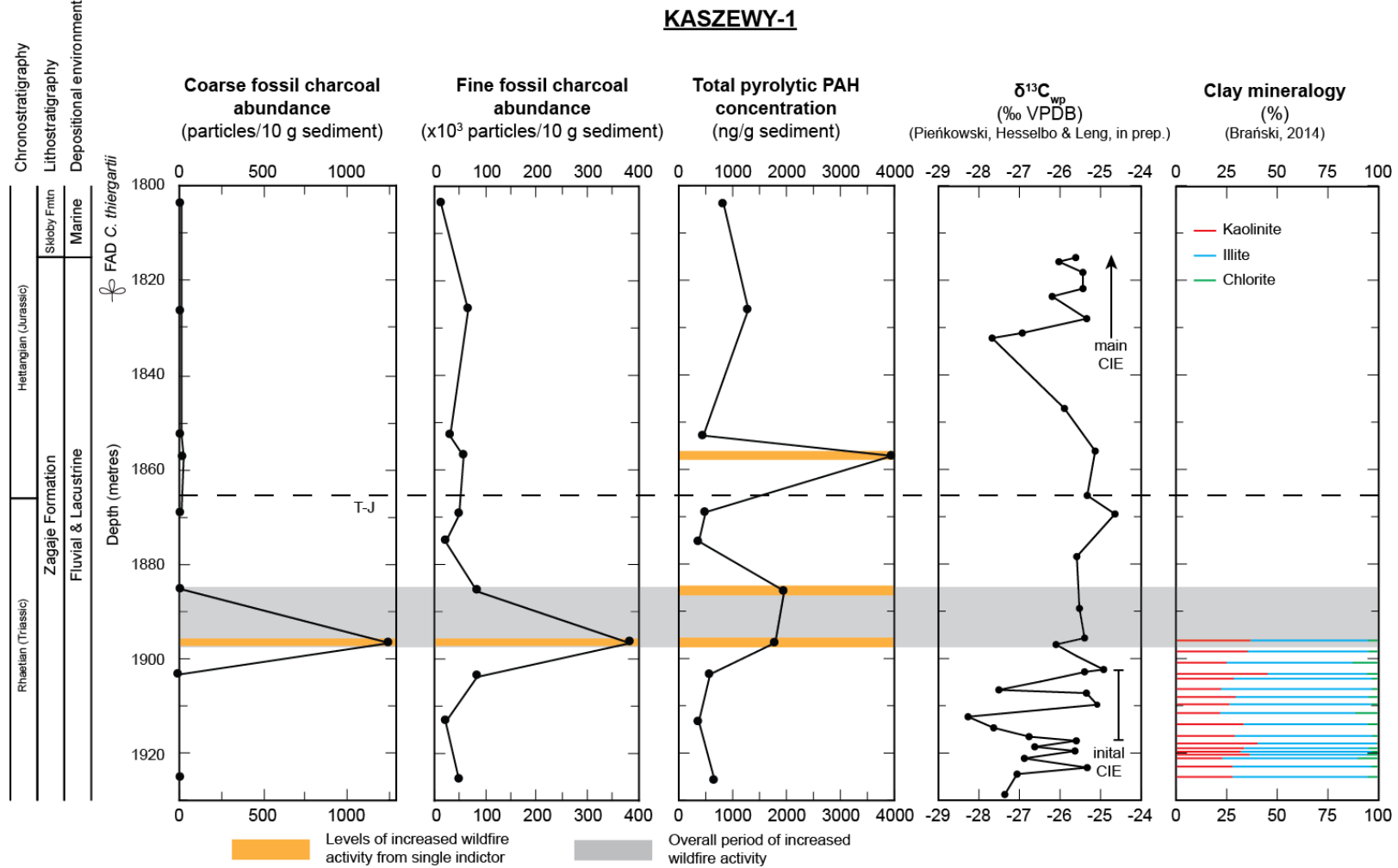
Figure 7.15 New fossil charcoal abundance and pyrolytic PAH concentration records from the Kaszewy-1 core correlated with δ13Corg (G. Pieńkowksi, pers. comm.) and clay mineralogy records (Brański, 2014). Levels of increased wildfire activity from a single indicator are highlighted in orange; overall periods of increased wildfire activity are highlighted in grey. T-J = Triassic-Jurassic Boundary. Lithological succession from G. Pieńkowski (pers. comm.).

The total concentration of pyrolytic PAHs in the study section suggests that there were at least two levels of increased wildfire activity: one in the middle of the Rhaetian section, and another just after the Triassic-Jurassic Boundary, in the Early Hettangian. Total pyrolytic PAH concentration is low in the lowest part of the Rhaetian section, before increasing between depths 1885.67 m & 1896.70 m, suggesting a period of increased wildfire activity, correlating with the high abundances of coarse and fine fossil charcoal. The total concentration of pyrolytic PAHs decreases in the top part of the Rhaetian section before then increasing again just after the inferred T-J Boundary at depth 1857.30 m, suggesting a second level of increased wildfire activity. This second peak in total pyrolytic PAH concentration is much sharper than the first one, suggesting that the second level of increased wildfire activity was more short-lived than the first one, assuming a constant sedimentation rate.

The size range of fossil charcoal present in a sedimentary sequence is thought to indicate the distance of the deposition site from the wildfire activity. Due to its hardy nature, charcoal is capable of being transported for large distance by water and air before final deposition; however, the smaller the charcoal particles, the further they are likely to be transported before deposition(Long et al., 1998; Tinner et al., 1998; Carcaillet et al., 2001). As discussed previously in **Section 7.5.3.**, the presence of coarse charcoal particles (greater than 125 µm in size) are thought to indicate local wildfire activity, and the presence of fine charcoal particles (less than 125 µm in size) are thought to indicate regional wildfire activity. There appear to be few studies detailing the transport of PAHs from their origin to the site of final deposition. PAHs can be present in both a gaseous and a solid form, adsorbed onto the surface of other particulate matter, it is possible that they can be transported for large distances before final deposition (Abdel-Shafy and Mansour, 2016). Considering this, it is most likely that the Kaszewy-1 pyrolytic PAH concentration record also reflects a mostly regional signal, rather than local, similar to the fossil charcoal records.

In the Kaszewy-1 samples, fine fossil charcoal is much more abundant than coarse fossil charcoal (**Figure 7.15**) suggesting a record of regional wildfire activity, rather than local activity. The peak in both coarse and fine fossil charcoal abundance in sample kk_10 at depth 1896.70 m suggests that there was an

increase in wildfire activity at the Kaszewy-1 site and in the region around it towards the end of the Rhaetian. The pyrolytic PAH data suggests a longer period of increased wildfire activity than the fossil charcoal datasets and possibly reflects a change in distance between the Kaszewy-1 site and the sites of wildfire activity. Increased concentrations of pyrolytic PAHs are detected in sample kk_10 along with an increased abundance of both coarse and fine fossil charcoal, lending further support to the idea that there was increased wildfire activity at and around the Kazewy-1 site towards the end of the Rhaetian. Both coarse and fine fossil charcoal abundance then decrease sharply in the next sample at 1885.67 m depth (kk_10b) but total pyrolytic PAH concentration remains high, suggesting that by this time, wildfire activity proximal to the Kaszewy-1 site had decreased, but wildfires were still burning in the region, away from the Kazewy-1 site. A second peak in total pyrolytic PAH concentration after the Triassic-Jurassic Boundary in sample kk_11b at depth 1857.30 m, but lack of increase in fossil charcoal abundance, suggests that there was a second level of increased regional wildfire activity, but that the area local to the Kaszewy-1 site did not experience significant levels of burning.

The fossil charcoal and geochemical data from the Kaszewy-1 samples shows evidence of three distinct levels of increased wildfire activity within the Polish Basin, which can be grouped into one period of increased wildfire activity below, and one level above the inferred Triassic-Jurassic Boundary. Changes in wildfire activity can be caused by many different factors and it is likely that multiple factors contributed to the periods of increased wildfire activity identified in the Kaszewy-1 study section (**Section 7.5.4.3.**; p. 221).

7.5.4.2. Increased Wildfire Activity Recorded Across the T-J Boundary in the Niekłan PIG-1 Core

The abundance of both coarse and fine fossil charcoal, as well as total pyrolytic PAH concentration is generally low in the Rhaetian part of the Niekłan PIG-1 core (**Figure 7.16**). However, sample NC6 at depth 160.00 m shows a high abundance of coarse fossil charcoal, suggesting a level of increased wildfire activity at the end of the Rhaetian prior to the inferred T-J Boundary. There is also a small increase in fine fossil charcoal abundance in the same sample, but it is still relatively low; no pyrolytic PAH data are available for this sample due to lack of

material. The large increase in coarse fossil charcoal abundance and smaller increase in fine fossil charcoal abundance suggests that this first level of intense wildfire activity was local to the Niekłan PIG-1 site. The presence of larger fragments of charcoal tend to reflect local wildfire activity, whereas smaller fragments of charcoal generally reflect regional wildfire activity (e.g. Carcaillet et al., 2001). This first level of increased wildfire activity correlates with a change in clay mineral assemblage from smectite-dominated to a kaolinite-illite-chlorite assemblage, likely reflecting a change from a warm climate with seasonal rainfall to a warm climate with year-round rainfall and increased humidity (Brański, 2014).

A second level of increased wildfire activity is indicated by a peak in fine fossil charcoal abundance in sample NC8 at depth 158.05 m immediately above the inferred T-J Boundary. Coarse fossil charcoal abundance is low in this sample, suggesting that this second level of increased wildfire activity was further from the Niekłan PIG-1 site than the first level immediately before the T-J Boundary. The total concentration of pyrolytic PAHs in sample NC8 shows a slight increase from the previous, Rhaetian-aged, samples, though it is still relatively low. The discrepancy between the fine fossil charcoal abundance and pyrolytic PAH concentration records perhaps reflects that a relatively low proportion of the pyrolytic PAHs generated during this second phase of intense wildfire activity are being deposited at the Niekłan PIG-1 site, while the majority are deposited elsewhere; perhaps the Niekłan PIG-1 site was downwind of the burning site. A peak in total pyrolytic PAH concentration (2327 ng/g sediment) in sample NC9 (depth: 155.50 m) suggests a third level of increased wildfire activity in the Early Hettangian. A relatively small increase in coarse fossil charcoal abundance is also observed. Fine fossil charcoal abundance is lower than in the previous sample, but still relatively high. The relatively high concentration of pyrolytic PAHs to fossil charcoal abundance suggests that this third level of intense wildfire activity was further from the Niekłan PIG-1 site than either of the previous two levels. The third level of increased wildfire activity correlates with the negative carbon-isotope excursion observed in the new $\delta^{13}C_{plant}$ record, and the negative trend in $\delta^{13}C_{wp}$ values.

After a decline in fossil charcoal abundance and total pyrolytic PAH concentration in sample NC12 (depth: 147.50 m), indicating a decline in wildfire activity on both
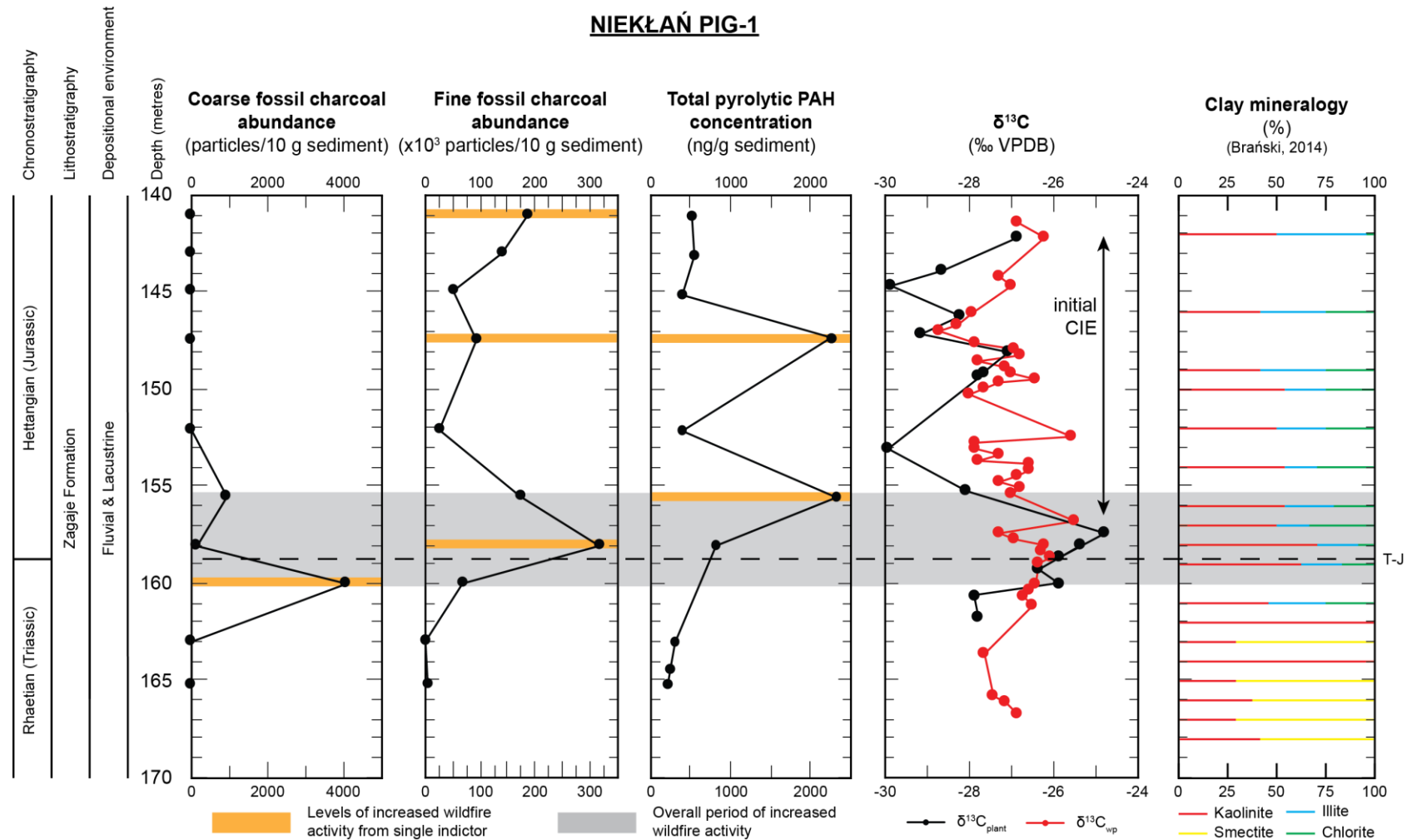
Figure 7.16 New fossil charcoal abundance and pyrolytic PAH concentration records from the Niekłań PIG-1 core correlated with new δ13C records and published clay mineralogy records (Brański, 2014). Levels of increased wildfire activity from a single indicator are highlighted in orange; overall periods of increased wildfire activity are highlighted in grey. T-J = Triassic-Jurassic Boundary; based on first occurrence of *C. thiergartii*.

a local and regional scale, a second peak in total pyrolytic PAH concentration is observed in sample NC13 (depth: 145.00 m). This second peak in total pyrolytic PAH concentration is comparable in magnitude to the first peak (2444 vs 2327 ng/g sediment). A relatively small increase in fine fossil charcoal abundance from the previous sample (NC9) is also observed in sample NC12, suggesting that the Niekłan PIG-1 site is closer to the site of burning than was the case for the third level of wildfire activity, though not necessarily as close as the second level. This fourth level of intense wildfire activity correlates with increased concentrations of pyrolytic PAHs at the nearby Sołtyków site (**Figure 7.17**; Marynowski and Simoneit, 2009). However, due to a lack of TOC data for the Niekłan PIG-1 samples, it is not possible to quantitatively compare the concentrations of pyrolytic PAHs at the Sołtyków and Niekłan PIG-1 sites.

Coarse and fine fossil charcoal abundance, as well as total pyrolytic PAH concentration, is generally low in the upper part of the study section, though a potential fifth level of increased wildfire activity is indicated by an increase in fine fossil charcoal abundance in the uppermost sample (NC15; depth: 141.10 m). Both coarse fossil charcoal abundance and total pyrolytic PAH concentration are, however, low in this sample. This potential fifth level of increased wildfire activity correlates with the end of the negative trends in the new $\delta^{13}C_{plant}$ and $\delta^{13}C_{wp}$ records.

The new fossil charcoal abundance and geochemical records generated from the Niekłan PIG-1 samples show evidence of at least five distinct levels of increased activity within the Polish Basin across the Triassic-Jurassic Boundary, the first three of which can be grouped into a larger period of increased wildfire activity. Similar to the new Kaszewy-1 wildfire activity proxy records, the Niekłan PIG-1 records show evidence of levels of intense wildfire activity both prior to, and immediately after, the T-J Boundary.

Up to three additional levels of intense wildfire activity are identified in the Hettangian section of the Niekłan PIG-1 core which are not identified in the Kaszewy-1 core, most likely due to the relatively low resolution of the new datasets. Changes in the level of wildfire activity are likely caused by a combination of factors, such as changing climatic conditions, and are discussed in detail in the following section (**Section 7.5.4.3.**; p. 221).
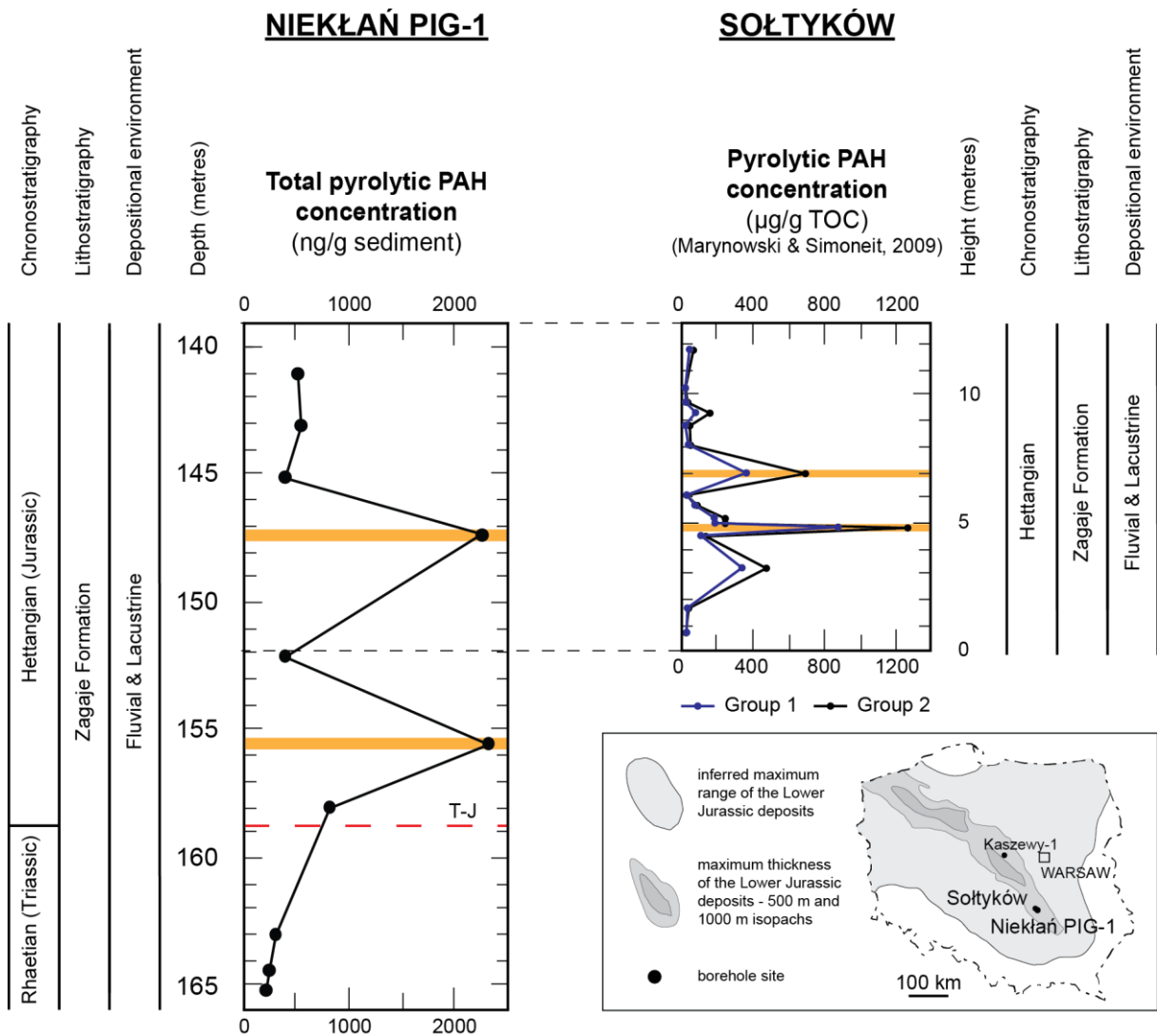
Figure 7.17 New pyrolytic PAH data from the Niekłan PIG-1 core correlated with pyrolytic PAH data from the nearby Sołtyków site (Marynowski and Simoneit, 2009). Stratigraphic correlation is made using sequence stratigraphy. Inset is a map of the Polish Basin and Lower Jurassic deposits showing the location of the Sołtyków outcrop in relation to the Kaszewy-1 and Niekłan PIG-1 borehole sites.

7.5.4.3. Comparison Between the Kaszewy-1 and Niekłań PIG-1 Cores

Comparison of the wildfire activity proxy records of the Kaszewy-1 and Niekłań PIG-1 cores is shown in **Figure 7.18**. The position of the T-J Boundary in the Kaszewy-1 core is based on sequence stratigraphy and located at a depth of ~1865 m; the first occurrence of the basal Jurassic palynomorph *C. thiergartii* is at a depth of ~1824 m (G. Pieńkowski, pers. comm.). The position of the T-J Boundary in the Niekłań PIG-1 core is based on the first occurrence of *C.*

thiergartii and is located at a depth of ~157 m (M. Hodbod, pers. comm.). The two cores are correlated using the position of the T-J Boundary in each.

Both cores show evidence of a double-peaked negative CIE towards the base of the study sections. The $\delta^{13}C_{wp}$ record from the Kaszewy-1 core shows a double-peaked negative CIE of ~4‰ magnitude between the depths of 1918.80 m and 1903.40 m, spanning a sediment thickness of ~15 m. Similarly, a double-peaked negative CIE of ~5‰ magnitude is observed in the Niekłań PIG-1 core $\delta^{13}C_{plant}$ record between the depths of 157.42 m and 142.10 m. A negative trend (~3.5%) in the Niekłań PIG-1 $\delta^{13}C_{wp}$ record is also observed between the depths of 158.00 m and 142.10 m. The Niekłań PIG-1 $\delta^{13}C_{plant}$ negative CIE and $\delta^{13}C_{wp}$ negative trend span sediments of ~15 m and ~16 m thickness. Despite similar magnitudes of the double-peaked negative CIEs observed in the Kaszewy-1 and Niekłań PIG-1 samples, the Kaszewy-1 negative CIE has been identified as the initial CIE, whereas the Niekłań PIG-1 CIE has been identified as the main CIE. This is due to the age of the sediments at these horizons: the Kaszewy-1 double-peaked negative CIE occurs in sediments of Rhaetian age, and the Niekłań PIG-1 doubled peaked negative CIE occurs in sediments of Hettangian age. The intial CIE is typically found in sediments of Rhaetian age.

Clay mineral assemblages in the two cores at similar depths also show a general agreement. A kaolinite-illite-chlorite assemblage is observed between the depths of ~1905 m and ~1895 m in the Kaszewy-1 core, and between the depths of ~160 m and ~140 m in the Niekłań PIG-1 core. A kaolinite-smectite assemblage is also observed between the depths of ~160 m and ~170 m in the Niekłań PIG-1 core, but is not observed in the Kaszewy-1 core. With the new proposed correlation, the two kaolinite-illite-chlorite assemblages occur at similar horizons in the two cores. There is a slight overlap between the Niekłań PIG-1 smectite-dominated assemblage and the bottom of the Kaszewy-1 illite/chlorite-dominated assemblage. This could be due to variations in sedimentation rate and/or weathering regime between the two sites.

The Kaszewy-1 and Niekłań PIG-1 wildfire activity proxy records show a major difference: periods of increased wildfire activity are identified in the Rhaetian-aged section of the Kazewy-1 core, whereas periods of increased wildfire activity are identified in the Hettangian-aged section of the Niekłań PIG-1 core. This
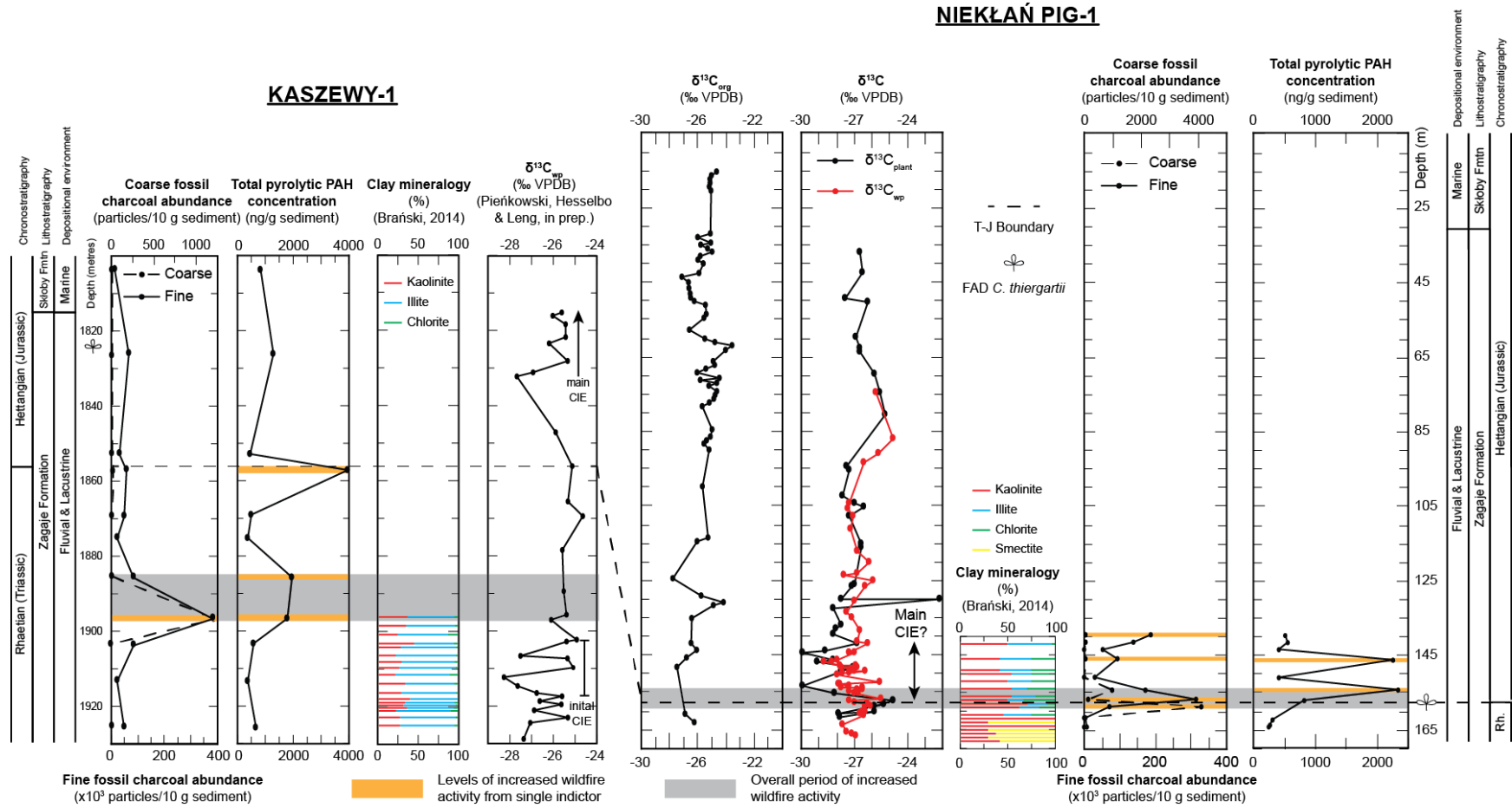
Figure 7.18 Correlation between the Kaszewy-1 and Niekłań PIG-1 cores. The T-J Boundary in the Kaszewy-1 core is based on carbon-isotope and sequence stratigraphy; the T-J Boundary in the Niekłań PIG-1 core is based on the FAD of *C.* thiergartii. Rh. = Rhaetian.

difference can likely be explained by the low resolution of the wildfire activity proxy records. This difference could perhaps also be explained by the different depositional environments at each site. Further study, increasing the resolution of these records, would improve our understanding of the T-J Boundary-related increased wildfire activity at these two Polish Basin sites.

A sequence of disturbed beds similar to the seismite identified at St Audrie's Bay (Mayall, 1983; Simms, 2003, 2007; Lindström et al., 2015) is observed between the depths of ~1910 m and ~1900 m in the Kaszewy-1 core. However, similarly-disturbed beds are not observed in the Niekłań PIG-1 core at all. It is possible that the cause of the disturbed bedding in the Kaszewy-1 core did not affect the Niekłań PIG-1 site, or that variations in sedimentation between the two sites resulted in this event not being recorded at the Niekłań PIG-1 site. It should also be noted that the lithology of the two study sections differ from each other; the Kaszewy-1 study section is dominated by sandstones whereas the Niekłań PIG-1 study section is dominated by mudstones. The lithologies of the two cores do not correlate very well, likely as a result of different depositional environments.

7.5.4.4. Causes of Changes in Wildfire Activity Level

In the fossil record, wildfire activity would have been caused by ignition of plant material by lightning strikes (Batchelder, 1967; Cope and Chaloner, 1980; Scott, 2000; Jones et al., 2002). Several factors can influence the intensity and frequency of wildfire activity such as atmospheric oxygen concentration, level of storm activity, availability of flammable material, and environmental conditions (see **Section 3.5.3.2.** for background).

A lack of published studies of the Kaszewy-1 and Niekłan PIG-1 cores does not allow for a detailed investigation into potential causes of the changing wildfire activity throughout the study sections, however they do provide some suggestions. A lack of palynology data from the cores makes it impossible to tell whether a change in vegetation was, in some way, responsible for the change in wildfire activity levels. However, palynology records from the contemporaneous Kamień Pomorski IG-1 core, located in the northwest Polish Basin, show evidence of a palynofloral turnover across the T-J Boundary, with a disappearance of xerophilous plants (Pienkowski et al., 2012), suggesting increased rainfall and humidity in the earliest Jurassic. Additional palaeobotanical

studies from Bornhølm, Denmark, suggest a ~3-4°C rise in temperatures across the T-J Boundary (McElwain et al., 1999; Belcher, Mander, et al., 2010).

In the fossil record, the most likely cause of increased wildfire activity is an increase in lightning strikes, as a result of increased storminess (Pyne et al., 1996). Clay mineralogy data available for the lower, Rhaetian-aged part of the Kaszewy-1 study section shows a kaolinite-illite-chlorite assemblage dominates (**Figure 7.15**); this kaolinite-illite-chlorite assemblage is associated with warm and humid conditions, with year-round rainfall (Brański, 2014). Conversely, clay mineralogy records of the Niekłan PIG-1 core show a smectite-dominated assemblage in the Rhaetian-aged part of the core, prior to the T-J Boundary (**Figure 7.16**), suggesting a warm environment with seasonal rainfall (Brański, 2014). A shift from this smectite-dominated assemblage to a kaolinite-illite-chlorite assemblage occurs prior to the inferred T-J Boundary, along with a shift to more negative $\delta^{13}C_{plant}$ and $\delta^{13}C_{wp}$ values (**Figure 7.16**).

Unpublished $\delta^{13}C_{org}$ data from the Kaszewy-1 core (Pieńkowski *et al.*, in prep.) shows two significant negative carbon-isotope excursions in the sediments below the first period of increased wildfire activity, thought to correlate with the 'initial' carbon-isotope excursion first identified at St Audrie's Bay, UK (**Figure 7.16**; Hesselbo et al., 2002); relatively positive $\delta^{13}C_{org}$ values correlate with the two periods of increased wildfire activity. The periods of intense wildfire activity recorded in the Niekłan PIG-1 are, however, associated with lighter $\delta^{13}C$ values. It has been suggested that an increase in carbon burial at the T-J Boundary limited the duration of the initial negative CIE, resulting in the relatively short, sharp negative CIE observed in many $\delta^{13}C$ records (Ruhl et al., 2011). An increase in carbon burial would have removed carbon from the atmosphere, and eventually increased the concentration of atmospheric oxygen and, as a result, the probability of wildfire ignition and spread. This could explain the pattern in wildfire activity observed in the Kaszewy-1 core. The periods of intense wildfire activity recorded in the Niekłan PIG-1 core are associated with relatively light $\delta^{13}C$ values, suggesting that while there was an increase in atmospheric carbon, oxygen levels remained high enough to sustain wildfire activity.

There are several discrepancies between the Kaszewy-1 and Niekłan PIG-1 palaeoenvironmental records, hindering interpretation of the wildfire activity

records. It is posible that these are caused by differences in depositional environments at the two sites, and/or the low resolution-nature of the studies. The current working hypothesis is that an increase in temperature across the T-J Boundary, most likely caused by an increase in atmospheric carbon dioxide, coupled with an increase in rainfall and humidity, resulted in increased storm activity. Elevated levels of storm activity likely increased rates of wildfire ignition. A change in vegetation recorded across the T-J Boundary could have provided a better, larger, fuel source, aiding the spread of wildfire. While there is evidence of increased atmospheric carbon dioxide across the T-J Boundary, atmospheric oxygen concentrations remained sufficiently high to support widespread wildfire activity. Further high-resolution studies of the Kaszewy-1 and Niekłan PIG-1 cores are required to test the robustness of this hypothesis, but whatever the cause, new wildfire activity proxy records from the central Polish Basin indicated multiple periods of intense wildfire activity around the T-J Boundary.

7.5.5. Environmental Changes in the Central Polish Basin in a Regional Context

Wildfire activity proxy data from across the Triassic-Jurassic Boundary are available from sites in eastern Greenland and the Danish Basin (see **Figure 7.19** for a palaeogeographic map of locations). At Astartekløft, Greenland, Belcher et al. (2010) discovered a five-fold increase in the number of charcoal particles >150 µm immediately above the T-J Boundary, and at sites in the Danish Basin, Petersen and Lindström (2012) documented that the average inertinite content of palynological samples increases above the T-J Boundary, and remains elevated for most of the Hettangian, before dropping again into the Sinemurian. It is worth nothing that Danish Basin is an extremely low resolution study and deals with relative values, rather than absolute values.

A period of increased wildfire activity immediately above the T-J Boundary is inferred at Astartekløft, Greenland (Belcher, Mander, et al., 2010), which appears to correlate with periods of intense wildfire activity at the Niekłan PIG-1 site; a period of intense wildfire activity at the Kaszewy-1 site instead occurs below the T-J Boundary (**Figure 7.20**). Increased inertinite content is also observed in samples from immediately above the T-J Boundary in Danish Basin sediments, but the inertinite record consists of a total of five data points spanning the
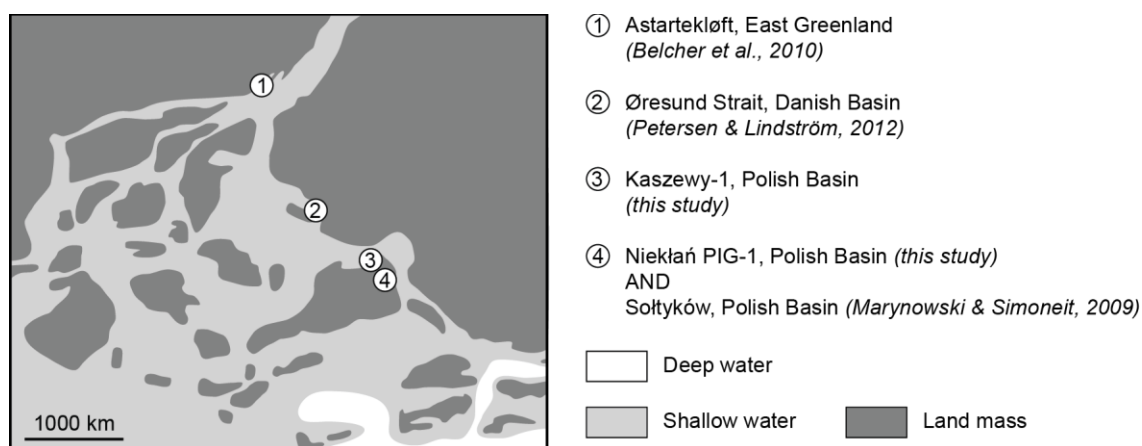
Figure 7.19 Palaeogeographic map of the NW Tethyan realm during the Late Triassic–Early Jurassic (~200 Ma) with localities of wildfire activity proxy studies labelled. Redrawn from (Blakey, 2018a).

Rhaetian – Sinemurian (Petersen and Lindström, 2012); this extremely low resolution does not allow for confident correlation with the new Polish Basin records, or the published record from Greenland. This period of increased wildfire activity immediately after the T-J Boundary is marked by significant increases in fossil charcoal abundance at both the Astartekløft and Polish Basin sites, as well as increasing concentrations of pyrolytic PAHs at the Polish Basin sites.

Additional levels of intense wildfire activity after the T-J Boundary are clearly recorded in the Niekłan PIG-1 fine fossil charcoal abundance and pyrolytic PAH concentration records, as well as the Kaszewy-1 geochemical record, but not in the Astartekløft record (**Figure 7.20**). The low-resolution Danish Basin wildfire record shows elevated inertinite content in three samples spanning the Hettangian stage, which the authors interpret to reflect increased wildfire levels throughout the Hettangian (Petersen and Lindström, 2012). However, the extremely low resolution of this study makes it difficult to correlate any of the later periods of wildfire activity identified in the Hettangian sections of the Kaszewy-1 and Niekłan PIG-1 cores with the Danish Basin record. Perhaps the relatively low resolution of the Astartekløft records have resulted in these additional periods of intense wildfire activity being missed, or perhaps they were not recorded there at all.
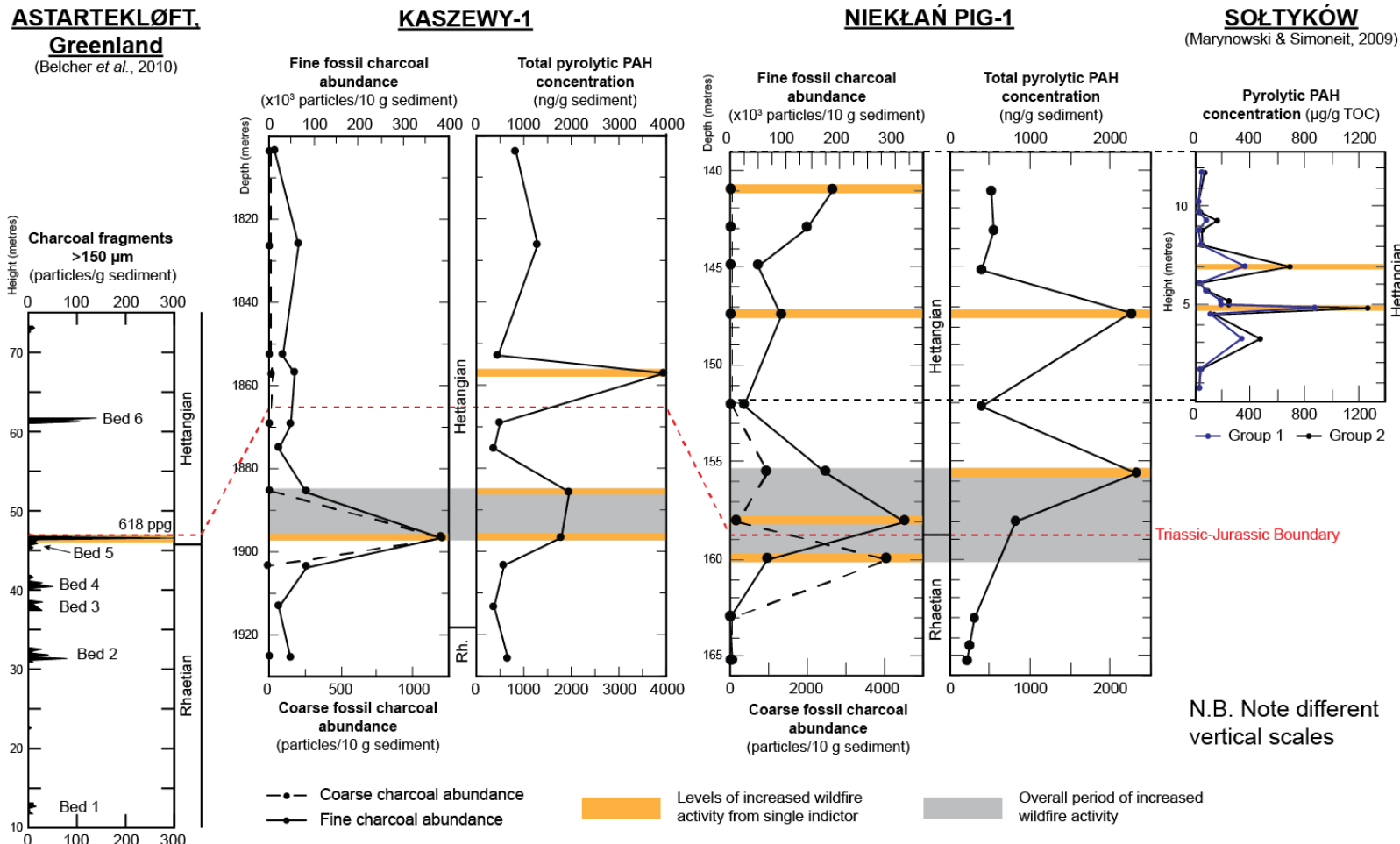
Figure 7.20 Wildfire activity proxy records from Astartekløft, East Greenland (Belcher et al., 2010), the Kaszewy-1 and Niekłań PIG-1 cores, Polish Basin (this study), and Sołtyków, Polish Basin (Marynowski and Simoneit, 2009). Note different vertical scales. Correlation between Niekłań PIG-1 and Sołtyków is based on sequence stratigraphy. The T-J Boundary is defined by: FO of *C. thiergartii* and C-isotope stratigraphy at Astartekløft; carbon-isotope stratigraphy in the Kaszewy-1 core; FO of *C. thiergartii* in the Niekłań PIG-1 core.

The post-T-J Boundary levels of intense wildfire activity recorded in the Niekłan PIG-1 core does not show increased abundances of coarse fossil charcoal, suggesting that the wildfire activity was not local to the Polish Basin sites at that time. A level of increased wildfire activity above the T-J Boundary at Astartekløft is inferred from the elevated level of fossil charcoal abundance in Bed 6 (**Figure 7.20**). It is possible that this elevated fossil charcoal abundance in Bed 6 at Astartekløft is related to the post-T-J Boundary levels of intense wildfire activity inferred at the Polish Basin sites. The lack of coarse fossil charcoal at the Polish Basin sites could be explained by the intense wildfire activity not extending extend far enough for the deposition of coarse charcoal in the Polish Basin, or the wildfire activity not being recorded at the Polish Basin sites at all..

Comparison of the new wildfire activity proxy records from the Kaszewy-1 and Niekłan PIG-1 cores with published records from Greenland and Denmark suggest that there were widespread periods of intense wildfire activity across the NW Tethyan realm during the latest Triassic and earliest Jurassic. However, the resolution of existing wildfire activity proxy records across the Triassic-Jurassic Boundary needs to be increased and new records from other sites need to be generated in order to produce a more confident correlation between sites.

7.6. Conclusions & Future Work

The following conclusions can be drawn from this study:

- Fossil charcoal abundance and pyrolytic PAH concentration datasets record a distinct period of intense wildfire activity around the Triassic-Jurassic Boundary in the region of the Kaszewy-1 and Niekłań PIG-1 sites.
- The new fossil charcoal abundance and pyrolytic PAH concentration datasets complement other published palaeo-wildfire studies, confirming widespread intense wildfire activity at times around the Triassic-Jurassic Boundary.
- New $\delta^{13}C$ records generated from macrofossil plant material and bulk woody phytoclast samples show evidence of the Triassic-Jurassic Boundary main negative carbon-isotope excursion.

- C_{org}/N_{total} ratios of the macrofossil plant material and bulk woody phytoclast samples confirm the origin of the organic matter.

There is a wide scope for further work based on that discussed in this chapter. Additional work is required to better constrain the wildfire activity history of the Kaszewy-1 and Niekłan PIG-1 sites, and to more confidently correlate the new Polish Basin records with existing records. Palynological studies will potentially reveal any vegetation changes in the Rhaetian and Hettangian sections of the Kaszewy-1 and Niekłań PIG-1 cores which, in turn, will help to further pinpoint the cause of the wildfire activity changes identified in this study. Increasing the resolution of the fossil charcoal and pyrolytic PAH records will provide a more informative record of wildfire activity in the Polish Basin across the Triassic-Jurassic Boundary, and would also help with correlation to other sites.

Additional carbon-isotope stratigraphy work would also be beneficial to this study. Reprocessing the bulk rock samples from the Niekłan PIG-1 core using a different method to ensure all inorganic carbon is removed prior to carbon-isotope analyses would provide a clearer $\delta^{13}C_{org}$ record of the Niekłan PIG-1 core, and help to identify the initial and main negative carbon isotope-excursions associated with the Triassic-Jurassic Boundary. Increasing the resolution of the new $\delta^{13}C_{plant}$ and $\delta^{13}C_{wp}$ records, as well as analysing samples from the upper part of the core, would also help to better constrain the nature of the observed negative CIEs and trends.

CHAPTER 8 APPLYING NOVEL ORGANIC GEOCHEMICAL PROXIES TO TRIASSIC AND JURASSIC SEDIMENTS OF THE POLISH AND BRISTOL CHANNEL BASINS

8.1 Introduction

There are various methods for estimating palaeotemperatures in the Mesozoic, though these are often focused on seawater temperatures (e.g. $\delta^{18}O$ values and Mg/Ca ratios of marine invertebrate calcite), or based on fossil leaf characteristics (e.g. leaf margin analysis). Compound-specific $\delta^{13}C$ records from fossil plant matter can also be used to estimate palaeotemperatures, but, along with records based on fossil leaf characteristics, rely on suitable sample material being available, and often require supporting evidence from additional sources.

The BIT index soil organic matter proxy (**Equation 4.6**) and MBT'-CBT palaeotemperature proxy (**Equations 4.7 – 4.10**) are frequently used to investigate palaeoenvironments in the Cenozoic (66 Ma – present). These two proxies involve analysing sediments for the presence of different types of glycerol dialkyl glycerol tetraethers (GDGTs), a type of lipid found synthesised by archaea and bacteria. GDGTs are ubiquitous in modern sediments and commonly found in sediments of Cenozoic age (Schouten et al., 2013); they have also been detected in sediments from the Early Jurassic (Jenkyns et al., 2012; Robinson et al., 2017). In this study, sediments of Early Jurassic and Late Triassic age are analysed from the Bristol Channel and Polish Basins in an attempt to evaluate the efficacy of these two proxies in Mesozoic sediments.

8.2. Aims

This study attempts to investigate geochemical palaeoenvironmental reconstructions at sites in the Central Polish Basin and in the southwest UK

during two key intervals of the Late Triassic and Early Jurassic. With the new data collected as part of this study, the following questions are answered:

- Can both branched and isoprenoidal GDGTs be detected in quantifiable amounts in sediment samples from Late Triassic-Early Jurassic-aged strata?

- If present, can these GDGTs be used to calculate BIT indices, and thus produce a record of terrestrial organic matter input to three selected sites in Europe?

- Are all the GDGTs required to calculate MBT' and CBT indices preserved in these strata of Rhaetian-Toarcian age, and if so is it possible to produce records of mean annual air temperature and soil pH changes?

8.3. Background

8.3.1. Glycerol Dialkyl Glycerol Tetraether Lipids

Glycerol dialkyl glycerol tetraether lipids (GDGTs) are a group of organic compounds that are integral cell membrane components for certain groups of archaea and bacteria. GDGTs are found in the majority of modern day ambient environments from terrestrial soils, peats and lakes, to the deep-sea, and in certain extreme environments such as cold seeps and hot springs (e.g. Schouten et al., 2013, and references therein) and can be classified into two main groups: isoprenoid and branched.

Isoprenoid GDGTs were first reported by De Rosa and Gambacorta (1988) and later by Koga et al. (1993) who reported that isoprenoid GDGTs comprised the majority of archaeal membranes. It was suggested by these authors that the isoprenoid GDGT compounds provide archaea with increased robustness to allow the organisms to cope with the extreme environments which they are often found in. More recent research, however, has found that isoprenoid GDGTs synthesised by archaea are also present in non-extreme lacustrine and marine environments (MacGregor et al., 1997; Vetriania et al., 1998), as well as soils (Herschberger et al., 1996).

GDGT Ia   *m/z 1022*

GDGT Ib   *m/z 1020*

GDGT Ic   *m/z 1018*

GDGT IIa   *m/z 1036*

GDGT IIb   *m/z 1034*

GDGT IIc   *m/z 1032*

GDGT IIIa   *m/z 1050*

GDGT IIIb   *m/z 1048*

GDGT IIIc   *m/z 1046*

Crenarchaeol   *m/z 1292*
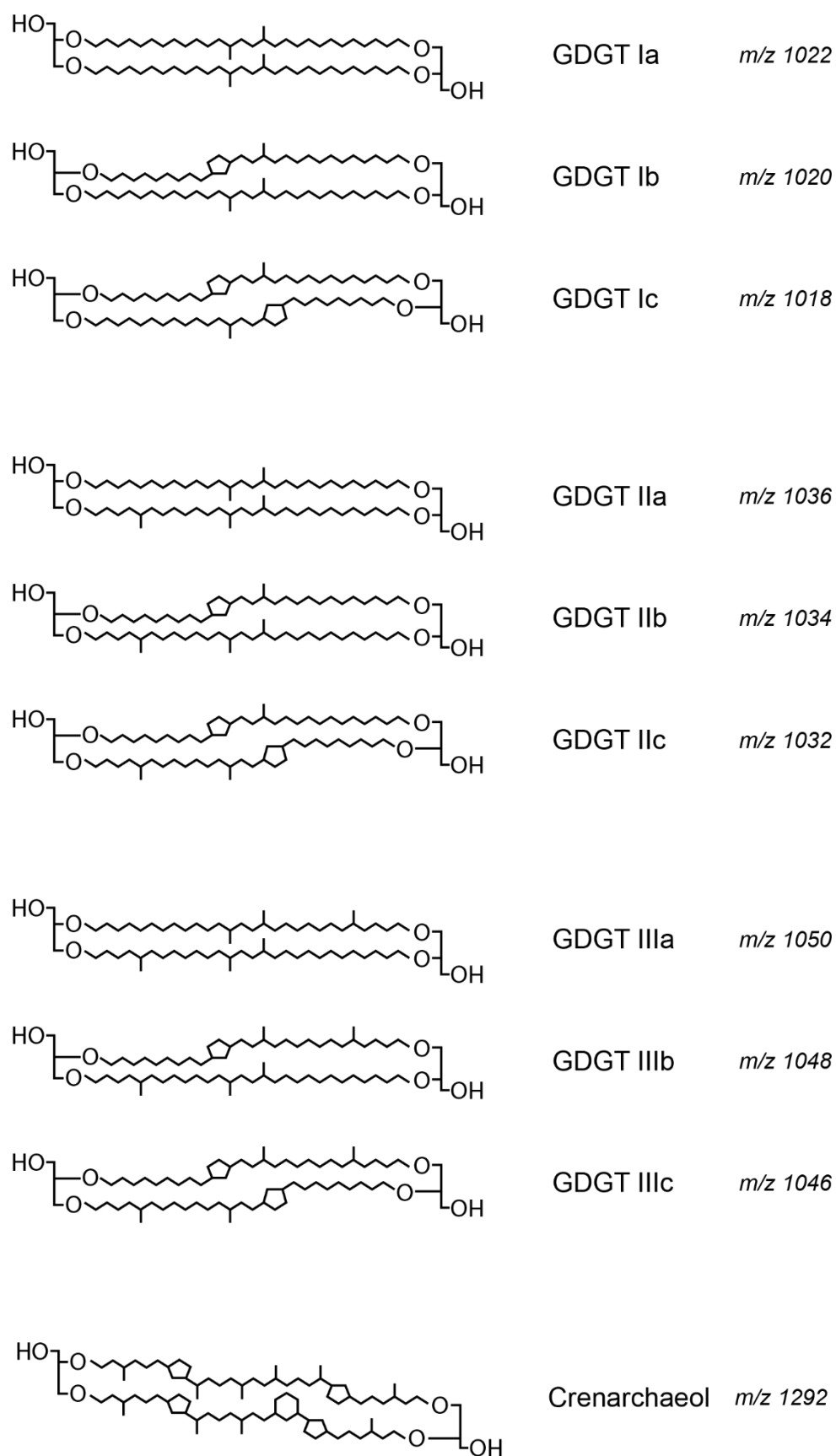
Figure 8.1 Structures and molecular weights (*m/z*) of key GDGTs discussed in this thesis. GDGTs I-III are branched GDGTs; crenarchaeol is an isoprenoid GDGT.

Branched GDGTs, however, were not first reported until much later from peats, as well as lacustrine and coastal marine sediments (Sinninghe Damsté et al. 2000).

The precise origin of branched GDGTs is still unknown, as the molecules exhibit both archaeal and bacterial properties (Schouten et al., 2013), though it is generally thought that branched GDGTs are likely produced by bacterial organisms (e.g. Weijers et al., 2006; Weijers, Schouten, Sluijs, et al., 2007; Weijers et al., 2009; Peterse et al., 2010) with acidobacteria being the most likely source (Schouten et al., 2013). Although they are thought to be predominantly produced in peats and soils, branched GDGTs have also been found to be produced in lacustrine environments (e.g. Tierney and Russell, 2009; Loomis et al., 2011) and marine sediments (Peterse et al., 2009).

A number of key isoprenoid and branched GDGTs (**Figure 8.1**) have been used to develop environmental proxies, reconstructing terrestrial soil input to the marine environment, as well as mean annual air temperature and soil pH. These proxies are discussed in detail in the following sections.

8.3.2. The BIT Index: A Proxy for Terrestrial Organic Matter Input to Deposition Sites

The branched and isoprenoid tetraether (BIT) index was developed by Hopmans et al. (2004) as a proxy for estimating the input of terrestrial organic matter into Holocene marine sediments. Sediment samples were collected from a range of locations, representing a range of depositional environments, including terrestrial peat and soil sites, as well as lacustrine, coastal marine, and open marine sediments, and investigated for GDGT content.

Branched GDGTs (I-III) were identified in all samples from both terrestrial and marine environments, however, crenarchaeol was found to only be present in marine sediment samples. The authors concluded that branched GDGTs are derived from organisms present in terrestrial soils and peats, and that crenarchaeol is usually derived from organisms present in seawater. From this, the authors concluded that branched GDGTs can be used as tracers for terrestrial organic matter and developed the BIT Index based on the relative abundance of branched GDGTs I, II and III with respect to crenarchaeol. The BIT Index is

defined by **Equation 4.6**, with the symbols referring to the GDGTs indicated in **Figure 8.1**.

The BIT Index indicates that as terrestrial soil input to a site increases, so does the measured BIT value of the sediments deposited there, and *vice versa*. Hopmans et al. (2004) tested the newly-developed BIT Index by applying it to sediment samples collected from multiple sites around the world, as well as calculated BIT values for a range of other Holocene-aged terrestrial and marine sediments. The authors found that the BIT values correlated well with the sample site locations and concluded that it can be successfully used as a proxy for soil organic matter input into sediments. Studies have found that soils generally have BIT values >0.9 (e.g. Weijers et al., 2006; Sinninghe Damsté et al., 2009; Loomis et al., 2011), lacustrine sediments have variable BIT Index values >0.5 depending on the type and setting of the lake (e.g. Blaga et al., 2009; Powers et al., 2010; Tierney et al., 2010), and sediments from open marine settings generally have BIT Index values <0.15 (e.g. Schouten et al., 2013). A subsequent study by Huguet et al. (2007) found that the BIT Index more accurately reflected only the soil input to a site, not the combined input of all terrestrial organic matter (i.e. soils and plant matter), revising interpretation of BIT values. Schouten et al. (2013) suggest that BIT values should only be interpreted in qualitative terms, unless accompanied by absolute concentrations of GDGTs, since the BIT Index is a relative measurement rather than an absolute one.

Subsequent studies have found evidence that isoprenoid GDGTs, such as crenarchaeol, can be produced *in situ* in terrestrial environments. A study of sediment and peat samples from a range of locations by Weijers et al. (2006) found that crenarchaeol was present in all samples, regardless of the depositional environment. The authors suggested that the transport of terrestrially-derived crenarchaeol to marine sites could influence the BIT values of marine sediments. However, the relatively low abundance of crenarchaeol in terrestrial sediments in comparison to that of branched GDGTs suggest that this influence would be minimal.Similarly, branched GDGTs may be produced *in situ* in some marine settings where terrestrial OM input is low (Peterse et al., 2009).

The BIT Index was originally developed using Holocene-aged surface sediment samples and is best used on immature sediments (Hopmans et al., 2004), though it should be noted that reproducibility between laboratories is often poor. As a

result, it is commonly used on relatively young sediments (e.g. Kim et al., 2006; Huguet et al., 2007; French et al., 2015; Zell et al., 2015; Cao et al., 2017) and is more rarely used on older sediments. However, branched GDGTs and crenarchaeol have both been detected in sediments of Cretaceous age (Kuypers et al., 2001; Hopmans et al., 2004), suggesting that the BIT Index can be used on older (e.g. Mesozoic) immature sediments. Jenkyns et al. (2012) successfully detected branched GDGTs in and calculated BIT indices from Middle Jurassic-Early Cretaceous-age marine sediments from the Falkland Plateau as part of a study reconstructing sea-surface temperatures. Robinson et al. (2017) attempted to analyse BIT Index values of sediments of Sinemurian and Pliensbachian age (~199 –183 Ma), though the amount of branched GDGTs in these Early Jurassic sediments are either below the limit of detection or not abundant enough to be quantified. The effect of diagenesis on BIT values is not well-known and therefore values of ancient sediments should be interpreted with caution (Schouten et al., 2013). Further work is required to investigate the impact of diagenesis on BIT values.

8.3.3. The MBT'-CBT Palaeothermometer & Soil pH Proxy

The distribution of branched GDGTs in sediments is related to both mean annual air temperature (MAAT) and soil pH (Weijers, Schouten, van den Donker, et al., 2007). Soil samples were collected from a number of localities around the world and analysed for their branched GDGT content.

In their study, Weijers et al. (2007) found that some branched GDGTs contained extra methyl groups (containing one carbon atom bonded to three hydrogen atoms) attached to the main branched structure, while others contained additional cyclopentyl groups (containing five carbon atoms bonded to nine hydrogen atoms). The authors developed the methylation Index of branched tetraethers (MBT; **Equation 8.1**, with the symbols referring to the GDGTs indicated in **Figure 8.1**) and the cyclisation Index of branched tetraethers (CBT; **Equation 4.8**, with the symbols referring to the GDGTs indicated in **Figure 8.1**).

$$(8.1) \quad MBT = \frac{Ia + Ib + Ic}{Ia + Ib + Ic + IIa + IIb + IIc + IIIa + IIIb + IIIc}$$

Weijers et al. (2007) found that the MBT and CBT indices were related to mean annual air temperature and soil pH, and therefore can be used to reconstruct environmental conditions. The authors determined that the MBT and CBT indices

are related to MAAT and soil pH using the following equations (**8.2** and **8.3**; MAAT is in °C):

(8.2) $CBT = 3.33 - (0.38 \times pH)$

(8.3) $MBT = 0.122 + (0.187 \times CBT) + (0.020 \times MAAT)$

The MBT'-CBT proxy is a revision by Peterse et al. (2012) of the original MBT-CBT proxy by Weijers et al. (2007) and is more frequently used for reconstructing MAAT and soil pH. Peterse et al. (2012) revised these original indices using additional data from soil studies to produce the updated MBT' Index (**Equation 4.7**, with the symbols referring to the GDGTs indicated in **Figure 8.1**). The authors also revised the mathematical relationship between the MBT' Index and MAAT (**Equation 4.9**). Peterse et al. (2012) did not revise the original CBT Index of Weijers et al. (2007), but did revise the mathematical relationship between the CBT Index and soil pH (**Equation 4.10**).

Similar to the BIT Index, the MBT(')-CBT proxy was developed using Holocene-aged sediments and consequently, the majority of published studies consist of its use on Cenozoic material (Peterse et al., 2009; Niemann et al., 2012; Sinninghe Damsté et al., 2012; Anderson et al., 2014; Hanna et al., 2016). It should be noted that for geologically young lake sediments, there appears to be a poor correlation between MBT-CBT/MBT'-CBT-based reconstructions and recorded air temperatures and nearby soil pH (Blaga et al., 2010; Zink et al., 2010; Tierney et al., 2010). The authors of these studies suggest that specific calibrations are required for each individual lake studied in order to obtain more accurate MAAT and soil pH reconstructions. The use of the MBT(')-CBT proxy on ancient sample material has provided mixed results. Analysis of ancient terrestrial material shows both poor MAAT and pH reconstructions (e.g. Weijers et al., 2011; Yang et al., 2011), and good correlations (e.g. Ballantyne et al., 2018; Hren et al., 2018; Zhou et al., 2011), but further work is needed to evaluate the efficacy of this proxy in relation to geological materials. Schouten et al. (2013) have carried out maturation studies in order to replicate ancient sediments and found that MBT values generally increased and CBT values generally decreased as sample material was artificially matured.

Studies of older geological material are scarce and include studies of Eocene-age (56 – 33.9 Ma) samples (Pross et al., 2012) and one focusing on the

Palaeocene-Eocene Thermal Maximum (~55.5 Ma; Weijers, Schouten, Sluijs, et al., 2007). A study by Kemp et al. (2014) where the authors apply the MBT-CBT proxy to latest Cretaceous-Palaeogene material appears to be the only published study involving material older than the Palaeogene. The use of the MBT-CBT or MBT'-CBT proxies on Mesozoic, or older, samples appears to be extremely limited.

8.4. Materials & Methods

8.4.1. Materials

Bulk rock samples were collected from sites in the Polish and Bristol Channel Basins for organic geochemical analyses (17 and 2, respectively). Samples collected consisted of mudstones and sandstones, and range in age from Late Triassic (Rhaetian) to Early Jurassic (Toarcian).

One core and one outcrop from the Polish Basin were sampled for BIT Index and MBT'-CBT analysis (see **Figure 8.2** for locations). Fifteen samples were collected from Rhaetian and Early Jurassic sections of the Kasewy-1 core, consisting of mudstones and sandstones that are interpreted to have been deposited in a range of terrestrial and shallow marine environments. The samples from the Kaszewy-1 core were chosen based on their interpreted depositional environments and limited available Rock Eval data (Pieńkowski, pers. comm.). Samples were taken from horizons with T_{max} values of <454°C where Rock-Eval data are available. The sample set analysed in this study reflects a range of inferred depositional environments, from terrestrial to shallow-marine.

Three mudstone samples were collected from the Toarcian-age Kozłowice outcrop in a working clay pit; these samples are thought to have been deposited in a shallow-marine environment and are poorly-consolidated, relatively immature sediments (Pieńkowski, pers. comm.). The immature nature of the Kozłowice sediments was the basis for their inclusion in this study, however these sediments are highly susceptible to contamination and therefore only a small number of samples were taken and analysed.

Two mudstone samples from St Audrie's Bay, SW United Kingdom, were also collected for analysis (see **Figure 8.2** for location). These samples are of

Figure 8.2 Map of present day NW Europe showing locations of the St Audrie's Bay section, United Kingdom, the Kozłowice section, Poland, and the Kaszewy-1 borehole, Poland.

Hettangian age and are thought to have been deposited in a deep marine environment in the Bristol Channel Basin. The least-consolidated St Audrie's Bay samples (2) were chosen for comparison to the Polish Basin samples.

8.4.2. Methods

A detailed discussion of the methods used in this study is provided in **Section 4.5.** (p. 110).

Samples were cleaned and crushed to a fine homogenous powder by the author at Camborne School of Mines, University of Exeter; subsequent preparation and analysis was carried out by R. A dos Santos and C. Vane at the Organic Geochemistry Facility, British Geological Survey. The total lipid extract (TLE) was taken from the powdered samples using a 9:1 mixture of dichloromethane and methanol. Column separation was then used to separate the TLE into an apolar and a polar fraction. The polar fraction was then filtered prior to high-performance liquid chromatography-mass spectrometry; GDGTs were identified and quantified using the resulting chromatograms. The BIT, MBT' and CBT indices were

calculated using **Equations 4.6, 4.7 & 4.8.** Mean annual air temperature and soil pH reconstructions were calculated using **Equations 4.9** and **4.10**.

8.5. Results

8.5.1. Pilot Study

The results of the pilot study are show in **Table 8.1**. Sufficient GDGTs were detected in 5 of 8 samples in order to calculate BIT indices. Sufficient GDGTs for MBT' and CBT indices calculations were only detected in one sample; reliable estimates of mean annual air temperature and pH were calculated for this one sample. MAAT estimates of the remaining 6 samples were also calculated but are not reliable due to lacking sufficient concentrations of the branched GDGTs required for the calculations.

The samples from St Audrie's Bay showed peaks below the limit of detection and as such, neither the BIT, MBT' or CBT indices were calculated. Sample KWE_2014_3 (-11.0 m in height) from the Kozłowice outcrop also showed peaks below the limit of detection.

The remaining 5 samples shows peaks above the limit of detection and have BIT indices ranging from 0.6 to 0.9. The Hettangian-age Kaszewy-1 sample has a BIT Index of 0.6, whereas the Toarcian-age Kaszewy-1 samples have values of 0.7 and 0.9. The Toarcian-aged Koslowice outcrop samples show similar BIT indices of 0.8 and 0.7.

Of the 5 samples which showed peaks above the limit of detection, only 1 sample (KWE_2014_1) presented all the branched GDGTs required to perform MBT' and CBT calculations. Sample KWE_2014_1 from the Kozłowice outcrop has a BIT Index of 0.7 and MBT' and CBT values of 0.17 and -0.02, respectively. The MBT' indices were calculated for the remaining 5 samples but are not reliable due to the lack of all branched GDGTs necessary for these calculations (see values in red in **Table 8.1**). The CBT indices were not calculated in these remaining 4 samples.

An estimate for mean annual air temperature and pH was calculated for sample KWE_2014_1. The mean annual air temperature is estimated to be 3.4°C and the soil pH is estimated to be 7.9. Mean annual air temperatures were also calculated for the other 6 samples where some branched GDGTs were detected.

Age	Locality	Sample Number	Depth in core (m)/Height in section (m)	BIT Index	MBT'	MAAT (°C)	CBT	Soil pH
Toarcian	Kozłowice outcrop	KWE_2014_1	+3.5	**0.7**	**0.17**	**3.36**	**-0.02**	**7.9**
Toarcian	Kozłowice outcrop	KWE_2014_3	-11.0					
Toarcian	Kozłowice outcrop	KWE_2014_5	-22.5	**0.8**	0.35	7.49	-	-
Toarcian	Kaszewy-1 core	KK-39	1250.75	**0.6**	0.25	5.1	-	-
Toarcian	Kaszewy-1 core	KK-37	1275.85	**0.9**	0.28	5.76	-	-
Hettangian	Kaszewy-1 core	KK-13	1822.7	**0.7**	0.32	6.7	-	-
Hettangian	St Audrie's Bay outcrop	StAB 127	23.3					
Hettangian	St Audrie's Bay outcrop	StAB 80	15.8					

Table 8.1 Results from MAAT and pH pilot study. Samples are listed in order from youngest to oldest. Results in red indicate samples where the full suite of branched GDGTs required for the calculation of mean annual air temperature were not detected. Greyed out boxes indicate samples where the levels of all required branched GDGTs were below the limit of detection. **Equations 4.6 – 4.10** were used to calculate BIT, MBT' and CBT indices, and MAAT and soil pH.

1 These MAAT estimates range from 5.0°C to 7.5°C but are not thought to be

2 reliable due to the lack of all branched GDGTs required for the calculation.

3 **8.5.2. Kaszewy-1 core study**

4 A further 12 samples from the Kaszewy-1 core were analysed in a second study.

5 The average concentration (ng/g TOC) of each GDGT was used to calculate BIT,

6 MBT' and CBT indices, mean annual air temperature and soil pH estimates

7 (**Table 8.2**)

8 8.5.2.1. Rhaetian-Hettangian Section

9 BIT indices of sediments from the Rhaetian section of the Kaszewy-1 core range

10 from 0.53 to 0.70; the two sediment samples from the Hettangian section of the

11 core have BIT indices of 0.44 and 0.69. MBT' and CBT indices were calculated

12 for the samples from the T-J Boundary section of the Kaszewy-1 core, but are not

13 reliable due to lacking all of the necessary measurements of branched GDGTs

14 required, consequently, MAAT and soil pH estimates are also not reliable. The

15 MBT' and CBT indices, as well as MAAT and soil pH estimates, are not discussed

16 further in this thesis.

17 The concentration of the sum of all branched GDGTs ([sum brGDGT]) in the T-J

18 Boundary samples varies from 0.20 ng/g TOC to 0.39 ng/g TOC. The

19 concentration of crenarchaeol ([cren]) in each sample is lower than [sum

20 brGDGT], and varies between samples from 0.04 ng/g TOC to 0.23 ng/g TOC.

21 The concentration of crenarchaeol is lower than [sum brGDGT] in each sample.

22 8.5.2.2. Pliensbachian-Toarcian Section

23 The two sediment samples from the Pliensbachian section of the Kaszewy-1 core

24 have BIT indices of 0.40 and 0.53; the BIT indices of samples from the Toarcian

25 section of the ranges from 0.44 to 0.86. All of the branched GDGDTs required to

26 calculate the MBT' Index accurately were detected in sample kk_41a at 1238.90

27 m depth; it has an MBT' Index of 0.53, which provides a MAAT estimate of

28 14.58°C. All other samples from this section of the Kaszewy-1 core were missing

29 at least one of the branched GDGTs required for accurate MBT'-CBT Index

30 calculations.

31 In one of the samples from the Pliensbachian-Toarcian section of the Kaszewy-

32 1 core, [cren] is higher than [sum br GDGT]; sample kk_35 at 1289.70 m depth

Age	Depth (m)	Sample	Average concentration (ng/g TOC)											BIT Index	MBT'	MAAT (°C)	CBT	Soil pH
			Cren.	Ia	Ib	Ic	IIa	IIb	IIc	IIIa	IIIb	IIIc	Sum brGDGT					
			1292	1022	1020	1018	1036	1034	1032	1050	1048	1046						
T/A?	1083.05	**KK_49**	0.25	0.11	0.00	0.00	0.17	0.06	0.02	0.08	0.00	0.00	0.44	**0.60**	0.25	4.57	0.69	6.54
Toarcian	1188.00	**KK_45f**	0.06	0.02	0.00	0.00	0.02	0.01	0.01	0.01	0.00	0.00	0.07	**0.44**	0.29	5.61	0.72	6.48
	1201.10	**KK_44**	0.36	0.17	0.00	0.00	0.23	0.05	0.03	0.07	0.00	0.00	0.54	**0.56**	0.31	5.21	0.90	6.13
	1219.00	**KK_42a**	0.08	0.04	0.00	0.00	0.05	0.02	0.02	0.01	0.00	0.00	0.13	**0.57**	0.30	5.95	0.76	6.41
	1238.90	**KK_41a**	0.17	0.49	0.24	0.05	0.49	0.09	0.02	0.10	0.00	0.00	1.48	**0.86**	0.53	14.58	0.47	6.96
Plien.	1260.10	**KK_38d**	0.16	0.07	0.00	0.00	0.08	0.02	0.01	0.02	0.00	0.00	0.20	**0.53**	0.36	6.50	0.98	5.98
	1289.70	**KK_35**	0.25	0.05	0.00	0.00	0.04	0.02	0.00	0.08	0.00	0.00	0.19	**0.40**	0.24	4.72	0.61	6.69
Hett.	1692.10	**KK_17**	0.23	0.07	0.00	0.00	0.09	0.05	0.16	0.02	0.00	0.00	0.39	**0.44**	0.17	3.36	0.47	6.97
	1796.60	**KK_14c**	0.05	0.05	0.00	0.00	0.05	0.08	0.03	0.01	0.00	0.00	0.21	**0.69**	0.21	6.90	0.07	7.76
Rhaetian	1891.37	**KK_10a**	0.05	0.06	0.00	0.00	0.04	0.07	0.01	0.01	0.00	0.00	0.20	**0.71**	0.31	9.41	0.18	7.54
	1920.68	**KK_6**	0.22	0.09	0.00	0.00	0.12	0.03	0.02	0.04	0.00	0.00	0.29	**0.53**	0.31	5.73	0.80	6.32
	1940.00	**KK_4**	0.04	0.02	0.00	0.00	0.03	0.25	0.02	0.01	0.00	0.00	0.33	**0.62**	0.07	6.67	-0.67	9.22

Table 8.2 Average concentrations (ng/g TOC) of the isoprenoid GDGT crenarchaeol and branched GDGTs Ia-c, IIa-c, IIIa-c; Sum brGDGT = the sum of concentrations of GDGTs Ia-c, IIa-c, and IIIa-c; BIT Indices; MBT' indices and MAAT estimates; CBT indices and soil pH estimates. **Equations 4.6 – 4.10** were used to calculate BIT indices, MBT' indices, MAAT, CBT indices and soil pH. Results in bold indicate samples where the full suite of GDGTs required for the calculation were detected; results in red indicate samples where the full suite of GDGTs required for the calculation were not detected (i.e. concentration of 0 ng/g TOC). Cren. = crenarchaeol. Hett. = Hettangian; Plien. = Pliensbachian; T/A? = Toarcian/Aalenian boundary?

has a higher concentration of crenarchaeol than [sum brGDGT]: 0.25 vs 0.19 ng/g TOC (**Table 8.2**).

In all other samples, the concentration of the sum of all branched GDGTs is higher than [cren], and ranges from 0.07 to 1.48 ng/g TOC. The concentration of crenarchaeol in these samples ranges from 0.02 to 0.49. Sample kk_41a (1238.90 m depth) has an anomalously high [sum brGDGT]: 1.48 ng/g TOC, far higher than any other sample from either this section, or the Rhaetian-Hettangian section of the Kaszewy-1 core.

8.6. Discussion

8.6.1. Contamination & Diagenetic Alteration

8.6.1.1. Potential For Contamination

Before interpreting the results from the analyses of the Polish Basin samples, the risk of contamination of the samples by modern soil bacteria must be evaluated. The structures of fossil and recent GDGTs are identical, therefore it is not possible to distinguish between them. If the samples have been contaminated by modern soil bacteria, the resulting BIT, MBT' & CBT Indices would reflect a mixture of both fossil and modern organic matter sources, rendering them useless for investigating palaeoenvironments and climatic conditions. Steps can be taken to limit the risk of contamination, such as digging back to an unweathered surface of an outcrop to take samples, taking samples of well consolidated sediments, and scraping off the exposed weathered surfaces of core rounds to expose the fresh samples.

The Kozłowice clay pit is a working clay pit which experiences a high level of weathering. The clay is extremely soft and highly unconsolidated which, combined with the significant level of rainfall that the area experiences, greatly increases the risk of contamination by modern soil bacteria and therefore modern GDGTs. The 3 samples collected from the Kozłowice site were collected from ~20-30 cm back from the exposed surface to try to minimise the risk of contamination. However, it is possible that modern soil bacteria could have contaminated this far back due to the unconsolidated nature of the sediments. Given the nature of the Kozłowice outcrop, it is highly likely that the samples have been contaminated by modern soil bacteria and, therefore, the BIT, MBT' and

CBT Indices of these samples are therefore, not thought to be reliable and are not discussed further.

The Kaszewy-1 core is stored in wooden boxes in a large metal structure similar to a shipping container at the Polish Geological Institute's site in Sosnowiec, southern Poland. The storage structure is a dusty building with no climate control or measures to reduce the level of dust. The Kaszewy-1 borehole was drilled in 2008 (10 years old) and has been sampled several times since the borehole was drilled. Many of the samples collected from the Kaszewy-1 core were small fragments which were loose. A minority of Kaszewy-1 core samples were fragments broken off larger sections of core. Prior to powdering the Kaszewy-1 samples, the outer surfaces were scraped off to remove any modern soil bacteria that may have contaminated the surfaces of the samples. It is much less likely that the Kaszewy-1 core samples have been contaminated by modern soil bacteria than the Kozłowice samples. However, caution should still be exercised when interpreting the BIT Indices of these samples given that there is little reference material to compare the results to.

8.6.1.2. Potential For Diagenetic Alteration

The effect of diagenesis on GDGTs of Mesozoic age is currently unknown. Artificial maturation experiments show a decrease in MBT and an increase in CBT values with increasing maturation (Schouten et al., 2013, and references therein). A study of peats and coals of different thermal maturities shows that brGDGTs are present only in low concentrations in mature coals; the study also shows that brGDGTs present in peats bias MAAT estimates towards warmer temperatures (Weijers et al., 2011). Considering the age of the Polish Basin sediments analysed here (Late Triassic–Early Jurassic), it is highly likely that diagenetic alteration of GDGTs has occurred. However, it has also been proposed that branched and isoprenoid GDGTs should undergo a similar degree of alteration during diagenesis due to their similar properties (Schouten et al., 2013, and references therein).

Samples from the Kaszewy-1 core were chosen based on T_{max} values <435°C (thermally immature) determined using Rock-Eval (Pieńkowski, pers. comm.) so as to minimise the effect of diagenesis. Whilst discussing the results from this study, it is important to remember that the values presented here are likely

affected by diagenesis, but with a lack of studies addressing this problem, it is not possible to evaluate the magnitude of diagenetic alteration. Further work is needed to better understand the effect of diagenesis on GDGTs in older, mature sediments.

8.6.2. Changes in the Composition of Organic Matter Deposited at the Kaszewy-1 Site During the Late Triassic and Early Jurassic

Changes in BIT indices throughout a sedimentary succession suggest that there are variations in the ratio of terrestrial OM to marine OM deposited in the sediments (Hopmans et al., 2004). Changes in BIT indices can be driven by changes in terrestrial OM input, marine OM input, or both. By comparing [sum brGDGT] and [cren], it is possible to identify what the change in BIT indices was driven by Schouten et al. (2013).

8.6.2.1. Rhaetian-Hettangian Section

The 3 Rhaetian-aged samples (all from the Kaszewy-1 core) show a range of BIT indices (0.53-0.71; **Figure 8.3**), though all sediments analysed are interpreted to have been deposited in terrestrial environments (kk_4, 1940.00 m depth: lacustrine-delta; kk_6, 1920.68 m depth: backswamp; kk_10a, 1891.37 m depth: fluvial-floodplain). These intermediate BIT indices suggest that there was a mixture of both terrestrial and marine organic matter deposited at the Kaszewy-1 site during the Rhaetian. However, the changing BIT indices suggest that the ratio of terrestrial to marine organic matter varied during this time. In all three Rhaetian-aged samples, the [sum brGDGT] is higher than [cren], indicating that there was a greater input of terrestrial OM than marine OM to the Kaszew-1 site at this time. However, these absolute concentrations both vary throughout the section, suggesting that both terrestrial and marine organic matter input changed during the Rhaetian.

The two samples from the Hettangian section of the Kaszewy-1 core both have intermediate values (0.69 and 0.44; **Figure 8.3**), similar to the Rhaetian-aged samples. Again, the BIT indices of the Hettangian-aged samples would suggest that there was a mixture of both terrestrial and marine organic matter deposited at the Kaszewy-1 site.
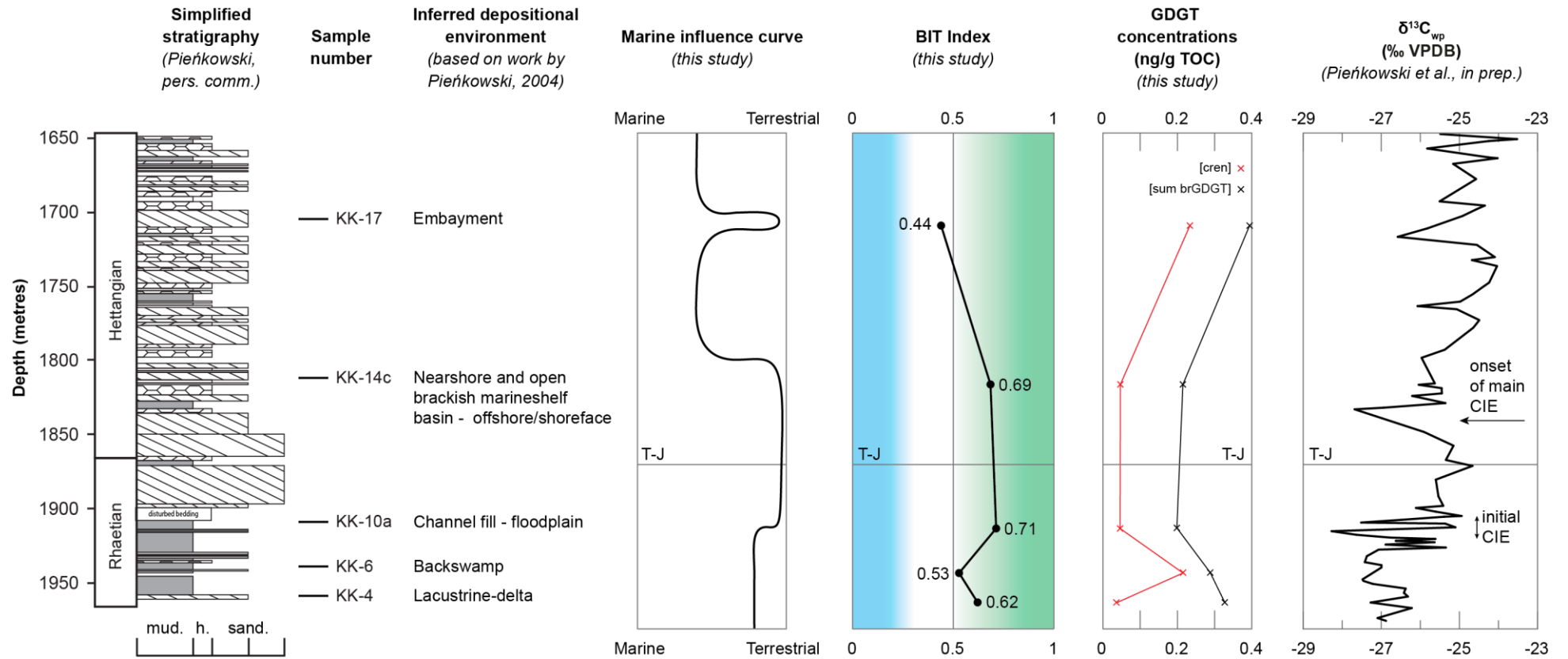
Figure 8.3 A generalised 'sea level' curve, BIT indices, [cren], [sum brGDGT] from this study plotted against a simplified stratigraphy column, inferred depositional environments and $\delta^{13}C_{wp}$ (all based on unpublished work by Pieńkowski) for the Triassic-Jurassic Boundary section of the Kaszewy-1 core. T-J = Triassic-Jurassic Boundary; [cren] = concentration of crenarchaeol; [sum brGDGT] = concentration of the sum of all branched GDGTs.

Similar to the samples from the lower, Rhaetian section, [sum brGDGT] is higher than [cren], indicating a higher input of terrestrial OM than marine OM to the Kaszewy-1 site during the Hettangian. Both the concentration of crenarchaeol and [sum brGDGT] varies in the Hettangian part of the study section, suggesting that BIT Index variations is driven by changes in both the amount of terrestrial and marine organic matter deposited at the site.

The BIT indices of the sediment samples from the Rhaetian-Hettangian section of the Kaszewy-1 core show a fair correlation with the inferred depositional environments of the samples (**Figure 8.3**). Three of the five samples analysed are interpreted to have been deposited in terrestrial environments (kk_4, depth 1940.00 m depth; kk_6, 1920.68 m depth; kk_10a, 1891.37 m depth), and the other two in more marine environments (kk_14c, 1796.60 m depth; kk_17, 1692.10 m depth). The two more marine samples are thought to have been deposited in environments which would have still received a significant amount of terrestrial organic matter, and this appears to be reflected in the intermediate BIT indices of the samples. However, the three more terrestrial samples have BIT indices which are slightly lower than expected.

Crenarchaeol does appear to be formed *in situ* in some terrestrial environments, though not in significant quantities (Weijers et al., 2006). The concentration of crenarchaeol and [sum brGDGT] covary to an extent (**Figure 8.3**), perhaps indicating that crenarchaeol was being produced *in situ* at the Kaszewy-1 site. Without the presence of sediments deposited in deep marine environments to compare to, it is hard to determine to what extent crenarchaeol may have been produced *in situ* at the Kaszewy-1 site.

Generally, the BIT indices of the samples from the Rhaetian-Hettangian section of the Kaszewy-1 core do reflect the inferred depositional environments of the sediments, and the concentrations of branched GDGTs and crenarchaeol identify changes in the amounts of terrestrial marine organic matter deposited at the site. The GDGT concentration data does also suggest that there may have been some *in situ* production of crenarchaeol at the Kaszewy-1 site during the Rhaetian and Hettangian, though the extent of this is not clear.

8.6.2.2. Pliensbachian-Toarcian Section

The two samples analysed from the Pliensbachian part of the Kaszewy-1 core all come from the upper part of the Pliensbachian section and show similar BIT indices (kk_35, 1289.70 m depth: 0.40; kk_38d, 1260.10 m depth: 0.53; **Figure 8.4**), though the sediments were thought to have been deposited in two different environments: nearshore and fluvial, respectively. Nearshore environments would still experience an influence from the terrestrial environment, with the input of significant amounts of terrestrial OM, reflected by the intermediate BIT Index of sample kk_35 at 1289.70 m depth. The concentration of crenarchaeol is slightly higher than [sum brGDGT] in sample kk_35, supporting the interpretation of sample kk_35 as nearshore sediments, since crenarchaeol is usually produced in marine environments (Weijers et al., 2006). The BIT Index of sample kk_38d at 1260.10 m depth is lower than expected for sediments that are thought to have been deposited in a fluvial environment. Marine influences to the Kaszewy-1 site at this time should have been minimal, if this interpretation is accurate.

Moving up the core past the Pliensbachian-Toarcian boundary, both the BIT Index (0.86) and [sum br GDGT] (1.48 ng/g TOC) increase greatly in sample kk_41a (1238.90 m depth), an interbedded sand- and mudstone thought to have been deposited in a deltaic environment. Deltaic environments are still relatively terrestrial environments, though some influence from the marine realm is expected. The sudden increase in [sum brGDGT] suggests that the high BIT Index for this sample was caused by a relatively large increase in terrestrial organic matter input, rather than a decrease in [cren], which is similar to the two previous samples from the Pliensbachian section of the core. Sample kk_41a (1238.90 m depth) coincides with the negative CIE associated with the Toarcian OAE, correlating with one of the most negative parts of the $\delta^{13}C_{wp}$ record.

The following two samples moving up the core also correlate with the Toarcian OAE negative carbon-isotope excursion. Both of these samples have intermediate BIT indices (kk_42a, 1219.00 m depth: 0.57; kk_44, 1201.10 m depth: 0.56), indicating a mixture of both terrestrial and marine OM deposited at the Kaszewy-1 site. However, [sum brGDGT] and [cren] of sample kk_44 (1201.10 m depth) is higher than sample kk_42a (1219.00 m depth), indicating a greater amount of both terrestrial and marine OM input during the deposition of
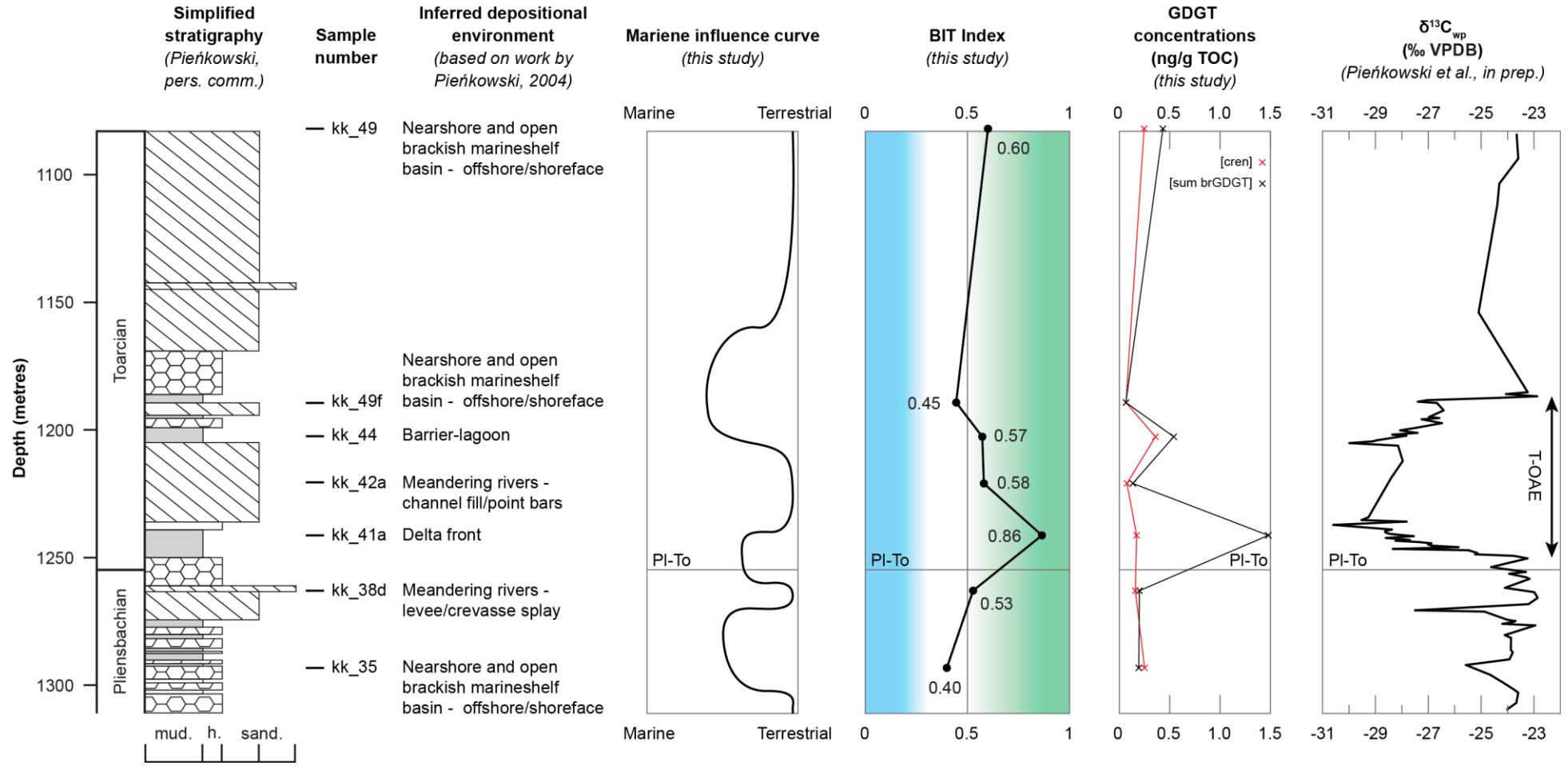
Figure 8.4 A generalised 'sea level' curve, BIT indices, [cren], [sum brGDGT] from this study plotted against a simplified stratigraphy column, inferred depositional environments and δ¹³Cwp (all based on unpublished work by Pieńkowski) for the Pliensbachian-Toarcian section of the Kaszewy-1 core. Pl-To = Pliensbachian-Toarcian Boundary; [cren] = concentration of crenarchaeol; [sum brGDGT] = concentration of the sum of all branched GDGTs.

the sediments of sample kk_44. The two peaks in [sum brGDGT] in samples kk_41a (1219.00 m depth) and kk_44 (1201.10 m depth) perhaps reflect increased weathering and increased transport of terrestrial organic matter to the Kaszewy-1 site during the Toarcian OAE, as indicated by changes in clay mineral assemblages (Brański, 2012).

Sample kk_45f at 1188.00 m depth corresponds with the recovery period of the Toarcian OAE, correlating with relatively positive $\delta^{13}C_{wp}$ values (**Figure 8.4**), and has an intermediate BIT Index of 0.45, and relatively low [cren] and [sum brGDGT]. The data suggest that there was a fairly even mixture of terrestrial and marine organic matter deposited at the Kaszewy-1 site at the end of the Toarcian OAE, which correlates well with the interpreted depositional environment: nearshore.

The uppermost Toarcian-aged sample (kk_49) is situated at the very top of the Toarcian section of the core, just below what is thought to be the Toarcian-Aalenian Boundary. Sample kk_49 has an intermediate BIT Index of 0.60, indicating a mixture of both terrestrial and marine OM input, and relatively low [cren] and [sum brGDGT], correlating well with its inferred depositional environment: nearshore.

Similar to the Rhaetian-Hettangian section of the Kaszewy-1 core, [cren] and [sum brGDGT] generally covary, with the exception of sample kk_41a. This covariance perhaps reflects some *in situ* production of crenarchaeol in the terrestrial sediments (Weijers et al., 2006). However, it is difficult to evaluate the extent of *in situ* production of crenarchaeol in terrestrial sediments without data from deep marine sediments from the Kaszewy-1 core (there are none).

Generally, the BIT indices of the samples from the Pliensbachian-Toarcian section of the Kaszewy-1 core reflect the inferred depositional environments of the sediments, and the concentrations of branched GDGTs and crenarchaeol identify changes in the composition of organic matter deposited at the site during the Pliensbachian and Toarcian. Changes in BIT indices appear to be driven by changes in both terrestrial OM and marine OM input to the Kaszewy-1 site, with the possibility of some *in situ* production of crenarchaeol in the terrestrial environments.

8.6.3. Mean Annual Air Temperature & Soil pH Reconstructions in the Polish Basin during the Late Triassic and Early Jurassic

MBT' and CBT Indices were calculated for 17 of the 20 samples analysed. However, all of the branched GDGTs required to calculate the indices accurately were only found in 2 of these 19 samples (**Equations 4.6 – 4.8**). As a result, the mean annual air temperature and soil pH estimates calculated using the MBT' and CBT Indices are only potentially reliable for these 2 samples (see values in bold in **Table 8.1** and **Table 8.2**). The MAAT and soil pH estimates for the remaining 17 samples are not deemed to be reliable (see values in red in **Table 8.1** and **Table 8.2**).

The average monthly temperature of Poland between the years 1901 and 2015 ranges from -2.6°C to 18.2°C, and has a mean annual temperature of 7.98°C (The World Bank Group, 2018). During the Early Jurassic, the Polish Basin was located a palaeolatitude of 40-45°N and was situated on the northern margin of the Tethys Ocean (Feist-Burkhardt et al., 2008; Barbacka et al., 2016). Previously published data indicates that seawater palaeotemperatures were warm during the Toarcian, particularly during the Toarcian Oceanic Anoxic Event (McArthur et al., 2000; Bailey et al., 2003; Rosales et al., 2004; Cohen et al., 2007). Published carbon-isotope data shows a prominent negative excursion in $\delta^{13}C_{org}$ and $\delta^{13}C_{carb}$ during the Toarcian, signalling the Toarcian OAE, and indicating a massive input of isotopically-light carbon into the ocean-atmosphere system (Hesselbo, Gröcke, et al., 2000; Kemp et al., 2005; Hesselbo, Jenkyns, et al., 2007; Hermoso et al., 2009; Jenkyns, 2010; Hesselbo and Pienkowski, 2011). This input of massive amounts of ^{12}C into the ocean-atmosphere system would likely have been accompanied by a rise in seawater and atmospheric temperatures (e.g. Jenkyns, 2003; Korte et al., 2015). To summarise, the evidence points to the Polish Basin being warmer during the Toarcian than modern-day Poland (mean annual termperature of 7.98°C).

Samples kk_41a (1238.90 m depth) is from the lowermost part of the Toarcian section of the Kaszewy-1 core and has an MBT' Index of 0.53, which provides a mean annual air temperature estimate of 14.6°C. Sample KWE_2014_1 is from the upper part of the Toarcian-aged Kozłowice outcrop and has an MBT' Index of 0.17, which provides a mean annual air temperature estimate of 3.4°C. These

two MAAT estimates are different by ~10°C, but it is important to note that sample KK_41a is from the beginning of the Toarcian, just after the Pliensbachian boundary, and sample KWE_2014_1 is from later during the Toarcian. The MAAT estimate for sample KWE_2014_1 (3.36°C) is significantly lower than expected. This sample was collected from within the Toarcian OAE, as indicated by carbon-isotope stratigraphy, when palaeotemperatures are thought to have been high. As discussed previously, it is very likely that sample KWE_2014_1 has been contaminated by modern-day soil bacteria, which could potentially lower the estimated MAAT. The MAAT estimate from sample KWE_2014_1 is, therefore, likely not reliable. The MAAT estimate from sample KK_41a (11.52°C) is higher than the annual temperature of modern-day Poland; evidence shows that the Toarcian was warmer than today (Bailey et al., 2003; Rosales et al., 2004). There is still a risk of contamination of this sample by modern-day soil bacteria, but it is much lower than the Kozłowice sample.

All branched GDGTs required to calculate the CBT Index were only present in sample KWE_2014_1. This sample has a CBT Index of -0.02, which results in a soil pH estimate of 7.9. However, due to the high probability of this sample being contaminated by modern-day soil bacteria, the soil pH estimate is likely unreliable and reflects a mixed source of both fossil and modern-day soil bacteria.

8.6.4. Efficacy of the BIT Index and MBT'-CBT Proxies as Applied to Late Triassic and Early Jurassic Sediments

The purpose of this small-scale study was threefold: 1) to determine whether GDGTs can be detected and quantified in Late Triassic and Early Jurassic sediments; 2) to determine whether BIT indices can be used to successfully investigate sources of organic matter in Early Jurassic-aged sediments; and 3) to determine whether the MBT'-CBT palaeotemperature proxy could be successfully used to reconstruct mean annual air temperature and soil pH from Mesozoic-aged sediments.

Various GDGTs were detected and quantified in 17 of the total 20 samples analysed as part of this small-scale study. Crenarchaeol and branched GDGTs
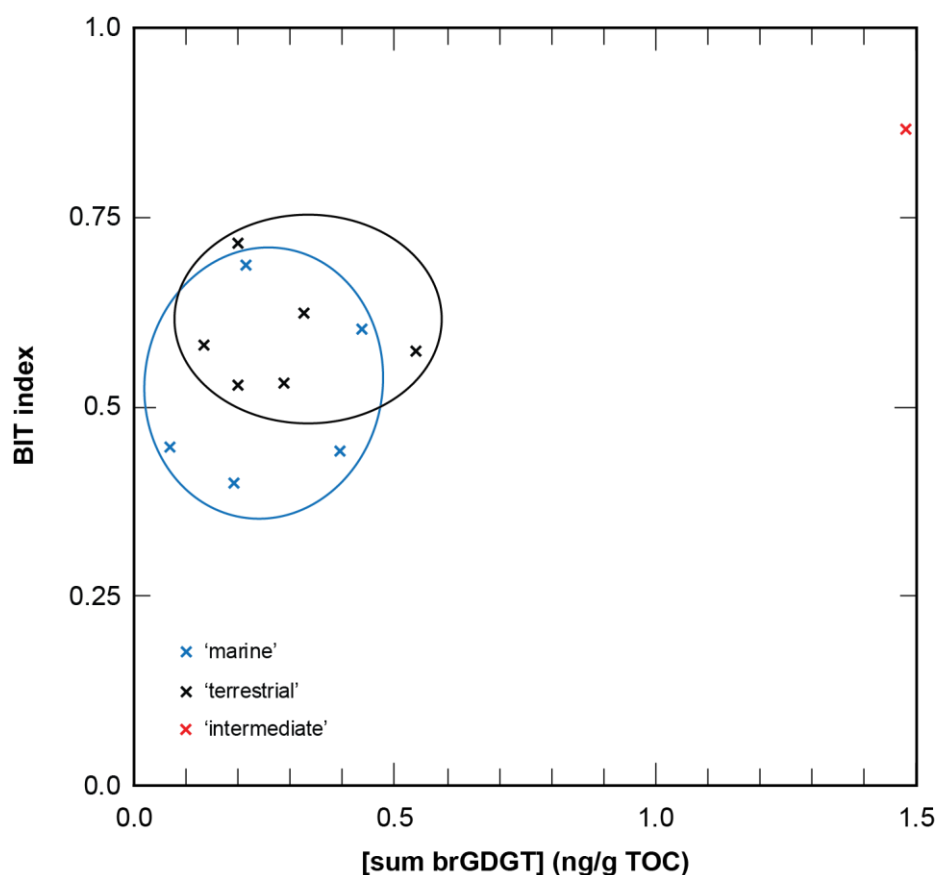
Figure 8.5 Concentrations of the sum of all branched GDGTs ([sum brGDGT]) plotted against BIT Index. Fields showing the range of BIT indices and [sum brGDGT] have been drawn around the 'marine' samples and 'terrestrial' samples. Samples have been categorised as deposited in either a marine, terrestrial or intermediate environment based on their lithology.

were detected in sediment samples from the Rhaetian and Hettangian sections of the Kaszewy-1 core, making them the current oldest-known detected and quantified GDGTs, surpassing the Middle Jurassic samples of Jenkyns et al. (2012) and Sinemurian-Pliensbachian samples of Robinson et al. (2017). This study pushes back the limit of GDGT detection and quantification to the Late Triassic.

The 3 branched GDGTs (Ia, IIa, IIIa) and the isoprenoid GDGT crenarchaeol required to calculate BIT indices were detected in 17 of the 20 samples analysed. After evaluating the potential for contamination by modern-day soil bacteria, it was determined that 15 of the 17 samples provided reliable BIT indices. The BIT indices of these 15 samples broadly correlated with the inferred depositional environments of the samples. However, crossplots of BIT indices against [sum brGDGT] and [cren] (**Figure 8.5** and **Figure 8.6**, respectively) show that there is
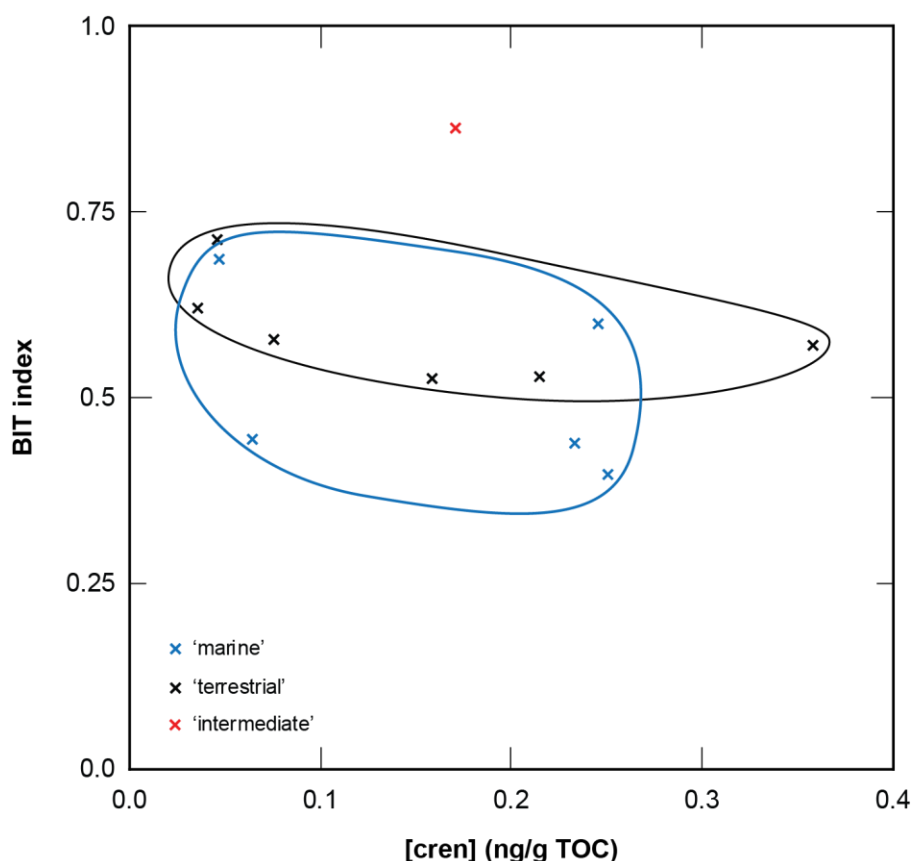
Figure 8.6 Concentrations of crenarchaeol ([cren]) plotted against BIT Index. Fields showing the range of BIT indices and [cren] have been drawn around the 'marine' samples and 'terrestrial' samples. Samples have been categorised as deposited in either a marine, terrestrial or intermediate environment based on their lithology.

significant overlap between samples thought to have been deposited in more marine environments and more terrestrial environments. The BIT indices of Middle Jurassic deep marine sediments analysed by Jenkyns et al. (2012) were consistently <0.1. While the BIT indices, [cren] and [sum brGDGT] all provide valuable information regarding the composition of organic matter input to the Kaszewy-1 site during key periods of the Early Jurassic, they cannot be used by themselves to differentiate between terrestrial and shallow marine environments. Additional information, such as lithology changes and palynology, should be used alongside BIT indices, [cren] and [sum brGDGT] to identify changes between terrestrial and shallow marine environments of Early Jurassic sediments.

The 7 branched GDGTs (Ia, Ib, Ic, IIa, IIb, IIc, IIIa) required to calculate the MBT' and CBT Indices were often not all present in the Late Triassic- and Early Jurassic-aged samples. Mean annual air temperature and soil pH estimates were

calculated from these indices but are not reliable due to the full suite of branched GDGTs not being present. The results of this study show that applying the MBT'-CBT proxy to Late Triassic- and Early Jurassic-aged sediments in the chosen cores does not produce reliable results. The use of this proxy is not recommended on Late Triassic- or Early Jurassic-aged sediments until further work has been carried out to improve the technique.

8.7. Conclusions & Future Work

The following conclusions can be drawn from this small-scale study of organic matter sources and mean annual air temperature & soil pH reconstructions from Early Jurassic-aged Polish Basin samples:

- Contamination of geological samples by modern soil bacteria is highly likely, and steps should be taken to prevent contamination of samples, particularly those collected from outcrops.

- The full suite of GDGTs required to calculate the BIT Index is present in some Early Jurassic-aged sediments. As a result, reliable estimates of the proportion of soil and marine organic matter input to a site can be estimated.

- Peaks in branched GDGT concentrations in Toarcian-aged samples from the Polish Basin can perhaps be linked to periods of increased weathering, as indicated by clay mineral assemblages.

- The BIT indices calculated from the Rhaetian and Hettangian sediments of the Kaszewy-1 core are possibly the oldest-known values calculated using this proxy.

- The BIT Index, [cren] and [sum brGDGT] can be used to investigate changes in organic matter composition deposited at a site during the Early Jurassic, but cannot be used by themselves to differentiate between terrestrial and shallow marine environments. Traditional sedimentological observations remain an invaluable part of characterising the palaeoenvironment of sediments used in Mesozoic palaeoclimate studies.

- The full suite of GDGTs required to calculate the MBT' Index is often not present in the selected Early Jurassic-aged sediments. As a result, reliable mean annual air temperature reconstructions cannot be calculated.

- The full suite of GDGTs require to calculate the CBT Index if often not present in the selected Early Jurassic-aged sediments. As a result, reliable soil pH reconstructions cannot be calculated.

- The MBT'-CBT proxy requires further development before it can be successfully used to reconstruct mean annual air temperatures and soil pH for Early Jurassic-aged sediments.

There is great scope for future work based on the data presented in this chapter. A large amount of sample material from the Kaszewy-1 core still remains, and could be analysed to provide a greater insight into changes in organic matter composition at the site during the Early Jurassic. Additional studies of the Kaszewy-1 core could form the basis of reference material for GDGT studies of Mesozoic sediments from other sites. Further analyses of Early Jurassic-aged sediments could potentially help to identify sediments which may be suitable for palaeotemperature and soil pH reconstructions using the MBT'-CBT proxy.

CHAPTER 9 CONCLUSIONS & FUTURE WORK

A new $\delta^{13}C$ record generated from measurements of individual woody phytoclasts shows that, despite $\delta^{13}C$ variations within discrete horizons, individual phytoclast $\delta^{13}C$ measurements can be used to identify major variations in $\delta^{13}C$, such as the Toarcian OAE negative CIE, but cannot be used to identify more minor fluctuations. The new $\delta^{13}C_{phytoclast}$ data also show that fossil woody phytoclasts are relatively isotopically-homogeneous. The single-phytoclast $\delta^{13}C$ study presented here shows that it has potential as a complementary tool for traditional chemostratigraphic techniques. The use of single-phytoclast $\delta^{13}C$ analyses could provide invaluable for interpreting $\delta^{13}C$ records generated from samples deposited in environments under both marine and terrestrial influences. Single-phytoclast $\delta^{13}C$ records could enable the disentangling of terrestrial and marine records at these sites, and assist in evaluating the relative influence of terrestrial and marine organic matter. Use of this new technique could also complement palynology studies, allowing for the generation of species-specific plant $\delta^{13}C$ records; interpretation of these records could improve understanding of the responses of individual plant species to environmental changes.

New wildfire activity proxy records from a site in the Central Polish Basin show evidence of supressed wildfire activity correlating with the negative carbon-isotope excursion of the Toarcian Oceanic Anoxic Event. The new proxy records also show evidence of a period of increased wildfire activity prior to and during the recovery period of the Toarcian OAE, correlating with more positive $\delta^{13}C$ values. These findings appear to correlate with other published contemporaneous records from the NW Tethyan realm, suggesting a regional control on wildfire activity across the Toarcian OAE. Evidence presented here suggests that there is a link between increased wildfire activity and positive $\delta^{13}C$ values; this link is interesting and worth further investigation. This relationship perhaps hints at increased wildfire activity associated with carbon burial events. Investigation of wildfire activity during major carbon burial events (e.g. the Cenomanian/Turonian oceanic anoxic event) would perhaps present similarities with the data presented here in this thesis.

Evidence presented here showcases the importance of wildfire activity in the Earth System. Wildfires play an important role in a postive feedback system involving primary production and atmospheric oxygen. The burning of plant biomass enhances soil weathering, leading to an increased input of phosphorous to the oceans. In turn, elevated levels of oceanic phosphorous stimulates primary production of oxygen in the ocean-atmosphere system. Wildfires are also required for the successful reproduction of some plant species and can play an important role in shaping plant assemblages. Wildfire activity in the geological record is somewhat overlooked in comparison to other paleoclimate indicators. The importance of wildfire activity in understanding past environmental changes cannot continue to be underestimated, and wildfire activity proxy records should be better utilised.

New carbon-isotope records generated from terrestrial organic matter from a site in the Central Polish Basin show evidence of a negative trend in $\delta^{13}C$ values after the Triassic-Jurassic Boundary, perhaps correlating with the 'main' negative CIE which has been observed at numerous contemporaneous sites. These new $\delta^{13}C$ records provide evidence of a perturbation to the terrestrial component of the carbon cycle at this time. Using these new $\delta^{13}C$ records, a new correlation between the two Central Polish Basin sites is also proposed. New wildfire activity proxy records from two sites in the Central Polish Basin show evidence of a period of increased wildfire activity across the Triassic-Jurassic Boundary, similar to contemporaneous wildfire activity proxy records from other European sites.

The exploratory investigation of the application of the BIT index and MBT'-CBT proxies to Mesozoic sediments from the Polish Basin provided mixed results, but nevertheless added to our existing understanding of these proxies. The GDGTs required for calculation of the BIT index were successfully identified and quantified in the majority of samples analysed, providing a semi-quantitative record of changes in terrestrial organic matter input at a site in the Central Polish Basin during two key intervals of the Late Triassic and Early Jurassic. However, the full suite of GDGTs required for calculation of the MBT' and CBT indices were not detected in the selected samples and therefore palaeotemperature and soil pH reconstructions were not possible. The BIT index cannot yet be used to distinguish between Mesozoic-aged sediments deposited in terrestrial and shallow-marine environments, or transitional ones between, but this investigation

has shown that it can be used to produce a record of changing terrestrial organic matter input to sites during the Mesozoic.

There is scope for future work to be carried out on the basis of the work presented here in this thesis; four key areas are identified as being of the most benefit to future studies. The generation of additional $\delta^{13}C_{phytoclast}$ data from Mochras phytoclast samples, increasing the number of data points, would provide a greater understanding of inter-phytoclast $\delta^{13}C$ variability. Increasing the resolution and stratigraphic extent of the wildfire activity proxy datasets would provide a better understanding of wildfire activity across the Triassic-Jurassic Boundary and Toarcian OAE and place in a longer time frame. Additional work to better constrain the position of the T-J Boundary in the Kaszewy-1 and Niekłań PIG-1 cores would improve correlation between these sites and other contemporaneous sites outside of the Polish Basin. The generation of additional BIT index data from new Kaszewy-1 sediment samples, increasing the number of data points, would provide a a better understanding of variations in terrestrial OM input to the site during the Early Jurassic, and improve understanding of the use of this proxy on Mesozoic sediments.

BIBLIOGRAPHY

Abdel-Shafy, H.I., and Mansour, M.S.M., 2016, A review on polycyclic aromatic hydrocarbons: Source, environmental impact, effect on human health and remediation: Egyptian Journal of Petroleum, v. 25, p. 107–123, doi: 10.1016/j.ejpe.2015.03.011.

Aberhan, M., and Fürsich, F.T., 1996, Diversity analysis of Lower Jurassic bivalves of the Andean Basin and the Pliensbachian-Toarcian mass extinction: Lethaia, v. 29, p. 181–195, doi: 10.1111/j.1502-3931.1996.tb01874.x.

Aceves, M., and Grimalt, J.O., 1993, Seasonally Dependent Size Distributions of Aliphatic and Polycyclic Aromatic Hydrocarbons in Urban Aerosols from Densely Populated Areas: Environmental Science & Technology, v. 27, p. 2896–2908, doi: 10.1021/es00049a033.

Akikuni, K., Vajda, V., Hori, R.S., Grant-Mackie, J.A., and Ikehara, M., 2010, Stratigraphy of Triassic-Jurassic boundary sequences from the Kawhia coast and Awakino gorge, Murihiku Terrane, New Zealand: Stratigraphy, v. 7, p. 7–24.

Al-Suwaidi, A., Angelozzi, G.N., Baudin, F., Damborenea, S.E., Hesselbo, S.P., Jenkyns, H.C., Mancenido, M.O., and Riccardi, A.C., 2010, First record of the Early Toarcian Oceanic Anocic event from the Southern Hemisphere, Nequen Basin, Argentina: Journal of the Geological Society, London, v. 167, p. 633–636, doi: 10.1144/0016-76492010-025.SPECIAL.

Al-Suwaidi, A.H., Steuber, T., and Suarez, M.B., 2016, The Triassic–Jurassic boundary event from an equatorial carbonate platform (Ghalilah Formation, United Arab Emirates): Journal of the Geological Society, v. 173, p. 949–953, doi: 10.1144/jgs2015-102.

Albini, F.A., 1976, Estimating wildfire behavior and effects:, doi: USDA Forest Service General Technical Report INT-30.

Anderson, V.J., Shanahan, T.M., Saylor, J.E., Horton, B.K., and Mora, A.R., 2014, Organic Geochemistry Sources of local and regional variability in the MBT'/CBT paleotemperature proxy: Insights from a modern elevation transect across the Eastern Cordillera of Colombia: Organic Geochemistry,

v. 69, p. 42–51, doi: 10.1016/j.orggeochem.2014.01.022.

Ascough, P.L., Bird, M.I., Scott, A.C., Collinson, M.E., Cohen-Ofri, I., Snape, C.E., and Le Manquais, K., 2010, Charcoal reflectance measurements: implications for structural characterization and assessment of diagenetic alteration: Journal of Archaeological Science, v. 37, p. 1590–1599, doi: 10.1016/j.jas.2010.01.020.

Bachan, A., van de Schootbrugge, B., Fiebig, J., McRoberts, C.A., Ciarapica, G., and Payne, J.L., 2012, Carbon cycle dynamics following the end-Triassic mass extinction: Constraints from paired δ13Ccarb and δ13Corg records: Geochem. Geophys. Geosyst., v. 13, p. Q09008, doi: 10.1029/2012gc004150.

Bacon, K.L., Belcher, C.M., Hesselbo, S.P., and McElwain, J.C., 2011, The Triassic-Jurassic Boundary carbon-isotope excursions in taxonomically identified leaf cuticles: Palaios, v. 26, p. 461–469, doi: 10.2110/palo.2010.p10-120r.

Bailey, T.R., Rosenthal, Y., McArthur, J.M., van de Schootbrugge, B., and Thirlwall, M.F., 2003, Paleoceanographic changes of the Late Pliensbachian-Early Toarcian interval: A possible link to the genesis of an Oceanic Anoxic Event: Earth and Planetary Science Letters, v. 212, p. 307–320, doi: 10.1016/S0012-821X(03)00278-4.

Baker, S.J., Hesselbo, S.P., Lenton, T.M., Duarte, L. V, and Belcher, C.M., 2017, Charcoal evidence that rising atmospheric oxygen terminated Early Jurassic ocean anoxia: Nature Communications, v. 8, p. 1–7, doi: 10.1038/ncomms15018.

Ballantyne, A.P., Greenwood, D.R., Sinninghe Damsté, J.S., Csank, A.Z., Eberle, J.J., and Rybczynski, N., 2018, Significantly warmer Arctic surface temperatures during the Pliocene indicated by multiple independent proxies: Geology, p. 603–606, doi: 10.1130/G30815.1.

Barbacka, M., Pacyna, G., Pieńkowski, G., and Ziaja, J., 2016, New data about matonia braunii (göppert) harris from the early jurassic of Poland and its ecology: Geological Quarterly, v. 60, p. 857–868, doi: 10.7306/gq.1322.

Barbacka, M., Ziaja, J., and Wcisło-Luraniec, E., 2010, Taxonomy and palaeoecology of the Early Jurassic macroflora from Odrowąż, central

Poland: Acta Geologica Polonica, v. 60, p. 373–392.

Barski, M., and Leonowicz, P., 2002, Dinoflagellates of Lower Jurassic outcrops at Kozłowice and Boroszów (southern Poland): Przegląd Geologiczny, v. 5, p. 411–414.

Barth, G., Pienkowski, G., Zimmermann, J., Franz, M., and Kuhlmann, G., 2018, Palaeogeographical evolution of the Lower Jurassic: high-resolution biostratigraphy and sequence stratigraphy in the Central European Basin: Geological Society, London, Special Publications,.

Barth, J.A.C., Veizer, J., and Mayer, B., 1998, Origin of particulate organic carbon in the upper St. Lawrence: Isotopic constraints: Earth and Planetary Science Letters, v. 162, p. 111–121, doi: 10.1016/S0012-821X(98)00160-5.

Bartolini, A., Guex, J., Spangenberg, J.E., Schoene, B., Taylor, D.G., Schaltegger, U., and Atudorei, V., 2012, Disentangling the Hettangian carbon isotope record: Implications for the aftermath of the end-Triassic mass extinction: Geochemistry, Geophysics, Geosystems, v. 13, p. 1–11, doi: 10.1029/2011GC003807.

Batchelder, R.B., 1967, Spatial and temporal patterns of fire in the tropical world: Proceedings of the Annual Tall Timbers Fire Ecology Conference, v. 6, p. 171–207, #.

Beerling, D.J., and Berner, R.A., 2002, Biogeochemical constraints on the Triassic-Jurassic boundary carbon cycle event: Global Biogeochemical Cycles, v. 16, p. 1–13.

Beerling, D.J., and Royer, D.L., 2002, Fossil Plants As Indicators of the Phanerozoic Global Carbon Cycle: Annual Review of Earth and Planetary Sciences, v. 30, p. 527–556, doi: 10.1146/annurev.earth.30.091201.141413.

Belcher, C.M., Collinson, M.E., and Scott, A.C., 2005, Constraints on the thermal energy released from the Chicxulub impactor; new evidence from multi-method charcoal analysis: Journal of the Geological Society of London, v. 162, p. 591–602, doi: http://dx.doi.org/10.1144/0016-764904-104.

Belcher, C.M., Finch, P., Collinson, M.E., Scott, A.C., and Grassineau, N. V., 2009, Geochemical evidence for combustion of hydrocarbons during the K-T impact event: Proceedings of the National Academy of Sciences, v. 106, p. 4112–4117, doi: 10.1073/pnas.0813117106.

Belcher, C.M., and Hudspith, V.A., 2016, The formation of charcoal reflectance and its potential use in post-fire assessments: International Journal of Wildland Fire, v. 25, p. 775–779, doi: 10.1071/WF15185.

Belcher, C.M., Mander, L., Rein, G., Jervis, F.X., Haworth, M., Hesselbo, S.P., Glasspool, I.J., and McElwain, J.C., 2010, Increased fire activity at the Triassic/Jurassic boundary in Greenland due to climate-driven floral change: Nature Geoscience, v. 3, p. 426–429, doi: 10.1038/ngeo871.

Belcher, C.M., and McElwain, J.C., 2008, Limits for Combustion in Low O2 Redefine Paleoatmospheric Predictions for the Mesozoic: Science, v. 321, p. 1197–1201.

Belcher, C.M., Yearsley, J.M., Hadden, R.M., Mcelwain, J.C., and Rein, G., 2010, Baseline intrinsic flammability of Earth's ecosystems estimated from paleoatmospheric oxygen over the past 350 million years: Proceedings of the National Academy of Sciences, p. 2–7, doi: 10.1073/pnas.1011974107.

Bender, M.M., and Berge, A.J., 1979, Influence of N and K Fertilization and Growth Temperature on 13C/12C Ratios of Timothy (Phleum pratense L.): Oecologia, v. 44, p. 117–118.

Benton, M.J., 1995, Diversification and Extinction in the History of Life: Science, v. 268, p. 52–58.

Benton, M.J., 1991, What really happened in the Late Triassic? Historical Biology, v. 5, p. 263–278, doi: 10.1080/10292389109380406.

Berner, R.A., 2006, GEOCARBSULF: A combined model for Phanerozoic atmospheric O2 and CO2: Geochimica et Cosmochimica Acta, v. 70, p. 5653–5664, doi: 10.1016/j.gca.2005.11.032.

Berner, R.A., Beerling, D.J., Dudley, R., Robinson, J.M., and Wildman Jr., R.A., 2003, Phanerozoic Atmospheric Oxygen: Annual Review of Earth and Planetary Sciences, v. 31, p. 105–134, doi: 10.1146/annurev.earth.31.100901.141329.

Berner, R.A., and Canfield, D.E., 1989, A new model for atmospheric oxygen over Phanerozoic time: American Journal of Science, v. 289, p. 333–361, doi: 10.2475/ajs.289.4.333.

Bice, D.M., Newton, C.R., Mccauley, S., Reiners, P.W., and Mcroberts, C.A., 1992, Shocked Quartz at the Triassic-Jurassic Boundary in Italy: Science, v.

255, p. 443–446.

Bird, M.I., Ascough, P.L., Young, I.M., Wood, C. V., and Scott, A.C., 2008, X-ray microtomographic imaging of charcoal: Journal of Archaeological Science, v. 35, p. 2698–2706, doi: 10.1016/j.jas.2008.04.018.

Blaga, C.I., Reichart, G.-J., Heiri, O., and Sinninghe Damsté, J.S., 2009, Tetraether membrane lipid distributions in water-column particulate matter and sediments: a study of 47 European lakes along a north–south transect: Journal of Paleolimnology, v. 41, p. 523–540, doi: 10.1007/s10933-008-9242-2.

Blaga, C.I., Reichart, G.-J., Schouten, S., Lotter, A.F., Werne, J.P., Kosten, S., Mazzeo, N., Lacerot, G., and Sinninghe Damsté, J.S., 2010, Branched glycerol dialkyl glycerol tetraethers in lake sediments: Can they be used as temperature and pH proxies? Organic Geochemistry, v. 41, p. 1225–1234, doi: 10.1016/j.orggeochem.2010.07.002.

Blakey, R., 2018a, Europe Series Thumbnails:, http://deeptimemaps.com/europe-series-thumbnails/ (accessed October 2018).

Blakey, R., 2018b, Global Paleogeography and Tectonics in Deep Time Series:, http://deeptimemaps.com/global-paleogeography-and-tectonics-in-deep-time-series/ (accessed October 2018).

Bocherens, H., Friis, E.M., Mariotti, A., and Pedersen, K.R., 1993, Carbon Isotopic Abundances in Mesozoic and Cenozoic Fossil Plants - Paleoecological Implications: Lethaia, v. 26, p. 347–358, //a1993nl49800008.

Bond, D.P.G., and Grasby, S.E., 2016, On the causes of mass extinctions: Palaeogeography, Palaeoclimatology, Palaeoecology, doi: 10.1016/j.palaeo.2016.11.005.

Bond, W.J., and van Wilgen, B.W., 1996, Fire and Plants (Population and Community Biology Series 14): Springer Netherlands.

Bonis, N.R., Kürschner, W.M., and Krystyn, L., 2009, A detailed palynological study of the Triassic-Jurassic transition in key sections of the Eiberg Basin (Northern Calcareous Alps, Austria): Review of Palaeobotany and Palynology, v. 156, p. 376–400, doi: 10.1016/j.revpalbo.2009.04.003.

Bonis, N.R., Ruhl, M., and Kurschner, W.M., 2010, Milankovitch-scale palynological turnover across the Triassic-Jurassic transition at St. Audrie's Bay, SW UK: Journal of the Geological Society, v. 167, p. 877–888, doi: 10.1144/0016-76492009-141.

Bordalo Da Rocha, R., Mattioli, E., Duarte, L.V., Pittet, B., Elmi, S., Mouterde, R., Cabral, M.C., Comas-Rengifo, M.J., Gomez, J.J., Goy, A., Hesselbo, S.P., Jenkyns, H.C., Littler, K., Mailliot, S., et al., 2016, Base of the Toarcian Stage of the Lower Jurassic defined by the Global Boundary Stratotype Section and Point (GSSP) at the Peniche section (Portugal): Episodes, v. 39, p. 460, doi: 10.18814/epiiugs/2016/v39i3/99741.

Bowman, D.M.J.S., Balch, J.K., Artaxo, P., Bond, W.J., Carlson, J.M., Cochrane, M.A., D'Antonio, C.M., DeFries, R.S., Doyle, J.C., Harrison, S.P., Johnston, F.H., Keeley, J.E., Krawchuk, M.A., Kull, C.A., et al., 2009, Fire in the Earth System: Science, v. 324, p. 481–485.

Bown, P.R., and Lord, A.R., 1990, The occurrence of calcareous nannofossils in the Triassic/Jurassic boundary interval: Les Cahiers de l'Université Catholique de Lyon, Serie Sciences, v. 3, p. 127–136.

Brand, W.A., Coplen, T.B., Vogl, J., Rosner, M., and Prohaska, T., 2014, Assessment of international reference materials for isotope-ratio analysis (IUPAC technical report): Pure and Applied Chemistry, v. 86, p. 425–467, doi: 10.1515/pac-2013-1023.

Brannon, J.M., Pennington, J.C., McFarland, V.A., and Hayes, C., 1995, The effects of sediment contact time on Koc of nonpolar organic contaminants: Environmental Science & Technology, v. 31, p. 3465–3473.

Brański, P., 2014, Climatic disaster at the Triassic-Jurassic boundary - a clay minerals and major elements record from the Polish Basin: Geological Quarterly, v. 58, p. 291–310, doi: 10.7306/gq.1161.

Brański, P., 2009, Influence of palaeoclimate and the green house effect on Hettangian clay mineral assemblages (Holy Cross Mts. area, Polish Basin): Geological Quarterly, v. 53, p. 363–368.

Brański, P., 2012, The mineralogical record of the Early Toarcian stepwise climate changes and other environmental variations (Ciechocinek Formation, Polish Basin): Volumina Jurassica, v. 10, p. 1–24.

Brański, P., and Mikulski, S.Z., 2016, Rare earth element distribution in fine-grained deposits from the uppermost Triassic and Lower Jurassic of the Polish Basin: provenance and weathering in the source area: Geological Quarterly, v. 60, doi: 10.7306/gq.1288.

Brooks, J.R., Flanagan, L.B., Buchmann, N., and Ehleringer, J.R., 1997, Carbon isotope composition of boreal plants: functional groupings of life forms: Oecologia, v. 110, p. 301–311.

Brooks, J.R., Flanagan, L.B., and Ehleringer, J.R., 1998, Responses of boreal conifers to climate fluctuations: indications from tree-ring widths and carbon isotope analyses: Canadian Journal of Forest Research, v. 28, p. 524–533, doi: 10.1139/x98-018.

Burgess, S.D., Bowring, S.A., Fleming, T.H., and Elliot, D.H., 2015, High-precision geochronology links the Ferrar large igneous province with early-Jurassic ocean anoxia and biotic crisis: Earth and Planetary Science Letters, v. 415, p. 90–99, doi: 10.1016/j.epsl.2015.01.037.

Cao, Y., Xing, L., Zhang, T., and Liao, W.-H., 2017, Science of the Total Environment Multi-proxy evidence for decreased terrestrial contribution to sedimentary organic matter in coastal areas of the East China Sea during the past 100 years: Science of the Total Environment, v. 599–600, p. 1895–1902, doi: 10.1016/j.scitotenv.2017.05.159.

Carcaillet, C., Almquist, H., Asnong, H., Bradshaw, R.H., Carrion, J.S., Gaillard, M.J., Gajewski, K., Haas, J.N., Haberle, S.G., Hadorn, P., Muller, S.D., Richard, P.J., Richoz, I., Rosch, M., et al., 2002, Holocene biomass burning and global dynamics of the carbon cycle: Chemosphere, v. 49, p. 845–863, doi: 10.1016/S0045-6535(02)00385-5.

Carcaillet, C., Bouvier, M., Fréchette, B., Larouche, A.C., and Richard, P.J.H., 2001, Comparison of pollen-slide and sieving methods in lacustrine charcoal analyses for local and regional fire history: The Holocene, v. 11, p. 467–476, doi: 10.1191/095968301678302904.

Caruthers, A.H., Gröcke, D.R., and Smith, P.L., 2011, The significance of an Early Jurassic (Toarcian) carbon-isotope excursion in Haida Gwaii (Queen Charlotte Islands), British Columbia, Canada: Earth and Planetary Science Letters, v. 307, p. 19–26, doi: 10.1016/j.epsl.2011.04.013.

Caruthers, A.H., Smith, P.L., and Gröcke, D.R., 2014, The Pliensbachian-Toarcian (Early Jurassic) extinction: A North American perspective: Geological Society of America Special Paper, v. 505, doi: 10.1130/2014.2505(11).For.

Chaloner, W.G., 1989, Fossil charcoal as an indicator of palaeoatmospheric oxygen level: Journal of the Geological Society, v. 146, p. 171–174, doi: 10.1144/gsjgs.146.1.0171.

Chiodini, G., Caliro, S., Aiuppa, A., Avino, R., Granieri, D., Moretti, R., and Parello, F., 2011, First 13C/12C isotopic characterisation of volcanic plume CO2: Bulletin of Volcanology, v. 73, p. 531–542, doi: 10.1007/s00445-010-0423-2.

Ciarapica, G., 2007, Regional and global changes around the Triassic-Jurassic boundary reflected in the late Norian-Hettangian history of the Apennine basins: Palaeogeography, Palaeoclimatology, Palaeoecology, v. 244, p. 34–51, doi: 10.1016/j.palaeo.2006.06.022.

Cieśla, E., 1979, Budowa geologiczna strefy wychodni liasu między Gowarczowem a Rozwadami: Kwartalnik Geologiczny, v. 5, p. 381–393.

Cirilli, S., Marzoli, A., Tanner, L., Bertrand, H., Buratti, N., Jourdan, F., Bellieni, G., Kontak, D., and Renne, P.R., 2009, Latest Triassic onset of the Central Atlantic Magmatic Province (CAMP) volcanism in the Fundy Basin (Nova Scotia): New stratigraphic constraints: Earth and Planetary Science Letters, v. 286, p. 514–525, doi: 10.1016/j.epsl.2009.07.021.

Clark, F.R.S., and Russell, D.A., 1981, Fossil charcoal and the palaeoatmosphere: Nature, v. 290, p. 428.

Clémence, M.E., Bartolini, A., Gardin, S., Paris, G., Beaumont, V., and Page, K.N., 2010, Early Hettangian benthic-planktonic coupling at Doniford (SW England). Palaeoenvironmental implications for the aftermath of the end-Triassic crisis: Palaeogeography, Palaeoclimatology, Palaeoecology, v. 295, p. 102–115, doi: 10.1016/j.palaeo.2010.05.021.

Cohen, A.S., Coe, A.L., Harding, S.M., and Schwark, L., 2004, Osmium isotope evidence for the regulation of atmospheric CO2 by continental weathering: Geology, v. 32, p. 157–160, doi: 10.1130/G20158.1.

Cohen, A.S., Coe, A.L., and Kemp, D.B., 2007, The Late Palaeocene Early

Eocene and Toarcian (Early Jurassic) carbon isotope excursions: a comparison of their time scales, associated environmental changes, causes and consequences: Journal of the Geological Society, v. 164, p. 1093–1108, doi: 10.1144/0016-76492006-123.

Cohen, K.M., Finney, S.C., Gibbard, P.L., and Fan, J.-X., 2013, The ICS International Chronostratigraphic Chart: Episodes, v. 36, p. 199–204.

Collister, J.W., Rieley, G., Stern, B., Eglinton, G., and Fry, B., 1994, Compound-specific $\delta13C$ analyses of leaf lipids from plants with differing carbon dioxide metabolisms: Organic Geochemistry, v. 21, p. 619–627, doi: 10.1016/0146-6380(94)90008-6.

Cope, M.J., and Chaloner, W.G., 1980, Fossil charcoal as evidence of past atmospheric composition: Nature, v. 283, p. 647–649.

Cope, M.J., and Chaloner, W.G., 1981, Reply: Nature, p. 428.

Coplen, T.B., 1995, Discontinuance of SMOW and PDB: Nature, v. 375, p. 285.

Coplen, T.B., Brand, W.A., Gehre, M., Gröning, M., Meijer, H.A.J., Toman, B., and Verkouteren, R.M., 2006, New guidelines for $\delta13C$ measurements: Analytical Chemistry, v. 78, p. 2439–2441, doi: 10.1021/ac052027c.

Cornelissen, J.H.C., Lavorel, S., Garnier, E., Diaz, S., Buchmann, N., Gurvich, D.E., Reich, P.B., Ter Steege, H., Morgan, H.D., Van Der Heijden, M.G.A., Pausas, J.G., and Pooter, H., 2003, Handbook of protocols for standardised and easy measurement of plant functional traits worldwide . Aust J Bot A handbook of protocols for standardised and easy measurement of plant functional traits worldwide: Australian Journal of Botany, v. 51, p. 335–380, doi: 10.1071/BT02124.

Craig, H., 1953, The geochemistry of the stable carbon isotopes: Geochimica et Cosmochimica Acta, v. 3, p. 53–92.

Cresta, S., Goy, A., Ureta, S., Arias, C., Barrón, E., Bernad, J., Canales, M., García-Joral, F., García-Romero, E., Gialanella, P.R., Gomez, J.J., Gonzalez, J.A., Herrero, C., Martinez, G., et al., 2001, The Global Boundary Stratotype Section and Point (GSSP) of the Toarcian-Aalenian boundary (Lower-Middle Jurassic): Episodes, v. 24, p. 166–175, doi: 10.1080/0969594X.2010.527701.

Črne, A.E., Weissert, H., Goričan, Š., and Bernasconi, S.M., 2011, A

biocalcification crisis at the Triassic-Jurassic boundary recorded in the Budva Basin (Dinarides, Montenegro): Bulletin of the Geological Society of America, v. 123, p. 40–50, doi: 10.1130/B30157.1.

Dadlez, R., 1962, Equivalents of the Połomia beds of the Częstochowa Lias in the western margin area of the Święty Krzyż Mountains (Polish, English Summary): Kwartalnik Geologiczny, v. 6, p. 447–459.

Dadlez, R., 2003, Mesozoic thickness pattern in the Mid-Polish Trough: Geological Quarterly, v. 47, p. 223–240.

Dadlez, R., and Kopik, J., 1972, Stratigraphy and palaeogeography of the Jurassic: Biuletyn Instytutu Geologicznego, v. 252, p. 149–171.

Danise, S., Twitchett, R.J., and Little, C.T.S., 2015, Environmental controls on Jurassic marine ecosystems during global warming: Geology, v. 43, p. 263–266, doi: 10.1130/G36390.1.

Deczkowski, Z., 1997, Jura dolna — formalne i nieformalne jednostki litostratygraficzne [Eng. Sum.]: Prace Państwowego Instytutu Geologicznego, v. 153, p. 195- 196; 205-206.

Deenen, M., Ruhl, M., and Bonis, N., 2010, A new chronology for the end-Triassic mass extinction: Earth and Planetary Science Letters, v. 291, p. 113–125, doi: 10.1016/j.epsl.2010.01.003.

Deines, P., 1980, The isotopic composition of reduced organic carbon, *in* Fritz, P. and Fontes, J.C. eds., Handbook of Environmental Isotope Geochemistry. The Terrestrial Environment, vol. 1, Amsterdam, Elsevier, p. 329–406.

Dera, G., Brigaud, B., Monna, F., Laffont, R., Pucéat, E., Deconinck, J.F., Pellenard, P., Joachimski, M.M., and Durlet, C., 2011, Climatic ups and downs in a disturbed Jurassic world: Geology, v. 39, p. 215–218, doi: 10.1130/G31579.1.

Dera, G., Pellenard, P., Neige, P., Deconinck, J.F., Pucéat, E., and Dommergues, J.L., 2009, Distribution of clay minerals in Early Jurassic Peritethyan seas: Palaeoclimatic significance inferred from multiproxy comparisons: Palaeogeography, Palaeoclimatology, Palaeoecology, v. 271, p. 39–51, doi: 10.1016/j.palaeo.2008.09.010.

Duarte, L. V, 1998, Clay minerais and geochemical evolution in the Toarcian-lower Aalenian of the lusitanian basin (Portugal): Cuadernos de Geologia

Iberica, v. 24, p. 69–98.

Eckmeier, E., Gerlach, R., Skjemstad, J.O., Ehrmann, O., and Schmidt, M.W.I., 2007, Minor changes in soil organic carbon and charcoal concentrations detected in a temperate deciduous forest a year after an experimental slash-and-burn: Biogeosciences, v. 4, p. 377–383, doi: 10.5194/bg-4-377-2007.

Eckmeier, E., Rosch, M., Ehrmann, O., Schmidt, M.W.I., Schier, W., and Gerlach, R., 2007, Conversion of biomass to charcoal and the carbon mass balance from a slash-and-burn experiment in a temperate deciduous forest: The Holocene, v. 17, p. 539–542, doi: 10.1177/0959683607077041.

Ehleringer, J.R., and Cerling, T.E., 1995, Atmospheric CO2 and the ratio of intercellular to ambient CO2 concentrations in plants: Tree Physiology, v. 15, p. 105–111, doi: 10.1093/treephys/15.2.105.

Elliott, J.G., and Parker, R.S., 2001, Developing a post-fire flood chronology and recurrence probability from alluvial stratigraphy in the Buffalo Creek watershed, Colorado, USA: Hydrological Processes, v. 15, p. 3039–3051, doi: 10.1002/hyp.390.

Ellis, L., Singh, R.A.J.K., Alexander, R., Kagi, R.I., and Ellis, L., 1995, Identification and occurrence of dihydro-ar-curcumene in crude oils and sediments: Organic Geochemistry, v. 23, p. 197–203.

Embry, A.F., and Suneby, L.B., 1994, The Triassic-Jurassic boundary in the Sverdrup Basin, Arctic Canada: Pangea: Global Environments and Resources, v. 17, p. 857–868.

Fantasia, A., Föllmi, K.B., Adatte, T., Bernárdez, E., and Jorge, E., 2018, The Toarcian Oceanic Anoxic Event in southwestern Gondwana: An example from the Andean Basin, northern Chile: Journal of the Geological Society, v. jgs2018-00.

Farquhar, G.D., Ehleringer, J.R., and Hubick, K.T., 1989, Carbon Isotope Discrimination And Photosynthesis: Annual Review of Plant Physiology & Plant Molecular Biology, v. 40, p. 503–537.

Farquhar, G., O'Leary, M., and Berry, J., 1982, On the Relationship Between Carbon Isotope Discrimination and the Intercellular Carbon Dioxide Concentration in Leaves: Australian Journal of Plant Physiology, v. 9, p. 121, doi: 10.1071/PP9820121.

Feist-Burkhardt, S., Götz, A.E., Szulc, J., Borkhataria, R., Jordan, P., Kempf, O., Michalík, J., Nawrocki, J., Reinhardt, L., Ricken, W., Röhling, H.-G., Rüffer, T., Török, Á., and Zühlke, R., 2008, Triassic, *in* McCann, T. ed., The Geology of Central Europe. Volume 2: Mesozoic and Cenozoic, Geological Society, London, p. 749–821.

Felber, R., Weissert, H.J., Furrer, H., and Bontognali, T.R.R., 2015, The Triassic-Jurassic boundary in the shallow-water marine carbonates from the western Northern Calcareous Alps (Austria): Swiss Journal of Geosciences, v. 108, p. 213–224, doi: 10.1007/s00015-015-0192-1.

Fernandez, P., Vilanova, R.M., Martinez, C., Appleby, P., and Grimalt, J.O., 2000, The Historical Record of Atmospheric Pyrolytic Pollution over Europe Registered in the Sedimentary PAH from Remote Mountain Lakes: Environmental Science & Technology, v. 34, p. 1906–1913.

Finkelstein, D.B., Pratt, L.M., Curtin, T.M., and Brassell, S.C., 2005, Wildfires and seasonal aridity recorded in Late Cretaceous strata from south-eastern Arizona, USA: Sedimentology, v. 52, p. 587–599, doi: 10.1111/j.1365-3091.2005.00712.x.

French, D.W., Huguet, C., Turich, C., Wakeham, S.G., Carlson, L.T., and Ingalls, A.E., 2015, Spatial distributions of core and intact glycerol dialkyl glycerol tetraethers (GDGTs) in the Columbia River Basin and Willapa Bay, Washingto : Insights into origin and implications for the BIT index: Organic Geochemistry, v. 88, p. 91–112, doi: 10.1016/j.orggeochem.2015.09.001.

French, K.L., Sepúlveda, J., Trabucho-Alexandre, J., Gröcke, D.R., and Summons, R.E., 2014, Organic geochemistry of the early Toarcian oceanic anoxic event in Hawsker Bottoms, Yorkshire, England: Earth and Planetary Science Letters, v. 390, p. 116–127, doi: 10.1016/j.epsl.2013.12.033.

Frenklach, M., 2002, Reaction mechanism of soot formation in flames: Physical Chemistry Chemical Physics, v. 4, p. 2028–2037, doi: 10.1039/b110045a.

Freyer, H.-D., 1980, Record of environmental variability by 13C measurements in tree rings, *in* Jacoby, G.C. ed., Proc. Int. Meeting on Stable Isotopes in Tree Ring Research, New York.

Friedman, I., O'Neil, J., and Cebula, G., 1982, Two New Carbonate Stable-Isotope Standards: Geostandards Newsletter, v. 6, p. 11–12.

Galli, M.T., Jadoul, F., Bernasconi, S.M., Cirilli, S., and Weissert, H., 2007, Stratigraphy and palaeoenvironmental analysis of the Triassic-Jurassic transition in the western Southern Alps (Northern Italy): Palaeogeography, Palaeoclimatology, Palaeoecology, v. 244, p. 52–70, doi: 10.1016/j.palaeo.2006.06.023.

Galli, M., Jadoul, F., Bernasconi, S.M., and Weissert, H., 2005, Anomalies in global carbon cycling and extinction at the Triassic/Jurassic boundary: evidence from a marine C-isotope record: Palaeogeography, Palaeoclimatology, Palaeoecology, v. 216, p. 203–214, doi: 10.1016/j.palaeo.2004.11.009.

George, S.C., 1992, Effect of igneous intrusion on the organic geochemistry of a siltstone and an oil shale horizon in the Midland Valley of Scotland: Organic Geochemistry, v. 18, p. 705–723, doi: 10.1016/0146-6380(92)90097-H.

Gierliński, G., 1991, New dinosaur ichnotaxa from the Early Jurassic of the Holy Cross Mountains, Poland: Palaeogeography, Palaeoclimatology, Palaeoecology, v. 85, p. 137–148.

Gierliński, G., Pieńkowski, G., and Niedźwiedzki, G., 2004, Tetrapod track assemblage in the Hettangian of Sołtyków, Poland, and its paleoenvironmental background: Ichnos, v. 11, p. 195–213, doi: 10.1080/10420940490444861.

Glasspool, I.J., and Scott, A.C., 2010, Phanerozoic concentrations of atmospheric oxygen reconstructed from sedimentary charcoal: Nature Geoscience, v. 3, p. 627–630, doi: 10.1038/ngeo923.

Golonka, J., 2007, Late Triassic and Early Jurassic palaeogeography of the world: Palaeogeography, Palaeoclimatology, Palaeoecology, v. 244, p. 297–307, doi: 10.1016/j.palaeo.2006.06.041.

Gómez, J.J., and Goy, A., 2005, Late Triassic and Early Jurassic palaeogeographic evolution and depositional cycles of the Western Tethys Iberian platform system (Eastern Spain): Palaeogeography, Palaeoclimatology, Palaeoecology, v. 222, p. 77–94, doi: 10.1016/j.palaeo.2005.03.010.

Gómez, J.J., and Goy, A., 2011, Warming-driven mass extinction in the Early Toarcian (Early Jurassic) of northern and central Spain. Correlation with

other time-equivalent European sections: Palaeogeography, Palaeoclimatology, Palaeoecology, v. 306, p. 176–195, doi: 10.1016/j.palaeo.2011.04.018.

Gómez, J., Goy, A., and Barrón, E., 2007, Events around the Triassic–Jurassic boundary in northern and eastern Spain: a review: Palaeogeography, Palaeoclimatology, Palaeoecology, v. 244, p. 89–110, doi: 10.1016/j.palaeo.2006.06.025.

Gómez, J.J., Goy, A., and Canales, M.L., 2008, Seawater temperature and carbon isotope variations in belemnites linked to mass extinction during the Toarcian (Early Jurassic) in Central and Northern Spain. Comparison with other European sections: Palaeogeography, Palaeoclimatology, Palaeoecology, v. 258, p. 28–58, doi: 10.1016/j.palaeo.2007.11.005.

Greene, S., Martindale, R., Ritterbush, K., Bottjer, D., Corsetti, F., and Berelson, W., 2012, Recognising ocean acidification in deep time: An evaluation of the evidence for acidification across the Triassic-Jurassic boundary: Earth-Science Reviews, v. 113, p. 72–93, doi: 10.1016/j.earscirev.2012.03.009.

Griffin, J.J., and Goldberg, E.D., 1979, Morphologies and Origin of Elemental Carbon in the Environment: Science, v. 206, p. 563–566.

Gröcke, D.R., Hori, R.S., Trabucho-Alexandre, J., Kemp, D.B., and Schwark, L., 2011, An open ocean record of the Toarcian oceanic anoxic event: Solid Earth, v. 2, p. 245–257, doi: 10.5194/se-2-245-2011.

Gröcke, D.R., Rimmer, S.M., Yoksoulian, L.E., Cairncross, B., Tsikos, H., and van Hunen, J., 2009, No evidence for thermogenic methane release in coal from the Karoo-Ferrar large igneous province: Earth and Planetary Science Letters, v. 277, p. 204–212, doi: 10.1016/j.epsl.2008.10.022.

Guex, J., Bartolini, A., Atudorei, V., and Taylor, D., 2004, High-resolution ammonite and carbon isotope stratigraphy across the Triassic–Jurassic boundary at New York Canyon (Nevada): Earth and Planetary Science Letters, v. 225, p. 29–41, doi: 10.1016/j.epsl.2004.06.006.

Guy, R.D., Reid, D.M., and Krouse, H.R., 1980, Shifts in Carbon Isotope Ratios of Two C3 Halophytes Under Natural and Artifical Conditions: Oecologia, v. 44, p. 241–247.

Haas, J., Götz, A.E., and Pálfy, J., 2010, Late Triassic to early Jurassic

palaeogeography and eustatic history in the NW Tethyan realm: New insights from sedimentary and organic facies of the Cso{double-acute}v??r Basin (Hungary): Palaeogeography, Palaeoclimatology, Palaeoecology, v. 291, p. 456–468, doi: 10.1016/j.palaeo.2010.03.014.

Haines, E.B., 1976, Stable carbon isotopes in the biota, soils and tidal waters of a Georgia salt marsh: Estuarine and Coastal Marine Science, v. 4, p. 604–609.

Hall, D.O., and Rao, K.K., 1999, Photosynthesis: Cambridge University Press, 1-214 p.

Hallam, A., 2001, A review of the broad pattern of Jurassic sea-level changes and their possible causes in the light of current knowledge: Palaeogeography, Palaeoclimatology, Palaeoecology, v. 167, p. 23–37, doi: 10.1016/S0031-0182(00)00229-7.

Hallam, A., 1997, Estimates of the amount and rate of sea-level change across the Rhaetian—Hettangian and Pliensbachian—Toarcian boundaries (latest Triassic to early Jurassic): Journal of the Geological Society, v. 154, p. 773–779, doi: 10.1144/gsjgs.154.5.0773.

Hallam, A., 1990, The end-Triassic mass extinction event: Geological Society of America Special Paper, v. 247, p. 577–583.

Hallam, A., and Goodfellow, W.D., 1990, Facies and geochemical evidence bearing on the end-Triassic disappearance of the Alpine reef ecosystem: Historical Biology, v. 4, p. 131–138, doi: 10.1080/08912969009386538.

Hallam, A., and Wignall, P., 1999, Mass extinctions and sea-level changes: Earth-Science Reviews, v. 48, p. 217–250.

Halsall, C.J., Sweetman, A.J., Barrie, L.A., and Jones, K.C., 2001, Modelling the behaviour of PAHs during atmospheric transport from the UK to the Arctic: Atmospheric Environment, v. 35, p. 255–267.

Handoh, I.C., and Lenton, T.M., 2003, Periodic mid-Cretaceous oceanic anoxic events linked by oscillations of the phosphorus and oxygen biogeochemical cycles: Global Biogeochemical Cycles, v. 17, p. n/a-n/a, doi: 10.1029/2003gb002039.

Hanna, A.J.M., Shanahan, T.M., and Allison, M.A., 2016, Distribution of branched GDGTs in surface sediments from the Colville River, Alaska: Implications for

the MBT'/CBT paleothermometer in Arctic marine sediments: Journal of Geophysical Research: Biogeosciences, v. 121, p. 1762–1780, doi: 10.1002/2015JG003266.Received.

Haq, B.U., Hardenbol, J.A.N., and Vail, P.R., 1987, Chronology of Fluctuating Sea Levels Since the Triassic: Science, v. 235, p. 1156–1167.

Harries, P., and Little, C., 1999, The early Toarcian (Early Jurassic) and the Cenomanian–Turonian (Late Cretaceous) mass extinctions: similarities and contrasts: Palaeogeography, Palaeoclimatology, Palaeoecology, v. 154, p. 39–66.

Hatzinger, P.B., and Alexander, M., 1995, Effect of Aging of Chemicals in Soil on Their Biodegradability and Extractability: Environmental Science & Technology, v. 29, p. 537–545.

Hautmann, M., 2004, Effect of end-Triassic CO2 maximum on carbonate sedimentation and marine mass extinction: Facies, v. 50, p. 257–261, doi: 10.1007/s10347-004-0020-y.

Hautmann, M., Benton, M.J., and Tomasovych, A., 2008, Catastrophic ocean acidification at the Triassic-Jurassic boundary: Neues Jahrbuch für Geologie und Paläontologie - Abhandlungen, v. 249, p. 119–127, doi: 10.1127/0077-7749/2008/0249-0119.

Helby, R.J., 1987, A palynological zonation of the Australian Mesozoic: Memoirs of the Association of Australasian Palaeontologists, v. 4, p. 1–94.

Hermoso, M., Le Callonnec, L., Minoletti, F., Renard, M., and Hesselbo, S.P., 2009, Expression of the Early Toarcian negative carbon-isotope excursion in separated carbonate microfractions (Jurassic, Paris Basin): Earth and Planetary Science Letters, v. 277, p. 194–203, doi: 10.1016/j.epsl.2008.10.013.

Herschberger, K.L., Barns, S.M., Reysenbach, A.-L., Dawson, S.C., and Pace, N.R., 1996, Wide diversity of Crenarchaeota: Nature, v. 384, p. 420.

Hesselbo, S.P., Bjerrum, C.J., Hinnov, L.A., MacNiocaill, C., Miller, K.G., Riding, J.B., Van De Schootbrugge, B., Abels, H., Belcher, C., Blau, J., Browning, J., Cartwright, J., Condon, D., Daines, S., et al., 2013, Mochras borehole revisited: A new global standard for Early Jurassic earth history: Scientific Drilling, p. 81–91, doi: 10.5194/sd-16-81-2013.

Hesselbo, S., Gröcke, D., and Jenkyns, H., 2000, Massive dissociation of gas hydrate during a Jurassic oceanic anoxic event: Nature, v. 406, p. 392–395.

Hesselbo, S., Jenkyns, H., Duarte, L. V, and Oliveria, L.C., 2007, Carbon-isotope record of the Early Jurassic (Toarcian) Oceanic Anoxic Event from fossil wood and marine carbonate (Lusitanian Basin, Portugal): Earth and Planetary Science Letters, v. 253, p. 455–470, doi: 10.1016/j.epsl.2006.11.009.

Hesselbo, S., McRoberts, C., and Pálfy, J., 2007, Triassic–Jurassic boundary events: problems, progress, possibilities: Palaeogeography, Palaeoclimatology, Palaeoecology, v. 244, p. 1–10, doi: 10.1016/j.palaeo.2006.06.020.

Hesselbo, S.P., Meister, C., and Gröcke, D.R., 2000, A potential global stratotype for the Sinemurian–Pliensbachian boundary (Lower Jurassic), Robin Hood's Bay, UK: ammonite faunas and isotope stratigraphy: Geological Magazine, v. 137, p. 601–607.

Hesselbo, S.P., and Pienkowski, G., 2011, Stepwise atmospheric carbon-isotope excursion during the Toarcian Oceanic Anoxic Event (Early Jurassic, Polish Basin): Earth and Planetary Science Letters, v. 301, p. 365–372, doi: 10.1016/j.epsl.2010.11.021.

Hesselbo, S.P., Robinson, S.A., and Surlyk, F., 2004, Sea-level change and facies development across potential Triassic-Jurassic boundary horizons, SW Britain: Journal of the Geological Society, v. 161, p. 365–379, doi: 10.1144/0016-764903-033.

Hesselbo, S.P., Robinson, S. a., Surlyk, F., and Piasecki, S., 2002, Terrestrial and marine extinction at the Triassic-Jurassic boundary synchronized with major carbon-cycle perturbation: A link to initiation of massive volcanism? Geology, v. 30, p. 251–254, doi: 10.1130/0091-7613(2002)030<0251.

Higuera, P.E., Peters, M.E., Brubaker, L.B., and Gavin, D.G., 2007, Understanding the origin and analysis of sediment-charcoal records with a simulation model: Quaternary Science Reviews, v. 26, p. 1790–1809, doi: 10.1016/j.quascirev.2007.03.010.

Hillebrandt, A. von, and Krystyn, L., 2009, On the oldest Jurassic ammonites of Europe (Northern Calcareous Alps, Austria) and their global significance:

Neues Jahrbuch für Geologie und Paläontologie - Abhandlungen, v. 253, p. 163–195, doi: 10.1127/0077-7749/2009/0253-0163.

Hillebrandt, A. v, Krystyn, L., Kürschner, W.M., Bonis, N.R., Ruhl, M., Richoz, S., Schobben, M. a, Urlichs, M., Bown, P.R., Kment, K., McRoberts, C. a, Simms, M., and Tomãsových, A., 2013, The Global Stratotype Sections and Point (GSSP) for the base of the Jurassic System at Kuhjoch (Karwendel Mountains, Northern Calcareous Alps, Tyrol, Austria): Episodes, v. 36, p. 162–198.

Hobbie, E.A., and Werner, R.A., 2004, Bulk carbon isotope patterns in C 3 and C 4 plants : a review and synthesis: New Phytologist, v. 161, p. 371–385, doi: 10.1046/j.1469-8137.2004.00970.x.

Hönig, M.R., John, C.M., and Manning, C., 2016, Development of an equatorial carbonate platform across the Triassic-Jurassic boundary and links to global palaeoenvironmental changes (Musandam Peninsula, UAE/Oman): Gondwana Research, doi: http://dx.doi.org/10.1016/j.gr.2016.11.007.

Hopmans, E.C., Weijers, J.W.H., Schefuß, E., Herfort, L., Sinninghe Damsté, J.S., and Schouten, S., 2004, A novel proxy for terrestrial organic matter in sediments based on branched and isoprenoid tetraether lipids: Earth and Planetary Science Letters, v. 224, p. 107–116, doi: 10.1016/j.epsl.2004.05.012.

Hounslow, M.W., Posen, P.E., and Warrington, G., 2004, Magnetostratigraphy and biostratigraphy of the Upper Triassic and lowermost Jurassic succession, St. Audrie's Bay, UK: Palaeogeography, Palaeoclimatology, Palaeoecology, v. 213, p. 331–358, doi: 10.1016/j.palaeo.2004.07.018.

Hren, M.T., Pagani, M., Erwin, D.M., and Brandon, M., 2018, Biomarker reconstruction of the early Eocene paleotopography and paleoclimate of the northern Sierra Nevada: Geology, p. 7–10, doi: 10.1130/G30215.1.

Hudspith, V.A., and Belcher, C.M., 2017, Observations of the structural changes that occur during charcoalification: implications for identifying charcoal in the fossil record: Palaeontology, v. Rapid Comm, p. 503–510, doi: 10.1111/pala.12304.

Huguet, C., Smittenberg, R.H., Boer, W., Sinninghe Damsté, J.S., and Schouten, S., 2007, Twentieth century proxy records of temperature and soil organic

matter input in the Drammensfjord, southern Norway: Organic Geochemistry, v. 38, p. 1838–1849, doi: 10.1016/j.orggeochem.2007.06.015.

Huynh, T., and Poulsen, C., 2005, Rising atmospheric CO2 as a possible trigger for the end-Triassic mass extinction: Palaeogeography, Palaeoclimatology, Palaeoecology, v. 217, p. 223–242, doi: 10.1016/j.palaeo.2004.12.004.

ICCP, 2001, New inertinite classification (ICCP System 1994): Fuel, v. 80, p. 459–471, doi: 10.1016/S0016-2361(00)00102-2.

Izumi, K., Kemp, D.B., Itamiya, S., and Inui, M., 2018, Sedimentary evidence for enhanced hydrological cycling in response to rapid carbon release during the early Toarcian oceanic anoxic event: Earth and Planetary Science Letters, v. 481, p. 162–170, doi: 10.1016/j.epsl.2017.10.030.

Javoy, M., Pineau, F., and Delorme, H., 1986, Carbon and nitrogen isotopes in the mantle: Chemical Geology, v. 57, p. 41–62, doi: 10.1016/0009-2541(86)90093-8.

Jenkyns, H.C., 2003, Evidence for rapid climate change in the Mesozoic-Palaeogene greenhouse world: Philosophical Transactions: Mathematical, Physical and Engineering Sciences, v. 361, p. 1885–1916.

Jenkyns, H., 2010, Geochemistry of oceanic anoxic events: Geochemistry, Geophysics, Geosystems, v. 11, p. n/a-n/a, doi: 10.1029/2009GC002788.

Jenkyns, H., 1988, The Early Toarcian (Jurassic) Anoxic Event: Stratigraphic, Sedimentary, and Geochemical Evidence: American Journal of Science, v. 288, p. 101–151.

Jenkyns, H.C., 1985, The early Toarcian and Cenomanian-Turonian anoxic events in Europe: comparisons and contrasts: Geologische Rundschau, v. 74, p. 505–518, doi: 10.1007/BF01821208.

Jenkyns, H.C., and Clayton, C.J., 1986, Black shales and carbon isotopes in pelagic sediments from the Tethyan Lower Jurassic: Sedimentology, v. 33, p. 87–106, doi: 10.1111/j.1365-3091.1986.tb00746.x.

Jenkyns, H.C., and Clayton, C., 1997, Lower Jurassic epicontinental carbonates and mudstones from England and Wales: chemostratigraphic signals and the early Toarcian anoxic event: Sedimentology, v. 44, p. 687–706.

Jenkyns, H.C., Jones, C.E., GrOcke, D.R., Hesselbo, S.P., and Parkinson, D.N.,

2002, Chemostratigraphy of the Jurassic System: applications, limitations and implications for palaeoceanography: Journal of the Geological Society, v. 159, p. 351–378, doi: 10.1144/0016-764901-130.

Jenkyns, H.C., Schouten-Huibers, L., Schouten, S., and Sinninghe Damsté, J.S., 2012, Warm Middle Jurassic-Early Cretaceous high-latitude sea-surface temperatures from the Southern Ocean: Climate of the Past, v. 8, p. 215–225, doi: 10.5194/cp-8-215-2012.

Jiang, C., Alexander, R., Kagi, R., and Murray, A., 1998, Polycyclic aromatic hydrocarbons in ancient sediments and their relationships to palaeoclimate: Organic Geochemistry, v. 29, p. 1721–1735.

Jimenez, A.P., Jimenez de Cisneros, C., Rivas, O., and Vera, J.A., 1996, The Early Toarcian Anoxic Event in the Westernmost Tethys (Subbetic): Paleogeographic and Paleobiogeographic Significance: The Journal of Geology, v. 104, p. 399–416.

Johnsen, A.R., Wick, L.Y., and Harms, H., 2005, Principles of microbial PAH-degradation in soil: Environmental Pollution, v. 133, p. 71–84, doi: 10.1016/j.envpol.2004.04.015.

Jones, T.P., Ash, S., and Figueiral, I., 2002, Late Triassic charcoal from Petrified Forest National Park, Arizona, USA: Palaeogeography, Palaeoclimatology, Palaeoecology, v. 188, p. 127–139.

Jones, T., and Chaloner, W., 1991, Fossil charcoal, its recognition and palaeoatmospheric significance: Palaeogeography, Palaeoclimatology, Palaeoecology, v. 7, p. 39–50.

Jones, T.P., and Lim, B., 2000, Extraterrestrial impacts and wildfires: Palaeogeography, Palaeoclimatology, Palaeoecology, v. 164, p. 57–66, doi: 10.1016/S0031-0182(00)00175-9.

Jones, T.P., Scott, A.C., and Cope, M., 1991, Reflectance Measurements and the Temperature of Formation of Modern Charcoals and Implications for Studies of Fusain: Bulletin De La Societe Geologique De France, v. 162, p. 193–200.

Jurkiewiczowa, I., 1967, The Lias of the Western part of the Mesozoic Zone surrounding the Świêtokrzyskie (Holy Cross) Mountains and its correlation with the Lias of the Cracow-Wieluń Range: Biuletyn Państwowego Instytutu

Geologicznego, v. 200, p. 5–32.

Karaszewski, W., 1962, The stratigraphy of the Lias in the northern Mesozoic zone surrounding the Święty Krzyż Mountains (Central Poland): Prace Państwowego Instytutu Geologicznego, v. 30, p. 333–416.

Kawano, T., Sasaki, N., Hayashi, T., and Takahara, H., 2012, Grassland and fire histroy since the late-glacial in northern part of Aso Caldera, central Kyusyu, Japan, inferred from phytolith and charcoal records: Quaternary International, v. 254, p. 18–27, doi: 10.1016/j.quaint.2010.12.008.

Kemp, D.B., Coe, A.L., Cohen, A.S., and Schwark, L., 2005, Astronomical pacing of methane release in the Early Jurassic period: Nature, v. 437, p. 396–399, doi: 10.1038/nature04361.

Kemp, D.B., and Izumi, K., 2014, Multiproxy geochemical analysis of a Panthalassic margin record of the early Toarcian oceanic anoxic event (Toyora area, Japan): Palaeogeography, Palaeoclimatology, Palaeoecology, v. 414, p. 332–341, doi: 10.1016/j.palaeo.2014.09.019.

Kemp, D.B., Robinson, S.A., Crame, J.A., Francis, J.E., Ineson, J., Whittle, R.J., and Brien, C.O., 2014, A cool temperate climate on the Antarctic Peninsula through the latest Cretaceous to early Paleogene: Geology, v. 42, p. 583–586, doi: 10.1130/G35512.1.

Kent, D. V., Olsen, P.E., and Muttoni, G., 2017, Astrochronostratigraphic polarity time scale (APTS) for the Late Triassic and Early Jurassic from continental sediments and correlation with standard marine stages: Earth-Science Reviews, v. 166, p. 153–180, doi: 10.1016/j.earscirev.2016.12.014.

Killops, S.D., and Massoud, M.S., 1992, Polycyclic aromatic hydrocarbons of pyrolytic origin in ancient sediments: evidence for Jurassic vegetation fires: Organic Geochemistry, v. 18, p. 1–7.

Kim, J., Schouten, S., Buscail, R., Ludwig, W., Bonnin, J., Sinninghe Damsté, J.S., and Bourrin, F., 2006, Origin and distribution of terrestrial organic matter in the NW Mediterranean (Gulf of Lions): Exploring the newly developed BIT index: Geochem. Geophys. Geosyst., v. 7, p. 1–20, doi: 10.1029/2006GC001306.

Kislov, V. V., Sadovnikov, A.I., and Mebel, A.M., 2013, Formation mechanism of polycyclic aromatic hydrocarbons beyond the second aromatic ring: Journal

of Physical Chemistry A, v. 117, p. 4794–4816, doi: 10.1021/jp402481y.

Knobbe, T.K., and Schaller, M.F., 2018, A tight coupling between atmospheric pCO2and sea-surface temperature in the Late Triassic: Geology, v. 46, p. 43–46, doi: 10.1130/G39405.1.

Koga, Y., Nishihara, M., Morii, H., and Akagawa-matsushita, M., 1993, Ether Polar Lipids of Methanogenic Bacteria: Structures, Comparative Aspects, and Biosyntheses: Microbiological Reviews, v. 57, p. 164–182.

Komarek, E. V., 1967, The nature of lightning fires.: Proceedings of the Tall Timbers Ecology Conference, v. 7, p. 5–41.

Kopik, J., 1964, Stratigraphy of the Lower Jurassic based on the fauna of the Mechowo IG-1 borehole: Biuletyn Instytutu Geologicznego, v. 189, p. 43–55.

Korte, C., Hesselbo, S.P., Jenkyns, H.C., Rickaby, R.E.M., and Spotl, C., 2009, Palaeoenvironmental significance of carbon- and oxygen-isotope stratigraphy of marine Triassic-Jurassic boundary sections in SW Britain: Journal of the Geological Society, v. 166, p. 431–445, doi: 10.1144/0016-76492007-177.

Korte, C., Hesselbo, S.P., Ullmann, C. V., Dietl, G., Ruhl, M., Schweigert, G., and Thibault, N., 2015, Jurassic climate mode governed by ocean gateway: Nature Communications, v. 6, p. 1–7, doi: 10.1038/ncomms10015.

Kozłowska, M., Barski, M., Mieszkowski, R., and Antoszewska, K., 2016, A new Triassic-Jurassic section in the southern part of the Holy Cross Mts. (Poland) – implications for palaeogeography: Geological Quarterly, v. 60, p. 365–384, doi: 10.7306/gq.1259.

Kozydra, Z., 1968, Deposits of Lower Jurassic refractory clays in the light of general geological structure in the northern margin ofthe Świêtokrzyskie Mountains [Eng. Sum.]: Biuletyn Instytutu Geologicznego, v. 216, p. 5–94.

Krzywiec, P., 2002, Mid-Polish Trough inversion – seismic examples, main mechanisms, and its relationship to the Alpine-Carpathian collision: Stephan Mueller Special Publication Series, v. 1, p. 151–165, doi: 10.5194/smsps-1-151-2002.

Kump, L., and Arthur, M., 1999, Interpreting carbon-isotope excursions: carbonates and organic matter: Chemical Geology, v. 161, p. 181–198.

Kuroda, J., Hori, R.S., Suzuki, K., Gröcke, D.R., and Ohkouchi, N., 2010, Marine

osmium isotope record across the Triassic-Jurassic boundary from a Pacific pelagic site: Geology, v. 38, p. 1095–1098, doi: 10.1130/G31223.1.

Kürschner, W.M., Bonis, N., and Krystyn, L., 2007, Carbon-isotope stratigraphy and palynostratigraphy of the Triassic–Jurassic transition in the Tiefengraben section—Northern Calcareous Alps (Austria): Palaeogeography, Palaeoclimatology, Palaeoecology, v. 244, p. 257–280, doi: 10.1016/j.palaeo.2006.06.031.

Küspert, W., 1982, Environmental changes during oil shale deposition as deduced from stable isotope ratios, *in* Cyclic and event stratification, Berlin, Springer, p. 482–501.

Kuypers, M.M.M., Blokker, P., Erbacher, J., Kinkel, H., Pancost, R.D., and Damsté, J.S.S., 2001, Massive expansion ofmarine Archaea during amid-Cretaceous oceanic anoxic event: Science, v. 293, p. 92–94.

Kvenvolden, K.A., 1995, A review of the geochemistry of methane in natural gas hydrate: Organic Geochemistry, v. 23, p. 997–1008, doi: 10.1016/0146-6380(96)00002-2.

Laflamme, R.E., and Hites, R.A., 1978, The global distribution of polycyclic aromatic hydrocarbons in recent sediments: Geochimica et Cosmochimica Acta, v. 42, p. 289–303, doi: 10.1016/0016-7037(78)90182-5.

Lake, J., Norwood, C., Dimock, C., and Robert, B., 1979, Origins of polycyclic aromatic hydrocarbons in estuarine sediments: Geochimica et Cosmochimica Acta, v. 43, p. 1847–1854, doi: 10.1016/0016-7037(79)90033-4.

Lamb, A.L., Vane, C.H., Wilson, G.P., Rees, J.G., and Moss-Hayes, V.L., 2007, Assessing ??13C and C/N ratios from organic material in archived cores as Holocene sea level and palaeoenvironmental indicators in the Humber Estuary, UK: Marine Geology, v. 244, p. 109–128, doi: 10.1016/j.margeo.2007.06.012.

Lamb, A.L., Wilson, G.P., and Leng, M.J., 2006, A review of coastal palaeoclimate and relative sea-level reconstructions using δ13C and C/N ratios in organic material: Earth-Science Reviews, v. 75, p. 29–57, doi: 10.1016/j.earscirev.2005.10.003.

Landrum, P.F., 1989, Bioavailability and Toxicokinetics of Polycyclic Aromatic

Hydrocarbons Sorbed to Sediments for the Amphipod Pontoporeia hoyi: Environmental Science & Technology, v. 23, p. 588–595.

Leavitt, S.W., and Long, A., 1991, Seasonal stable-carbon isotope variability in tree rings: possible paleoenvironmental signals: Chemical Geology: Isotope Geoscience section, v. 87, p. 59–70, doi: 10.1016/0168-9622(91)90033-S.

Ledesma, E.B., Kalish, M.A., Nelson, P.F., Wornat, M.J., and Mackie, J.C., 2006, Formation and fate of PAH during the pyrolysis and fuel-rich combustion of coal primary tar: Fuel, v. 79, p. 1801–1814.

Leister, D.L., and Baker, J.E., 1994, Atmospheric deposition of organic contaminants to the Chesapeake Bay: Atmospheric Environment, v. 28, p. 1499–1520.

Lenton, T.M., 2003, The coupled evolution of life and atmospheric oxygen, *in* Rothschild, L. and Lister, A. eds., Evolution on Planet Earth: Impact of the Physical Environment, Academic Press.

Lenton, T.M., and Watson, A.J., 2000, Redfield revisited 2. What regulates the oxygen content of the atmosphere? Global Biogeochemical Cycles, v. 14, p. 249–268, doi: 10.1002/(ISSN)1944-9224.

Leonowicz, P., 2004, Trace fossils from the Lower Jurassic Ciechocinek Formation, SW Poland: Volumina Jurassica, v. 6, p. 89–98.

Lindström, S., Pedersen, G.K., Van De Schootbrugge, B., Hansen, K.H., Kuhlmann, N., Thein, J., Johansson, L., Petersen, H.I., Alwmark, C., Dybkjær, K., Weibel, R., Erlström, M., Nielsen, L.H., Oschmann, W., et al., 2015, Intense and widespread seismicity during the end-Triassic mass extinction due to emplacement of a large igneous province: Geology, v. 43, p. 387–390, doi: 10.1130/G36444.1.

Lindström, S., van de Schootbrugge, B., Dybkjær, K., Pedersen, G.K., Fiebig, J., Nielsen, L.H., and Richoz, S., 2012, No causal link between terrestrial ecosystem change and methane release during the end-Triassic mass extinction: Geology, v. 40, p. 531–534, doi: 10.1130/G32928.1.

Lindström, S., van de Schootbrugge, B., Hansen, K.H., Pedersen, G.K., Alsen, P., Thibault, N., Dybkjær, K., Bjerrum, C., and Nielsen, L.H., 2016, A new correlation of Triassic–Jurassic boundary successions in NW Europe, Nevada and Peru, and the Central Atlantic Magmatic Province: A time-line

for the end-Triassic mass extinction: Palaeogeography, Palaeoclimatology, Palaeoecology, doi: 10.1016/j.palaeo.2016.12.025.

Little, C.T.S., and Benton, M.J., 1995, Early Jurassic mass extinction: a global long-term event: Geology, v. 23, p. 495–498, doi: 10.1130/0091-7613(1995)023<0495.

Long, C.J., Whitlock, C., Bartlein, P.J., and Millspaugh, S.H., 1998, A 9000-year fire history from the Oregon Coast Range, based on a high-resolution charcoal study: Canadian Journal of Forest Research, v. 28, p. 774–787, doi: 10.1139/cjfr-28-5-774.

Loomis, S.E., Russell, J.M., and Sinninghe Damsté, J.S., 2011, Distributions of branched GDGTs in soils and lake sediments from western Uganda: Implications for a lacustrine paleothermometer: Organic Geochemistry, v. 42, p. 739–751, doi: 10.1016/j.orggeochem.2011.06.004.

Lopes dos Santos, R.A., and Vane, C.H., 2016, Organic Geochemistry Signatures of tetraether lipids reveal anthropogenic overprinting of natural organic matter in sediments of the Thames Estuary, UK: Organic Geochemistry, v. 93, p. 68–76, doi: 10.1016/j.orggeochem.2016.01.003.

Lucas, S.G., 1994, Triassic Tetrapod Extinctions and the Compiled Correlation Effect: Pangea: Global Environments and Resources, p. 869–875.

Lucas, S.G., and Tanner, L.H., 2007, The nonmarine Triassic-Jurassic boundary in the Newark Supergroup of eastern North America: Earth-Science Reviews, v. 84, p. 1–20, doi: 10.1016/j.earscirev.2007.05.002.

Lund, J.J., 1977, Rhaetic to Lower Liassic palynology of the onshore south-eastern North Sea Basin: Danmarks Geologiske UndersÝgelse, v. 2, p. 1–129.

MacGregor, B.J., Moser, D.P., Alm, E.W., Nealson, K.H., and Stahl, D.A., 1997, Crenarchaeota in Lake Michigan Sediment: Applied and Environmental Microbiology, v. 63, p. 1178–1181.

Mander, L., Kuerschner, W.M., and McElwain, J.C., 2010, An explanation for conflicting records of Triassic–Jurassic plant diversity: Proceedings of the National Academy of Sciences, v. 107, p. 15351–15356, doi: 10.1073/pnas.1004207107.

Marcinkiewicz, T., 1960, Megaspores analysis of Jurassic deposits in the Gorzów

Śląski-Praszka area [Eng. Sum.]: Kwartalnik Geologiczny, v. 4, p. 713–733.

Marlon, J., Bartlein, P.J., and Whitlock, C., 2006, Fire-fuel-climate linkages in the northwestern USA during the Holocene: The Holocene, v. 16, p. 1059–1071, doi: 10.1177/0959683606069396.

Marynowski, L., and Filipiak, P., 2007, Water column euxinia and wildfire evidence during deposition of the Upper Famennian Hangenberg event horizon from the Holy Cross Mountains (central Poland): Geological Magazine, v. 144, p. 569–595, doi: 10.1017/S0016756807003317.

Marynowski, L., Scott, A., Zatoń, M., Parent, H., and Garrido, A., 2011, First multi-proxy record of Jurassic wildfires from Gondwana: Evidence from the Middle Jurassic of the Neuquén Basin, Argentina: Palaeogeography, Palaeoclimatology, Palaeoecology, v. 299, p. 129–136, doi: 10.1016/j.palaeo.2010.10.041.

Marynowski, L., and Simoneit, B.R.T., 2009, Widespread Upper Triassic To Lower Jurassic Wildfire Records From Poland: Evidence From Charcoal and Pyrolytic Polycyclic Aromatic Hydrocarbons: Palaios, v. 24, p. 785–798, doi: 10.2110/palo.2009.p09-044r.

Marzoli, A., Bertrand, H., Knight, K., and Cirilli, S., 2004, Synchrony of the Central Atlantic magmatic province and the Triassic-Jurassic boundary climatic and biotic crisis: Geology, v. 32, p. 973–976, doi: 10.1130/G20652.1.

Mayall, M.J., 1983, An earthquake origin for synsedimentary deformation in a late Triassic (Rhaetian) lagoonal sequence, southwest Britain: Geological Magazine, v. 120, p. 613–622, doi: 10.1017/S001675680002776X.

McArthur, J.M., Donovan, D.T., Thirlwall, M.F., Fouke, B.W., and Mattey, D., 2000, Strontium isotope profile of the early Toarcian (Jurassic) oceanic anoxic event, the duration of ammonite biozones, and belemnite palaeotemperatures: Earth and Planetary Science Letters, v. 179, p. 269–285, doi: 10.1016/S0012-821X(00)00111-4.

McCarroll, D., Gagen, M.H., Loader, N.J., Robertson, I., Anchukaitis, K.J., Los, S., Young, G.H.F., Jalkanen, R., Kirchhefer, A., and Waterhouse, J.S., 2009, Correction of tree ring stable carbon isotope chronologies for changes in the carbon dioxide content of the atmosphere: Geochimica et Cosmochimica Acta, v. 73, p. 1539–1547, doi: 10.1016/j.gca.2008.11.041.

McElwain, J.C., Beerling, D.J., and Woodward, F.I., 1999, Fossil Plants and Global Warming at the Triassic-Jurassic Boundary: Science, v. 285, p. 1386–1390, doi: 10.1126/science.285.5432.1386.

McElwain, J.C., Popa, M.E., Hesselbo, S.P., Haworth, M., and Surlyk, F., 2007, Macroecological Responses of Terrestrial Vegetation to Climatic and Atmospheric Change across the Triassic/Jurassic Boundary in East Greenland: Paleobiology, v. 33, p. 547–573.

McElwain, J., Wade-Murphy, J., and Hesselbo, S., 2005, Changes in carbon dioxide during an oceanic anoxic event linked to intrusion into Gondwana coals: Nature, v. 435, p. 479–482, doi: 10.1038/nature03618.

McElwain, J., Wagner, P., and Hesselbo, S., 2009, Fossil plant relative abundances indicate sudden loss of Late Triassic biodiversity in East Greenland: Science, v. 324, p. 1554–1556, doi: 10.1126/science.1171706.

McGrath, T.E., Chan, W.G., and Hajaligol, M.R., 2003, Low temperature mechanism for the formation of polycyclic aromatic hydrocarbons from the pyrolysis of cellulose: Journal of Analytical and Applied Pyrolysis, v. 66, p. 51–70.

McParland, L., Collinson, M., Scott, A., and Campbell, G., 2009, The use of reflectance values for the interpretation of natural and anthropogenic charcoal assemblages: Archaeological and Anthropological Sciences, v. 1, p. 249–261, doi: 10.1007/s12520-009-0018-z.

McRoberts, C., Furrer, H., and Jones, D., 1997, Palaeoenvironmental interpretation of a Triassic-Jurassic boundary section from Western Austria based on palaeoecological and geochemical data: Palaeogeography, Palaeoclimatology, Palaeoecology, v. 136, p. 79–95.

Medina, E., and Minchin, P., 1980, Stratification of δ13C values of leaves in Amazonian rain forests: Oecologia, v. 45, p. 377–378, doi: 10.1007/BF00540209.

Meija, J., Coplen, T.B., Berglund, M., Brand, W.A., De Bièvre, P., Gröning, M., Holden, N.E., Irrgeher, J., Loss, R.D., Walczyk, T., and Prohaska, T., 2016a, Atomic weights of the elements 2013 (IUPAC Technical Report): Pure and Applied Chemistry, v. 88, p. 265–291, doi: 10.1515/pac-2015-0305.

Meija, J., Coplen, T.B., Berglund, M., Brand, W.A., De Bièvre, P., Gröning, M.,

Holden, N.E., Irrgeher, J., Loss, R.D., Walczyk, T., and Prohaska, T., 2016b, Isotopic compositions of the elements 2013 (IUPAC Technical Report): Pure and Applied Chemistry, v. 88, p. 293–306, doi: 10.1515/pac-2015-0503.

Meister, C., Aberhan, M., Blau, J., Dommergues, J., Feist-burkhardt, S., Hailwood, E.A., Hart, M., and Hesselbo, S.P., 2006, The Global Boundary Stratotype Section and Point (GSSP) for the base of the Pliensbachian Stage (Lower Jurassic), Wine Haven, Yorkshire, UK: Episodes, v. 29, p. 93–106.

Meyers, P. a., 1997, Organic geochemical proxies of paleoceanographic, paleolimnologic, and paleoclimatic processes: Organic Geochemistry, v. 27, p. 213–250, doi: 10.1016/S0146-6380(97)00049-1.

Meyers, P. a., 1994, Preservation of elemental and isotopic source identification of sedimentary organic matter: Chemical Geology, v. 114, p. 289–302, doi: 10.1016/0009-2541(94)90059-0.

Meyers, P.A., and Ishiwatari, R., 1993, Lacustrine organic geochemistry-an overview of indicators of organic matter sources and diagenesis in lake sediments: Organic Geochemistry, v. 20, p. 867–900, doi: 10.1016/0146-6380(93)90100-P.

Middelburg, J.J., and Nieuwenhuize, J., 1998, Carbon and nitrogen stable isotopes in suspended matter and sediments from the Schelde Estuary: Marine Chemistry, v. 60, p. 217–225, doi: 10.1016/S0304-4203(97)00104-7.

Morante, R., and Hallam, A., 1996, Organic carbon isotopic record across the Triassic-Jurassic boundary in Austria and its bearing on the cause of the mass extinction: Geology, v. 24, p. 391–394, doi: 10.1130/0091-7613(1996)024<0391.

Mossoczy, Z., 1961, New stratigraphic division of Lias in the northern part of Cracow-Czêstochowa Jura [Eng. Sum.]: Kwartalnik Geologiczny, v. 5, p. 81–100.

Murchison, D.G., and Raymond, A.C., 1989, Igneous activity and organic maturation in the Midland Valley of Scotland: International Journal of Coal Geology, v. 14, p. 47–82, doi: 10.1016/0166-5162(89)90078-5.

Nabbefeld, B., Grice, K., Summons, R.E., Hays, L.E., and Cao, C., 2010, Applied Geochemistry Significance of polycyclic aromatic hydrocarbons (PAHs) in Permian/Triassic boundary sections: Applied Geochemistry, v. 25, p. 1374–

1382, doi: 10.1016/j.apgeochem.2010.06.008.

Nichols, G.J., Cripps, J.A., Collinson, M.E., and Scott, A.C., 2000, Experiments in waterlogging and sedimentology of charcoal: Results and implications: Palaeogeography, Palaeoclimatology, Palaeoecology, v. 164, p. 43–56, doi: 10.1016/S0031-0182(00)00174-7.

Niedźwiedzki, G., and Pienkowski, G., 2005, A dinosaur track association from the Early Jurassic deltaic deposits of Podole near Opatów, Poland: Geological Quarterly, v. 48, p. 333–338.

Niedźwiedzki, G., and Pieńkowski, G., 2016, A dinosaur track assemblage from the Upper Hettangian (Lower Jurassic) marginal-marine deposits of Zapniów, Holy Cross Mountains, Poland: Geological Quarterly, v. 60, p. 840–856, doi: 10.7306/gq.1310.

Nielsen, L.H., and Japsen, P., 1991, Deep wells in Denmark 1935-1990.: Danmarks Geologiske Undersøgelse Serie A, v. 31, p. 1–177.

Niemann, H., Stadnitskaia, A., Wirth, S.B., Gilli, A., Anselmetti, F.S., Sinninghe Damsté, J.S., Schouten, S., Hopmans, E.C., and Lehmann, M.F., 2012, Bacterial GDGTs in Holocene sediments and catchment soils of a high Alpine lake: application of the MBT/CBT-paleothermometer: Climate of the Past, v. 8, p. 889–906, doi: 10.5194/cp-8-889-2012.

Nordt, L., Tubbs, J., and Dworkin, S., 2016, Stable carbon isotope record of terrestrial organic materials for the last 450 Ma yr: Earth-Science Reviews, v. 159, p. 103–117, doi: 10.1016/j.earscirev.2016.05.007.

O'Leary, M., 1981, Carbon Isotope Fractionation in Plants: Phytochemistry, v. 20, p. 553–567.

O'Leary, M.H., 1988, Carbon Isotopes in Photosynthesis: BioScience, v. 38, p. 328–336, doi: 10.2307/1310735.

Olsen, P., Kent, D., Sues, H.-D., and Koeberl, C., 2002, Ascent of dinosaurs linked to an iridium anomaly at the Triassic-Jurassic boundary: Science, v. 296, p. 1305–1307, doi: 10.1126/science.1065522.

Oros, D.R., and Simoneit, B.R.T., 2000, Identification and emission rates of molecular tracers in coal smoke particulate matter: Fuel, v. 79, p. 515–536.

Pacyna, G., 2013, Critical review of research on the Lower Jurassic flora of Poland: Acta Palaeobotanica, v. 53, p. 141–163, doi: 10.2478/acpa-2013-

0015.

Pacyna, G., 2014, Plant remains from the Polish Triassic. Present knowledge and future prospects: Acta Palaeobotanica, v. 54, p. 3–33, doi: 10.2478/acpa-2014-0001.

Page, D.S., Boehm, P.D., Douglas, G.S., Bence, A.E., Burns, W.A., and Mankiewicz, P.J., 1999, Pyrogenic Polycyclic Aromatic Hydrocarbons in Sediments Record Past Human Activity: A Case Study in Prince William Sound, Alaska: Marine Pollution Bulletin, v. 38, p. 247–260.

Pálfy, J., Demény, A., Haas, J., Carter, E.S., Görög, Á., Halász, D., Oravecz-Scheffer, A., Hetényi, M., Márton, E., Orchard, M.J., Ozsvárt, P., Veto, I., and Zajzon, N., 2007, Triassic-Jurassic boundary events inferred from integrated stratigraphy of the Csovár section, Hungary: Palaeogeography, Palaeoclimatology, Palaeoecology, v. 244, p. 11–33, doi: 10.1016/j.palaeo.2006.06.021.

Pálfy, J., Demény, A., Haas, J., and Hetényi, M., 2001, Carbon isotope anomaly and other geochemical changes at the Triassic-Jurassic boundary from a marine section in Hungary: Geology, v. 29, p. 1047–1050, doi: 10.1130/0091-7613(2001)029<1047.

Pálfy, J., and Kocsis, Á., 2014, Volcanism of the Central Atlantic magmatic province as the trigger of environmental and biotic changes around the Triassic-Jurassic boundary: The Geological Society of America, v. 505, p. 245–261, doi: 10.1130/2014.2505(12).

Park, R., and Epstein, S., 1960, Carbon isotope fractionation during photosynthesis: Geochimica et Cosmochimica Acta, v. 21.

Percival, L.M.E., Cohen, A.S., Davies, M.K., Dickson, A.J., Hesselbo, S.P., Jenkyns, H.C., Leng, M.J., Mather, T.A., Storm, M.S., and Xu, W., 2016, Osmium isotope evidence for two pulses of increased continental weathering linked to Early Jurassic volcanism and climate change: Geology, v. 44, p. 759–762, doi: 10.1130/G37997.1.

Percival, L.M.E., Ruhl, M., Hesselbo, S.P., Jenkyns, H.C., Mather, T.A., and Whiteside, J.H., 2017, Mercury evidence for pulsed volcanism during the end-Triassic mass extinction: Proceedings of the National Academy of Sciences, p. 201705378, doi: 10.1073/PNAS.1705378114.

Percival, L.M.E., Witt, M.L.I., Mather, T.A., Hermoso, M., Jenkyns, H.C., Hesselbo, S.P., Al-Suwaidi, A.H., Storm, M.S., Xu, W., and Ruhl, M., 2015, Globally enhanced mercury deposition during the end-Pliensbachian extinction and Toarcian OAE: A link to the Karoo-Ferrar Large Igneous Province: Earth and Planetary Science Letters, v. 428, p. 267–280, doi: 10.1016/j.epsl.2015.06.064.

Peters, K.E., Sweeney, R.E., and Kaplan, I.R., 1978, Correlation of carbon and nitrogen stable isotope ratios in sedimentary organic matter: Limnology and Oceanography, v. 23, p. 598–604.

Peters, K.E., Walters, C.C., and Moldowan, J.M., 2007, Source- and age-related biomarker parameters, *in* The Biomarker Guide, Volume 2: Biomarkers and Isotopes in Petroluem Exploration and Earth History, Cambridge University Press, p. 483–607.

Peterse, F., Kim, J.H., Schouten, S., Kristensen, D.K., Koç, N., and Sinninghe Damsté, J.S., 2009, Constraints on the application of the MBT/CBT palaeothermometer at high latitude environments (Svalbard, Norway): Organic Geochemistry, v. 40, p. 692–699, doi: 10.1016/j.orggeochem.2009.03.004.

Peterse, F., van der Meer, J., Schouten, S., Weijers, J.W.H., Fierer, N., Jackson, R.B., Kim, J.-H., and Sinninghe Damsté, J.S., 2012, Revised calibration of the MBT–CBT paleotemperature proxy based on branched tetraether membrane lipids in surface soils: Geochimica et Cosmochimica Acta, v. 96, p. 215–229, doi: 10.1016/j.gca.2012.08.011.

Peterse, F., Nicol, G.W., Schouten, S., and Sinninghe, J.S., 2010, Organic Geochemistry Influence of soil pH on the abundance and distribution of core and intact polar lipid-derived branched GDGTs in soil: Organic Geochemistry, v. 41, p. 1171–1175, doi: 10.1016/j.orggeochem.2010.07.004.

Petersen, H.I., and Lindström, S., 2012, Synchronous Wildfire Activity Rise and Mire Deforestation at the Triassic-Jurassic Boundary: PLoS ONE, v. 7, p. e47236, doi: 10.1371/journal.pone.0047236.

Peterson, B., Fry, B., Hullar, M., Saupe, S., and Wright, R., 1994, The Distribution and Stable Carbon Isotopic Composition of Dissolved Organic Carbon in

Estuaries: Estuaries, v. 17, p. 111–121, doi: 10.2307/1352560.

Pieńkowski, G., 1998, Dinosaur nesting ground from the Early Jurassic fluvial deposits, Holy Cross Mountains (Poland): Geological Quarterly, v. 42, p. 461–476.

Pieńkowski, G., 2015, Geologiczne składowanie ditlenku węgla (CCS) jest metodą bezpieczną–dowody geologiczne: Przegląd Geologiczny, v. 63, p. 48–54.

Pieńkowski, G., 2004, The epicontinental Lower Jurassic of Poland: Polish Geological Institute Special Papers, v. 12, p. 5–154.

Pieńkowski, G., 2014, The first Early Jurassic ammonite find in central Poland: Volumina Jurassica, v. 12, p. 99–104.

Pienkowski, G., and Niedźwiedzki, G., 2010, Invertebrate trace fossil assemblages from the Lower Hettangian of Soltyków, Holy Cross Mountains, Poland: Volumina Jurassica, v. 6, p. 109–131.

Pienkowski, G., Niedzwiedzki, G., and Branski, P., 2014, Climatic reversals related to the Central Atlantic magmatic province caused the end-Triassic biotic crisis - Evidence from continental strata in Poland: Geological Society of America Special Paper, v. 505, doi: 10.1130/2014.2505(13).

Pienkowski, G., Niedzwiedzki, G., and Waksmundzka, M., 2012, Sedimentological, palynological and geochemical studies of the terrestrial Triassic–Jurassic boundary in northwestern Poland: Geological Magazine, v. 149, p. 308–332, doi: 10.1017/S0016756811000914.

Pieńkowski, G., Schudack, M.E., Bosák, P., Enay, R., Feldman-Olszewska, A., Golonka, J., Krobicki, M., Lathuliere, B., Leinfelder, R.R., Michalík, J., Mönnig, E., Noe-Nygaard, N., Pálfy, J., Pint, A., et al., 2008, Jurassic, *in* McCann, T. ed., The Geology of Central Europe. Volume 2: Mesozoic and Cenozoic, Geological Society, London, p. 823–922.

Pieńkowski, G., and Uchman, A., 2010, Ptychoplasma conica isp. nov.-a new bivalve locomotion trace fossil from the Lower Jurassic (Hettangian) alluvial sediments of Soltyków, Holy Cross Mountains,: Geological Quarterly, v. 53, p. 397–406, https://gq.pgi.gov.pl/article/view/7528 (accessed December 2014).

Pienkowski, G., and Waksmundzka, M., 2009, Palynofacies in Lower Jurassic

epicontinental deposits of Poland: Tool to interpret sedimentary environments: Episodes, v. 32, p. 21–32.

Power, M.J., Marlon, J., Ortiz, N., Bartlein, P.J., Harrison, S.P., Mayle, F.E., Ballouche, A., Bradshaw, R.H.W., Carcaillet, C., Cordova, C., Mooney, S., Moreno, P.I., Prentice, I.C., Thonicke, K., et al., 2007, Changes in fire activity since the Last Glacial Maximum: an assessment based on a global synthesis and analysis of charcoal data: Climate Dynamics, v. 30, p. 887–907, doi: 10.1007/s00382-007-0334-x.

Powers, L., Werne, J.P., Vanderwoude, A.J., Sinninghe Damsté, J.S., Hopmans, E.C., and Schouten, S., 2010, Organic Geochemistry Applicability and calibration of the TEX86 paleothermometer in lakes: Organic Geochemistry, v. 41, p. 404–413, doi: 10.1016/j.orggeochem.2009.11.009.

Prahl, F.G., Bennett, J.T., and Carpenter, R., 1980, The early diagenesis of aliphatic hydrocarbons and organic matter in sedimentary particulates from Dabob Bay, Washington: Geochimica et Cosmochimica Acta, v. 44, p. 1967–1976, doi: 10.1016/0016-7037(80)90196-9.

Price, C., 2000, Evidence for a link between global lightning activity and upper tropospheric water vapour: Nature, v. 406, p. 290–3, doi: 10.1038/35018543.

Price, C., and Rind, D., 1994, The Impact of a 2 x CO2 Climate of Lightning-Caused Fires: Journal of Climate, p. 1484–1494.

Pross, J., Contreras, L., Bijl, P.K., Greenwood, D.R., Bohaty, S.M., Schouten, S., Bendle, J.A., Tauxe, L., Raine, J.I., Huck, C.E., Flierdt, T. Van De, Jamieson, S.S.R., Stickley, C.E., Rohl, U., et al., 2012, Persistent near-tropical warmth on the Antarctic continent during the early Eocene epoch: Nature, v. 488, p. 3–7, doi: 10.1038/nature11300.

Pyne, S.J., Andrews, P.L., and Laven, R.D., 1996, Introduction to wildland fire: New York City, John Wiley and Sons.

Quan, T.M., van de Schootbrugge, B., Field, M.P., Rosenthal, Y., and Falkowski, P.G., 2008, Nitrogen isotope and trace metal analyses from the Mingolsheim core (Germany): Evidence for redox variations across the Triassic-Jurassic boundary: Global Biogeochemical Cycles, v. 22, p. 1–14, doi: 10.1029/2007GB002981.

Rasbash, D.J., and Langford, B., 1968, Burning of wood in atmospheres of

reduced oxygen concentation: Combustion & Flame, v. 12, p. 33–40.

Reeve, N., and Toumi, R., 1999, Lightning activity as an indicator of climate change: Quarterly Journal of the Royal Meteorological Society, v. 125, p. 893–903.

Reymanówna, M., 1993, Forest fire in the lower Liassic of Odrowąż, Poland: Plants and their Environment. Resumes des Communications presentees lors du Premier Congres Europeen de Paleontologie: Organismes-paleoenvironnement interactions. Lyon University, Lyon, v. 111.

Reymanówna, M., 1991, Two conifers from the Liassic flora of Odrowąż in Poland: Palaeovegetational development in Europe and Regions relevant to its palaeofloristic evolution, p. 307–310.

Richter, H., and Howard, J.., 2000, Formation of polycyclic aromatic hydrocarbons and their growth to soot - a review of chemical reaction pathways: v. 26, 565-608 p., doi: 10.1016/S0360-1285(00)00009-5.

Rizzo, A.L., Liuzzo, M., Ancellin, M.A., and Jost, H.J., 2015, Real-time measurements of $\delta^{13}C$, CO_2 concentration, and CO_2/SO_2 in volcanic plume gases at Mount Etna, Italy, over 5 consecutive days: Chemical Geology, v. 411, p. 182–191, doi: 10.1016/j.chemgeo.2015.07.007.

Robinson, S.A., Ruhl, M., Astley, D.L., Naafs, B.D.A., Farnsworth, A.J., Bown, P.R., Jenkyns, H.C., Lunt, D.J., O'Brien, C., Pancost, R.D., and Markwick, P.J., 2017, Early Jurassic North Atlantic sea-surface temperatures from TEX86 palaeothermometry: Sedimentology, v. 64, p. 215–230, doi: 10.1111/sed.12321.

van Roij, L., Sluijs, A., Laks, J.J., and Reichart, G.-J., 2017, Stable carbon isotope analyses of ng quantities of particulate organic carbon (pollen) with laser ablation nano combustion gas chromatography isotope ratio mass spectrometry: Rapid Communications in Mass Spectrometry, v. 31, p. 47–58, doi: 10.1002/rcm.7769.

De Rosa, M., and Gambacorta, A., 1988, The lipids of archaebacteria: Progress in Lipid Research, v. 27, p. 153–175.

Rosales, I., Barnolas, A., Goy, A., Sevillano, A., Armendáriz, M., and López-García, J.M., 2018, Isotope records (C-O-Sr) of late Pliensbachian-early

Toarcian environmental perturbations in the westernmost Tethys (Majorca Island, Spain): Palaeogeography, Palaeoclimatology, Palaeoecology, v. 497, p. 168–185, doi: 10.1016/j.palaeo.2018.02.016.

Rosales, I., Quesada, S., and Robles, S., 2004, Paleotemperature variations of Early Jurassic seawater recorded in geochemical trends of belemnites from the Basque-Cantabrian basin, northern Spain: Palaeogeography, Palaeoclimatology, Palaeoecology, v. 203, p. 253–275, doi: 10.1016/S0031-0182(03)00686-2.

Royer, D., 2001, Stomatal density and stomatal index as indicators of paleoatmospheric CO_2 concentration: Review of Palaeobotany and Palynology, v. 114.

Ruhl, M., Bonis, N., G-J, R., Damsté, J.S.S., and Kuerschner, W.M., 2011, Atmospheric carbon injection linked to end-Triassic mass extinction: Science, v. 430, p. 430–434, doi: 10.1126/science.1204255.

Ruhl, M., Deenen, M.H.L., Abels, H.A., Bonis, N.R., Krijgsman, W., and Kürschner, W.M., 2010, Astronomical constraints on the duration of the early Jurassic Hettangian stage and recovery rates following the end-Triassic mass extinction (St Audrie's Bay/East Quantoxhead, UK): Earth and Planetary Science Letters, v. 295, p. 262–276, doi: 10.1016/j.epsl.2010.04.008.

Ruhl, M., and Kürschner, W.M., 2011, Multiple phases of carbon cycle disturbance from large igneous province formation at the Triassic-Jurassic transition: Geology, v. 39, p. 431–434, doi: 10.1130/G31680.1.

Ruhl, M., Kürschner, W.M., and Krystyn, L., 2009, Triassic – Jurassic organic carbon isotope stratigraphy of key sections in the western Tethys realm (Austria): Earth and Planetary Science Letters, v. 281, p. 169–187, doi: 10.1016/j.epsl.2009.02.020.

Ruhl, M., Veld, H., and Kürschner, W.M., 2010, Sedimentary organic matter characterization of the Triassic-Jurassic boundary GSSP at Kuhjoch (Austria): Earth and Planetary Science Letters, v. 292, p. 17–26, doi: 10.1016/j.epsl.2009.12.046.

Rybicki, M., Marynowski, L., Misz-Kennan, M., and Simoneit, B.R.T., 2016, Organic Geochemistry Molecular tracers preserved in Lower Jurassic

"Blanowice brown coals" from southern Poland at the onset of coalification: Organic geochemical and petrological characteristics: Organic Geochemistry, v. 102, p. 77–92, doi: 10.1016/j.orggeochem.2016.09.012.

Sadori, L., and Giardini, M., 2007, Charcoal analysis, a method to study vegetation and climate of the Holocene: The case of Lago di Pergusa (Sicily, Italy): Geobios, v. 40, p. 173–180, doi: 10.1016/j.geobios.2006.04.002.

Saelen, G., Doyle, P., and Talbot, M.R., 1996, Stable-Isotope Analyses of Belemnite Rostra from the Whitby Mudstone Fm., England: Surface Water Conditions during Deposition of a Marine Black Shale: Palaios, v. 11, p. 97, doi: 10.2307/3515065.

Sage, R.F., 2004, The evolution of C4 photosynthesis: New Phytologist, v. 161, p. 341–370, doi: 10.1046/j.1469-8137.2004.00974.x.

Salomons, W., and Mook, W.G., 1981, Field observation of the isotopic composition of particulate organic carbon in the Southern North Sea and adjacent estuaries: Marine Geology, v. 41, p. M11–M20.

Sandoval, J., Henriques, M.H., Chandler, R.B., and Ureta, S., 2012, Latest Toarcian-earliest Bajocian (Jurassic) Grammoceratinae (Hildoceratidae, Ammonitina) of the western Tethys: Their palaeobiogeographic and phylogenetic significance: Geobios, v. 45, p. 109–119, doi: 10.1016/j.geobios.2011.11.001.

Sanford, R.L., Saldarriage, J., Clark, K.E., Uhl, C., and Herrera, R., 1985, Amazon Rain-Forest Fires: Science, v. 227, p. 53–55.

Sarmiento, J.L., and Toggweiler, J.R., 1984, A new model for the role of the oceans in determining atmospheric PCO2: Nature, v. 308, p. 621–624, doi: 10.1038/308621a0.

Saurer, M., Siegenthaler, U., and Schweingruber, F.H., 1995, The climate-carbon isotope relationship in tree rings and the significance of site conditions: Tellus, v. 47B, p. 320–330.

Saurer, M., Siegwolf, R.T.W., and Schweingruber, F.H., 2004, Carbon isotope discrimination indicates improving water-use efficiency of trees in northern Eurasia over the last 100 years: Global Change Biology, v. 10, p. 2109–2120, doi: 10.1111/j.1365-2486.2004.00869.x.

Schaller, M.F., Wright, J.D., and Kent, D. V, 2011, Atmospheric pCO2

perturbations associated with the Central Atlantic Magmatic Province: Science, v. 331, p. 1404–1409.

Schidlowski, M., Hayes, J.M., and Kaplan, I.R., 1983, Isotopic inferences of ancient biochemistries - Carbon, sulfur, hydrogen, and nitrogen, *in* Scholf, J.W. ed., Earth's Earliest Biosphere, Its Origin and Evolution, Princeton, Princeton University Press, p. 1490186.

Schleser, G.H., 1992, d13C Pattern in a Forest Tree as an Indicator of Carbon Transfer in Trees: Ecology, v. 73, p. 1922–1925.

Schleser, G.H., 1995, Parameters determining carbon isotope ratios in plants, *in* Problems of Stable Isotopes in Tree-Rings, Lake Sediments and Peat Bogs as Climate Evidence for the Holocene, Stuttgart, Fischer Verlag, p. 71–96.

Schoene, B., Guex, J., Bartolini, A., Schaltegger, U., and Blackburn, T.J., 2010, Correlating the end-Triassic mass extinction and flood basalt volcanism at the 100 ka level: Geology, v. 38, p. 387–390, doi: 10.1130/G30683.1.

Van de Schootbrugge, B., Bachan, A., Suan, G., Richoz, S., and Payne, J.L., 2013, Microbes, mud and methane: Cause and consequence of recurrent early Jurassic anoxia following the end-Triassic mass extinction: Palaeontology, v. 56, p. 685–709, doi: 10.1111/pala.12034.

van de Schootbrugge, B., Payne, J.L., Tomasovych, A., Pross, J., Fiebig, J., Benbrahim, M., Föllmi, K.B., and Quan, T.M., 2008, Carbon cycle perturbation and stabilization in the wake of the Triassic-Jurassic boundary mass-extinction event: Geochemistry, Geophysics, Geosystems, v. 9, p. 1–16, doi: 10.1029/2007GC001914.

van de Schootbrugge, B., Quan, T.M., Lindström, S., Püttmann, W., Heunisch, C., Pross, J., Fiebig, J., Petschick, R., Röhling, H.-G., Richoz, S., Rosenthal, Y., and Falkowski, P.G., 2009, Floral changes across the Triassic/Jurassic boundary linked to flood basalt volcanism: Nature Geoscience, v. 2, p. 589–594, doi: 10.1038/ngeo577.

Schouten, S., Hopmans, E.C., and Sinninghe Damsté, J.S., 2013, The organic geochemistry of glycerol dialkyl glycerol tetraether lipids: A review: Organic Geochemistry, v. 54, p. 19–61, doi: 10.1016/j.orggeochem.2012.09.006.

Scott, A.C., 2010, Charcoal recognition, taphonomy and uses in palaeoenvironmental analysis: Palaeogeography, Palaeoclimatology,

Palaeoecology, v. 291, p. 11–39, doi: 10.1016/j.palaeo.2009.12.012.

Scott, A., 2009, Forest Fire in the Fossil Record, *in* Cerda, A. ed., Fire Effects on Soils and Restoration Strategies, CRC Press, p. 1–37, doi: 10.1201/9781439843338-c1.

Scott, A., 1990, Preservation, evolution, and extinction of plants in Lower Carboniferous volcanic sequences in Scotland: Volcanism and Fossil Biotas, v. 244, p. 25–38, doi: 10.1130/SPE244-p25.

Scott, A.C., 2000, The Pre-Quaternary history of fire: Palaeogeography, Palaeoclimatology, Palaeoecology, v. 164, p. 281–329, doi: 10.1016/S0031-0182(00)00192-9.

Scott, A.C., 1988, Volcanoes, fires and the Lower Carboniferous vegetation Scotland: Open University Geological Society Journal, v. 8, p. 27–31.

Scott, A.C., and Damblon, F., 2010, Charcoal: Taphonomy and significance in geology, botany and archaeology: Palaeogeography, Palaeoclimatology, Palaeoecology, v. 291, p. 1–10, doi: 10.1016/j.palaeo.2010.03.044.

Scott, A.C., and Glasspool, I.J., 2005, Charcoal reflectance as a proxy for the emplacement temperature of pyroclastic flow deposits: Geology, v. 33, p. 589, doi: 10.1130/G21474.1.

Scott, A.C., and Glasspool, I.J., 2007, Observations and experiments on the origin and formation of inertinite group macerals: International Journal of Coal Geology, v. 70, p. 53–66, doi: 10.1016/j.coal.2006.02.009.

Scott, A.C., and Glasspool, I.J., 2006, The diversification of Paleozoic fire systems and fluctuations in atmospheric oxygen concentration.: Proceedings of the National Academy of Sciences, v. 103, p. 10861–5, doi: 10.1073/pnas.0604090103.

Scott, A., and Jones, T., 1991, Fossil charcoal: a plant-fossil record preserved by fire: Geology Today, v. 7, p. 214–216.

Sell, B., Ovtcharova, M., Guex, J., Bartolini, A., Jourdan, F., Spangenberg, J.E., Vicente, J.C., and Schaltegger, U., 2014, Evaluating the temporal link between the Karoo LIP and climatic-biologic events of the Toarcian Stage with high-precision U-Pb geochronology: Earth and Planetary Science Letters, v. 408, p. 48–56, doi: 10.1016/j.epsl.2014.10.008.

Sellwood, B.W., and Jenkyns, H.C., 1975, Basins and swells and the evolution of

an epeiric sea (Pliensbachian-Bajocian of Great Britain): Journal of the Geological Society of London, v. 131, p. 373–388.

Shen, W., Sun, Y., Lin, Y., Liu, D., and Chai, P., 2011, Evidence for wildfire in the Meishan section and implications for Permian-Triassic events: Geochimica et Cosmochimica Acta, v. 75, p. 1992–2006, doi: 10.1016/j.gca.2011.01.027.

Simms, M.J., 2003, Uniquely extensive seismite from the latest Triassic of the United Kingdom: Evidence for bolide impact? Geology, v. 31, p. 557, doi: 10.1130/0091-7613(2003)031<0557:UESFTL>2.0.CO;2.

Simms, M.J., 2007, Uniquely extensive soft-sediment deformation in the Rhaetian of the UK: Evidence for earthquake or impact? Palaeogeography, Palaeoclimatology, Palaeoecology, v. 244, p. 407–423, doi: 10.1016/j.palaeo.2006.06.037.

Simoneit, B.R.T., 2002, Biomass burning - a review of organic tracers for smoke from incomplete combustion: Applied Geochemistry, v. 17, p. 129–162.

Sinninghe Damsté, J.S., Hopmans, E.C., Pancost, R.D., and Geenevasen, J.A.J., 2000, Newly discovered non-isoprenoid glycerol dialkyl glycerol tetraether lipids in sediments: Chemical Communications, v. 17, p. 1683–1684, doi: 10.1039/b004517i.

Sinninghe Damsté, J.S., Ossebaar, J., Abbas, B., Schouten, S., and Verschuren, D., 2009, Fluxes and distribution of tetraether lipids in an equatorial African lake: Constraints on the application of the TEX86 palaeothermometer and BIT index in lacustrine settings: Geochimica et Cosmochimica Acta, v. 73, p. 4232–4249, doi: 10.1016/j.gca.2009.04.022.

Sinninghe Damsté, J.S., Ossebaar, J., Schouten, S., and Verschuren, D., 2012, Distribution of tetraether lipids in the 25-ka sedimentary record of Lake Challa: extracting reliable TEX86 and MBT/CBT palaeotemperatures from an equatorial African lake: Quaternary Science Reviews, v. 50, p. 43–54, doi: 10.1016/j.quascirev.2012.07.001.

Sluijs, A., van Roij, L., Frieling, J., Laks, J., and Reichart, G.J., 2018, Single-species dinoflagellate cyst carbon isotope ecology across the Paleocene-Eocene Thermal Maximum: Geology, v. 46, p. 79–82, doi: 10.1130/G39598.1.

Smith, B.N., Herath, H.M.W., and Chase, J.B., 1973, Effect of growth temperature

on carbon isotopic ratios in barley, pea and rape: Plant and Cell Physiology, v. 14, p. 177–181.

Smith, B.N., Oliver, J., and Millan, C.M.C., 1976, Influence of Carbon Source, Oxygen Concentration, Light Intensity, and Temperature on 13C/12C Ratios in Plant Tissues: Botanical Gazette, v. 137, p. 99–104.

Steinthorsdottir, M., Bacon, K.L., Popa, M.E., Bochner, L., and Mcelwain, J.C., 2011, Bennettitalean leaf cuticle fragments (here Anomozamites and Pterophyllum) can be used interchangeably in stomatal frequency-based palaeo-CO 2 reconstructions: Palaeontology, v. 54, p. 867–882, doi: 10.1111/j.1475-4983.2011.01060.x.

Steinthorsdottir, M., Jeram, A.J., and McElwain, J.C., 2011, Extremely elevated CO2 concentrations at the Triassic/Jurassic boundary: Palaeogeography, Palaeoclimatology, Palaeoecology, v. 308, p. 418–432, doi: 10.1016/j.palaeo.2011.05.050.

Suan, G., Mattioli, E., Pittet, B., Lécuyer, C., Suchéras-Marx, B., Duarte, L.V., Philippe, M., Reggiani, L., and Martineau, F., 2010, Secular environmental precursors to Early Toarcian (Jurassic) extreme climate changes: Earth and Planetary Science Letters, v. 290, p. 448–458, doi: 10.1016/j.epsl.2009.12.047.

Suan, G., Mattioli, E., Pittet, B., Mailliot, S., and Lécuyer, C., 2008, Evidence for major environmental perturbation prior to and during the Toarcian (Early Jurassic) oceanic anoxic event from the Lusitanian Basin, Portugal: Paleoceanography, v. 23, p. 1–14, doi: 10.1029/2007PA001459.

Suan, G., Nikitenko, B.L., Rogov, M. a., Baudin, F., Spangenberg, J.E., Knyazev, V.G., Glinskikh, L. a., Goryacheva, A. a., Adatte, T., Riding, J.B., Föllmi, K.B., Pittet, B., Mattioli, E., and Lécuyer, C., 2011, Polar record of Early Jurassic massive carbon injection: Earth and Planetary Science Letters, v. 312, p. 102–113, doi: 10.1016/j.epsl.2011.09.050.

Suan, G., Pittet, B., Bour, I., Mattioli, E., Duarte, L., and Mailliot, S., 2008, Duration of the Early Toarcian carbon isotope excursion deduced from spectral analysis: Consequence for its possible causes: Earth and Planetary Science Letters, v. 267, p. 666–679, doi: 10.1016/j.epsl.2007.12.017.

Svensen, H., Planke, S., Chevallier, L., Malthe-Sørenssen, A., Corfu, F., and

Jamtveit, B., 2007, Hydrothermal venting of greenhouse gases triggering Early Jurassic global warming: Earth and Planetary Science Letters, v. 256, p. 554–566, doi: 10.1016/j.epsl.2007.02.013.

Svensen, H., Planke, S., Polozov, A.G., Schmidbauer, N., Corfu, F., Podladchikov, Y.Y., and Jamtveit, B., 2009, Siberian gas venting and the end-Permian environmental crisis: Earth and Planetary Science Letters, v. 277, p. 490–500, doi: 10.1016/j.epsl.2008.11.015.

Taiz, L., and Zeiger, E., 2010, Plant Physiology: Sinauer Associates, 1-782 p.

Tanner, L.H., Hubert, J.F., and Coffey, B.P., 2001, Stability of atmospheric CO2 levels across the Triassic/Jurassic boundary: Nature, v. 411, p. 675–677.

Taylor, R., 1990, Interpretation of the Correlation Coefficient: A Basic Review: Journal of Diagnostic Medical Sonography, v. 6, p. 35–39.

The World Bank Group, 2018, Country Historical Climate - Poland:, http://sdwebx.worldbank.org/climateportal/index.cfm?page=country_historical_climate&ThisCCode=POL (accessed January 2018).

Them, T.R., Gill, B.C., Caruthers, A.H., Grï¿½cke, D.R., Tulsky, E.T., Martindale, R.C., Poulton, T.P., and Smith, P.L., 2017, High-resolution carbon isotope records of the Toarcian Oceanic Anoxic Event (Early Jurassic) from North America and implications for the global drivers of the Toarcian carbon cycle: Earth and Planetary Science Letters, v. 459, p. 118–126, doi: 10.1016/j.epsl.2016.11.021.

Thevenon, F., Bard, E., Williamson, D., and Beaufort, L., 2004, A biomass burning record from the West Equatorial Pacific over the last 360 ky: Methodological, climatic and anthropic implications: Palaeogeography, Palaeoclimatology, Palaeoecology, v. 213, p. 83–99, doi: 10.1016/j.palaeo.2004.07.003.

Thornton, S.F., and McManus, J., 1994, Application of organic carbon and nitrogen stable isotope and C/N ratios as source indicators of organic matter provenance in estuarine systems: Evidence for the Tay Estuary, Scotland: Estuarine, Coastal and Shelf Science, v. 38, p. 219–233, doi: 10.1006/ecss.1994.1015.

Tierney, J.E., and Russell, J.M., 2009, Distributions of branched GDGTs in a tropical lake system: Implications for lacustrine application of the MBT/CBT

paleoproxy: Organic Geochemistry, v. 40, p. 1032–1036, doi: 10.1016/j.orggeochem.2009.04.014.

Tierney, J.E., Russell, J.M., Eggermont, H., Hopmans, E.C., Verschuren, D., and Sinninghe Damsté, J.S., 2010, Environmental controls on branched tetraether lipid distributions in tropical East African lake sediments: Geochimica et Cosmochimica Acta, v. 74, p. 4902–4918, doi: 10.1016/j.gca.2010.06.002.

Tinner, W., Ammann, B., Conedera, M., Gaggeler, H.W., Sagesser, B., Gedye, S., and Jones, R., 1998, Pollen and charcoal in lake sediments compared with historically documented forest fires in southern Switzerland since AD 1920: The Holocene, v. 8, p. 31–42, doi: 10.1191/095968398667205430.

Troughton, J.H., and Card, K.A., 1975, Temperature Effects on the Carbon-isotope Ratio of C3, C4 and Crassulacean-acid-metabolism (CAM) Plants: Planta, v. 123, p. 185–190, doi: 10.1007/BF00383867.

Troughton, J.H., Card, K.A., and Hendy, C.H., 1974, Photosynthetic pathways and carbon isotope discrimination by plants: Carnegie Institution Yearbook, v. 73, p. 768–780.

Tsapakis, M., Stephanou, E.G., and Karakassis, I., 2003, Evaluation of atmospheric transport as a nonpoint source of polycyclic aromatic hydrocarbons in marine sediments of the Eastern Mediterranean: Marine Chemistry, v. 80, p. 283–298.

Tukey, J.W., 1977, Exploratory Data Analysis: Addison-Wesley, 688 p.

Tyson, R. V, 1995, Sedimentary Organic Matter: Organic Facies and Palynofacies: London, Chapman & Hall.

Uhl, C., and Kauffman, J.B., 1990, Deforestation, Fire Susceptibility, and Potential Tree Responses to Fire in the Eastern Amazon: Ecology, v. 71, p. 437–449.

Uhl, D., and Montenari, M., 2011, Charcoal as evidence of palaeo-wildfires in the Late Triassic of SW Germany: Geological Journal, v. 46, p. 34–41, doi: 10.1002/gj.1229.

Ullmann, C.V., Thibault, N., Ruhl, M., Hesselbo, S.P., and Korte, C., 2014, Effect of a Jurassic oceanic anoxic event on belemnite ecology and evolution.: Proceedings of the National Academy of Sciences, v. 111, p. 10073–6, doi:

10.1073/pnas.1320156111.

Unrug, R., and Calikowski, A., 1960, Sedymentacja i petrografia warstw połomskich: Rocznik Polskiego Towarzystwa Geologicznego, v. 30, p. 129–170.

Urey, H.C., Lowenstam, H. a., Epstein, S., and McKinney, C.R., 1951, Measurement of Paleotemperatures and Temperatures and the Southeastern United States: Bulletin of the geological society of America, v. 62, p. 399–416, doi: 10.1130/0016-7606(1951)62[399:MOPATO]2.0.CO;2.

Vakhrameev, V.A., 1981, Pollen Classopolis: Indicator of Jurassic and Cretaceous Environments: The Palaeobotanist, v. 28–29, p. 301–307.

Venkatesan, M.I., and Dahl, J., 1989, Organic geochemical evidence fpr global fires at the Cretaceous/Tertiary boundary: Nature, v. 338, p. 57–60.

Vetriania, C., Reysenbach, A., and Dore, J., 1998, Recovery and phylogenetic analysis of archaeal rRNA sequences from continental shelf sediments: FEMS Microbiology Letters, v. 161, p. 83–88.

Vogel, G.C., 1978, Recycling of carbon in a forest environment: Oecologia Plant Sciences, v. 13, p. 89–94.

Ward, P.D., Garrison, G.H., Haggart, J.W., Kring, D. a., and Beattie, M.J., 2004, Isotopic evidence bearing on Late Triassic extinction events, Queen Charlotte Islands, British Columbia, and implications for the duration and cause of the Triassic/Jurassic mass extinction: Earth and Planetary Science Letters, v. 224, p. 589–600, doi: 10.1016/j.epsl.2004.04.034.

Ward, P.D., Garrison, G.H., Williford, K.H., Kring, D. a., Goodwin, D., Beattie, M.J., and McRoberts, C. a., 2007, The organic carbon isotopic and paleontological record across the Triassic–Jurassic boundary at the candidate GSSP section at Ferguson Hill, Muller Canyon, Nevada, USA: Palaeogeography, Palaeoclimatology, Palaeoecology, v. 244, p. 281–289, doi: 10.1016/j.palaeo.2006.06.042.

Ward, P.D., Haggart, J.W., Carter, E.S., Wilbur, D., Tipper, H.W., and Evans, T., 2001, Sudden productivity collapse associated with the Triassic-Jurassic boundary mass extinction.: Science, v. 292, p. 1148–51, doi: 10.1126/science.1058574.

Watson, A.J., 1978, Consequences for the biosphere of grassland and forest

fires: University of Reading.

Watson, A., Lovelock, J.E., and Margulis, L., 1978, Methanogenesis, fires and the regulation of atmospheric oxygen: BioSystems, v. 10, p. 293–298, doi: 10.1016/0303-2647(78)90012-6.

Wcislo-Luraniec, E., 1991, Flora from Odrowaz in Poland-a typical Lower Liassic European flora, *in* Kovar-Eder, J. ed., Proceedings, Pan- European Palaeobotanical Conference, Vienna, Vienna, p. 331–334.

Weems, R.E., 1992, The "terminal Triassic catastrophic extinction event" in perspective: a review of Carboniferous through Early Jurassic terrestrial vertebrate extinction patterns: Palaeogeography, Palaeoclimatology, Palaeoecology, v. 94, p. 1–29.

Wegierek, P., and Zherikhin, V.V., 1997, An Early Jurassic insect fauna in the Holy Cross mountains: Acta Palaeontologica Polonica, v. 42, p. 539–543.

Weijers, J.W.H., Panoto, E., Bleijswijk, J. Van, Schouten, S., Rijpstra, I.C., Balk, M., Stams, A.J.M., Damsté, J.S.S., Weijers, J.W.H., Panoto, E., Bleijswijk, J. Van, Schouten, S., Rijpstra, W.I.C., Balk, M., et al., 2009, Constraints on the Biological Source(s) of the Orphan Branched Tetraether Membrane Lipids: Geomicrobiology Journal, v. 26, p. 402–414, doi: 10.1080/01490450902937293.

Weijers, J.W.H., Schouten, S., van den Donker, J.C., Hopmans, E.C., and Sinninghe Damsté, J.S., 2007, Environmental controls on bacterial tetraether membrane lipid distribution in soils: Geochimica et Cosmochimica Acta, v. 71, p. 703–713, doi: 10.1016/j.gca.2006.10.003.

Weijers, J.W.H., Schouten, S., Sluijs, A., Brinkhuis, H., and Sinninghe Damsté, J.S., 2007, Warm arctic continents during the Palaeocene–Eocene thermal maximum: Earth and Planetary Science Letters, v. 261, p. 230–238, doi: 10.1016/j.epsl.2007.06.033.

Weijers, J.W.H., Schouten, S., Spaargaren, O.C., and Sinninghe Damsté, J.S., 2006, Occurrence and distribution of tetraether membrane lipids in soils: Implications for the use of the TEX86 proxy and the BIT index: Organic Geochemistry, v. 37, p. 1680–1693, doi: 10.1016/j.orggeochem.2006.07.018.

Weijers, J.W.H., Steinmann, P., Hopmans, E.C., Schouten, S., and Sinninghe

Damsté, J.S., 2011, Bacterial tetraether membrane lipids in peat and coal: Testing the MBT–CBT temperature proxy for climate reconstruction: Organic Geochemistry, v. 42, p. 477–486, doi: 10.1016/j.orggeochem.2011.03.013.

Whelan, J.R., 1995, The Ecology of Fire: Cambridge University Press.

Whiteside, J.H., Olsen, P.E., Eglinton, T., Brookfield, M.E., and Sambrotto, R.N., 2010, Compound-specific carbon isotopes from Earth's largest flood basalt eruptions directly linked to the end-Triassic mass extinction.: Proceedings of the National Academy of Sciences, v. 107, p. 6721–5, doi: 10.1073/pnas.1001706107.

Whiteside, J.H., Olsen, P.E., Kent, D. V., Fowell, S.J., and Et-Touhami, M., 2007, Synchrony between the Central Atlantic magmatic province and the Triassic–Jurassic mass-extinction event? Palaeogeography, Palaeoclimatology, Palaeoecology, v. 244, p. 345–367, doi: 10.1016/j.palaeo.2006.06.035.

Whitlock, C., 2001, Variations in Holocene Fire Frequency: A View from the Western United States: Biology and Environment: Proceedings of the Royal Irish Academy, v. 101, p. 65–77.

Whitlock, C., Bianchi, M.M., Bartlein, P.J., Markgraf, V., Marlon, J., Walsh, M., and McCoy, N., 2006, Postglacial vegetation, climate, and fire history along the east side of the Andes (lat 41-42.5°S), Argentina: Quaternary Research, v. 66, p. 187–201, doi: 10.1016/j.yqres.2006.04.004.

Wildman, R.A., Hickey, L.J., Dickinson, M.B., Berner, R.A., Robinson, J.M., Dietrich, M., Essenhigh, R.H., and Wildman, C.B., 2004, Burning of forest materials under late Paleozoic high atmospheric oxygen levels: Geology, p. 457–460, doi: 10.1130/G20255.1.

Williford, K.H., Grice, K., Holman, A., and Mcelwain, J.C., 2014, An organic record of terrestrial ecosystem collapse and recovery at the Triassic - Jurassic boundary in East Greenland: Geochimica et Cosmochimica Acta, v. 127, p. 251–263.

Williford, K.H., Ward, P.D., Garrison, G.H., and Buick, R., 2007, An extended organic carbon-isotope record across the Triassic–Jurassic boundary in the Queen Charlotte Islands, British Columbia, Canada: Palaeogeography, Palaeoclimatology, Palaeoecology, v. 244, p. 290–296, doi:

10.1016/j.palaeo.2006.06.032.

Wyrwicki, R., 1996, Ferruginous deposits of the wiêtokrzyskie Mountains [Eng. Sum.]: Biuletyn Instytutu Geologicznego, v. 195, p. 71–158.

Xie, S., Pancost, R.D., Chen, L., Evershed, R.P., Yang, H., Zhang, K., Huang, J., and Xu, Y., 2012, Microbial lipid records of highly alkaline deposits and enhanced aridity associated with significant uplift of the Tibetan Plateau in the Late Miocene: Geology, v. 40, p. 291–294, doi: 10.1130/G32570.1.

Xu, W., Ruhl, M., Jenkyns, H.C., Hesselbo, S.P., Riding, J.B., Selby, D., Naafs, B.D.A., Weijers, J.W.H., Pancost, R.D., Tegelaar, E.W., and Idiz, E.F., 2017, Carbon sequestration in an expanded lake system during the Toarcian oceanic anoxic event: Nature Geoscience, v. 10, p. 129–134, doi: 10.1038/ngeo2871.

Xu, W., Ruhl, M., Jenkyns, H.C., Leng, M.J., Huggett, J.M., Minisini, D., Ullmann, C. V, Riding, J.B., Weijers, J.W.H., Storm, M.S., Percival, L.M.E., Tosca, N.J., Idiz, E.F., Tegelaar, E.W., et al., 2018, Evolution of the Toarcian (Early Jurassic) carbon-cycle and global climatic controls on local sedimentary processes (Cardigan Bay Basin, UK): Earth and Planetary Science Letters, v. 484, p. 396–411, doi: 10.1016/j.epsl.2017.12.037.

Yang, H., Ding, W., Zhang, C.L., Wu, X., Ma, X., He, G., Huang, J., and Xie, S., 2011, Occurrence of tetraether lipids in stalagmites: Implications for sources and GDGT-based proxies: Organic Geochemistry, v. 42, p. 108–115, doi: 10.1016/j.orggeochem.2010.11.006.

Zell, C., Kim, J., Dorhout, D., Baas, M., and Damsté, J.S.S., 2015, Sources and distributions of branched tetraether lipids and crenarchaeol along the Portuguese continental margin: Implications for the BIT index: Continental Shelf Research, v. 96, p. 34–44, doi: 10.1016/j.csr.2015.01.006.

Zhou, H., Hu, J., Ming, L., Peng, P., and Zhang, G., 2011, Branched glycerol dialkyl glycerol tetraethers and paleoenviron- mental reconstruction in Zoigê peat sediments during the last 150 years: Chinese Science Bulletin, v. 56, p. 2456–2463, doi: 10.1007/s11434-011-4594-9.

Zhou, H., Wu, C., Onwudili, J.A., Meng, A., Zhang, Y., and Williams, P.T., 2015, Polycyclic aromatic hydrocarbons (PAH) formation from the pyrolysis of different municipal solid waste fractions: Waste Management, v. 36, p. 136–

146, doi: 10.1016/j.wasman.2014.09.014.

Ziaja, J., 2006, Lower Jurassic spores and pollen grains from Odrowąż, Mesozoic margin of the Holy Cross Lower Jurassic spores and pollen grains from Odrowąż, Mesozoic margin of the Holy Cross Mountains, Poland: Acta Palaeobotanica, v. 46, p. 3–83.

Zink, K., Vandergoes, M.J., Mangelsdorf, K., Dieffenbacher-Krall, A.C., and Schwark, L., 2010, Organic Geochemistry Application of bacterial glycerol dialkyl glycerol tetraethers (GDGTs) to develop modern and past temperature estimates from New Zealand lakes: Organic Geochemistry, v. 41, p. 1060–1066, doi: 10.1016/j.orggeochem.2010.03.004.

Znosko, J., 1959, Preliminary description of stratigraphy of Jurassic sediments in southwestern part of Polish Lowland [Eng. Sum.]: Kwartalnik Geologiczny, v. 3, p. 501–528.

APPENDIX A MOCHRAS SINGLE-PHYTOCLAST δ^{13}C RAW DATA

Appendix A contains all of the uncorrected raw data generated during the δ^{13}C analysis of the Mochras single phytoclast samples. A discussion of this data is provided in **Chapter 5** (p. 113).

Table A.1 shows samples descriptions, identifications, and images of phytoclasts analysed. Descriptions and identifications are based on when viewed using a microscope, and not based on the images seen here, which tend to distort colours and lustre. All images taken at x5 magnification; image width is equivalent to 1.8 mm at x1 magnification.

Table A.2 shows the uncorrected raw data collected during LA/nC/GC/IRMS analysis of the Mochras individual phytoclast samples. First column identifies whether peaks refer to reference gas (R), standard (PE), or sample (S).
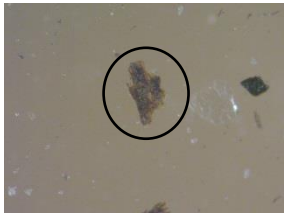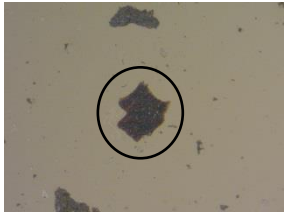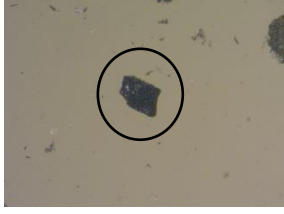
Sample	Colour	Shape	Identification	Image
M256031	Dark grey, brown edges	Angular	Woody phytoclast	
M256035	Dark grey, brown edges	Angular, elongate	Woody phytoclast	
M256037	Dark grey/black, brown edges	Angular	Woody phytoclast	
M256039	Dark grey/black, brown edges	Sub-angular, elongate	Woody phytoclast	
M2560310	Dark black (shiny)	Angular	Charcoal	
M2560311	Dark grey/translucent brown	Sub-angular	Woody phytoclast	

Table A.1 Description, identification, and images of phytoclasts analysed in the single phytoclast carbon-isotope study. When more than one phytoclast is present in the image, the ringed particle is the one analysed. Images at x5 magnification; width of image equivalent to 1.8 mm at x1 magnification.
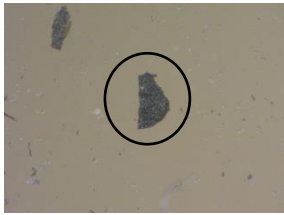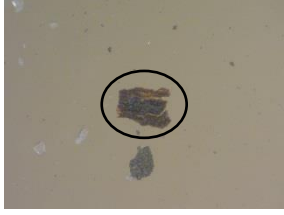
Sample	Colour	Shape	Identification	Image
M2560312	Dark grey/black	Sub-angular	Woody phytoclast	
M2560313 **M2560313(1)**	Dark grey/black	Angular, elongate	Woody phytoclast	
M2560314 **M2560314(1)** **M2560314(2)**	Dark grey/black, brown edges	Sub-angular	Woody phytoclast	
M2560315	Dark grey/black, brown edges	Sub-angular	Woody phytoclast	
M25783	Dark grey/black	Sub-rounded	Woody phytoclast	
M257810	Dark grey, brown edges	Sub-angular	Woody phytoclast	

Table A.1 (cont.) Description, identification, and images of phytoclasts analysed in the single phytoclast carbon-isotope study. When more than one phytoclast is present in the image, the ringed particle is the one analysed. Images at x5 magnification; width of image equivalent to 1.8 mm at x1 magnification.

Sample	Colour	Shape	Identification	Image
M259271	Dark grey, brown edges	Sub-angular	Woody phytoclast	
M259272	Dark grey, brown edges	Sub-angular	Woody phytoclast	
M259273	Dark grey, brown edges	Sub-angular	Woody phytoclast	
M259274	Dark grey, brown edges	Sub-angular	Woody phytoclast	
M259275	Dark grey, brown edges	Sub-angular	Woody phytoclast	
M259276 **M259276(1)**	Dark black	Angular	Charcoal	

Table A.1 (cont.) Description, identification, and images of phytoclasts analysed in the single phytoclast carbon-isotope study. When more than one phytoclast is present in the image, the ringed particle is the one analysed. Images at x5 magnification; width of image equivalent to 1.8 mm at x1 magnification.
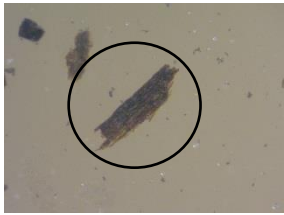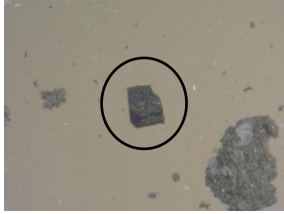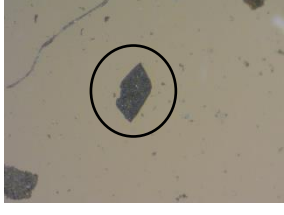
Sample	Colour	Shape	Identification	Image
M259277	Dark grey, brown edges	Sub-angular	Woody phytoclast	
M259278	Dark grey/black	Angular	Charcoal	
M259279	Dark grey, brown edges	Sub-angular	Woody phytoclast	
M2592711 **M2592711(1)** **M2592711(2)**	Dark grey, brown edges	Angular	Woody phytoclast	
M2592712	Dark grey, brown edges	Sub-angular	Woody phytoclast	
M2592713	Dark grey, brown edges	Angular	Woody phytoclast	

Table A.1 (cont.) Description, identification, and images of phytoclasts analysed in the single phytoclast carbon-isotope study. When more than one phytoclast is present in the image, the ringed particle is the one analysed. Images at x5 magnification; width of image equivalent to 1.8 mm at x1 magnification.

Sample	Colour	Shape	Identification	Image
M261193	Dark grey, brown edges	Sub-angular	Woody phytoclast	
M261196	Dark grey/black, brown edges	Sub-angular	Woody phytoclast	
M2611915	Dark grey, brown edges	Sub-angular	Woody phytoclast	
M263141	Dark grey, brown edges	Sub-angular	Woody phytoclast	
M263143	Dark grey, brown edges	Sub-angular	Woody phytoclast	
M263144	Dark grey, brown edges	Sub-angular	Woody phytoclast	

Table A.1 (cont.) Description, identification, and images of phytoclasts analysed in the single phytoclast carbon-isotope study. When more than one phytoclast is present in the image, the ringed particle is the one analysed. Images at x5 magnification; width of image equivalent to 1.8 mm at x1 magnification.

Sample	Colour	Shape	Identification	Image
M263145	Dark grey, brown edges	Sub-angular	Woody phytoclast	
M263147	Dark grey, brown edges	Sub-angular	Woody phytoclast	
M263149	Dark grey, brown edges	Sub-angular	Woody phytoclast	
M2631410	Translucent brown, some grey	Sub-angular	Woody phytoclast	
M2631411	Dark grey/black	Sub-angular	Woody phytoclast	
M2631412	Dark grey, brown edges	Sub-angular	Woody phytoclast	

Table A.1 (cont.) Description, identification, and images of phytoclasts analysed in the single phytoclast carbon-isotope study. When more than one phytoclast is present in the image, the ringed particle is the one analysed. Images at x5 magnification; width of image equivalent to 1.8 mm at x1 magnification.
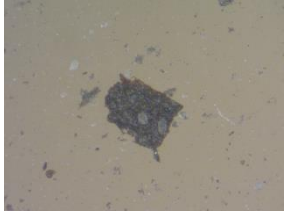
Sample	Colour	Shape	Identification	Image
M2631413	Dark grey, brown edges	Sub-angular	Woody phytoclast	
M2631414	Dark grey/black	Sub-angular	Woody phytoclast	
M2631415	Dark grey, brown edges	Sub-angular	Woody phytoclast	
M264181	Dark grey, brown edges	Sub-angular	Woody phytoclast	
M264182	Dark grey/translucent brown	Sub-angular	Woody phytoclast	
M264184	Dark grey, brown edges	Sub-angular	Woody phytoclast	

Table A.1 (cont.) Description, identification, and images of phytoclasts analysed in the single phytoclast carbon-isotope study. When more than one phytoclast is present in the image, the ringed particle is the one analysed. Images at x5 magnification; width of image equivalent to 1.8 mm at x1 magnification.
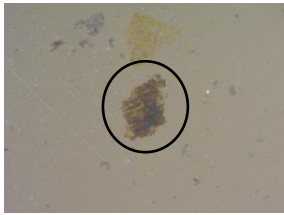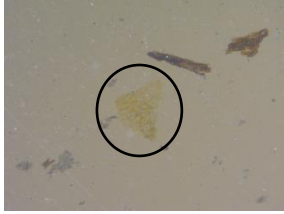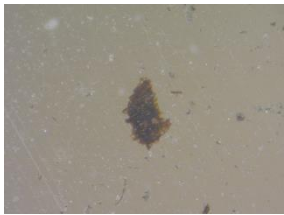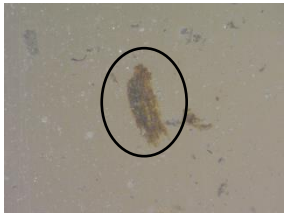
Sample	Colour	Shape	Identification	Image
M264185	Translucent brown/dark grey	Sub-angular	Woody phytoclast	
M264186	Translucent brown	Sub-angular	Woody phytoclast	
M264187 M264187(1) M264187(2)	Dark grey, brown edges	Sub-angular	Woody phytoclast	
M264188	Dark grey, brown edges	Sub-angular	Woody phytoclast	
M264189	Translucent brown/dark grey	Sub-angular	Woody phytoclast	
M2641810	Dark grey, brown edges	Sub-angular	Woody phytoclast	

Table A.1 (cont.) Description, identification, and images of phytoclasts analysed in the single phytoclast carbon-isotope study. When more than one phytoclast is present in the image, the ringed particle is the one analysed. Images at x5 magnification; width of image equivalent to 1.8 mm at x1 magnification.

Sample	Colour	Shape	Identification	Image
M2641812	Dark grey, brown edges	Sub-angular	Woody phytoclast	
M2641813	Dark grey, brown edges	Sub-angular	Woody phytoclast	
M2641814	Dark grey/translucent brown	Sub-angular	Woody phytoclast	Image file corrupted
M26701	Dark grey/translucent brown	Elongate	Woody phytoclast	
M26702	Dark grey/translucent brown	Elongate	Woody phytoclast	
M26703	Translucent brown/dark grey	Sub-angular	Woody phytoclast	

Table A.1 (cont.) Description, identification, and images of phytoclasts analysed in the single phytoclast carbon-isotope study. When more than one phytoclast is present in the image, the ringed particle is the one analysed. Images at x5 magnification; width of image equivalent to 1.8 mm at x1 magnification.
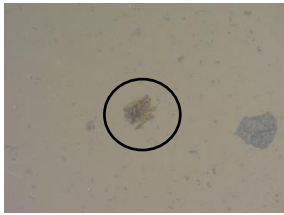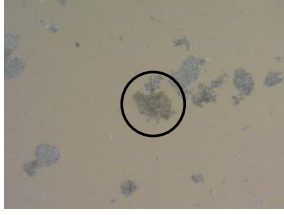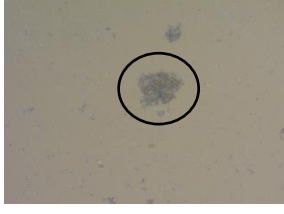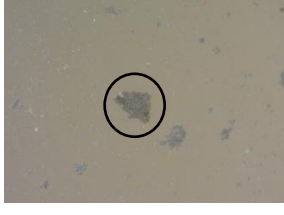
Sample	Colour	Shape	Identification	Image
M26704	Translucent brown	Sub-angular	Woody phytoclast	
M26705	Dark grey	Sub-angular	Woody phytoclast	
M26706	Translucent brown/dark grey	Sub-angular	Woody phytoclast	
M26707	Dark grey	Sub-angular	Woody phytoclast	
M26708	Translucent brown	Sub-rounded	Woody phytoclast	
M26709	Translucent brown	Sub-angular	Woody phytoclast	

Table A.1 (cont.) Description, identification, and images of phytoclasts analysed in the single phytoclast carbon-isotope study. When more than one phytoclast is present in the image, the ringed particle is the one analysed. Images at x5 magnification; width of image equivalent to 1.8 mm at x1 magnification.
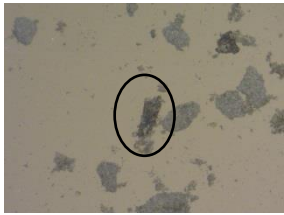
Sample	Colour	Shape	Identification	Image
M267011	Dark grey/black	Sub-angular	Woody phytoclast	
M267012	Dark grey/black	Sub-rounded	Woody phytoclast	
M267013	Dark grey/black	Elongate	Woody phytoclast	
M267014	Translucent brown	Elongate	Woody phytoclast	
M267015	Translucent brown	Elongate	Woody phytoclast	
M270161 M270161(1)	Translucent brown	Sub-angular	Woody phytoclast	

Table A.1 (cont.) Description, identification, and images of phytoclasts analysed in the single phytoclast carbon-isotope study. When more than one phytoclast is present in the image, the ringed particle is the one analysed. Images at x5 magnification; width of image equivalent to 1.8 mm at x1 magnification.

Sample	Colour	Shape	Identification	Image
M270162	Dark grey, brown edges	Sub-angular	Woody phytoclast	
M270164	Dark grey, brown edges	Sub-angular	Woody phytoclast	
M270165	Dark grey, brown edges	Sub-angular	Woody phytoclast	
M270168	Translucent brown/dark grey	Sub-angular	Woody phytoclast	
M270169	Dark grey, brown edges	Sub-angular	Woody phytoclast	
M2701610	Translucent brown	Sub-angular	Woody phytoclast	

Table A.1 (cont.) Description, identification, and images of phytoclasts analysed in the single phytoclast carbon-isotope study. When more than one phytoclast is present in the image, the ringed particle is the one analysed. Images at x5 magnification; width of image equivalent to 1.8 mm at x1 magnification.
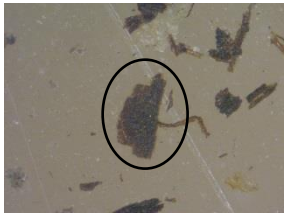
Sample	Colour	Shape	Identification	Image
M2701611	Dark grey, brown edges	Sub-angular	Woody phytoclast	
M2701612	Dark grey, brown edges	Sub-angular	Woody phytoclast	
M2701613	Dark grey, brown edges	Elongate	Woody phytoclast	
M2701615	Translucent brown	Sub-angular	Woody phytoclast	
M272921	Black (shiny)	Sub-rounded	Charcoal	
M272922	Black (shiny)	Sub-rounded	Charcoal	

Table A.1 (cont.) Description, identification, and images of phytoclasts analysed in the single phytoclast carbon-isotope study. When more than one phytoclast is present in the image, the ringed particle is the one analysed. Images at x5 magnification; width of image equivalent to 1.8 mm at x1 magnification.
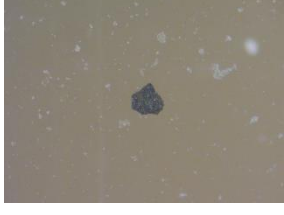
Sample	Colour	Shape	Identification	Image
M272923	Dark grey/black	Angular	Woody phytoclast	
M272924	Black (shiny)	Sub-rounded	Charcoal	
M272925	Dark grey, brown edges	Sub-angular	Woody phytoclast	
M272926	Translucent brown/dark grey	Sub-angular	Woody phytoclast	
M272927	Dark grey, brown edges	Sub-angular	Woody phytoclast	
M272928 **M272928(1)** **M272928(2)**	Dark grey/black	Sub-rounded	Woody phytoclast	

Table A.1 (cont.) Description, identification, and images of phytoclasts analysed in the single phytoclast carbon-isotope study. When more than one phytoclast is present in the image, the ringed particle is the one analysed. Images at x5 magnification; width of image equivalent to 1.8 mm at x1 magnification.

Sample	Colour	Shape	Identification	Image
M272929	Dark grey, brown edges	Sub-angular	Woody phytoclast	
M2729210	Dark grey, brown edges	Sub-angular	Woody phytoclast	
M2729211	Dark grey/black	Sub-rounded	Woody phytoclast	
M2729212	Black (shiny)	Angular	Charcoal	
M2729214	Dark grey/black	Sub-angular	Woody phytoclast	
M276541	Black (shiny)	Sub-angular	Charcoal	

Table A.1 (cont.) Description, identification, and images of phytoclasts analysed in the single phytoclast carbon-isotope study. When more than one phytoclast is present in the image, the ringed particle is the one analysed. Images at x5 magnification; width of image equivalent to 1.8 mm at x1 magnification.

Sample	Colour	Shape	Identification	Image
M276542	Dark grey/black	Sub-angular	Woody phytoclast	
M276543	Dark grey/black (shiny)	Elongate	Charcoal	
M276544	Dark grey/black (shiny)	Elongate	Charcoal	
M276545 **M276545(1)** **M276545(2)** **M276545(3)**	Dark grey/translucent brown	Sub-angular	Woody phytoclast	
M276546	Dark grey/black	Elongate	Woody phytoclast	
M276547	Dark grey/black	Sub-angular	Woody phytoclast	

Table A.1 (cont.) Description, identification, and images of phytoclasts analysed in the single phytoclast carbon-isotope study. When more than one phytoclast is present in the image, the ringed particle is the one analysed. Images at x5 magnification; width of image equivalent to 1.8 mm at x1 magnification.
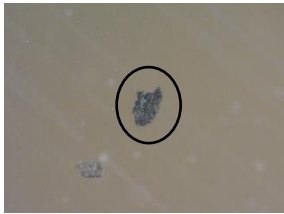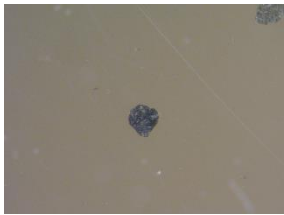
Sample	Colour	Shape	Identification	Image
M276548	Dark grey/black	Sub-angular	Woody phytoclast	
M276549	Dark grey/translucent brown	Sub-angular	Woody phytoclast	
M2765410 M2765410(1)	Black (shiny)	Sub-angular	Charcoal	
M2765411	Translucent brown/dark grey	Sub-angular	Woody phytoclast	
M2765412	Dark grey/black	Sub-rounded	Woody phytoclast	
M2765414	Dark grey/black	Sub-rounded	Woody phytoclast	

Table A.1 (cont.) Description, identification, and images of phytoclasts analysed in the single phytoclast carbon-isotope study. When more than one phytoclast is present in the image, the ringed particle is the one analysed. Images at x5 magnification; width of image equivalent to 1.8 mm at x1 magnification.
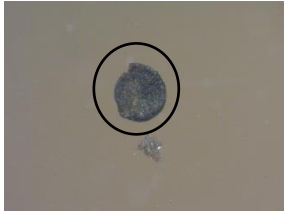
Sample	Colour	Shape	Identification	Image
M2765415	Dark grey/black	Sub-rounded	Woody phytoclast	

Table A.1 (cont.) Description, identification, and images of phytoclasts analysed in the single phytoclast carbon-isotope study. When more than one phytoclast is present in the image, the ringed particle is the one analysed. Images at x5 magnification; width of image equivalent to 1.8 mm at x1 magnification.

	Identifier 1	Date	Time	Peak Nr	Start	Rt	End	Area All	Ampl 44	BGD 44	BGD 45	BGD 46	d13C/12C
R	M256037	04/03/18	11:54:37	1	26.5	47.2	50.8	57.812	2900	2.6	3.0	4.4	-35.915
R	M256037	04/03/18	11:54:37	2	66.3	86.9	90.7	57.652	2895	2.7	3.2	4.7	-36.1
R	M256037	04/03/18	11:54:37	3	106.2	126.9	130.4	57.717	2910	2.8	3.2	4.7	-36.203
PE	M256037	04/03/18	11:54:37	4	201.9	209.4	214.4	3.141	574	2.4	2.8	4.1	-32.378
PE	M256037	04/03/18	11:54:37	5	214.4	218.4	269.2	4.242	228	2.4	2.8	4.1	-33.931
PE	M256037	04/03/18	11:54:37	6	523.8	531.7	536.9	3.866	579	3.5	4.0	5.6	-32.701
PE	M256037	04/03/18	11:54:37	7	536.9	541.1	608.6	6.932	321	3.5	4.0	5.6	-33.013
S	M256037	04/03/18	11:54:37	8	840.2	865.3	942	25.767	854	4.4	5.2	7.3	-27.22
S	M256037	04/03/18	11:54:37	9	1134	1154.3	1233.7	24.351	856	9.8	11.4	14.8	-27.202
S	M256037	04/03/18	11:54:37	10	1428.7	1449.6	1540.1	19.229	735	13.0	15.1	19.0	-27.298
PE	M256037	04/03/18	11:54:37	11	1733.9	1741.6	1745.8	1.532	263	13.5	15.7	19.1	-32.554
PE	M256037	04/03/18	11:54:37	12	1745.8	1750.4	1812.4	4.629	229	13.5	15.7	19.1	-33.722
S	M256037	04/03/18	11:54:37	13	2042.6	2058.4	2114.5	14.381	635	12.5	14.5	18.0	-27.07
S	M256037	04/03/18	11:54:37	14	2363	2368.8	2387.4	0.359	27	10.9	12.6	15.6	-25.759
S	M256037	04/03/18	11:54:37	15	2597.7	2605.8	2646.6	1.598	67	11.1	12.9	15.9	-28.897
PE	M256037	04/03/18	11:54:37	16	2972.6	2980.5	2986.2	3.108	430	8.9	10.3	12.8	-34.09
PE	M256037	04/03/18	11:54:37	17	2986.2	2989.7	3055.2	5.345	244	8.9	10.3	12.8	-32.974
PE	M256037	04/03/18	11:54:37	18	3233.6	3242.2	3247.2	2.859	412	8.0	9.3	11.6	-32.175
PE	M256037	04/03/18	11:54:37	19	3247.2	3251.6	3303.7	5.097	243	8.0	9.3	11.6	-36.178
R	M256037	04/03/18	11:54:37	20	3469.8	3490.3	3494.3	57.872	2904	8.3	9.7	12.1	-35.931
R	M256037	04/03/18	11:54:37	21	3509.5	3530.2	3533.8	57.801	2913	7.8	9.1	11.4	-36.1
R	M256037	04/03/18	11:54:37	22	3549.4	3569.9	3573.9	57.818	2916	7.4	8.5	10.8	-36.203
	Identifier 1	**Date**	**Time**	**Peak Nr**	**Start**	**Rt**	**End**	**Area All**	**Ampl 44**	**BGD 44**	**BGD 45**	**BGD 46**	**d13C/12C**
R	M270161	04/03/18	13:52:29	1	26.5	47.2	51	52.93	2660	2.8	3.3	5.1	-35.965
R	M270161	04/03/18	13:52:29	2	66.3	86.9	90.7	53.196	2674	2.9	3.5	5.4	-36.1
R	M270161	04/03/18	13:52:29	3	106.2	126.9	130.4	53.267	2685	2.9	3.5	5.4	-36.178
PE	M270161	04/03/18	13:52:29	4	224	235.8	251.8	0.539	33	2.7	3.2	5.1	-37.817
PE	M270161	04/03/18	13:52:29	5	484.3	499.3	543.8	5.007	291	3.8	4.5	6.6	-33.337
S	M270161	04/03/18	13:52:29	6	830.6	844.2	893.9	5.033	247	5.1	5.9	8.3	-33.272

Table A.2 R = reference gas; PE = PE standard; S = sample. Date in MM/DD/YY format. Time is in Central European Standard Time (UTC +2). Peak Nr = peak number. Start = peak start time (s). Rt = retention time (s). End = end peak time (s). Area all = peak area (Vs). Ampl 44 = peak amplitude. BGD 44, BGD 45, BGD 46 = background gas levels. d13C/12C = $\delta^{13}C$.

	Identifier 1	Date	Time	Peak Nr	Start	Rt	End	Area All	Ampl 44	BGD 44	BGD 45	BGD 46	d13C/12C
R	M270161(1)	04/03/18	15:57:02	1	26.5	47.2	50.8	57.218	2884	4.3	5.1	7.7	-35.968
R	M270161(1)	04/03/18	15:57:02	2	66.3	86.9	90.7	57.193	2876	4.5	5.3	8.0	-36.1
R	M270161(1)	04/03/18	15:57:02	3	106.2	126.9	130.4	57.318	2875	4.3	5.1	7.8	-36.201
PE	M270161(1)	04/03/18	15:57:02	4	265.4	273.4	329	5.359	257	4.0	4.8	7.4	-33.262
PE	M270161(1)	04/03/18	15:57:02	5	558.9	569.3	624.7	5.848	295	5.3	6.2	9.0	-32.989
S	M270161(1)	04/03/18	15:57:02	6	838.7	857.7	933.4	11.36	451	6.1	7.1	10.3	-31.619
S	M270161(1)	04/03/18	15:57:02	7	1143.4	1161.4	1225.8	9.933	431	7.6	9.0	12.4	-31.617
S	M270161(1)	04/03/18	15:57:02	8	1446.9	1464.9	1535.9	11.969	530	8.1	9.5	12.9	-31.66
PE	M270161(1)	04/03/18	15:57:02	9	1769.2	1777.3	1823.3	3.928	189	8.4	9.8	13.1	-32.92
S	M270161(1)	04/03/18	15:57:02	10	2044.9	2063.5	2163.8	19.339	819	8.0	9.4	12.8	-31.359
S	M270161(1)	04/03/18	15:57:02	11	2337.2	2355.4	2417.1	9.072	397	10.9	12.7	16.7	-31.223
S	M270161(1)	04/03/18	15:57:02	12	2648	2666.2	2734.6	7.536	344	10.0	11.7	15.3	-31.57
PE	M270161(1)	04/03/18	15:57:02	13	2940.2	2960.1	3018.8	9.578	303	10.2	11.9	15.5	-33.396
PE	M270161(1)	04/03/18	15:57:02	14	3235.5	3253.3	3305.5	8.183	280	10.2	11.9	15.5	-33.555
R	M270161(1)	04/03/18	15:57:02	15	3469.6	3490.3	3493.9	57.637	2890	11.6	13.4	17.2	-35.942
R	M270161(1)	04/03/18	15:57:02	16	3509.5	3530.2	3533.6	57.535	2887	11.0	12.9	16.6	-36.1
R	M270161(1)	04/03/18	15:57:02	17	3549.2	3569.9	3573.3	57.473	2887	10.5	12.2	15.8	-36.19

	Identifier 1	Date	Time	Peak Nr	Start	Rt	End	Area All	Ampl 44	BGD 44	BGD 45	BGD 46	d13C/12C
R	M276547	04/03/18	17:46:33	1	26.5	47.2	50.6	53.561	2701	5.0	5.9	9.7	-35.99
R	M276547	04/03/18	17:46:33	2	66.3	86.9	90.5	53.652	2704	5.2	6.1	10.0	-36.1
R	M276547	04/03/18	17:46:33	3	106.2	126.9	130.4	54.087	2725	5.1	6.1	9.9	-36.138
PE	M276547	04/03/18	17:46:33	4	252.9	260.6	264.8	3.27	594	4.7	5.6	9.2	-32.307
PE	M276547	04/03/18	17:46:33	5	264.8	269.4	321.2	8.593	430	4.7	5.6	9.2	-33.295
S	M276547	04/03/18	17:46:33	6	567.9	583.7	669.8	14.481	700	6.8	8.0	12.1	-27.307
PE	M276547	04/03/18	17:46:33	7	884.5	902.3	968.5	11.486	425	7.6	9.0	12.9	-32.859
R	M276547	04/03/18	17:46:33	8	1180.8	1201.5	1205.1	56.401	2832	8.3	9.7	13.7	-35.935
R	M276547	04/03/18	17:46:33	9	1220.8	1240.8	1245.2	56.505	2843	7.9	9.3	13.3	-36.1
R	M276547	04/03/18	17:46:33	10	1260.7	1281.2	1284.7	56.572	2841	7.8	9.1	12.9	-36.19

	Identifier 1	Date	Time	Peak Nr	Start	Rt	End	Area All	Ampl 44	BGD 44	BGD 45	BGD 46	d13C/12C
R	M276542	04/04/18	10:33:08	1	26.5	47.2	50.8	56.23	2826	2.7	3.2	5.1	-35.922

Table A.2 (cont.) R = reference gas; PE = PE standard; S = sample. Date in MM/DD/YY format. Time is in Central European Standard Time (UTC +2). Peak Nr = peak number. Start = peak start time (s). Rt = retention time (s). End = end peak time (s). Area all = peak area (Vs). Ampl 44 = peak amplitude. BGD 44, BGD 45, BGD 46 = background gas levels. d13C/12C = $\delta^{13}C$.

	Identifier 1	Date	Time	Peak Nr	Start	Rt	End	Area All	Ampl 44	BGD 44	BGD 45	BGD 46	d13C/12C
R	M276542	04/04/18	10:33:08	2	66.3	86.9	90.7	56.146	2829	2.8	3.4	5.3	-36.1
R	M276542	04/04/18	10:33:08	3	106.2	113.7	130.4	56.339	2827	2.8	3.4	5.3	-36.202
PE	M276542	04/04/18	10:33:08	4	251.6	265.6	319.4	7.814	406	2.5	2.9	4.7	-33.098
S	M276542	04/04/18	10:33:08	5	546.3	561.8	600.2	2.267	108	4.3	5.0	7.2	-26.953
PE	M276542	04/04/18	10:33:08	6	842.9	857.3	886	1.055	53	4.3	5.1	7.2	-26.65
R	M276542	04/04/18	10:33:08	7	1180.8	1198	1205.1	56.74	2845	3.8	4.4	6.4	-35.953
R	M276542	04/04/18	10:33:08	8	1220.8	1241.3	1245	56.861	2858	4.1	4.8	6.7	-36.1
R	M276542	04/04/18	10:33:08	9	1260.5	1281.2	1284.9	56.72	2852	4.1	4.8	6.7	-36.209
	Identifier 1	**Date**	**Time**	**Peak Nr**	**Start**	**Rt**	**End**	**Area All**	**Ampl 44**	**BGD 44**	**BGD 45**	**BGD 46**	**d13C/12C**
R	M2765415	04/04/18	12:08:58	1	26.5	47.2	50.8	55.997	2824	2.6	3.0	5.0	-35.96
R	M2765415	04/04/18	12:08:58	2	66.3	86.9	90.5	56.292	2837	2.6	3.2	5.2	-36.1
R	M2765415	04/04/18	12:08:58	3	106.2	126.9	130.4	56.117	2822	2.6	3.1	5.1	-36.177
PE	M2765415	04/04/18	12:08:58	4	240.4	246.8	251	0.794	161	2.3	2.7	4.6	-31.664
S	M2765415	04/04/18	12:08:58	5	251	256.7	298.9	4.392	353	2.3	2.7	4.6	-33.124
	Identifier 1	**Date**	**Time**	**Peak Nr**	**Start**	**Rt**	**End**	**Area All**	**Ampl 44**	**BGD 44**	**BGD 45**	**BGD 46**	**d13C/12C**
R	M259274	04/04/18	14:01:24	1	26.5	47.2	50.6	54.444	2740	3.2	3.8	7.4	-35.941
R	M259274	04/04/18	14:01:24	2	66.3	86.9	90.5	54.411	2731	3.3	4.0	7.7	-36.1
R	M259274	04/04/18	14:01:24	3	106.2	126.9	130.4	54.431	2744	3.4	4.1	7.8	-36.155
PE	M259274	04/04/18	14:01:24	4	234.1	248.9	303.7	6.289	343	3.0	3.6	7.0	-32.867
S	M259274	04/04/18	14:01:24	5	540.3	556.8	597.5	3.146	159	4.1	4.9	8.7	-26.806
PE	M259274	04/04/18	14:01:24	6	846	855.4	925.2	10.257	430	4.6	5.4	8.9	-32.72
R	M259274	04/04/18	14:01:24	7	1180.8	1201.5	1204.9	56.463	2840	5.2	6.2	9.6	-35.931
R	M259274	04/04/18	14:01:24	8	1220.6	1241.3	1244.8	56.394	2849	5.2	6.2	9.7	-36.1
R	M259274	04/04/18	14:01:24	9	1260.500	1281.2	1284.5	56.648	2851	5.1	6.1	9.5	-36.157
	Identifier 1	**Date**	**Time**	**Peak Nr**	**Start**	**Rt**	**End**	**Area All**	**Ampl 44**	**BGD 44**	**BGD 45**	**BGD 46**	**d13C/12C**
R	M257810	04/04/18	15:42:37	1	26.5	47.2	50.8	49.773	2505	3.2	3.9	6.9	-36.031
R	M257810	04/04/18	15:42:37	2	66.3	86.9	90.5	49.981	2518	3.4	4.1	7.0	-36.1
R	M257810	04/04/18	15:42:37	3	106.200	126.9	130.4	50.318	2538	3.4	4.1	7.1	-36.163
PE	M257810	04/04/18	15:42:37	4	240.400	255.4	321.4	9.11	407	3.1	3.7	6.6	-32.988
S	M257810	04/04/18	15:42:37	5	542.8	561	626.6	6.716	330	4.7	5.6	9.1	-24.971

Table A.2 (cont.) R = reference gas; PE = PE standard; S = sample. Date in MM/DD/YY format. Time is in Central European Standard Time (UTC +2). Peak Nr = peak number. Start = peak start time (s). Rt = retention time (s). End = end peak time (s). Area all = peak area (Vs). Ampl 44 = peak amplitude. BGD 44, BGD 45, BGD 46 = background gas levels. d13C/12C = $\delta^{13}C$.

	Identifier 1	Date	Time	Peak Nr	Start	Rt	End	Area All	Ampl 44	BGD 44	BGD 45	BGD 46	d13C/12C
PE	M257810	04/04/18	15:42:37	6	845.4	860.000	927.8	7.497	352	5.3	6.3	9.8	-32.756
R	M257810	04/04/18	15:42:37	7	1180.8	1201.5	1205.1	55.29	2774	5.2	6.2	9.6	-35.9
R	M257810	04/04/18	15:42:37	8	1220.8	1241.5	1245	55.368	2782	5.3	6.3	9.8	-36.1
R	M257810	04/04/18	15:42:37	9	1260.5	1281.2	1284.7	55.393	2783	5.2	6.1	9.6	-36.141

	Identifier 1	Date	Time	Peak Nr	Start	Rt	End	Area All	Ampl 44	BGD 44	BGD 45	BGD 46	d13C/12C
R	M263146	04/04/18	16:43:37	1	26.5	47.2	50.6	54.739	2770	4.3	5.1	9.3	-36.006
R	M263146	04/04/18	16:43:37	2	66.3	86.9	90.5	54.971	2763	4.3	5.2	9.4	-36.1
R	M263146	04/04/18	16:43:37	3	106.2	126.9	130.4	55.245	2781	4.3	5.2	9.4	-36.176
PE	M263146	04/04/18	16:43:37	4	241.4	257.1	333.8	13.35	594	3.9	4.8	8.7	-32.979
S	M263146	04/04/18	16:43:37	5	536.3	553.6	595.9	2.886	122	6.3	7.4	12.0	-27.443
PE	M263146	04/04/18	16:43:37	6	841.2	857.5	935.1	15.374	546	5.6	6.6	10.7	-32.579
R	M263146	04/04/18	16:43:37	7	1180.8	1201.5	1205.1	55.886	2807	6.4	7.6	11.6	-35.952
R	M263146	04/04/18	16:43:37	8	1220.8	1241.5	1244.8	55.928	2813	6.3	7.4	11.5	-36.1
R	M263146	04/04/18	16:43:37	9	1260.5	1281.2	1284.7	55.895	2808	6.0	7.2	11.1	-36.189

	Identifier 1	Date	Time	Peak Nr	Start	Rt	End	Area All	Ampl 44	BGD 44	BGD 45	BGD 46	d13C/12C
R	M2641813	04/04/18	17:23:08	1	26.5	47.2	50.8	54.691	2755	4.5	5.4	10.3	-35.99
R	M2641813	04/04/18	17:23:08	2	66.3	86.9	90.5	54.862	2764	4.6	5.5	10.4	-36.1
R	M2641813	04/04/18	17:23:08	3	106.2	126.9	130.4	54.832	2758	4.7	5.6	10.4	-36.121
PE	M2641813	04/04/18	17:23:08	4	239.5	254.4	317.9	11.523	530	4.3	5.1	9.7	-32.825

	Identifier 1	Date	Time	Peak Nr	Start	Rt	End	Area All	Ampl 44	BGD 44	BGD 45	BGD 46	d13C/12C
R	M261196	04/05/18	10:42:02	1	26.5	47	50.8	57.662	2895	2.6	3.1	5.2	-35.933
R	M261196	04/05/18	10:42:02	2	66.3	86.9	90.7	57.786	2899	2.7	3.2	5.4	-36.1
R	M261196	04/05/18	10:42:02	3	106.2	126.9	130.4	57.729	2903	2.9	3.4	5.6	-36.198
PE	M261196	04/05/18	10:42:02	4	223	232	237.8	3.702	531	2.5	2.9	4.9	-32.269
PE	M261196	04/05/18	10:42:02	5	237.8	240.1	285.1	3.414	239	2.5	2.9	4.9	-32.191
S	M261196	04/05/18	10:42:02	6	524.8	537.5	566.2	1.092	69	3.7	4.3	6.6	-27.718
PE	M261196	04/05/18	10:42:02	7	836	844.8	906	7.813	447	3.5	4.1	6.3	-32.975
R	M261196	04/05/18	10:42:02	8	1180.8	1201.5	1205.1	58.689	2955	4.1	4.8	7.0	-35.913
R	M261196	04/05/18	10:42:02	9	1220.6	1241.3	1244.8	58.581	2946	4.2	4.9	7.2	-36.1
R	M261196	04/05/18	10:42:02	10	1260.5	1281.2	1284.7	58.489	2947	4.1	4.9	7.2	-36.176

Table A.2 (cont.) R = reference gas; PE = PE standard; S = sample. Date in MM/DD/YY format. Time is in Central European Standard Time (UTC +2). Peak Nr = peak number. Start = peak start time (s). Rt = retention time (s). End = end peak time (s). Area all = peak area (Vs). Ampl 44 = peak amplitude. BGD 44, BGD 45, BGD 46 = background gas levels. d13C/12C = δ^{13}C.

	Identifier 1	Date	Time	Peak Nr	Start	Rt	End	Area All	Ampl 44	BGD 44	BGD 45	BGD 46	d13C/12C
R	M272922	04/05/18	12:11:26	1	26.5	47	50.8	55.59	2797	3.3	3.9	7.2	-35.977
R	M272922	04/05/18	12:11:26	2	66.3	86.9	90.7	55.765	2810	3.5	4.1	7.4	-36.1
R	M272922	04/05/18	12:11:26	3	106.2	126.9	130.4	55.817	2804	3.5	4.1	7.3	-36.173
PE	M272922	04/05/18	12:11:26	4	237.6	253.5	297.6	7.171	327	3.1	3.7	6.7	-33.073
S	M272922	04/05/18	12:11:26	5	532.1	546.5	575.2	1.288	71	4.4	5.2	8.5	-27.211
PE	M272922	04/05/18	12:11:26	6	841.6	856.1	909.8	6.49	315	3.9	4.6	7.5	-32.557
R	M272922	04/05/18	12:11:26	7	1180.8	1201.5	1205.1	57.825	2911	4.3	5.1	8.0	-35.921
R	M272922	04/05/18	12:11:26	8	1220.6	1241.3	1244.8	57.88	2910	4.4	5.3	8.2	-36.1
R	M272922	04/05/18	12:11:26	9	1260.5	1281.2	1284.7	58.061	2925	4.4	5.2	8.1	-36.175

	Identifier 1	Date	Time	Peak Nr	Start	Rt	End	Area All	Ampl 44	BGD 44	BGD 45	BGD 46	d13C/12C
R	M26703	04/05/18	13:20:34	1	26.3	47	50.6	57.957	2910	3.5	4.2	7.7	-35.942
R	M26703	04/05/18	13:20:34	2	66.3	86.9	90.5	57.727	2917	3.6	4.4	7.9	-36.1
R	M26703	04/05/18	13:20:34	3	106.2	126.7	130.2	57.694	2896	3.7	4.4	8.0	-36.158
PE	M26703	04/05/18	13:20:34	4	231.4	247.2	330.6	13.692	518	3.3	3.9	7.4	-32.744
S	M26703	04/05/18	13:20:34	5	533.4	538	541.7	0.057	11	5.8	6.8	10.7	-22.718
S	M26703	04/05/18	13:20:34	6	541.7	548.2	572.5	0.768	47	5.8	6.8	10.7	-28.63
PE	M26703	04/05/18	13:20:34	7	845	861.3	951.2	14.905	518	4.4	5.2	8.6	-32.564
R	M26703	04/05/18	13:20:34	8	1180.8	1201.5	1204.9	58.227	2928	6.3	7.4	11.0	-35.948
R	M26703	04/05/18	13:20:34	9	1220.6	1241.3	1245	58.275	2934	6.1	7.2	10.9	-36.1
R	M26703	04/05/18	13:20:34	10	1260.5	1281.2	1284.7	58.177	2936	5.8	6.8	10.5	-36.148

	Identifier 1	Date	Time	Peak Nr	Start	Rt	End	Area All	Ampl 44	BGD 44	BGD 45	BGD 46	d13C/12C
R	M2611915	04/05/18	14:07:00	1	26.3	47	50.6	56.371	2841	4.4	5.3	9.9	-35.982
R	M2611915	04/05/18	14:07:00	2	66.3	86.9	90.5	56.293	2836	4.5	5.4	10.0	-36.1
R	M2611915	04/05/18	14:07:00	3	106.2	126.7	130.2	56.546	2838	4.6	5.5	9.9	-36.181
PE	M2611915	04/05/18	14:07:00	4	224.3	240.4	317.7	15.863	603	4.1	4.9	9.1	-32.861
S	M2611915	04/05/18	14:07:00	5	523.3	538.4	580.4	3.129	124	6.7	8.0	12.9	-27.346
PE	M2611915	04/05/18	14:07:00	6	837.9	853.8	911.7	13.313	561	5.7	6.7	10.9	-32.707
R	M2611915	04/05/18	14:07:00	7	1180.8	1201.5	1204.9	57.842	2913	6.6	7.8	11.9	-36.003
R	M2611915	04/05/18	14:07:00	8	1220.6	1240.2	1245	58.058	2919	6.5	7.7	11.9	-36.1

Table A.2 (cont.) R = reference gas; PE = PE standard; S = sample. Date in MM/DD/YY format. Time is in Central European Standard Time (UTC +2). Peak Nr = peak number. Start = peak start time (s). Rt = retention time (s). End = end peak time (s). Area all = peak area (Vs). Ampl 44 = peak amplitude. BGD 44, BGD 45, BGD 46 = background gas levels. d13C/12C = $\delta^{13}C$.

	Identifier 1	Date	Time	Peak Nr	Start	Rt	End	Area All	Ampl 44	BGD 44	BGD 45	BGD 46	d13C/12C
R	M2611915	04/05/18	14:07:00	9	1260.5	1281.2	1284.7	57.998	2914	6.3	7.5	11.6	-36.202

	Identifier 1	Date	Time	Peak Nr	Start	Rt	End	Area All	Ampl 44	BGD 44	BGD 45	BGD 46	d13C/12C
R	M2560311	04/05/18	16:47:06	1	26.3	47	50.6	58.493	2944	3.7	4.5	7.3	-35.975
R	M2560311	04/05/18	16:47:06	2	66.3	86.9	90.3	58.626	2952	3.8	4.6	7.4	-36.1
R	M2560311	04/05/18	16:47:06	3	106	126.7	130.2	58.932	2961	3.8	4.5	7.5	-36.133
PE	M2560311	04/05/18	16:47:06	4	229.9	246	330.6	14.928	577	3.4	4.0	6.8	-32.817
S	M2560311	04/05/18	16:47:06	5	529	545.3	590.6	3.937	183	5.7	6.7	10.2	-27.191
PE	M2560311	04/05/18	16:47:06	6	838.9	854.8	904.1	11.626	550	5.0	5.9	8.9	-32.934
R	M2560311	04/05/18	16:47:06	7	1180.8	1201.5	1205.1	59.312	2985	5.6	6.6	9.7	-35.923
R	M2560311	04/05/18	16:47:06	8	1220.6	1241.3	1244.6	59.259	2974	5.6	6.6	9.8	-36.1
R	M2560311	04/05/18	16:47:06	9	1260.5	1281.2	1284.5	59.153	2976	5.4	6.4	9.5	-36.177

	Identifier 1	Date	Time	Peak Nr	Start	Rt	End	Area All	Ampl 44	BGD 44	BGD 45	BGD 46	d13C/12C
R	M263145	04/05/18	17:34:56	1	26.3	47	50.6	56.873	2866	4.2	5.0	9.8	-36.016
R	M263145	04/05/18	17:34:56	2	66.3	86.9	90.3	56.944	2867	4.3	5.2	9.8	-36.1
R	M263145	04/05/18	17:34:56	3	106	126.7	130.2	57.144	2875	4.4	5.3	9.9	-36.161
PE	M263145	04/05/18	17:34:56	4	232.2	247.5	294.3	6.014	284	3.9	4.7	9.0	-33.193
S	M263145	04/05/18	17:34:56	5	536.7	555.7	596.5	4.032	169	5.0	6.0	10.8	-25.432
PE	M263145	04/05/18	17:34:56	6	830.4	846.7	897.4	6.056	268	5.3	6.3	10.5	-32.849
R	M263145	04/05/18	17:34:56	7	1180.8	1201.3	1205.1	58.776	2964	5.4	6.5	10.5	-35.934
R	M263145	04/05/18	17:34:56	8	1220.6	1241.3	1244.6	58.67	2950	5.6	6.6	10.7	-36.1
R	M263145	04/05/18	17:34:56	9	1260.5	1281.2	1284.5	58.654	2952	5.4	6.5	10.5	-36.176

	Identifier 1	Date	Time	Peak Nr	Start	Rt	End	Area All	Ampl 44	BGD 44	BGD 45	BGD 46	d13C/12C
R	M2701611	04/06/18	10:10:50	1	26.3	47	51	61.729	3093	2.4	2.8	3.8	-35.913
R	M2701611	04/06/18	10:10:50	2	66.3	86.9	90.7	61.599	3098	2.6	3.0	4.0	-36.1
R	M2701611	04/06/18	10:10:50	3	106	126.7	130.6	61.891	3102	2.7	3.2	4.2	-36.2
PE	M2701611	04/06/18	10:10:50	4	226.6	235.5	304.1	8.094	389	2.2	2.5	3.4	-32.943
S	M2701611	04/06/18	10:10:50	5	527.3	541.9	584.8	6.206	311	3.8	4.4	5.7	-31.923
PE	M2701611	04/06/18	10:10:50	6	826	842.3	908.1	8.732	313	5.0	5.8	7.3	-33.384
R	M2701611	04/06/18	10:10:50	7	1180.8	1201.3	1205.5	61.839	3106	5.9	6.8	8.5	-35.926
R	M2701611	04/06/18	10:10:50	8	1220.6	1241.3	1245	61.479	3097	5.9	6.8	8.5	-36.1

Table A.2 (cont.) R = reference gas; PE = PE standard; S = sample. Date in MM/DD/YY format. Time is in Central European Standard Time (UTC +2). Peak Nr = peak number. Start = peak start time (s). Rt = retention time (s). End = end peak time (s). Area all = peak area (Vs). Ampl 44 = peak amplitude. BGD 44, BGD 45, BGD 46 = background gas levels. d13C/12C = δ13C.

	Identifier 1	Date	Time	Peak Nr	Start	Rt	End	Area All	Ampl 44	BGD 44	BGD 45	BGD 46	d13C/12C
R	M2701611	04/06/18	10:10:50	9	1260.5	1281.2	1284.9	61.392	3086	5.6	6.5	8.1	-36.185

	Identifier 1	Date	Time	Peak Nr	Start	Rt	End	Area All	Ampl 44	BGD 44	BGD 45	BGD 46	d13C/12C
R	M256035	04/06/18	11:43:03	1	26.3	47	50.6	53.739	2704	4.1	4.9	9.2	-36.043
R	M256035	04/06/18	11:43:03	2	66.3	86.9	90.5	54.065	2731	4.2	5.0	9.3	-36.1
R	M256035	04/06/18	11:43:03	3	106	126.7	130.4	54.512	2740	4.2	5.1	9.3	-36.188
PE	M256035	04/06/18	11:43:03	4	242	258.1	345.9	14.387	618	3.8	4.5	8.6	-32.744
S	M256035	04/06/18	11:43:03	5	587.3	604.2	644.3	2.918	129	5.7	6.8	11.4	-27.182
PE	M256035	04/06/18	11:43:03	6	835.2	851.7	932.8	15.64	589	5.5	6.6	10.7	-32.574
R	M256035	04/06/18	11:43:03	7	1180.8	1201.3	1205.1	58.331	2944	6.5	7.6	11.8	-35.938
R	M256035	04/06/18	11:43:03	8	1220.6	1241.3	1244.8	58.3	2932	6.4	7.6	11.7	-36.1
R	M256035	04/06/18	11:43:03	9	1260.5	1281.2	1284.7	58.305	2928	6.1	7.3	11.4	-36.165

	Identifier 1	Date	Time	Peak Nr	Start	Rt	End	Area All	Ampl 44	BGD 44	BGD 45	BGD 46	d13C/12C
R	M2701615	04/06/18	12:32:12	1	26.3	47	50.6	57.23	2876	4.5	5.4	10.7	-36
R	M2701615	04/06/18	12:32:12	2	66.3	86.9	90.3	57.218	2884	4.7	5.6	10.8	-36.1
R	M2701615	04/06/18	12:32:12	3	106	126.7	130.4	57.322	2891	4.6	5.6	10.6	-36.177
PE	M2701615	04/06/18	12:32:12	4	220.9	236.8	310.8	14.429	653	4.1	5.0	9.8	-32.802
S	M2701615	04/06/18	12:32:12	5	522.5	539	601.7	6.759	336	6.6	7.8	13.1	-31.365
PE	M2701615	04/06/18	12:32:12	6	820.7	827.8	915.8	15.804	649	6.3	7.4	12.1	-32.466
R	M2701615	04/06/18	12:32:12	7	1180.8	1201.5	1205.1	58.853	2963	6.3	7.4	11.9	-35.937
R	M2701615	04/06/18	12:32:12	8	1220.6	1241.3	1245.2	59.123	2976	6.4	7.6	12.1	-36.1
R	M2701615	04/06/18	12:32:12	9	1260.5	1281.2	1284.7	59.047	2965	6.0	7.1	11.6	-36.162

	Identifier 1	Date	Time	Peak Nr	Start	Rt	End	Area All	Ampl 44	BGD 44	BGD 45	BGD 46	d13C/12C
R	M2560313(1)	05/07/18	10:31:08	1	26.3	47	50.8	58.834	2962	4.3	5.1	9.7	-35.989
R	M2560313(1)	05/07/18	10:31:08	2	66.3	86.9	90.7	59.016	2963	4.4	5.2	9.8	-36.1
R	M2560313(1)	05/07/18	10:31:08	3	106	126.7	130.4	58.959	2976	4.3	5.1	9.7	-36.162
PE	M2560313(1)	05/07/18	10:31:08	4	243.9	256.2	312.9	6.668	502	3.7	4.3	8.4	-32.465
S	M2560313(1)	05/07/18	10:31:08	5	528.8	544.9	591.5	3.285	169	5.1	6.0	10.4	-26.788
PE	M2560313(1)	05/07/18	10:31:08	6	831.2	840.4	893.3	6.671	456	4.7	5.5	9.4	-32.664
R	M2560313(1)	05/07/18	10:31:08	7	1180.6	1201.3	1205.3	59.239	2987	4.8	5.6	9.3	-35.993
R	M2560313(1)	05/07/18	10:31:08	8	1220.6	1241.3	1244.8	59.303	2988	4.9	5.8	9.6	-36.1

Table A.2 (cont.) R = reference gas; PE = PE standard; S = sample. Date in MM/DD/YY format. Time is in Central European Standard Time (UTC +2). Peak Nr = peak number. Start = peak start time (s). Rt = retention time (s). End = end peak time (s). Area all = peak area (Vs). Ampl 44 = peak amplitude. BGD 44, BGD 45, BGD 46 = background gas levels. d13C/12C = δ^{13}C.

	Identifier 1	Date	Time	Peak Nr	Start	Rt	End	Area All	Ampl 44	BGD 44	BGD 45	BGD 46	d13C/12C
R	M2560313(1)	05/07/18	10:31:08	9	1260.3	1281	1284.7	59.308	2982	4.8	5.6	9.4	-36.163

	Identifier 1	Date	Time	Peak Nr	Start	Rt	End	Area All	Ampl 44	BGD 44	BGD 45	BGD 46	d13C/12C
R	M2631412	05/07/18	11:17:21	1	26.3	47	50.6	58.427	2935	4.5	5.5	21.4	-36.03
R	M2631412	05/07/18	11:17:21	2	66.3	86.9	90.5	58.525	2938	4.6	5.5	21.2	-36.1
R	M2631412	05/07/18	11:17:21	3	106	126.7	130.4	58.461	2947	4.7	5.6	21.0	-36.163
PE	M2631412	05/07/18	11:17:21	4	234.1	242.2	247.5	1.819	298	4.1	4.9	19.1	-31.902
PE	M2631412	05/07/18	11:17:21	5	247.5	250.2	294.5	2.29	133	4.1	4.9	19.1	-33.395
S	M2631412	05/07/18	11:17:21	6	533.4	551.8	627.4	16.948	712	4.6	5.4	18.5	-25.076
PE	M2631412	05/07/18	11:17:21	7	831.6	840.6	902.3	6.558	290	6.8	8.1	19.9	-33.328
R	M2631412	05/07/18	11:17:21	8	1180.8	1201.5	1204.9	58.464	2938	5.3	6.3	16.8	-35.976
R	M2631412	05/07/18	11:17:21	9	1220.6	1240.2	1244.8	58.45	2937	5.5	6.5	17.1	-36.1
R	M2631412	05/07/18	11:17:21	10	1260.5	1281.2	1284.7	58.451	2942	5.4	6.3	16.9	-36.169

	Identifier 1	Date	Time	Peak Nr	Start	Rt	End	Area All	Ampl 44	BGD 44	BGD 45	BGD 46	d13C/12C
R	M2701610	05/07/18	11:49:46	1	26.3	47	50.6	57.274	2880	5.2	6.3	23.3	-36.011
R	M2701610	05/07/18	11:49:46	2	66.3	86.9	90.3	57.375	2887	5.2	6.3	23.0	-36.1
R	M2701610	05/07/18	11:49:46	3	106	126.7	130.4	57.653	2911	5.2	6.3	22.7	-36.161
PE	M2701610	05/07/18	11:49:46	4	229.9	239.1	305.1	8.677	396	4.6	5.6	20.7	-33.148
S	M2701610	05/07/18	11:49:46	5	534.6	540.7	555.9	0.215	17	7.9	9.4	23.4	-34.382

	Identifier 1	Date	Time	Peak Nr	Start	Rt	End	Area All	Ampl 44	BGD 44	BGD 45	BGD 46	d13C/12C
R	M276543	05/07/18	12:47:04	1	26.3	47	50.6	57.301	2888	5.1	6.1	26.8	-35.974
R	M276543	05/07/18	12:47:04	2	66.3	86.9	90.3	57.363	2886	5.2	6.3	26.7	-36.1
R	M276543	05/07/18	12:47:04	3	106	126.7	130.2	57.475	2892	5.2	6.3	26.4	-36.164
PE	M276543	05/07/18	12:47:04	4	228.9	238.7	246.6	3.133	382	4.7	5.6	24.1	-32.085
PE	M276543	05/07/18	12:47:04	5	246.6	247	281.7	1.108	72	4.7	5.6	24.1	-37.326
S	M276543	05/07/18	12:47:04	6	524.8	541.5	563.5	0.885	40	5.2	6.3	22.7	-25.378
PE	M276543	05/07/18	12:47:04	7	834.5	841.4	847.5	0.999	169	4.7	5.6	20.4	-31.498
PE	M276543	05/07/18	12:47:04	8	847.5	851.7	881.8	1.159	57	4.7	5.6	20.4	-34.698
R	M276543	05/07/18	12:47:04	9	1180.6	1201.3	1204.9	57.724	2908	5.0	5.9	19.5	-35.957
R	M276543	05/07/18	12:47:04	10	1220.6	1241.3	1244.6	57.858	2901	5.2	6.2	19.8	-36.1
R	M276543	05/07/18	12:47:04	11	1260.3	1281	1284.3	57.92	2920	5.0	6.1	19.7	-36.147

Table A.2 (cont.) R = reference gas; PE = PE standard; S = sample. Date in MM/DD/YY format. Time is in Central European Standard Time (UTC +2). Peak Nr = peak number. Start = peak start time (s). Rt = retention time (s). End = end peak time (s). Area all = peak area (Vs). Ampl 44 = peak amplitude. BGD 44, BGD 45, BGD 46 = background gas levels. d13C/12C = $\delta^{13}C$.

	Identifier 1	Date	Time	Peak Nr	Start	Rt	End	Area All	Ampl 44	BGD 44	BGD 45	BGD 46	d13C/12C
R	M256039	05/07/18	13:57:24	1	26.3	47	50.6	47.909	2413	3.0	3.6	13.3	-36.155
R	M256039	05/07/18	13:57:24	2	66.3	86.9	90.3	48.275	2433	3.1	3.8	13.8	-36.1
R	M256039	05/07/18	13:57:24	3	106	126.7	130.2	48.756	2456	3.2	3.9	14.0	-36.043
PE	M256039	05/07/18	13:57:24	4	228.2	243.1	289.5	4.091	190	3.0	3.6	13.8	-32.957
S	M256039	05/07/18	13:57:24	5	527.1	544	579.8	1.863	89	4.0	4.8	15.3	-28.033
PE	M256039	05/07/18	13:57:24	6	826	841.4	884.1	2.902	149	4.3	5.2	15.5	-33.285
S	M256039	05/07/18	13:57:24	7	1180.6	1201.3	1204.7	55.771	2812	4.3	5.1	15.1	-35.946
R	M256039	05/07/18	13:57:24	8	1220.4	1241	1244.6	55.977	2813	4.4	5.3	15.4	-36.1
R	M256039	05/07/18	13:57:24	9	1260.3	1281	1284.5	55.947	2813	4.6	5.5	15.6	-36.183

	Identifier 1	Date	Time	Peak Nr	Start	Rt	End	Area All	Ampl 44	BGD 44	BGD 45	BGD 46	d13C/12C
R	M263143	05/07/18	14:44:26	1	26.3	47	50.6	55.894	2816	4.9	5.9	22.6	-36.007
R	M263143	05/07/18	14:44:26	2	66.3	86.9	90.3	55.94	2814	5.0	6.1	22.6	-36.1
R	M263143	05/07/18	14:44:26	3	106	126.7	130.2	56.078	2817	5.0	6.0	22.3	-36.168
PE	M263143	05/07/18	14:44:26	4	233.7	253.1	308.3	7.031	261	4.5	5.5	20.8	-33.598
S	M263143	05/07/18	14:44:26	5	541.1	547.8	595	2.443	137	7.3	8.7	23.2	-28.227
PE	M263143	05/07/18	14:44:26	6	833.7	852.1	906.4	4.695	194	5.2	6.2	19.1	-33.096
R	M263143	05/07/18	14:44:26	7	1180.8	1201.5	1204.9	57.118	2871	5.2	6.2	18.3	-35.923
R	M263143	05/07/18	14:44:26	8	1220.6	1241.3	1244.6	57.282	2889	5.3	6.4	18.5	-36.1
R	M263143	05/07/18	14:44:26	9	1260.5	1281.2	1284.7	57.198	2872	5.4	6.5	18.6	-36.161

	Identifier 1	Date	Time	Peak Nr	Start	Rt	End	Area All	Ampl 44	BGD 44	BGD 45	BGD 46	d13C/12C
R	M270168	05/07/18	15:28:49	1	26.3	47	50.6	52.57	2649	4.7	5.8	20.7	-36.102
R	M270168	05/07/18	15:28:49	2	66.3	86.9	90.5	53.318	2682	4.9	6.0	21.0	-36.1
R	M270168	05/07/18	15:28:49	3	106	126.7	130	53.592	2697	4.9	5.9	20.8	-36.119
PE	M270168	05/07/18	15:28:49	4	229.5	239.5	284.7	8.088	661	4.4	5.3	19.5	-32.374
S	M270168	05/07/18	15:28:49	5	527.1	542.6	575.4	1.353	71	5.3	6.3	19.8	-29.843
PE	M270168	05/07/18	15:28:49	6	827.6	836.6	843.7	3.102	325	4.8	5.8	18.2	-31.699
PE	M270168	05/07/18	15:28:49	7	843.7	845.4	887.4	2.186	138	4.8	5.8	18.2	-32.469
R	M270168	05/07/18	15:28:49	8	1180.8	1201.5	1204.7	56.762	2859	4.9	5.9	17.5	-35.909
R	M270168	05/07/18	15:28:49	9	1220.6	1241.3	1244.6	56.811	2861	5.1	6.2	18.0	-36.1

Table A.2 (cont.) R = reference gas; PE = PE standard; S = sample. Date in MM/DD/YY format. Time is in Central European Standard Time (UTC +2). Peak Nr = peak number. Start = peak start time (s). Rt = retention time (s). End = end peak time (s). Area all = peak area (Vs). Ampl 44 = peak amplitude. BGD 44, BGD 45, BGD 46 = background gas levels. d13C/12C = δ^{13}C.

	Identifier 1	Date	Time	Peak Nr	Start	Rt	End	Area All	Ampl 44	BGD 44	BGD 45	BGD 46	d13C/12C
R	M270168	05/07/18	15:28:49	10	1260.5	1281.2	1284.5	56.916	2863	5.1	6.1	17.9	-36.132
	Identifier 1	**Date**	**Time**	**Peak Nr**	**Start**	**Rt**	**End**	**Area All**	**Ampl 44**	**BGD 44**	**BGD 45**	**BGD 46**	**d13C/12C**
R	M2765410(1)	05/07/18	16:15:30	1	26.3	47	50.6	51.688	2606	4.2	5.1	15.7	-36.14
R	M2765410(1)	05/07/18	16:15:30	2	66.3	86.9	90.3	51.987	2622	4.4	5.3	15.9	-36.1
R	M2765410(1)	05/07/18	16:15:30	3	106	126.7	130.2	52.266	2637	4.5	5.5	16.2	-36.126
PE	M2765410(1)	05/07/18	16:15:30	4	224.7	233.5	238.7	2.783	422	4.1	4.9	15.4	-32.1
PE	M2765410(1)	05/07/18	16:15:30	5	238.7	242.2	295.9	3.849	219	4.1	4.9	15.4	-33.765
S	M2765410(1)	05/07/18	16:15:30	6	518.5	527.9	568.1	2.755	129	5.1	6.1	16.6	-23.118
PE	M2765410(1)	05/07/18	16:15:30	7	820.7	828.7	867.1	4.766	478	4.9	5.9	15.8	-32.502
R	M2765410(1)	05/07/18	16:15:30	8	1180.6	1201.3	1204.9	56.264	2833	4.6	5.6	15.1	-35.954
R	M2765410(1)	05/07/18	16:15:30	9	1220.6	1241.3	1244.6	56.611	2850	4.9	5.9	15.5	-36.1
R	M2765410(1)	05/07/18	16:15:30	10	1260.3	1281	1284.5	56.479	2843	4.8	5.8	15.4	-36.198
	Identifier 1	**Date**	**Time**	**Peak Nr**	**Start**	**Rt**	**End**	**Area All**	**Ampl 44**	**BGD 44**	**BGD 45**	**BGD 46**	**d13C/12C**
R	M2560314(2)	05/08/18	10:34:48	1	26.5	47	50.6	52.75	2649	2.5	2.9	7.0	-36.024
R	M2560314(2)	05/08/18	10:34:48	2	66.3	86.9	90.5	52.877	2663	2.6	3.1	7.2	-36.1
R	M2560314(2)	05/08/18	10:34:48	3	106.2	126.9	130.2	53.032	2664	2.7	3.2	7.3	-36.162
PE	M2560314(2)	05/08/18	10:34:48	4	224.7	233	240.8	2.957	416	2.4	2.8	6.8	-32.113
PE	M2560314(2)	05/08/18	10:34:48	5	240.8	241.2	280.9	1.763	122	2.4	2.8	6.8	-35.918
S	M2560314(2)	05/08/18	10:34:48	6	521.9	537.8	600.9	6.592	344	3.2	3.8	8.1	-25.429
PE	M2560314(2)	05/08/18	10:34:48	7	825.5	833.9	887.6	4.902	234	4.1	4.8	9.0	-32.92
R	M2560314(2)	05/08/18	10:34:48	8	1180.8	1201.5	1204.9	57.297	2882	3.7	4.3	8.4	-35.924
R	M2560314(2)	05/08/18	10:34:48	9	1220.6	1241.3	1244.8	57.483	2887	3.9	4.6	8.8	-36.1
R	M2560314(2)	05/08/18	10:34:48	10	1260.5	1281.2	1284.7	57.509	2897	3.9	4.6	8.9	-36.171
	Identifier 1	**Date**	**Time**	**Peak Nr**	**Start**	**Rt**	**End**	**Area All**	**Ampl 44**	**BGD 44**	**BGD 45**	**BGD 46**	**d13C/12C**
R	M263144	05/08/18	11:21:07	1	26.3	47	50.4	57.031	2870	4.6	5.6	15.6	-36.018
R	M263144	05/08/18	11:21:07	2	66.3	86.9	90.5	57.135	2875	4.8	5.7	15.7	-36.1
R	M263144	05/08/18	11:21:07	3	106	126.9	130.2	57.313	2877	4.7	5.6	15.4	-36.148
PE	M263144	05/08/18	11:21:07	4	230.5	239.5	305.3	7.672	411	4.2	4.9	14.1	-32.638
S	M263144	05/08/18	11:21:07	5	528.6	545.1	606.1	6.884	325	5.0	5.9	14.6	-27.9
PE	M263144	05/08/18	11:21:07	6	858.6	867.3	919.6	4.837	236	5.0	5.9	13.8	-33.083

Table A.2 (cont.) R = reference gas; PE = PE standard; S = sample. Date in MM/DD/YY format. Time is in Central European Standard Time (UTC +2). Peak Nr = peak number. Start = peak start time (s). Rt = retention time (s). End = end peak time (s). Area all = peak area (Vs). Ampl 44 = peak amplitude. BGD 44, BGD 45, BGD 46 = background gas levels. d13C/12C = $\delta^{13}C$.

	Identifier 1	Date	Time	Peak Nr	Start	Rt	End	Area All	Ampl 44	BGD 44	BGD 45	BGD 46	d13C/12C
R	M263144	05/08/18	11:21:07	7	1180.8	1201.3	1204.9	57.991	2924	4.8	5.7	13.1	-35.913
R	M263144	05/08/18	11:21:07	8	1220.6	1241.3	1244.6	57.859	2911	4.8	5.7	13.1	-36.1
R	M263144	05/08/18	11:21:07	9	1260.5	1281.2	1284.5	58.056	2916	4.7	5.6	13.1	-36.159

	Identifier 1	Date	Time	Peak Nr	Start	Rt	End	Area All	Ampl 44	BGD 44	BGD 45	BGD 46	d13C/12C
R	M270162	05/08/18	12:20:44	1	26.5	47	50.6	52.995	2673	5.1	6.2	17.5	-36.02
R	M270162	05/08/18	12:20:44	2	66.3	86.9	90.5	53.322	2687	5.2	6.3	17.6	-36.1
R	M270162	05/08/18	12:20:44	3	106.2	126.9	130	53.597	2698	5.1	6.2	17.4	-36.188
PE	M270162	05/08/18	12:20:44	4	241.4	253.7	269.6	0.416	23	4.9	5.9	16.6	-40.233
S	M270162	05/08/18	12:20:44	5	526.5	544.4	600	7.705	337	5.0	6.1	16.8	-29.881
PE	M270162	05/08/18	12:20:44	6	839.8	854.2	872.6	0.549	26	6.5	7.8	17.5	-40.428
R	M270162	05/08/18	12:20:44	7	1180.8	1201.5	1204.9	56.667	2847	5.2	6.2	15.3	-35.909
R	M270162	05/08/18	12:20:44	8	1220.6	1241.3	1244.8	56.709	2857	5.4	6.5	15.6	-36.1
R	M270162	05/08/18	12:20:44	9	1260.5	1281.2	1284.5	56.9	2866	5.5	6.5	15.7	-36.13

	Identifier 1	Date	Time	Peak Nr	Start	Rt	End	Area All	Ampl 44	BGD 44	BGD 45	BGD 46	D13C/12C
R	M276545(2)	05/08/18	14:09:06	1	26.5	47	50.4	55.456	2793	5.2	6.3	17.5	-36.004
R	M276545(2)	05/08/18	14:09:06	2	66.3	86.9	90.3	55.356	2791	5.3	6.5	17.5	-36.1
R	M276545(2)	05/08/18	14:09:06	3	106.2	126.9	130	55.517	2799	5.3	6.4	17.4	-36.132
PE	M276545(2)	05/08/18	14:09:06	4	237.2	247.9	266.7	0.554	34	4.9	6.0	16.5	-37.951

	Identifier 1	Date	Time	Peak Nr	Start	Rt	End	Area All	Ampl 44	BGD 44	BGD 45	BGD 46	d13C/12C
R	M276545(3)	05/08/18	14:57:29	1	26.3	47	50.6	49.588	2500	4.4	5.3	13.9	-36.088
R	M276545(3)	05/08/18	14:57:29	2	66.3	86.9	90.3	49.826	2509	4.6	5.5	14.2	-36.1
R	M276545(3)	05/08/18	14:57:29	3	106.2	126.7	130.2	49.995	2512	4.6	5.5	14.3	-36.033
PE	M276545(3)	05/08/18	14:57:29	4	230.7	238.9	243.9	2.803	442	4.2	5.0	13.5	-31.716
PE	M276545(3)	05/08/18	14:57:29	5	243.9	248.1	301.8	5.074	264	4.2	5.0	13.5	-32.388
S	M276545(3)	05/08/18	14:57:29	6	527.7	534.8	578.1	2.023	83	5.3	6.3	15.2	-25.761
PE	M276545(3)	05/08/18	14:57:29	7	827.6	836.8	842.3	3.174	450	5.0	6.0	14.4	-32.019
PE	M276545(3)	05/08/18	14:57:29	8	842.3	845.6	898.1	3.892	204	5.0	6.0	14.4	-33.045
R	M276545(3)	05/08/18	14:57:29	9	1180.8	1201.5	1204.9	55.534	2797	5.3	6.3	14.5	-35.916
R	M276545(3)	05/08/18	14:57:29	10	1220.6	1241.3	1244.8	55.736	2803	5.3	6.4	14.7	-36.1
R	M276545(3)	05/08/18	14:57:29	11	1260.5	1281.2	1284.5	56.021	2810	5.3	6.3	14.6	-36.144

Table A.2 (cont.) R = reference gas; PE = PE standard; S = sample. Date in MM/DD/YY format. Time is in Central European Standard Time (UTC +2). Peak Nr = peak number. Start = peak start time (s). Rt = retention time (s). End = end peak time (s). Area all = peak area (Vs). Ampl 44 = peak amplitude. BGD 44, BGD 45, BGD 46 = background gas levels. d13C/12C = $\delta^{13}C$.

	Identifier 1	Date	Time	Peak Nr	Start	Rt	End	Area All	Ampl 44	BGD 44	BGD 45	BGD 46	d13C/12C
R	M256031	05/08/18	15:45:15	1	26.5	47	50.6	54.419	2738	4.8	5.8	14.8	-36.024
R	M256031	05/08/18	15:45:15	2	66.3	86.9	90.3	54.737	2751	4.9	5.9	14.9	-36.1
R	M256031	05/08/18	15:45:15	3	106.2	126.9	130.2	54.737	2751	4.9	5.9	14.8	-36.149
PE	M256031	05/08/18	15:45:15	4	224.7	241.2	303.5	9.246	364	4.5	5.5	14.1	-32.863
S	M256031	05/08/18	15:45:15	5	520.6	538.4	590.4	5.956	235	5.8	7.0	16.3	-26.39
PE	M256031	05/08/18	15:45:15	6	822.6	838.3	896.8	6.875	273	6.1	7.3	15.6	-33.009
R	M256031	05/08/18	15:45:15	7	1180.8	1201.5	1204.9	56.898	2864	5.7	6.9	14.8	-35.918
R	M256031	05/08/18	15:45:15	8	1220.6	1241.3	1244.6	57.081	2863	5.8	6.9	14.9	-36.1
R	M256031	05/08/18	15:45:15	9	1260.5	1281.2	1284.5	57.001	2867	5.7	6.9	14.9	-36.123

	Identifier 1	Date	Time	Peak Nr	Start	Rt	End	Area All	Ampl 44	BGD 44	BGD 45	BGD 46	d13C/12C
R	M270163	05/08/18	16:37:11	1	26.5	47	50.6	51.422	2595	4.1	5.0	12.0	-36.019
R	M270163	05/08/18	16:37:11	2	66.3	86.9	90.3	51.791	2606	4.3	5.2	12.2	-36.1
R	M270163	05/08/18	16:37:11	3	106.2	126.9	130.2	52.111	2633	4.3	5.2	12.2	-36.116
PE	M270163	05/08/18	16:37:11	4	225.5	234.3	294.9	6.905	398	4.0	4.8	11.8	-32.732
S	M270163	05/08/18	16:37:11	5	523.5	541.9	609.4	7.749	359	5.1	6.1	13.7	-30.783
PE	M270163	05/08/18	16:37:11	6	825.1	833.3	899.3	9.029	490	5.6	6.7	13.9	-32.43
R	M270163	05/08/18	16:37:11	7	1180.8	1201.5	1204.7	56.174	2823	5.2	6.3	13.2	-35.926
R	M270163	05/08/18	16:37:11	8	1220.6	1241.3	1244.8	56.229	2831	5.4	6.4	13.4	-36.1
R	M270163	05/08/18	16:37:11	9	1260.5	1281.2	1284.5	56.355	2837	5.3	6.4	13.4	-36.162

	Identifier 1	Date	Time	Peak Nr	Start	Rt	End	Area All	Ampl 44	BGD 44	BGD 45	BGD 46	d13C/12C
R	M276546	05/08/18	17:26:18	1	26.5	47.2	50.6	56.313	2837	5.0	6.1	15.8	-35.992
R	M276546	05/08/18	17:26:18	2	66.3	86.9	90.3	56.28	2833	5.1	6.3	16.0	-36.1
R	M276546	05/08/18	17:26:18	3	106.2	126.9	130.2	56.341	2832	5.0	6.2	15.8	-36.162
PE	M276546	05/08/18	17:26:18	4	222.2	231.2	236.6	5.154	717	4.7	5.8	15.0	-32.235
PE	M276546	05/08/18	17:26:18	5	236.8	240.4	296.6	0.215	54	290.2	335.5	411.1	12.387
S	M276546	05/08/18	17:26:18	6	523.8	541.1	597.9	8.246	387	5.8	7.0	16.2	-24.465
PE	M276546	05/08/18	17:26:18	7	823.5	831.8	837	3.535	549	5.9	7.1	15.7	-32.551
PE	M276546	05/08/18	17:26:18	8	837	840.2	895.4	5.481	290	5.9	7.1	15.7	-31.744
R	M276546	05/08/18	17:26:18	9	1180.8	1201.5	1204.9	57.72	2901	5.6	6.7	14.7	-35.926

Table A.2 (cont.) R = reference gas; PE = PE standard; S = sample. Date in MM/DD/YY format. Time is in Central European Standard Time (UTC +2). Peak Nr = peak number. Start = peak start time (s). Rt = retention time (s). End = end peak time (s). Area all = peak area (Vs). Ampl 44 = peak amplitude. BGD 44, BGD 45, BGD 46 = background gas levels. d13C/12C = δ^{13}C.

	Identifier 1	Date	Time	Peak Nr	Start	Rt	End	Area All	Ampl 44	BGD 44	BGD 45	BGD 46	d13C/12C
R	M276546	05/08/18	17:26:18	10	1220.8	1241.3	1244.6	57.724	2913	5.7	6.9	15.0	-36.1
R	M276546	05/08/18	17:26:18	11	1260.5	1281.2	1284.7	57.987	2913	5.7	6.9	15.1	-36.145
	Identifier 1	**Date**	**Time**	**Peak Nr**	**Start**	**Rt**	**End**	**Area All**	**Ampl 44**	**BGD 44**	**BGD 45**	**BGD 46**	**d13C/12C**
R	M263149	05/09/18	11:07:33	1	26.5	47	50.6	51.075	2565	3.8	4.5	8.3	-35.947
R	M263149	05/09/18	11:07:33	2	66.3	86.9	90.3	51.34	2597	3.9	4.6	8.4	-36.1
R	M263149	05/09/18	11:07:33	3	106.2	126.9	130.2	51.527	2594	3.9	4.6	8.5	-36.178
PE	M263149	05/09/18	11:07:33	4	224.9	234.1	239.7	4.503	598	3.5	4.2	7.9	-32.348
PE	M263149	05/09/18	11:07:33	5	239.7	243.1	302.6	5.614	286	3.5	4.2	7.9	-32.617
S	M263149	05/09/18	11:07:33	6	520.4	536.7	606.7	8.019	366	4.9	5.7	10.1	-28.894
PE	M263149	05/09/18	11:07:33	7	821	828.1	892	7.422	358	5.2	6.1	10.2	-32.75
R	M263149	05/09/18	11:07:33	8	1180.8	1201.5	1205.1	55.765	2808	4.8	5.7	9.6	-35.925
R	M263149	05/09/18	11:07:33	9	1220.6	1241.5	1245	55.803	2806	5.1	6.0	10.0	-36.1
R	M263149	05/09/18	11:07:33	10	1260.5	1281.2	1284.5	55.783	2805	4.9	5.8	9.8	-36.164
	Identifier 1	**Date**	**Time**	**Peak Nr**	**Start**	**Rt**	**End**	**Area All**	**Ampl 44**	**BGD 44**	**BGD 45**	**BGD 46**	**d13C/12C**
R	M270164	05/09/18	12:15:19	1	26.5	47	50.4	52.579	2651	4.8	5.8	14.0	-35.993
R	M270164	05/09/18	12:15:19	2	66.3	86.9	90.3	52.741	2655	4.8	5.8	13.8	-36.1
R	M270164	05/09/18	12:15:19	3	106.2	126.9	130.2	52.928	2665	4.8	5.8	13.8	-36.141
PE	M270164	05/09/18	12:15:19	4	223.8	232.8	279.9	4.488	347	4.4	5.4	13.0	-32.66
S	M270164	05/09/18	12:15:19	5	519.6	524.4	529.2	0.127	23	5.0	6.0	13.4	-28.345
S	M270164	05/09/18	12:15:19	6	529.2	533.8	558	0.543	38	5.0	6.0	13.4	-30.323
PE	M270164	05/09/18	12:15:19	7	823.5	832.4	880.9	5.547	414	4.5	5.4	12.2	-32.622
R	M270164	05/09/18	12:15:19	8	1180.8	1201.5	1204.7	55.421	2785	4.9	5.8	12.5	-35.925
R	M270164	05/09/18	12:15:19	9	1220.6	1241.3	1244.8	55.747	2794	5.0	5.9	12.6	-36.1
R	M270164	05/09/18	12:15:19	10	1260.5	1281.2	1284.7	55.694	2802	4.9	5.9	12.6	-36.139
	Identifier 1	**Date**	**Time**	**Peak Nr**	**Start**	**Rt**	**End**	**Area All**	**Ampl 44**	**BGD 44**	**BGD 45**	**BGD 46**	**d13C/12C**
R	M270165	05/09/18	13:58:45	1	26.5	47	50.6	56.611	2854	3.5	4.2	9.7	-35.992
R	M270165	05/09/18	13:58:45	2	66.3	86.9	90.5	56.796	2860	3.7	4.5	10.1	-36.1
R	M270165	05/09/18	13:58:45	3	106.2	126.7	130	56.85	2859	3.8	4.6	10.2	-36.197
PE	M270165	05/09/18	13:58:45	4	229.3	239.3	292.2	6.504	409	3.5	4.2	9.6	-33.008
S	M270165	05/09/18	13:58:45	5	527.7	547.2	592.3	4.903	188	4.5	5.3	11.3	-30.457

Table A.2 (cont.) R = reference gas; PE = PE standard; S = sample. Date in MM/DD/YY format. Time is in Central European Standard Time (UTC +2). Peak Nr = peak number. Start = peak start time (s). Rt = retention time (s). End = end peak time (s). Area all = peak area (Vs). Ampl 44 = peak amplitude. BGD 44, BGD 45, BGD 46 = background gas levels. d13C/12C = $\delta^{13}C$.

	Identifier 1	Date	Time	Peak Nr	Start	Rt	End	Area All	Ampl 44	BGD 44	BGD 45	BGD 46	d13C/12C
PE	M270165	05/09/18	13:58:45	6	826.2	835.2	841.6	3.949	531	5.1	6.1	11.6	-32.548
PE	M270165	05/09/18	13:58:45	7	841.6	843.7	891.2	3.332	173	5.1	6.1	11.6	-33.199
R	M270165	05/09/18	13:58:45	8	1180.8	1201.5	1204.9	56.76	2858	4.8	5.7	11.0	-35.928
R	M270165	05/09/18	13:58:45	9	1220.6	1241.3	1244.6	56.844	2858	5.0	6.0	11.3	-36.1
R	M270165	05/09/18	13:58:45	10	1260.5	1281.2	1284.5	56.856	2860	4.9	5.8	11.1	-36.14
	Identifier 1	**Date**	**Time**	**Peak Nr**	**Start**	**Rt**	**End**	**Area All**	**Ampl 44**	**BGD 44**	**BGD 45**	**BGD 46**	**d13C/12C**
R	M2560310	05/09/18	14:45:49	1	26.5	47	50.6	53.565	2694	4.7	5.6	12.7	-36.034
R	M2560310	05/09/18	14:45:49	2	66.3	86.9	90.3	53.89	2707	4.8	5.8	12.9	-36.1
R	M2560310	05/09/18	14:45:49	3	106.2	126.9	130.2	53.992	2708	4.7	5.6	12.7	-36.143
PE	M2560310	05/09/18	14:45:49	4	227.8	236	241.2	2.687	447	4.4	5.3	12.0	-31.964
PE	M2560310	05/09/18	14:45:49	5	241.2	244.3	296.4	3.944	225	4.4	5.3	12.0	-33.219
S	M2560310	05/09/18	14:45:49	6	521.5	540.3	623.4	16.221	654	5.3	6.4	13.5	-25.191
PE	M2560310	05/09/18	14:45:49	7	831	840.2	897	6.392	371	9.0	10.6	17.9	-32.621
R	M2560310	05/09/18	14:45:49	8	1180.8	1201.5	1204.9	56.269	2837	6.0	7.2	13.6	-35.936
R	M2560310	05/09/18	14:45:49	9	1220.8	1241.3	1244.8	56.16	2829	6.2	7.4	13.8	-36.1
R	M2560310	05/09/18	14:45:49	10	1260.5	1281.2	1284.5	56.232	2833	5.9	7.1	13.5	-36.141
	Identifier 1	**Date**	**Time**	**Peak Nr**	**Start**	**Rt**	**End**	**Area All**	**Ampl 44**	**BGD 44**	**BGD 45**	**BGD 46**	**d13C/12C**
R	M2631411	05/09/18	15:37:17	1	26.5	47.2	50.4	53.459	2702	5.2	6.3	14.5	-35.981
R	M2631411	05/09/18	15:37:17	2	66.3	86.9	90.3	53.628	2698	5.2	6.3	14.5	-36.1
R	M2631411	05/09/18	15:37:17	3	106.2	126.9	130.2	53.569	2695	5.3	6.4	14.5	-36.149
PE	M2631411	05/09/18	15:37:17	4	225.7	233.9	270.4	1.907	111	5.0	6.0	13.8	-33.813
S	M2631411	05/09/18	15:37:17	5	522.1	529.8	569.5	1.295	59	5.5	6.6	14.3	-28.89
PE	M2631411	05/09/18	15:37:17	6	836	849.2	881.1	2.118	150	5.2	6.3	13.4	-33.831
R	M2631411	05/09/18	15:37:17	7	1180.8	1201.3	1204.7	55.937	2808	5.4	6.5	13.3	-35.887
R	M2631411	05/09/18	15:37:17	8	1220.6	1241.3	1244.8	55.725	2802	5.6	6.7	13.6	-36.1
R	M2631411	05/09/18	15:37:17	9	1260.5	1281.2	1284.5	55.765	2810	5.6	6.7	13.6	-36.147
	Identifier 1	**Date**	**Time**	**Peak Nr**	**Start**	**Rt**	**End**	**Area All**	**Ampl 44**	**BGD 44**	**BGD 45**	**BGD 46**	**d13C/12C**
R	M270169	05/09/18	17:45:37	1	26.5	47.2	50.4	54.804	2763	5.3	6.4	13.5	-35.979
R	M270169	05/09/18	17:45:37	2	66.3	86.9	90.3	54.818	2750	5.5	6.7	13.9	-36.1
R	M270169	05/09/18	17:45:37	3	106.2	126.9	130.2	54.894	2761	5.6	6.8	14.0	-36.143

Table A.2 (cont.) R = reference gas; PE = PE standard; S = sample. Date in MM/DD/YY format. Time is in Central European Standard Time (UTC +2). Peak Nr = peak number. Start = peak start time (s). Rt = retention time (s). End = end peak time (s). Area all = peak area (Vs). Ampl 44 = peak amplitude. BGD 44, BGD 45, BGD 46 = background gas levels. d13C/12C = δ^{13}C.

	Identifier 1	Date	Time	Peak Nr	Start	Rt	End	Area All	Ampl 44	BGD 44	BGD 45	BGD 46	d13C/12C
PE	M270169	05/09/18	17:45:37	4	226.6	235.3	241.4	4.693	659	5.1	6.2	13.2	-32.369
PE	M270169	05/09/18	17:45:37	5	241.4	243.9	298.7	5.9	311	5.1	6.2	13.2	-33.123
S	M270169	05/09/18	17:45:37	6	521.9	539.2	613	12.088	466	6.5	7.8	15.8	-29.932
PE	M270169	05/09/18	17:45:37	7	827	835.6	908.1	9.841	382	6.9	8.3	15.4	-32.52
R	M270169	05/09/18	17:45:37	8	1180.8	1201.5	1205.3	56.068	2819	6.5	7.7	14.5	-35.924
R	M270169	05/09/18	17:45:37	9	1220.6	1241.3	1244.8	56.035	2821	6.6	7.9	14.7	-36.1
R	M270169	05/09/18	17:45:37	10	1260.5	1281.2	1284.5	56.041	2823	6.5	7.9	14.6	-36.169
	Identifier 1	**Date**	**Time**	**Peak Nr**	**Start**	**Rt**	**End**	**Area All**	**Ampl 44**	**BGD 44**	**BGD 45**	**BGD 46**	**d13C/12C**
R	M2765412	05/11/18	14:39:55	1	26.3	47	50.4	50.27	2533	4.8	5.7	14.2	-35.926
R	M2765412	05/11/18	14:39:55	2	66.3	86.9	90.3	50.753	2559	4.9	5.9	14.4	-36.1
R	M2765412	05/11/18	14:39:55	3	106	126.7	130	50.97	2565	5.0	6.0	14.6	-36.17
PE	M2765412	05/11/18	14:39:55	4	229.9	238.7	298.9	6.435	328	4.9	5.9	14.3	-33.035
S	M2765412	05/11/18	14:39:55	5	523.5	530.7	589.6	5.585	194	6.1	7.3	16.3	-24.607
PE	M2765412	05/11/18	14:39:55	6	832.9	842.5	902	8.204	357	6.7	7.9	16.5	-32.664
R	M2765412	05/11/18	14:39:55	7	1180.8	1201.3	1204.7	56.045	2822	6.8	8.2	16.5	-35.956
R	M2765412	05/11/18	14:39:55	8	1220.6	1241.3	1244.8	56.155	2825	6.9	8.3	16.6	-36.1
R	M2765412	05/11/18	14:39:55	9	1260.5	1281.2	1284.5	56.223	2830	6.8	8.1	16.5	-36.144
	Identifier 1	**Date**	**Time**	**Peak Nr**	**Start**	**Rt**	**End**	**Area All**	**Ampl 44**	**BGD 44**	**BGD 45**	**BGD 46**	**d13C/12C**
R	M2560312	05/11/18	15:26:42	1	26.3	47	50.4	53.579	2699	5.6	6.7	15.2	-36.019
R	M2560312	05/11/18	15:26:42	2	66.3	86.9	90.3	53.896	2723	5.7	6.9	15.4	-36.1
R	M2560312	05/11/18	15:26:42	3	106	126.7	130	54.1	2721	5.6	6.7	15.3	-36.125
PE	M2560312	05/11/18	15:26:42	4	223.4	233.5	293.2	7.324	406	5.4	6.5	14.8	-32.818
S	M2560312	05/11/18	15:26:42	5	516.9	534.4	580.8	6.849	283	6.6	7.9	16.9	-28.548
PE	M2560312	05/11/18	15:26:42	6	814.9	822.8	876.3	6.276	374	7.3	8.6	16.8	-32.403
R	M2560312	05/11/18	15:26:42	7	1180.8	1201.3	1204.7	56.607	2848	6.7	7.9	15.7	-35.944
R	M2560312	05/11/18	15:26:42	8	1220.6	1241.3	1244.6	56.566	2850	6.7	8.0	15.9	-36.1
R	M2560312	05/11/18	15:26:42	9	1260.5	1281.2	1284.5	56.633	2853	6.6	7.9	15.7	-36.15
	Identifier 1	**Date**	**Time**	**Peak Nr**	**Start**	**Rt**	**End**	**Area All**	**Ampl 44**	**BGD 44**	**BGD 45**	**BGD 46**	**d13C/12C**
R	M2631414	05/11/18	16:27:42	1	26.3	47	50.6	56.111	2830	5.5	6.7	16.1	-35.987
R	M2631414	05/11/18	16:27:42	2	66.3	86.9	90.3	56.281	2831	5.7	6.9	16.2	-36.1

Table A.2 (cont.) R = reference gas; PE = PE standard; S = sample. Date in MM/DD/YY format. Time is in Central European Standard Time (UTC +2). Peak Nr = peak number. Start = peak start time (s). Rt = retention time (s). End = end peak time (s). Area all = peak area (Vs). Ampl 44 = peak amplitude. BGD 44, BGD 45, BGD 46 = background gas levels. d13C/12C = $\delta^{13}C$.

	Identifier 1	Date	Time	Peak Nr	Start	Rt	End	Area All	Ampl 44	BGD 44	BGD 45	BGD 46	d13C/12C
R	M2631414	05/11/18	16:27:42	3	106	126.7	130	56.2	2830	5.6	6.8	16.1	-36.174
PE	M2631414	05/11/18	16:27:42	4	226.1	236.4	283.8	7.897	610	5.3	6.4	15.4	-32.698
S	M2631414	05/11/18	16:27:42	5	519.8	537.8	605.7	8.947	431	6.8	8.1	17.7	-28.286
PE	M2631414	05/11/18	16:27:42	6	823.7	833.1	873.8	5.777	444	7.4	8.8	17.5	-32.267
R	M2631414	05/11/18	16:27:42	7	1180.8	1201.5	1204.9	56.892	2872	6.8	8.1	16.3	-35.952
R	M2631414	05/11/18	16:27:42	8	1220.6	1241.3	1244.8	56.954	2860	6.9	8.3	16.5	-36.1
R	M2631414	05/11/18	16:27:42	9	1260.5	1281.2	1284.3	57.001	2867	6.8	8.1	16.3	-36.155
	Identifier 1	**Date**	**Time**	**Peak Nr**	**Start**	**Rt**	**End**	**Area All**	**Ampl 44**	**BGD 44**	**BGD 45**	**BGD 46**	**d13C/12C**
R	M2701612	05/14/18	10:01:59	1	26.3	47	51.2	61.272	3084	2.3	2.6	3.3	-35.935
R	M2701612	05/14/18	10:01:59	2	66.3	86.9	90.9	61.191	3074	2.5	2.9	3.5	-36.1
R	M2701612	05/14/18	10:01:59	3	106.2	126.9	130.8	61.237	3073	2.5	2.9	3.5	-36.185
PE	M2701612	05/14/18	10:01:59	4	224.5	237.8	285.5	5.148	315	2.1	2.4	3.0	-32.977
S	M2701612	05/14/18	10:01:59	5	516.6	532.5	564.3	1.673	87	3.9	4.5	5.6	-29.083
PE	M2701612	05/14/18	10:01:59	6	820.1	832.9	876.1	4.612	280	3.5	4.0	4.9	-32.981
R	M2701612	05/14/18	10:01:59	7	1180.8	1201.5	1205.7	61.539	3092	4.0	4.5	5.5	-35.936
R	M2701612	05/14/18	10:01:59	8	1220.6	1241.3	1245.6	61.492	3089	4.2	4.9	5.9	-36.1
R	M2701612	05/14/18	10:01:59	9	1260.5	1281.2	1285.1	61.238	3071	4.4	5.1	6.2	-36.19
	Identifier 1	**Date**	**Time**	**Peak Nr**	**Start**	**Rt**	**End**	**Area All**	**Ampl 44**	**BGD 44**	**BGD 45**	**BGD 46**	**d13C/12C**
R	M2631413	05/14/18	10:50:49	1	26.3	47	50.8	57.612	2897	3.7	4.4	7.2	-36.002
R	M2631413	05/14/18	10:50:49	2	66.3	86.9	90.7	57.636	2898	3.8	4.5	7.4	-36.1
R	M2631413	05/14/18	10:50:49	3	106	126.7	130.4	57.731	2894	3.8	4.6	7.4	-36.16
PE	M2631413	05/14/18	10:50:49	4	222.8	233	289	6.602	379	3.4	3.9	6.5	-32.718
S	M2631413	05/14/18	10:50:49	5	518.7	525.4	529.8	0.818	149	4.4	5.1	7.9	-24.763
S	M2631413	05/14/18	10:50:49	6	529.8	534.8	587.5	3.955	219	4.4	5.1	7.9	-26.595
PE	M2631413	05/14/18	10:50:49	7	821.6	831.4	883.7	4.712	206	4.3	5.0	7.5	-33.074
R	M2631413	05/14/18	10:50:49	8	1180.8	1201.3	1205.1	58.693	2952	4.4	5.1	7.5	-35.973
R	M2631413	05/14/18	10:50:49	9	1220.6	1241.3	1245	58.732	2958	4.5	5.3	7.8	-36.1
R	M2631413	05/14/18	10:50:49	10	1260.5	1281.2	1284.9	58.788	2950	4.6	5.4	7.8	-36.197
	Identifier 1	**Date**	**Time**	**Peak Nr**	**Start**	**Rt**	**End**	**Area All**	**Ampl 44**	**BGD 44**	**BGD 45**	**BGD 46**	**d13C/12C**
R	M259271	05/14/18	11:38:08	1	26.3	47	50.8	55.968	2816	3.9	4.7	9.3	-36.02

Table A.2 (cont.) R = reference gas; PE = PE standard; S = sample. Date in MM/DD/YY format. Time is in Central European Standard Time (UTC +2). Peak Nr = peak number. Start = peak start time (s). Rt = retention time (s). End = end peak time (s). Area all = peak area (Vs). Ampl 44 = peak amplitude. BGD 44, BGD 45, BGD 46 = background gas levels. d13C/12C = $\delta^{13}C$.

	Identifier 1	Date	Time	Peak Nr	Start	Rt	End	Area All	Ampl 44	BGD 44	BGD 45	BGD 46	d13C/12C
R	M259271	05/14/18	11:38:08	2	66.3	86.9	90.5	56.129	2829	4.0	4.9	9.5	-36.1
R	M259271	05/14/18	11:38:08	3	106.2	126.9	130.4	56.387	2839	4.0	4.8	9.4	-36.13
PE	M259271	05/14/18	11:38:08	4	220.3	230.3	275.9	5.836	439	3.6	4.3	8.5	-32.818
S	M259271	05/14/18	11:38:08	5	515.2	519.8	524.4	0.13	24	5.0	5.9	10.2	-24.206
S	M259271	05/14/18	11:38:08	6	524.4	530.2	559.1	1.021	62	5.0	5.9	10.2	-27.673
PE	M259271	05/14/18	11:38:08	7	819.3	831.4	871.3	3.841	314	4.4	5.2	9.0	-32.573
R	M259271	05/14/18	11:38:08	8	1180.8	1201.3	1204.9	58.259	2931	5.0	5.9	9.6	-35.927
R	M259271	05/14/18	11:38:08	9	1220.6	1241.3	1244.8	58.344	2931	5.1	6.1	9.8	-36.1
R	M259271	05/14/18	11:38:08	10	1260.5	1281.2	1284.7	58.252	2938	5.1	6.1	9.8	-36.158
	Identifier 1	**Date**	**Time**	**Peak Nr**	**Start**	**Rt**	**End**	**Area All**	**Ampl 44**	**BGD 44**	**BGD 45**	**BGD 46**	**d13C/12C**
R	M259272	05/14/18	12:32:44	1	26.3	47	50.8	56.796	2863	4.0	4.8	9.8	-36.012
R	M259272	05/14/18	12:32:44	2	66.3	86.9	90.5	56.861	2867	4.1	4.9	9.9	-36.1
R	M259272	05/14/18	12:32:44	3	106	126.7	130.2	56.759	2854	4.1	4.9	9.8	-36.192
PE	M259272	05/14/18	12:32:44	4	223.6	232	279	3.83	186	3.7	4.4	9.0	-33.205
S	M259272	05/14/18	12:32:44	5	520.6	539.4	571.4	1.706	75	5.0	5.9	10.6	-26.906
PE	M259272	05/14/18	12:32:44	6	819.3	832.2	873.2	3.911	216	4.8	5.7	10.1	-33.24
R	M259272	05/14/18	12:32:44	7	1180.8	1201.3	1205.1	57.595	2900	5.0	6.0	10.1	-35.962
R	M259272	05/14/18	12:32:44	8	1220.6	1241.3	1244.8	57.622	2899	5.3	6.3	10.6	-36.1
R	M259272	05/14/18	12:32:44	9	1260.5	1281.2	1284.5	57.7	2897	5.2	6.2	10.4	-36.151
	Identifier 1	**Date**	**Time**	**Peak Nr**	**Start**	**Rt**	**End**	**Area All**	**Ampl 44**	**BGD 44**	**BGD 45**	**BGD 46**	**d13C/12C**
R	M259273	05/14/18	13:36:45	1	26.5	47	50.8	48.559	2452	3.1	3.8	7.5	-36.172
R	M259273	05/14/18	13:36:45	2	66.3	86.9	90.5	48.953	2463	3.3	4.0	7.7	-36.1
R	M259273	05/14/18	13:36:45	3	106.2	126.7	130.4	49.368	2489	3.4	4.1	7.8	-36.075
PE	M259273	05/14/18	13:36:45	4	227.6	235.3	293.4	5.181	263	3.1	3.7	7.4	-32.611
S	M259273	05/14/18	13:36:45	5	523.1	539	573.1	1.613	78	4.2	5.0	9.2	-26.976
PE	M259273	05/14/18	13:36:45	6	827.2	837.5	843.1	3.991	445	4.5	5.3	9.3	-32
PE	M259273	05/14/18	13:36:45	7	843.1	845.4	898.7	4.179	218	4.5	5.3	9.3	-32.963
R	M259273	05/14/18	13:36:45	8	1180.6	1201.3	1204.9	56.108	2835	4.8	5.6	9.5	-35.953
R	M259273	05/14/18	13:36:45	9	1220.6	1241.3	1245	56.381	2833	4.9	5.9	9.9	-36.1
R	M259273	05/14/18	13:36:45	10	1260.5	1281.2	1284.7	56.353	2841	4.8	5.7	9.7	-36.183

Table A.2 (cont.) R = reference gas; PE = PE standard; S = sample. Date in MM/DD/YY format. Time is in Central European Standard Time (UTC +2). Peak Nr = peak number. Start = peak start time (s). Rt = retention time (s). End = end peak time (s). Area all = peak area (Vs). Ampl 44 = peak amplitude. BGD 44, BGD 45, BGD 46 = background gas levels. d13C/12C = δ^{13}C.

	Identifier 1	Date	Time	Peak Nr	Start	Rt	End	Area All	Ampl 44	BGD 44	BGD 45	BGD 46	d13C/12C
R	M259277	05/14/18	15:15:38	1	26.3	47	50.6	50.669	2550	4.0	4.9	10.5	-35.975
R	M259277	05/14/18	15:15:38	2	66.3	86.9	90.5	50.975	2578	4.1	5.0	10.7	-36.1
R	M259277	05/14/18	15:15:38	3	106	126.7	130.2	51.403	2587	4.2	5.1	10.7	-36.099
PE	M259277	05/14/18	15:15:38	4	219.9	228.9	285.5	8.192	554	3.8	4.7	10.1	-32.605
S	M259277	05/14/18	15:15:38	5	520	537.8	606.5	10.566	493	5.1	6.1	12.3	-25.067
PE	M259277	05/14/18	15:15:38	6	818.9	828.5	883.9	7.713	503	6.3	7.5	13.2	-32.632
R	M259277	05/14/18	15:15:38	7	1180.8	1201.5	1204.9	56.353	2832	5.5	6.5	11.7	-35.979
R	M259277	05/14/18	15:15:38	8	1220.6	1241.3	1244.8	56.426	2841	5.6	6.7	12.1	-36.1
R	M259277	05/14/18	15:15:38	9	1260.5	1281.2	1284.7	56.569	2848	5.7	6.8	12.1	-36.166

	Identifier 1	Date	Time	Peak Nr	Start	Rt	End	Area All	Ampl 44	BGD 44	BGD 45	BGD 46	d13C/12C
R	M259279	05/14/18	16:17:17	1	26.5	47	50.6	52.538	2645	4.6	5.6	11.3	-36.023
R	M259279	05/14/18	16:17:17	2	66.3	86.9	90.5	52.992	2675	4.8	5.8	11.4	-36.1
R	M259279	05/14/18	16:17:17	3	106.2	126.7	130.2	53.218	2682	4.8	5.8	11.4	-36.129
PE	M259279	05/14/18	16:17:17	4	213.6	224.3	230.9	6.071	697	4.3	5.2	10.5	-32.39
PE	M259279	05/14/18	16:17:17	5	230.9	233.2	284	5.043	263	4.3	5.2	10.5	-32.854
S	M259279	05/14/18	16:17:17	6	512.9	533	579.3	4.046	172	5.6	6.7	12.4	-26.189
PE	M259279	05/14/18	16:17:17	7	813.6	822.4	828.3	4.251	589	5.4	6.5	11.6	-32.486
PE	M259279	05/14/18	16:17:17	8	828.3	831.4	885.3	5.074	253	5.4	6.5	11.6	-32.684
R	M259279	05/14/18	16:17:17	9	1180.8	1201.5	1204.9	56.597	2855	5.4	6.4	11.2	-35.916
R	M259279	05/14/18	16:17:17	10	1220.6	1241.3	1244.8	56.714	2851	5.5	6.6	11.4	-36.1
R	M259279	05/14/18	16:17:17	11	1260.5	1281.2	1284.5	56.721	2850	5.4	6.4	11.2	-36.166

	Identifier 1	Date	Time	Peak Nr	Start	Rt	End	Area All	Ampl 44	BGD 44	BGD 45	BGD 46	d13C/12C
R	M2592711(2)	05/15/18	10:28:12	1	26.3	47	50.6	52.577	2648	3.0	3.6	5.7	-35.993
R	M2592711(2)	05/15/18	10:28:12	2	66.3	86.9	90.5	52.84	2667	3.1	3.7	5.8	-36.1
R	M2592711(2)	05/15/18	10:28:12	3	106	126.7	130.2	53.105	2677	3.1	3.8	5.8	-36.161
PE	M2592711(2)	05/15/18	10:28:12	4	223	233.2	273.4	4.188	355	2.8	3.3	5.2	-32.549
S	M2592711(2)	05/15/18	10:28:12	5	519.4	536.7	587.3	4.623	205	3.4	4.0	6.2	-25.357
PE	M2592711(2)	05/15/18	10:28:12	6	821.4	829.9	870.7	3.967	317	3.9	4.6	6.5	-32.363
R	M2592711(2)	05/15/18	10:28:12	7	1180.8	1201.3	1204.9	58.236	2936	3.7	4.3	6.0	-35.955
R	M2592711(2)	05/15/18	10:28:12	8	1220.6	1241.3	1244.8	58.278	2936	3.8	4.5	6.3	-36.1

Table A.2 (cont.) R = reference gas; PE = PE standard; S = sample. Date in MM/DD/YY format. Time is in Central European Standard Time (UTC +2). Peak Nr = peak number. Start = peak start time (s). Rt = retention time (s). End = end peak time (s). Area all = peak area (Vs). Ampl 44 = peak amplitude. BGD 44, BGD 45, BGD 46 = background gas levels. d13C/12C = $\delta^{13}C$.

	Identifier 1	Date	Time	Peak Nr	Start	Rt	End	Area All	Ampl 44	BGD 44	BGD 45	BGD 46	d13C/12C
R	M2592711(2)	05/15/18	10:28:12	9	1260.5	1281	1284.7	58.386	2935	3.9	4.5	6.4	-36.123

	Identifier 1	Date	Time	Peak Nr	Start	Rt	End	Area All	Ampl 44	BGD 44	BGD 45	BGD 46	d13C/12C
R	M26709	05/15/18	11:17:35	1	26.3	47	50.6	56.027	2833	4.2	5.0	9.2	-36.027
R	M26709	05/15/18	11:17:35	2	66.3	86.9	90.5	56.234	2825	4.2	5.0	9.2	-36.1
R	M26709	05/15/18	11:17:35	3	106	126.7	130.2	56.361	2830	4.2	5.1	9.1	-36.159
PE	M26709	05/15/18	11:17:35	4	224.5	234.7	274.6	2.312	124	3.8	4.5	8.4	-33.321
S	M26709	05/15/18	11:17:35	5	517.5	534.2	580	3.452	182	4.4	5.3	9.3	-31.57
PE	M26709	05/15/18	11:17:35	6	819.3	832	873.6	2.523	138	4.5	5.4	8.9	-34.017
R	M26709	05/15/18	11:17:35	7	1180.6	1201.3	1204.9	58.117	2914	4.4	5.2	8.5	-35.956
R	M26709	05/15/18	11:17:35	8	1220.6	1241.3	1244.8	58.028	2924	4.6	5.4	8.8	-36.1
R	M26709	05/15/18	11:17:35	9	1260.3	1279.5	1284.5	58.265	2926	4.6	5.5	8.9	-36.178

	Identifier 1	Date	Time	Peak Nr	Start	Rt	End	Area All	Ampl 44	BGD 44	BGD 45	BGD 46	d13C/12C
R	M267011	05/15/18	11:59:53	1	26.3	47	50.6	54.919	2759	4.3	5.1	8.5	-36.073
R	M267011	05/15/18	11:59:53	2	66.3	86.9	90.5	55.07	2772	4.4	5.2	8.6	-36.1
R	M267011	05/15/18	11:59:53	3	106	126.7	130.2	55.348	2779	4.4	5.3	8.7	-36.117
PE	M267011	05/15/18	11:59:53	4	217.6	227	279.4	7.134	583	4.0	4.8	8.1	-32.355
S	M267011	05/15/18	11:59:53	5	533.2	539.4	543.8	0.479	90	4.6	5.4	9.0	-28.31
S	M267011	05/15/18	11:59:53	6	543.8	549.3	594.4	3.23	183	4.6	5.4	9.0	-29.846
PE	M267011	05/15/18	11:59:53	7	816.1	824.7	831.8	3.228	393	4.9	5.7	9.1	-32.376
PE	M267011	05/15/18	11:59:53	8	831.8	832.9	876.1	2.221	134	4.9	5.7	9.1	-34.05
R	M267011	05/15/18	11:59:53	9	1180.8	1201.3	1204.9	58.043	2918	4.5	5.3	8.5	-35.937
R	M267011	05/15/18	11:59:53	10	1220.6	1241.3	1244.8	58.029	2919	4.6	5.5	8.7	-36.1
R	M267011	05/15/18	11:59:53	11	1260.5	1281.2	1284.5	58.106	2918	4.7	5.5	8.8	-36.167

	Identifier 1	Date	Time	Peak Nr	Start	Rt	End	Area All	Ampl 44	BGD 44	BGD 45	BGD 46	d13C/12C
R	M267012	05/15/18	13:27:15	1	26.3	47	50.6	56.798	2858	4.1	5.0	9.9	-36.003
R	M267012	05/15/18	13:27:15	2	66.3	86.9	90.5	56.817	2855	4.2	5.1	9.9	-36.1
R	M267012	05/15/18	13:27:15	3	106	126.7	130.2	56.898	2863	4.3	5.2	10.0	-36.152
PE	M267012	05/15/18	13:27:15	4	218.4	227.6	235.3	4.74	538	3.9	4.7	9.2	-32.22
PE	M267012	05/15/18	13:27:15	5	235.3	237	283.8	3.038	177	3.9	4.7	9.2	-33.237
S	M267012	05/15/18	13:27:15	6	512.5	517.1	522.3	0.214	39	5.0	5.9	10.7	-28.216

Table A.2 (cont.) R = reference gas; PE = PE standard; S = sample. Date in MM/DD/YY format. Time is in Central European Standard Time (UTC +2). Peak Nr = peak number. Start = peak start time (s). Rt = retention time (s). End = end peak time (s). Area all = peak area (Vs). Ampl 44 = peak amplitude. BGD 44, BGD 45, BGD 46 = background gas levels. d13C/12C = δ^{13}C.

	Identifier 1	Date	Time	Peak Nr	Start	Rt	End	Area All	Ampl 44	BGD 44	BGD 45	BGD 46	d13C/12C
S	M267012	05/15/18	13:27:15	7	522.3	527.7	556.6	1.19	78	5.0	5.9	10.7	-29.518
PE	M267012	05/15/18	13:27:15	8	819.3	827.4	833.9	3.32	471	4.5	5.4	9.6	-32.213
PE	M267012	05/15/18	13:27:15	9	833.9	836.2	877.8	2.394	141	4.5	5.4	9.6	-32.924
R	M267012	05/15/18	13:27:15	10	1180.8	1201.3	1204.9	58.207	2937	4.5	5.3	9.4	-35.952
R	M267012	05/15/18	13:27:15	11	1220.6	1241.3	1244.6	58.185	2931	4.8	5.7	9.8	-36.1
R	M267012	05/15/18	13:27:15	12	1260.5	1281.2	1284.7	58.189	2923	4.8	5.7	9.8	-36.162
	Identifier 1	**Date**	**Time**	**Peak Nr**	**Start**	**Rt**	**End**	**Area All**	**Ampl 44**	**BGD 44**	**BGD 45**	**BGD 46**	**d13C/12C**
R	M267013	05/15/18	15:18:09	1	26.3	47	50.6	52.439	2641	4.3	5.2	10.7	-36.004
R	M267013	05/15/18	15:18:09	2	66.3	86.9	90.5	52.663	2657	4.4	5.4	10.8	-36.1
R	M267013	05/15/18	15:18:09	3	106.2	126.7	130.2	53.094	2675	4.4	5.4	10.8	-36.17
PE	M267013	05/15/18	15:18:09	4	219.4	228.4	278	6.02	460	4.1	5.0	10.1	-32.545
S	M267013	05/15/18	15:18:09	5	520	534.2	568.9	1.73	93	4.8	5.8	10.9	-27.602
PE	M267013	05/15/18	15:18:09	6	819.7	828.9	835.6	3.591	507	4.6	5.6	10.2	-32.43
PE	M267013	05/15/18	15:18:09	7	835.6	837.5	873.2	2.134	138	4.6	5.6	10.2	-32.594
R	M267013	05/15/18	15:18:09	8	1180.8	1201.5	1205.1	57.345	2889	4.6	5.6	10.0	-35.942
R	M267013	05/15/18	15:18:09	9	1220.6	1241.3	1244.6	57.499	2902	4.9	5.9	10.4	-36.1
R	M267013	05/15/18	15:18:09	10	1260.5	1281.2	1284.5	57.661	2897	5.0	6.0	10.6	-36.16
	Identifier 1	**Date**	**Time**	**Peak Nr**	**Start**	**Rt**	**End**	**Area All**	**Ampl 44**	**BGD 44**	**BGD 45**	**BGD 46**	**d13C/12C**
R	M267015	05/15/18	16:13:30	1	26.3	47	50.6	56.836	2849	4.6	5.6	11.2	-36.019
R	M267015	05/15/18	16:13:30	2	66.3	86.9	90.3	56.772	2860	4.8	5.9	11.5	-36.1
R	M267015	05/15/18	16:13:30	3	106.2	126.7	130.4	56.907	2862	4.8	5.8	11.4	-36.183
PE	M267015	05/15/18	16:13:30	4	220.7	229.5	269.4	6.523	557	4.3	5.2	10.5	-32.605
S	M267015	05/15/18	16:13:30	5	521	538	582.1	3.086	138	5.1	6.1	11.5	-30.346
PE	M267015	05/15/18	16:13:30	6	820.1	831.2	878.6	6.549	464	5.1	6.2	11.1	-32.46
R	M267015	05/15/18	16:13:30	7	1180.8	1201.5	1205.1	58.209	2937	5.1	6.1	10.9	-35.943
R	M267015	05/15/18	16:13:30	8	1220.6	1241.3	1244.8	58.325	2934	5.3	6.3	11.2	-36.1
R	M267015	05/15/18	16:13:30	9	1260.5	1281.2	1284.5	58.451	2939	5.2	6.2	11.0	-36.13
	Identifier 1	**Date**	**Time**	**Peak Nr**	**Start**	**Rt**	**End**	**Area All**	**Ampl 44**	**BGD 44**	**BGD 45**	**BGD 46**	**d13C/12C**
R	M26707	05/15/18	17:02:56	1	26.3	47	50.4	56.972	2872	4.5	5.5	11.6	-35.99
R	M26707	05/15/18	17:02:56	2	66.3	86.9	90.5	57.124	2872	4.8	5.8	11.8	-36.1
R	M26707	05/15/18	17:02:56	3	106	126.7	130.2	57.051	2869	4.7	5.7	11.7	-36.13

Table A.2 (cont.) R = reference gas; PE = PE standard; S = sample. Date in MM/DD/YY format. Time is in Central European Standard Time (UTC +2). Peak Nr = peak number. Start = peak start time (s). Rt = retention time (s). End = end peak time (s). Area all = peak area (Vs). Ampl 44 = peak amplitude. BGD 44, BGD 45, BGD 46 = background gas levels. d13C/12C = $\delta^{13}C$.

	Identifier 1	Date	Time	Peak Nr	Start	Rt	End	Area All	Ampl 44	BGD 44	BGD 45	BGD 46	d13C/12C
PE	M26707	05/15/18	17:02:56	4	225.3	232.6	241.8	3.939	515	4.3	5.2	10.9	-32.184
PE	M26707	05/15/18	17:02:56	5	241.8	242.4	282.4	1.84	118	4.3	5.2	10.9	-33.214
S	M26707	05/15/18	17:02:56	6	529.6	547.6	584.6	2.808	131	5.1	6.1	11.8	-29.738
PE	M26707	05/15/18	17:02:56	7	825.1	835	842.3	4.776	519	5.1	6.2	11.3	-32.366
PE	M26707	05/15/18	17:02:56	8	842.3	844.8	891.4	3.672	186	5.1	6.2	11.3	-32.308
R	M26707	05/15/18	17:02:56	9	1180.8	1201.5	1204.9	58.263	2938	5.3	6.4	11.4	-35.967
R	M26707	05/15/18	17:02:56	10	1220.6	1241.3	1244.8	58.234	2937	5.4	6.4	11.4	-36.1
R	M26707	05/15/18	17:02:56	11	1260.5	1281.2	1284.5	58.524	2944	5.3	6.4	11.4	-36.159
	Identifier 1	**Date**	**Time**	**Peak Nr**	**Start**	**Rt**	**End**	**Area All**	**Ampl 44**	**BGD 44**	**BGD 45**	**BGD 46**	**d13C/12C**
R	M26704	05/16/18	10:17:23	1	26.3	47	50.8	54.313	2736	2.9	3.4	5.6	-35.985
R	M26704	05/16/18	10:17:23	2	66.3	86.9	90.5	54.568	2755	3.0	3.5	5.7	-36.1
R	M26704	05/16/18	10:17:23	3	106	126.7	130.4	54.792	2756	3.1	3.6	5.8	-36.192
PE	M26704	05/16/18	10:17:23	4	220.5	227.4	232	4.118	812	2.7	3.2	5.2	-32.275
PE	M26704	05/16/18	10:17:23	5	232	237.4	327.3	14.706	610	2.7	3.2	5.2	-33.353
S	M26704	05/16/18	10:17:23	6	513.7	531.3	575	3.142	134	6.0	7.0	9.9	-30.912
PE	M26704	05/16/18	10:17:23	7	814.1	821.4	826.4	4.431	773	5.3	6.1	8.5	-32.444
PE	M26704	05/16/18	10:17:23	8	826.4	831	914	10.727	448	5.3	6.1	8.5	-32.95
R	M26704	05/16/18	10:17:23	9	1180.8	1201.5	1205.1	58.185	2928	5.5	6.4	8.9	-35.944
R	M26704	05/16/18	10:17:23	10	1220.6	1241.3	1244.8	58.374	2941	5.6	6.5	9.0	-36.1
R	M26704	05/16/18	10:17:23	11	1260.5	1281.2	1284.7	58.407	2934	5.4	6.3	8.8	-36.154
	Identifier 1	**Date**	**Time**	**Peak Nr**	**Start**	**Rt**	**End**	**Area All**	**Ampl 44**	**BGD 44**	**BGD 45**	**BGD 46**	**d13C/12C**
R	M272921	05/16/18	11:08:55	1	26.3	47	50.6	56.898	2855	3.8	4.6	8.9	-35.994
R	M272921	05/16/18	11:08:55	2	66.3	86.9	90.5	56.767	2852	4.0	4.8	9.1	-36.1
R	M272921	05/16/18	11:08:55	3	106	126.7	130.2	56.764	2859	4.0	4.8	8.9	-36.16
PE	M272921	05/16/18	11:08:55	4	225.3	241.2	303.7	10.554	420	3.6	4.2	8.2	-32.986
S	M272921	05/16/18	11:08:55	5	521.2	540.1	618.6	10.841	492	5.9	7.0	11.4	-26.257
PE	M272921	05/16/18	11:08:55	6	824.5	841	903.1	6.615	259	7.7	9.0	13.6	-33.61
R	M272921	05/16/18	11:08:55	7	1180.8	1201.5	1205.1	58.022	2918	6.4	7.5	11.5	-35.933
R	M272921	05/16/18	11:08:55	8	1220.6	1241.3	1244.8	58.159	2925	6.4	7.5	11.5	-36.1
R	M272921	05/16/18	11:08:55	9	1260.5	1281.2	1284.7	58.187	2927	6.2	7.3	11.2	-36.13

Table A.2 (cont.) R = reference gas; PE = PE standard; S = sample. Date in MM/DD/YY format. Time is in Central European Standard Time (UTC +2). Peak Nr = peak number. Start = peak start time (s). Rt = retention time (s). End = end peak time (s). Area all = peak area (Vs). Ampl 44 = peak amplitude. BGD 44, BGD 45, BGD 46 = background gas levels. d13C/12C = δ^{13}C.

	Identifier 1	Date	Time	Peak Nr	Start	Rt	End	Area All	Ampl 44	BGD 44	BGD 45	BGD 46	d13C/12C
R	M272923	05/16/18	11:57:06	1	26.3	47	50.6	54.257	2734	4.2	5.1	10.4	-36.044
R	M272923	05/16/18	11:57:06	2	66.3	86.9	90.5	54.588	2760	4.3	5.1	10.5	-36.1
R	M272923	05/16/18	11:57:06	3	106	126.7	130.4	54.9	2762	4.4	5.3	10.5	-36.137
PE	M272923	05/16/18	11:57:06	4	220.5	229.7	235.1	4.643	733	4.0	4.8	9.7	-32.258
PE	M272923	05/16/18	11:57:06	5	235.1	237.8	296.4	6.214	332	4.0	4.8	9.7	-32.927
S	M272923	05/16/18	11:57:06	6	516.9	523.3	527.9	0.667	112	6.1	7.3	12.8	-26.012
S	M272923	05/16/18	11:57:06	7	527.9	533	578.5	3.321	190	6.1	7.3	12.8	-26.757
PE	M272923	05/16/18	11:57:06	8	820.3	829.5	836.6	7.63	1025	5.7	6.8	11.5	-32.138
PE	M272923	05/16/18	11:57:06	9	836.6	838.7	894.9	4.945	245	5.7	6.8	11.5	-32.549
R	M272923	05/16/18	11:57:06	10	1180.8	1201.3	1205.1	57.914	2911	6.3	7.5	12.2	-35.934
R	M272923	05/16/18	11:57:06	11	1220.6	1241.3	1244.8	58.085	2926	6.4	7.6	12.2	-36.1
R	M272923	05/16/18	11:57:06	12	1260.5	1281.2	1284.7	58.191	2926	6.2	7.4	12.0	-36.15

	Identifier 1	Date	Time	Peak Nr	Start	Rt	End	Area All	Ampl 44	BGD 44	BGD 45	BGD 46	d13C/12C
R	M272924	05/16/18	13:31:43	1	26.3	47	50.6	57.37	2891	4.1	5.0	10.4	-36.016
R	M272924	05/16/18	13:31:43	2	66.3	86.9	90.5	57.409	2886	4.4	5.3	10.7	-36.1
R	M272924	05/16/18	13:31:43	3	106	125.4	130.2	57.323	2887	4.4	5.3	10.7	-36.155
PE	M272924	05/16/18	13:31:43	4	226.8	234.9	243.1	7.933	1086	3.9	4.8	9.8	-32.294
PE	M272924	05/16/18	13:31:43	5	243.1	244.5	297	4.152	214	3.9	4.8	9.8	-33.068
S	M272924	05/16/18	13:31:43	6	526.1	542.8	588.8	3.624	164	6.2	7.4	13.1	-25.647
PE	M272924	05/16/18	13:31:43	7	829.3	837.7	845	7.571	1063	5.9	7.1	12.1	-32.091
PE	M272924	05/16/18	13:31:43	8	845	847.5	905.8	4.595	222	5.9	7.1	12.1	-32.167
R	M272924	05/16/18	13:31:43	9	1180.8	1201.3	1204.9	58.109	2923	6.3	7.4	12.3	-35.962
R	M272924	05/16/18	13:31:43	10	1220.6	1241.3	1244.8	58.116	2926	6.3	7.5	12.4	-36.1
R	M272924	05/16/18	13:31:43	11	1260.5	1279.5	1284.5	58.339	2926	6.1	7.2	12.1	-36.155
	M272924	05/16/18	13:31:43	12	3531.7	3532.7	3537.1	0.091	26	1.3	1.4	2.0	60541.4

	Identifier 1	Date	Time	Peak Nr	Start	Rt	End	Area All	Ampl 44	BGD 44	BGD 45	BGD 46	d13C/12C
R	M272925	05/16/18	15:09:48	1	26.3	47	50.6	53.596	2699	4.2	5.1	11.0	-35.976
R	M272925	05/16/18	15:09:48	2	66.3	86.9	90.3	53.919	2722	4.3	5.2	11.1	-36.1
R	M272925	05/16/18	15:09:48	3	106	126.7	130.2	53.974	2722	4.3	5.3	11.1	-36.142
PE	M272925	05/16/18	15:09:48	4	222.4	231.4	237.4	8.496	1145	4.0	4.8	10.3	-32.343

Table A.2 (cont.) R = reference gas; PE = PE standard; S = sample. Date in MM/DD/YY format. Time is in Central European Standard Time (UTC +2). Peak Nr = peak number. Start = peak start time (s). Rt = retention time (s). End = end peak time (s). Area all = peak area (Vs). Ampl 44 = peak amplitude. BGD 44, BGD 45, BGD 46 = background gas levels. d13C/12C = $\delta^{13}C$.

	Identifier 1	Date	Time	Peak Nr	Start	Rt	End	Area All	Ampl 44	BGD 44	BGD 45	BGD 46	d13C/12C
PE	M272925	05/16/18	15:09:48	5	237.4	239.9	307	11.013	518	4.0	4.8	10.3	-33.093
S	M272925	05/16/18	15:09:48	6	520.6	539.2	587.3	4.723	193	6.9	8.2	14.7	-27.765
PE	M272925	05/16/18	15:09:48	7	820.1	828.9	834.7	8.588	1265	6.4	7.6	13.1	-32.252
PE	M272925	05/16/18	15:09:48	8	834.7	837.7	921.5	11.845	507	6.4	7.6	13.1	-32.358
R	M272925	05/16/18	15:09:48	9	1180.8	1201.5	1204.9	57.676	2903	7.0	8.3	13.7	-35.937
R	M272925	05/16/18	15:09:48	10	1220.6	1241.3	1244.8	57.728	2911	6.9	8.2	13.6	-36.1
R	M272925	05/16/18	15:09:48	11	1260.5	1281.2	1284.7	57.808	2913	6.6	7.9	13.2	-36.154
	Identifier 1	**Date**	**Time**	**Peak Nr**	**Start**	**Rt**	**End**	**Area All**	**Ampl 44**	**BGD 44**	**BGD 45**	**BGD 46**	**d13C/12C**
R	M272927	05/16/18	15:43:28	1	26.3	47	50.6	54.635	2753	4.7	5.7	11.9	-36.037
R	M272927	05/16/18	15:43:28	2	66.3	86.9	90.3	55.005	2773	4.7	5.7	11.8	-36.1
R	M272927	05/16/18	15:43:28	3	106	126.7	130.2	55.177	2775	4.7	5.7	11.8	-36.115
PE	M272927	05/16/18	15:43:28	4	214.9	226.8	294.7	11.649	499	4.4	5.3	11.1	-32.788
	Identifier 1	**Date**	**Time**	**Peak Nr**	**Start**	**Rt**	**End**	**Area All**	**Ampl 44**	**BGD 44**	**BGD 45**	**BGD 46**	**d13C/12C**
R	M272928	05/16/18	17:22:08	1	26.3	47	50.6	54.021	2720	4.6	5.7	14.1	-35.958
R	M272928	05/16/18	17:22:08	2	66.3	86.9	90.3	54.217	2738	4.8	5.9	14.1	-36.1
R	M272928	05/16/18	17:22:08	3	106	126.7	130	54.605	2751	4.7	5.9	14.0	-36.153
PE	M272928	05/16/18	17:22:08	4	226.8	238.5	264.8	0.918	46	4.3	5.3	13.1	-36.077
S	M272928	05/16/18	17:22:08	5	534.4	543.6	611.1	11.201	493	5.1	6.2	15.0	-25.418
PE	M272928	05/16/18	17:22:08	6	830.1	847.9	878.8	1.308	52	6.1	7.3	14.3	-34.786
	Identifier 1	**Date**	**Time**	**Peak Nr**	**Start**	**Rt**	**End**	**Area All**	**Ampl 44**	**BGD 44**	**BGD 45**	**BGD 46**	**d13C/12C**
R	M272928(1)	05/17/18	10:09:04	1	26.3	47	50.6	55.938	2812	2.4	2.9	8.1	-35.953
R	M272928(1)	05/17/18	10:09:04	2	66.3	86.9	90.5	56.178	2832	2.6	3.0	8.2	-36.1
R	M272928(1)	05/17/18	10:09:04	3	106	126.7	130.4	56.301	2838	2.6	3.0	8.0	-36.204
	Identifier 1	**Date**	**Time**	**Peak Nr**	**Start**	**Rt**	**End**	**Area All**	**Ampl 44**	**BGD 44**	**BGD 45**	**BGD 46**	**d13C/12C**
R	M272928(2)	05/17/18	11:06:19	1	26.3	47	50.6	56.608	2847	3.9	4.6	10.3	-36.048
R	M272928(2)	05/17/18	11:06:19	2	66.3	86.9	90.5	56.73	2858	4.0	4.8	10.5	-36.1
R	M272928(2)	05/17/18	11:06:19	3	106	126.7	130	56.89	2864	4.1	4.9	10.5	-36.183
PE	M272928(2)	05/17/18	11:06:19	4	228.2	240.1	283.4	5.352	378	3.8	4.5	10.0	-32.624
S	M272928(2)	05/17/18	11:06:19	5	524	541.9	609.7	12.184	495	4.7	5.5	11.4	-26.014
PE	M272928(2)	05/17/18	11:06:19	6	827	840	874.9	2.185	103	6.4	7.5	13.1	-34.381

Table A.2 (cont.) R = reference gas; PE = PE standard; S = sample. Date in MM/DD/YY format. Time is in Central European Standard Time (UTC +2). Peak Nr = peak number. Start = peak start time (s). Rt = retention time (s). End = end peak time (s). Area all = peak area (Vs). Ampl 44 = peak amplitude. BGD 44, BGD 45, BGD 46 = background gas levels. d13C/12C = δ^{13}C.

	Identifier 1	Date	Time	Peak Nr	Start	Rt	End	Area All	Ampl 44	BGD 44	BGD 45	BGD 46	d13C/12C
R	M272928(2)	05/17/18	11:06:19	7	1180.6	1201.3	1204.9	58.48	2949	5.0	5.9	10.9	-35.945
R	M272928(2)	05/17/18	11:06:19	8	1220.6	1241.3	1244.6	58.505	2940	5.3	6.3	11.4	-36.1
R	M272928(2)	05/17/18	11:06:19	9	1260.3	1281	1284.5	58.518	2943	5.2	6.1	11.2	-36.157
	Identifier 1	**Date**	**Time**	**Peak Nr**	**Start**	**Rt**	**End**	**Area All**	**Ampl 44**	**BGD 44**	**BGD 45**	**BGD 46**	**d13C/12C**
R	M2729210	05/17/18	11:54:27	1	26.3	47	50.8	55.224	2777	4.3	5.2	12.7	-36.036
R	M2729210	05/17/18	11:54:27	2	66.3	86.9	90.3	55.528	2794	4.6	5.5	13.0	-36.1
R	M2729210	05/17/18	11:54:27	3	106	126.7	130.2	55.828	2809	4.6	5.5	12.9	-36.145
PE	M2729210	05/17/18	11:54:27	4	224.7	232.8	285.1	7.065	466	4.1	4.9	11.9	-32.559
S	M2729210	05/17/18	11:54:27	5	527.3	545.3	589	3.642	152	5.3	6.3	13.6	-26.491
PE	M2729210	05/17/18	11:54:27	6	826.2	837.3	875.7	3.458	215	5.5	6.5	13.1	-32.663
R	M2729210	05/17/18	11:54:27	7	1180.6	1201.3	1204.9	57.984	2916	5.5	6.5	12.7	-35.943
R	M2729210	05/17/18	11:54:27	8	1220.6	1241.3	1244.6	57.833	2907	5.6	6.6	12.9	-36.1
R	M2729210	05/17/18	11:54:27	9	1260.5	1281.2	1284.5	57.996	2917	5.6	6.7	12.9	-36.166
	Identifier 1	**Date**	**Time**	**Peak Nr**	**Start**	**Rt**	**End**	**Area All**	**Ampl 44**	**BGD 44**	**BGD 45**	**BGD 46**	**d13C/12C**
R	M264181	05/17/18	12:47:19	1	26.3	47	50.6	54.571	2742	3.0	3.6	9.4	-36.009
R	M264181	05/17/18	12:47:19	2	66.3	86.9	90.3	54.89	2756	3.1	3.8	9.7	-36.1
R	M264181	05/17/18	12:47:19	3	106	126.7	130.2	55.2	2777	3.2	3.8	9.7	-36.135
PE	M264181	05/17/18	12:47:19	4	235.3	246.8	274.4	1.917	146	3.0	3.6	9.3	-32.303
S	M264181	05/17/18	12:47:19	5	528.1	542.8	583.5	3.211	195	3.2	3.8	9.9	-27.141
PE	M264181	05/17/18	12:47:19	6	829.1	838.1	870.5	2.394	216	3.6	4.3	9.7	-32.576
R	M264181	05/17/18	12:47:19	7	1180.6	1201.3	1204.7	58.211	2938	3.5	4.2	9.4	-35.962
R	M264181	05/17/18	12:47:19	8	1220.6	1241.3	1244.6	58.19	2927	3.7	4.4	9.7	-36.1
R	M264181	05/17/18	12:47:19	9	1260.3	1281	1284.7	58.342	2935	3.8	4.6	9.9	-36.177
	Identifier 1	**Date**	**Time**	**Peak Nr**	**Start**	**Rt**	**End**	**Area All**	**Ampl 44**	**BGD 44**	**BGD 45**	**BGD 46**	**d13C/12C**
R	M264184	05/17/18	14:16:48	1	26.3	47	50.4	54.176	2727	3.2	3.9	9.8	-36.025
R	M264184	05/17/18	14:16:48	2	66.3	86.9	90.5	54.407	2745	3.3	4.0	9.9	-36.1
R	M264184	05/17/18	14:16:48	3	106	126.7	130.2	54.744	2758	3.4	4.1	10.1	-36.173
PE	M264184	05/17/18	14:16:48	4	228.6	239.5	277.6	3.077	258	3.1	3.7	9.4	-33.253
S	M264184	05/17/18	14:16:48	5	520	539.4	609.2	13.881	526	4.1	4.8	11.5	-26.47
PE	M264184	05/17/18	14:16:48	6	824.5	832.7	875.1	3.459	229	6.1	7.2	13.2	-32.897

Table A.2 (cont.) R = reference gas; PE = PE standard; S = sample. Date in MM/DD/YY format. Time is in Central European Standard Time (UTC +2). Peak Nr = peak number. Start = peak start time (s). Rt = retention time (s). End = end peak time (s). Area all = peak area (Vs). Ampl 44 = peak amplitude. BGD 44, BGD 45, BGD 46 = background gas levels. d13C/12C = δ13C.

	Identifier 1	Date	Time	Peak Nr	Start	Rt	End	Area All	Ampl 44	BGD 44	BGD 45	BGD 46	d13C/12C
R	M264184	05/17/18	14:16:48	7	1180.8	1201.3	1204.9	57.824	2906	5.0	5.8	11.3	-35.95
R	M264184	05/17/18	14:16:48	8	1220.6	1241.3	1244.8	57.986	2920	5.1	6.0	11.5	-36.1
R	M264184	05/17/18	14:16:48	9	1260.5	1281.2	1284.5	57.926	2901	5.1	6.1	11.6	-36.173
	Identifier 1	**Date**	**Time**	**Peak Nr**	**Start**	**Rt**	**End**	**Area All**	**Ampl 44**	**BGD 44**	**BGD 45**	**BGD 46**	**d13C/12C**
R	M264185	05/17/18	15:29:52	1	26.3	47	50.4	48.687	2455	3.2	3.9	8.8	-36.096
R	M264185	05/17/18	15:29:52	2	66.3	86.7	90.3	48.907	2466	3.4	4.1	9.1	-36.1
R	M264185	05/17/18	15:29:52	3	106	126.7	130	49.374	2492	3.3	4.0	9.0	-36.091
PE	M264185	05/17/18	15:29:52	4	229.3	238.1	267.9	1.947	185	3.2	3.8	8.6	-32.694
S	M264185	05/17/18	15:29:52	5	523.1	542.6	593.4	7.016	311	4.0	4.8	10.7	-26.269
PE	M264185	05/17/18	15:29:52	6	827.2	835.4	886.6	4.383	319	5.1	6.0	11.4	-32.367
R	M264185	05/17/18	15:29:52	7	1180.6	1201.3	1204.9	56.843	2874	5.1	6.1	11.4	-35.923
R	M264185	05/17/18	15:29:52	8	1220.6	1241.3	1244.6	57.091	2867	5.1	6.1	11.5	-36.1
R	M264185	05/17/18	15:29:52	9	1260.3	1281	1284.5	57.174	2871	5.3	6.3	11.7	-36.167
	Identifier 1	**Date**	**Time**	**Peak Nr**	**Start**	**Rt**	**End**	**Area All**	**Ampl 44**	**BGD 44**	**BGD 45**	**BGD 46**	**d13C/12C**
R	M264187	05/17/18	16:06:04	1	26.3	47	50.4	56.092	2821	4.8	5.9	13.4	-36.045
R	M264187	05/17/18	16:06:04	2	66.3	86.9	90.3	56.221	2838	4.9	5.9	13.4	-36.1
R	M264187	05/17/18	16:06:04	3	106	126.7	130.4	56.363	2838	5.0	6.0	13.5	-36.163
PE	M264187	05/17/18	16:06:04	4	234.7	247.5	270	0.736	35	4.6	5.5	12.8	-36.438
	Identifier 1	**Date**	**Time**	**Peak Nr**	**Start**	**Rt**	**End**	**Area All**	**Ampl 44**	**BGD 44**	**BGD 45**	**BGD 46**	**d 3C/12C**
R	M264187(1)	05/17/18	16:12:38	1	26.3	47	50.4	57.172	2870	6.2	7.4	14.7	-36.062
R	M264187(1)	05/17/18	16:12:38	2	66.3	86.9	90.3	57.301	2883	6.0	7.2	14.4	-36.1
R	M264187(1)	05/17/18	16:12:38	3	106	126.7	130.4	57.569	2892	5.8	7.0	14.2	-36.124
PE	M264187(1)	05/17/18	16:12:38	4	236.6	248.1	264.6	0.361	20	5.2	6.2	13.0	-38.377
	Identifier 1	**Date**	**Time**	**Peak Nr**	**Start**	**Rt**	**End**	**Area All**	**Ampl 44**	**BGD 44**	**BGD 45**	**BGD 46**	**d13C/12C**
R	M264187(2)	05/17/18	16:59:27	1	26.3	47	50.4	55.845	2808	5.0	6.1	15.1	-36.037
R	M264187(2)	05/17/18	16:59:27	2	66.3	86.9	90.5	56	2819	5.1	6.2	15.2	-36.1
R	M264187(2)	05/17/18	16:59:27	3	106	126.7	130	56.163	2831	5.2	6.3	15.1	-36.163
PE	M264187(2)	05/17/18	16:59:27	4	226.8	237	268.1	2.431	207	4.6	5.6	13.9	-33.347
S	M264187(2)	05/17/18	16:59:27	5	522.9	542.4	588.5	6.594	281	5.3	6.4	15.0	-29.123

Table A.2 (cont.) R = reference gas; PE = PE standard; S = sample. Date in MM/DD/YY format. Time is in Central European Standard Time (UTC +2). Peak Nr = peak number. Start = peak start time (s). Rt = retention time (s). End = end peak time (s). Area all = peak area (Vs). Ampl 44 = peak amplitude. BGD 44, BGD 45, BGD 46 = background gas levels. d13C/12C = $\delta^{13}C$.

	Identifier 1	Date	Time	Peak Nr	Start	Rt	End	Area All	Ampl 44	BGD 44	BGD 45	BGD 46	d13C/12C
PE	M264187(2)	05/17/18	16:59:27	6	823.5	832.2	880.5	4.628	344	6.0	7.2	14.8	-32.562
R	M264187(2)	05/17/18	16:59:27	7	1180.6	1201.3	1204.7	58.77	2959	5.5	6.6	13.6	-35.922
R	M264187(2)	05/17/18	16:59:27	8	1220.6	1241.3	1244.8	58.888	2960	5.6	6.8	13.9	-36.1
R	M264187(2)	05/17/18	16:59:27	9	1260.3	1281	1284.3	58.935	2966	5.7	6.8	13.8	-36.163
	Identifier 1	**Date**	**Time**	**Peak Nr**	**Start**	**Rt**	**End**	**Area All**	**Ampl 44**	**BGD 44**	**BGD 45**	**BGD 46**	**d13C/12C**
R	M264188	05/17/18	17:27:50	1	26.3	47	50.6	57.138	2881	5.3	6.4	17.0	-36.032
R	M264188	05/17/18	17:27:50	2	66.3	86.9	90.1	57.27	2885	5.5	6.7	17.1	-36.1
R	M264188	05/17/18	17:27:50	3	106	126.7	130	57.225	2883	5.4	6.6	16.8	-36.16
PE	M264188	05/17/18	17:27:50	4	228.4	239.3	269.8	1.74	134	4.8	5.9	15.5	-33.831
	Identifier 1	**Date**	**Time**	**Peak Nr**	**Start**	**Rt**	**End**	**Area All**	**Ampl 44**	**BGD 44**	**BGD 45**	**BGD 46**	**d13C/12C**
R	M264189	05/18/18	10:24:24	1	26.3	47	50.4	53.383	2692	3.0	3.6	7.0	-35.956
R	M264189	05/18/18	10:24:24	2	66.3	86.9	90.3	53.573	2693	3.2	3.8	7.3	-36.1
R	M264189	05/18/18	10:24:24	3	106	126.7	130.2	53.998	2716	3.2	3.8	7.2	-36.161
PE	M264189	05/18/18	10:24:24	4	222.6	231.6	261.3	2.701	329	2.9	3.4	6.8	-32.657
S	M264189	05/18/18	10:24:24	5	517.1	531.3	573.9	2.891	138	3.8	4.4	8.1	-27.218
PE	M264189	05/18/18	10:24:24	6	826.4	837.3	852.3	0.249	15	4.2	4.9	8.3	-36.339
R	M264189	05/18/18	10:24:24	7	1180.6	1201.3	1204.9	58.115	2928	3.8	4.4	7.4	-35.9
R	M264189	05/18/18	10:24:24	8	1220.6	1241.3	1244.6	58.125	2924	4.1	4.8	8.0	-36.1
R	M264189	05/18/18	10:24:24	9	1260.3	1281	1284.5	58.235	2921	4.1	4.8	8.0	-36.133
	Identifier 1	**Date**	**Time**	**Peak Nr**	**Start**	**Rt**	**End**	**Area All**	**Ampl 44**	**BGD 44**	**BGD 45**	**BGD 46**	**d13C/12C**
R	M2641812	05/18/18	11:17:29	1	26.3	47	50.6	57.079	2868	3.9	4.7	10.1	-36.036
R	M2641812	05/18/18	11:17:29	2	66.3	86.9	90.5	57.15	2878	4.0	4.8	10.2	-36.1
R	M2641812	05/18/18	11:17:29	3	106	125.4	130	57.043	2859	4.0	4.8	10.2	-36.17
PE	M2641812	05/18/18	11:17:29	4	228	236.2	286.1	7.073	489	3.7	4.4	9.5	-32.625
S	M2641812	05/18/18	11:17:29	5	526.1	533.4	538.4	0.536	82	4.7	5.6	10.9	-25.977
S	M2641812	05/18/18	11:17:29	6	538.4	544	572.9	1.327	76	4.7	5.6	10.9	-28.282
PE	M2641812	05/18/18	11:17:29	7	826.4	834.5	882	5.25	286	4.3	5.2	9.8	-32.982
R	M2641812	05/18/18	11:17:29	8	1180.6	1201.3	1204.7	58.314	2926	4.6	5.4	10.0	-35.928
R	M2641812	05/18/18	11:17:29	9	1220.6	1241.3	1244.8	58.351	2935	4.7	5.6	10.2	-36.1
R	M2641812	05/18/18	11:17:29	10	1260.3	1281	1284.5	58.441	2933	4.7	5.6	10.1	-36.141

Table A.2 (cont.) R = reference gas; PE = PE standard; S = sample. Date in MM/DD/YY format. Time is in Central European Standard Time (UTC +2). Peak Nr = peak number. Start = peak start time (s). Rt = retention time (s). End = end peak time (s). Area all = peak area (Vs). Ampl 44 = peak amplitude. BGD 44, BGD 45, BGD 46 = background gas levels. d13C/12C = $\delta^{13}C$.

	Identifier 1	Date	Time	Peak Nr	Start	Rt	End	Area All	Ampl 44	BGD 44	BGD 45	BGD 46	d13C/12C
R	M252976	05/18/18	11:43:13	1	26.8	47	66.5	57.593	3295	436.5	488.6	5105.5	-56763.322
R	M252976	05/18/18	11:43:13	2	66.5	69.4	106.2	63.208	3304	436.5	488.6	5105.5	-36.1
R	M252976	05/18/18	11:43:13	3	106.2	110.1	160.1	56.016	2884	436.5	488.6	5105.5	5089619.47

	Identifier 1	Date	Time	Peak Nr	Start	Rt	End	Area All	Ampl 44	BGD 44	BGD 45	BGD 46	d13C/12C
R	M252976(1)	05/18/18	13:25:52	1	26.3	47	50.6	59.339	2985	3.5	4.2	13.0	-35.925
R	M252976(1)	05/18/18	13:25:52	2	66.3	86.9	90.3	59.348	2984	3.7	4.4	13.2	-36.1
R	M252976(1)	05/18/18	13:25:52	3	106	126.7	130.2	59.423	2989	3.8	4.5	13.4	-36.153
PE	M252976(1)	05/18/18	13:25:52	4	223.4	231.8	238.7	3.239	488	3.4	4.0	12.6	-32.252
PE	M252976(1)	05/18/18	13:25:52	5	238.7	240.4	281.3	1.741	93	3.4	4.0	12.6	-29.922
S	M252976(1)	05/18/18	13:25:52	6	527.9	544.7	566	0.714	33	4.2	4.9	13.3	-28.656
PE	M252976(1)	05/18/18	13:25:52	7	819.7	827.4	835.4	2.7	375	4.1	4.8	12.8	-32.3
PE	M252976(1)	05/18/18	13:25:52	8	835.4	836.4	880.5	1.692	85	4.1	4.8	12.8	-32.773
R	M252976(1)	05/18/18	13:25:52	9	1180.6	1201.3	1205.1	59.444	2990	4.2	4.9	12.6	-35.949
R	M252976(1)	05/18/18	13:25:52	10	1220.6	1241.3	1244.8	59.365	2988	4.4	5.3	13.0	-36.1
R	M252976(1)	05/18/18	13:25:52	11	1260.3	1281	1284.5	59.56	2990	4.4	5.2	13.0	-36.17

	Identifier 1	Date	Time	Peak Nr	Start	Rt	End	Area All	Ampl 44	BGD 44	BGD 45	BGD 46	d13C/12C
R	M2729214	05/18/18	13:59:34	1	26.3	47	50.6	57.274	2891	4.4	5.3	16.6	-35.992
R	M2729214	05/18/18	13:59:34	2	66.3	86.9	90.3	57.238	2880	4.5	5.5	16.7	-36.1
R	M2729214	05/18/18	13:59:34	3	106	126.7	130.2	57.527	2903	4.5	5.5	16.7	-36.136
PE	M2729214	05/18/18	13:59:34	4	223.6	231.6	263.1	1.998	187	4.2	5.0	15.7	-33.211

	Identifier 1	Date	Time	Peak Nr	Start	Rt	End	Area All	Ampl 44	BGD 44	BGD 45	BGD 46	d13C/12C
R	M2701613	05/18/18	14:48:30	1	26.3	47	50.4	56.112	2823	4.3	5.2	17.7	-35.993
R	M2701613	05/18/18	14:48:30	2	66.3	86.9	90.1	56.199	2829	4.4	5.3	17.8	-36.1
R	M2701613	05/18/18	14:48:30	3	106	126.7	130.2	56.378	2834	4.4	5.4	17.7	-36.154
PE	M2701613	05/18/18	14:48:30	4	221.1	229.3	236.2	3.207	453	4.1	4.9	16.7	-31.951
PE	M2701613	05/18/18	14:48:30	5	236.2	238.3	274.2	2.151	139	4.1	4.9	16.7	-31.569
S	M2701613	05/18/18	14:48:30	6	526.1	540.7	572.2	1.536	87	4.7	5.7	16.9	-30.731
PE	M2701613	05/18/18	14:48:30	7	819.5	827.4	868.2	3.556	327	4.7	5.6	16.1	-32.74

Table A.2 (cont.) R = reference gas; PE = PE standard; S = sample. Date in MM/DD/YY format. Time is in Central European Standard Time (UTC +2). Peak Nr = peak number. Start = peak start time (s). Rt = retention time (s). End = end peak time (s). Area all = peak area (Vs). Ampl 44 = peak amplitude. BGD 44, BGD 45, BGD 46 = background gas levels. d13C/12C = $\delta^{13}C$.

R	M2701613	05/18/18	14:48:30	8	1180.6	1201.3	1204.9	58.213	2929	4.5	5.4	15.4	-35.931
R	M2701613	05/18/18	14:48:30	9	1220.6	1241.3	1244.8	58.212	2931	4.8	5.7	15.7	-36.1
R	M2701613	05/18/18	14:48:30	10	1260.3	1281	1284.5	58.256	2926	4.8	5.8	15.8	-36.162

Table A.2 (cont.) R = reference gas; PE = PE standard; S = sample. Date in MM/DD/YY format. Time is in Central European Standard Time (UTC +2). Peak Nr = peak number. Start = peak start time (s). Rt = retention time (s). End = end peak time (s). Area all = peak area (Vs). Ampl 44 = peak amplitude. BGD 44, BGD 45, BGD 46 = background gas levels. d13C/12C = $\delta^{13}C$.

APPENDIX B MOCHRAS SINGLE-PHYTOCLAST δ^{13}C RANDOM NUMBER GENERATOR RECORDS

Appendix B contains the results of the twenty single measurement $\delta^{13}C_{phytoclast}$ records produced using a random number generator (RNG) function (=RANDBETWEEN) in Microsoft Excel 2013. A discussion of this data is provided in **Chapter 5, Section 5.5.2.6.** (p. 142).

Table A.3 shows the numbers assigned to each individual phytoclast per sample.

Table A.4 shows the phytoclast chosen by the random number generator function for each sample, for twenty total runs.

Figures A.1- A.3 show the results of runs 6-20 graphically. The results of run 1-5 are shown in **Figure 5.16.**

Sample	M25603	M25927	M26314	M26418	M26670	M27016	M27292	M27654
Depth (m)	780.36	790.22	802.03	805.18	813.82	823.42	831.85	842.87
Fragment	$\delta^{13}C$	$\delta^{13}C$	$\delta^{13}C$	$\delta^{13}C$	$\delta^{13}C$	$\delta^{13}C$	$\delta^{13}C$	$\delta^{13}C$
1	-25.6	-27.13	-27.03	-25.55	-28.13	-30.43	-25.11	-25.86
2	-26.67	-25.84	-27.19	-25.89	-30.7	-29.83	-26.55	-26.05
3	-26.15	-26.82	-24.56	-28.71	-29.61	-29.83	-26.71	-24.22
4	-27.23	-26.16	-28.5	-25.33	-29.63	-29.96	-25.61	-26.57
5	-25.05	-28.53	-25.85		-29.45	-29.64	-27.62	-22.97
6	-26.47	-24.6	-27.96		-27.27	-30.91	-25.54	-23.91
7	-28.09	-25.9			-29.97	-28.26	-26.03	
8	-26.38	-25.05				-29.91		
9	-25.06					-30.88		

Table A.3 The numbers assigned to each single-phytoclast $\delta^{13}C$ measurement per sample, for use with the =RANDBETWEEN function.

Sample		M25603	M25927	M26314	M26418	M26670	M27016	M27292	M27654
Depth (m)		780.36	790.22	802.03	805.18	813.82	823.42	831.85	842.87
Run 1	Phyto.	4	5	1	3	2	1	7	2
	$\delta^{13}C$	-27.23	-28.53	-27.03	-28.71	-30.7	-30.43	-26.03	-26.05
Run 2	Phyto.	8	2	1	4	7	1	2	6
	$\delta^{13}C$	-26.38	-25.84	-27.03	-25.33	-29.97	-30.43	-26.55	-23.91
Run 3	Phyto.	8	6	2	1	2	1	3	3
	$\delta^{13}C$	-26.38	-24.6	-27.19	-25.55	-30.7	-30.43	-26.71	-24.22
Run 4	Phyto.	8	5	5	1	2	4	7	1
	$\delta^{13}C$	-26.38	-28.53	-25.85	-25.55	-30.7	-29.96	-26.03	-25.86
Run 5	Phyto.	2	1	6	4	6	7	2	6
	$\delta^{13}C$	-26.67	-27.13	-27.96	-25.33	-27.27	-28.26	-26.55	-23.91
Run 6	Phyto.	2	4	2	2	6	9	2	4
	$\delta^{13}C$	-26.67	-26.16	-27.19	-25.89	-27.27	-30.88	-26.55	-26.57
Run 7	Phyto.	5	2	2	2	2	7	6	1
	$\delta^{13}C$	-25.05	-25.84	-27.19	-25.89	-30.7	-28.26	-25.54	-25.86
Run 8	Phyto.	7	7	2	1	3	8	5	2
	$\delta^{13}C$	-28.09	-25.9	-27.19	-25.55	-29.61	-29.91	-27.62	-26.05

Table A.4 Results of runs 1-16 of the random number generator. Phyto. = Phytoclast.

Sample		M256 03	M2592 7	M2631 4	M2641 8	M267 0	M2701 6	M2729 2	M2765 4
Depth (m)		780.3 6	790.22	802.03	805.18	813.8 2	823.42	831.85	842.87
Run 9	Phyto.	5	8	1	4	2	9	1	1
	δ¹³C	- 25.05	-25.05	-27.03	-25.33	-30.7	-30.88	-25.11	-25.86
Run 10	Phyto.	6	7	4	1	5	7	2	4
	δ¹³C	- 26.47	-25.9	-28.5	-25.55	- 29.45	-28.26	-26.55	-26.57
Run 11	Phyto.	6	7	6	3	3	8	6	6
	δ¹³C	- 26.47	-25.9	-27.96	-28.71	- 29.61	-29.91	-25.54	-23.91
Run 12	Phyto.	3	8	6	3	2	7	3	3
	δ¹³C	- 26.15	-25.05	-27.96	-28.71	-30.7	-28.26	-26.71	-24.22
Run 13	Phyto.	1	8	1	1	7	6	4	4
	δ¹³C	-25.6	-25.05	-27.03	-25.55	- 29.97	-30.91	-25.61	-26.57
Run 14	Phyto.	9	5	1	1	2	3	2	3
	δ¹³C	- 25.06	-28.53	-27.03	-25.55	-30.7	-29.83	-26.55	-24.22
Run 15	Phyto.	4	2	5	3	2	2	6	4
	δ¹³C	- 27.23	-25.84	-25.85	-28.71	-30.7	-29.83	-30.91	-26.57
Run 16	Phyto.	3	4	5	1	7	8	3	6
	δ¹³C	- 26.15	-26.16	-25.85	-25.55	- 29.97	-29.91	-26.71	-23.91
Run 19	Phyto.	5	4	3	2	4	5	7	3
	δ¹³C	- 25.05	-26.16	-24.56	-25.89	- 29.63	-26.64	-26.03	-24.22
Run 20	Phyto.	1	4	2	3	2	9	5	6
	δ¹³C	-25.6	-26.16	-27.19	-28.71	-30.7	-30.88	-27.62	-23.91

Table A.4 (cont.) Results of runs 17-20 of the random number generator. Phyto. = Phytoclast.
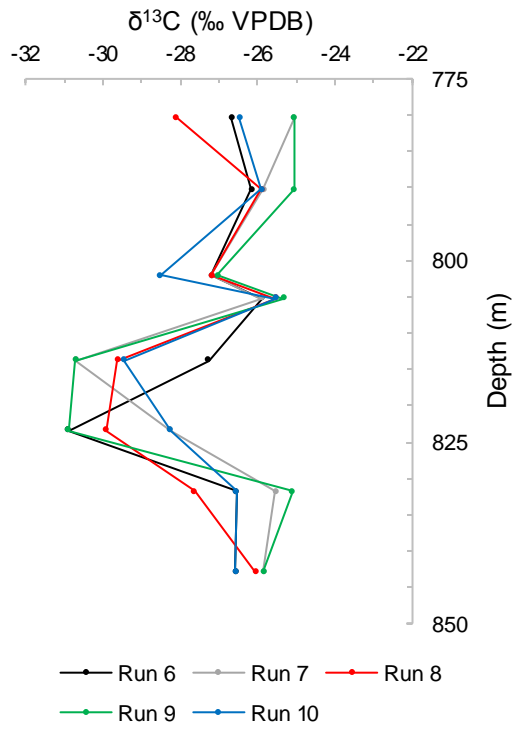
Figure A.1 The results of RNG runs 6-10. $\delta^{13}C_{phytoclast}$ is plotted against depth for each run.
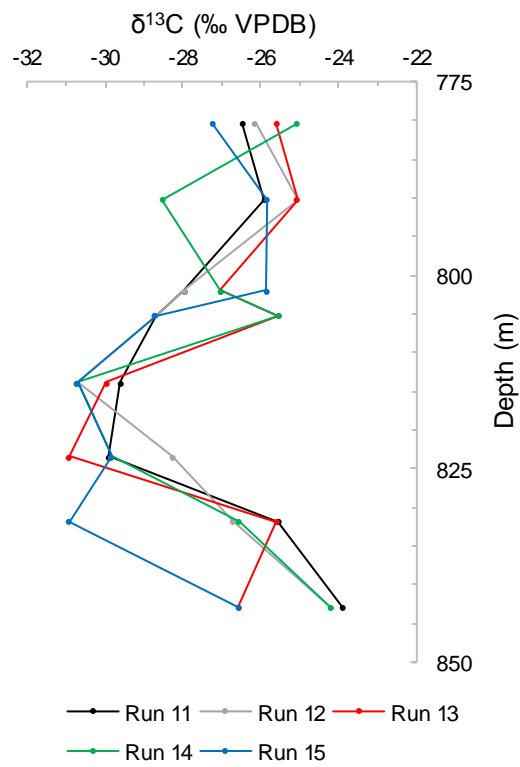
Figure A.2 The results of RNG runs 11-15. $\delta^{13}C_{phytoclast}$ is plotted against depth for each run.
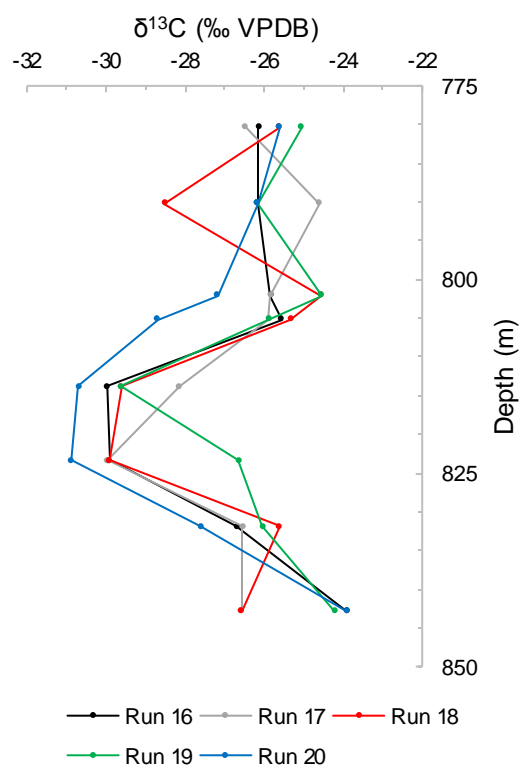
Figure A.3 The results of RNG runs 16-20. $\delta^{13}C_{phytoclast}$ is plotted against depth for each run.

APPENDIX C FOSSIL CHARCOAL ABUNDANCE DATA

Appendix C contains all of the fossil charcoal and non-charcoal particle counts.

Tables A.5 – A.7 show the coarse fossil charcoal counts for the Kaszewy-1 Pliensbachian-Toarcian, Kaszewy-1 Rhaetian-Hettangian, and Niekłań PIG-1 Rhaetian-Hettangian study sections. A discussion of this data is provided in **Chapter 6** (p. 149) and **Chapter 7** (p. 176).

Tables A.8 – A.10 show the fine fossil charcoal and non-charcoal counts for the Kaszewy-1 Pliensbachian-Toarcian, Kaszewy-1 Rhaetian-Hettangian, and Niekłań PIG-1 Rhaetian-Hettangian study sections. A discussion of this data is provided in **Chapter 6** (p. 149) and **Chapter 7** (p. 176).

Sample	Depth (m)	Charcoal fragments counted	Non-charcoal fragments counted	Number of fields of view counted	Area counted (mm²)	Total sample area (mm²)	Volume of water (ml)	Weight of sample (g)	Charcoal fragments per 10 g bulk rock sample	Non-charcoal fragments per 10 g bulk rock sample	Charcoal %
kk_34 1	1297.20	44	265	90	85.50	484.00	45.48	10.25	187879	1131542	14.2
kk_34 2	1297.20	22	136	91	86.45	376.97	45.48	10.25	72362	447328	13.9
kk_35 1	1289.70	41	257	80	76.00	287.10	21.57	10.80	52587	329631	13.8
kk_35 2	1289.70	31	211	80	76.00	484.00	21.57	10.80	67030	456236	12.8
kk_38 1	1265.90	16	320	80	76.00	484.00	24.48	8.12	52222	1044446	4.8
kk_38 2	1265.90	29	600	77	73.15	484.00	24.48	8.12	98341	2034635	4.6
kk_39 1	1250.75	39	1124	65	61.75	484.00	34.74	5.84	309128	8909239	3.4
kk_39 2	1250.75	26	950	66	62.70	484.00	34.74	5.84	202963	7415959	2.7
kk_42 1	1238.07	16	267	84	79.80	484.00	18.60	11.31	27131	452744	5.7
kk_42 2	1238.07	15	207	86	81.70	484.00	18.60	11.31	24844	342841	6.8
kk_42c 1	1215.75	5	62	83	78.85	484.00	22.28	10.08	11532	143001	7.5
kk_42c 2	1215.75	5	49	77	73.15	484.00	22.28	10.08	12431	121823	9.3
kk_45y 1	1188.15	15	67	76	72.20	484.00	25.62	7.25	60407	269819	18.3
kk_45y 2	1188.15	14	84	78	74.10	484.00	25.62	7.25	54935	329607	14.3
kk_46b 1	1178.00	15	137	80	76.00	309.55	26.87	10.48	26630	243217	9.9
kk_47 1	1169.10	54	371	80	76.00	484.00	29.38	8.07	212840	1462288	12.7
kk_47 2	1169.10	38	262	82	77.90	454.48	29.38	8.07	137211	946032	12.7

Table A.5 Fine fossil charcoal and non-charcoal particle counts for the Kaszewy-1 Pliensbachian-Toarcian study section. The numbers 1 and 2 following each sample number denote the slide analysed.

Sample	Depth (m)	Charcoal fragments counted	Non-charcoal fragments counted	Number of fields of view counted	Area counted (mm²)	Total sample area (mm²)	Volume of water (ml)	Weight of sample (g)	Charcoal fragments per 10 g bulk rock sample	Non-charcoal fragments per 10 g bulk rock sample	Charcoal %
kk_5 1	1925.56	31	141	83	78.85	484.00	13.88	9.76	46004	209243	18.0
kk_5 2	1925.56	38	163	84	79.80	484.00	13.88	9.76	55720	239011	18.9
kk_8 1	1913.40	8	61	79	75.05	484.00	20.05	14.85	11842	90295	11.6
kk_8 2	1913.40	33	234	82	77.90	373.89	20.05	14.85	36354	257786	12.4
kk_9 1	1903.55	40	155	42	39.90	129.67	21.97	10.53	46108	178669	20.5
kk_9 2	1903.55	56	175	85	80.75	484.00	21.97	10.53	119053	372042	24.2
kk_10 1	1896.70	107	545	81	76.95	484.00	23.38	7.59	352429	1795084	16.4
kk_10 2	1896.70	130	686	83	78.85	484.00	23.38	7.59	417868	2205055	15.9
kk_10b 1	1885.67	33	66	80	76.00	392.40	23.97	7.59	91475	182951	33.3
kk_10b 3	1885.67	24	30	69	65.55	413.93	23.07	7.59	78311	97888	44.4
kk_10d 1	1875.30	23	47	84	79.80	472.19	17.90	14.66	28249	57727	32.9
kk_10d 2	1875.30	10	55	81	76.95	484.00	17.90	14.66	13056	71807	15.4
kk_11 1	1869.30	13	41	81	76.95	484.00	40.98	7.78	73219	230920	24.1
kk_11 2	1869.30	6	28	80	76.00	399.83	40.98	7.78	28265	131905	17.6
kk_11b 2	1857.30	16	40	80	76.00	484.00	38.54	10.03	66560	166399	28.6
kk_11b 3	1857.30	15	43	81	76.95	418.29	38.54	10.03	53262	152685	25.9
kk_11c 1	1852.80	25	79	80	76.00	163.66	29.09	10.68	24928	78773	24.0
kk_11c 2	1852.80	14	37	80	76.00	445.82	29.09	10.68	38027	100501	27.5
kk_12a 1	1826.30	18	96	53	50.35	170.70	47.89	7.82	63532	338838	15.8
kk_12a 2	1826.30	24	115	56	53.20	156.88	47.89	7.82	73681	353054	17.3
kk_14b 1	1803.80	9	46	53	50.35	199.99	28.91	10.10	17395	88908	16.4
kk_14b 2	1803.80	6	36	31	29.45	142.90	28.91	10.10	14167	85001	14.3

Table A.6 Fine fossil charcoal and non-charcoal particle counts for the Kaszewy-1 Rhaetian-Hettangian study section. The numbers 1, 2 and 3 following each sample number denote the slide analysed.

Sample	Depth (m)	Charcoal fragments counted	Non-charcoal fragments counted	Number of fields of view counted	Area counted (mm²)	Total sample area (mm²)	Volume of water (ml)	Weight of sample (g)	Charcoal fragments per 10 g bulk rock sample	Non-charcoal fragments per 10 g bulk rock sample	Charcoal %
NC1 1	165.20	3	46	85	80.75	273.57	16.28	9.97	2821	43261	6.1
NC1 2	165.20	6	87	94	89.30	411.54	16.28	9.97	7676	111298	6.5
NC4 1	163.00	1	46	81	76.95	350.12	21.37	15.00	1102	50691	2.1
NC4 2	163.00	2	62	80	76.00	484.00	21.37	15.00	3085	95628	3.1
NC6 1	160.00	49	253	87	82.65	484.00	14.94	8.90	81886	422798	16.2
NC6 3	160.00	78	481	100	95.00	241.31	14.94	8.90	56540	348663	14.0
NC8 1	158.05	119	706	80	76.00	190.83	32.53	7.20	229499	1361565	14.4
NC8 2	158.05	154	933	84	79.80	268.71	32.53	7.20	398293	2413032	14.2
NC9 1	155.50	61	248	84	79.80	484.00	27.62	11.42	152117	618444	19.7
NC9 2	155.50	73	279	80	76.00	484.00	27.62	11.42	191144	730537	20.7
NC10 1	152.10	16	326	83	78.85	484.00	22.35	11.13	33527	683113	4.7
NC10 2	152.10	13	278	100	95.00	484.00	22.35	11.13	22610	483502	4.5
NC12 1	147.50	56	318	97	92.15	484.00	20.49	9.44	108532	616305	15.0
NC12 2	147.50	35	301	88	83.60	484.00	20.49	9.44	74770	643020	10.4
NC13 1	145.00	28	132	90	85.50	484.00	13.55	9.18	39772	187499	17.5
NC13 2	145.00	40	170	84	79.80	484.00	13.55	9.18	60876	258724	19.0
NC14 2	143.00	107	491	75	71.25	198.36	29.62	10.85	138247	634388	17.9
NC15 1	141.10	91	450	75	71.25	268.02	32.48	11.22	168460	833042	16.8
NC15 2	141.10	117	465	84	79.80	284.39	32.48	11.22	205196	815523	20.1

Table A.7 Fine fossil charcoal and non-charcoal particle counts for the Niekłań PIG-1 Rhaetian-Hettangian study section. The numbers 1 and 2 following each sample number denote the slide analysed.

Sample	Depth (m)	Total charcoal fragments counted	Weight of sample (g)	Charcoal per 10 g sample
kk_47	1169.10	0	8.07	0
kk_46b	1178.00	4	10.48	4
kk_45y	1188.15	11	7.25	15
kk_42c	1215.75	0	10.08	0
kk_42	1238.07	0	11.31	0
kk_39	1250.75	1	5.84	2
kk_38	1265.90	0	8.12	0
kk_34	1297.20	1	10.25	1

Table A.8 Coarse charcoal counts per sample, weight of sample, and charcoal count per 10 g sample for the Kaszewy-1 Pliensbachian-Toarcian study section.

Sample	Depth (m)	Total charcoal fragments counted	Weight of sample (g)	Charcoal per 10 g sample
kk_5	1925.56	3	9.76	3
kk_9	1903.55	0	10.53	0
kk_10	1896.70	953	7.59	1256
kk_10b	1885.67	7	7.59	9
kk_11	1869.30	8	7.78	10
kk_11b	1857.30	24	10.03	24
kk_11c	1852.80	14	10.68	13
kk_12a	1826.30	11	7.82	14
kk_14b	1803.80	5	10.10	5

Table A.9 Coarse charcoal counts per sample, weight of sample, and charcoal count per 10 g sample for the Kaszewy-1 Rhaetian-Hettangian study section.

Sample	Depth (m)	Total charcoal fragments counted	Weight of sample (g)	Charcoal per 10 g sample
NC1	165.20	0	9.97	0
NC4	163.00	0	15.00	0
NC6	160.00	3656	8.90	4108
NC8	158.05	91	7.20	126
NC9	155.50	1090	11.42	954
NC10	152.10	0	11.13	0
NC12	147.50	17	9.44	18
NC13	145.00	0	9.18	0
NC14	143.00	16	10.85	15
NC15	141.10	34	11.22	30

Table A.10 Coarse charcoal counts per sample, weight of sample, and charcoal count per 10 g sample for the Niekłan PIG-1 Rhaetian-Hettangian study section.

APPENDIX D PAH DATA

Appendix D contains all of the peak areas, and uncorrected and corrected concentrations of the polycyclic aromatic hydrocarbons quantified as part of this thesis. A discussion of this data is provided in **Chapter 6** (p. 149) and **Chapter 7** (p. 176).

Tables A.11 – A.12 show the peak areas as measured from the GC-MS chromatograms of the polycyclic aromatic hydrocarbons quantified for the Kaszewy-1 Pliensbachian-Toarcian study section, Kaszewy-1 Rhaetian-Toarcian study section, and Niekłan PIG-1 Rhaetian-Toarcian study section.

Tables A.13 – A.14 show the uncorrected concentrations (ng/g sediment) of the polycyclic aromatic hydrocarbons quantified for the Kaszewy-1 Pliensbachian-Toarcian study section, Kaszewy-1 Rhaetian-Toarcian study section, and Niekłan PIG-1 Rhaetian-Toarcian study section.

Tables A.15 – A.16 show the corrected concentrations (ng/g sediment) of the polycyclic aromatic hydrocarbons quantified for the Kaszewy-1 Pliensbachian-Toarcian study section, Kaszewy-1 Rhaetian-Toarcian study section, and Niekłan PIG-1 Rhaetian-Toarcian study section.

PAH		fluorene	phenanthrene	fluoranthene	pyrene	benz-anthracene	benzo(k)fluor anthene	Indeno[1,2,3-cd]pyrene	coronene
Retention time (min)		18.11	21.65	26.28	27.01	31.96	36.64	40.90	44.80
Molecular weight		166	178	202	202	228	252	276	300
Sample	Depth (m)	Peak area							
KK34	1297.20	22895293.71	229194789.2	27640864.08	39602228.61	50737424.63	111148423.5	83135616.53	14630382.75
KK35	1289.70	24143978.52	189594937.7	15455484.62	29172563.59	35395468.88	64110807.27	39016216.29	5058512.53
KK38	1265.90	41471273.96	390403278.9	32881091.41	68647150.23	196013978.6	45928871.37	19722829.17	713363.966
KK40	1247.40	4781327.578	73344711.63	4555166.955	8849498.448	6115728.045	7097686.136	7334232.308	191676.206
KK42	1238.07	463888.851	20951726.08	2593461.343	3451295.026	3115845.265	1677541.654	684535.964	142342.549
KK42c	1215.75		4951374.028	2886249.63	1575186.933	997709.134	467923.273	154235.746	153310.703
KK45e	1188.60		4127479.328	3059944.721	2009853.029	1446321.13	1850512.132	606260.307	
KK46b	1178.00	10266516.78	125109386.2	21249782.14	30525177.22	22956342.24	27607721.02	28133898.2	759732.892
KK47	1169.10		163647972.6	44544730.54	48778926.88	41636995.37	32664016.8	24066792.74	
KK5	1925.56		32321930.82	8030252.591	11518633.82	25820267.28	46982886.07	12624874.99	284046.727
KK8	1913.40		5867355.954	2767573.127	3926545.67	3179099.539	4019666.661	1999088.604	95538.185
KK9	1903.55	2806920.451	50183949.62	8164370.233	9158752.123	18611134.93	20811533.62	5969921.929	92108.216
KK10	1896.70	38127329.84	337019714.5	28017637.52	51771406.18	46492414.46	51855783.15	22026409.16	699971.514
KK10b	1885.67	8885121.395	301558574.7	42809276.23	53515494.21	106169124.1	91560909.04	66769503.9	10423161.23
KK10d	1875.30	530443.102	15820850.41	2164431.489	3446366.496	3618581.89	3019659.164	1417997.778	
KK11	1869.30	351915.572	19396320.98	3894716.076	5078298.093	16584470.51	29158708.24	12809876.89	
KK11b	1857.30	16536493.78	844779359.9	134597100.9	125751755.9	188361298.6	128400079.5	36905549.56	324341.671
KK11c	1852.80	338712.719	17867714.2	3357853.998	4529733.53	6681438.228	6627349.481	3370693.456	355826.094
KK12a	1826.30	19247687.66	246763966.9	23361753.52	35130044.23	38076412.93	29080389.61	8383692.072	332526.602
KK14b	1803.80	7162481.387	91714841.7	10458494.82	12914398	24941384.42	30007204.59	10830053.08	350891.574

Table A.11 Peak areas (no units) of the pyrolytic PAHs identified and quantified as part of this thesis.

PAH		fluorene	phenanthrene	fluoranthene	pyrene	benz-anthracene	benzo(k)fluoranthene	Indeno[1,2,3-cd]pyrene	coronene
Retention time (minutes)		18.11	21.65	26.28	27.01	31.96	36.64	40.90	44.80
Molecular weight		166	178	202	202	228	252	276	300
Sample	**Depth (m)**	**Peak area**							
NC1	165.20		731299.122	1007086.321	251813.907	33942.679		138680.838	107406.447
NC2	164.40		11631157.66	2543768.753	854860.649	378279.255	190659.947	70934.22	178790.234
NC4	163.00		4903387.23	1655327.658	742752.933	22343.726	128371.372	904814.705	82121.88
NC8	158.05	3987314.084	162406377	38163017.2	69210608.2	32346120.74	40898146.15	15783359.75	930888.232
NC9	155.50	2486402.75	81940878.89	43910589.73	147453381.4	72050592.8	317183457.9	281653009.1	
NC10	152.10		7466929.743	1992763.946	1759611.838	953323.373	17408262.91	21533632.12	162037.074
NC12	147.50	9953176.715	185217486	46476670.29	92949753.82	58256176.4	326441444	250104313.6	12445786.21
NC13	145.00		20612011.16	8307401.914	9016916.425	3500164.54	13221970.53	12912826.73	304965.559
NC14	143.00		68317019.2	13135270.79	17099813.38	7700846.223	27577158.3	37630044.93	234419.964
NC15	141.10		48168836.64	12509450.45	17098387.84	8301575.136	24464709.28	41160335.01	496549.514

Table A.11 (cont.) Peak areas (no units) of the pyrolytic PAHs identified and quantified as part of this thesis.

PAH		2-methylnaphthalene	1,7-dimethylnaphthalene	2-methylphenanthrene	9-methyphenanthrene	2,5-dimethylphenanthrene	1-methylpyrene	retene
Retention time (min)		12.16	14.93	23.80	24.10	26.04	28.58	28.91
Molecular weight		142	156	192	192	206	216	234
Sample	**Depth (m)**	Peak area						
KK34	1297.20	87759046.36	106045098.4	95833405.32	108950470.3	80231393.98	90535016.23	65723475.04
KK35	1289.70	104267224.9	115779527.8	83210045.35	80195925.65	69181166.31	64180201.36	44238132.75
KK38	1265.90	407830484	362770416.4	188482994.1	199138888.4	195967916.5	142366244.8	176261125.4
KK40	1247.40	32050818.9	43927118.64	32422230.16	30656122.18	28430197.4	13826710.63	9132262.307
KK42	1238.07		183775.06	13067419.59	10209133.75	11952245.81	7251189.934	2775050.291
KK42c	1215.75	46856.024	1080966.266	2297932.165	2547794.171	4108988.138	2044874.703	2060793.644
KK45e	1188.60	245057.579	705759.026	1917193.468	2011066.311	1908296.4	141970.756	1407260.855
KK46b	1178.00	32852780.47	46391112.94	57328435.07	86195610.29	75820764.18	54399650.44	109004169.2
KK47	1169.10	43213711.86	44752698.12	109406516.7	144497890.4	143535090.3	115350672.8	162349558.8
KK5	1925.56	30704.278	662689.829	9719847.096	4725960.531	1925199.521	6817285.156	3687462.655
KK8	1913.40		433119.133	2848884.879	1728954.289	1108695.379	3022024.608	67415.68
KK9	1903.55	3140329.575	3027867.122	32810037.42	25363561.06	22982438.27	26309253.06	7127980.134
KK10	1896.70	71454892.23	82228020.87	180420342.7	182451664.8	152531102.9	115265206.2	46772121.84
KK10b	1885.67	4563268.128	2804903.817	182789516.3	183829887.3	121621956	191825847.6	36395794
KK10d	1875.30		763630.699	11929935.92	10150643.84	10030602.06	8182174.678	2748681.602
KK11	1869.30		718422.88	17455407.77	14993932.6	14021735.66	12865997.39	3263472.805
KK11b	1857.30	28561655.99	14514980.15	492523788.6	439717497.4	430904567.9	453520068	111791225.3
KK11c	1852.80			12278561.84	10579028.92	10340305.09	13520489.45	3061375.184
KK12a	1826.30	8368798.482	16990499.38	141161862.9	133475839.7	128999818.3	81591453.64	44499662.06
KK14b	1803.80	1925190.366	6622666.633	48917533.69	44027461.33	46618169.8	48176998.37	14914004.14

Table A.12 Peak areas (no units) of the petrogenic and biomarker PAHs identified and quantified as part of this thesis.

PAH		2-methylnaphthalene	1,7-dimethylnaphthalene	2-methylphenanthrene	9-methyphenanthrene	2,5-dimethylphenanthrene	1-methylpyrene	retene
Retention time (minutes)		12.16	14.93	23.80	24.10	26.04	28.58	28.91
Molecular weight		142	156	192	192	206	216	234
Sample	**Depth (m)**				**Peak area**			
NC1	165.20		637874.164	944860.364	630230.637	800397.727		
NC2	164.40		645797.375	3420722.819	2558268.999	1531610.801		
NC4	163.00		735932.802	2434957.788	1696464.287	1445144.1		194579.085
NC8	158.05	2989594.801	19521004.46	82122594.31	96797282.59	76106854.88	61979171.15	58923677.34
NC9	155.50	1935307.296	4224954.511	54097878.99	78149054.02	42864337.24	95257059.88	105540670.2
NC10	152.10		698605.337	3418008.496	2566495.91	2120168.159	705666.972	1404775.638
NC12	147.50	5291519.491	23216521.28	83421742.04	94797143.14	70270453.92	87627638.57	85000461.73
NC13	145.00		1518183.244	8217945.758	8762230.847	5674028.32	5342689.305	4907422.684
NC14	143.00		970626.009	25926627.32	29698295.09	14783503.68	13891698.06	14100462.29
NC15	141.10	609100.146	675013.224	16031253.06	17450002.05	7499401.614	11485274.39	8468699.516

Table A.12 (cont.) Peak areas (no units) of the petrogenic and biomarker PAHs identified and quantified as part of this thesis.

PAH		fluorene	phenanthrene	fluoranthene	pyrene	benz-anthracene	benzo(k)fluoranthene	indeno[1,2,3-cd]pyrene	coronene
Retention time (minutes)		18.11	21.65	26.28	27.01	31.96	36.64	40.9	44.8
Molecular weight		166	178	202	202	228	252	276	300
Sample	Depth (m)	Uncorrected concentration (ng/ g sediment)							
KK34	1297.20	82.64989154	480.1441025	91.7935724	114.8405176	136.2956159	252.6944576	198.7198777	66.7252076
KK35	1289.70	82.51210939	391.7662387	66.27193387	91.91133381	103.5429325	157.2164622	110.3106847	46.83834118
KK38	1265.90	117.9870901	787.7222243	101.4992158	170.148081	414.6141624	126.5429393	76.24343411	39.7569366
KK40	1247.40	36.49680056	137.4738021	36.16372158	42.48821568	38.46204425	39.908227	40.25660134	29.73737291
KK42	1238.07	39.73570651	79.51791471	43.87079872	45.5364952	44.88513644	42.09231389	40.1641475	39.11134476
KK42c	1215.75		44.71572406	41.01478428	38.66520956	37.63030311	36.68086608	36.11870205	36.11704427
KK45e	1188.60		44.02824695	42.0801911	40.16396538	39.1356225	39.87319732	37.60266479	
KK46b	1178.00	57.65050816	276.3988309	78.57101359	96.23843279	81.82160426	90.68137336	91.68361563	39.54234837
KK47	1169.10		343.910061	120.8702819	128.7994885	115.425085	98.6217543	82.52208378	
KK5	1925.56		102.1912711	54.74658709	61.55983167	89.49270952	130.8259494	63.72045896	39.61727876
KK8	1913.40		47.72574899	42.00659249	44.14491821	42.76586631	44.31672816	40.58872436	37.07663872
KK9	1903.55	39.45833988	121.4255184	48.72728414	50.44766803	66.8012715	70.60818966	44.93066078	34.7614329
KK10	1896.70	112.4319726	690.5603762	92.877442	138.8228359	128.6120202	138.9860409	81.28899256	40.03862962
KK10b	1885.67	54.19347354	603.2993898	117.8410436	137.9277565	236.7150546	209.3075217	162.7945664	57.07910174
KK10d	1875.30	36.33706744	63.39973524	39.22908228	41.4979938	41.80279981	40.74275958	37.90796067	
KK11	1869.30	37.4805075	72.5530773	44.00500198	46.18471104	67.37471549	90.53169106	60.42334602	
KK11b	1857.30	70.26248804	1663.037231	297.3021171	280.2918383	400.6948049	285.3847682	109.4337492	39.08527244
KK11c	1852.80	37.94535955	70.64872053	43.57808582	45.76442823	49.77880266	49.67789082	43.60204003	37.97728749
KK12a	1826.30	72.5465576	493.0942087	80.15111556	101.9039635	107.3501163	90.72160742	52.46523488	37.58322847
KK14b	1803.80	52.9483068	217.7677226	59.37328425	64.16061988	87.60503785	97.47993098	60.09756936	39.67035395

Table A.13 Uncorrected concentrations (ng/g sediment) of the pyrolytic PAHs identified and quantified as part of this thesis.

PAH		fluorene	phenanthrene	fluoranthene	pyrene	benz-anthracene	benzo(k)fluoranthene	indeno[1,2,3-cd]pyrene	coronene
Retention time (minutes)		18.11	21.65	26.28	27.01	31.96	36.64	40.9	44.8
Molecular weight		166	178	202	202	228	252	276	300
Sample	Depth (m)	Uncorrected concentration (ng/ g sediment)							
NC1	165.20		38.24962938	38.75846185	37.36497031	36.96299387		37.15623771	37.09853588
NC2	164.40		51.34928191	36.5970272	33.85529326	33.08162217	32.77704537	32.58268542	32.75777635
NC4	163.00		47.98340507	41.72510146	39.96676866	38.57869697	38.78298916	40.27902641	38.69387645
NC8	158.05	46.21833157	351.4573737	112.0674705	171.8894185	100.8595775	117.3374685	68.94674326	40.32926442
NC9	155.50	42.5073776	192.704875	120.8139692	316.5470348	174.008682	637.397841	570.2325314	
NC10	152.10		54.82421106	43.89773243	43.43235896	41.82300074	74.66719143	82.90146131	40.24358697
NC12	147.50	57.82466547	396.1727528	128.3333403	218.0497178	151.0736996	668.8058765	521.4368988	62.63665292
NC13	145.00		79.94490386	55.72323211	57.11991422	46.26016642	65.39757978	64.789029	39.97040464
NC14	143.00		171.8229946	64.46550737	72.17862525	53.89269693	92.56256478	112.12071	39.36657581
NC15	141.10		126.0052433	60.09140564	68.57372983	52.31344757	82.1898508	113.0505268	37.88641315

Table A.13 (cont.) Uncorrected concentrations (ng/g sediment) of the pyrolytic PAHs identified and quantified as part of this thesis.

PAH		2-methyl naphthalene	1,7-dimethyl naphthalene	2-methyl phenanthrene	9-methyl phenanthrene	2,5-dimethyl phenanthrene	1-methyl pyrene	retene
Retention time (min)		12.16	14.93	23.8	24.1	26.04	28.58	28.91
Molecular weight		142	156	192	192	206	216	234
Sample	Depth (m)	Uncorrected concentration (ng/ g sediment)						
KK34	1297.20	207.6282203	242.8614612	223.1857521	248.4594803	193.1240732	212.9769099	165.1704721
KK35	1289.70	232.2751868	253.7935099	192.9159726	187.282104	166.6937688	157.3461708	120.0712762
KK38	1265.90	821.1717543	734.6841006	400.1592976	420.6120699	414.5257514	311.643464	376.7008165
KK40	1247.40	76.65805435	94.14892288	77.20505179	74.6040091	71.32576936	49.81842508	42.9046573
KK42	1238.07		39.19179623	64.20858173	58.65851214	62.04319574	52.91493191	44.22339862
KK42c	1215.75	35.92626528	37.77950944	39.96045191	40.40823328	43.20607193	39.50694391	39.53547248
KK45e	1188.60	36.94353573	37.7842318	39.99487859	40.1661794	39.97864307	36.75542109	39.06434463
KK46b	1178.00	100.6719628	126.4592627	147.2922573	202.2773529	182.5157413	141.7136199	245.7222271
KK47	1169.10	118.3777376	121.2597343	242.334301	308.0484839	306.2454875	253.4656794	341.4785745
KK5	1925.56	39.12246929	40.35681607	58.04657636	48.29289166	42.82265531	52.37751007	46.2645755
KK8	1913.40		37.6994818	42.15661417	40.09032157	38.94593243	42.47606016	37.02475218
KK9	1903.55	40.03517228	39.84060056	91.36684674	78.48366965	74.36408005	80.11981498	46.93422169
KK10	1896.70	176.8953428	197.7331158	387.6602374	391.5892935	333.7158663	261.6348282	129.1530403
KK10b	1885.67	46.08493082	42.78593587	380.4681356	382.4200512	265.7072345	397.4218528	105.8082439
KK10d	1875.30		36.74978885	56.51316092	53.36397139	53.15150807	49.87995518	40.26315328
KK11	1869.30		38.15547492	68.97865151	64.44554806	62.65513012	60.52669869	42.84249135
KK11b	1857.30	93.38779999	66.37496182	985.6226703	884.0721104	867.1241691	910.6155154	253.4446641
KK11c	1852.80			60.22119747	57.05042709	56.60504681	62.53822659	245.8791517
KK12a	1826.30	52.43770514	68.37430569	297.8962345	283.6891676	275.4155607	187.7845724	119.2230352
KK14b	1803.80	42.73916251	51.89603632	134.3421709	124.8098661	129.8599801	132.8986323	68.05848759

Table A.14 Uncorrected concentrations (ng/g sediment) of the petrogenic and biomarker PAHs identified and quantified as part of this thesis.

PAH		2-methyl naphthalene	1,7-dimethyl naphthalene	2-methyl phenanthrene	9-methyl phenanthrene	2,5-dimethyl phenanthrene	1-methyl pyrene	retene
Retention time (minutes)		12.16	14.93	23.8	24.1	26.04	28.58	28.91
Molecular weight		142	156	192	192	206	216	234
Sample	Depth (m)	Uncorrected concentration (ng/ g sediment)						
NC1	165.20		38.07725861	38.64365381	38.06315616	38.37711758		
NC2	164.40		33.51590483	38.02065393	36.62056656	34.95391364		
NC4	163.00		39.95362775	43.22727897	41.80436279	41.32012351		38.910557
NC8	158.05	44.29594374	76.14837083	196.7680044	225.0429337	185.1769844	157.9560138	152.0687425
NC9	155.50	41.46560926	45.79386486	140.0716049	185.5369641	118.8361763	217.8772399	237.3169568
NC10	152.10		41.31458151	46.74253193	45.04290601	44.15203225	41.32867659	42.72410307
NC12	147.50	48.8253272	83.42957777	199.6558727	221.6161065	174.2672856	207.775364	202.7035941
NC13	145.00		42.35862843	55.54713732	56.61856466	50.53942583	49.88718367	49.03035961
NC14	143.00		40.79888329	89.35141502	96.68929006	67.67218614	65.93715576	66.34331185
NC15	141.10	38.09445498	38.21629062	66.60120713	69.22366367	50.8306869	58.19828907	52.62236509

Table A.14 (cont.) Uncorrected concentrations (ng/g sediment) of the petrogenic and biomarker PAHs identified and quantified as part of this thesis.

PAH		fluorene	phenanthrene	fluoranthene	pyrene	benz-anthracene	benzo(k)fluoranthene	indeno[1,2,3-cd]pyrene	coronene
Retention time (minutes)		18.11	21.65	26.28	27.01	31.96	36.64	40.9	44.8
Molecular weight		166	178	202	202	228	252	276	300
Sample	Depth (m)	Corrected concentration (ng/ g sediment)							
KK34	1297.20	103.3123644	600.1801281	114.7419655	143.5506469	170.3695198	315.868072	248.3998471	83.4065095
KK35	1289.70	103.1401367	489.7077983	82.83991733	114.8891673	129.4286656	196.5205777	137.8883558	58.54792647
KK38	1265.90	147.4838627	984.6527804	126.8740197	212.6851013	518.267703	158.1786741	95.30429264	49.69617074
KK40	1247.40	45.6210007	171.8422526	45.20465198	53.1102696	48.07755531	49.88528376	50.32075167	37.17171614
KK42	1238.07	49.66963313	99.39739339	54.83849841	56.920619	56.10642055	52.61539236	50.20518438	48.88918094
KK42c	1215.75		55.89465508	51.26848035	48.33151195	47.03787888	45.8510826	45.14837757	45.14630534
KK45e	1188.60		55.03530869	52.60023887	50.20495673	48.91952813	49.84149665	47.00333099	
KK46b	1178.00	72.0631352	345.4985387	98.21376699	120.298041	102.2770053	113.3517167	114.6045195	49.42793546
KK47	1169.10		429.8875763	151.0878524	160.9993607	144.2813562	123.2771929	103.1526047	
KK5	1925.56		127.7390889	68.43323386	76.94978959	111.8658869	163.5324367	79.6505737	49.52159845
KK8	1913.40		59.65718624	52.50824061	55.18114776	53.45733289	55.3959102	50.73590545	46.3457984
KK9	1903.55	49.32292485	151.781898	60.90910518	63.05958504	83.50158938	88.26023707	56.16332597	43.45179112
KK10	1896.70	140.5399658	863.2004703	116.0968025	173.5285449	160.7650253	173.7325511	101.6112407	50.04828703
KK10b	1885.67	67.74184192	754.1242372	147.3013045	172.4096956	295.8938182	261.6344021	203.493208	71.34887718
KK10d	1875.30	45.4213343	79.24966905	49.03635285	51.87249225	52.25349976	50.92844948	47.38495084	
KK11	1869.30	46.85063437	90.69134663	55.00625248	57.7308888	84.21839436	113.1646138	75.52918252	
KK11b	1857.30	87.82811005	2078.796538	371.6276463	350.3647978	500.8685062	356.7309603	136.7921864	48.85659056
KK11c	1852.80	47.43169944	88.31090066	54.47260727	57.20553528	62.22350333	62.09736353	54.50255004	47.47160936
KK12a	1826.30	90.683197	616.3677609	100.1888944	127.3799543	134.1876454	113.4020093	65.5815436	46.97903559
KK14b	1803.80	66.1853835	272.2096533	74.21660531	80.20077486	109.5062973	121.8499137	75.1219617	49.58794243

Table A.15 Corrected concentrations (ng/g sediment) of the pyrolytic PAHs identified and quantified as part of this thesis.

PAH		fluorene	phenanthrene	fluoranthene	pyrene	benz-anthracene	benzo(k)fluoranthene	indeno[1,2,3-cd]pyrene	coronene
Retention time (minutes)		18.11	21.65	26.28	27.01	31.96	36.64	40.9	44.8
Molecular weight		166	178	202	202	228	252	276	300
Sample	**Depth (m)**	**Corrected concentration (ng/ g sediment)**							
NC1	165.20		47.81203672	48.44807731	46.70621289	46.20374234		46.44529714	46.37316985
NC2	164.40		64.18660239	45.746284	42.31911658	41.35202771	40.97130671	40.72835678	40.94722044
NC4	163.00		59.97925633	52.15637683	49.95846082	48.22337121	48.47873645	50.34878301	48.36734557
NC8	158.05	57.77291446	439.3217171	140.0843381	214.8617731	126.0744719	146.6718356	86.18342908	50.41158052
NC9	155.50	53.134222	240.8810938	151.0174616	395.6837935	217.5108526	796.7473012	712.7906643	
NC10	152.10		68.53026383	54.87216553	54.2904487	52.27875093	93.33398929	103.6268266	50.30448372
NC12	147.50	72.28083184	495.2159411	160.4166754	272.5621472	188.8421245	836.0073456	651.7961235	78.29581614
NC13	145.00		99.93112983	69.65404014	71.39989278	57.82520802	81.74697472	80.98628625	49.9630058
NC14	143.00		214.7787432	80.58188422	90.22328156	67.36587116	115.703206	140.1508875	49.20821976
NC15	141.10		157.5065541	75.11425704	85.71716229	65.39180946	102.7373135	141.3131585	47.35801644

Table A.15 (cont.) Corrected concentrations (ng/g sediment) of the pyrolytic PAHs identified and quantified as part of this thesis.

PAH		2-methyl naphthalene	1,7-dimethyl naphthalene	2-methyl phenanthrene	9-methyl phenanthrene	2,5-dimethyl phenanthrene	1-methyl pyrene	retene
Retention time (min)		12.16	14.93	23.8	24.1	26.04	28.58	28.91
Molecular weight		142	156	192	192	206	216	234
Sample	Depth (m)	Corrected concentration (ng/ g sediment)						
KK34	1297.20	259.5352754	303.5768265	278.9821901	310.5743503	241.4050915	266.2211374	206.4630902
KK35	1289.70	290.3439835	317.2418873	241.1449658	234.10263	208.367211	196.6827135	150.0890952
KK38	1265.90	1026.464693	918.3551258	500.1991221	525.7650874	518.1571893	389.55433	470.8760207
KK40	1247.40	95.82256793	117.6861536	96.50631473	93.25501137	89.1572117	62.27303135	53.63082163
KK42	1238.07		48.98974529	80.26072716	73.32314018	77.55399468	66.14366489	55.27924828
KK42c	1215.75	44.90783159	47.2243868	49.95056489	50.5102916	54.00758991	49.38367989	49.4193406
KK45e	1188.60	46.17941966	47.23028975	49.99359824	50.20772425	49.97330383	45.94427636	48.83043078
KK46b	1178.00	125.8399535	158.0740784	184.1153216	252.8466912	228.1446766	177.1420249	307.1527838
KK47	1169.10	147.972172	151.5746679	302.9178762	385.0606049	382.8068594	316.8320992	426.8482181
KK5	1925.56	48.90308662	50.44602009	72.55822045	60.36611458	53.52831914	65.47188759	57.83071937
KK8	1913.40		47.12435224	52.69576771	50.11290196	48.68241554	53.0950752	46.28094022
KK9	1903.55	50.04396534	49.8007507	114.2085584	98.10458707	92.95510006	100.1497687	58.66777711
KK10	1896.70	221.1191785	247.1663948	484.5752967	489.4866169	417.1448328	327.0435352	161.4413004
KK10b	1885.67	57.60616353	53.48241983	475.5851695	478.025064	332.1340431	496.777316	132.2603049
KK10d	1875.30		45.93723606	70.64145115	66.70496424	66.43938508	62.34994398	50.3289416
KK11	1869.30		47.69434365	86.22331438	80.55693508	78.31891265	75.65837336	53.55311419
KK11b	1857.30	116.73475	82.96870227	1232.028338	1105.090138	1083.905211	1138.269394	316.8058301
KK11c	1852.80			75.27649684	71.31303386	70.75630851	78.17278324	307.3489397
KK12a	1826.30	65.54713143	85.46788212	372.3702931	354.6114595	344.2694509	234.7307154	149.028794
KK14b	1803.80	53.42395313	64.8700454	167.9277137	156.0123327	162.3249751	166.1232904	85.07310949

Table A.16 Corrected concentrations (ng/g sediment) of the petrogenic and biomarker PAHs identified and quantified as part of this thesis.

PAH		2-methyl naphthalene	1,7-dimethyl naphthalene	2-methyl phenanthrene	9-methyl phenanthrene	2,5-dimethyl phenanthrene	1-methyl pyrene	retene
Retention time (minutes)		12.16	14.93	23.8	24.1	26.04	28.58	28.91
Molecular weight		142	156	192	192	206	216	234
Sample	Depth (m)	Corrected concentration (ng/ g sediment)						
NC1	165.20		47.59657326	48.30456726	47.5789452	47.97139697		
NC2	164.40		41.89488104	47.52581741	45.7757082	43.69239205		
NC4	163.00		49.94203469	54.03409872	52.25545349	51.65015438		48.63819625
NC8	158.05	55.36992967	95.18546354	245.9600056	281.3036671	231.4712304	197.4450172	190.0859281
NC9	155.50	51.83201157	57.24233108	175.0895061	231.9212052	148.5452203	272.3465498	296.646196
NC10	152.10		51.64322689	58.42816491	56.30363251	55.19004032	51.66084574	53.40512884
NC12	147.50	61.031659	104.2869722	249.5698408	277.0201331	217.8341069	259.719205	253.3794926
NC13	145.00		52.94828554	69.43392165	70.77320582	63.17428228	62.35897959	61.28794952
NC14	143.00		50.99860411	111.6892688	120.8616126	84.59023267	82.4214447	82.92913981
NC15	141.10	47.61806873	47.77036327	83.25150892	86.52957959	63.53835863	72.74786134	65.77795637

Table A.16 (cont.) Corrected concentrations (ng/g sediment) of the petrogenic and biomarker PAHs identified and quantified as part of this thesis.

APPENDIX E NIEKŁAŃ PIG-1 CARBON-ISOTOPE DATA

Appendix E contains all of the new carbon- and nitrogen-isotope data from the Niekłań PIG-1 bulk organic matter, macrofossil plant material, and bulk woody phytoclast samples. A discussion of this data is provided in **Chapter 7** (p. 176).

Table A.17 shows the carbon-isotope values ($\delta^{13}C$) and percentage of all carbon present in each sample for the bulk organic matter samples.

Table A.18 shows the percentage of nitrogen, percentage of carbon, $\delta^{13}C$ values, and C_{org}/N_{total} ratios for the macrofossil plant material samples.

Table A.19 shows the $\delta^{13}C$ values, percentage of carbon, percentage of nitrogen, and C_{org}/N_{total} ratios of the bulk woody phytoclast samples. Blank cells indicate no available data.

Sample	Depth (m)	δ^{13}C (‰ VPDB)	% carbon	Notes
NC1	165.20	-	0.1	Too small for analysis
NC2	164.40	-	0.1	Too small for analysis
NC4	163.00	-13.6	0.3	
NC5	162.25	-26.3	0.5	
NC6	160.00	-26.9	13.7	
NC7	159.00	-17.3	1.9	
NC8	158.05	-18.0	1.4	
NC9	155.50	-20.3	2.8	
NC10	152.10	-11.6	2.8	
NC11	151.00	-15.5	1.2	
NC12	147.50	-27.5	1.5	
NC13	145.00	-26.8	0.5	
NC14	143.00	-26.1	0.3	
NC15	141.10	-26.5	0.4	
NC16	136.00	-23.2	0.5	
NC17	134.50	-26.5	0.4	
NC20	131.00	-24.9	0.2	
NC21	130.25	-24.2	1.0	
NC22	128.50	-25.8	0.4	
NC24	123.85	-27.8	0.8	
NC25	122.20	-6.2	3.6	
NC26	121.40	-20.6	0.5	
NC27	119.10	-24.1	0.2	
NC28	118.50	-24.0	1.6	
NC29	116.00	-24.6	0.3	
NC31	114.00	-26.1	0.6	
NC32	113.00	-25.3	0.2	
NC33	112.40	-23.1	0.3	
NC34	110.00	-7.8	2.1	
NC35	109.30	-8.5	2.8	
NC36	108.00	-	0.3	Too small for analysis
NC38	101.20	-23.5	0.5	
NC39	100.20	-	0.2	Too small for analysis
NC40	99.40	-25.7	0.3	
NC41	98.00	-	0.2	Too small for analysis
NC42	97.00	-18.2	0.3	
NC43	96.10	-17.1	0.3	
NC45	94.00	-18.3	0.4	
NC46	92.30	-	0.1	Too small for analysis
NC47	91.00	-	0.3	Too small for analysis
NC48	89.60	-25.2	0.7	
NC49	88.00	-25.6	0.2	
NC50	87.10	-25.4	0.2	

Table A.17 Sample number, depth in core (m), δ^{13}C, and % carbon of each sample for bulk organic matter δ^{13}C analysis.

Sample	Depth (m)	δ¹³C (‰ VPDB)	% carbon	Notes
NC50	87.10	-25.4	0.2	
NC51	86.10	-25.1	0.5	
NC52	85.00	-11.9	3.0	
NC53	84.20	-25.0	0.2	
NC54	83.00	-9.8	1.6	
NC55	82.20	-15.5	1.2	
NC57	81.00	-16.6	0.6	
NC59	79.00	-16.7	0.4	
NC61	78.00	-25.7	8.4	
NC63	77.00	-25.2	7.6	
NC65	76.00	-24.9	9.0	
NC67	75.00	-24.8	6.6	
NC68	74.00	-24.7	0.4	
NC70	73.00	-22.7	0.3	
NC71	72.60	-25.3	1.7	
NC72	71.80	-24.7	3.1	
NC73	71.00	-25.9	0.4	
NC74	70.50	-24.5	0.4	
NC76	69.00	-26.1	1.1	
NC78	68.00	-25.5	0.6	
NC80	67.00	-24.9	0.6	
NC82	66.00	-25.0	0.6	
NC84	65.00	-22.0	0.5	
NC86	64.00	-20.5	0.4	
NC88	63.00	-24.1	1.6	
NC90	61.80	-23.6	1.5	
NC91	60.90	-24.8	0.2	
NC92	60.00	-25.5	0.4	
NC94	58.50	-19.0	0.9	
NC96	57.60	-26.6	0.4	
NC98	56.50	-23.4	0.4	
NC100	55.50	-	0.2	Need more sample to repeat
NC102	54.50	-25.6	0.3	
NC104	53.50	-25.4	0.4	
NC106	52.00	-	0.1	Need more sample to repeat
NC108	51.00	-25.5	0.6	
NC110	50.00	-26.3	1.7	
NC111	49.10	-26.6	5.6	
NC112	48.00	-26.6	4.8	
NC113	46.50	-26.7	3.0	
NC114	45.00	-26.7	3.0	
NC116	43.50	-27.2	39.2	

Table A.17 (cont.) Sample number, depth in core (m), δ¹³C, and % carbon of each sample for bulk organic matter δ¹³C analysis.

Sample	Depth (m)	δ¹³C (‰ VPDB)	% carbon	Notes
NC118	42.50	-26.0	0.7	
NC120	41.30	-22.8	0.3	
NC122	40.00	-25.7	0.4	
NC124	39.00	-26.0	0.8	
NC126	38.00	-25.9	0.4	
NC128	36.80	-25.0	1.6	
NC129	36.00	-25.3	0.4	
NC131	35.00	-25.8	1.3	
NC132	34.40	-25.1	0.6	
NC134	33.00	-26.0	0.8	
NC136	32.00	-25.2	0.8	
NC138	20.60	-25.1	1.1	
NC140	19.50	-25.2	1.2	
NC142	18.50	-25.2	1.1	
NC144	17.50	-25.2	0.7	
NC146	16.50	-25.1	0.9	
NC148	15.50	-24.7	0.6	

Table A.17 (cont.) Sample number, depth in core (m), δ^{13}C, and % carbon of each sample for bulk organic matter δ^{13}C analysis.

Sample number	Depth (m)	% N	% C	δ¹³C	C/N
NC1	161.70	0.256844	16.88996	-27.8029	65.75953
NC2	160.12	0.541779	44.08189	-25.8508	81.36501
NC3	160.75	0.26163	16.93672	-27.8739	64.73533
NC4	159.24	0.72823	33.31686	-26.3525	45.75044
NC5	158.08	0.161065	19.92292	-25.3467	123.6952
NC6	158.69	0.356646	18.85528	-25.8208	52.86841
NC7	157.42	0.104085	1.214535	-24.7622	11.66864
NC8	155.30	0.084484	1.1001	-28.0892	13.02133
NC9	153.10	0.184154	4.495846	-29.9157	24.41352
NC10	149.11	0.35861	14.59186	-27.6333	40.69011
NC11	149.38	0.442195	17.99945	-27.7564	40.70481
NC12	148.12	0.391937	17.53415	-27.0789	44.73723
NC13	147.08	0.371175	10.70638	-29.1229	28.84456
NC14	146.23	0.210236	4.007031	-28.2121	19.05967
NC15	144.57	0.261216	2.992025	-29.897	11.4542
NC16	143.83	0.232656	5.530069	-28.6548	23.76929
NC17	142.10	0.561917	20.46588	-26.8721	36.42154
NC18	139.51	1.406375	2.765051	-28.2288	1.966084
NC19	138.18	0.427311	20.46254	-28.0203	47.88676
NC20	137.07	0.478158	20.25553	-27.7067	42.36156
NC21	132.63	0.192309	5.024246	-28.2181	26.12592
NC22	130.25	0.282322	17.01735	-22.1269	60.27637
NC23	129.86	0.224932	15.93004	-27.7741	70.82168
NC24	126.43	1.042284	75.908	-27.1572	72.82849
NC24b	126.23	0.870346	69.82276	-27.0133	80.2241
NC25	116.35	0.902039	61.20357	-26.6184	67.85023
NC26	115.40	0.13692	11.42831	-26.6248	83.4671
NC27	107.60	0.999271	72.73606	-27.3255	72.78912
NC28	105.24	0.522812	41.97701	-26.4925	80.29079
NC29	104.09	0.838451	67.60569	-26.9779	80.63168
NC30	102.50	0.876621	67.51774	-27.6692	77.02041
NC31	95.50	1.018417	69.95467	-27.3174	68.68963
NC32	94.55	0.239169	8.368649	-27.4344	34.99055
NC33	80.35	0.195992	8.471753	-25.2324	43.22489
NC35	74.66	0.132118	2.332135	-25.5897	17.6519
NC36	69.84	0.555322	31.86655	-25.8446	57.38389
NC37	63.45	0.707358	44.76676	-26.7123	63.28732
NC38	62.70	0.906402	53.62253	-26.6641	59.15979
NC39	59.85	0.756782	51.9327	-26.911	68.62302
NC40	50.10	0.614209	52.51097	-26.2018	85.49361
NC41	49.09	0.791451	71.59369	-27.5183	90.45874
NC42	42.20	0.985728	74.365	-26.5356	75.44171
NC43	37.10	0.299934	18.53572	-26.7033	61.79938

Table A.18 Sample number, depth in core (m), percentage of nitrogen, percentage of carbon, δ¹³C value, and C_{org}/N_{total} ratio of the macrofossil plant material samples.

Sample Number	Depth (m)	δ¹³C	%C	%N	C/N
NK15	166.70	-26.9			
NK17	166.10	-27.1			
NK18	165.80	-27.4			
NK25	163.70	-27.6			
NK31	161.10	-26.5	36.8	0.6	62.0
NK32	160.70	-26.7	44.3	0.8	59.0
NK33	160.30	-26.6	69.0	1.4	50.8
NK34	160.00	-26.4	49.1	0.8	59.7
NK35	158.90	-26.4	37.2	0.8	46.7
NK36	158.60	-26.1	51.9	0.8	61.7
NK37	158.30	-26.3	48.5	1.0	48.6
NK37a	158.30	-26.3			
NK38	158.00	-26.2	49.2	0.9	52.5
NK39	157.70	-27.0	50.9	1.1	46.4
NK40	157.40	-27.3			
NK42	156.80	-25.5	67.4	1.5	44.4
NK43	155.40	-27.0	38.0	0.5	74.6
NK44	155.10	-26.8			
NK45	154.80	-27.3			
NK46	154.50	-26.8			
NK47	154.20	-26.6	58.9	1.0	61.6
NK48	153.90	-26.5	71.8		
NK49	153.60	-27.8	73.6	1.5	49.5
NK50	153.30	-27.3	61.4	1.5	41.0
NK51	153.00	-27.8	67.2	1.7	40.0
NK52	152.70	-27.9	69.7	1.7	40.4
NK53	152.40	-25.5	40.7	2.7	14.8
NK60	150.30	-28.0	54.8	1.5	36.7
NK61	150.00	-27.7	66.4		
NK62	149.70	-27.3	69.7	1.7	41.6
NK63	149.40	-26.4	67.9	2.6	26.1
NK64	149.10	-27.0	54.7		
NK65	148.80	-27.1	62.6		
NK66	148.50	-27.7	60.5	1.6	37.1
NK67	148.20	-26.8	63.0	1.7	36.9
NK68	147.90	-26.9	64.6	1.6	40.9
NK69	147.60	-27.8	67.9	1.6	42.3
NK71	147.00	-28.7	76.8	1.6	48.1
NK72	146.70	-28.3	76.5	1.7	44.6
NK74	146.10	-28.0			
NK79	144.60	-27.0	76.5	2.0	37.4

Table A.19 Sample number, depth in core (m), δ¹³C value, percentage of carbon, percentage of nitrogen, and C_{org}/N_{total} ratios of the bulk woody phytoclast samples. Blank cells indicate no available data.

Sample Number	Depth (m)	δ¹³C	%C	%N	C/N
NK80	144.20	-27.3	74.8	1.6	46.7
NK83	142.10	-26.2	75.2		
NK84	141.30	-26.8			
NK88	138.20	-26.7	68.7		
NK92	135.20	-27.1			
NK94	133.40	-27.4			
NK97	130.60	-27.0			
NK100	126.50	-26.4	69.5		
NK101	125.30	-25.9			
NK102	123.80	-27.6			
NK103	123.00	-26.8	78.9		
NK106	120.10	-26.2	77.8		
NK108	117.10	-26.9			
NK113	111.10	-27.2			
NK117	107.60	-27.1	66.6		
NK118	105.70	-27.4	74.7	1.2	61.0
NK119	104.10	-27.3			
NK127	93.60	-26.4	62.1		
NK130	90.80	-25.7			
NK133	86.80	-24.8	79.7		
NK144	74.60	-25.8	81.2	0.8	99.6

Table A.19 (cont.) Sample number, depth in core (m), δ¹³C value, percentage of carbon, percentage of nitrogen, and C_{org}/N_{total} ratios of the bulk woody phytoclast samples. Blank cells indicate no available data.